Physics of the Solid State, Vol. 42, No. 11, 2000, pp. 1973–1989. Translated from Fizika Tverdogo Tela, Vol. 42, No. 11, 2000, pp. 1921–1937.

REVIEW

Very Low-Energy Electron Diffraction as a Method of Band Structure Investigations: Applications in Photoelectron Spectroscopy

V. N. Strocov

Institute of High-Performance Computations and Data Bases, Ministry of Science of the Russian Federation, St. Petersburg, 194291 Russia

e-mail: F1XVS@fy.chalmers.se

Received November 11, 1999; in final form, April 4, 2000

Abstract—This review presents the theoretical and experimental foundations of very low-energy electron diffraction (VLEED) spectroscopy, which is the most direct method of studying the band structure $E(\mathbf{k})$ of unoccupied higher-lying electronic states. The experimental results presented here indicate that, contrary to the generally accepted point of view, these states may differ significantly from free-electron dispersion and may experience considerable many-electron effects. It is shown that the higher-lying states observed in the experiment can be used directly in photoelectron spectroscopy, which is the basic method for studying valence states. This makes it possible to solve the basic problem of resolving the band structure in the three-dimensional quasi-wave vector. © *2000 MAIK "Nauka/Interperiodica".*

1. INTRODUCTION

The electronic band structure $E(\mathbf{k})$, viz., the dependence of energy on the wave vector, is a fundamental characteristic of solids, which determines, for example, optical properties and transport phenomena. Not only the energies of electron states, but also their position in the $\mathbf{k}$ space, play an important role. For example, wide application of GaAs in modern optoelectronics [1] is due to the fact that it is a direct-band semiconductor; i.e., the top of its valence band and the bottom of the conduction band coincide in $\mathbf{k}$.

Photoemission (PE) spectroscopy with angular resolution is the basic experimental method of studying $E(\mathbf{k})$ of the valence band with resolution in $\mathbf{k}$ (see, for example, [2–5]). In this method, the sample is exposed to monochromatic light in the UV range. Figure 1 shows that light induces electronic transitions from occupied valence states to unoccupied higher-lying states (HSs) (above the vacuum level E_{vac}), followed by the emission of photoelectrons to vacuum. The measurable quantity is the photocurrent I^{ph} for a certain emission angle and the kinetic energy of the photoelectrons. The $E(\mathbf{k})$ dependence for the conduction band is studied by using the inverse PE [6], which is a time-reversed analog of PE (the sample is bombarded by electrons, and the intensity of radiation is measured). The subsequent analysis will be carried out for PE with an obvious generalization for inverse PE.

The physical foundations for determining $E(\mathbf{k})$ by using PE are illustrated in Fig. 1. The energy E^i of the initial state in the valence band is determined directly as the energy E^f of the final higher-lying state for the PE spectrum peak minus the energy $h\nu$ of the quantum:

$$E^i = E^f - h\nu.$$

The determination of the corresponding $\mathbf{k}^i$ of the initial state is based on the fact that photoinduced transitions in the crystal are direct, i.e., are made with the conservation of the three-dimensional $\mathbf{k}$ in the reduced Brillouin zone (BZ):

$$\mathbf{k}^i = \mathbf{k}^f.$$

When an electron is emitted to vacuum, the $\mathbf{k}_\parallel$ component of $\mathbf{k}$, which is parallel to the surface, is conserved due to the two-dimensional translational symmetry of the surface. This component is determined directly in the experiment as the parallel component $\mathbf{K}_\parallel$ of the wave vector in vacuum (accurate to the vector $\mathbf{g}$ of the surface reciprocal lattice):

$$\mathbf{k}_\parallel = \mathbf{K}_\parallel + \mathbf{g}.$$

However, the perpendicular component $k_\perp$ is distorted as the electron escapes to vacuum. In order to find this component, we must return to the dispersion $E(k_\perp)$ for HS in the bulk of the crystal, which is usually simulated by using the empirical free-electron (FE) approximation.

In PE experiments, the dependence $E(\mathbf{k})$ in the valence band can be determined by plotting the energy E^i of spectral peaks as a function of $\mathbf{k}$. In this case, the value of $\mathbf{k}$ is varied either in $\mathbf{k}_\parallel$ (by changing the emission angle) or in $k_\perp$ (by changing $h\nu$). Modern sources of radiation used are usually synchrotrons ensuring a

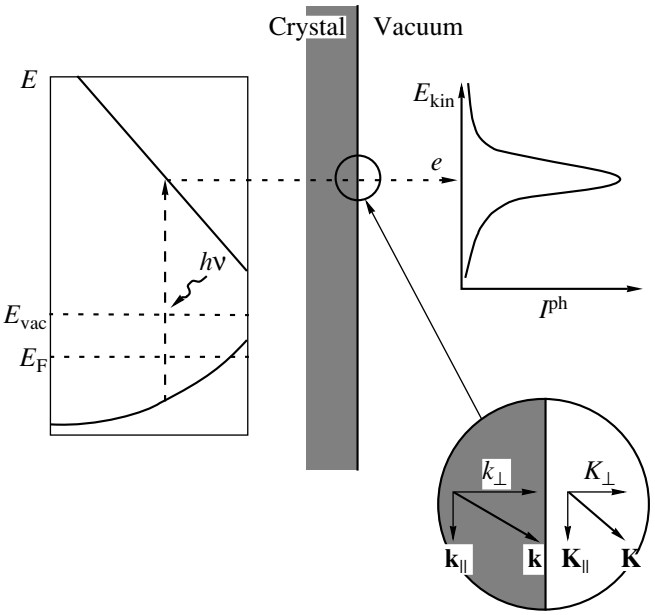

Fig. 1. Principles of PE spectroscopy: valence electrons undergo photoinduced transitions to HSs in the bulk of the crystal (left) and are emitted from these states into vacuum, forming the PE spectrum (right). The photoinduced transitions are made so that the three-dimensional wave vector **k** is conserved, but, when the electrons are emitted into vacuum, only the component parallel to the surface is conserved (inset).

wide range of $h\nu$, high intensity, and a high degree of polarization of radiation.

The main problem in PE spectroscopy is the control of $k_\perp$ (and hence the three-dimensional **k**). Its solution requires the knowledge of $E(k_\perp)$ for HS. The applicability of the FE approximation can be limited in this case by overly strong scattering from the crystal potential. Attempts to solve this problem in PE spectroscopy (e.g., by using the triangulation method) are impractical and confined to individual points in the **k** space. It has been proven recently that very low-energy electron diffraction (VLEED) is an optimal method for independent analysis of $E(\mathbf{k})$ for HS with a resolution in **k**. The application of VLEED together with PE spectroscopy is based on the fact that electron diffraction states are time-inverted final states of PE.

The VLEED spectroscopy involves the measurement of the coefficient of elastic electron reflection from the crystal surface in the primary electron energy range up to ~40 eV. This energy range is characterized by the following two features. (1) The inelastic electron absorption characterized by the absorption potential V_i is relatively weak. The VLEED spectra are formed by elastic scattering, and, moreover, since the mean free path is increased, they reflect $E(\mathbf{k})$ of HS in the bulk of the crystal. However, the sensitivity to the geometrical structure of the surface is reduced as compared to the conventional low-energy electron diffraction (LEED), which employs higher energies [7, 8]. (2) This energy range is suitable for PE spectroscopy since it corresponds to typical final-state energies employed in the regime of measuring $E(\mathbf{k})$ with resolution in **k**.

This review is devoted to the VLEED spectroscopy as a method of investigating $E(\mathbf{k})$ for higher-lying states and to its applications, together with PE spectroscopy, for studying $E(\mathbf{k})$ in the valence band with a resolution in three-dimensional **k**.

2. PRINCIPLES OF VLEED SPECTROSCOPY

*2.1. Relation between VLEED and E(**k**)*

Elastic reflection of electrons from the crystal surface can be described by matching (on the crystal surface) the wave function Φ_{vac} in vacuum and the wave function Φ_c excited in the crystal [7–11]. The former is the sum of plane waves

$$\Phi_{vac} = e^{i\mathbf{K}\cdot\mathbf{r}} + \sum_{\mathbf{g}} R_{\mathbf{g}} e^{-i\mathbf{K}_{\mathbf{g}}\cdot\mathbf{r}},$$

corresponding to the primary beam and all diffracted beams characterized by the surface reciprocal lattice vectors **g** (including the specularly reflected beam with $\mathbf{g} = 0$). The latter wave function is the sum of Bloch waves

$$\Phi_c = \sum_{\mathbf{k}} T_{\mathbf{k}} \phi_{\mathbf{k}}$$

with quasi-wave vectors **k**; their $\mathbf{k}_\parallel$ being determined by the conservation of the wave vector component $\mathbf{K}_\parallel$ of the primary beam, which is parallel to the surface ($\mathbf{k}_\parallel = \mathbf{K}_\parallel + \mathbf{g}$), while $k_\perp$ is determined by the band structure $E(k_\perp)$ along BZ directions specified by this condition and perpendicular to the surface. Consequently, elastic scattering is formed by the set of $\phi_{\mathbf{k}}$ corresponding to $E(k_\perp)$ along the BZ directions $\mathbf{k}_\parallel = \mathbf{K}_\parallel + \mathbf{g}$. At the critical points (CPs) of $E(k_\perp)$, such as the edge of the local band gap or the inflection point of the band dispersion curve, the composition of the $\phi_{\mathbf{k}}$ changes abruptly. The elastic reflection coefficient R integrated over all diffraction beams also changes sharply (henceforth, we will use the elastic transmission coefficient $T = 1 - R$ instead of R). This is manifested as extrema of the derivative dT/dE of its energy dependence, viz., the VLEED spectrum. Consequently, as shown in Figs. 2a and 2b, the extrema of the VLEED spectra reveal the energy position of CPs in $E(k_\perp)$ along the BZ directions $\mathbf{k}_\parallel = \mathbf{K}_\parallel + \mathbf{g}$ perpendicular to the surface. This relationship forms the basis of an experimental investigation of HSs using VLEED [12, 13].

This somewhat simplified pattern should be supplemented with a number of important amendments.

Contributions of individual Bloch waves. The effect of individual $\phi_{\mathbf{k}}$ constituting the overall wave function in the crystal on the formation of the VLEED

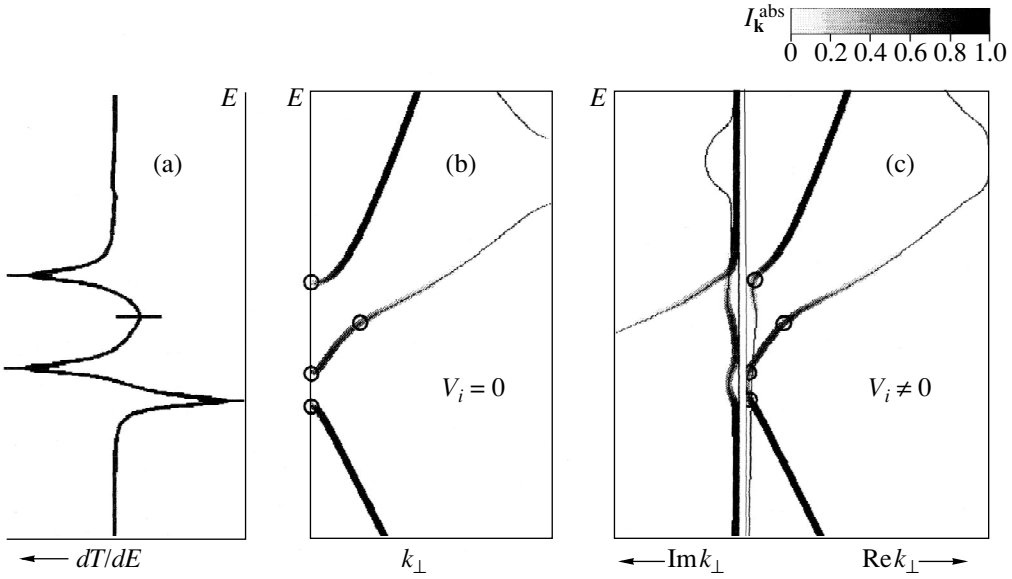

Fig. 2. Relationship between VLEED and band structure (model calculations): (a) the derivative dT/dE of the elastic transmission coefficient and (b, c) the corresponding $E(k_\perp)$ with and without the absorption V_i, respectively. The extrema of dT/dE reveal the critical points in the bands whose Bloch waves are effectively coupled with the primary plane wave and take up significant absorbed currents $I_{\mathbf{k}}^{abs}$ (shown by greyscale).

spectrum is determined primarily by (1) the effectiveness of their matching with the primary plane wave, i.e., the excitation amplitude $T_{\mathbf{k}}$, and (2) the effectiveness of their propagation to the bulk of the crystal, i.e., the group velocity $v_{g\perp}$ normal to the surface. These two factors are combined in partially absorbed currents [14, 15]

$$I_{\mathbf{k}}^{abs} = |T_{\mathbf{k}}|^2 v_{g\perp},$$

which comprise the total current I^{abs} in the crystal. Consequently, the main contribution to the VLEED spectrum will come from $\phi_{\mathbf{k}}$ associated with significant $I_{\mathbf{k}}^{abs}$. The bands in $E(k_\perp)$ corresponding to them are referred to as coupling bands. It can be seen from Figs. 2a and 2b that it is only the CPs of coupling bands that are manifested as dT/dE extrema, while the remaining CPs are not seen. (The same coupling bands also dominate in PE; see Subsection 5.1). The coupling bands can be identified qualitatively by using the Fourier expansion of $\phi_{\mathbf{k}}$ in the vectors of the three-dimensional reciprocal lattice; the Fourier component $\phi_{\mathbf{k}} = \sum_{\mathbf{G}} C_{\mathbf{G}} e^{i(\mathbf{k}+\mathbf{G})\cdot\mathbf{r}}$ similar to the primary plane wave must be large [11–13] (see Subsection 4.2.2 for more details).

Effect of inelastic scattering. The inelastic scattering characterized by absorption V_i has not been taken into account thus far. In fact, it efficiently "washes out" electrons from the elastic scattering channel. This leads to the exponential attenuation of all $\phi_{\mathbf{k}}$ into the bulk of the crystal (but attenuation along the surface is absent in view of the translational invariance of the VLEED process in this direction). Such a behavior of $\phi_{\mathbf{k}}$ can be described by a complex-valued $k_\perp$ and a real-valued $\mathbf{k}_\parallel$. As compared to $E(k_\perp)$ with $V_i = 0$ (see Fig. 2b), the band dispersions $E(\mathrm{Re}k_\perp)$ (Fig. 2c) are smoothed and close, without local band gaps, coming closer to being FE dispersion. On account of all these factors, we must generalize the concepts of CPs and partial currents [15]. We now define critical points as points of extremal curvature of band dispersion, which can be conveniently identified as extrema of $d^2\mathrm{Re}k_\perp/dE^2$. In this case, the currents $I_{\mathbf{k}}^{abs}$ can no longer be treated as currents in the conventional sense (associated with a propagating wave) since all $\phi_{\mathbf{k}}$ attenuate. However, currents are generated due to electron absorption from coherent $\phi_{\mathbf{k}}$ with subsequent cascade transitions to the Fermi level, where electrons can carry current to the bulk of the crystal through the conventional mechanism since $V_i = 0$. In this case, the currents $I_{\mathbf{k}}^{abs}$ become proportional to electron densities integrated over the entire crystal volume:

$$I_{\mathbf{k}}^{abs} \propto V_i \int (T_{\mathbf{k}}\phi_{\mathbf{k}})^* (T_{\mathbf{k}}\phi_{\mathbf{k}}) dr_\perp$$

(the total current I^{abs} also includes the interference terms $V_i \int (T_{\mathbf{k}'}\phi_{\mathbf{k}'})^* (T_{\mathbf{k}}\phi_{\mathbf{k}}) dr_\perp$ vanishing for $V_i \longrightarrow 0$). These two generalizations allow us to extend the above relationship between VLEED and $E(\mathbf{k})$ to the real situation taking inelastic scattering into consideration. It should be noted that, under the influence of V_i, the CPs are slightly shifted in energy and $\mathbf{k}$ relative to their posi-

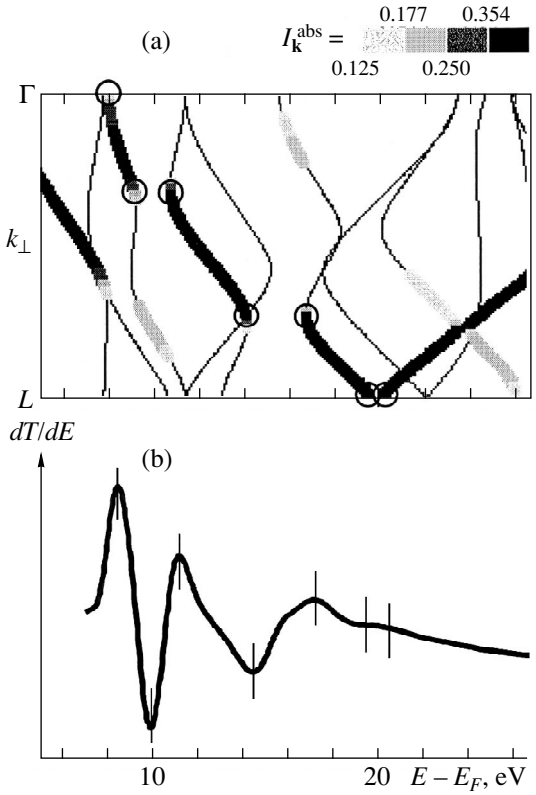

Fig. 3. Identification of the VLEED spectrum with specific CPs using model calculations, the H–Si (111) surface (1 × 1): (a) model $E(\mathbf{k})$ ($V_i = 0$) along ΓL, $I_{\mathbf{k}}^{abs}$ are shown by grey-scale, and (b) the corresponding normal-incidence experimental VLEED spectrum. The obvious correspondence of the CPs of coupling bands to *dT*/*dE* extrema makes it possible to determine the experimental position of these CPs.

tion for $V_i = 0$; however, such displacements are small for moderate values of V_i. Consequently, the structure of the VLEED spectrum can be related to CPs in $E(k_\perp)$ for $V_i = 0$. This simplified approach is known as the $V_i = 0$ approximation, which is usually highly applicable in the energy range of VLEED.

Influence of the surface. The surface potential barrier mainly affects the form of the VLEED spectrum, while the change in the energy corresponding to its dominating features associated with the bulk $E(\mathbf{k})$ is relatively small [15, 16]. The spectra may acquire a weaker structure associated with surface resonances [17]. This structure can be easily distinguished due to its small energy broadening (the electron density and, accordingly, V_i decrease near the surface) and its position immediately under diffraction thresholds.

*2.2. Methods of Determining E(**k**)*

The VLEED data analysis is based on determination of CPs in $E(k_\perp)$. The energy corresponding to the CPs can be determined directly as the energy of the *dT*/*dE* extrema. However, it is difficult to identify these extrema with specific CPs, since the $E(\mathbf{k})$ dependence in the HS range is normally characterized by a large number of bands and, hence, by a large number of CPs. This difficulty can be overcome by identifying a few (usually, one or two) bands in this multitude which are coupling bands and actually form the VLEED spectrum [12, 13]. In actual practice, such an analysis involves model calculations of $E(\mathbf{k})$ and $I_{\mathbf{k}}^{abs}$ for individual bands and often makes use of simplified methods (see Subsection 4.2). The application of such calculations for tracing the VLEED spectrum to individual CPs is shown in Fig. 3 for the 1 × 1 surface of Si(111) (unreconstructed surface prepared by saturation of dangling bonds of Si surface atoms by H atoms, leading to an almost undistorted bulk $E(\mathbf{k})$) [18]. The VLEED spectrum for the normal incidence of the primary beam corresponds to $E(k_\perp)$ along the Γ*L* direction of the BZ. It can be seen from the figure that all the extrema of the *dT*/*dE* spectrum correspond to the CPs of the coupling bands. For such a large number of bands, the tracing of the experimental spectrum to specific CPs is hardly possible without identifying the coupling bands.

It must be remarked that, like any other spectroscopy, the VLEED spectroscopy has its own intrinsic accuracy: the *dT*/*dE* extrema may be displaced insignificantly (usually by 0.1–0.3 eV) as a result of monotonic variations in $T(E)$, the influence of the surface barrier, and, above all, the overlapping of the effects of adjacent CPs. The magnitude of this displacement is quite small in comparison with the bandwidth and is smaller than the analogous displacements in the PE spectroscopy. The compensation of such displacements requires a correction of the experimental energies of the extrema by an amount equal to the displacements obtained in model calculations [12, 18].

The continuous dispersion dependences in $E(\mathbf{k})$ can be obtained from the experimental CPs by using the following methods.

2.2.1. Determination of $E(\mathbf{k})$ as $E(k_\perp)$ (band fitting method). This method [15] is used for determining $E(\mathbf{k})$ as a function of $k_\perp$ for a fixed $\mathbf{k}_\parallel$. It is based on the model calculation of $E(k_\perp)$ (e.g., by the empirical pseudopotential method) and the corresponding VLEED spectrum. Through optimization of the crystal potential parameters, the extremal energies of the model *dT*/*dE* are fitted to the experimental values by minimizing the standard deviation of energies of N extrema, $\frac{1}{N}\sum_N (E_{\text{calc}} - E_{\text{exp}})^2$. The obtained model dependence $E(k_\perp)$ optimally conforms to the experimental data: its CPs are in their experimental positions and connected by optimally smooth dispersion branches (any peculiarity of dispersion would be manifested in the spectrum). It should be noted that such a procedure does not ensure the exact position of the

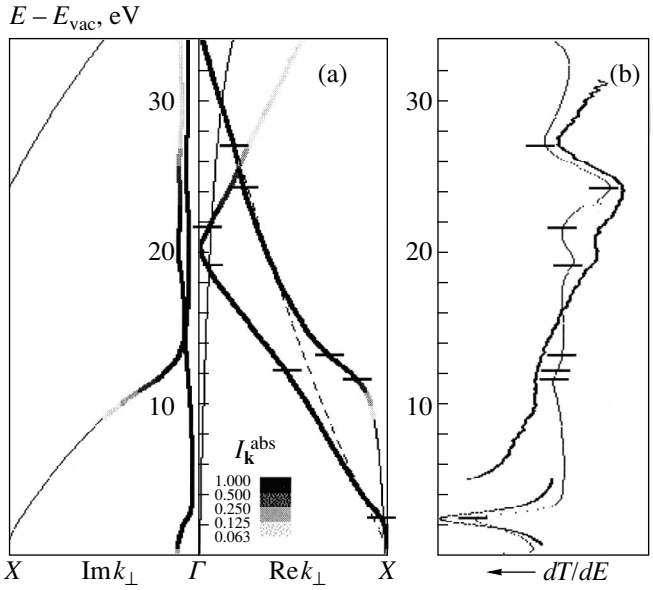

Fig. 4. Determination of $E(\mathbf{k})$ as $E(k_\perp)$ (band fitting method) from the VLEED spectrum for normal incidence on the Cu (100) surface. (a) $E(\mathbf{k})$ obtained along the ΓX direction (for V_i). The bands Δ_1 of the allowed symmetry are shown. (b) Experimental spectrum (bold curves) and the theoretical spectrum with the energies of extrema fitted to the experiment. The correspondence of CPs to the dT/dE extrema is indicated. The doublet of coupling bands radically distinguishes the experimental $E(\mathbf{k})$ from the FE dispersion (dashed curve).

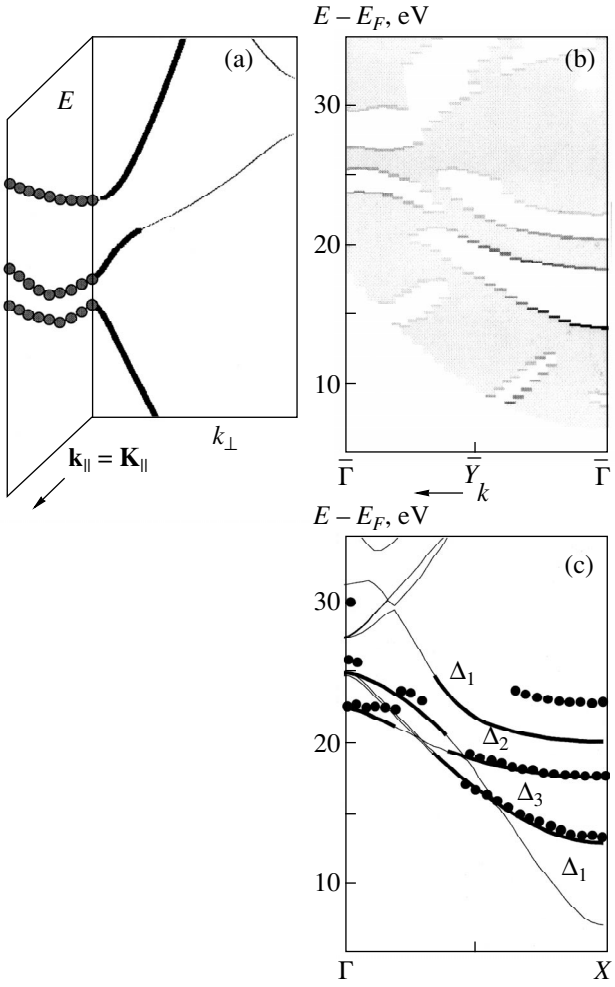

Fig. 5. Determination of $E(\mathbf{k})$ as $E(\mathbf{k}_\parallel)$ from VLEED angular dependences (direct band mapping method). (a) The idea of the method and (b) its application for the Cu (110) surface; experimental $\mathbf{K}_\parallel$ dispersion of the dT/dE. Dots correspond to dT/dE extrema (projections of the CPs of coupling bands of $E(k_\perp)$ along the directions $\mathbf{k}_\parallel = \mathbf{K}_\parallel + \mathbf{g}$, and the shaded segments are the dT/dE maximum–minimum intervals (internal parts of these bands). Extrema are shown by the greyscale representing their amplitude and sharpness as $\left|\frac{d^2}{dE^2}(dT/dE)\right|$. (c) Experimental $E(\mathbf{k})$ along the ΓX direction (dots). This was obtained from (b) by identification of the CPs lying on this symmetry direction. The theoretical $E(\mathbf{k})$ calculated in the DFT framework is also shown. The shifts of experimental points reflect many-electron effects of the excited VLEED state, which depend on the spatial localization of $\phi_{\mathbf{k}}$ (see Subsection 3.2).

bands with $I_{\mathbf{k}}^{abs} \sim 0$ which are not manifested in the VLEED spectrum. However, this is not important in subsequent applications of PE spectroscopy, as such bands are not manifested therein either (see Subsection 5.1).

The band fitting method can be illustrated as applied to determining $E(\mathbf{k})$ for copper along the ΓX direction from the VLEED spectrum for the normal incidence on the (001) surface [15]. Model calculations were made using actual values for V_i [19] with the help of the empirical pseudopotential method with subsequent determining of dT/dE by the matching method (see Subsection 4.2.1). Fitting was carried out using global optimization with the variation of principal Fourier components of the pseudopotential. The obtained experimental $E(\mathbf{k})$ is presented in Fig. 4. It will be shown below that it differs radically from the FE dispersion.

2.2.2. Determination of $E(\mathbf{k})$ as $E(\mathbf{k}_\parallel)$ (direct band mapping method). This method [13, 20, 21] is used for constructing $E(\mathbf{k})$ as a function of $\mathbf{k}_\parallel$ for a fixed $k_\perp$. In contrast to the previous method based on the modeling of $E(\mathbf{k})$, this method is direct. The idea of the method is illustrated in Fig. 5a. The VLEED spectra are measured upon variation of the angle of incidence of the primary beam. Then, the energies corresponding to CPs lying along a BZ symmetry direction parallel to the surface are plotted as functions of $\mathbf{k}_\parallel$. Such a construction directly maps $E(\mathbf{k})$ along this direction. In this case, complete localization in the $\mathbf{k}$ space is attained: $\mathbf{k}_\parallel$ is fixed by the $\mathbf{K}_\parallel$ component of the primary beam, whereas $k_\perp$ is specified by the position on the symmetry direction (in fact, the influence of V_i leads to a certain

displacement of CPs (see Fig. 2c), but this effect is insignificant).

The direct band mapping method can be illustrated as applied to the determination of $E(\mathbf{k})$ for copper along the ΓX direction [21]. This dependence was constructed from the data obtained on the (110) surface, and the angle of incidence was varied in the $\overline{\Gamma Y}$ azimuth on the surface BZ.

The $\mathbf{K}_\parallel$ dispersion of the VLEED spectra presented in Fig. 5b is the prototype of $E(\mathbf{k})$. Here, the dT/dE extrema are shown by dots and the intervals between the maxima and the next minima on the energy scale are shaded. It should be noted that such a representation has a direct physical meaning. Indeed, the dots are the projections of CPs of coupling bands lying along the BZ directions defined by the condition $\mathbf{k}_\parallel = \mathbf{K}_\parallel + \mathbf{g}$, while the shading corresponds to the interior of these bands. In this case, the $\mathbf{K}_\parallel$ dispersion of the VLEED spectra actually maps (with intrinsic accuracy) the projection of $E(\mathbf{k})$ of the coupling bands onto the surface.

The $E(\mathbf{k})$ mapping with resolution in three-dimensional $\mathbf{k}$ is now reduced to a separation from the projection of CPs lying on a symmetry direction parallel to the surface (ΓX in our case). Such CPs were identified by using simple model calculations of $E(\mathbf{k})$ and $I_\mathbf{k}^{\text{abs}}$ (see Subsection 4.2), which allowed us to analyze the entire body of experimental data rapidly and, in addition, to take into account the insignificant displacement of the CPs due to the effect of V_i. The experimental dependence $E(\mathbf{k})$ obtained in this way is presented in Fig. 5c. It is shifted relative to the theoretical curve calculated using the formalism of the density functional theory, which reflects many-electron effects in the excited state (see Subsection 3.2 for details).

The experimental dependence $E(\mathbf{k})$ illustrates two interesting aspects of the VLEED spectroscopy. First, the bands manifested in this $E(\mathbf{k})$ differ from those obtained along the same direction ΓX from the spectra for the normal incidence on the (100) surface (see Fig. 4). This is due to the different experimental geometries and, hence, to the different coupling properties of the bands. Second, the obtained $E(\mathbf{k})$ preserves the band gaps (at points Γ and X), although one should expect that they would vanish due to the action of V_i. This is a consequence of the fact that the given $E(\mathbf{k})$ dependence was measured as a function of $\mathbf{k}_\parallel$, which remains real-valued, in contrast to $k_\perp$, in view of the translational invariance of the VLEED process in a direction parallel to the surface.

2.3. Determination of Absorption Potential V_i

In addition to the determination of $E(\mathbf{k})$, VLEED spectroscopy provides information on V_i. This is important for subsequent applications in PE since V_i in fact determines the $k_\perp$ resolution of PE experiments (see Subsection 5.2). The effect of V_i is manifested in the VLEED spectra as a broadening of spectral structures and a suppression of their amplitudes. The values of V_i can be determined directly from this broadening, but their simulation on the basis of calculations with the variation of V_i [18, 22] makes it possible to compensate the effect of intraband changes in $T(E)$ and gives a higher accuracy. A typical energy dependence of V_i is a smoothly increasing function corresponding to electron–electron scattering combined with a pronounced threshold at the excitation energy $\hbar\omega_p$ of a bulk plasmon (if the latter is well defined as a quasiparticle).

2.4. Comparison with Other Methods

The traditional methods used for studying HSs are x-ray absorption spectroscopy (XAS) and bremsstrahlung isochromat spectroscopy (BIS) [6, 23]. However, these methods give only the characteristic integrated over the $\mathbf{k}$ space (like the density of states) and draw on the matrix element of photoinduced transitions, since they inherently involve two electron states. Inverse PE, which is a version of BIS in the UV range, ensures, in principle, a resolution in $\mathbf{k}_\parallel$, but determination of $k_\perp$ again requires the knowledge of $E(k_\perp)$ for one of the two states. Another traditional method is secondary electron emission spectroscopy. In this case, however, the information on $E(\mathbf{k})$ is strongly distorted due to the combined effect of the one-dimensional density of states (which increases at band edges), the transmission coefficient of the surface for secondary electrons emitted to vacuum (which, on the contrary, decreases at band edges), and the complex dynamics of many-electron relaxation.

The advantages of VLEED spectroscopy over traditional methods are obvious (resolution in the three-dimensional wave vector $\mathbf{k}$ and independent access to the one electron state). A practical advantage is its exceptionally simple experimental technique (see Subsection 4.1). However, the most important feature is its direct relationship with the PE spectroscopy, which is the main tool for studying the valence band.

3. PROPERTIES OF THE HIGHER LYING STATES

The application of VLEED spectroscopy to a wide class of materials has made it possible to study in detail the peculiarities of their HSs, such as deviation from the FE dispersion and many-electron effects in the excited state.

3.1. Deviations from Free-Electron States

Under the action of V_i, the dispersion of HSs is smoothed and comes closer to being FE dispersion. However, contrary to the generally accepted point of view, the difference can remain significant in the case of strong scattering from the crystal potential. Usually,

by FE dispersion we mean an optimal approximation of the actual $E(\mathbf{k})$ using the relation

$$E_{FE}(\mathbf{k}) = \frac{\hbar^2}{2m^*}(\mathbf{k} + \mathbf{G})^2 + V_{000},$$

where the effective mass m^* and the inner potential V_{000} are empirical parameters, which to a certain extent take into account the influence of the crystal potential and many-electron effects. This dispersion has only one coupling band, the $\mathbf{k} + \mathbf{G}$ of which corresponds to the primary plane wave.

Metals. The deviations from the FE dispersion for metals are usually insignificant, because the crystal potential is only slightly modulated in view of a strong screening of ionic potential by valence electrons. However, deviations can be significant in some regions of the $\mathbf{k}$ space. For example, the experimental $E(\mathbf{k})$ dependence for copper in the ΓX direction (see Fig. 4) is characterized by a multiband composition: between 15 and 25 eV, it contains two coupling bands with almost identical values of $I_{\mathbf{k}}^{\text{abs}}$ [15]. In the case of photoemission, such a feature of HSs forms spectral multiplet peaks reflecting different values of $k_\perp$ for various coupling bands (see Subsection 5.3). Moreover, the dispersion of each band differs significantly from a parabolic dependence even though it is smoothed due to the action of V_i. It should be noted that the multiband composition of $E(\mathbf{k})$ is formed by the lower, and, hence, most significant, Fourier components of the potential (V_{111} in the present case). For high energies, this type of composition becomes the main manifestation of the difference between HS and FE dispersion. For other symmetry directions of the BZ, the deviation of $E(\mathbf{k})$ for copper from the FE dispersion is less significant [15, 21].

For the off-symmetry directions of the BZ, the deviations are usually stronger in view of the removal of the band degeneracy. For example, the deviations in the experimental $\mathbf{K}_\parallel$ dispersion of the VLEED spectra on the Cu(110) surface (see Fig. 5b) are manifested as nonparabolicity and discontinuities of dispersions in some regions of $\mathbf{k}_\parallel$.

Nonmetals. In the case of nonmetals, the screening of the ionic potential is normally weaker and the deviations from the FE dispersion increase. For example, $E(\mathbf{k})$ of silicon along the ΓL direction [18] exhibits a clearly manifested multiband composition in a much wider energy range. Such a composition of HS is also inherent in other diamond-like semiconductors (Ge, GaAs, etc.).

Layered materials. The most significant deviations from the FE dispersion are observed for layered materials like graphite and chalcogenides of transition metals [22, 24, 25], in which the weak interlayer coupling leads to a considerable potential modulation in the direction perpendicular to the layers. By way of an example, Fig. 6 illustrates the determination of $E(\mathbf{k})$ for

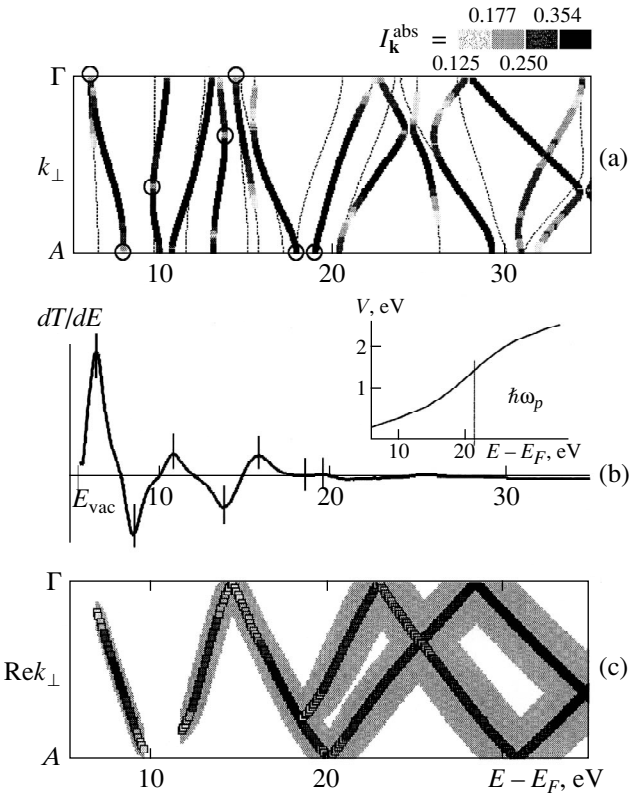

Fig. 6. Determination of HSs for VSe_2 (a) Model $E(\mathbf{k})$ (V_i = 0); $I_{\mathbf{k}}^{\text{abs}}$ are shown by greyscale. (b) Experimental VLEED spectrum whose extrema are identified with the CPs of the coupling bands; the inset shows the experimental dependence $V_i(E)$. (c) Experimental $E(\mathbf{k})$ (main coupling bands) taking V_i into account. Im$k_\perp$ is depicted by shading. This $E(\mathbf{k})$ represents the photoemission FS, and Im$k_\perp$ shows their $k_\perp$ broadening. The experimental $E(\mathbf{k})$ differs radically from the FE dispersion.

VSe_2 along the ΓA direction, which corresponds to the VLEED spectrum for normal incidence on the (0001) surface. We employed the band fitting method with certain modifications dictated by the complexity of the $E(\mathbf{k})$ calculations for VSe_2 associated with a large unit cell and the presence of d bands. First, the fitting itself was carried out by using the $V_i = 0$ approximation. We used a model calculation of $E(\mathbf{k})$ in which the values of $I_{\mathbf{k}}^{\text{abs}}$ were determined within the CFC–$\mathbf{v}_g$ approximation (see Subsection 4.2.2). The critical points of coupling bands for the model $E(\mathbf{k})$ (see Fig. 6a) were identified with the extrema of the experimental spectrum (see Fig. 6b), which determined the energies of these CPs. The $E(\mathbf{k})$ dispersions between these points were then determined by interpolation between the experimental CPs. Second, the energy dependence of V_i was determined from the broadening of the extrema (see the inset to Fig. 6b). The pronounced threshold is associated with the excitation of a volume plasmon with $\hbar\omega_p \sim 21.5$ eV. Above the threshold, the values of V_i are much larger than the separation between individual

CPs, and the spectral structure is suppressed due to the averaging of their effects. Third, we simulated the effect of V_i by smoothing the main coupling bands using a Lorentzian with a half-width V_i. The obtained $E(\mathbf{k})$ dependence is presented together with $\mathrm{Im}k_\perp \sim V_i/v_{g\perp}$ in Fig. 6c.

The experimental $E(\mathbf{k})$ dependence differs significantly from the FE dispersion: (1) it displays a clear two-band character above 20 eV; (2) the FE approximation for each band is only local; the value of V_{000} varies up to 10 eV in the indicated energy range and up to 20 eV within the BZ. These peculiarities in HSs strongly affect the results of the PE experiment (see Subsection 5.3.1).

3.2. Many-Electron Effects

The experimental $E(\mathbf{k})$ dependence usually displays significant and regular displacements relative to the theoretical curve obtained using the standard density functional theory (DFT) [26]. Indeed, the experiments reflect an excited state of a system of interacting electrons in a crystal, which is created by an external factor (e.g., an outer electron in VLEED). However, the static exchange–correlation potential V_{XC} used in the DFT reflects many-electron effects only in the ground state. An excited state is usually described by a dynamic exchange–correlation potential, which is a complex nonlocal self-energy operator $\mathbf{\Sigma}$ [2, 6, 23, 27]:

$$\mathbf{\Sigma}\phi_k(\mathbf{r}) = \int \Sigma(\mathbf{r}, \mathbf{r}', E)\phi_\mathbf{k}(\mathbf{r})d\mathbf{r}'.$$

The deviation of quasiparticle energy levels $E(\mathbf{k})$ from the DFT energy levels is determined by the matrix element $\mathrm{Re}\langle\phi_\mathbf{k}|\mathbf{\Sigma} - V_{XC}|\phi_\mathbf{k}\rangle$, where $\phi_\mathbf{k}$ is the one-electron wave function. It is referred to as the self-energy correction $\mathrm{Re}\Delta\Sigma$ (for the uppermost occupied state, $\mathrm{Re}\Delta\Sigma = 0$ by virtue of the DFT analog of the Koopmans theorem [28]). Energy level broadening is determined by $\mathrm{Im}\,\mathbf{\Sigma} = V_i$. It should be noted that a rigorous description of dynamic many-electron effects does not exist; only various poorly controlled approximations of the *GW* type have been proposed [27, 29].

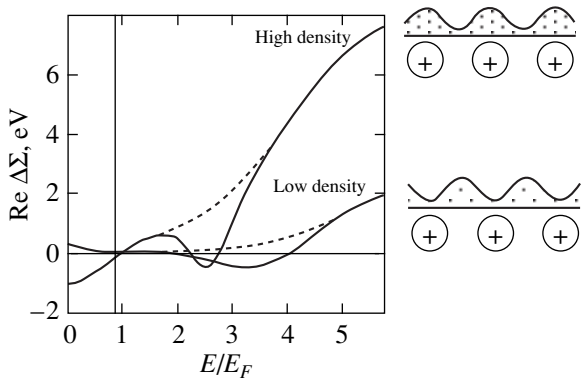

Fig. 7. $\mathrm{Re}\Delta\Sigma$ for a homogeneous electron gas. In a real crystal, the local electron density $n(\mathbf{r})$ is modulated. In this case, the plasmon minimum is suppressed (dashed curve) and the effective density and, hence, $\mathrm{Re}\Delta\Sigma$ depend on the spatial localization of $\phi_\mathbf{k}$ (on the right).

The value of $\mathrm{Re}\Delta\Sigma$ for HSs can differ considerably from the monotonic energy shift, displaying a dependence on $\mathbf{k}$ and the specific band. A comparison of the experimental $E(\mathbf{k})$ of copper with the DFT calculation (see Fig. 5c) reveals a clear $\mathrm{Re}\Delta\Sigma$ anomaly in the upper Δ_1 band on top of an average shift of about +1 eV. It should be noted that these calculations correspond to a practically "ideal" $E(\mathbf{k})$, since they were carried out using the most advanced method of full potential linearized augmented plane waves (FLAPW) [30] and were almost independent of the form of approximation for the static V_{XC}. Similar $\mathrm{Re}\Delta\Sigma$ anomalies were also detected for Ni [20].

The $\mathrm{Re}\Delta\Sigma$ anomalies for HSs are largely associated with the spatial localization effect [31, 32], i.e., the dependence of $\mathrm{Re}\Delta\Sigma$ on the distribution of $|\phi_\mathbf{k}|^2$ within the unit cell. In order to elucidate the mechanism of this effect, we consider the model of a homogeneous electron gas. The corresponding energy dependences of $\mathrm{Re}\Delta\Sigma$ obtained from the calculations [33] are presented in Fig. 7. A characteristic feature of these dependences is an increase in $\mathrm{Re}\Delta\Sigma$ with the electron density n. A generalization for a real crystal with a modulated electron density $n(\mathbf{r})$ can be obtained by introducing the effective $\phi_\mathbf{k}$-weighted electron density

$$\langle n\rangle_\mathbf{k} = \int \phi_\mathbf{k}^*(\mathbf{r})n(\mathbf{r})\phi_\mathbf{k}(\mathbf{r})d\mathbf{r},$$

where the integration is carried out over the unit cell. In the region of ion cores, the value of $n(\mathbf{r})$ increases due to core electrons. In this case, the $\phi_\mathbf{k}$ that have a larger weight in this region (right diagram in Fig. 7) are characterized by a larger $\langle n\rangle_\mathbf{k}$ and, hence, a larger $\mathrm{Re}\Delta\Sigma$ as compared to $\phi_\mathbf{k}$, with a considerable weight between the cores since $\mathrm{Re}\Delta\Sigma$ depends on the spatial localization of $\phi_\mathbf{k}$. This effect determines, for example, $\mathrm{Re}\Delta\Sigma$ anomalies for the $E(\mathbf{k})$ of copper in Fig. 5c [31] (the monotonic part of $\mathrm{Re}\Delta\Sigma$ is also affected by interband transitions and plasmon excitation). It is interesting to note that, in keeping with $\langle n\rangle_\mathbf{k}$, the effective V_i also increases, which is manifested in a larger broadening of the corresponding structures of the VLEED spectrum [34]. The spatial localization effect is also manifested in the valence band (see Subsection 5.3.2).

4. TECHNIQUE OF VLEED SPECTROSCOPY

4.1. Experimental Technique

In VLEED spectroscopy, the dependence $R(E)$ of the integral elastic reflection coefficient on the primary beam energy is measured (for interpreting experimental data, $T(E) = 1 - R(E)$ is normally used). This experi-

ment is characterized by remarkable simplicity. It can be made on any experimental setup with a low-energy electron gun. Figure 8 schematically shows the experiment with a standard LEED module. Instead of taking the $R(E)$ measurements, it is sufficient to measure the total reflection coefficient $R_{tot}(E)$, including elastic and inelastic reflection, since the inelastic component has a smooth energy dependence. Such measurements are most conveniently carried out by measuring the current through the sample, which is complementary to the current of reflected electrons if the gun output current is constant [35, 36] (total current spectroscopy technique).

The optimal operation of the electron gun down to zero energy is ensured by the retarding field mode. For this purpose, the required accelerating voltages (usually, 100–300 V at the last electrode) relative to the cathode are fed to all the electrodes of the gun (Fig. 8) and the energy of the primary beam, with the grounded sample, is controlled by the voltage on the cathode (practical aspects, including electron optics adjustments, are considered in [22, 36, 37]). The retarding field created between the gun and the sample decelerates the electrons to the required primary energy. Since the energy of the electrons over the main part of their path remains quite high, the effect of the stray magnetic fields is minimized and the beam spot can be kept <1.5 mm even when the standard LEED optics are used. Moreover, such a regime ensures the energy independence of the beam, which is of particularly importance in measuring the current targets.

Measurements of angular dependences in the retarding field mode have some peculiarities [37]. The rotation of the sample through an angle α gives rise to the distortion of the field in the region near the sample, where primary electrons incident at a certain angle to equipotential lines are deflected from the rectilinear path (Fig. 9a). This leads to a displacement of the beam over the surface, which depends on the angle α and energy of primary electrons, and, most importantly, to a distortion of the vector $\mathbf{K}_\parallel$ determining the BZ direction being probed. These effects can be taken into account by explicit ray-tracing calculations, which involve the computation of the electrostatic field $U(x, y, z)$ through the solution of the three-dimensional Laplace equation $\sum_i \frac{\partial^2 U}{\partial x_i^2} = 0$ ($x_i = x, y, z$) and the subsequent integration of the equations of motion $\frac{\partial^2 x_i}{\partial t^2} = -\frac{e}{m}\frac{\partial U}{\partial x_i}$ (details and a particular implementation are described in [37]). Figure 9 shows typical results for such computations. The displacement of the beam (see Fig. 9b) is quite large, but the compensating shift of the axis of rotation by 1–3 mm below the sample surface makes it possible to reduce it to less than ±1 mm. As compared to the zero-field mode, $\mathbf{K}_\parallel$ (Fig. 9c) increases and

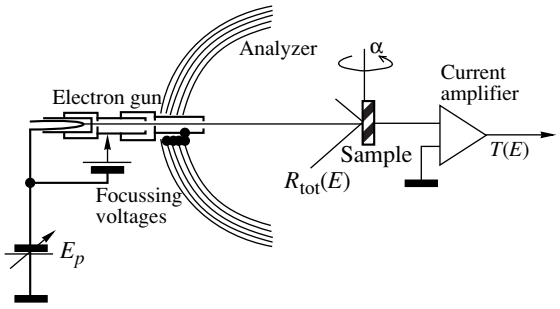

Fig. 8. Schematic diagram of a VLEED experiment with standard four-grid LEED optics. The spectra are measured in the target current. Optimal operation of the electron gun is ensured by applying the required focussing voltages relative to the cathode. This results in a retarding field between the gun and the sample.

depends on energy less strongly. In this case, the dependence $K_\parallel(\alpha, E)$ can be parametrized to within an acceptable accuracy by the biquadratic function $K_\parallel(\alpha, E) = A_1\alpha + A_2\alpha^2 + A_3\alpha E + A_4\alpha^2 E$. Application of this formula allows one to avoid cumbersome ray-tracing computations: $K_\parallel(\alpha, E)$ can be easily found by fitting the coefficients A_1–A_4 to some experimental points for which $K_\parallel$ is fixed by characteristic spectral structures and diffraction patterns [37].

4.2. Theoretical Approaches

Model computations in which $E(\mathbf{k})$ and $I_\mathbf{k}^{abs}$ are determined form an important component of data processing in VLEED spectroscopy, since they are used to identify the structures in the experimental spectra with specific CPs in $E(\mathbf{k})$. In such computations, one can use either rigorous approaches within the semi-infinite crystal model or approximations within the bulk crystals model suitable for a qualitative description.

4.2.1. Model of a semi-infinite crystal. This model takes into account the confinement of the crystal by the surface. The wave function in such a crystal includes both the bulk $\phi_\mathbf{k}$ propagating to the bulk of the crystal and characterized by real-valued $k_\perp$ and the surface wave functions attenuating away from the surface and having complex-valued $k_\perp$. When V_i is taken into consideration, the bulk $\phi_\mathbf{k}$ also become attenuating, but their damping is weaker than that for surface wave functions. In the model calculations, one first calculates $E(\mathbf{k})$ depending on the complex $k_\perp$ and then determines the excitation amplitudes $\phi_\mathbf{k}$, and hence their $I_\mathbf{k}^{abs}$, using the matching technique (see Subsection 2.1). It should be noted that the methods of the multiple scattering theory [7, 8] are more efficient in numerical calculations than the matching method, but they are less suitable for analyzing $E(\mathbf{k})$, since they yield the total wave field in the crystal without its decomposition in $\phi_\mathbf{k}$.

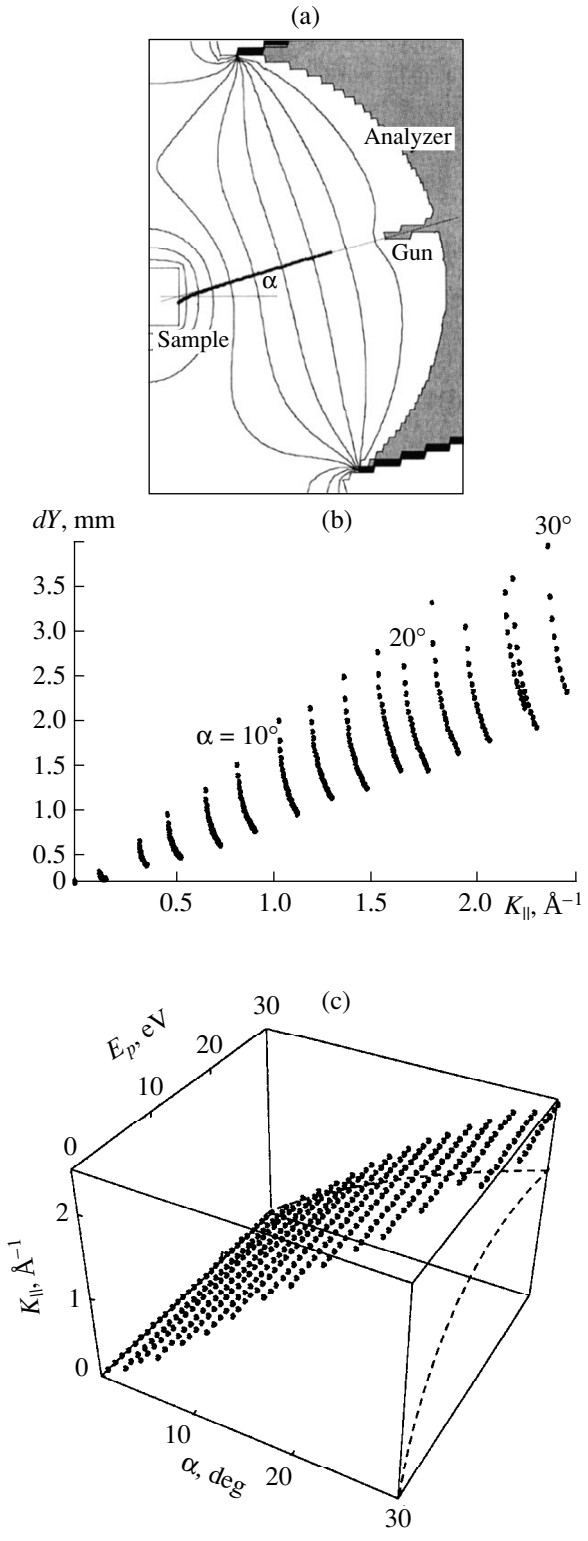

Fig. 9. Typical results of ray-tracing calculations for the retarding field under variations of the sample rotation angle α and the energy of primary electrons (with standard LEED optics and a gun accelerating voltage of 300 V): (a) equipotential lines and the deviation of the primary beam; (b) displacement of the beam (each branch corresponds to a change in energy for α = const, and (c) $K_\parallel$ dependence. The dashed curves above the axes depict this dependence in the zero-field mode.

In order to find $E(\mathbf{k})$, we must solve the Schrödinger equation [7, 15]

$$\left(-\frac{\hbar^2}{2m}\nabla^2 + \mathbf{V} - iV_i - E\right)\phi_\mathbf{k} = 0.$$

For this purpose, use is normally made of the pseudopotential method, which leads to a secular equation of the form

$$\det\{(|\mathbf{k}+\mathbf{G}|^2 + iV_i - E)\delta_{\mathbf{G}\mathbf{G}'} + V_{\mathbf{G}\mathbf{G}'}\} = 0,$$

connecting E and $\mathbf{k}$. In conventional computations of $E(\mathbf{k})$ for an infinite crystal with real $\mathbf{k}$, this equation is solved for E at a fixed $\mathbf{k}$, which can be reduced to the simple eigenvalue problem for the Hamiltonian matrix. However, for $E(\mathbf{k})$ of a semi-infinite crystal with a complex $\mathbf{k}$, the energy remains real-valued only along definite lines in the complex $\mathbf{k}$ space even for $V_i = 0$. Consequently, we must solve the secular equation for $\mathbf{k}$ for a fixed E, which is much more difficult from the computational point of view [9, 10, 38, 39]. In actual practice, this is possible (requiring a reasonable computational effort) only with a local pseudopotential; in this case, the problem is reduced to determining $k_\perp$ as a spectrum of a complex-valued matrix with doubled dimensionality [10, 39]. The **k**–**p** expansion [39, 40], which makes it possible to use any standard computational procedure for $E(\mathbf{k})$ (e.g., the LAPW method), is a promising approach for solving the secular equation.

The matching procedure itself, with known $E(\mathbf{k})$ and $\phi_\mathbf{k}$, is quite trivial. By expanding the wave functions in vacuum and in the crystal in the plane waves $e^{i(\mathbf{k}_\parallel + \mathbf{g})\mathbf{r}_\parallel}$ parallel to the surface, matching can be reduced to the solution of the system of linear equations with a dimensionality equal to the doubled number of the included $\mathbf{g}$. The criterion for the accuracy of the computations is the conservation of current, which includes partial currents $I_\mathbf{k}^{abs}$ in the crystal and interference terms for $V_i \neq 0$ (see Subsection 2.1).

The model for a semi-infinite crystal (naturally, including $V_i \neq 0$) ensures the most accurate description of the VLEED process. However, the calculations based on this model involve considerable computational difficulties [40].

4.2.2. Approximations of a bulk crystal. These approximations presume that $V_i = 0$ and deal only with the bulk $\phi_\mathbf{k}$. Model calculations in this case are considerably simplified since they are, in fact, reduced to the standard calculation of the bulk $E(\mathbf{k})$ on a grid of real-valued $\mathbf{k}$.

An effective method of this type is the coupling Fourier component–group velocity (CFC–$\mathbf{v}_g$) approximation [14]. It is based on an analysis of the Fourier expansion $\phi_\mathbf{k} = \sum_\mathbf{G} C_\mathbf{G} e^{i(\mathbf{k}+\mathbf{G})\mathbf{r}}$. The currents $I_\mathbf{k}^{abs}$ are considered as monotonic functions of two variables: (1) the partial content of the so-called coupling Fourier

components, which resemble the primary plane wave $e^{i\mathbf{Kr}}$ in the sense of the equivalence of the parallel wave vectors and the codirectionality of the perpendicular wave vectors

$$\begin{cases}\mathbf{k}_\parallel + \mathbf{G}_\parallel = \mathbf{K}_\parallel \\ (k_\perp + G_\perp)/K_\perp > 0;\end{cases}$$

and (2) the surface-perpendicular group velocity $v_{g\perp}$. The dependence of $I_{\mathbf{k}}^{\text{abs}}$ on these factors can be expressed as an empirical formula whose parameters are determined by fitting to matching computations for a model semi-infinite crystal. It is shown in Fig. 10 that, despite certain amplitude errors, the CFC–$\mathbf{v}_g$ approximation very accurately reproduces the energy positions of the $I_{\mathbf{k}}^{\text{abs}}$ features corresponding to the CPs determined in the experiments. This makes it possible to successfully use this approximation in analyzing the VLEED spectroscopic data.

Another promising method is the asymptotic approximation based on the multiple scattering theory [41]. In this case, the wave functions in the vacuum and in the crystal are replaced by their asymptotic representations, which makes it possible to derive an analytic expression for $I_{\mathbf{k}}^{\text{abs}}$. The accuracy of this approximation is higher than that of the CFC–$\mathbf{v}_g$ approximation, but it requires an extension of the unit cell in some cases, which slightly increases the computation time.

The implementation of the bulk crystal approximation can employ any standard code for $E(\mathbf{k})$ computations, e.g., the pseudopotential method [18] or the LAPW method [21, 22]. In this case, the functions $\phi_{\mathbf{k}}$ are generated as a byproduct of the computations. The run time is reduced by several orders of magnitude (especially if the CFC–$\mathbf{v}_g$ approximation is used) as compared to the semi-infinite crystal approach. This makes it possible to easily carry out an analysis of the VLEED data for materials with a large number of atoms in the unit cell, even HTSC. A considerable disadvantage of this method is that the influence of V_i on $E(\mathbf{k})$ cannot be taken into account, although the effect on the VLEED spectrum can be simulated by its convolution with a Lorentzian having a half-width V_i and the corresponding suppression of spectral structure.

5. APPLICATIONS IN PHOTOEMISSION SPECTROSCOPY

The dispersion $E(\mathbf{k})$ of the valence band near the Fermi level is of particular interest when considering the physicochemical properties of solids. This dispersion is studied using PE spectroscopy, but resolution in this case, i.e., in the three-dimensional $\mathbf{k}$, requires the knowledge of $E(\mathbf{k})$ for HSs (see Introduction). This is the main field of application of VLEED spectroscopy.

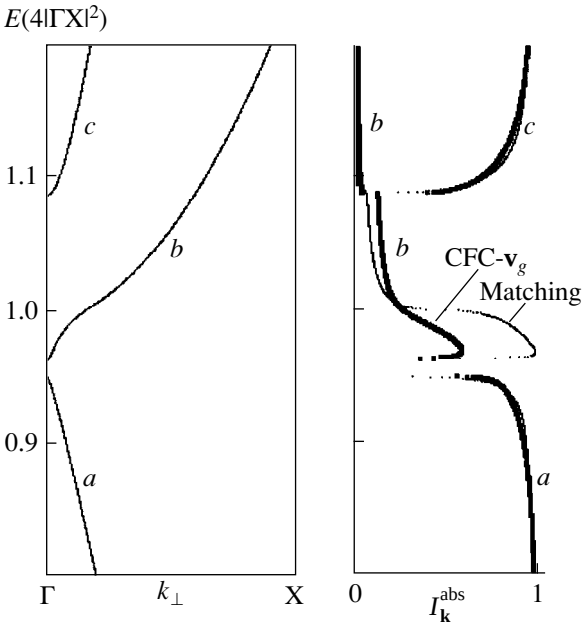

Fig. 10. Comparison of the CFC–$\mathbf{v}_g$ approximation with the accurate matching calculations on a model crystal (cubic unit cell, $V_i = 0$) $E(\mathbf{k})$ and corresponding $I_{\mathbf{k}}^{\text{abs}}$ for bands *a*–*c*.

Its applications for studying the conduction band by inverse PE are analogous.

5.1. Relationship between VLEED and Photoemission

A close connection between VLEED and photoemission is observed in the one-step theory of PE in which photoexcitation, photoelectron transport, and its emission to vacuum are regarded as a single quantum-mechanical process [2–4]. The photocurrent is proportional to the matrix element of the operator $\mathbf{A} \cdot \mathbf{p}$ ($\mathbf{A}$ is the vector potential of the electromagnetic field) for a transition between the initial one-electron state (IS) Φ^i and the final state (FS) Φ^f:

$$I^{\text{ph}} \propto \left|\left\langle \Phi^{f*} | \mathbf{A} \cdot \mathbf{p} | \Phi^i \right\rangle\right|^2.$$

Here, Φ^f is the time-reversed VLEED state which would be excited in the crystal by an electron gun mounted in place of the PE analyzer (if we neglect the electron–hole interaction). Henceforth, we refer to these states alternatively as final states in connection with PE and, as before, higher-lying states in connection with VLEED.

The connection between VLEED and photoemission also extends to the contributions from individual $\phi_{\mathbf{k}}$ constituting the FS. Indeed, the partial photocurrents $I_{\mathbf{k}}^{\text{ph}}$ are proportional to $\left|M_{\mathbf{k}}^{fi}\right|^2 \left|T_{\mathbf{k}}\right|^2$, where $T_{\mathbf{k}}$ is the surface transmission coefficient equal to the excitation

amplitude of $\phi_{\mathbf{k}}$ in VLEED [4]. Expressing $|T_{\mathbf{k}}|^2$ in terms of $I_{\mathbf{k}}^{\text{abs}}$, we obtain [15]

$$I_{\mathbf{k}}^{\text{ph}} \propto \left(\frac{1}{V_i}\left|M_{\mathbf{k}}^{fi}\right|^2\right) \cdot I_{\mathbf{k}}^{\text{abs}}.$$

Consequently, the values of $I_{\mathbf{k}}^{\text{ph}}$ for PE are proportional to $I_{\mathbf{k}}^{\text{abs}}$ for VLEED. This means that, in both processes, the same coupling bands dominate in a multitude of bands.

Such a detailed connection makes it possible to use the experimental HSs determined by VLEED as FSs in PE spectroscopy. Such a combined VLEED–PE method ensures an absolute (with complete control over three-dimensional **k**) determination of the valence band $E(\mathbf{k})$ [21, 22]. Since the experimental HSs already contain true deviations from the FE dispersion, as well as the dynamic many-electron effects, this method ensures a fundamentally higher accuracy as compared to the traditional approaches based on empirical or calculated HSs.

5.2. Intrinsic $k_\perp$ Resolution of PE Spectroscopy

Apart from the knowledge of $E(\mathbf{k})$ for the FS, the exact determination of the valence bands $E(\mathbf{k})$ requires a sufficiently high resolution in $k_\perp$, which is limited by the very physics of the PE process. Let us consider the mechanism of PE peak broadening based on the bulk $E(\mathbf{k})$ picture [2, 3, 25, 42].

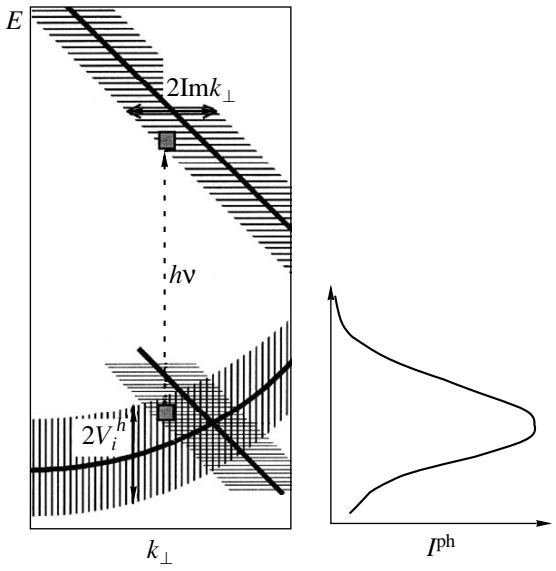

Fig. 11. Development of the PE peak profile as a result of $k_\perp$ broadening $\Delta k_\perp$ in the FS combined with the energy broadening ΔE in the IS.

The spectral function $A(E, \mathbf{k})$ of the Bloch wave for the FS is reduced in energy (in spite of V_i) to a fixed E^f detected by the PE analyzer. However, because of attenuation of $\phi_{\mathbf{k}}$, it has a Lorentzian distribution of real-valued $k_\perp$ centered at $\text{Re}k_\perp^f$ and having a half-width $\text{Im}k_\perp^f$:

$$A^f(k_\perp - \text{Re}k_\perp^f) = \frac{1}{(k_\perp - \text{Re}k_\perp^f)^2 + (\text{Im}k_\perp^f)^2}.$$

In contrast to this, the function $A(E, \mathbf{k})$ of the Bloch wave for the initial state is reduced in $k_\perp$ to a real-valued $k_\perp^i$ because $\phi_{\mathbf{k}}$ almost does not attenuate in view of a large light absorption length. However, because of the hole absorption V_i^h, it has a Lorentzian energy distribution centered on the $E^i(k_\perp)$ band dispersion and with a half-width V_i^h:

$$A^i(E - E^i(k_\perp)) = \frac{1}{(E - E^i(k_\perp))^2 + (V_i^h)^2}.$$

It is shown in Fig. 11 that the PE current is formed at the initial energy $E^i = E^f - h\nu$ as a result of the integration of the elementary currents from the intervals $dk_\perp$:

$$I^{\text{ph}}(E^f, h\nu) = \left|M_{\mathbf{k}}^{fi}\right|^2 |T_{\mathbf{k}}|^2 \times \int A^f(k_\perp - \text{Re}k_\perp^f) A^i(E - E^i(k_\perp)) dk_\perp$$

(the amplitude factors $M_{\mathbf{k}}^{fi}$ and $T_{\mathbf{k}}$ are assumed to be constant). The profile of the PE peak is then formed by the $k_\perp$ broadening of the FS together with the energy broadening of the IS. Since $A^f(k_\perp - \text{Re}k_\perp^f)$ determines the weight of the $dk_\perp$ states in the **k** space, its half-width $\text{Im}k_\perp^f$ is the intrinsic $k_\perp$ resolution of the PE experiment [25]. In contrast to the $\mathbf{k}_\parallel$ resolution limited by the aperture of the PE analyzer, the $k_\perp$ resolution cannot be improved instrumentally.

The maxima of PE peaks correspond in principle to the direct transitions $\text{Re}k_\perp^f = k_\perp^i$; this fact forms the basis for determining $E(\mathbf{k})$ with the help of PE. However, an insufficient intrinsic resolution might lead to a displacement of the peaks from these positions (intrinsic shifts) [21, 22, 43]. For example, if the initial-state $E(k_\perp)$ is nonlinear, the total numbers of the $dk_\perp$ states lying above and below the direct transition energy are different and the peak becomes asymmetric and displaced towards the larger number of states. In the band interior, the shift is directed to the bottom of the band (see Fig. 11), while at the bottom of the band it is directed into the band (there are no states below the bot-

tom) [21]. Intrinsic shifts can also be due to sharp changes in $M_{\mathbf{k}}^{fi}$ within the PE profile [22].

The intrinsic shifts can be minimized by reducing $\mathrm{Im}k_\perp^f$ (the remaining factors are the inherent properties of the valence states) to

$$\mathrm{Im}k_\perp^f \ll k_\perp^{BZ},$$

where $k_\perp^{BZ}$ is the size of the BZ along the normal to the surface. It is this condition that ensures the correct analysis of $E(\mathbf{k})$ with a resolution in $k_\perp$ (the band structure regime) [4, 43]. Under the opposite condition $\mathrm{Im}k_\perp^f \gg k_\perp^{BZ}$, averaging over $k_\perp$ takes place and PE spectra reflect the one-dimensional density of states (density-of-states regime).

Tuning of the $k_\perp$ resolution can be carried out by varying the FS energy. Tendencies of the corresponding dependence are described by the well-known "universal curve" as the energy dependence of the mean free path $\lambda = (2\mathrm{Im}k_\perp)^{-1}$ [2, 4]. For E^f smaller than ~30 eV, the band-structure regime usually takes place (λ is large). It is gradually transformed into the density-of-states regime, which sets in near 100 eV. Starting from ~1000 eV, the band-structure regime sets in again, but, in this region, technical difficulties associated with the $\mathbf{k}_\parallel$ resolution are encountered. The PE experiments at the minimal E^f (below ~20 eV) make it possible to ensure the best resolution both in $k_\perp$ and in $\mathbf{k}_\parallel$. In view of the large value of λ, the contribution of the surface region in which $E(\mathbf{k})$ might be distorted also decreases [44]. In this energy range, final states differ considerably from the FE dispersion, thus, the application of the VLEED–PE technique is required.

The $k_\perp$ resolution can be controlled by using the VLEED experimental data on $E(\mathbf{k})$ and V_i ($\mathrm{Im}k_\perp^f$ is determined from these data as $\sim\frac{\partial k_\perp^f}{\partial E}$). It should be noted that the range of the most accurate determination of the FS in VLEED spectroscopy (where V_i remains smaller than the separation between CPs) almost coincides with the range of the best resolution in PE spectroscopy.

*5.3. Examples of Absolute Determination of E(**k**) by the VLEED–PE Method*

In PE spectroscopy, the $E(\mathbf{k})$ dispersions can be determined either as ($E(k_\perp)$, when the value of $k_\perp$ is varied by changing $h\nu$, or as $E(\mathbf{k}_\parallel)$, when $\mathbf{k}_\parallel$ is varied by changing the emission angle. In accordance with these two methods, the VLEED determination of $E(\mathbf{k})$ for the FSs is carried out either by the band fitting method or by direct band mapping (see Subsection 2.2).

5.3.1. Determination of $E(\mathbf{k})$ as $E(k_\perp)$ by varying $h\nu$. In this method of determining $E(\mathbf{k})$, the VLEED–PE approach was demonstrated for the first time [22] for VSe_2 (ΓA direction) as a representative of the layered materials characterized by strong deviations of HSs from FE dispersion. Indeed, the VLEED experiments (see Subsection 3.1) revealed a multiband composition of $E(\mathbf{k})$ and, in addition, a sharp increase in $\mathrm{Im}k_\perp$ above $\hbar\omega_p$ (see Fig. 6c).

Optimization of the PE experiment. Knowledge of the HS peculiarities has made it possible to optimize PE experiments for accurate determination of $E(k_\perp)$. In order to ensure the band-structure regime $\mathrm{Im}k_\perp^f \ll k_\perp^{BZ}$ (this condition is critical for layered materials in view of the small size of the BZ along the normal to the surface), it was found expedient to choose values of E^f below the plasmon energy. For higher values of E^f, considerable intrinsic shifts could be expected, along with difficulties associated with resolving PE peaks from different FS bands.

Determination of the valence band. The corresponding PE experiments were made under normal emission using synchrotron radiation tunable in $h\nu$. The results are presented in Fig. 12a as a map of the PE intensity as a function of $h\nu$ and E^i. Such a representation makes it possible to easily determine the nature of spectral structures. For example, the descending straight lines correspond to secondary emission peaks with E^f = const, while the ascending lines correspond to core energy levels excited by higher-order light (they have nothing to do with the valence band). The remaining peaks correspond to different valence bands, with their $h\nu$ dispersion reflecting the $k_\perp$ dispersion of these bands. The doublet structure of the FSs (see Fig. 6c) is manifested, for example, as two peaks in the Se $4p_z^*$ band near $h\nu$ = 30 eV. In the deeper Se $4p_z$ band, analogous peaks merge into one broad peak due to the strong broadening associated with an increase in V_i^h.

The energy $E_{e\text{–}h}$ of the electron–hole interaction was estimated as the difference between the FS energies and the corresponding HS energies (in VLEED). For this purpose, we used the points of extremal dispersion of the PE peaks for which $k_\perp$ lies at the symmetry points of the BZ. In this case, it was found that $E_{e\text{–}h} \sim 0$, indicating a considerable delocalization of electrons and holes.

Direct determination of $E(k_\perp)$ for the valence band involved the standard construction of E^i corresponding to spectral peaks as a function of $k_\perp$ (see Introduction). In this procedure, $k_\perp$ was determined from the experimental FSs shown in Fig. 6c. The obtained $E(\mathbf{k})$ is presented in Fig. 12b. The same figure shows the theoretical $E(\mathbf{k})$ calculated in the DFT framework by the LAPW method. All points in the band structure regime

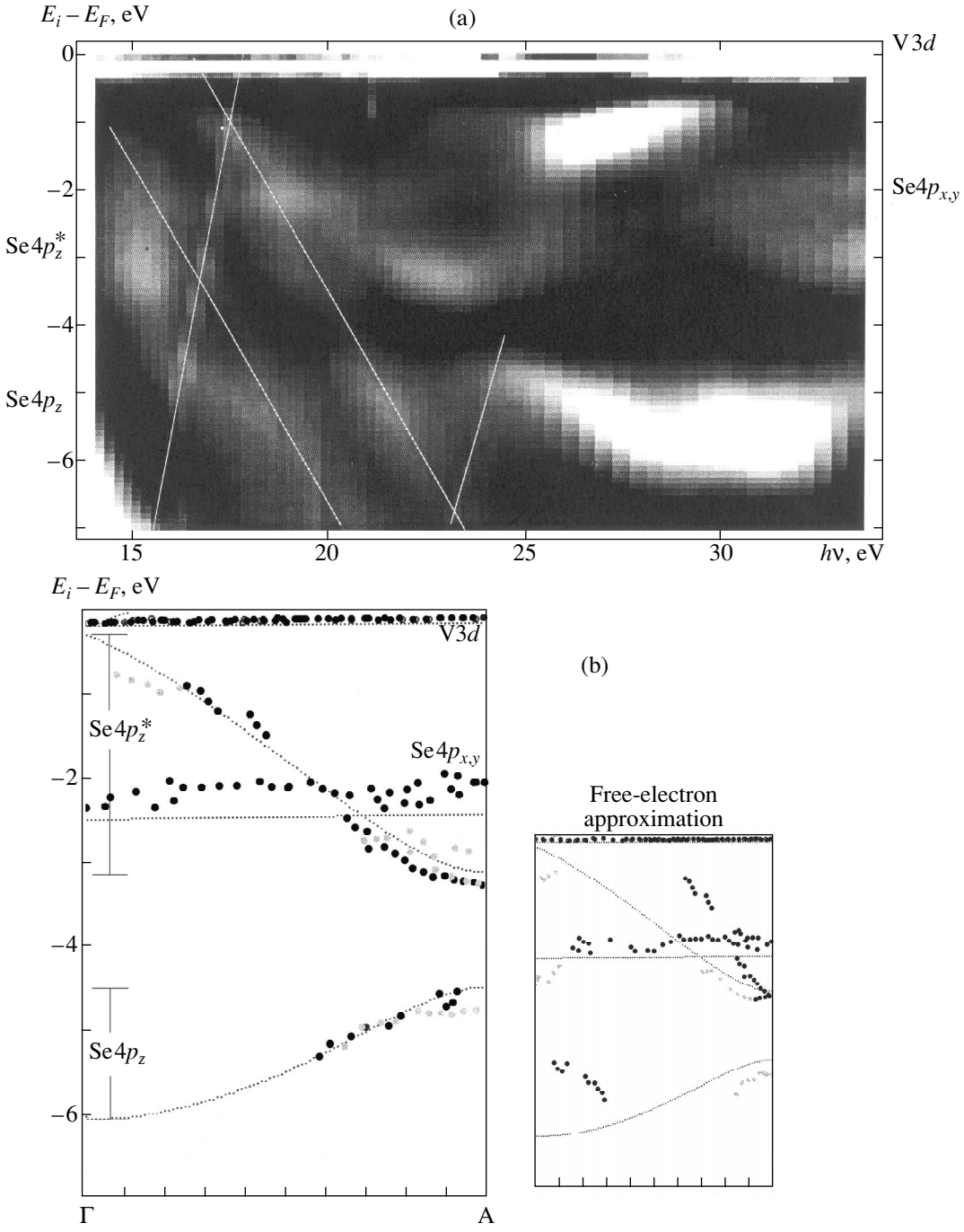

Fig. 12. Absolute determination of the valence band $E(\mathbf{k})$ of VSe_2 by the VLEED–PE method varying $h\nu$. (a) Dependence of the PE intensity on $h\nu$ and the IS energy, shown in greyscale (white corresponds to the maximum intensity). Secondary emission and core level peaks are indicated. The remaining peaks correspond to the valence band, and their $h\nu$ dispersion reflects the $k_\perp$ dispersion of these bands. (b) Experimental valence-band $E(\mathbf{k})$. Black points correspond to the region of the band structure regime and grey ones lie outside this region. This $E(\mathbf{k})$ was obtained from the FSs determined by VLEED (Fig. 6c). Its integrity is contrasted with the results of the FE approximation of FSs (with V_{000} at the valence band bottom), which are presented on the right.

$E^f < \hbar\omega_p$ (black points) demonstrate truly consistent dispersions, although they are displaced relative to theoretical $E(\mathbf{k})$ (presumably, because of the many-electron effects). The sharp contrast with the results of the application of the FE approximation (see the inset) demonstrates the importance of using correct FSs. Moreover, the points outside the region of the band structure regime (grey points) for the same ISs are displaced to the interior of the band, demonstrating the importance of a sufficiently high $k_\perp$ resolution (see

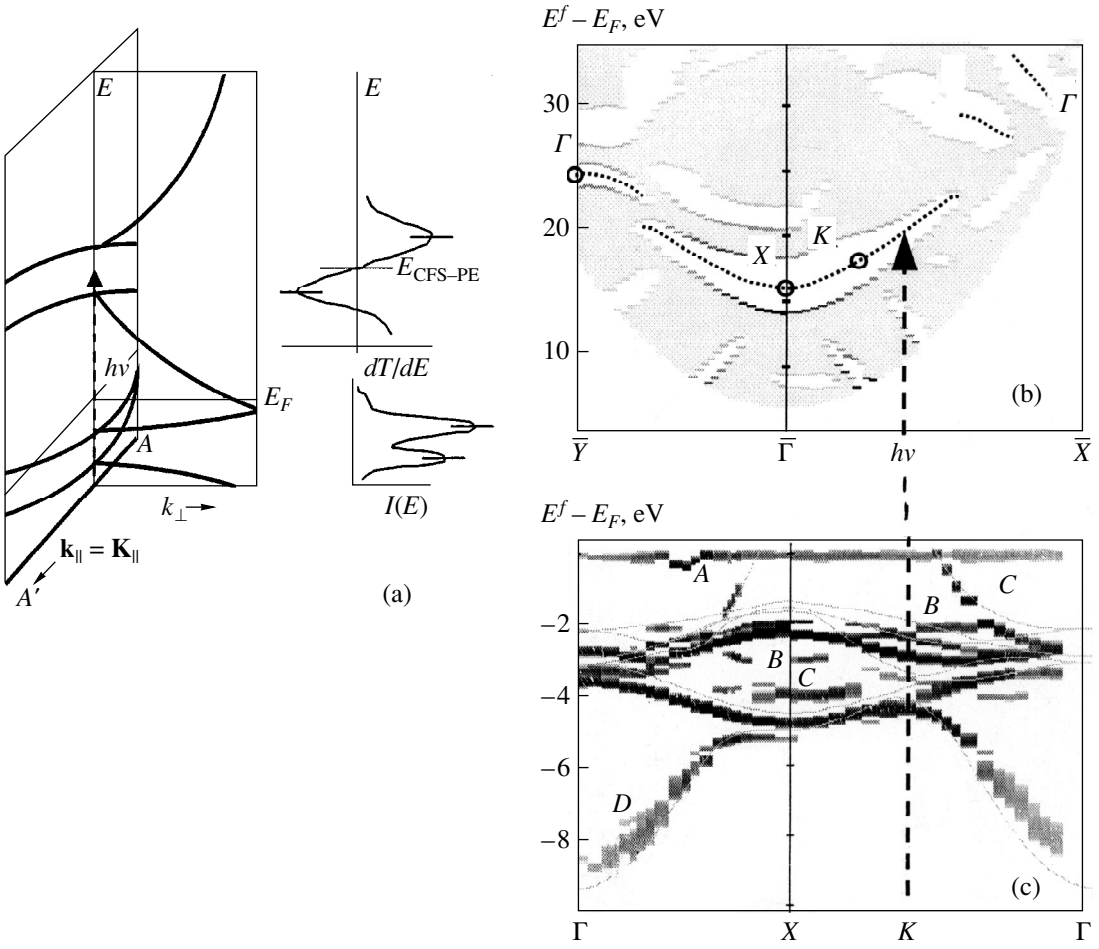

Fig. 13. Absolute determination of $E(\mathbf{k})$ for the valence band of Cu by the VLEED–PE method of angular dependences on the (110) surface. (a) The idea of the method. The wave vector $k_\perp$ is localized on the *AA*' symmetry direction if the FS energy is at the middle of the band gap $E(k_\perp)$ (minimum–maximum of dT/dE). (b) Experimental dispersion of the VLEED spectra, presented as in Fig. 5b. The dashed curve corresponds to E^f localizing $k_\perp$ on the Γ*X* and Γ*KX* of the bulk BZ. (c) The experimental valence-band $E(\mathbf{k})$, obtained with the chosen E^f, which is presented as $-\frac{d^2 I^{\mathrm{ph}}}{dE^2} > 0$ (shown by greyscale). The *A*–*D* peaks are not connected directly with $E(\mathbf{k})$. The DFT theoretical $E(\mathbf{k})$ is also shown. The signs of $\mathrm{Re}\Delta\Sigma$ in the *d* and *sp* bands are opposite due to the different spatial localizations of the corresponding $\phi_{\mathbf{k}}$.

Subsection 5.2). It should be noted that the VLEED–PE method has made it possible to attain, for the first time, a consistent resolution of the valence band in $k_\perp$ for the class of layered materials characterized by strong deviations of HSs from the FE dispersion.

Similarly, $E(\mathbf{k})$ was determined for TiS_2 [22]. Considerable intrinsic shifts were observed due to strong variations of M_k^{fi}.

5.3.2. Determination of $E(\mathbf{k})$ as $E(\mathbf{k}_\parallel)$ by varying the emission angle. In this method of determining $E(\mathbf{k})$, the VLEED–PE approach is also referred to as the VLEED–PE method of angular dependences [21]. It is most effective in measurements of the PE spectra in the constant-final-state mode as a function of $h\nu$ with a fixed E^f. The idea of the method is illustrated in Fig. 13a. Let *AA*' be a certain symmetry direction of the BZ parallel to the surface. First, the $E(\mathbf{k})$ of the HSs along *AA*' is constructed from the angular dependences of VLEED using the direct band mapping method (see Subsection 2.2.2). The pair of its bands corresponds to local band gaps of $E(k_\perp)$ (minimum–maximum of dT/dE) in this symmetry direction. For the energy lying between these two bands, $k_\perp$ is localized on *AA*' (taking into account the smoothing effect of V_i; see Fig. 2c). Second, these energies E^f are chosen as constant FS energies and the PE angular dependences are measured. Then, $k_\perp$ is localized on the chosen direction and the $\mathbf{K}_\parallel$ dispersions of the PE peaks directly form the valence band $E(\mathbf{k})$, the three-dimensional $\mathbf{k}$ being completely fixed. Such a determination of $E(\mathbf{k})$ is direct. It should be noted that the attenuation of $\phi_{\mathbf{k}}$ associated with the

emission from energy gaps is not a specific feature of the method, since V_i also leads to the attenuation of $\phi_{\mathbf{k}}$ outside the band gaps. The method was tested on Cu using the (110) surface, which gives access to all BZ directions in the symmetry plane $\Gamma KLUX$ [21].

Determination of FS. The determination of $E(\mathbf{k})$ for HSs was discussed earlier in connection with VLEED band mapping (see Subsection 2.2.2). The experimental $\mathbf{K}_\parallel$ dispersion of dT/dE extrema in azimuths $\overline{\Gamma Y}$ and $\overline{\Gamma X}$ of the surface BZ is presented in Fig. 13b. As before, the bands corresponding to the symmetry directions of the bulk BZ were identified in them (ΓX and ΓKX in this case). In addition, the pairs corresponding to the $E(k_\perp)$ extrema of the opposite curvature were identified in them (otherwise, the effect of V_i would lead to a certain displacement of $k_\perp$ from the symmetry direction; see Fig. 2c). It is these pairs that gave the E^f values localizing $k_\perp$ on symmetry directions for the PE experiments. In Fig. 13b, these energies are shown by dashed curves. It is worth noting that the $E^f(\mathbf{K}_\parallel)$ dispersions have discontinuities in the regions of strong multiband hybridization, where $E(k_\perp)$ deviates considerably from the FE dispersion.

Determination of the valence-band $E(\mathbf{k})$. The corresponding PE experiment was carried out using synchrotron radiation, which makes it possible to scan $h\nu$. The results of such an experiment are presented in Fig. 13c as the dispersion of negative values of the second derivative of the PE intensity, $\frac{d^2 I^{\mathrm{ph}}}{dE^2} < 0$. Such a representation makes it possible to identify the spectral structure against the background of monotonic variations of I^{ph} and, in fact, directly maps the valence-band $E(\mathbf{k})$ (except the bands with too small values of $M_{\mathbf{k}}^{fi}$). Indeed, the peaks $-\frac{d^2 I^{\mathrm{ph}}}{dE^2}$ reveal the peaks and shoulders of the energy dependence of the I^{ph} corresponding to the $E(\mathbf{k})$ bands. The obtained $E(\mathbf{k})$ perfectly agrees with the entire body of previous experimental data (see the review [5]) obtained by traditional PE methods. The experimental data exhibit exceptional internal consistency: dispersion remains smooth even at E^f discontinuities occurring in regions of strong hybridization of HSs. Moreover, the energy of the PE peaks was found to remain constant upon a change in E^f through the discontinuities (only the intensity changes due to the variation of $M_{\mathbf{k}}^{fi}$), which can be explained by the almost vertical $k_\perp$ dispersion of corresponding FSs.

The theoretical valence-band $E(\mathbf{k})$, which was calculated in the DFT framework using the LAPW method, is also shown in Fig. 13c. The experimental $E(\mathbf{k})$ agrees well with it (the *A*–*D* peaks are connected with the surface states, the maxima of the one-dimensional density of states, and the multiband composition of the FSs). However, regular deviations amounting to –0.5 eV for the *d* bands and +0.4 eV for the bottom of the *sp* band can be clearly seen. These deviations are due to many-electron effects in the excited PE state. As in the case of HSs (see Subsection 3.2), these $\mathrm{Re}\Delta\Sigma$ anomalies are connected with different spatial localizations of $\phi_{\mathbf{k}}$ in the *d* and *sp* bands [31, 32].

Peculiarities of the method. The intrinsic accuracy of the method [21] may seem limited since the value of $\mathrm{Im}k_\perp$ increases slightly in the band gap, thus deteriorating the $k_\perp$ resolution (see Subsection 5.2). In fact, such an increase is much smaller than the main contribution to $\mathrm{Im}k_\perp$ due to V_i. Moreover, the possibility of using low E^f characterized by small values of V_i makes it possible even to improve the $k_\perp$ resolution comparatively with traditional methods. However, the main factor determining the high accuracy of the VLEED–PE method of angular dependences is the direct mapping of $E(\mathbf{k})$.

A practical advantage of this method is the possibility of analyzing several BZ directions using a single crystalline surface. For example, the present experiment alone covers almost the entire previous experimental data on Cu [5]. This is especially important for materials with only one stable surface (such as layered materials). The method is most efficient in cases where deviations of FSs from FE dispersion are strong.

6. CONCLUSIONS

Photoemission spectroscopy is the main tool for analyzing the $E(\mathbf{k})$ band structure with $\mathbf{k}$ resolution. However, controlling $k_\perp$, which is distorted during the photoelectron emission to vacuum, and, thus, three-dimensional $\mathbf{k}$ requires knowledge of $E(\mathbf{k})$ for unoccupied higher-lying states.

Very low-energy electron diffraction spectroscopy is the most direct method for studying HSs. It is based on the connection between the elastic electron reflection spectra and the critical points in the $E(k_\perp)$ dispersion of the Bloch states that are effectively coupled with the wave function in vacuum. This makes it possible to find the experimental positions of such points and to use them to determine $E(\mathbf{k})$ itself by fitting the model calculations or by direct mapping of VLEED angular dependences.

According to experimental data, HSs (1) can be characterized by strong deviations from the free-electron dispersion, especially for nonmetals, and (2) can experience noticeable shifts relative to the ground state $E(\mathbf{k})$ due to excited-state many-electron effects. The experimental technique of VLEED spectroscopy is extremely simple, but data processing requires a certain numerical simulation.

The VLEED states are the time-reversed PE states. This makes it possible to employ VLEED spectroscopy for determining the final-state $E(\mathbf{k})$ for PE spectros-

copy, which ensures the resolution of the valence-band $E(\mathbf{k})$ in the three-dimensional vector $\mathbf{k}$ in the PE determination. Such a combined VLEED–PE method is most efficient when one uses angular dependences and the constant-final-state mode of the PE measurements; this permits a direct determination of $E(\mathbf{k})$. The advantage of this method is that it allows one to use low $h\nu$ in attaining the best $\mathbf{k}$ resolution of the PE experiment.

The fundamentals of VLEED spectroscopy as a method of band structure investigation $E(\mathbf{k})$ and the principles of its application in PE spectroscopy have been developed quite recently. Having demonstrated its potential, VLEED spectroscopy passes over to a stage of wide application, providing information on the electronic structure of solids which was not previously available.

ACKNOWLEDGMENTS

The author is grateful to H. I. Starnberg and P.-O. Nilsson (Chalmers University of Technology), R. Claessen (Universität, Augsburg), and S. A. Komolov (Physical Research Institute, St. Petersburg State University), who took part in the development of VLEED spectroscopy as a band structure method.

REFERENCES

1. Zh. I. Alferov, Fiz. Tekh. Poluprovodn. (St. Petersburg) **32** (1), 3 (1999) [Semiconductors **32**, 1 (1998)].
2. *Angle-Resolved Photoemission*, Ed. by S. D. Kevan (Elsevier, Amsterdam, 1992).
3. S. Hüfner, *Photoelectron Spectroscopy* (Springer-Verlag, Berlin, 1995).
4. P. J. Feibelman and D. E. Eastman, Phys. Rev. B **10**, 4932 (1974).
5. R. Courths and S. Hüfner, Phys. Rep. **112**, 53 (1984).
6. *Unoccupied Electronic States*, Ed. by J. C. Fuggle and J. E. Inglesfield (Springer-Verlag, Berlin, 1992).
7. J. B. Pendry, *Low Energy Electron Diffraction* (Academic, London, 1974).
8. M. A. van Hove and S. Y. Tong, *Surface Crystallography by LEED* (Springer-Verlag, Berlin, 1979).
9. G. Capart, Surf. Sci. **13**, 361 (1969).
10. J. B. Pendry, J. Phys. C **2**, 2273 (1969).
11. R. C. Jaklevic and L. C. Davis, Phys. Rev. B **26**, 5391 (1982).
12. V. N. Strocov, Solid State Commun. **78**, 545 (1991); V. N. Strocov and S. A. Komolov, Phys. Status Solidi B **167**, 605 (1991).
13. V. N. Strocov, Int. J. Mod. Phys. B **9**, 1755 (1995).
14. V. N. Strocov, Solid State Commun. **106**, 101 (1998).
15. V. N. Strocov, H. I. Starnberg, and P. O. Nilsson, J. Phys.: Condens. Matter **8**, 7539 (1996); Phys. Rev. B **56**, 1717 (1997).
16. J.-V. Peetz, W. Schattke, H. Carstensen, *et al.*, Phys. Rev. B **46**, 10127 (1992).
17. E. G. McRae, Rev. Mod. Phys. **51**, 541 (1979); R. O. Jones and P. J. Jennings, Surf. Sci. Rep. **9**, 165 (1988).
18. V. N. Strocov, S. Mankefors, P. O. Nilsson, *et al.*, Phys. Rev. B **59**, 5296 (1999).
19. A. Goldmann, W. Altmann, and V. Dose, Solid State Commun. **79**, 511 (1991).
20. V. N. Strocov, Int. J. Mod. Phys. B **7**, 2813 (1993).
21. V. N. Strocov, R. Claessen, C. Nicolay, *et al.*, Phys. Rev. Lett. **81**, 4943 (1998); Phys. Rev. B (2000) (in press).
22. V. N. Strocov, H. I. Statnberg, P. O. Nilsson, *et al.*, Phys. Rev. Lett. **79**, 467 (1997); J. Phys.: Condens. Matter **10**, 5749 (1998).
23. W. B. Jackson and J. W. Allen, Phys. Rev. B **37**, 4618 (1988).
24. V. N. Strocov, P. Blaha, H. I. Starnberg, *et al.*, Phys. Rev. B **61**, 4994 (2000).
25. V. N. Strocov, in *Electron Spectroscopies Applied to Low-Dimensional Materials*, Ed. by H. I. Starnberg and H. P. Hughes (Kluwer, Dordrecht, 2000).
26. P. Hohenberg and W. Kohn, Phys. Rev. B **136**, 864 (1964); W. Kohn and L. J. Sham, Phys. Rev. A **140**, 1133 (1965); W. Kohn, Rev. Mod. Phys. **71**, 1253 (1999).
27. L. Hedin and S. Lundquist, in *Solid State Physics*, Ed. by H. Ehrenreich, F. Seitz, and D. Turnbull (Academic, New York, 1969), Vol. 23.
28. M. Levy, J. P. Perdew, and V. Sahni, Phys. Rev. A **30**, 2745 (1984); C.-O. Almbladh and U. von Barth, Phys. Rev. B **31**, 3231 (1985).
29. M. S. Hybertsen and S. G. Louie, Phys. Rev. Lett. **55**, 1418 (1985); Phys. Rev. B **34**, 5390 (1986).
30. P. Blaha, K. Schwarz, and J. Luitz, *WIEN97, A Full Potential Linearized Augmented Plane Wave Package for Calculating Crystal Properties* (Techn. Univ. Vienna, Vienna, 1999).
31. V. N. Strocov, P. O. Nilsson, P. Blaha, *et al.* (in press).
32. P. O. Nilsson and C. G. Larsson, Phys. Rev. B **27**, 6143 (1983).
33. L. Hedin and B. I. Lundquist, J. Phys. C **4**, 2064 (1971).
34. I. Bartoš, M. A. van Hove, and M. S. Altmann, Surf. Sci. **352–354**, 660 (1996).
35. V. Heinrich, Rev. Sci. Instrum. **44**, 456 (1973).
36. S. A. Komolov, *Total Current Spectroscopy of Surfaces* (Gordon and Breach, Philadelphia, 1992).
37. V. N. Strocov, Meas. Sci. Technol. **7**, 1636 (1996).
38. H. Bross, Surf. Sci. **213**, 215 (1989).
39. D. L. Smith and C. Mailhiot, Rev. Mod. Phys. **62**, 173 (1990).
40. E. E. Krasovskii and W. Schattke, Phys. Rev. B **56**, 12874 (1997); Phys. Rev. B **59**, R15609 (1999).
41. G. V. Vol'f, Yu. P. Chuburin, D. V. Fedorov, and V. N. Strocov, Fiz. Tverd. Tela (St. Petersburg) **41** (12), 2105 (1999) [Phys. Solid State **41**, 1929 (1999)].
42. R. Matzdorf, Appl. Phys. A **A63**, 549 (1996); Surf. Sci. Rep. **30**, 153 (1998).
43. E. Pehlke and W. Schattke, Solid State Commun. **69**, 419 (1989).
44. E. Pehlke and W. Schattke, J. Phys. C **20**, 4437 (1987).

Translated by N. Wadhwa

Physics of the Solid State, Vol. 42, No. 11, 2000, pp. 1990–1994. Translated from Fizika Tverdogo Tela, Vol. 42, No. 11, 2000, pp. 1938–1942.

METALS AND SUPERCONDUCTORS

Heat Conductivity of $LuAgCu_4$

A. V. Golubkov*, L. S. Parfen'eva*, I. A. Smirnov*, H. Misiorek, J. Mucha**, and A. Jezowski****

**Ioffe Physicotechnical Institute, Russian Academy of Sciences, ul. Politekhnicheskaya 26, St. Petersburg, 194021 Russia*
e-mail: Igor.Smirnov@shuvpop.ioffe.rssi.ru
***Institute of Low-Temperature and Structural Studies, Polish Academy of Sciences, Wroclaw, 53-529 Poland*
Received March 30, 2000

Abstract—The electrical resistivity and heat conductivity of $LuAgCu_4$ have been studied within the 4.2–300-K range. An additional contribution to heat conductivity, most probably due to the bipolar component, has been revealed at $T \geq 100$ K. The conclusion is drawn that $LuAgCu_4$ is apparently a semimetal. © *2000 MAIK "Nauka/Interperiodica".*

1. INTRODUCTION

This work is a continuation of studies of the heat conductivity of $LnMCu_4$ intermetallic compounds (here, Ln stands for a rare-earth metal and M, for a transition metal) crystallizing in an $AuBe_5$ fcc lattice [$C15b$ structure, space group $F\bar{4}3m(T_d^2)$] [1, 2].

$LnMCu_4$ compounds exhibit interesting and sometimes unusual physical properties. Two representatives of this class of materials, $YbInCu_4$ and $YbAgCu_4$, have recently been attracting considerable attention from both experimenters and theorists. The former material initiated interest because of a specific isostructural phase transition of the first kind that it undergoes at $T_v \sim 40$–80 K and at atmospheric pressure. For $T > T_v$, $YbInCu_4$ is a Curie–Weiss paramagnet (a state with localized magnetic moments), while for $T < T_v$, it is a Pauli paramagnet (a nonmagnetic Fermi-liquid state); it is a compound with a mixed valence of the rare-earth ion called the light heavy-fermion system. The references to most experimental and theoretical works dealing with $YbInCu_4$ are summarized in [1, 3, 4].

$YbAgCu_4$ is a representative of the nonmagnetic moderately heavy-fermion system possessing properties characteristic of dense Kondo lattices [4–6]. This compound has been dealt with in an enormous number of publications. To isolate the lattice, electric, and magnetic effects in $YbAgCu_4$ (heat conductivity [4, 7–9], magnetic susceptibility [4, 10], neutron scattering [11], electrical conductivity [8, 12], x-ray L_{III} absorption spectra [4, 13, 14], volume expansion coefficient [13], and XPS spectra [15]), one used $LuAgCu_4$ as a reference material, which has the structure of $YbAgCu_4$ and similar lattice parameters. Yb and Lu occupy adjacent places in the periodic table.

In addition to the above parameters, there are literature data on such characteristics of $LuAgCu_4$ as the lattice constant [4], the γ and β parameters in the $C = \gamma T + \beta T^2$ relation for heat capacity (different authors quote values of γ ranging from 8.7 to 11 mJ/mol K [4, 7, 8, 13], and those of β, from 0.55 to 0.58 mJ/K^4 mol [7, 8]), Debye temperature Θ (from 205 to 257 K [4, 8, 12]), and the Hall constant [4, 13]. Electronic band structure calculations can be found in [17, 18]. Unfortunately, we have not been able to locate any literature data on the heat conductivity of $LuAgCu_4$. They may, however, be of interest in a number of areas. They are needed for thermodynamic calculations and estimation of thermal regimes for single-crystal growth, and they could also be employed as a reference when analyzing heat conductivity data for $YbAgCu_4$. A study of the electronic component of the heat conductivity of $LuAgCu_4$ could yield additional information on specific features of the electronic band structure of this compound.

We have performed measurements of the heat conductivity (κ_{tot}) and electrical resistivity (ρ_{tot}) on a cast polycrystalline sample of $LuAgCu_4$ in the temperature range 4.2–300 K.

2. EXPERIMENTAL

The metals used in preparing $LuAgCu_4$ were 0-grade Lu, 99.99%-pure Ag, and OSCh V3-grade Cu. The components taken in the stoichiometric ratio were melted in a thin-walled (wall thickness ~0.1 mm) sealed tantalum container evacuated to 10^{-4} mm Hg. The samples were melted in an RF-heated furnace. The ingot thus obtained was annealed at 800°C for 75 h. The technique used to synthesize RE-based compounds is described in considerable detail in [19, 20].

The $LuAgCu_4$ sample to be studied was subjected to x-ray diffraction analysis on a DRON-2 setup (with CuK_α radiation). The lattice constant was found to be 7.070(4) Å. The value of a for $LuAgCu_4$ is quoted [4] as 7.094 Å. The available data on the lattice constants

of a number of $LnMCu_4$ compounds, where Ln stands for Yb or Lu, and M is Ag, Au, In, Zn, Cd, Tl, or Mg, were analyzed in [4]. The variation of the parameter $B = \dfrac{a(YbMCu_4) - a(LuMCu_4)}{a(LuMCu_4)}$ for various M was studied. Except for the $YbAgCu_4$–$LuAgCu_4$ pair, the parameter B was positive (the constant a for lutetium compounds is always smaller than that for ytterbium, which correlates with the variation of the ionic radii of these elements). The parameter B was found [4] to be negative (B = –0.155%) only for the $YbAgCu_4$–$LuAgCu_4$ pair. No satisfactory explanation was presented in [4] for the observed anomaly. The assumption as to the band structure of $LuAgCu_4$ proposed appears fairly exotic. The value of a used in [4] to calculate B for $YbAgCu_4$ was 7.083 Å (the numerous literature data place the value of a for $YbAgCu_4$ within the interval from 7.054 to 7.087 Å [5, 6, 11, 16, 17, 21–26]), and for $LuAgCu_4$, a = 7.094 Å [4]. We have not been able to find any publication, except [4], with a measurement of a for $LuAgCu_4$.

Taking the value of a obtained here for $LuAgCu_4$, and that for $YbAgCu_4$ from [4], one finds a positive value of 0.183% for B. According to [4], the values of B, for instance, for the $YbZnCu_4$–$LuZnCu_4$, $YbInCu_4$–$LuInCu_4$, and $YbCdCu_4$–$LuCdCu_4$ pairs, are 0.171, 0.140, and 0.168%, respectively. Thus, the anomaly found in [4] for the $YbAgCu_4$–$LuAgCu_4$ pair apparently does not exist. It may be conjectured that the parameter a quoted in [4] for $LuAgCu_4$ was overestimated for some reason.

The total heat conductivity κ_{bot} and total electrical resistivity ρ_{tot} were measured on a setup similar to that described in [26].

3. RESULTS AND DISCUSSION

Figure 1 presents our data and the figures quoted in [12] for $\rho_{tot}(T)$ of the $LuAgCu_4$ samples. For $T \gtrsim 25$ K, ρ_{tot} depends linearly on the temperature, which is characteristic of metals (and semimetals). For $T \lesssim 25$ K (down to 4.2 K), $\rho_{tot} \simeq \rho_0$ (ρ_0 is the residual electrical resistivity). As is seen from Fig. 1, ρ_0 turned out to be larger for the sample studied here than for the sample used in [12].

Figure 2 displays data on $\kappa_{tot}(T)$ for $LuAgCu_4$. For metals, one can write

$$\kappa_{tot} = \kappa_{ph} + \kappa_e, \quad (1)$$

where κ_{ph} and κ_e are the lattice and electronic heat conductivity components, respectively. By the classical theory of heat conductivity of metals [27, 28], κ_e obeys the Wiedemann–Franz relation

$$\kappa_e = LT/\rho_{tot}, \quad (2)$$

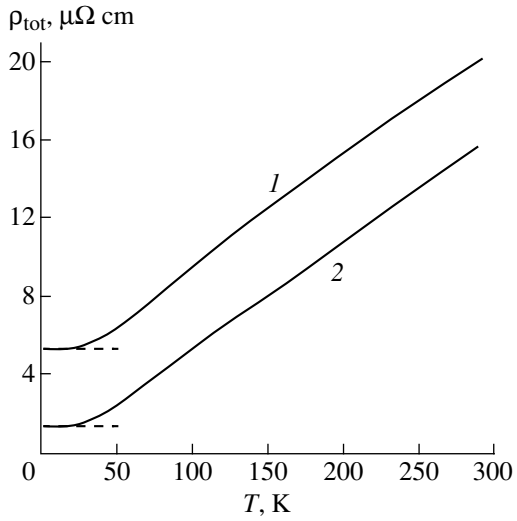

Fig. 1. Temperature dependence of ρ_{tot}: (*1*) our data, (*2*) data from [12].

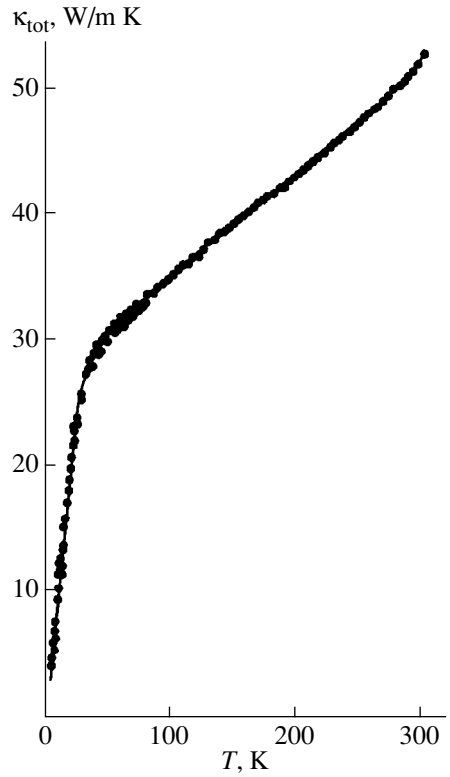

Fig. 2. Temperature dependence of κ_{tot} for the $LuAgCu_4$ sample studied.

where L is the Lorenz number. For moderate temperatures and "clean" metals, as well as for low and high temperatures and "dirty" metals, $L = L_0$, where L_0 is the Sommerfeld value of the Lorenz number ($L_0 = 2.45 \times 10^{-8}$ WΩ/K^2). The $LuAgCu_4$ sample we studied has a fairly large value of ρ_0. This suggests that we are deal-

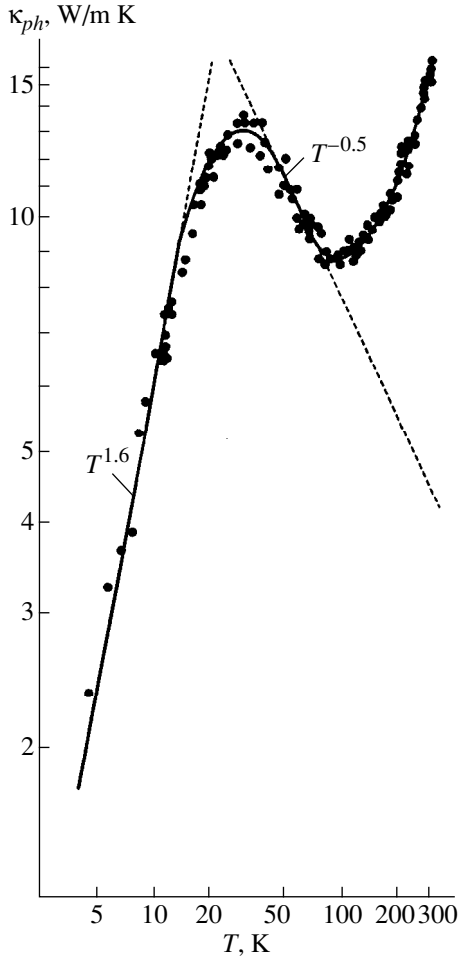

Fig. 3. Temperature dependence of κ_{ph} for the $LuAgCu_4$ sample studied. κ_e was calculated under the assumption $L = L_0$.

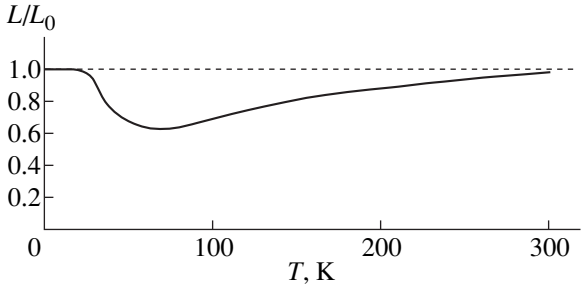

Fig. 4. Temperature dependence of L/L_0 for $LuAgCu_4$. Calculation made according to [32–34].

ing with a not very "clean" metal, so that one may accept $L = L_0$ throughout the temperature range studied in this paper.

Figure 3 presents data for κ_{ph} obtained using Eqs. (1) and (2). In calculating κ_e, we assumed $L = L_0$. As is seen from the figure, in the low-temperature domain, $\kappa_{ph} \sim T^{1.6}$, while in the interval from 30 to 100 K, we have $\kappa_{ph} \sim T^{-0.5}$. Such temperature dependences for κ_{ph} are characteristic of materials with defects. The defects present in the sample studied by us are probably not associated with the purity of the starting materials used to prepare $LuInCu_4$, but rather form as a result of Ag occupying Lu sites or Cu substituting for Ag, as was the case with $YbInCu_4$, where the experimentally observed "amorphous" behavior of $\kappa_{ph}(T)$ for $T > T_v$ [1] is connected either with In occupying Yb sites [29] or with Cu substituting for In [30].

For $T > 100$ K, $LuAgCu_4$ exhibits a deviation from the $\kappa_{ph} \sim T^{-0.5}$ relation. The heat conductivity κ_{ph} increases fairly strongly with temperature. This behavior of $\kappa_{ph}(T)$ could be accounted for by the emergence of a bipolar heat-conductivity component (κ_{bip}), characteristic of semimetals [2, 27, 32], for $T \gtrsim 100$ K. This conclusion is, however, at odds with the available literature data on measurements of the Hall constant [4, 13] and with theoretical calculations of the $LuAgCu_4$ band structure [17, 18], which suggest that this compound is apparently a metal (rather than a semimetal).

How else could one explain (other than by the semimetal concept proposed above and the emergence of κ_{bip}) the observed increase in κ for $T \gtrsim 100$ K in a metallic $LuAgCu_4$?

We have not been able to relate it to any effects exhibited within this temperature interval by the lattice component of heat conductivity. The only way out is to conjecture that it may be due to some errors made in the calculation of κ_e, namely, that L in the Wiedemann–Franz relation is not equal to L_0.

Consider some cases in which L may not equal L_0.

1. In order for $LuAgCu_4$ not to exhibit this effect of increase in κ, L for $T \gtrsim 100$ K must be larger than L_0. In metals, this can be observed under the conditions of interband interaction between heavy and light carriers in crossing subbands that form, for instance, the conduction band, when the heavy subband containing the Fermi level lies higher than the light one [27, 31, 32].

This situation can hardly be realized in $LuAgCu_4$, because it appears impossible that within a fairly broad temperature range (4.2–100 K) $L = L_0$, while for $T \gtrsim 100$ K, $L > L_0$. Such a behavior of $L(T)$ has not been observed thus far for any material, and it is not anticipated to occur within the above model [31].

2. It is possible that $L \neq L_0$ throughout the temperature range studied. For metals both above and below the

Debye temperature Θ, the ratio L/L_0 can be presented in the form [32–34]

$$L/L_0 = \left[\frac{\rho_0}{4A_0} + \left(\frac{T}{\Theta}\right)^5 I_5\left(\frac{\Theta}{T}\right)\right] \Big/ \left[\frac{\rho_0}{4A_0} + \chi\left(\frac{T}{\Theta}, \frac{D}{\xi}\right)\right], \quad (3)$$

where ρ_0 is the residual electrical resistivity;

$$\chi\left(\frac{T}{\Theta}, \frac{D}{\xi}\right) = \left(\frac{T}{\Theta}\right)^5 \times \left\{\left[1 + \frac{3}{2\pi^2}\frac{\xi}{D}\left(\frac{\Theta}{T}\right)^2\right] I_5\left(\frac{\Theta}{T}\right) - \frac{1}{2\pi^2} I_7\left(\frac{\Theta}{T}\right)\right\}; \quad (4)$$

ξ is the Fermi energy for the carriers; $I_5(\Theta/T)$ and $I_7(\Theta/T)$ are integrals tabulated in [35, 36]; and A_0 is a constant including the electron–phonon coupling constant and depending on the lattice constant, Fermi energy, atomic mass, and Debye temperature. D is also a constant. The quantities D/ξ and A_0 can be roughly estimated from the following relations [32, 34]:

$$D/\xi = 2^{-1/3} N_a^{-2/3}, \quad (5)$$

$$\rho_i = \rho_{tot} - \rho_0 = \frac{A_0 T}{\Theta} \quad (\text{at } T/\Theta \gtrsim 0.6), \quad (6)$$

where N_a is the number of free electrons per atom and ρ_i is the part of the electrical resistivity due to scattering from lattice vibrations.

A very rough estimate of L/L_0 made using Eqs. (3)–(6) for the $LuAgCu_4$ sample studied by us is shown graphically in Fig. 4. The Debye temperature accepted in the calculations is 257 K [4]. One readily sees that, within the 25–300-K range, L is even somewhat smaller than L_0. Figure 5 (curve *1*) plots κ_{ph} calculated from Eqs. (1) and (2), with κ_e in the Wiedemann–Franz relation obtained using the values of L from Fig. 4. Shown also for comparison are data for $\kappa_{ph}(T)$ obtained in the calculation of κ_e with $L = L_0$ from Fig. 3. The two $\kappa_{ph}(T)$ plots (curves *1*, *2* in Fig. 5) do not differ qualitatively from one another. In both cases, an additional contribution to κ is seen to exist for $T \gtrsim 100$ K.

It should be pointed out that the $\kappa_{ph}(T)$ relation constructed using data for L from Fig. 4 (curve *1* in Fig. 5) is consistent with the real pattern of behavior of lattice heat conductivity.

One might question the weak temperature dependence for the linear region, $\kappa_{ph} \sim T^{-0.2}$, within the 30–100-K interval and the very approximate and, possibly, not fully valid estimation of the L/L_0 ratio from expressions (3)–(6) for such a complex metal as $LuAgCu_4$.

We believe that the data obtained in the calculation of $\kappa_{ph}(T)$ made under the assumption of $L = L_0$ are more trustworthy.

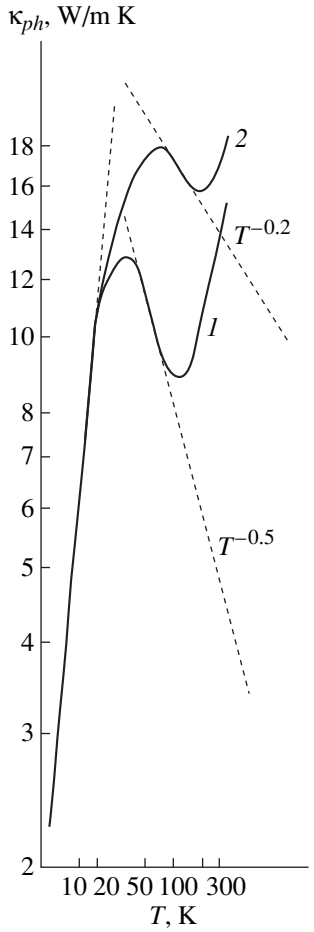

Fig. 5. Temperature dependence of κ_{ph} for $LuAgCu_4$. The calculation was made with κ_e determined under various assumptions: (*1*) $L = L_0$, (*2*) data for L taken from Fig. 4.

Thus, the above reasoning suggests that $LuAgCu_4$ is a semimetal. The related compounds $LuInCu_4$, $YbInCu_4$ (for $T > T_v$), and $YInCu_4$ are also known to be semimetals [2, 37–39].

4. CONCLUSIONS

We reached the following conclusions:

(1) There is apparently no anomaly associated with the lattice constant of $LuAgCu_4$ reported in [4].

(2) An analysis of the heat conductivity data for $LuAgCu_4$ suggests that this compound is a semimetal, similar to its related compounds $LuInCu_4$, $YbInCu_4$ (for $T > T_v$), and $YInCu_4$.

ACKNOWLEDGMENTS

The authors are indebted to N.F. Kartenko and N.V. Sharenkova for the x-ray structural measurements.

The work was conducted as a bilateral agreement between the Russian and Polish Academies of Sciences. This study was supported by the Russian Foundation for Basic Research, grant no. 99-02-18078.

REFERENCES

1. I. A. Smirnov, L. S. Parfen'eva, A. Jezowski, *et al.*, Fiz. Tverd. Tela (St. Petersburg) **41** (9), 1548 (1999) [Phys. Solid State **41**, 1418 (1999)].
2. A. V. Golubkov, L. S. Parfen'eva, I. A. Smirnov, *et al.*, Fiz. Tverd. Tela (St. Petersburg) **42** (8), 1357 (2000) [Phys. Solid State **42**, 1394 (2000)].
3. A. V. Gotsev and G. Bruls, submitted to Phys. Rev. B.
4. J. L. Sarrao, C. D. Immer, Z. Fisk, *et al.*, Phys. Rev. B **59** (10), 6855 (1999).
5. E. Bauer, Adv. Phys. **40** (4), 417 (1991).
6. N. Tsujii, J. He, K. Yoshimura, *et al.*, Phys. Rev. B **55** (2), 1032 (1997).
7. M. J. Besnus, P. Haen, N. Hamdaoui, *et al.*, Physica B (Amsterdam) **163**, 571 (1990).
8. N. Pilmayr, E. Bauer, and K. Yoshimura, J. Magn. Magn. Mater. **104–107**, 639 (1992).
9. P. Schlottmann, J. Appl. Phys. **73** (10), 5412 (1993).
10. T. Graf, J. M. Lawrence, M. F. Hundley, *et al.*, Phys. Rev. B **51** (21), 15053 (1995).
11. A. Severing, A. P. Murani, J. D. Thompson, *et al.*, Phys. Rev. B **41** (4), 1739 (1990).
12. E. Bauer, R. Hauser, E. Gratz, *et al.*, Phys. Rev. B **48** (21), 15873 (1993).
13. A. L. Cornelius, J. M. Lawrence, J. L. Sarrao, *et al.*, Phys. Rev. B **56** (13), 7993 (1997).
14. J. M. Lawrence, G. H. Kwei, P. C. Canfield, *et al.*, Phys. Rev. B **49** (3), 1627 (1994).
15. J. S. Kang, J. W. Allen, C. Rossel, *et al.*, Phys. Rev. B **41** (7), 4078 (1991).
16. H. Nakamura, K. Nakajima, Y. Kitaoka, *et al.*, Physica B (Amsterdam) **171**, 238 (1990).
17. A. Continenza and P. Monachesi, J. Appl. Phys. **79** (8), 6423 (1996).
18. P. Monachesi and A. Continenza, Phys. Rev. B **54** (19), 13558 (1996).
19. A. V. Golubkov, T. B. Zhukova, and V. M. Sergeeva, Izv. Akad. Nauk SSSR, Neorg. Mater. **2** (11), 77 (1966).
20. A. V. Golubkov and V. M. Sergeeva, Preprint (Institute of Metal Physics, Ural Division, USSR Academy of Sciences, Sverdlovsk, 1977).
21. R. Casanova, D. Jaccard, C. Marcenat, *et al.*, J. Magn. Magn. Mater. **90/91**, 587 (1990).
22. D. T. Adroja, S. K. Malik, B. D. Padalia, and R. Vijayaraghavan, J. Phys. C: Solid State Phys. **20**, L307 (1987).
23. C. Rossel, K. N. Yang, M. B. Maple, *et al.*, Phys. Rev. B **35** (4), 1914 (1987).
24. J. L. Sarrao, C. L. Benton, Z. Fisk, *et al.*, Physica B (Amsterdam) **223/224**, 366 (1996).
25. J. L. Sarrao, C. D. Immer, C. L. Benton, *et al.*, Phys. Rev. B **54** (17), 12207 (1996).
26. A. Jezowski, J. Mucha, and G. Pompe, J. Phys. D **20**, 1500 (1987).
27. I. A. Smirnov and V. I. Tamarchenko, *Electron Heat Conductivity in Metals and Semiconductors* [in Russian] (Nauka, Leningrad, 1977).
28. R. Berman, *Thermal Conduction in Solids* (Clarendon Press, Oxford, 1976; Mir, Moscow, 1979).
29. J. M. Lawrence, G. H. Kwei, J. L. Sarrao, *et al.*, Phys. Rev. B **54** (9), 6011 (1996).
30. A. Loffert, M. L. Aigner, F. Ritter, and W. Assmus, Cryst. Res. Technol. **34**, 267 (1999).
31. N. V. Kolomoets, Fiz. Tverd. Tela (Leningrad) **8** (4), 997 (1966) [Sov. Phys. Solid State **8**, 799 (1966)].
32. V. S. Oskotskiĭ and I. A. Smirnov, *Defects in Crystals and Thermal Conductivity* [in Russian] (Nauka, Leningrad, 1972).
33. A. H. Wilson, *The Theory of Metals* (Cambridge Univ. Press, Cambridge, 1954).
34. J. L. Olsen and H. M. Rosenberg, Adv. Phys. **2**, 28 (1953).
35. L. Colquitt, J. Appl. Phys. **36**, 2454 (1965).
36. E. H. Sondheimer, Proc. R. Soc. London, Ser. A **203**, 75 (1950).
37. H. Nakamura, K. Ito, and M. Shiga, J. Phys.: Condens. Matter **6**, 9201 (1994).
38. K. Takegahara and T. Kasuya, J. Phys. Soc. Jpn. **59** (9), 3299 (1990).
39. H. Nakamura, K. Ito, A. Uenishi, *et al.*, J. Phys. Soc. Jpn. **62** (5), 1446 (1993).

Translated by G. Skrebtsov

Physics of the Solid State, Vol. 42, No. 11, 2000, pp. 1995–1999. Translated from Fizika Tverdogo Tela, Vol. 42, No. 11, 2000, pp. 1943–1947.

METALS AND SUPERCONDUCTORS

Self-Consistent Band Structure Calculations for the Compounds TiN, $Ti_{0.75}Zr_{0.25}N$, $Ti_{0.25}Zr_{0.75}N$, and ZrN by the Linear Method of Augmented Slater Orbitals

N. G. Yakutovich*, N. N. Dorozhkin*, V. M. Anishchik*, and B. V. Novysh**

**Belarussian State University, ul. Leningradskaya 14, Minsk, 220080 Belarus*

e-mail: yakutovich@phys.bsu.unibel.by

***Institute of Solid-State and Semiconductor Physics, Belarussian Academy of Sciences, ul. Brovki 17, Minsk, 220072 Belarus*

Received November 26, 1999; in final form, April 10, 2000

Abstract—The physical properties of the stoichiometric compounds in the series Ti–Zr–N are studied theoretically, including electronic structure calculations by the linear augmented Slater orbitals method, as well as calculation of the bulk elastic moduli and the equilibrium lattice constant. The results obtained can be used for determining the phases of the materials used for protective coatings. *© 2000 MAIK "Nauka/Interperiodica".*

Research and development of new technological materials with unique physical properties and a comparatively low cost constitute one of the most important problems of modern materials science. Considerable attention is paid to materials that could be used for creating protective coatings. Protective coatings usually contain metals like Ti, Mo, Cr, and Zr that have a large number of *d* electrons and form well-defined covalent bonds with the metalloids present in the coating. The compounds obtained have a high strength and a high melting point. Binary systems of the type Me–X (Me stands for a *d* metal and X for a metalloid) have been investigated quite comprehensively. At present, investigations of ternary and more complex compounds are being carried out.

Calculations of the energy band structure form the basis for the theoretical investigations of the physical and chemical properties of materials. A large number of different methods, each with its own advantages and drawbacks, have been developed for calculating the electronic structure of crystalline solids [1–3]. For example, the traditional augmented plane wave (APW) and Korringa–Kohn–Rostocker (KKR) methods have a high accuracy, but a low count rate, and are unsuitable for self-consistent calculations of complex crystalline systems with a large number of atoms in the unit cell. Linear methods (LAPW, LMTO, etc.) are faster at the expense of computational accuracy and are actively used for calculating the electronic structure and physical properties of quite diverse solids with different crystal structures and all kinds of chemical bonds. The speed of the calculations depends on the available computational facilities. The electronic structure of systems containing several hundred atoms in the unit cell can be calculated with the help of supercomputers. Such calculations require high-precision and efficient methods. One of these is the linearized augmented Slater orbital (LASTO) method developed by Davenport *et al.* [4–7]. Among other things, this method was used for a theoretical interpretation of the x-ray absorption spectra and the short-range order in Au–Ta alloys [8].

The formalism of the LASTO method for an arbitrary number of atoms in the unit cell has not been published in the literature thus far. In order to fill this gap, we present in the Appendix all the expressions required for calculating the band structure of crystalline solids with an arbitrary basis.

The wave function in the LASTO method [4–7] is presented in the form

$$\Psi_k(\mathbf{r}) = \sum_N c_N \psi_N(\mathbf{r}), \tag{1}$$

where

$$\psi_N(\mathbf{r}) = \frac{1}{\sqrt{N_c}} \sum_{\mathbf{R}_\nu} e^{i\mathbf{k}\mathbf{R}_\nu} \phi_{nlm}(\mathbf{r} - \boldsymbol{\tau}_i - \mathbf{R}_\nu), \tag{2}$$

$N = \{i, nlm\}$ is the position of the ith atom in the unit cell, $\mathbf{R}_\nu$ is the lattice vector, and $\phi_{nlm}(\mathbf{r})$ is the Slater orbital outside the MT spheres joined at the MT boundary with the exact solution of the Schrödinger equation inside the MT spheres:

$$\phi_{nlm}(\mathbf{r}) = A_n r^{n-1} e^{-\xi r} Y_{lm}(\mathbf{r}), \tag{3}$$

$$A_n = (2\xi)^{n+\frac{1}{2}} [(2n)!]^{-\frac{1}{2}}. \tag{4}$$

1063-7834/00/4211-1995$20.00

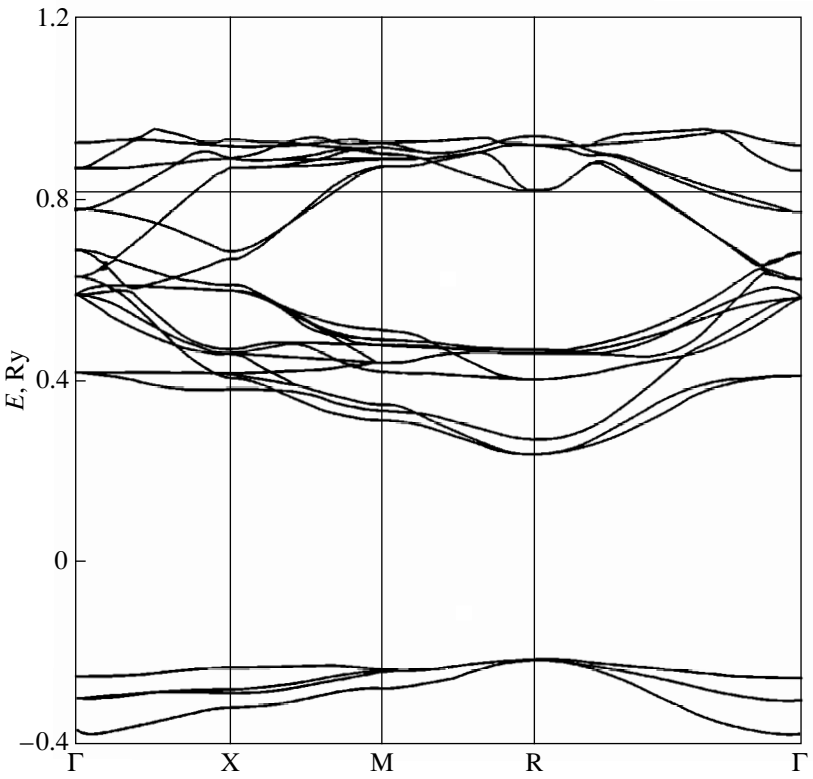

Fig. 1. Band structure of $Zr_{0.25}Ti_{0.75}N$.

The Fourier transform of Slater's orbital is known and has a simple form:

$$\phi_{nL}(\mathbf{q}) = \frac{4\pi}{\Omega}(i)^{-l}Y_L(\mathbf{r})\int_0^\infty dr\, j_l(qr)r^{n+1}\exp(-\xi r), \quad (5)$$

where Ω is the primitive unit cell volume. The integral in Eq. (5) can easily be evaluated analytically. In light of the above relations, the function $\psi_N(\mathbf{r})$ can be presented in the form

$$\psi_N(\mathbf{r}) = \frac{1}{\sqrt{N_c}}\sum_{\mathbf{q}} e^{i\mathbf{q}\cdot\mathbf{r}}e^{i\mathbf{q}\cdot\tau_i}\phi_{nL}(\mathbf{q}), \quad (6)$$

where $\mathbf{q} = \mathbf{k} + \mathbf{g}$. The function $\psi(\mathbf{r})$ in the form of Eq.(2) is used only outside the MT spheres, while the numerical solution of the radial Schrödinger equation is used inside the MT spheres. Inside the *j*th sphere, the basis function is chosen in the form of a linear combination of radial wave functions $g_{j\lambda}(\mathbf{r}_j)$ and their energy derivatives $\dot{g}_{j\lambda}(\mathbf{r}_j)$:

$$\psi_N(\mathbf{r}) = \sum_\Lambda [\beta_{N,j\Lambda}g_{j\lambda} + \alpha_{N,j\Lambda}\dot{g}_{j\lambda(\mathbf{r}_j)}]Y_\Lambda(\mathbf{r}_j), \quad (7)$$

where the coefficients $\beta_{N,j\Lambda}$ and $\alpha_{N,j\Lambda}$ are determined from the joining condition for the basis functions at the surface of the MT spheres.

The matrix elements of the Hamiltonian *H* and the overlapping matrix *S* are defined in the standard form:

$$H_{NN'} = \int \psi_N^*(\mathbf{r})H\psi_{N'}(\mathbf{r})d\mathbf{r}, \quad (8)$$

$$S_{NN'} = \int \psi_N^*(\mathbf{r})\psi_{N'}(\mathbf{r})d\mathbf{r}. \quad (9)$$

The explicit form of the matrix elements is presented in the Appendix.

In this work, we present the results of calculations for a number of compounds of the system (Ti–Zr)N, which can also be used to determine some of their physical properties. Calculations were made for the compounds TiN, $Zr_{0.25}Ti_{0.75}N$, $Ti_{0.25}Zr_{0.75}N$, and ZrN by using the extended unit cell. This cell belongs to a simple cubic lattice and contains eight atoms. The compounds TiN and ZrN have two types of nonequivalent atoms, while the compounds $Zr_{0.25}Ti_{0.75}N$ and $Ti_{0.25}Zr_{0.75}N$ have four types of nonequivalent metal atoms and two types of nitrogen atoms each. Calculations were made for 56 vectors of the irreducible part of the Brillouin zone with the Barth–Hedin exchange-correlation potential. The total and partial densities of states were calculated by the method of tetrahedra. Figure 1 shows the band structure of the compound

$Zr_{0.25}Ti_{0.75}N$ calculated from the standard contour for a simple cubic lattice. As usual, the *s* bands of TiN and ZrN have a three-fold degeneracy at the point Γ, while one band is split off in $Zr_{0.25}Ti_{0.75}N$ and $Ti_{0.25}Zr_{0.75}N$, and the *s* band has only a two-fold degeneracy. This can be attributed to the emergence of a different kind of atom in the unit cell, which lowers its local symmetry. The bands in the vicinity of the Fermi level are flatter for $Zr_{0.25}Ti_{0.75}N$ (since they are predominantly populated by the *p* electrons of nitrogen) than the analogous bands for ZrN and $Ti_{0.25}Zr_{0.75}N$, which is due to the heavy mixture of *d* states in these compounds. The total density of states for the compound $Zr_{0.25}Ti_{0.75}N$ is shown in Fig. 2. The densities of states for all the compounds investigated are identical on the whole. Three peaks can be singled out in the diagram, the first of which is associated with the *s* electrons of nitrogen. The second peak is split into two parts, which are occupied predominantly by the *p* electrons of the metal and the *p* electrons of nitrogen. The third peak is mainly associated with the *p* and *d* electrons of the metal. The Fermi level is usually located on the left side of this peak. For the materials $Ti_{0.25}Zr_{0.75}N$ and ZrN, two-thirds of this peak is due to the *p* electrons of nitrogen and metals, while the remaining states are occupied by the *d* electrons of Zr. For the two other compounds, the *p* states of nitrogen mainly contribute to the density of states near the Fermi level, while the contribution of *d* electrons of the metals is negligible. The band structure calculations were used to estimate the bulk elastic moduli for these compounds. The diagram of state $p = p(V)$ can be constructed by varying the lattice constant for a compound and calculating the electron gas pressure in the MT spheres. The bulk moduli can then be easily evaluated from the formula

$$B = V\left(\frac{dp}{dV}\right)_{V = V_0},$$

where V_0 is the equilibrium volume of a unit cell. Self-consistent band calculations were made for various lattice constants of the investigated compounds near the equilibrium value for each compound. The results of calculations of the bulk elastic moduli and the theoretically calculated equilibrium lattice constants of the compounds are in good agreement with the experimental values. Since this system forms a continuous series of solutions, the values of the lattice constants depend almost linearly on the concentration of metals in the compound. The table contains the calculated values of the equilibrium lattice constants of the compounds.

The theoretical values of the elastic moduli of the compounds were found to be slightly higher than the experimental values [9]. This is probably due to the difficulty in obtaining purely stoichiometric compositions. For example, the Ti sublattice in TiN may contain a large number of vacancies, which considerably lower the bulk elastic modulus. The same case occurs for other compounds in the system (Ti–Zr)N.

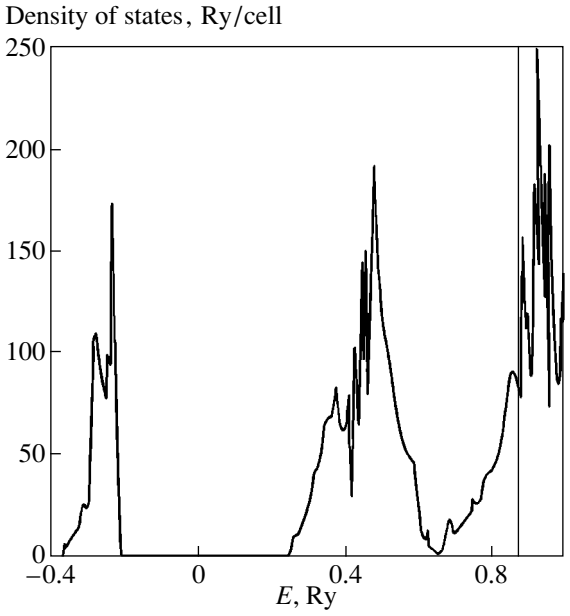

Fig. 2. Density of States of $Zr_{0.25}Ti_{0.75}N$.

In a number of recent works on the sputtering technique and investigations of protective coatings based on TiN and ZrN [10], the bulk elastic moduli were measured for the composite materials obtained. These moduli were calculated from the experimental data on the velocity of sound in film coatings. The critical review by Kral *et al*. [11] contains the values of Young's moduli for TiN and ZrN, which are found to differ from the theoretical values by not more than 10%.

Thus, the results of our investigations indicate that this method can be used effectively for calculating the physical properties of crystalline materials. This method can also be modified easily for calculating the properties of two-dimensional, quasi-one-dimensional, and nano systems, as well as for three-dimensional crystals with lattice defects, which is undoubtedly interesting for the study of implanted crystals. The LASTO method has a high accuracy and a higher speed than the method of linearized augmented plane waves and can be used effectively for calculating the energy band structure of ternary stoichiometric compounds. The inclusion of non-MT corrections in the computations should lead to a more correct description of the

Equilibrium lattice constants and bulk elastic moduli for compounds of the system (Ti–Zr)N

Compound	Lattice constant, nm	Bulk elastic modulus, GPa
TiN	0.4180	346.7
$Zr_{0.25}Ti_{0.75}N$	0.4422	224.0
$Ti_{0.25}Zr_{0.75}N$	0.4537	194.6
ZrN	0.4557	258.8

peculiarities of the chemical bonds in the compounds investigated.

APPENDIX

The matrix elements of the Hamiltonian can be presented as the sum of matrix elements of the Hamiltonian with the MT potential and non-MT corrections:

$$H_{NN'} = H_{NN'}^{MT} + H_{NN'}^{NMT}. \quad \text{(A1)}$$

In turn, the non-MT corrections can be presented as the sum of components for the regions inside the spheres and between them:

$$H_{NN'}^{NMT} = H_{NN'}^{\text{sp}} + H_{NN'}^{\text{out}}. \quad \text{(A2)}$$

As usual, the crystal potential is expanded into a Fourier series in the region between the spheres,

$$V(\mathbf{r}) = \sum_{\mathbf{g}} \exp(i\mathbf{g}\cdot\mathbf{r})V(\mathbf{g}), \quad \text{(A3)}$$

and is expanded into a series in spherical harmonics for the MT spheres,

$$V(\mathbf{r}) = \sum_{L} V_L(r_j)Y_L(\mathbf{r}_j). \quad \text{(A4)}$$

It can be shown [5] that the contribution $H_{NN'}^{\text{sp}}$ has the form

$$\begin{aligned} H_{NN'}^{\text{sp}} = \sum_{\Lambda,\Lambda',L} \int Y_L Y_\Lambda^* Y_{\Lambda'} d\dot{r} \Big[& \beta_{N,j\Lambda}^* \beta_{N',j\Lambda'} \int g_{j\lambda} V_L^j g_{j\lambda'} r^2 dr \\ & + \beta_{N,j\Lambda}^* \alpha_{N',j\Lambda'} \int g_{j\lambda} V_L^j \dot{g}_{j\lambda'} r^2 dr \\ & + \alpha_{N,j\Lambda}^* \beta_{N',j\Lambda'} \int \dot{g}_{j\lambda} V_L^j g_{j\lambda'} r^2 dr \\ & + \alpha_{N,j\Lambda}^* \alpha_{N',j\Lambda'} \int \dot{g}_{j\lambda} V_L^j \dot{g}_{j\lambda'} r^2 dr \Big]. \end{aligned} \quad \text{(A5)}$$

We define the function $\theta(\mathbf{r})$ as follows:

$$\theta(\mathbf{r}) = \begin{cases} 1 & \text{in the space between spheres} \\ 0 & \text{outside it.} \end{cases}$$

The Fourier transform $\theta(\mathbf{g})$ of this function can be determined easily in this case [7]:

$$\theta(\mathbf{g}) = \delta_{\mathbf{g},0} - \frac{4\pi}{\Omega} \sum_{\gamma} \frac{\exp(-i\mathbf{g}\cdot\boldsymbol{\tau}_\gamma) R_\gamma^3 j_1(gR_\gamma)}{gR_\gamma}. \quad \text{(A6)}$$

We can now obtain the following expression for the interspherical part of the non-MT corrections:

$$H_{NN'}^{\text{int}} = \Omega \sum_{\mathbf{g}} \phi_N^*(\mathbf{g}) T_i^*(\mathbf{g}) \sum_{\mathbf{g}} f(\mathbf{g}-\mathbf{g}')\phi_N(\mathbf{g}')T_i(\mathbf{g}'), \quad \text{(A7)}$$

where $f(\mathbf{r}) = V(\mathbf{r})\theta(\mathbf{r})$, and $f(\mathbf{g}-\mathbf{g}')$ is defined with the help of the fast Fourier transformation.

Let us now calculate the matrix elements of the Hamiltonian with the MT potential and the elements of the overlapping matrix. For this purpose, we compute the matrix elements involving the functions in Eq.(7) with the MT potential inside the MT spheres (region I) and replace the integral over the outer region (II) by the integral over the entire space with the Hamiltonian $H_{\text{II}} = [-\nabla^2 + V_0]$ minus the integral over the MT spheres with the same Hamiltonian H_{II}. The matrix elements can be written as the sum of three integrals:

$$H_{NN'}^{MT} = H_1 + H_2 + H_3, \quad \text{(A8)}$$

$$S_{NN'}^{MT} = S_1 + S_2 + S_3, \quad \text{(A9)}$$

$$H_1 = N_c \sum_{\nu} \int_{\Omega_\nu} \psi_N^*(\mathbf{r}) H_{\text{I}} \psi_{N'}(\mathbf{r}) d\mathbf{r}, \quad \text{(A10)}$$

$$H_2 = \int_V \psi_N^*(\mathbf{r}) H_{\text{II}} \psi_{N'}(\mathbf{r}) d\mathbf{r}, \quad \text{(A11)}$$

$$H_3 = -N_c \sum_{\nu} \int_{\Omega_\nu} \psi_N^*(\mathbf{r}) H_{\text{II}} \psi_{N'}(\mathbf{r}) d\mathbf{r}. \quad \text{(A12)}$$

Let us now evaluate each integral successively:

$$\begin{aligned} H_1 &= N_c \sum_{\nu} \int_{\Omega_\nu} \psi_N^*(\mathbf{r}) H_{\text{I}} \psi_{N'}(\mathbf{r}) d\mathbf{r} \\ &= \sum_{\nu} \int_{\Omega_\nu} \left(\sum_{\Lambda} [\beta_{N,\nu\Lambda}^* g_{\nu\lambda}(r_\nu) + \alpha_{N,\nu\Lambda}^* \dot{g}_{\nu\lambda}(r_\nu)] Y_\Lambda^*(\mathbf{r}_\nu) \right) \\ &\times H_{\text{I}} \left(\sum_{\Lambda'} [\beta_{N',\nu\Lambda'} g_{\nu\lambda'}(r_\nu) + \alpha_{N',\nu\Lambda'} \dot{g}_{\nu\lambda'}(r_\nu)] Y_{\Lambda'}(\mathbf{r}_\nu) \right) \quad \text{(A13)} \\ &= \sum_{\nu} \sum_{\Lambda} \epsilon (\beta_{N,\nu\lambda}^* \beta_{N',\nu\Lambda} + \alpha_{N,\nu\Lambda}^* \alpha_{N',\nu\Lambda} \langle \dot{g}_{\nu\lambda} | \dot{g}_{\nu\lambda} \rangle \\ &+ \beta_{N,\nu\Lambda}^* \alpha_{N',\nu\Lambda} + \alpha_{N,\nu\Lambda}^* \beta_{N',\nu\Lambda}), \end{aligned}$$

$$H_2 = \int_V \psi_N^*(\mathbf{r})[-\nabla^2 + V_0]\psi_{N'}(\mathbf{r}) d\mathbf{r}$$

$$= \int_V \frac{1}{\sqrt{N_c}}\frac{1}{\nu}\sum_{\mathbf{g}} e^{-i(\mathbf{k}+\mathbf{g})\mathbf{r}}\phi_N^*(\mathbf{g})T_i^*(\mathbf{g})\frac{1}{\sqrt{N_c}}\frac{1}{\nu}$$

$$\times \sum_{\mathbf{g}'} e^{-i(\mathbf{k}+\mathbf{g})\mathbf{r}}(|\mathbf{k}+\mathbf{g}|^2 + V_0)\phi_{N'}(\mathbf{g})T_j(\mathbf{g}')d\mathbf{r} \quad \text{(A14)}$$

$$= \frac{1}{\nu}\sum_{\mathbf{g}} T_i^*(\mathbf{g})\phi_N^*(\mathbf{k}+\mathbf{g})(|\mathbf{k}+\mathbf{g}|^2 + V_0)\phi_{N'}(\mathbf{k}+\mathbf{g})T_j(\mathbf{g}),$$

$$H_3 = -N_c\sum_{\nu}\int_{\Omega_\nu}\psi_N^*(\mathbf{r})[-\nabla^2 + V_0]\psi_{N'}(\mathbf{r})d\mathbf{r}$$

$$= \sum_{\nu}\int_{\Omega_\nu}\psi_N^*(\mathbf{r})\nabla^2\psi_{N'}(\mathbf{r})d\mathbf{r} - V_0\sum_{\nu}\int_{\Omega_\nu}\psi_N^*(\mathbf{r})\psi_{N'}(\mathbf{r})d\mathbf{r}$$

$$= -\frac{1}{\nu^2}\sum_{\mathbf{g}}\sum_{\mathbf{g}'} T_i^*(\mathbf{g})\phi_N^*(\mathbf{g})[(\mathbf{k}+\mathbf{g})(\mathbf{k}+\mathbf{g}) + V_0] \quad \text{(A15)}$$

$$\times \phi_{N'}(\mathbf{g}')T_j(\mathbf{g}')\sum_{\nu} 4\pi R_\nu^2\frac{j_1(|\mathbf{g}-\mathbf{g}'|R_\nu)}{|\mathbf{g}-\mathbf{g}'|}e^{i(\mathbf{g}'-\mathbf{g})\mathbf{r}_\nu}$$

$$+ \sum_{\nu}\sum_{\Lambda}[\beta_{N,\nu\Lambda}^*\beta_{N',\nu\Lambda}g_{\nu\lambda}g'_{\nu\lambda} + \beta_{N,\nu\Lambda}^*\alpha_{N',\nu\Lambda}g_{\nu\lambda}\dot{g}'_{\nu\lambda}$$

$$+ \alpha_{N,\nu\Lambda}^*\beta_{N',\nu\Lambda}\dot{g}_{\nu\lambda}g'_{\nu\lambda} + a_{N,\nu\Lambda}^*\alpha_{N',\nu\lambda}\dot{g}'_{\nu\lambda}]R_\nu^2.$$

Combining all three integrals, we finally obtain the following expression for the matrix elements of the Hamiltonian operator:

$$H_{NN'}^{MT} = \sum_{\nu}\sum_{\Lambda}\epsilon(\beta_{N,\nu\Lambda}^*\beta_{N',\nu\Lambda} + \alpha_{N,\nu\Lambda}^*\alpha_{N',\nu\Lambda}\langle\dot{g}_{\nu\lambda}|\dot{g}_{\nu\lambda}\rangle)$$

$$+ \sum_{\nu}\sum_{\Lambda}R_\nu^2[g'_{\nu\lambda}\dot{g}_{\nu\lambda}(\beta_{N,\nu\Lambda}^*\alpha_{N',\nu\Lambda} + \alpha_{N,\nu\Lambda}^*\beta_{N',\nu\Lambda})$$

$$+ \beta_{N,\nu\Lambda}^*\beta_{N',\nu\Lambda}g_{\nu\lambda}g'_{\nu\lambda} + \alpha_{N,\nu\Lambda}^*\alpha_{N',\nu\Lambda}\dot{g}_{\nu\lambda}\dot{g}'_{\nu\lambda}] \quad \text{(A16)}$$

$$+ \frac{1}{\nu}\sum_{\mathbf{g}} T_i^*(\mathbf{g})\phi_N^*(\mathbf{k}+\mathbf{g})(|\mathbf{k}+\mathbf{g}|^2 + V_0)\phi_{N'}(\mathbf{k}+\mathbf{g})T_j(\mathbf{g})$$

$$- \frac{1}{\nu^2}\sum_{\mathbf{g}}\sum_{\mathbf{g}''} T_i^*(\mathbf{g})\phi_N^*(\mathbf{g})[(\mathbf{k}+\mathbf{g})(\mathbf{k}+\mathbf{g}') + V_0]$$

$$\times \phi_{N'}(\mathbf{g}')T_j(\mathbf{g}')\sum_{\nu} 4\pi R_\nu^2\frac{j_1(|\mathbf{g}-\mathbf{g}'|R_\nu)}{|\mathbf{g}-\mathbf{g}'|}e^{i(\mathbf{g}'-\mathbf{g})\mathbf{r}_\nu}.$$

The elements of the overlapping matrix are obtained in an analogous manner and have the form

$$S_{NN'}^{MT} = \sum_{\nu}\sum_{\Lambda}\epsilon(\beta_{N,\nu\Lambda}^*\beta_{N',\nu\Lambda} + \alpha_{N,\nu\Lambda}^*\alpha_{N',\nu\Lambda}\langle\dot{g}_{\nu\lambda}|\dot{g}_{\nu\lambda}\rangle)$$

$$+ \frac{1}{\nu}\sum_{\mathbf{g}} T_i^*(\mathbf{g})\phi_N^*(\mathbf{k}+\mathbf{g})\phi_{N'}(\mathbf{k}+\mathbf{g})T_j(\mathbf{g}) \quad \text{(A17)}$$

$$- \frac{1}{\nu^2}\sum_{\mathbf{g}}\sum_{\mathbf{g}'} T_i^*(\mathbf{g})\phi_N^*(\mathbf{g})\phi_{N'}(\mathbf{g}')T_j(\mathbf{g}')$$

$$\times \sum_{\nu} 4\pi R_\nu^2\frac{j_1(|\mathbf{g}-\mathbf{g}'|R_\nu)}{|\mathbf{g}-\mathbf{g}'|}e^{i(\mathbf{g}'-\mathbf{g})\mathbf{r}_\nu}.$$

REFERENCES

1. G. G. Koelling, Rep. Prog. Phys. **44** (2), 139 (1981).
2. O. K. Andersen, Phys. Rev. B **12** (8), 3060 (1975).
3. D. D. Koelling and G. O. Arbman, J. Phys. F **5** (11), 2041 (1975).
4. J. W. Davenport, Phys. Rev. B **29** (6), 2896 (1984).
5. J. W. Davenport, M. Weinert, and R. E. Watson, Phys. Rev. B **32** (8), 4876 (1985).
6. J. W. Davenport, R. E. Watson, and M. Weinert, Phys. Rev. B **32** (8), 4883 (1985).
7. G. W. Fernando, J. W. Davenport, R. E. Watson, and M. Weinert, Phys. Rev. B **40** (5), 2757 (1989).
8. M. Khun, R. Sammynaiken, and T. K. Sham, Physica B (Amsterdam) **252** (11), 114 (1998).
9. G. V. Samsonov and I. M. Vinitskii, *Handbook of Refractory Compounds* (Metallurgiya, Moscow, 1976; Plenum, New York, 1980).
10. E. Kusano, M. Kitagawa, Y. Kuroda, *et al.*, Thin Solid Films **334**, 151 (1998).
11. C. Kral, W. Lengauer, D. Rafaja, and P. Ettmayer, J. Alloys Compd. **265** (1–2), 215 (1998).

Translated by N. Wadhwa

Physics of the Solid State, Vol. 42, No. 11, 2000, pp. 2000–2003. Translated from Fizika Tverdogo Tela, Vol. 42, No. 11, 2000, pp. 1948–1951.

METALS AND SUPERCONDUCTORS

Splitting of Dislocations in Low-Angle Grain Boundaries in Oxide Superconductors

M. Yu. Gutkin and I. A. Ovid'ko

Institute of Problems of Machine Science, Russian Academy of Sciences, Bol'shoĭ pr. 61, Vasil'evskiĭ Ostrov, St. Petersburg, 199178 Russia

e-mail: ovidko@def.ipme.ru

Received March 28, 2000

Abstract—A theoretical model for the description of the experimentally observed ([1] M.F. Chisholm, D.A. Smith, Philos. Mag. A **59** (2) 181 (1989)) formation of split dislocations in low-angle tilt boundaries in oxide superconductors is suggested. Conditions under which the splitting of dislocations in low-angle [100] tilt boundaries is energetically favorable are determined theoretically. *© 2000 MAIK "Nauka/Interperiodica".*

INTRODUCTION

Grain boundaries in oxide superconductors with a high superconducting transition temperature (T_c) dramatically decrease the critical current in polycrystalline samples as compared to single crystals (see, e.g., [2–7]). To explain this effect, several models [8–16] have been suggested, but the physical mechanism of the influence of grain boundaries on high-temperature superconductivity has not been determined unambiguously at present (see, e.g., the discussion in the review articles [6, 7, 17]). The most remarkable fact established experimentally in this field is the significant difference between the character of the effect of low-angle and high-angle grain boundaries on high-temperature superconductivity [2–7]. Thus, the critical current density J_c through low-angle boundaries decreases sharply with an increasing misorientation angle θ of the boundary approximately by the following exponential law: $J_c(\theta) = J_0(0)\exp(-\theta/8^\circ)$, where θ varies from 0° to about 15°. High-angle grain boundaries are characterized by extremely low densities of the critical current $J_c \approx (10^{-3}$ to $10^{-2})J_c(0)$, which depend only weakly on the misorientation angle θ for angles exceeding 15°. In order to explain the differences between the superconducting properties of low-angle and high-angle grain boundaries, the models developed in [8–11, 16] relate these properties to the effect on the high-temperature superconductivity exerted by the boundary cores and the fields of mechanical stresses due to grain boundaries. In the context of these models, it is of greatest interest to analyze the transformations of the grain boundaries in which the structure of the cores and the stress fields due to the grain boundaries suffer significant changes. The main aim of this work is to construct a theoretical model that would describe the experimentally observed [1] splitting of dislocations that constitute low-angle tilt boundaries in oxide superconductors.

1. MODEL OF A LOW-ANGLE TILT BOUNDARY WITH SPLIT DISLOCATIONS

Low-angle grain boundaries, which are characterized by misorientation angles $\theta \le 15^\circ$, are usually represented as walls of perfect lattice dislocations (with Burgers vectors that are full vectors of the crystal lattice) [18] (Fig. 1a). At the same time, it has been established experimentally [1] that the structure of low-angle [100] tilt boundaries in the superconducting ceramic compound $YBa_2Cu_3O_7$ differs from the "conventional" structure shown in Fig. 1a. At $\theta = 5^\circ$, the boundary represents a wall of partial edge dislocations united into triples of dislocations with a net Burgers vector $B \approx 1.17$ nm [1] (Fig. 1b). Within each triple, identical dislocations with the Burgers vector $b = B/3$ stand one above another and the separation p between them is about $12b$ at $\theta = 5^\circ$. For angles $\theta \le 5^\circ$, the structure of such boundaries has virtually not been studied, and we may assume that it also consists of either analogous triples of partial dislocations or perfect unextended edge dislocations with the Burgers vector $B \approx 1.17$ nm.

Let us first consider under which conditions extended dislocations can form in low-angle tilt boundaries. We will distinguish two main states of the structure of such boundaries: (*1*) a wall of unsplit edge dislocations with the Burgers vectors B and period h_1 (Fig. 1a) and (*2*) a wall of split edge dislocations with the same net Burgers vectors B, but consisting of partial dislocations with the Burgers vectors $b = B/3$, separations p, and period h_2 (Fig. 1b). Since we are interested in the transition between the above two states, we will assume that the new state (Fig. 1b) nucleates inside the previous one shown in Fig. 1a. Then, the problem reduces to finding the conditions under which the formation of one new structural element in place of one old element becomes energetically favorable, while all

1063-7834/00/4211-2000$20.00

the other structural elements of the boundary remain unchanged (Fig. 2).

Geometrically, to form a new structural element *2* (Fig. 2) in place of the old element *1*, it is sufficient to add to an unsplit dislocation with the Burgers vector *B* two dipoles of partial edge dislocations: one ("upper") of the intrinsic (vacancy) type and another ("lower") of the extrinsic (interstitial) type. Then, the lower dislocation of the upper dipole and the upper dislocation of the lower dipole interact with the initial dislocation to transform it into a partial dislocation of the same type as the two remaining dislocations (the upper dislocation of the upper dipole and the lower dislocation of the lower dipole).

2. ENERGY CONDITIONS FOR THE SPLITTING OF DISLOCATIONS IN LOW-ANGLE TILT BOUNDARIES

Let us now consider what changes in the total energy will occur upon the replacement of an old structural element with a new one (Fig. 2). The energy of the boundary in the first state may be represented by the sum

$$W_1 = RW_1^{\text{el}} + \frac{R}{h_1}W_1^{\text{c}}, \tag{1}$$

where R is the characteristic length for the boundary, W_1^{el} is the elastic energy density per unit length of the boundary, and W_1^{c} is the core energy of an undissociated grain-boundary dislocation.

The energy of the boundary in a transition state (Fig. 2) is

$$W_{1-2} = RW_1^{\text{el}} + \left(\frac{R}{h_1} - 1\right)W_1^{\text{c}} + 2W_{\text{dip}}^{\text{el}} + 3W_2^{\text{c}} + W_{\text{int}}^{\text{dip}} + 2W_{\text{int}}^{\text{dip}-b1} + 2(p - 2r_{0_2})\gamma, \tag{2}$$

where $W_{\text{dip}}^{\text{el}}$ is the elastic self-energy of the dipole of partial dislocations, W_2^{c} is the core energy of the partial dislocation, $W_{\text{int}}^{\text{dip}}$ is the energy of the interaction of the dipoles with one another, $W_{\text{int}}^{\text{dip}-b1}$ is the energy of the interaction of the dipole with the initial boundary in state *1*, r_{0_2} is the radius of the partial-dislocation core, and γ is the energy of the stacking fault enclosed between the partial dislocations.

Thus, as the structure of the boundary changes from state *1* into a transition state, the energy changes by an amount

$$\Delta W_{1-2} = W_{1-2} - W_1 = -W_1^{\text{c}} + 2W_{\text{dip}}^{\text{el}} + 3W_2^{\text{c}} + W_{\text{int}}^{\text{dip}} + 2W_{\text{int}}^{\text{dip}-b1} + 2(p - 2r_{0_2})\gamma; \tag{3}$$

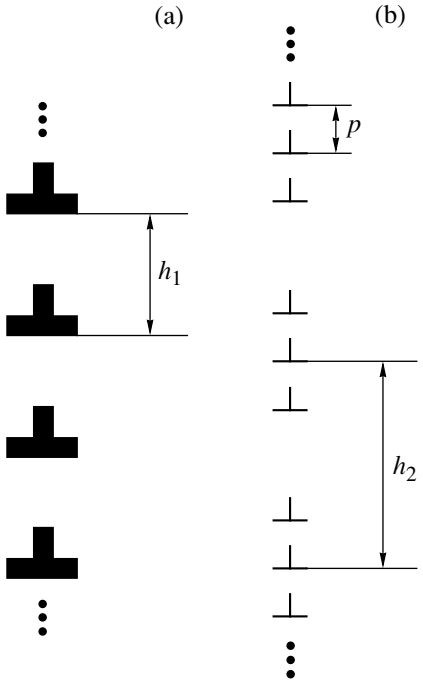

Fig. 1. Structure of low-angle tilt boundaries: (a) a wall of perfect lattice dislocations (structure 1) and (b) a wall of split dislocations (structure 2).

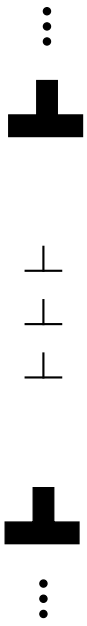

Fig. 2. Split dislocation in a low-angle boundary consisting of perfect lattice dislocations.

the critical condition for the transition is that this difference equals zero. The core energies of the initial unsplit dislocation W_1^{c} and partial dislocations W_2^{c} are given

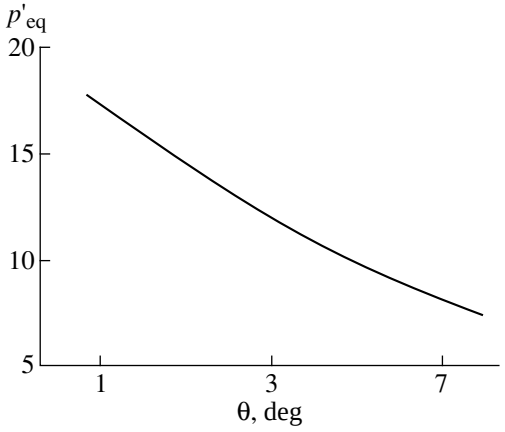

Fig. 3. Variation of p'_{eq} ($= p_{eq}/b$) as a function of the misorientation angle θ of the boundary.

by the known expression [18]

$$W_i^c = \frac{Gb_i^2 Z_i}{4\pi(1-\nu)}, \tag{4}$$

where G is the shear modulus; ν is the Poisson ratio; Z_i are dimensionless constants of order unity; $i = 1, 2$; $b_1 = B$; and $b_2 = b$. The elastic self-energy of the dipole of partial dislocations can easily be calculated as the work spent for the nucleation of a dipole in its self field of elastic stresses σ_{xx}^{dip} $(x = 0, y)$ [18]:

$$W_{dip}^{el} = \frac{b}{2}\int_{r_{0_2}}^{p-r_{0_2}} \sigma_{xx}^{dip}(x = 0, y)dy = -\frac{Gb^2}{4\pi(1-\nu)} \times \int_{r_{0_2}}^{p-r_{0_2}} \left(\frac{1}{y-p} - \frac{1}{y}\right)dy = \frac{Gb^2}{2\pi(1-\nu)}\ln\left(\frac{p-r_{0_2}}{r_{0_2}}\right). \tag{5}$$

The energies of interaction of dipoles with one another, W_{int}^{dip}, and with the initial boundary W_{int}^{dip-b1} are calculated in a similar way. The first is determined as the work spent on the nucleation of one dipole in the elastic field of another:

$$W_{int}^{dip} = b\int_{r_{0_2}}^{p} \sigma_{xx}^{dip}(x = 0, y)dy = \frac{Gb^2}{2\pi(1-\nu)} \times \int_{r_{0_2}}^{p} \left(\frac{1}{y+p} - \frac{1}{y}\right)dy = -\frac{Gb^2}{2\pi(1-\nu)}\ln\left(\frac{p+r_{0_2}}{2r_{0_2}}\right). \tag{6}$$

The second is calculated as the work done on the nucleation of a dipole in the elastic field of the initial boundary $\sigma_{xx}^{b1}(x, y)$, which is written as [18]

$$\sigma_{xx}^{b1}(x, y) = -\frac{GB\sin\tilde{y}(\cosh\tilde{x} - \cos\tilde{y} + \tilde{x}\sinh\tilde{x})}{2(1-\nu)h_1(\cosh\tilde{x} - \cos\tilde{y})^2}, \tag{7}$$

where the designation $\tilde{t} = 2\pi t/h_1$ is introduced. Then, the total energy W_{int}^{dip-b1} is determined by the expression

$$W_{int}^{dip-b1} = b\int_{r_{0_1}}^{p} \sigma_{xx}^{b1}(x = 0, y)dy = -\frac{GBb}{4\pi(1-\nu)}\ln\frac{1-\cos\tilde{p}}{1-\cos\tilde{r}_{0_1}}, \tag{8}$$

where r_{0_1} is the cutoff parameter of the elastic field of the initial dislocation at its core.

Substituting (4)–(6) and (8) into (3), we obtain

$$\Delta W_{1-2} = \frac{Gb^2}{4\pi(1-\nu)}\left(3Z_2 + \frac{B^2}{b^2}Z_1 + 2\ln\frac{2(p-r_{0_2})^2}{r_{0_2}(p+r_{0_2})} - 2\frac{B}{b}\ln\frac{1-\cos\tilde{p}}{1-\cos\tilde{r}_{0_1}}\right) + 2(p-2r_{0_2})\gamma. \tag{9}$$

The stacking-fault energy can be taken from [1], where the estimate $\gamma \approx 7GB/[324\pi \times (1-\nu)]$ was obtained.

The numerical analysis of expression (9) was performed for the following values of the parameters: $B = 3b$, $Z_1 \approx Z_2 \approx 1$, $r_{0_1} \approx B$, and $r_{0_2} \approx b$. In the range of small angles $\theta \approx B/h_1$ from 0° to 7°, the change in the total energy ΔW_{1-2} at $2b \le p \le 17b$ proved to be negative. This means that, at such misorientation angles, the existence of triples of partial dislocations is always more favorable energetically than the occurrence of perfect grain-boundary dislocations. It also turned out that, with increasing θ, the equilibrium separation p_{eq} between the partial dislocations in the triples (i.e., such p at which the gain in energy ΔW_{1-2} becomes maximum by the absolute value) decreases (Fig. 3). Note that, for $\theta = 5°$, our calculations yield $p_{eq} \approx 11b$, which agrees well with the magnitude $12b$ observed in [1].

CONCLUSIONS

Thus, the theoretical model developed in this work satisfactorily describes the conditions for the formation of dissociated dislocations in low-angle tilt boundaries in oxide superconductors. Within this model, the main driving force for the splitting of dislocations in low-angle boundaries is related to the decrease in the elastic energy of the boundary that takes place upon splitting. The splitting of dislocations in low-angle [100] tilt boundaries in $YBa_2Cu_3O_{7-\delta}$ is energetically favorable

for boundaries with misorientation angles $\theta \leq 7°$, which agrees with experimental data [1].

The critical current density J_c through low-angle tilt boundaries in oxide superconductors drops sharply as the misorientation angle of the boundary increases from $\theta = 0°$ to approximately 15° [2–7]. The models [8–16] in which the effect of grain boundaries on high-temperature superconductivity is considered usually employ the conventional concept of low-angle boundaries as walls of perfect lattice dislocations (Fig. 1a). However, in the context of the experiments described in [1] and of the theoretical analysis of this paper, the results of the models [8–16] seem to be debatable in the general case. In particular, the possibility of dislocation splitting in low-angle [100] tilt boundaries (Figs. 1b, 2) should necessarily be taken into account in future works concerning the theoretical description of the effects of the structure of cores and stress fields at grain boundaries on high-temperature superconductivity.

ACKNOWLEDGMENTS

This work was supported in part by the Russian Foundation for Basic Research, project no. 98-02-16075, and the US Office of Naval Research, grant no. N00014-99-1-0896.

REFERENCES

1. M. F. Chisholm and D. A. Smith, Philos. Mag. A **59** (2), 181 (1989).
2. D. Dimos, P. Chaudhari, J. Mannhart, and F. K. LeGoues, Phys. Rev. Lett. **61** (2), 219 (1988).
3. D. Dimos, P. Chaudhari, and J. Mannhart, Phys. Rev. B: Condens. Matter **41** (7), 4038 (1990).
4. Z. G. Ivanov, P.-A. Nilsson, D. Winkler, *et al.*, Appl. Phys. Lett. **59** (24), 3030 (1991).
5. S. E. Russek, D. K. Lathrop, B. H. Moeckly, R. A. Buhrmann, and D. H. Shin, Appl. Phys. Lett. **57** (11), 1155 (1990).
6. S. E. Babcock and J. L. Vargas, Annu. Rev. Mater. Sci. **25**, 193 (1995).
7. M. Prester, Supercond. Sci. Technol. **11** (3), 333 (1998).
8. M. F. Chisholm and S. J. Pennycook, Nature **351**, 47 (1991).
9. K. Jagannadham and J. Narayan, Philos. Mag. B **61** (2), 129 (1990).
10. D. Agassi, C. S. Pande, and R. A. Masumura, Phys. Rev. B: Condens. Matter **52** (22), 16237 (1995).
11. D. M. Kroeger, A. Choudhary, J. Brynestad, *et al.*, J. Appl. Phys. **64** (1), 331 (1988).
12. H. Hilgenkamp, J. Mannhart, and B. Mayer, Phys. Rev. B: Condens. Matter **53** (21), 14586 (1996).
13. H. Hilgenkamp and J. Mannhart, Appl. Phys. A **A64** (4), 553 (1997).
14. H. Hilgenkamp and J. Mannhart, Appl. Phys. Lett. **73** (3), 265 (1998).
15. J. Mannhart and H. Hilgenkamp, Supercond. Sci. Technol. **10** (6), 880 (1997).
16. S. A. Kukushkin, A. V. Osipov, and I. A. Ovid'ko, Mater. Phys. Mech. **1** (1), 49 (2000).
17. N. D. Browning, E. M. James, K. Kishida, *et al.*, Rev. Adv. Mater. Sci. **1** (1), 1 (2000).
18. J. P. Hirth and J. Lothe, *Theory of Dislocations* (Wiley, New York, 1982).

Translated by S. Gorin

Physics of the Solid State, Vol. 42, No. 11, 2000, pp. 2004–2013. Translated from Fizika Tverdogo Tela, Vol. 42, No. 11, 2000, pp. 1952–1960.

SEMICONDUCTORS AND DIELECTRICS

Effect of Normal Phonon–Phonon Scattering on the Mutual Electron–Phonon Drag and Kinetic Phenomena in Degenerate Conductors

I. G. Kuleev

Institute of Metal Physics, Ural Division, Russian Academy of Sciences, ul. S. Kovalevskoĭ 20, Yekaterinburg, 620219 Russia

e-mail: kuleev@imp.uran.ru

Received March 2, 2000

Abstract—The effect of normal phonon–phonon scattering processes on momentum relaxation in a nonequilibrium electron–phonon system is considered. A system of rate equations for the electron and phonon distribution functions has been solved with the inclusion of mutual electron–phonon drag. The kinetic coefficients of conductors have been calculated in a linear approximation in the degeneracy parameter. The effect of normal phonon–phonon scattering processes on the electron–phonon drag and on the kinetic phenomena in conductors with degenerate carrier statistics is analyzed. © *2000 MAIK "Nauka/Interperiodica".*

Studies dealing with the electron–phonon drag in metals and semiconductors published to date [1–13] were undertaken assuming that the momentum relaxation of both electrons and phonons in a nonequilibrium electron–phonon system can be described by introducing, in order, the total relaxation frequencies of electrons $\nu_e(k)$ and phonons $\nu_{ph}(q)$. This approximation was justified by the complexity of solving coupled integral equations for nonequilibrium electron and phonon distribution functions. These equations were solved in a zero approximation in the electron-gas degeneracy parameter $k_BT/\zeta \ll 1$ (ζ is the Fermi energy) [10, 11]. The present author succeeded in solving coupled rate equations for a nonequilibrium electron–phonon system in a linear approximation in the degeneracy parameter and for an arbitrary degree of the mutual effect of electrons and phonons not in equilibrium [12, 13]. This permitted the valid determination of the effect of mutual electron–phonon drag on the kinetic effects in conductors with degenerate carrier statistics [12, 13] within a one-parameter formulation.

The results obtained in [12, 13] are grounds for reaching beyond the one-parameter description of a nonequilibrium electron–phonon system and for taking into consideration normal phonon–phonon scattering (N-processes). These scattering processes do not contribute to the phonon momentum relaxation or, accordingly, to thermal resistance [14–18]. However, they determine the nonequilibrium phonon distribution function and result in the relaxation of the phonon subsystem to a local equilibrium distribution characterized by an average drift velocity of **u** [14–18]. The N-processes redistribute the energy and momentum among the various phonon modes, thereby inhibiting strong deviations from the equilibrium population of each mode, because most of the phonon momentum relaxation mechanisms depend on the phonon frequency. The part played by the N-processes in the theory of lattice heat conductivity was thoroughly studied in [14–18]. These scattering processes must be taken into account under the conditions where the phonon relaxation frequency for N-processes, $\nu_{phN}(q)$, is higher than, or comparable to, the resistive frequency $\nu_{phR}(q)$ associated with phonon relaxation at the boundaries in impurities, in electrons, and in Umklapp processes. We will show that the inclusion of the N-processes is also necessary when considering the effect of electron–phonon drag on kinetic phenomena in solids.

The point is that thermopower, heat conductivity, and thermomagnetic effects are determined from the condition of vanishing total electric current through a sample. In this case, the average velocity of ordered electron motion in any physically small volume of a sample is zero. Therefore, the momentum transfer from ordered electron motion to phonons is small and arises only in the first order in the degeneracy parameter. On the other hand, if there is a temperature gradient, there is also a stationary phonon flux from the hot to the cold end of the sample and momentum transfer from ordered phonon motion to electrons already occurs in the zeroth approximation in the degeneracy parameter. Note that, at low temperatures, where electron–phonon drag contributes noticeably to the thermopower, the phonon relaxation frequency $\nu_{phN}(q) > \nu_{phR}(q)$. It thus follows that phonon momentum relaxation in a nonequilibrium electron–phonon system should be taken into account more rigorously than was done in the case of the one-parameter formulation [1–13]. In this paper, the nonequilibrium state of the phonon subsystem is specified by three parameters, namely, the two relax-

1063-7834/00/4211-2004$20.00

ation frequencies $\nu_{phN}(q)$ and $\nu_{phR}(q)$ and the drift velocity $\mathbf{u}$. This formulation of the problem is appropriate for conductors with degenerate carrier statistics.

This paper studies the effect of normal phonon–phonon scattering processes on mutual electron–phonon drag and on kinetic phenomena in conductors with degenerate carrier statistics. In Section 1, a system of rate equations, complemented by the electron momentum balance equation, is transformed into coupled integral equations for the functions describing a nonequilibrium state of electrons. In Section 2, this system is solved in a linear approximation in the degeneracy parameter. Section 3 calculates the electrical conductivity and thermopower of degenerate conductors. Section 4 contains an analysis of the Onsager symmetry relations and of the part played by the normal phonon scattering processes in heat conductivity.

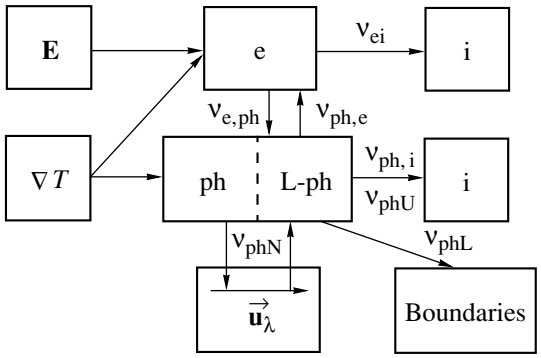

Scheme illustrating momentum relaxation of the electron–phonon system with inclusion of normal phonon-scattering processes. Here, $\nu_{ph,i}$, ν_{phL}, and ν_{phN} are the frequencies of phonon relaxation due to impurities (the Rayleigh mechanism), boundaries, and normal phonon–phonon scattering, respectively.

1. COUPLED RATE EQUATIONS FOR A NONEQUILIBRIUM ELECTRON–PHONON SYSTEM WITH INCLUSION OF NORMAL PHONON SCATTERING PROCESSES

It is well known [14–18] that normal phonon scattering processes do not contribute to the phonon momentum relaxation while driving the phonon subsystem to a local equilibrium Planck distribution characterized by an average drift velocity $\mathbf{u}_\lambda$, which can be different for phonons with different polarizations λ:

$$N(\mathbf{q}, \mathbf{u}_\lambda) = \left(\exp\left(\frac{\hbar\omega_{q\lambda} - \hbar\mathbf{q}\mathbf{u}_\lambda}{k_B T}\right) - 1\right)^{-1} \cong N^0_{q\lambda} + \frac{\hbar\mathbf{q}\mathbf{u}_\lambda}{k_B T} N^0_{q\lambda}(N^0_{q\lambda} + 1), \quad (1)$$

where $N^0_{q\lambda}$ is the Planck function. The figure illustrates schematically the redistribution and relaxation of the momentum acquired by the electron–phonon system from an electric field and a temperature gradient. The electron–phonon relaxation mechanisms characterized by the frequencies ν_{eph} and ν_{phe} bring about a redistribution of the momentum within an electron–phonon system. The scattering of electrons from impurities (ν_{ei}), of phonons from the boundaries (ν_{phL}), and of phonons from impurities (the Rayleigh mechanism, ν_{phi}), and the phonon–phonon Umklapp scattering (ν_{phU}) result in the relaxation of the total momentum of the electron–phonon system. The N-processes redistribute the momentum among the various phonon modes and give rise to a drift of phonons with a velocity of $\mathbf{u}_\lambda$.

The coupled rate equations for the nonequilibrium electron $f(\mathbf{k}, \mathbf{r})$ and the phonon $N^\lambda(\mathbf{q}, \mathbf{r})$, with the distribution functions taking the normal phonon–phonon scattering processes into account, can be written in the form [12–18]

$$\frac{e}{\hbar}\mathbf{E}_0\frac{\partial f_\mathbf{k}}{\partial \mathbf{k}} + (\mathbf{v}_k\nabla_\mathbf{r}) f_\mathbf{k} = I_{ei}(f_\mathbf{k}) + I_{eph}(f_\mathbf{k}, N^\lambda_\mathbf{q}),$$

$$\mathbf{v}^\lambda_\mathbf{q}\nabla_\mathbf{r} N^\lambda_\mathbf{q} = -(N^\lambda_\mathbf{q} - N^0_{q\lambda})\nu^{(1)\lambda}_{ph} - (N^\lambda_q - N(\mathbf{q}, \mathbf{u}_\lambda))\nu^\lambda_{phN} + I_{ph,e}(N^\lambda_\mathbf{q}, f_\mathbf{k}). \quad (2)$$

Here, $\mathbf{v}^\lambda_\mathbf{q} = s_\lambda\mathbf{q}/q$ is the group velocity of acoustic phonons with polarization λ and the relaxation frequency $\nu^{(1)\lambda}_{ph}(q)$ includes all nonelectronic resistive mechanisms of phonon scattering, namely, phonon scattering from phonons (Umklapp processes) from defects and from the sample boundaries. The collision integrals of electrons with impurities I_{ei} and with phonons $I_{e,ph}$ and of phonons with electrons $I_{ph,e}$ were specified in [3, 5, 12]. According to expression (2), the phonon subsystem is described not by one parameter $\nu^\lambda_{ph}(q) = \nu^\lambda_{phN}(q) + \nu^\lambda_{phR}(q)$, i.e., the total phonon momentum relaxation frequency [1–13], but by three parameters: the two relaxation frequencies $\nu^\lambda_{phN}(q)$ and $\nu^\lambda_{phR}(q)$ [$\nu^\lambda_{phR}(q) = \nu^\lambda_{ph,i}(q) + \nu^\lambda_{phL}(q) + \nu^\lambda_{ph,e}(q) + \nu^\lambda_{phU}(q)$ is the resistive phonon relaxation frequency] and the average phonon drift velocity $\mathbf{u}_\lambda$. There are two known mechanisms of normal three-phonon scattering, one due to Herring [19] and the other to Simons [20]. The scattering mechanism of Herring, which involves phonons of different polarizations ($t + l \longleftrightarrow l$, $t + l \longleftrightarrow t$), tends to establish the same drift velocity for phonons of both polarizations, $u_l = u_t = u_{ph}$. The phonons participating in the mechanism of Simons [20] are of the same polarization. Therefore, in the case of normal scattering by this mechanism, the drift velocity will be different for the longitudinal and transverse

phonons. The resistive frequency will likewise be different for longitudinal and transverse phonons. Therefore, in what follows, we will consider a more general case of the different drift velocities for longitudinal and transverse phonons, $u_l \neq u_t$. Note that, in some studies, the N-processes of phonon scattering are treated in a fairly arbitrary manner. For instance, the authors of [21], who studied the effect of mutual electron–phonon drag on thermomagnetic phenomena, included the relaxation mechanism of Simons as the only nonelectronic mechanism of phonon scattering. This mechanism, however, was formally included in the resistive frequency of the phonon momentum relaxation. This being considered, the results obtained in those studies cannot be considered fully valid.

To find $\mathbf{u}_\lambda$, the coupled rate equations (2) should be complemented with the phonon-momentum balance equation obtained by multiplying Eq. (1) by the phonon momentum vector $\hbar\mathbf{q}$ and by running this summation over all $\mathbf{q}$ vectors. In doing this, one should bear in mind that, in normal phonon–phonon scattering processes, the total phonon subsystem momentum is conserved:

$$\frac{1}{V}\sum_{\mathbf{q}}\hbar\mathbf{q}\nu^{\lambda}_{\mathrm{phN}}(q)(N^{\lambda}_{\mathbf{q}} - N(\mathbf{q}, \mathbf{u}_\lambda)) = \frac{1}{V}\sum_{\mathbf{q}}\hbar\mathbf{q}\nu^{\lambda}_{\mathrm{phN}}(q) \times\left[g_\lambda(\mathbf{q}) - \frac{\hbar\mathbf{q}\mathbf{u}_\lambda}{k_\mathrm{B}T}N^0_{q\lambda}(N^0_{q\lambda}+1)\right] = 0. \tag{3}$$

The electron and phonon distribution functions are presented in the form

$$f_{\mathbf{k}} = f_0(\varepsilon_k) + \delta f_{\mathbf{k}}, \quad N^{\lambda}_{\mathbf{q}} = N^0_{q\lambda} + g_\lambda(\mathbf{q}), \tag{4}$$

where $f_0(\varepsilon_k)$ and $N^0_{q\lambda}$ are the local equilibrium distribution functions for the electrons and phonons, respectively, and $\delta f_{\mathbf{k}}$ and $g_\lambda(\mathbf{q})$ are nonequilibrium terms (linear in external factors) added to the distribution functions. Let us linearize the collision integrals in these terms. The collision integrals $I_{\mathrm{ie}}(\delta f_{\mathbf{k}})$ and $I_{\mathrm{ph,\,e}}(f_0, g_\lambda(\mathbf{q}))$, as well as $I_{\mathrm{e,\,ph}}(\delta f_{\mathbf{k}}, N^0_{q\lambda})$, can be expressed in terms of the relaxation frequencies in the elastic-scattering approximations [12, 13]. When calculating the collision integral $I_{\mathrm{e,\,ph}}(f_0, g_\lambda(\mathbf{q}))$, we take into account the inelasticity of the electron–phonon collisions to the first order in the inelasticity parameter $\hbar\omega_{q\lambda}/\zeta$. We present the electron distribution function $\delta_{\mathbf{k}}$ in the standard form [2–13]

$$\delta f_{\mathbf{k}} = \left(-\frac{\partial f_0}{\partial\varepsilon_k}\right)(\mathbf{v}_k\boldsymbol{\chi}(\varepsilon)). \tag{5}$$

Substituting Eqs. (1), (4), and (5) in Eq. (2), we obtain an equation for the phonon distribution function. Because the corresponding manipulations are similar to those made in [12], we shall write out the expression for the function $g_\lambda(\mathbf{q})$ directly:

$$g_\lambda(\mathbf{q}) = -\frac{N^0_{q\lambda}(N^0_{q\lambda}+1)}{\nu^{\lambda}_{\mathrm{ph}}(q)}\frac{\hbar\omega_{q\lambda}}{k_\mathrm{B}T^2}(\mathbf{v}^{\lambda}_q\nabla T) + \frac{\hbar\mathbf{q}\mathbf{u}_\lambda}{k_\mathrm{B}T}N^0_{q\lambda}(N^0_{q\lambda}+1)\frac{\nu^{\lambda}_{\mathrm{phN}}(q)}{\nu^{\lambda}_{\mathrm{ph}}(q)} - \frac{\nu^{\lambda}_{\mathrm{ph,\,e}}(q)}{\nu^{\lambda}_{\mathrm{ph}}(q)}\frac{N^0_{q\lambda}(N^0_{q\lambda}+1)}{k_\mathrm{B}T}\int_{\varepsilon_{q/2}}^{\infty}d\varepsilon\left(-\frac{\partial f_0(\varepsilon)}{\partial\varepsilon}\right)\tilde{m}(\varepsilon)(\hbar\mathbf{q}\boldsymbol{\chi}(\varepsilon)) = g_{0\lambda}(\mathbf{q}) + g_{u\lambda}(\mathbf{q}) + g^2_\lambda(\mathbf{q}). \tag{6}$$

Here, $\nu^{\lambda}_{\mathrm{ph}} = \nu^{(1)\lambda}_{\mathrm{ph}} + \nu^{\lambda}_{\mathrm{ph,\,e}}$, where $\nu^{\lambda}_{\mathrm{ph,\,e}}(k_\mathrm{F}, q)$ is the frequency of phonon-momentum relaxation due to electrons [10–12]. The nonequilibrium term $g_{0\lambda}(\mathbf{q})$ is due to the action of the temperature gradient on the phonon subsystem, and the $g^2_\lambda(\mathbf{q})$ function takes into account the effect of the electrons in nonequilibrium. The quantity $g_{u\lambda}(\mathbf{q})$ originates from the normal phonon–phonon scattering processes, which give rise to phonon drift with a velocity of $\mathbf{u}_\lambda$. Relations (2), (3), and (6) can be used to derive a phonon momentum balance equation, from which the phonon drift velocity $\mathbf{u}_\lambda$ can be expressed through the $\boldsymbol{\chi}(\varepsilon)$ function in the following way:

$$\mathbf{u}_\lambda = \frac{s^2_\lambda\Psi^{\lambda}_N}{k_\mathrm{B}T\Psi^{\lambda}_{NR}}(-k_\mathrm{B}\nabla T) + \frac{2s^2_\lambda}{k_\mathrm{B}T\Psi^{\lambda}_{NR}}\left(\frac{k_\mathrm{F}}{q_{T\lambda}}\right)^3 \times\int_0^{\infty}d\varepsilon\left(-\frac{\partial f_0}{\partial\varepsilon}\right)\tilde{m}(\varepsilon)\psi^{\lambda}_{\mathrm{e,\,phN}}(\varepsilon)\boldsymbol{\chi}(\varepsilon) = \mathbf{u}_{0\lambda} + \Delta\mathbf{u}_\lambda. \tag{7}$$

In the function

$$z^{\lambda}_q = \frac{\hbar\omega_{q\lambda}}{k_\mathrm{B}T} = \frac{q}{q_{T\lambda}}, \quad q_{T\lambda} = \frac{k_\mathrm{B}T}{\hbar s_\lambda}, \quad z^{\lambda}_{2k} = \frac{2k}{q_{T\lambda}},$$

$$\tilde{m}(\varepsilon) = \frac{m(\varepsilon)}{m_\mathrm{F}},$$

$m_\mathrm{F} = m(\zeta)$ is the electron effective mass at the Fermi level and the other functions are given by the expressions

$$\psi^{\lambda}_{\mathrm{e,\,phN}}(\varepsilon) = \left\langle\frac{\nu^{\lambda}_{\mathrm{e,\,ph}}(k_\mathrm{F}, q)\nu^{\lambda}_{\mathrm{phN}}(q)}{\nu^{\lambda}_{\mathrm{ph}}(q)}\right\rangle_{z^{\lambda}_{2k}} \equiv\int_0^{z^{\lambda}_{2k}}dz^{\lambda}_q\frac{\nu^{\lambda}_{\mathrm{e,\,ph}}(k_\mathrm{F}, q)\nu^{\lambda}_{\mathrm{phN}}(q)}{\nu^{\lambda}_{\mathrm{ph}}(q)},$$

$$\Psi^{\lambda}_N = \left\langle\frac{\nu^{\lambda}_{\mathrm{phR}}(q)}{\nu^{\lambda}_{\mathrm{ph}}(q)}\right\rangle_{z_{d\lambda}} \equiv\int_0^{z_{d\lambda}}dz^{\lambda}_q(z^{\lambda}_q)^4\frac{\nu^{\lambda}_{\mathrm{phR}}(q)}{\nu^{\lambda}_{\mathrm{ph}}(q)}N^0_{q\lambda}(N^0_{q\lambda}+1), \tag{8}$$

$$\Psi_{\mathrm{NR}}^{\lambda} = \left\langle \frac{\nu_{\mathrm{phR}}^{\lambda}(q)\nu_{\mathrm{phN}}^{\lambda}(q)}{\nu_{\mathrm{ph}}^{\lambda}(q)} \right\rangle_{z_{d\lambda}},$$

where $z_{d\lambda} = \hbar\omega_{d\lambda}/k_{\mathrm{B}}T$ ($\omega_{d\lambda}$ is the Debye frequency of phonons of polarization λ). We isolated two parts of the phonon drift velocity $\mathbf{u}_{\lambda}$. The first part, $\mathbf{u}_{0\lambda}$, is due to the direct action of the temperature gradient on the phonon subsystem, and the second part, $\Delta\mathbf{u}_{\lambda}$, is associated with the effect of the nonequilibrium electron distribution function.

Prior to turning to further calculations, we will insert Eq. (7) in expression (6) for the phonon distribution function $g_{\lambda}(\mathbf{q})$ and rearrange the terms, which will considerably simplify the subsequent work. To do this, we combine the $g_{0\lambda}(\mathbf{q})$ term in the $g_{\lambda}(\mathbf{q})$ function with the $g_{u\lambda}(\mathbf{q})$ contribution, which is proportional to the phonon drift velocity $\mathbf{u}_{0\lambda}$, to obtain

$$\begin{aligned} g_{\lambda}(\mathbf{q}) &= g_{\lambda}^{(1)}(\mathbf{q}) + g_{\Delta u\lambda}(\mathbf{q}) + g_{\lambda}^{(2)}(\mathbf{q}), \\ g_{\Delta u\lambda}(\mathbf{q}) &= \frac{(\hbar\mathbf{q}\Delta\mathbf{u}_{\lambda})}{k_{\mathrm{B}}T} N_{q\lambda}^{0}(N_{q\lambda}^{0}+1)\frac{\nu_{\mathrm{phN}}^{\lambda}(q)}{\nu_{\mathrm{ph}}^{\lambda}(q)}, \end{aligned} \tag{9}$$

$$\begin{aligned} g_{\lambda}^{(1)}(\mathbf{q}) &= -\frac{N_{q\lambda}^{0}(N_{q\lambda}^{0}+1)}{\tilde{\nu}_{\mathrm{ph}}^{\lambda}(q)}\frac{\hbar\omega_{q\lambda}}{k_{\mathrm{B}}T^{2}}(\mathbf{v}_{q}^{\lambda}\nabla T), \\ \tilde{\nu}_{\mathrm{ph}}^{\lambda}(q) &= \nu_{\mathrm{ph}}^{\lambda}(q)\left(1 + \nu_{\mathrm{phN}}^{\lambda}(q)\frac{\Psi_{\mathrm{N}}^{\lambda}}{\Psi_{\mathrm{NR}}^{\lambda}}\right)^{-1}, \end{aligned} \tag{10}$$

where $\tilde{\nu}_{\mathrm{ph}}^{\lambda}(q)$ is the effective phonon-momentum relaxation frequency renormalized by the normal phonon-scattering processes. It is known [14–18] that the lattice heat conductivity is determined by this frequency. We will show here that the drag thermopower will likewise be determined by the effective phonon-momentum relaxation frequency. Obviously, when the inequality $\nu_{\mathrm{phN}}^{\lambda}(q) \ll \nu_{\mathrm{phR}}^{\lambda}(q)$ holds, the phonon drift contribution $\tilde{\nu}_{\mathrm{ph}}^{\lambda}(q) \approx \nu_{\mathrm{phR}}^{\lambda}(q)$ to the $g_{\lambda}(\mathbf{q})$ distribution function is negligible. In this limiting case, the one-parameter approximation accepted in [1–13] for the description of the effect of the nonequilibrium phonon subsystem on electron transport phenomena in conductors with degenerate carrier statistics is valid. In the opposite limiting case of $\nu_{\mathrm{phN}}^{\lambda}(q) \gg \nu_{\mathrm{phR}}^{\lambda}(q)$, one has to take into account the effect of phonon drift on momentum exchange in the nonequilibrium electron–phonon system. Thus, under the conditions where normal processes play a substantial role in phonon momentum repartitioning, one has to describe the phonon subsystem in terms of an augmented basis, i.e., within a three-parameter approximation.

The purpose of this work is to investigate the part played by the phonon drift, induced by the N-processes, on electron transport phenomena. For semimetals and semiconductors with degenerate carrier statistics with $n_e < n_a/4$ (n_a is the number of atoms per unit volume), the inequality $2k_{\mathrm{F}} < q_d$ is met (q_d is the Debye wave vector) [22]. In this case, one can obtain an equation for the $\boldsymbol{\chi}(\varepsilon)$ function in much the same way as was done in [12]. This equation is conveniently presented in the form of Volterra's inhomogeneous integral equation

$$\begin{aligned} \boldsymbol{\chi}(\varepsilon) &= \boldsymbol{\chi}_{1}(\varepsilon) + \boldsymbol{\chi}_{\Lambda}(\varepsilon) + \frac{\tilde{m}^{2}(\varepsilon)\tau(\varepsilon)}{\tilde{k}^{3}}\mathbf{Q}(\varepsilon) \\ &\equiv \boldsymbol{\chi}_{1\Lambda}(\varepsilon) + \boldsymbol{\chi}_{2}(\varepsilon), \\ \mathbf{Q}(\varepsilon) &= \Phi(\varepsilon)\int_{\varepsilon}^{\infty} d\varepsilon'\left(-\frac{\partial f_{0}}{\partial\varepsilon'}\right)\tilde{m}(\varepsilon')\boldsymbol{\chi}(\varepsilon') \\ &\quad + \int_{0}^{\varepsilon} d\varepsilon'\left(-\frac{\partial f_{0}}{\partial\varepsilon'}\right)\tilde{m}(\varepsilon')\Phi(\varepsilon')\boldsymbol{\chi}(\varepsilon') \\ &= \Phi(\varepsilon)\mathbf{K}^{>}(\varepsilon) + \mathbf{K}^{<}(\varepsilon), \\ \Phi(\varepsilon) &= \sum_{\lambda}\langle\Phi_{\lambda}(q)\rangle_{z_{2k}^{\lambda}}, \\ \Phi_{\lambda}(q) &= \frac{\nu_{\mathrm{ph,\,e}}^{\lambda}(k_{\mathrm{F}},q)\nu_{\mathrm{e,\,ph}}^{\lambda}(k_{\mathrm{F}},q)}{\nu_{\mathrm{ph}}^{\lambda}(q)}. \end{aligned} \tag{11}$$

Here, $\tilde{k} = k/k_{\mathrm{F}}$, $\hbar k_{\mathrm{F}}$ is the Fermi momentum, $\tau(\varepsilon)$ is the total electron relaxation time, $\tau^{-1}(\varepsilon_k) = \nu_{\mathrm{e}}(k) = \nu_{\mathrm{ei}}(k) + \nu_{\mathrm{e,\,ph}}(k)$, and $\nu_{\mathrm{ei}}(k)$ and $\nu_{\mathrm{e,\,ph}}(k)$ are the frequencies of electron relaxation due to impurities and phonons, respectively. The reciprocal quantity $(\Phi(\varepsilon))^{-1}$ determines the time $\tau_{\mathrm{e-ph-e}}$ during which the momentum imparted by the electrons to the phonon subsystem is recovered by the electrons [12]. The $\boldsymbol{\chi}_{2}(\varepsilon)$ function accounts for the effect of nonequilibrium electrons on electrons through the phonon subsystem and is related to mutual electron–phonon drag. The $\boldsymbol{\chi}_{1}(\varepsilon)$ function takes into account the direct action of the electric field and the temperature gradient on the electron subsystem, as well as the electron drag by phonons:

$$\begin{aligned} \boldsymbol{\chi}_{1}(\varepsilon) &= -e\tau(\varepsilon)\left(\mathbf{E} + \frac{k_{\mathrm{B}}}{e}\left(\frac{(\tilde{m}(\varepsilon))^{2}}{\tilde{k}^{3}}\tilde{A}_{\mathrm{ph}}(\varepsilon) + \frac{\varepsilon-\zeta}{k_{\mathrm{B}}T}\right)\nabla T\right), \\ \tilde{A}_{\mathrm{ph}}(\varepsilon) &= \sum_{\lambda}\frac{m_{\mathrm{F}}s_{\lambda}^{2}}{k_{\mathrm{B}}T}\left\langle\frac{\nu_{\mathrm{e,\,ph}}^{\lambda}(k_{\mathrm{F}},q)}{\tilde{\nu}_{\mathrm{ph}}^{\lambda}(q)}\right\rangle_{z_{2k}^{\lambda}} \\ &\equiv \sum_{\lambda}\frac{m_{\mathrm{F}}s_{\lambda}^{2}}{k_{\mathrm{B}}T}\int_{0}^{z_{2k}^{\lambda}} dz_{q}^{\lambda}\frac{\nu_{\mathrm{e,\,ph}}^{\lambda}(k_{\mathrm{F}},q)}{\tilde{\nu}_{\mathrm{ph}}^{\lambda}(q)}. \end{aligned} \tag{12}$$

The quantities $\tilde{A}_{ph}(\varepsilon)$ and $\Phi(\varepsilon)$ depend on energy ε only through the upper limit of integration $z^{\lambda}_{2k(\varepsilon)}$ [12]. The quantity $\boldsymbol{\chi}_{\lambda}(\varepsilon)$ reflects the effect of phonon drift on the electron distribution function. It can be written as

$$\boldsymbol{\chi}_{\Lambda}(\varepsilon) = \frac{\tilde{m}^2(\varepsilon)\tau(\varepsilon)}{\tilde{k}^3}\Lambda(\varepsilon),$$

$$\Lambda(\varepsilon) = \sum_{\lambda} m_F \Delta \mathbf{u}_{\lambda} \psi^{\lambda}_{e,\,phN}(\varepsilon), \tag{13}$$

$$\boldsymbol{\Lambda}(\varepsilon) = \sum_{\lambda} \frac{2m_F s^2_{\lambda}\psi^{\lambda}_{e,\,phN}(\varepsilon)}{k_B T \Psi^{\lambda}_{NR}}\left(\frac{k_F}{q_{T\lambda}}\right)^3$$

$$\times \int_0^{\infty} d\varepsilon\left(-\frac{\partial f}{\partial \varepsilon}\right)\tilde{m}(\varepsilon)\psi^{\lambda}_{e,\,phN}(\varepsilon)\boldsymbol{\chi}(\varepsilon). \tag{14}$$

Expressions (11)–(14) make up a system of two integral equations for the quantities $\boldsymbol{\chi}(\varepsilon)$ and $\boldsymbol{\Lambda}(\varepsilon)$, characterizing the nonequilibrium state of the electron subsystem. It was shown [12] that one can construct a regular scheme for calculating the $\boldsymbol{\chi}(\varepsilon)$ function from the integral equation (11) without recourse to expansion in a small parameter related to the weakness of the electron–phonon coupling or to the smallness of the mutual effect of electrons and phonons which have nonequilibrium distributions. We will now show that the coupled equations (11)–(14), including normal phonon scattering processes, can also be solved using only the strong degeneracy condition $k_B T/\zeta \ll 1$.

2. SOLUTION OF THE RATE EQUATION FOR ELECTRONS IN DEGENERATE SEMICONDUCTORS

It is convenient to look for $\mathbf{Q}(\varepsilon)$ rather than the function $\boldsymbol{\chi}(\varepsilon)$ in the solution to the integral equation (11). Using Eqs. (11) and (12), we obtain

$$\mathbf{Q}(\varepsilon) = \mathbf{Q}_1(\varepsilon) + \int_0^{\varepsilon} d\varepsilon'\left(-\frac{\partial f_0}{\partial \varepsilon'}\right)\Phi(\varepsilon')\varphi(\varepsilon')\mathbf{Q}(\varepsilon')$$

$$+ \Phi(\varepsilon)\int_{\varepsilon}^{\infty} d\varepsilon'\left(-\frac{\partial f_0}{\partial \varepsilon'}\right)\varphi(\varepsilon')\mathbf{Q}(\varepsilon'),$$

$$\mathbf{Q}_1(\varepsilon) = \int_0^{\varepsilon} d\varepsilon'\left(-\frac{\partial f_0}{\partial \varepsilon'}\right)\Phi(\varepsilon')\tilde{m}(\varepsilon')\boldsymbol{\chi}_{1\Lambda}(\varepsilon') + \Phi(\varepsilon) \tag{15}$$

$$\times \int_{\varepsilon}^{\infty} d\varepsilon'\left(-\frac{\partial f_0}{\partial \varepsilon'}\right)\tilde{m}(\varepsilon')\boldsymbol{\chi}_{1\Lambda}(\varepsilon'),$$

$$\varphi(\varepsilon) = \left(\frac{\tilde{m}(\varepsilon)}{\tilde{k}(\varepsilon)}\right)^3 \tau(\varepsilon).$$

The quantity $\boldsymbol{\Lambda}(\varepsilon)$, describing the effect of phonon drift on the electron distribution function, is expressed through the $\mathbf{Q}(\varepsilon)$ function as

$$\boldsymbol{\Lambda}(\varepsilon) = \frac{1}{1 - K_u(\varepsilon)}\sum_{\lambda} K^{\lambda}_u(\varepsilon)\left\{-e\mathbf{E}^{\lambda}_{Au} + \frac{\nu_F}{\psi^{\lambda}_{e,\,phN}(\zeta)}\right.$$

$$\left.\times \int_0^{\infty} d\varepsilon\left(-\frac{\partial f_0}{\partial \varepsilon}\right)\varphi(\varepsilon)\psi^{\lambda}_{e,\,phN}(\varepsilon)\mathbf{Q}(\varepsilon)\right\}, \tag{16}$$

where

$$\mathbf{E}^{\lambda}_{Au} = \mathbf{E}_A + \frac{k_B \pi^2}{e}\frac{D^{\lambda}_{e,\,phN}}{3}\nabla T,$$

$$\mathbf{E}_A = \mathbf{E} + \frac{k_B}{e}\tilde{A}_{ph}(\zeta)\nabla T,$$

$$K^{\lambda}_u(\varepsilon) = \frac{2m_F s^2_{\lambda}}{k_B T}\left(\frac{k_F}{q_{T\lambda}}\right)^3 \frac{\psi^{\lambda}_{e,\,phN}(\zeta)\psi^{\lambda}_{e,\,phN}(\varepsilon)}{\nu_F \Psi^{\lambda}_{NR}},$$

$$D^{\lambda}_{e,\,phN} = k_B T \frac{d}{d\varepsilon}[\ln(m(\varepsilon)\tau(\varepsilon)\psi^{\lambda}_{e,\,phN}(\varepsilon))]_{\varepsilon = \zeta}.$$

The coupled integral equations (15) and (16) could be solved using the method of Gurevich and Korenblit [10] by introducing a replacement $(-\partial f_0/\partial\varepsilon) \cong \delta(\varepsilon - \zeta)$ in the integral operator (15), which is valid in strong degeneracy conditions. However, this method allows for the rigorous analysis of kinetic coefficients, with the inclusion of mutual drag only in the zeroth approximation in electron gas degeneracy. Using this approximation in [21] in analyzing thermomagnetic effects led to incorrect calculations.

Therefore, we shall use the method proposed in [12], which is the best suited to seeking parametric solutions to coupled integral equations. It allows one, without specifying the $\Phi(\varepsilon)$, $\tau(\varepsilon)$, and $m(\varepsilon)$ functions of the electron energy ε, to find a solution to these equations in a linear approximation in the $(k_B T/\zeta)$ parameter. Using this method, a solution is found in two stages. First, one determines the energy dependence of the $\mathbf{Q}(\varepsilon)$ function. After this, the coupled integral equations (15) and (16) can be reduced to a system of algebraic equations.

We start by expanding the $\mathbf{Q}(\varepsilon)$ function in powers of the parameter $(\varepsilon - \zeta)$, because, due to the Fermi function derivative $(-\partial f_0/\partial\varepsilon)$, only a narrow energy interval

$|\varepsilon - \zeta| \leq k_B T$ will provide a dominant contribution to the integrals (15):

$$\mathbf{Q}(\varepsilon) = \mathbf{Q}(\zeta) + \sum_{n=1}^{\infty} \frac{(\varepsilon-\zeta)^n}{n!}\mathbf{Q}^{(n)}(\zeta),$$
$$\mathbf{Q}^{(n)}(\zeta) = \left(\frac{d^n\mathbf{Q}(\varepsilon)}{d\varepsilon^n}\right)_{\varepsilon=\zeta}. \quad (17)$$

It was shown [12] that the energy expansion studied actually occurs in the parameter $\eta = (\varepsilon - \zeta)/k_B T$. In the vicinity of the Fermi level, the strict inequality $|\eta| \ll 1$ does not hold, which does not allow one to limit the results to a finite number of terms. Summation of the infinite series yields [12]

$$\mathbf{Q}(\varepsilon) = \mathbf{Q}(\zeta) + k_B T \Psi^{(1)}(\zeta) \times \{\eta \mathbf{K}^{>}(\zeta) - f_1(\eta)\boldsymbol{\chi}(\zeta) - f_2(\eta)\tau_F(-k_B \nabla T)\}, \quad (18)$$

where

$$\mathbf{K}^{>}(\zeta) = \int_{\zeta}^{\infty} d\varepsilon \left(-\frac{\partial f_0}{\partial \varepsilon}\right)\tilde{m}(\varepsilon)\boldsymbol{\chi}(\varepsilon),$$
$$f_1(\eta) = \ln(1+\exp(-\eta)) - \ln(2) + \eta/2,$$
$$f_2(\eta) = \eta f_1(\eta) - 2\int_0^{\eta} d\eta' f_1(\eta').$$

Note that the function $f_1(\eta)$ is symmetric with respect to the replacement of η by $(-\eta)$ and $f_2(\eta)$ is antisymmetric with respect to this replacement, so that $\mathbf{Q}(\varepsilon)$ may also be divided into two parts: a symmetric $\mathbf{Q}_s(\varepsilon)$ and an antisymmetric $\mathbf{Q}_a(\varepsilon)$.

Thus, in order to solve the coupled equations (15) and (16), we have only to determine the functions $\mathbf{Q}(\zeta)$ and $\mathbf{K}^{>}(\zeta)$, and the quantity $\boldsymbol{\Lambda}(\zeta)$. We use the expansion $\Phi(\varepsilon) - \Phi(\zeta) \approx (\varepsilon - \zeta)\Phi^{(1)}(\zeta)$ and limit ourselves to a linear approximation in $(k_B T/\zeta)$ to recast Eq. (15) in the form

$$\mathbf{Q}(\zeta) = \int_{-\infty}^{\infty} d\eta \left(-\frac{\partial f_0}{\partial \eta}\right)\Phi(\varepsilon)\tilde{m}(\varepsilon)\boldsymbol{\chi}(\varepsilon) - \Phi(\zeta)D_{\Phi}\int_0^{\infty} d\eta\left(-\frac{\partial f_0}{\partial \eta}\right)\eta\,\tilde{m}(\varepsilon)\boldsymbol{\chi}(\varepsilon), \quad (19)$$

where $\varepsilon = \zeta + \eta k_B T$ and $D_{\Phi} = k_B T d/d\varepsilon[\ln(\Phi(\varepsilon))]_{\varepsilon=\zeta}$. To zero order in the degeneracy parameter, the second term in (19) can be neglected, after which one easily finds expressions for $\mathbf{Q}_0(\zeta)$ and $\boldsymbol{\Lambda}(\zeta)$:

$$\mathbf{Q}_0(\zeta) = -e\Gamma\mathbf{E}_A(1-\Gamma-K_u)^{-1},$$
$$\boldsymbol{\Lambda}^{(0)} = -eK_u\mathbf{E}_A(1-\Gamma-K_u)^{-1}, \quad (20)$$

where $\Gamma = \tau_F/\tau_{e\text{–}ph\text{–}e}$ is a parameter characterizing the degree of the mutual effect of the electron and phonon distribution functions in nonequilibrium. This parameter is equal to the ratio of the electron relaxation time τ_F to the time $\tau_{e\text{–}ph\text{–}e}$ during which the momentum imparted by electrons to phonons is recovered by the electron system. As seen from Eq. (20), taking the normal phonon scattering into account enhances the mutual electron–phonon drag effect.

To find the functions $\mathbf{Q}(\zeta)$, $\mathbf{K}^{>}(\zeta)$, and $\boldsymbol{\Lambda}(\zeta)$ to first order in the degeneracy parameter, we insert Eq. (18) in Eqs. (16) and (19) and integrate over η. As a result, we come to coupled algebraic equations for the sought functions, whose solution can be written in the form

$$\mathbf{Q}(\zeta) = \frac{-e\Gamma}{(1-\Gamma-K_u)} \times \left\{\mathbf{E}_A\left(1 - \frac{D_{\Phi}[J_1\Gamma + (1-K_u)\ln(2)]}{(1-\Gamma-K_u)}\right) + \frac{\pi^2}{3}\frac{k_B}{e}[(1-K_u)D_Q + \Delta_u]\nabla T\right\}, \quad (21)$$

$$\boldsymbol{\Lambda} = \frac{-e}{(1-\Gamma-K_u)}\left\{K_u\mathbf{E}_A\left(1 - \frac{C_1\Gamma D_{\Phi}}{(1-\Gamma-K_u)}\right) + \frac{\pi^2}{3}\frac{k_B}{e} - [K_u\Gamma D_Q + (1-\Gamma)\Delta_u]\nabla T\right\},$$

where

$$J_1 = \int_{-\infty}^{\infty} d\eta\left(-\frac{\partial f_0}{\partial \eta}\right)f_1(\eta) \cong 0.31,$$
$$D_Q = k_B T \frac{d}{d\varepsilon}[\ln(m(\varepsilon)\tau(\varepsilon)\Phi^{1/2}(\varepsilon))]_{\varepsilon=\zeta},$$
$$C_1 = J_1 + \ln(2) \approx 1, \quad \Delta_u = \sum_{\lambda} K_u^{\lambda}(\zeta)D_{e,\,phN}^{\lambda}(\zeta),$$
$$K_u = \sum_{\lambda} K_u^{\lambda}(\zeta).$$

To zero order in the degeneracy parameter, the $\mathbf{K}^{>}(\zeta)$ function has the form

$$\mathbf{K}_0^{>}(\zeta) = -\frac{e}{2\nu_F}\left\{\mathbf{E}_A(1-\Gamma-K_u)^{-1} + \frac{k_B}{2}2\ln(2)\nabla T\right\}. \quad (22)$$

Substituting Eqs. (21) and (22) in Eq. (18) yields a solution to the integral equation for the $\chi(\varepsilon)$ function, which is valid in the linear approximation in the degeneracy parameter. This solution allows one to calculate the conduction current and the heat flux and to analyze the

effect of normal phonon scattering on the kinetic coefficients of conductors with degenerate carrier statistics in the cases of both weak ($\Gamma \ll 1$) and strong mutual electron–phonon drag.

3. CALCULATION OF THE ELECTRICAL CONDUCTIVITY AND THERMOPOWER OF DEGENERATE CONDUCTORS

Let us calculate the conduction current $\mathbf{j}$ by dividing it into three parts proportional to the nonequilibrium terms added to the electron distribution function $\boldsymbol{\chi}(\varepsilon)$:

$$\mathbf{j} = -\frac{en_e}{m_F}\int_0^\infty d\varepsilon\left(-\frac{\partial f_0}{\partial\varepsilon}\right)\frac{\tilde{k}^3}{\tilde{m}(\varepsilon)} \times (\boldsymbol{\chi}_1(\varepsilon) + \boldsymbol{\chi}_\Lambda(\varepsilon) + \boldsymbol{\chi}_2(\varepsilon)) = \mathbf{j}_1 + \mathbf{j}_\Lambda + \mathbf{j}_2. \quad (23)$$

To calculate these fluxes, we insert Eqs. (18), (21), and (22) in Eq. (23) and integrate over the parameter η to obtain, in the linear approximation in (k_BT/ζ),

$$\mathbf{j} = \sigma_0\left\{\mathbf{E}_A + \frac{k_B}{e}\frac{\pi^2}{3}D_j\nabla T - \frac{1}{e}[\boldsymbol{\Lambda}(\zeta) + \mathbf{Q}(\zeta) - J_1\Gamma D_\Phi\boldsymbol{\chi}(\zeta)]\right\}. \quad (24)$$

Here,

$$\sigma_0 = \frac{e^2n_e\tau_F}{m_F}, \quad D_j = k_BT\frac{d}{d\varepsilon}\left[\ln\left(\frac{k^3(\varepsilon)\tau(\varepsilon)}{m(\varepsilon)}\right)\right]_{\varepsilon=\zeta}.$$

In Eq. (24), the first two terms in the braces give the current $\mathbf{j}_1$, the term proportional to $\boldsymbol{\Lambda}(\zeta)$ determines the current $\mathbf{j}_\Lambda$ caused by the effect of the phonon system drift on the conduction electrons, and the last two terms in the brackets determine the mutual-drag current. Substituting Eqs. (21) and (22) in Eq. (24) yields an expression for the conduction current:

$$\mathbf{j} = \tilde{\sigma}_0\left\{\mathbf{E}_A\left[1 - \frac{C_1\Gamma D_\Phi}{1-\Gamma-K_u}\right] + \frac{\pi^2}{3}\frac{k_B}{e}[\Gamma D_Q + (1-\Gamma-K_u)D_j + \Delta_u]\nabla T\right\}, \quad (25)$$

where $\tilde{\sigma}_0 = e^2n_e\tilde{\tau}_F/m_F$ and $\tilde{\tau}_F = \tau_F(1-\Gamma-K_u)^{-1}$.

From Eq. (25) one can derive expressions for the kinetic coefficients σ_{xx} and β_{xx}:

$$\sigma_{xx} = \tilde{\sigma}_0\{1 - \Gamma D_\Phi C_1(1-\Gamma-K_u)^{-1}\},$$
$$\beta_{xx} = -\frac{k_B}{e}\left\{\sigma_{xx}\tilde{A}_{ph}(\zeta) + \frac{\pi^2}{3}\tilde{\sigma}_0[(1-\Gamma-K_u)D_j + \Gamma D_Q + \Delta_u]\right\}. \quad (26)$$

For $\nu^\lambda_{phN}(q) = 0$, the quantity $K_u(\zeta) = 0$ and expressions (26) for σ_{xx} and β_{xx} transform to the corresponding expressions in [12]. As seen from Eq. (26), taking the drift of the phonon subsystem associated with normal phonon scattering into account results in an increase in the fraction of the momentum transferred by the phonons to the electrons. This enhances the effect of mutual electron–phonon drag on the electrical conductivity and brings about the renormalization of the phonon relaxation frequency by N-processes in the expression for the thermoelectric coefficient β_{xx}. The appearance of a term linear in the degeneracy parameter in the expression for σ_{xx} is a result of the mutual electron–phonon drag.

Consider the effect of normal phonon–phonon scattering on the thermopower of conductors with degenerate carrier statistics. We find from the $\mathbf{j} = 0$ condition that

$$\alpha = -\frac{k_B}{e}\left\{\tilde{A}_{ph}(\zeta) + \frac{\pi^2}{3}[(1-\Gamma-K_u)D_j + \Gamma D_Q + \Delta_u]\right\}\alpha_{ph} + \alpha_{dif}. \quad (27)$$

For $\nu^\lambda_{phN}(q) = 0$, we obtain $K_u(\zeta) = 0$ and $\tilde{A}_{ph}(\zeta) = A_{ph}(\zeta)$, and the expression for thermopower (27) transforms to Eq. (46) of [12]. We note first of all that the phonon component of thermopower σ_{ph} is determined not by the total phonon relaxation frequency $\nu^\lambda_{ph}(q)$ but rather by the resistive phonon relaxation frequency (10), which is renormalized by the N-processes. In the limiting case of $\nu_{phN}(q) \ll \nu_{phR}(q)$, the quantity $\tilde{A}_{ph}(\zeta) = A_{ph}(\zeta)$, and one can use the expression for the drag thermopower obtained earlier within the one-parameter approximation [1–13]. For $\nu_{phN}(q) \geq \nu_{phR}(q)$, normal phonon scattering processes give rise to an increase in magnitude of the drag thermopower:

$$\alpha_{ph} = -\frac{k_B}{e}\sum_\lambda\frac{m_Fs^2_\lambda}{k_BT} \times \int_0^{z^\lambda_{2k}} dz^\lambda_q\frac{\nu^\lambda_{e,ph}(k_F,q)}{\nu^\lambda_{ph}(q)}\left(1 + \nu^\lambda_{phN}(q)\frac{\Psi^\lambda_N}{\Psi^\lambda_{NR}}\right). \quad (28)$$

Therefore, when interpreting the experimental data, one should take into account the drift of the phonon system and use expression (28). Thus, we have shown that the drag thermopower, as well as the lattice heat conductivity, contains a phonon momentum relaxation frequency renormalized by the N-processes. As seen from Eq. (27), mutual electron–phonon drag contrib-

utes only to the diffusion component of the thermopower. The physics of this is clear. For $\mathbf{j} = 0$, the momentum is transferred from electrons to the phonon subsystem (see figure) through processes of diffusion arising in first order in the degeneracy parameter $k_B T/\zeta$. On the other hand, in the presence of a temperature gradient, a steady-state phonon flux propagates through a conductor and momentum transfer from the phonon subsystem to electrons is already nonzero in the first order in the degeneracy parameter. This is what follows from Eq. (27).

In [21], the method proposed in [10] was used to calculate thermopower, which resulted in a loss of the ΓD_Q term in Eqs. (26) and (27). When this approximation is applied in cases where a magnetic field is present, the Nernst–Ettingshausen coefficients are found to be erroneously magnetic-field dependent [21]. A correct calculation of these coefficients, with inclusion of the mutual drag effect [23] made within a one-parameter approach, does not show any deviation from their classical behavior in strong magnetic fields.

4. CALCULATION OF THE ELECTRONIC AND PHONON HEAT FLUXES AND ANALYSIS OF THE ONSAGER RELATIONS

Let us calculate the electronic heat flux $\mathbf{W}_e$ by dividing it into three parts proportional to the nonequilibrium terms added to the electron distribution function $\boldsymbol{\chi}(\varepsilon)$:

$$\mathbf{W}_e = \frac{n_e}{m_F}\int_0^\infty d\varepsilon\left(-\frac{\partial f_0}{\partial\varepsilon}\right)(\varepsilon-\zeta)\frac{\tilde{k}^3}{\tilde{m}(\varepsilon)} \times(\boldsymbol{\chi}_1(\varepsilon)+\boldsymbol{\chi}_\Lambda(\varepsilon)+\boldsymbol{\chi}_2(\varepsilon)) = \mathbf{W}_e^{(1)}+\mathbf{W}_{e\Lambda}+\mathbf{W}_e^{(2)}. \quad (29)$$

A calculation of this flux using Eqs. (18), (21), and (22) yields

$$\mathbf{W}_e = -L_0 T\sigma_0\left\{\frac{e}{k_B}\left[\mathbf{E}D_j+\mathbf{E}_A\frac{\Gamma D_Q+\Delta_u}{1-\Gamma-K_u}\right] + \frac{\pi^2}{3}\frac{k_B}{e}[1+D_\Phi\Gamma C_2+\tilde{A}_{ph}(\zeta)D_A]\nabla T\right\}, \quad (30)$$

where

$$L_0 = \frac{\pi^2}{3}\left(\frac{k_B}{e}\right)^2,$$

$$D_A = k_B T\frac{d}{d\varepsilon}[\ln(m(\varepsilon)\tau(\varepsilon)\tilde{A}_{ph}(\varepsilon))]_{\varepsilon=\zeta},$$

$$J_3 = \int_0^\infty d\eta\left(-\frac{\partial f_0}{\partial\eta}\right)\eta f_2(\eta)\cong 0.381,$$

$$C_2 = \ln(2)-\frac{3}{\pi^2}J_3\cong 0.577.$$

One can readily verify that the Onsager relations for the thermoelectric coefficients characterizing the fluxes of heat $\mathbf{W}_e$ and charge $\mathbf{j}$ are not met. As shown in [12], one has to take into account the heat flux transported by phonons, but also associated with electrons, in a nonequilibrium state.

The heat flux transported by phonons can be divided into three parts:

$$\mathbf{W}_{ph} = \frac{1}{V}\sum_{\mathbf{q},\lambda}\hbar\omega_{q\lambda}\mathbf{v}_q^\lambda(g_\lambda^{(1)}(\mathbf{q})+g_{\Delta u\lambda}(\mathbf{q})+\mathbf{g}_\lambda^{(2)}(\mathbf{q})) = \mathbf{W}_{ph1}+\mathbf{W}_{\Delta u}+\mathbf{W}_{ph,e}. \quad (31)$$

The heat flux $\mathbf{W}_{ph1}$ is due to both diffusion and drift motion of phonons driven by a temperature gradient. The calculation of the N-processes, which result in phonon drift, reduces to renormalization of the phonon-momentum relaxation frequency:

$$\mathbf{W}_{ph} = -\kappa_{ph}^{(1)}\nabla T,$$
$$\kappa_{ph}^{(1)} = \sum_\lambda\frac{k_B s_\lambda^2 q_{T\lambda}^3}{6\pi^2}\int_0^{z_d^\lambda}dz_q^\lambda\frac{(z_q^\lambda)^4}{\tilde{\nu}_{ph}^\lambda(q)}N_{q\lambda}^0(N_{q\lambda}^0+1). \quad (32)$$

Expression (32) coincides with the relation of Callaway for lattice heat conductivity [14–18]. The heat flux $\mathbf{W}_{\Delta u}$ originates from the effect of electrons on the drift motion of phonons. The heat flux $\mathbf{W}_{ph,e}$ results from the effect of nonequilibrium electrons on the phonon subsystem. These fluxes can be written in the form

$$\mathbf{W}_{\Delta u} = \frac{1}{V}\sum_{\mathbf{q},\lambda}s_\lambda^2\hbar\mathbf{q}g_{\Delta u\lambda}(\mathbf{q}) = \frac{n_e}{m_F}\sum_\lambda\frac{m_F s_\lambda^2\Psi_N^\lambda}{\Psi_{NR}^\lambda}\int_0^\infty d\varepsilon\left(-\frac{\partial f_0}{\partial\varepsilon}\right)\tilde{m}(\varepsilon)\psi_{e,phN}^\lambda(\varepsilon)\boldsymbol{\chi}(\varepsilon), \quad (33)$$

$$\mathbf{W}_{ph,e} = \frac{1}{V}\sum_{\mathbf{q},\lambda}s_\lambda^2\hbar\mathbf{q}g_\lambda^{(2)}(\mathbf{q}) = \frac{k_B T n_e}{m_F}\int_0^\infty d\varepsilon\left(-\frac{\partial f_0}{\partial\varepsilon}\right)\tilde{m}(\varepsilon)A_{ph}(\varepsilon)\boldsymbol{\chi}(\varepsilon). \quad (34)$$

Because the nonequilibrium state of the electron system is due not only to the effect of the electric field and temperature gradient but also to the drag of electrons by phonons, both the nonequilibrium electrons and the effect of nonequilibrium phonons on phonons through the electron subsystem contribute to the fluxes (33) and (34). Therefore, these fluxes bring about renormaliza-

tion of both the electron and phonon heat fluxes. These fluxes can be calculated as

$$\mathbf{W}_{\text{ph, e}} + \mathbf{W}_{\Delta u} = -\frac{k_B}{e} T \tilde{A}_{\text{ph}}(\zeta) \times \left\{ \sigma_{xx} \mathbf{E}_A + \frac{k_B}{e} \frac{\pi^2}{3} \tilde{\sigma}_0 [(1 - \Gamma - K_u) D_A + \Gamma D_Q + \Delta_u] \nabla T \right\}. \quad (35)$$

As in the analysis of the $\mathbf{W}_{\text{ph, e}}$ flux made in [12, 13], we include the drift and diffusion heat-flux components (35) caused by nonequilibrium electrons in the total electron heat flux:

$$W_{\text{etx}} = \gamma_{xx} E_x - \kappa^e_{xx} \nabla_x T. \quad (36)$$

The terms proportional to $(A_{\text{ph}}(\zeta))^2 \nabla T$ in expression (35), which are associated with the effect of nonequilibrium phonons on phonons through the conduction electrons, contribute to the phonon heat flux. As a result of this separation, the expressions for the kinetic coefficients assume the form

$$\gamma_{xx} = T \beta_{xx},$$

$$\kappa_{\text{ph}} = \kappa^{(1)}_{\text{ph}} + \frac{3}{\pi^2} L_0 T \sigma_{xx} (\tilde{A}_{\text{ph}}(\zeta))^2, \quad (37)$$

$$\kappa^e_{xx} = L_0 \sigma_0 T \times \left\{ 1 + D_\Phi \Gamma C_2 + 2 \tilde{A}_{\text{ph}}(\zeta) \left[D_A + \frac{\Gamma D_Q + \Delta_u}{1 - \Gamma - K_u} \right] \right\},$$

where β_{xx} is given by Eq. (26). Thus, we have verified by direct calculation that the Onsager relations for the thermoelectric coefficients β_{xx} and γ_{xx}, calculated in a linear approximation in the degeneracy parameter are satisfied in the case where the nonequilibrium state of the phonon system is described in terms of a three-parameter approximation. Note that the Onsager relations follow from the thermodynamics of irreversible processes and must always be satisfied. However, a solution of the coupled rate equations and a calculation of the kinetic coefficients are performed by making a number of approximations, which may result in a violation of these relations. The Onsager relations are a necessary (but not sufficient) condition to the validity of approximate calculations. The fact that these relations are satisfied for the kinetic coefficients calculated in this paper means that we have correctly taken into account both the effect of nonequilibrium electrons on electrons through the phonon subsystem and the effect of nonequilibrium phonons on phonons through the conduction electrons.

The electronic heat conductivity is usually found under the condition $\mathbf{j} = 0$. In this case, it can be presented in the form

$$\kappa_e = \kappa^e_{xx} - T \beta_{xx} \alpha = L_0 \sigma_0 T \times \left\{ 1 + D_\Phi \gamma C_2 + 2 \tilde{A}_{\text{ph}}(\zeta)(D_A - D_j) - \frac{3}{\pi^2} (\tilde{A}_{\text{ph}}(\zeta))^2 \frac{\sigma_{xx}}{\sigma_0} \right\}. \quad (38)$$

Note that, in the total heat conductivity $\kappa = \kappa_{\text{ph}} + \kappa_e$, the electron–phonon drag contribution proportional to $(A_{\text{ph}})^2$ cancels due to the $\mathbf{j} = 0$ condition:

$$\kappa = \kappa^{(1)}_{\text{ph}} + L_0 \sigma_0 T \times \{ 1 + C_2 \Gamma D_\Phi + 2 \tilde{A}_{\text{ph}}(\zeta)(D_A - D_j) \}. \quad (39)$$

A comparison of expressions (26) and (39) shows that the Wiedemann–Franz law is not satisfied. This is associated with the inelasticity of electron–phonon scattering, which results in electron drag by phonons $[A_{\text{ph}}(\zeta)]$ and their subsequent mutual drag (Γ). Neglecting the terms proportional to the degeneracy parameter, we obtain for the effective Lorenz factor $L^* = L/L_0$

$$L^* = \frac{\kappa_e}{L_0 T \sigma_{xx}} = \left\{ 1 - \Gamma - K_u - \frac{3}{\pi^2} (\tilde{A}_{\text{ph}}(\zeta))^2 \right\}. \quad (40)$$

It is evident that the electron drag by phonons and their subsequent mutual drag, as well as the contribution due to normal phonon–phonon scattering, may result in a considerable decrease in the Lorenz factor L^* and should be taken into account when interpreting experimental data.

5. CONCLUSIONS

Thus, we have solved coupled rate equations for the electron and phonon distribution functions with inclusion of normal phonon–phonon scattering for conductors with degenerate carrier statistics. The kinetic coefficients were calculated in a linear approximation in the degeneracy parameter. The part played by the mutual electron–phonon drag, as well as by the normal phonon-scattering processes, in electrical resistivity, thermopower, and heat conductivity of degenerate conductors has been analyzed. Formulating the nonequilibrium state of the phonon subsystem in terms of a three-parameter approximation allowed for a more correct analysis of the kinetic effects. It was shown that, under the conditions where the phonon relaxation frequency due to N-processes is of the order of or exceeds the resistive frequency, the drift of the phonon system caused by the N-processes brings about an enhancement of the mutual drag effect on the electrical conductivity and a considerable increase in the phonon component in the thermopower. In this case, one should use the expressions obtained in this work when interpreting experimental data on the electrical conductivity, thermopower, and heat conductivity of conductors with degenerate carrier statistics. Investigation into elec-

tron–phonon drag in degenerate conductors can be extended by considering normal electron–electron scattering, which, along with the phonon N-processes, does not contribute to the electron momentum relaxation but results instead in the drift of the electron system. Description of the nonequilibrium state of both electrons and phonons in terms of a three-parameter approximation would allow for a more adequate analysis of electron–phonon drag and of the kinetic phenomena exhibited in conductors with degenerate carrier statistics.

REFERENCES

1. L. É. Gurevich, Zh. Éksp. Teor. Fiz. **16** (3), 193 (1946); **16** (5), 416 (1946).
2. I. M. Tsidil'kovskiĭ, *Thermomagnetic Effects in Semiconductors* (Fizmatgiz, Moscow, 1960; Academic, New York, 1962).
3. V. M. Askerov, *Electronic Transport Phenomena in Semiconductors* (Nauka, Moscow, 1985).
4. F. J. Blatt, P. A. Schroeder, C. L. Foiles, and D. Greig, *Thermoelectric Power of Metals* (Plenum, New York, 1976; Metallurgiya, Moscow, 1980).
5. P. S. Zyryanov and M. I. Klinger, *Quantum Theory of Electronic Transport Phenomena in Crystalline Semiconductors* (Nauka, Moscow, 1976).
6. P. S. Zyryanov and G. I. Guseva, Usp. Fiz. Nauk **95** (4), 565 (1968); R. T. Delves, Rep. Prog. Phys. **28** (2), 249 (1965).
7. J. E. Parrott, Proc. Phys. Soc. London, Sect. B **70** (6), 590 (1957).
8. J. Appel, Z. Naturforsch. A **12** (5), 410 (1957); A **13** (5), 386 (1958).
9. I. I. Hanna and E. H. Sondheimer, Proc. R. Soc. London, Ser. A **239** (1217), 247 (1957).
10. L. É. Gurevich and I. Ya. Korenblit, Fiz. Tverd. Tela (Leningrad) **6** (3), 856 (1964) [Sov. Phys. Solid State **6**, 661 (1964)].
11. I. G. Lang and S. T. Pavlov, Zh. Éksp. Teor. Fiz. **63** (4), 1495 (1972) [Sov. Phys. JETP **36**, 793 (1973)].
12. I. G. Kuleev, Fiz. Met. Metalloved. **87** (6), 5 (1999).
13. I. G. Kuleev, Fiz. Tverd. Tela (St. Petersburg) **41** (10), 1753 (1999) [Phys. Solid State **41**, 1608 (1999)].
14. J. Callaway, Phys. Rev. **113** (4), 1046 (1959).
15. R. Berman, *Thermal Conduction in Solids* (Clarendon Press, Oxford, 1976; Mir, Moscow, 1979).
16. J. M. Ziman, *Electrons and Phonons* (Clarendon Press, Oxford, 1960; Inostrannaya Literatura, Moscow, 1962).
17. B. M. Mogilevskiĭ and A. F. Chudnovskiĭ, *Thermal Conductivity of Semiconductors* (Nauka, Moscow, 1972).
18. V. S. Oskotskiĭ and I. A. Smirnov, *Defects in Crystals and Thermal Conductivity* (Nauka, Leningrad, 1972).
19. C. Herring, Phys. Rev. **95** (2), 954 (1954).
20. S. Simons, Proc. Phys. Soc. London **82** (2), 401 (1963); **83** (3), 799 (1963).
21. I. I. Lyapilin and Kh. M. Bikkin, Fiz. Tekh. Poluprovodn. (St. Petersburg) **33** (3), 701 (1999) [Semiconductors **33**, 648 (1999)]; Kh. M. Bikkin, A. T. Lonchakov, and I. I. Lyapilin, Fiz. Tverd. Tela (St. Petersburg) **42** (2), 202 (2000) [Phys. Solid State **42**, 207 (2000)].
22. A. H. Wilson, *The Theory of Metals* (Cambridge Univ. Press, Cambridge, 1954).
23. I. G. Kuleev, Fiz. Tverd. Tela (St. Petersburg) **42** (6), 979 (2000) [Phys. Solid State **42**, 1009 (2000)].

Translated by G. Skrebtsov

Physics of the Solid State, Vol. 42, No. 11, 2000, pp. 2014–2016. Translated from Fizika Tverdogo Tela, Vol. 42, No. 11, 2000, pp. 1961–1963.

SEMICONDUCTORS AND DIELECTRICS

Fundamental Reflection Spectrum and the Electronic Band Structure of Chlorine-Doped CdTe

P. N. Tkachuk

Chernovtsy State University, Chernovtsy, 58012 Ukraine

e-mail: ptkachuk@chdu.cv.ua

Received March 7, 2000

Abstract—The effect of chlorine impurity on the fundamental reflection spectrum and the electronic band structure of cadmium telluride crystals has been studied. At the impurity concentration $N_{Cl} > 5.0 \times 10^{19}$ cm^{-3}, a peak appears in the reflectance spectra. This peak is due to electron transitions at the *X* point of the Brillouin zone from the upper split valence band to Cl levels lying 0.05 eV above the Γ minimum of the conduction band. The other features in the reflectance spectra and band structure are explained as being due to the effect of spin–orbit splitting at the *X* point and to indirect electronic transitions from the Cl levels to the Γ minimum.

Cadmium telluride is a wide-bandgap semiconducting material (E_g = 1.606 eV at 4.2 K) with direct transitions [1]. Doping of CdTe by Group-III and Group-VII elements of the periodic table places them in sites of the Cd and Te sublattices, respectively, where they act as donors. The donor levels lying below the Γ minimum of the conduction band (CB) are mainly shallow (up to 0.02 eV) and are calculated in terms of the hydrogenic model. A study [2] of the pressure dependences of the electrical resistivity and the Hall coefficient of CdTe doped by Ga, In, Cl, Br, and other donor impurities led to the development of the model of a non-Γ center. This model takes into account lattice rearrangement around donor impurities, which gives rise to the formation of states differing from the hydrogen-like ones. By [2], the Cl impurity levels lie 0.05 eV above the CB minimum and are not at the Γ point of the Brillouin zone (BZ). The symmetry of the center was not specified. Taking into account the possibility of indirect transitions, this model was found to be applicable to the interpretation of experimental data in studies of electron trapping centers in [3] and photoluminescence (PL) bands beyond the fundamental absorption edge in [4]. It was proposed [5] to place the off-center CB minimum associated with the above-mentioned impurities at the *X* point of the BZ; however, this refinement of the non-Γ center requires experimental support.

The purpose of this work was to investigate the effect of chlorine impurity on the fundamental reflection spectrum and electronic band structure of cadmium telluride, as well as to check the validity of the non-Γ-center model.

1. SAMPLE PREPARATION AND EXPERIMENTAL TECHNIQUES

CdTe single crystals were grown from the melt by the Bridgman method. The crystals were doped during growth by adding a corresponding amount of $CdCl_2$ into the ampoule with the preliminarily synthesized CdTe. The concentration of the chlorine impurity introduced into the melt was within the range of 10^{18}–10^{20} cm^{-3}.

Measurements of the electrical conductivity σ and the Hall constant R_H were carried out within the 300–420 K range on mechanically polished parallelepiped-shaped samples 1.5 × 2 × 8 mm in size. The undoped CdTe samples had hole conduction at room temperature, with carrier concentration $p \approx 10^{15}$ cm^{-3} and mobility μ_p = 80–90 cm^2/V s. The CdTe:Cl samples exhibited electronic conduction with $n \approx 10^6$ cm^{-3} and μ_n = 300–400 cm^2/V s. A characteristic feature of chlorine-compensated CdTe single crystals is the stability of their electrophysical parameters and the same spectral response of the low-temperature PL over the length of the ingot [6].

Fundamental reflection spectra $R(\lambda)$were obtained at room temperature on a HITACHI-356 double-beam spectrometer. The measurements were performed on naturally cleaved crystals under practically normal incidence of light on the surface of the studied sample.

2. RESULTS AND DISCUSSION

$R(\lambda)$ spectra of undoped CdTe and of CdTe:Cl (inset to Fig. 1) exhibit an E_0 peak (the Γ_8–Γ_6 transition, see Fig. 2). The peak positions, 1.64 and 1.65 eV, respectively, agree well with the theoretical value of 1.65 eV [1].

1063-7834/00/4211-2014$20.00

The chlorine-induced short-wavelength shift of the E_0 peak by 0.01 eV is accompanied by its spread, which washes out the free-exciton structure E_{ex} at 1.599 eV. The latter is most probably associated with free-exciton dissociation in the field of a large number of charged centers (in our case, Cl_{Te} donors). The shift of the peak is apparently caused by the CB shift induced by the strong interaction of electrons with phonons emitted in indirect transitions from the off-center CB minimum. In this connection, we note the large value of the Fröhlich constant (α_{Fr} = 0.39 [7]) characterizing CB electron coupling with optical phonons in CdTe, as well as the maximum value of the acoustic phonon energy at the BZ edge. The assumption of a strong electron–phonon coupling in *n*-CdTe:Cl crystals with a high chlorine-impurity concentration is argued for by an analysis of the $\mu \sim T^{\alpha}$ relations. For samples with N_{Cl} = 10^{18}–10^{19} cm^{-3}, α = –(1.5–1.6). This value of α is typical of *n*-CdTe [8] and is in accord with the theoretical figure, –1.5, associated with scattering from acoustic lattice vibrations. In samples with N_{Cl} = 5.0×10^{19}–10^{20} cm^{-3}, α = –4.5, which implies a comparable contribution of various scattering mechanisms to the total carrier mobility. In this case, one should apparently take into account two-phonon scattering from acoustic vibrations with α = –3 [9] and scattering from optical lattice vibrations, where α is determined by the quantity $\exp(\hbar\omega_{LO}/kT - 1)$. Note that the energy position of the donors can provide, in an indirect transition, the creation of a longitudinal optical ($\hbar\omega_{LO}$ = 0.0213 eV [1]) or two longitudinal acoustic phonons with the maximum energy $\hbar\omega_{LA} \approx 0.014$ eV. This value of $\hbar\omega_{LA}$ is in good agreement with the known experimental and calculated *LA* phonon energies at the BZ edges [1].

In the UV region, *R* shows the following features. In CdTe, this is the doublet E_1 and E_2 ($E_1 + \Delta_1$) at 3.64 and 4.27 eV, respectively (curve *1* in Fig. 1), which corresponds to the $L_{4.5}$–L_6 and L_6–L_6 transitions (Fig. 2). The magnitude of the spin–orbit splitting Δ_1 = 0.63 eV is in accord with the literature data of 0.6–0.7 eV [10], although the doublet peak positions are somewhat higher than the typical theoretical figures of 3.49 and 4.04 eV [1, 10]. By [1, 10], the E_0 peak at 5.16 eV corresponds to the Δ_5–Δ_5 transition. It should be pointed out that the relatively weak intensity of the E_0 peak (Δ_5–Δ_5) is at odds with earlier studies of the fundamental reflectivity spectra of cadmium telluride, while agreeing with the calculated figures quoted in the papers where more complex models involving transitions within the BZ are proposed for the nature of the structure of *R* [10]. The CdTe:Cl curves (*2*, *3*) are characterized by equal intensities of the E_1 and E_2 peaks resulting in some uncertainty as to their energy positions, as well as by the appearance of a *W* peak at 3.23 eV, which is not known from the literature. At first glance, the overall structure of the reflectance spectrum of CdTe:Cl crystals in the UV region is very similar to

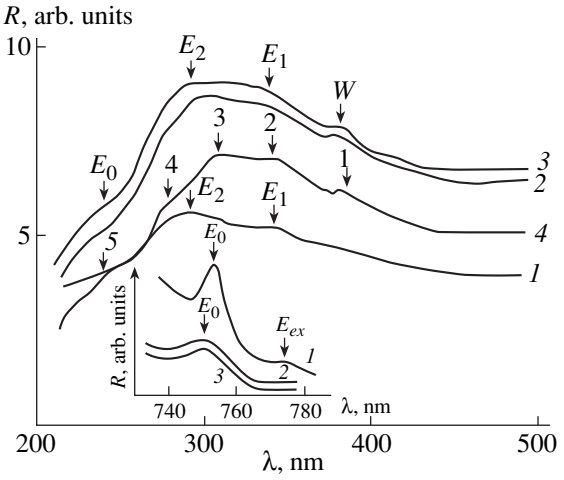

Fig. 1. Fundamental reflectance in the long-wavelength (inset) and UV regions of (*1*) CdTe, (*2*, *3*) CdTe:Cl, and (*4*) Si. Chlorine impurity concentration (cm^{-3}): (*2*) 2–5.0×10^{19} and (*3*) 10^{20}.

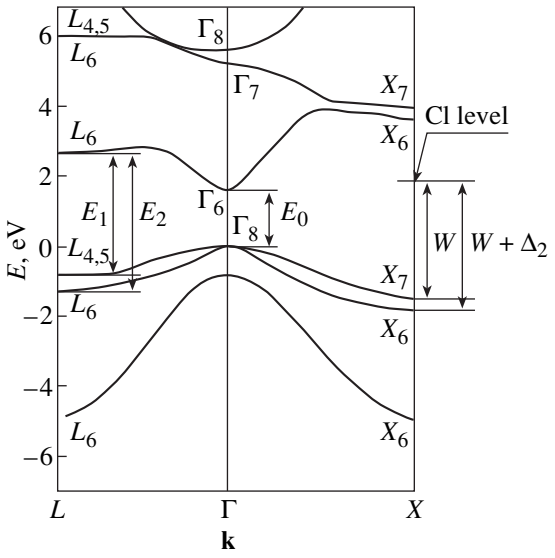

Fig. 2. Chlorine energy level position at the *X* point in the Brillouin zone and the main transitions corresponding to the fundamental reflectance peaks in CdTe and CdTe:Cl single crystals. The CdTe band structure was taken from [1].

the *R* structure for Si (curve *4*). Note that the positions of peaks 1, 2, 3, 4, and 5 at 3.2, 3.5, 3.9, 4.5, and 5.16 eV, respectively, correlate with the energies of the main transitions in Si crystals [10], namely, $L_3' - L_1'$ (3.2 eV), $\Gamma_{25}' - \Gamma_{15}'$ (3.5 eV), X_4–X_1 (4.0 eV), Σ_2–Σ_1 (4.4 eV), and L_3'–L_1 (5.2 eV). Hence, the similarity between the fundamental reflectance spectra is due to the formation of

the W peak and the relatively weak R intensity in the 5.16- to 5.20-eV region.

The position of the chlorine energy levels at the BZ X point, 0.05 eV above the Γ minimum (Fig. 2), permits one to relate the nature of the W peak in crystals with $N_{Cl} > 5.0 \times 10^{19}$ cm^{-3} to electron transitions from the X_{7v} point to the off-center CB minimum associated with the donor impurity band. In addition, the valence-band spin–orbit splitting at the X point (Δ_2 = 0.32–0.46 eV [10]) results in a "superposition" of the transitions $L_{4.5}$–L_6 (E_1) and the transitions to the X_{6v} off-center minimum ($W + \Delta_2$). This brings about an increase in intensity of the E_1 peak; however, compared with the case of undoped CdTe, one may observe its shift and some washing out of the E_1 and E_2 doublet structure.

Thus, the band structure of CdTe doped by the chlorine donor impurity undergoes substantial changes at high enough doping levels, which becomes manifest in a shift of the CB and the formation of a donor impurity band with a minimum at the X point in the Brillouin zone.

ACKNOWLEDGMENTS

The author expresses gratitude to M.I. Kurik and N.D. Raranskiĭ for their assistance in the work and valuable discussions.

REFERENCES

1. K. R. Zanio, in *Semiconductors and Semimetals* (Academic, New York, 1978), Vol. 113.
2. G. W. Iseler, J. A. Kafalas, A. J. Strauss, *et al.*, Solid State Commun. **10**, 619 (1972).
3. R. O. Bell and F. V. Wald, IEEE Trans. Nucl. Sci. **22**, 241 (1975).
4. P. N. Tkachuk, V. I. Tkachuk, N. D. Korbutjak, *et al.*, J. Cryst. Growth **184/185**, 536 (1998).
5. R. Legros, Y. Marfaing, and R. J. Tribulet, Phys. Chem. Solids **39**, 179 (1978).
6. D. V. Korbutjak, S. G. Krylyuk, P. M. Tkachuk, *et al.*, J. Cryst. Growth **197**, 659 (1999).
7. B. M. Askerov, *Electronic Transport Phenomena in Semiconductors* [in Russian] (Nauka, Moscow, 1989).
8. A. V. Savitskiĭ, V. I. Tkachuk, and P. N. Tkachuk, Fiz. Tekh. Poluprovodn. (St. Petersburg) **26**, 952 (1992) [Sov. Phys. Semicond. **26**, 536 (1992)].
9. E. V. Kuchis, *Methods for Researching the Hall Effect* [in Russian] (Sov. Radio, Moscow, 1974).
10. V. V. Sobolev and V. V. Nemoshkalenko, *The Methods of Computational Physics in the Theory of the Solid State: Electronic Structure of Semiconductors* [in Russian] (Naukova Dumka, Kiev, 1988).

Translated by G. Skrebtsov

Physics of the Solid State, Vol. 42, No. 11, 2000, pp. 2017–2021. Translated from Fizika Tverdogo Tela, Vol. 42, No. 11, 2000, pp. 1964–1968.

SEMICONDUCTORS AND DIELECTRICS

On the Mechanism of Luminescence of Silicon Nanostructures

P. M. Tomchuk, D. B. Dan'ko, and O. É. Kiyaev

Institute of Physics, National Academy of Sciences of Ukraine, pr. Nauki 144, Kiev-39, UA-03039 Ukraine

e-mail: fedorov@iop.kiev.ua

Received March 21, 2000

Abstract—A new model of porous-silicon (PS) luminescence based on hot-electron generation in silicon nanoparticles is proposed. This mechanism was used earlier for interpretation of light emission in island metal films (IMF). This paper offers a theoretical analysis of possible mechanisms capable of producing light emission in hot-electron collisions with a surface. Experimental data are presented in support of the applicability of this model to PS and silicon nanoparticles (the existence of electron emission in semiconductor structures and the correlation between the electron emission current and the luminescence intensity). © *2000 MAIK "Nauka/Interperiodica".*

Studies of the luminescence observed in porous silicon (PS) and similar silicon nanostructures have been dealt with in many publications and are summed up in monograph [1] and reviews [2, 3]. Nevertheless, the nature of the visible PS luminescence remains unclear. One of the first models proposed was based on size quantization of the energy levels in small silicon particles making up pore walls [4]. Photoluminescence (PL) is related in this model to radiative interband transitions through the energy gap enlarged by the quantum confinement (QC) effect. This model accounts well for the shift of the PL response toward shorter wavelengths as the pores are made progressively larger by chemical etching and the pore walls decrease in size.

There are, however, many observations defying explanation within the quantum model. Among them is the temperature dependence of the PL intensity and its quenching at temperatures of 600–800 K [5]. The width of the PL response (about 0.6 eV) also suggests that, according to the model of [4], the wall size scatter should be very small, which has not been observed experimentally [6]. The authors of [6] believe that the red PL in PS is due to molecular recombination in the near-surface region of the crystal rather than to a size quantization effect.

Alternative theories relating the visible PL from PS to molecular compounds present on the PS surface are usually called "molecular factor" theories. Molecular compounds capable of emitting visible PL themselves may form on the PS surface during etching. This may be the siloxane molecule consisting of Si, H, and O, as well as SiH_x complexes, polysilane, etc. [7]. This theory accounts well for the PL temperature dependence, because some of the above molecules are observed to decompose at the same temperatures at which the PL disappears [8]. It is difficult to understand within this theory, however, why PS layers subjected to an additional treatment (passivation) of the surface in hydrogen and in pure oxygen exhibit a similarly strong luminescence [7].

The so-called smart quantum model [7] is in a certain sense a combination of the preceding ones. Similar to the quantum model, it assumes that the visible PL is due to the increased width of the bandgap in small silicon particles; however, the molecules adsorbed on the PS surface are also believed to play an important role. More specifically, the adsorbed molecules of hydrogen, oxygen, and hydrogen-containing compounds deposited on the PS surface as a result of etching or some other specific additional treatment passivate this surface and, thus, increase the probability of radiative interband recombination.

Observation of the visible PL in PS stimulated studies of the PS electroluminescence (EL). These studies have a larger application potential, because they offer the promise of developing PS-based light-emitting devices and of the integration of optical and electronic components on a silicon substrate.

Primarily, the electroluminescence of various variants of sandwich structures has been studied. The EL properties of planar structures based on PS [9] and Si nanoparticles [10, 11] have recently become the focus of several studies. The PS EL studies are considered in detail in review paper [3]. In contrast to photoluminescence investigations, the results quoted by various authors on EL are more contradictory even in the case where the same object is studied. No common opinion has thus far been formed on the nature of the discrete pattern of luminescence of the sample surface and on the shape of the *I–V* curves, which determines effective luminescence. The need of electroforming for the formation of local luminescence centers likewise remains unclear. In some cases, the maxima of the EL and PL spectral responses coincide [12], while in others they differ in position [13]. The position of the maxima can also be affected by interference effects [14].

1063-7834/00/4211-2017$20.00

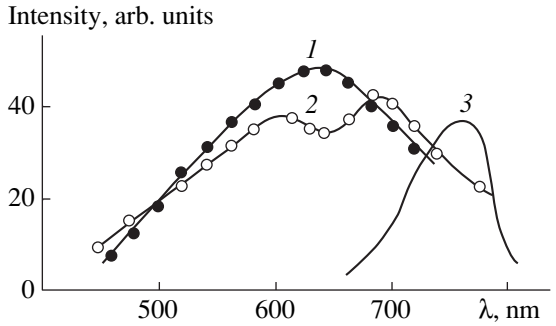

Fig. 1. Radiation spectrum of current-carrying gold island films. (*1*), (*2*) Relate to emission from individual centers. (*3*) Plots the emission of a chain-structured island film.

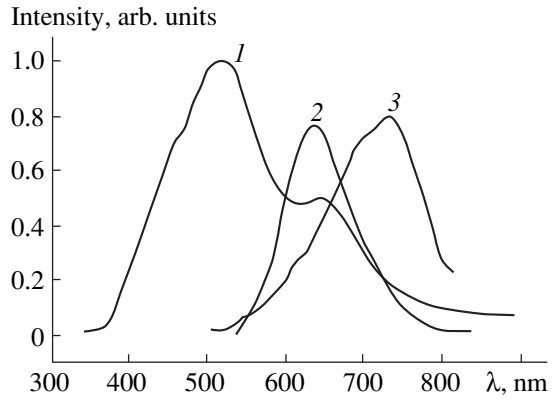

Fig. 2. Electroluminescence spectra of porous-silicon-based structures. (*1*) Refers to [15], (*2*) to [12], and (*3*) to [16].

While the first PS-based light-emitting devices were Schottky diodes, further research led to the development of PS *p–n* junctions characterized by a much more efficient carrier injection into the region of the *p–n* junction [12]. The mechanism of the emission was believed [12] to consist in the injection of electrons from the *n*-layer and of holes from the *p*-layer into the region of the *p–n* junction, where they underwent radiative recombination. The PS bandgap width in the region of the *p–n* junction was increased by the QC effect. The observed luminescence degradation with time is assigned [12] to depassivation of the emitting layers. The breaking of the passivating bonds may take place as the sample is heated in the course of work.

We noticed that the spectral response of the luminescence of current-carrying island metal films [10] reveals a close similarity with those of PS-based structures. This is seen, for instance, from Figs. 1 and 2 showing the spectra of luminescence of Au island films and of the PS EL when a current is passed through them [12, 15, 16]. The observations of the emission from island metal films (IMF) were interpreted by us in terms of a model which takes into account the possibility of strong nonequilibrium electron-gas heating in nanoobjects [17, 18]. A weighty argument for a model involving hot electrons and for the luminescence excited by them in islands came from the experiments that showed that the luminescence and electron emission are produced by the same centers and that the luminescence intensity and the electron emission current are correlated [19]. We suggested that the luminescence in island films and in PS may occur by the same mechanism [20]. This paper develops theoretical concepts on hot electrons in PS and reports a number of new experiments. Among them is an investigation of electron emission from PS and Si nanoparticles and of the correlation between electroluminescence and electron emission.

1. THEORY

IMFs on dielectric substrates (glass, SiO_2, SiO, sapphires, etc.) are known to emit electrons and photons when power is delivered to the islands by a variety of means, for example, by passing a electric current [19, 21] or by irradiation by electrons [22], laser light [23], or microwaves [24]. The characteristics of the electronic and photon emission allow the simplest and least contradictory interpretation within the hot-electron model [17, 18].

Hot-electron generation in IMFs is initiated by a combination of three factors: (i) a sharp decrease in the electron–lattice coupling in islands whose size is less than the electron mean free path, (ii) the possibility of injecting large power fluxes into a particular island, and (iii) the thermal stability of small islands on dielectric substrates with a good thermal contact.

Note that, when electrons are heated by an electric current, injection of high power fluxes into a particular island is made possible by the creation of high current-density channels in the course of electroforming. In laser heating, this possibility is associated with efficient light absorption by small particles [18, 25]. The increase in the thermal stability of an island with a decrease in its size is due to the increased ratio of the surface area of an island to its volume [17]. All the above factors are also characteristic, in various degrees, of porous silicon. The luminescence observed in IMFs may be connected with the bremsstrahlung of hot electrons and the inverse surface photoeffect in collisions of hot electrons with the island surface, as well as with inelastic tunneling from one island to another. The efficiency of light emission from an IMF is determined by two factors, namely, by the presence of hot electrons and by an extended surface. Both these factors are inherent in PS. Hot electrons produced in photoluminescence in semiconductors are capable of initiating an internal photoeffect. In this case, the hot-electron distribution function in energy is determined by the interaction of the primary nonequilibrium electrons with lattice vibrations. In the case of electroluminescence, the electron distribution function in energy is formed by

the competing effects of the electric field and electron scattering from the lattice vibrations.

By the model proposed here, the luminescence will appear if the presence of hot electrons in the size-quantized components of a silicon structure (islands, walls, filaments, etc.) is combined with the structure surface being in a specific condition.

When a hot nonequilibrium electron is scattered by a potential barrier, the component of the electron velocity normal to the barrier changes abruptly from $\nu_\perp$ to $-\nu_\perp$.

The bremsstrahlung spectrum is given by the expression [17]

$$\varepsilon(\omega) = \frac{16e^2}{3\pi mc^3}\sqrt{\varepsilon_\perp(\varepsilon_\perp - \hbar\omega)}, \quad (1)$$

where e and m are the electronic charge and mass, respectively, and c is the velocity of light.

Expression (1) is valid if

$$\varepsilon_\perp > \hbar\omega. \quad (2)$$

As is seen from Eq. (1), the spectral distribution of the radiation emitted by any one electron depends only weakly on the frequency. However, condition (2) imposes a stronger frequency dependence on an electron ensemble, because it relates the radiation spectrum to the distribution of hot electrons by the energy in the conduction band. In particular, if one accepts a Maxwellian function with an effective electron temperature T_e for the hot-electron distribution in energy, the bremsstrahlung spectrum due to collisions with the surface can be written as [1]

$$E(\omega) \approx S_c \frac{2e^2\mu^2}{3(\pi c\hbar)^3}\hbar\omega e^{-\hbar\omega/kT_e} \quad (\text{at } \hbar\omega < \mu). \quad (3)$$

Here, S_c is the surface area and μ is the Fermi energy.

We see that, in the case of a Maxwellian distribution function, the bremsstrahlung at the boundary should pass through a maximum in intensity at the frequency $\hbar\omega = kT_e$. For other mechanisms of light emission by hot electrons (for instance, for an effect inverse to the Drude absorption), this maximum can be shifted toward higher frequencies. Its position can also be affected by a deviation of the electron energy distribution from the Maxwellian function.

The energy distribution function of excited valence-band electrons in the PS conduction band usually has two maxima. One of them is due to the distribution of the electronic density of states in the valence band. The specific features of this maximum are determined by the electrons that did not have enough time to emit acoustic and optical phonons more than once. The other maximum lies at moderate energies, which in this case are not equal to the lattice temperature.

We believe that the presence of hot electrons and of an extended PS surface should favor bremsstrahlung generation and the onset of the inverse photoeffect when electrons hit the inner surface of the pores (Fig. 3). Moreover, such collisions may also initiate interband transitions with the emission of light. The band bending near the surface affects the height and the shape of the surface barrier. This may account for the luminescence sensitivity to surface contamination. In particular, adsorbed oxides are capable of substantially reducing the surface work function and, thus, of enhancing the surface photoeffect initiated by electron collisions with the pore surface.

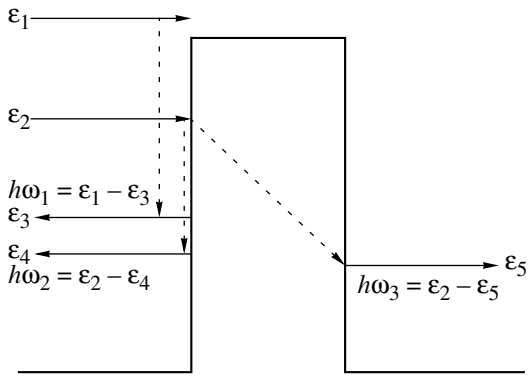

Fig. 3. Schematic of light emission in inverse photoeffect ($h\omega_1$), in inelastic electron scattering from a potential barrier between nanoparticles ($h\omega_2$), and in inelastic electron tunneling ($h\omega_3$).

2. RESULTS OF THE EXPERIMENT AND DISCUSSION

We studied the electroluminescence and electronic emission from PS-based sandwich structures, as well as from planar systems made up of Si islands.

The PS layers were prepared by standard electrochemical etching of *p*-type single-crystal plates 200 μm thick and with an electrical resistivity of 7 Ω cm. The porous layer was a few microns thick. An aluminum layer was deposited on the back side of the plate to provide an ohmic contact (see inset in Fig. 4). A gold grid electrode was deposited on the PS layer to facilitate electron escape into vacuum when observing electronic emission from the sample. In some samples, the top gold electrode was replaced by a spring-type contact. The measurements were carried out in a vacuum, with a residual gas pressure at a level of 10^{-4} Pa. To measure the electronic emission, an electron collector biased at +100 V with respect to the top gold electrode was placed above the sample. The *I–V* curves of the conduction and electronic-emission currents, as well as the radiation spectrum, were studied by applying dc and ac voltages.

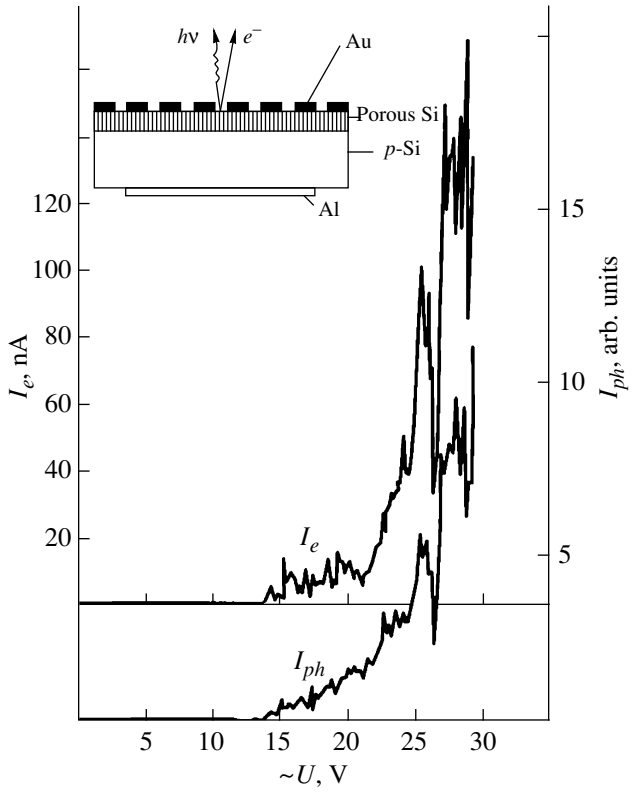

Fig. 4. Dependence of the electron emission current (I_e) and integrated luminescence intensity (I_{ph}) on the ac voltage (frequency 500 Hz) applied to a porous-silicon-based sandwich structure. The inset shows a schematic of the structure under study.

Figure 5 presents an *I–V* curve of the conduction current through a dc-biased experimental structure shown in Fig. 4. The structure had rectifying properties with a rectification factor of 50 at a voltage of about 10 V. Forward bias is obtained by applying a negative potential to the top gold electrode, which agrees with the published data [3]. The conduction-current *I–V* curves measured under forward bias exhibit a clearly pronounced nonohmic pattern. Conduction-current *I–V* characteristics of this kind were also observed when an ac voltage was applied to a sample.

EL was seen under a forward bias of about 13 V in the form of separate red luminous dots, which could be observed by the unaided eye in the dark. The EL intensity observed when applying an ac voltage of the same effective magnitude was somewhat higher than that under a dc bias. This is similar to EL observations in IMFs [10]. The appearance of the luminescence was accompanied by the onset of electronic emission from the diode. The inset to Fig. 5 presents oscillograms of the ac voltage *U* applied to the structure and of the conduction (I_c) and emission (I_e) currents. One readily sees that an emission current is observed in a forward-biased sample, where a noticeable conduction current also sets in. The dependences of the luminescence intensity (λ_{max} = 700 nm) and of the electron emission current on the applied ac voltage are shown in Fig. 4. These dependences are seen to be well correlated, including their noise, which suggests that electron emission and the EL processes are interrelated. As was already mentioned, a similar correlation was observed in the case of IMFs [19].

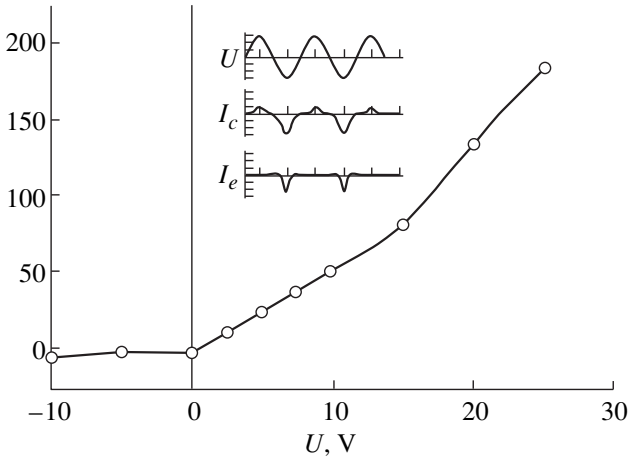

Fig. 5. *I–V* characteristic of the conduction current of a porous-silicon-based sandwich structure under a dc bias. The schematic of the structure is shown in the inset to Fig. 4. The inset in this figure presents oscillograms of the conduction current I_c and the electron emission current I_e with an ac voltage *U* at a frequency of 500 Hz applied to the structure.

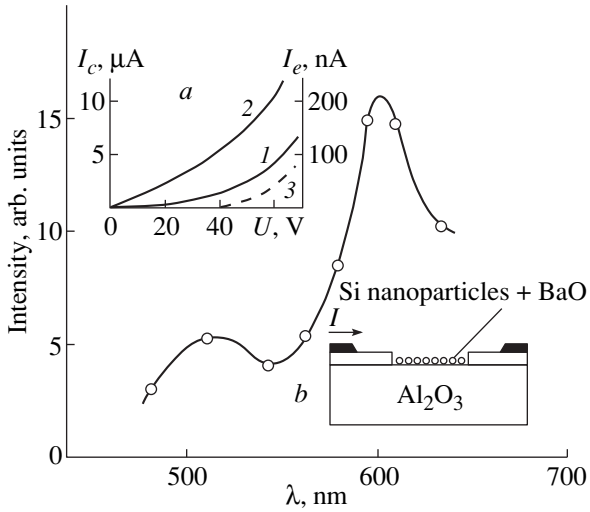

Fig. 6. Spectral response of radiation of the nanostructure shown in inset *b*. Inset *a* shows an *I–V* characteristic of the conduction current I_c of a clean silicon island film (*1*) and after a reduction of the film work function (*2*), as well as an *I–V* curve of the electron emission current I_e after the lowering of the film work function (*3*).

In addition to the sandwich configurations, we also studied the planar silicon island structures [10], which were prepared in a high vacuum on a dielectric substrate in the gap between the Si contacts (inset *b* in Fig. 6). To reduce the electron work function, a BaO layer was deposited on the Si island film. Deposition of BaO on Si islands increased film conductivity, and an electron emission current accompanied by luminescence set in at a voltage of 40 V (Fig. 6). Also shown in the figure is the spectral response of the luminescence of a BaO-coated Si island film.

The observation of electron emission in PS and silicon island films argues for the presence of hot electrons in them. The similarity between the spectral responses gives one grounds to maintain that the EL in these materials has the same nature. The presence of hot electrons in silicon nanoparticles with a reduced work function and of an extended surface in PS makes the operation of luminescence generation mechanisms involving bremsstrahlung, the inverse surface photoeffect, and inelastic tunneling possible.

ACKNOWLEDGMENTS

The authors are indebted to A.G. Naumovets and R.D. Fedorovich for fruitful discussions.

REFERENCES

1. *Properties of Porous Silicon*, Ed. by L. T. Canham (IEE INSPEC, The Inst. of Electrical Engineers, London, 1997).
2. S. V. Svechnikov, A. V. Sachenko, G. A. Sukach, *et al.*, Optoélektron. Poluprovodn. Tekh. **27**, 3 (1994).
3. S. V. Svechnikov, É. G. Manoĭlov, É. B. Kaganovich, and V. S. Dvirnyak, Optoélektron. Poluprovodn. Tekh. **32**, 19 (1997).
4. L. T. Canham, Appl. Phys. Lett. **57**, 1046 (1990).
5. S. H. Perry, F. Lu, F. Namavar, *et al.*, Appl. Phys. Lett. **60**, 3117 (1992).
6. B. M. Shutov and O. I. Datsenko, Ukr. Fiz. Zh. **43** (4), 489 (1998).
7. M. Koch, Mater. Res. Soc. Symp. Proc. **298**, 319 (1993).
8. E. A. Shelonin, M. V. Naĭdenkova, A. M. Khort, *et al.*, Fiz. Tekh. Poluprovodn. (St. Petersburg) **32** (4), 494 (1998) [Semiconductors **32**, 443 (1998)].
9. C. C. Yeh, C. H. Lee, H. L. Hwang, and K. G. J. Hsu, Thin Solid Films **255**, 262 (1995); M. Takanahi, N. Araki, and N. Koshida, Jpn. J. Appl. Phys. Part 2 **37**, L1017 (1998).
10. P. G. Borziak, D. B. Dan'ko, R. D. Fedorovich, *et al.*, Prog. Surf. Sci. **53** (2–4), 171 (1996).
11. A. G. Nassiopoulov, P. Photopolos, and A. Travlos, in *Physics, Chemistry and Application of Nanostructures: Reviews and Short Notes to Nanomeeting 99*, Ed. by V. E. Borisenko, A. B. Filonov, S. V. Gaponenko, and V. S. Gurin (World Scientific, Singapore, 1999), p. 356.
12. P. Steiner, F. Kozlovski, and W. Lang, Appl. Phys. Lett. **62** (21), 2700 (1993).
13. R. Sabet-Dariani, N. S. McAlpine, and D. Haneman, J. Appl. Phys. **75** (12), 8008 (1994).
14. V. G. Golubev, A. V. Medvedev, A. B. Pevtsov, *et al.*, Fiz. Tverd. Tela (St. Petersburg) **41**, 153 (1999) [Phys. Solid State **41**, 137 (1999)].
15. W. Lang, P. Steiner, F. Kozlowski, and P. Ramm, Thin Solid Films **255**, 224 (1995).
16. S. N. Kuznetsov, M. Ya. Berezin, and G. B. Stefanovich, Pis'ma Zh. Tekh. Fiz. **18** (22), 72 (1992) [Sov. Tech. Phys. Lett. **18**, 753 (1992)].
17. E. Belotskij and P. Tomchuk, Surf. Sci. **239**, 143 (1990).
18. P. M. Tomchuk, Surf. Sci. **330**, 350 (1995).
19. P. G. Borzyak and Yu. A. Kulyupin, *Electronic Processes in Island Metallic Films* [in Russian] (Naukova Dumka, Kiev, 1980).
20. P. Tomchuk, D. Dan'ko, and O. Kiyayev, in *Final Book of Abstracts E-MRS Spring Meeting, Strasbourg, 1994*, F-V/P47.
21. H. Pagnia and N. Sotnik, Phys. Status Solidi A **108** (1), 11 (1988).
22. R. D. Fedorovich, O. E. Kiyayev, A. G. Naumovets, *et al.*, Phys. Low-Dimens. Semicond. Struct. **1**, 83 (1994).
23. A. A. Benditskii, D. V. Danko, R. D. Fedorovich, *et al.*, Int. J. Electron. **77**, 985 (1994).
24. D. A. Ganichev, V. S. Dokuchaev, S. A. Fridrikhov, *et al.*, Pis'ma Zh. Tekh. Fiz. **1** (8), 386 (1975) [Sov. Tech. Phys. Lett. **1**, 180 (1975)].
25. P. M. Tomchuk and B. P. Tomchuk, Zh. Éksp. Teor. Fiz. **112**, 661 (1997) [JETP **85**, 360 (1997)].

Translated by G. Skrebtsov

Physics of the Solid State, Vol. 42, No. 11, 2000, pp. 2022–2029. Translated from Fizika Tverdogo Tela, Vol. 42, No. 11, 2000, pp. 1969–1975.

SEMICONDUCTORS AND DIELECTRICS

Generation of Thermal Donors in Silicon: Effect of Self-Interstitials

V. V. Voronkov, G. I. Voronkova, A. V. Batunina, V. N. Golovina, M. G. Mil'vidskiĭ, A. S. Gulyaeva, N. B. Tyurina, and L. V. Arapkina

State Research Institute for Rare Metals (GIREDMET), B. Tolmachevskiĭ per. 5, Moscow, 109017 Russia

e-mail: icpm@mail.girmet.ru

Received April 10, 2000

Abstract—The generation of low-temperature thermal donors (TD) in silicon is sensitive to the sample cooling rate (from the anneal to room temperature) and the ambient (air or vacuum). This effect is most clearly pronounced in the case of annealing at 500°C, is noticeable at 480°C, and is practically undetectable at 450°C. The results are interpreted satisfactorily as being due to the TD generation becoming enhanced in the presence of silicon self-interstitial (Si_I) atoms. These atoms are emitted by thermal donors, to be subsequently absorbed by sinks, particularly the sample surface and grown-in microdefects (vacancy voids). When annealing in a vacuum, the surface acts as the main sink. If the anneal is done in air, this sink is passivated as a result of oxidation and/or contamination, with voids becoming the main sinks; as a result, the concentration of Si_I atoms increases substantially and the generation rate is enhanced. Rapid cooling brings about a partial passivation of the voids (as a result of their becoming decorated by rapidly diffusing impurities) and an additional enhancement of the generation rate. The calculated rate curves obtained within this model are well fitted to the experiment.

The kinetics of oxygen thermal-donor (TD) buildup in silicon in the course of low-temperature annealing (usually in the temperature region from 400 to 550°C) is dealt with in a wealth of publications; they are reviewed, for instance, in [1–4]. The experimental data are characterized by very poor reproducibility; indeed, the $N(t)$ rate curves, i.e., the dependences of the TD concentration on anneal time, obtained at a given anneal temperature T and oxygen concentration C, may differ both in shape (in the characteristic time needed to reach saturation) and in the magnitude of N (by a few multiples). This scatter can be partially attributed to the difference in the content of some concomitant impurities, such as carbon [5, 6], hydrogen [7, 8], or nitrogen [9, 10], among the samples studied. However, the high-purity crystals (where the above impurities are practically absent) studied also exhibited this strong difference in $N(t)$ at the same T and C. There is obviously an intimate and fundamental reason for this difference, which is not merely associated with the different impurity contents in a material. Such a fundamental factor would most probably result from the silicon self-interstitial atoms emitted by oxygen aggregates [3, 11]. This paper presents experimental data as evidence of the appreciable significance of this factor. The rate curves obtained were successfully fitted to the relations calculated in terms of a simple quantitative model.

1. EXPERIMENT

We studied silicon samples cut from adjacent plates of the same crystal with the following characteristics: diameter 150 mm; vacancy growth regime [12]; a relatively high growth rate, 0.8 mm/min; oxygen content $C = 1 \times 10^{18}$ cm^{-3} (obtained using the presently accepted calibration of 3.14×10^{17} cm^{-2} for the optical absorption peak); carbon content below the sensitivity threshold (approximately 2×10^{15} cm^{-3}); crystal boron-doped to a concentration $N_B = 1.7 \times 10^{15}$ cm^{-3}. Some of the samples were studied in the starting (post-growth) conditions, but the majority were studied after a fast thermal anneal (at 1250°C 35 s in a nitrogen atmosphere). This preliminary anneal dissolves native oxygen clusters [13], so that subsequent oxygen agglomeration should start anew. A qualitative difference between the above two groups of samples was not, however, observed. All the data presented in what follows refer to samples that were subjected to preliminary anneal. This was done because, in such samples, the effects to be described below manifest themselves more clearly in these conditions.

Thermal donor annealing was carried out both in air (in several three to four hour long steps adding up to about 80 h, with each step finalized either by quenching, at a cooling rate of about 60 K/s, or by slow cooling in a furnace at a rate of 0.2 K/s after switching the heating off) and in an evacuated quartz tube at a fixed cool-

ing rate of 0.8 K/s, which is intermediate between the two figures mentioned in parentheses.

The TD concentration was derived from the temperature dependence of the electron concentration $n(T)$ measured using the Hall effect (see Fig. 1 for illustration). The theoretical (solid) line is drawn under the assumption that the double TDs of different size and, accordingly, with slightly differing energy levels can be formally described by one (averaged) deep level and one shallow level. Despite this simplification, the smallest rms deviation of the theoretical curve from experimental points did not usually exceed 3%. The parameters to be determined were the concentration of double thermal donors N, their averaged deep (E_d) and shallow (E_s) energy levels, and the effective compensating concentration (which is equal to the difference between the concentrations of shallow (boron) acceptors and shallow (phosphorus) donors, as well as of shallow single thermal donors, STDs [14, 15]).

The rate curves $N(t)$ obtained under a 500°C anneal in the three regimes studied (namely, (I) anneal in air with subsequent quenching, (II) anneal in air with subsequent slow cooling, and (III) anneal in vacuum) are presented in Fig. 2. These three curves differ strongly in shape and in absolute concentrations, despite the samples being identical. Annealing in vacuum results in a comparatively low concentration of double thermal donors, and the rate curve can be fitted by a simple exponential (except for a small drop occurring in long time intervals). Annealing in air produces a significantly larger N and a cupola-shaped curve. The solid lines in Fig. 2 were calculated in terms of the model described below, in which the main parameter is the sink power for the Si_I atoms (which depends strongly on the actual anneal conditions).

Some series of anneals were done with regime switching (Fig. 3). When several anneals in air with quenching were followed by annealing in a vacuum furnace, $N(t)$ dropped to the level characteristic of the new conditions (Fig. 3a). When switched to the reverse direction, from the initial anneal in vacuum to that in air (with quenching), $N(t)$ started to increase immediately to the values typical of the new regime (Fig. 3b).

The effect of the anneal conditions were weaker at lower T; indeed, while it remained substantial at 480°C (Fig. 4a), it nearly disappeared at 450°C (Fig. 4b).

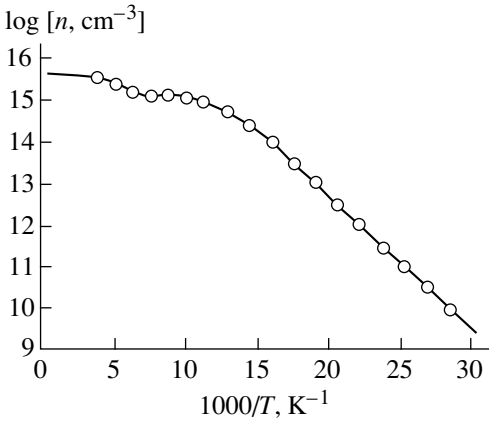

Fig. 1. Illustration of the temperature dependence of the electron concentration derived from the Hall effect. The sample was annealed for 8 h at 500°C in air (with subsequent quenching). The TD parameters found from the best fit of the theoretical (solid) curve to experimental points: $N = 2.45 \times 10^{15}$ cm^{-3}, a deep energy level of 133 meV, a shallow level of 60 meV, a difference between the boron acceptor and STD concentrations of 1×10^{15} cm^{-3}.

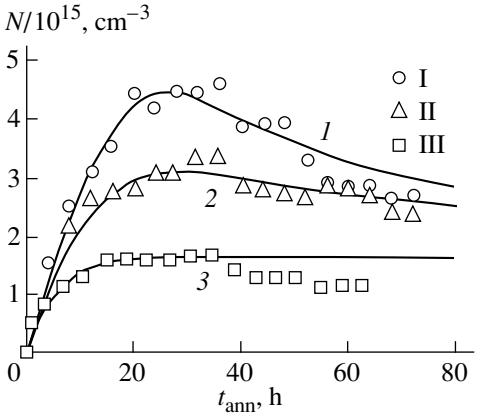

Fig. 2. TD generation rate curves obtained at 500°C [(I) anneal in air with quenching, (II) anneal in air followed by slow cooling, (III) anneal in vacuum]: (*1–3*) were calculated within the model of oxygen agglomeration enhanced by self-interstitials.

2. MODEL

The strong sensitivity of the rate curve $N(t)$ to the anneal conditions can be readily accounted for, both qualitatively and quantitatively, within a simple model reducing to four main points:

(1) The TD generation rate G increases rapidly if the concentration C_I of the self-interstitial atoms is sufficiently high [3, 11]; the $G(C_I)$ dependence, which is discussed below, can be reduced to a linear function.

(2) The interstitials Si_I are emitted by thermal-donor oxygen clusters O_n (where n is the number of oxygen atoms in a cluster). Emission transforms these clusters to vacancy-type clusters O_nV (removal of a silicon atom is equivalent to adding a vacancy).

(3) The emitted Si_I atoms are absorbed by sinks, i.e., the sample surface and volume sinks (voids in a vacancy-type material). Under prolonged annealing, absorption of Si_I atoms by vacancy clusters O_nV also becomes significant.

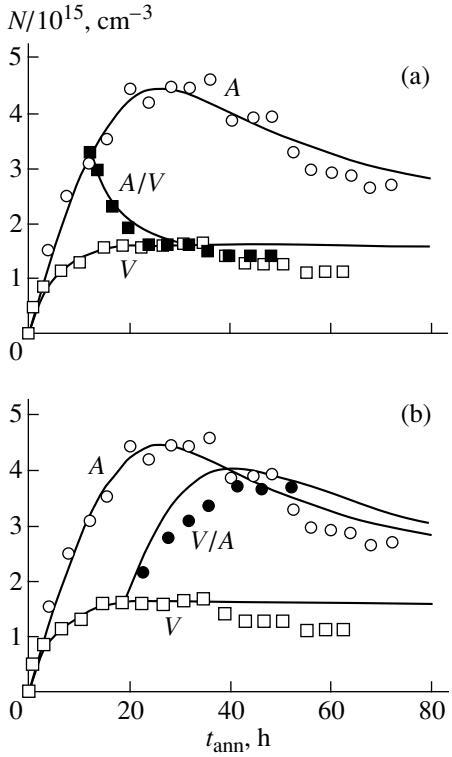

Fig. 3. Transient TD-generation processes after the switching of the anneal conditions: (a) anneal in vacuum after a preliminary anneal in air with quenching (*A*/*V* curve, filled squares) and (b) anneal in air with quenching after a preliminary anneal in vacuum (*V*/*A* curve, filled circles). Shown for comparison are curves obtained in a fixed regime, (*A*) in air and (*V*) in vacuum. Solid curves are the calculation.

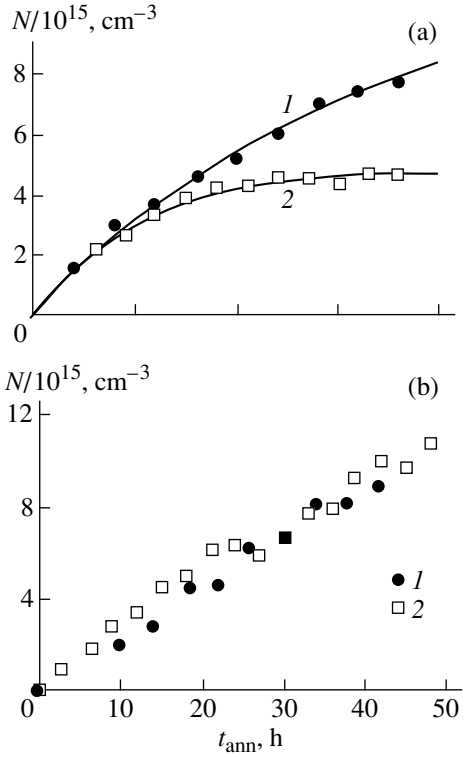

Fig. 4. Comparison of TD generation rate curves for two anneal conditions: (*1*) in air with quenching and (*2*) in vacuum, obtained at (a) 480°C and (b) 450°C.

(4) The sink power depends on the actual anneal conditions, and it is this factor that accounts for the sensitivity of the rate curves to these conditions.

The flux of diffusing interstitials to voids, normalized to the product D_IC_I of the diffusion coefficient by the concentration, is equal to $4\pi R_V N_V$ (where R_V is the average radius of the voids, and N_V is their density). The quantity $4\pi R_V N_V$ may be called the void sink power and be denoted by β_V. The typical void parameters [12] correspond to $\beta_V = 150$ cm^{-2}.

Diffusion to the sample surface acting as a sink results in C_I being dependent on the depth z, a relation which can be approximated by the $\sin(\pi z/d)$ profile. The loss of interstitials (per unit volume) corresponds to the sink power $\beta_S = (\pi/d)^2 = 2000$ cm^{-2} (in our case, the sample thickness $d = 675$ μm). The diffusion flux to the surface is substantially stronger than that to the voids; the β_S/β_V ratio is approximately 14.

The substantial increase in the TD concentration observed when crossing over from annealing in vacuum to that in air (Figs. 2, 3) may be attributed to the fact that the flow to the surface, under the relatively clean conditions of vacuum anneal, is limited only by diffusion; i.e., it is strong (and the concentration of interstitial atoms is too low to enhance the TD generation). Conversely, when annealing in air, the surface is passivated either by a growing oxide layer or by surface contamination (or both), which makes the voids the main (but less powerful) sink. Accordingly, the C_I concentration grows, and the TD generation rate increases. The further increase in the generation rate, observed after the transition from slow cooling to quenching, indicates partial void passivation in the case of annealing in air. It appears natural to relate this effect to void decoration by rapidly diffusing impurities (such as copper), which penetrate into the bulk of the sample under annealing. Under the slow cooling conditions, these impurities diffuse back to the surface. However, when quenched, the impurities remain in the sample and decorate the voids. It is essential that only part of the voids (in a general case, microdefects) are decorated by impurities during the quench [16]; one may, therefore, anticipate that the void passivation will be far from complete. Indeed, an estimation made below suggests that the void sink power decreases by only a factor of 1.5. This reasoning is supported by sample etching experiments; while before, thermal donor anneal etch-

ing did not reveal microdefects, after an anneal for several hours (in air with subsequent quenching), microdefects with a volume density of the order of 2×10^6 cm^{-3} were observed, which, in order of magnitude, is equal to a typical void density in vacancy silicon [12].

We are turning now to a quantitative theory of kinetic phenomena based on the above general model.

2.1. TD Generation Rate as a Function of the Concentration of Interstitials

Oxygen thermal-donor clusters are generated (nucleated) as a result of consecutive transitions in a chain of states. Two adjacent states are denoted by indices k and $k + 1$; they differ either in the size n (the number of aggregated oxygen atoms) or in atomic configuration. In the first case, the transition indicates the attachment of another oxygen atom, while in the second, it indicates the atomic rearrangement. In terms of classical nucleation theory, the generation rate G is expressed as a sum over consecutive transitions [17]:

$$1/G = \sum 1/J_k, \tag{1}$$

where J_k is the flux from k to the next state, $k + 1$, for the particular case where clusters are in equilibrium with the monomer solution (so that their concentration C_k is given by the law of active masses and is proportional to C^n). The flux J_k is equal to the product of C_k and the transition frequency ν_k. Both types of transitions, the attachment and rearrangement, can be enhanced in the presence of Si_I atoms. The reaction of the attachment is enhanced through oxygen transport by the rapid diffusion (and rapid dissociation) of OSi_I complexes [3, 11]. The rearrangement is enhanced if the Si_I atoms act as mobile catalysts in this reaction; indeed, an Si_I atom then becomes the nearest neighbor of a cluster and lowers the barrier to rearrangement, to subsequently recede again from it.

For both types of transitions, the frequency ν_k (and, hence, the flux J_k) is a linearly growing function of the concentration of interstitials C_I. The nucleation rate in Eq. (1) is frequently controlled by only one (critical) transition, in which case it is also the linearly growing function

$$G = G_0 + \alpha C_I, \tag{2}$$

where G_0 is the "intrinsic" nucleation rate (in the absence of Si_I atoms) and α is a "catalytic coefficient" describing the generation enhanced by the Si_I atoms.

In earlier papers [3, 11], it was assumed that Si_I atom emission can also be a transition in the chain leading to the formation of thermal-donor clusters, which in this case would be vacancy-type clusters, such as O_nV. The vacancy cluster concentration can be measured using the platinum diffusion technique [18, 19]. This technique was employed to determine the vacancy concentration in the starting and quenched silicon samples (vacancies are bound to oxygen atoms to form O_nV below a certain temperature, near 1020°C [20]). When applied to samples annealed at 500°C [21], this technique revealed that vacancy complexes are indeed introduced in the course of thermal-donor anneal, but their concentration is less than N by two to three orders of magnitude. Thus, the emission transitions are not involved directly in the formation of TDs (which should be identified with the simple O_n clusters). The emission of Si_I by the already formed TDs is, however, an effect of fundamental significance; indeed, the interstitials emitted in relatively small numbers enhance the TD generation catalytically, thereby producing feedback in the system under consideration.

2.2. The Rate of Emission and Reabsorption of Si_I Atoms

The emission rate is proportional to the emitter (thermal donor) concentration and is equal to μN, where μ is the emission frequency. Strictly speaking, this frequency varies with time as the average cluster size increases. However, the average size of thermal donors rapidly attains a constant level, about 10 oxygen atoms per cluster [22], which justifies the use of a time-independent averaged value of μ.

The emission is balanced by the reabsorption of Si_I atoms by vacancy clusters (their concentration is denoted by N_V), in which case the concentrations of the three reagents (emitters, absorbers, and Si_I atoms) satisfy the mass action law

$$C_I N_V / N = \chi, \tag{3}$$

where χ is the equilibrium emission constant. The total vacancy-cluster generation rate is equal to the difference between the emission and absorption fluxes:

$$dN_V/dt = \mu(N - C_I N_V/\chi). \tag{4}$$

It becomes zero when the equilibrium relation (3) is satisfied.

2.3 The Balance Equation for Self-Interstitials

Interstitial atoms are generated at the same rate in Eq. (4) as the vacancy clusters (the difference between the emission and reabsorption); moreover, they are absorbed by sinks (this process is practically irreversibly because of the low equilibrium Si_I concentration at low T) at the rate $\beta D_I C_I$:

$$dC_I/dt = \mu(N - C_I N_V/\chi) - \beta D_I C_I. \tag{5}$$

The sink power β defined earlier depends noticeably on the actual anneal conditions.

The Si_I diffusion coefficient is very large even below room temperature [23]; at the melting point, it was estimated at 3×10^{-4} cm^2/s [24]. Extrapolation to 500°C

made for a reasonably low migration energy (0.25 eV), yielding $D_I = 4 \times 10^{-5}$ cm^2/s. By Eq. (5), the actual concentration C_I very rapidly (in about 3 min or less) reaches a quasi-stationary value corresponding to the nearly zero right-hand part of the equation

$$C_I = \mu N/(\beta D_I + \mu N_V/\chi). \quad (6)$$

In particular, in an earlier anneal stage, when the vacancy cluster concentration is still not high, expression (6) reduces to direct proportionality between C_I and the emitter (thermal donor) concentration:

$$C_I = \mu N/\beta D_I. \quad (7)$$

However, at a later stage, as the vacancy cluster concentration builds up, the magnitude of C_I, by Eq. (6), is controlled by the ratio N/N_V. Because N is limited and N_V continues to grow (as a result of the emission and subsequent removal of the interstitials by the sinks), C_I falls off with time in a later anneal stage and the thermal donor generation rate decreases accordingly. This effect accounts for the dropping branch of rate curves *1* and *2* in Fig. 2.

2. 4. Rate Equation for Thermal Donors

TDs are generated at a rate given by expression (2). The generated thermal donors, on the other hand, disappear with a characteristic lifetime τ, which is evidenced by the dropping branches of the rate curves (particularly by the decrease following the regime switching in Fig. 3a). The net rate equation includes generation and losses:

$$dN/dt = G_0 + \alpha C_I - N/\tau. \quad (8)$$

There are two general thermal-donor loss mechanisms: (1) dissolution (dissociation) and (2) transformation to neutral clusters O_n^* either through a slow rearrangement to a neutral configuration or as a result of growing to a size at which the electrical activity is zero.

In the first case, the concentration N would tend to a constant value (determined by the mass action law), which is at odds with the behavior of the curves in Fig. 2. We shall therefore accept the second mechanism, namely, transformation to the neutral clusters O_n^*. Generation of these clusters requires certain refinements be introduced into the model: (i) These clusters are assumed to be weaker emitters than the thermal donors themselves, so that their contribution to the balance equation (6) can be neglected. (ii) The thermal-donor lifetime (the time for O_n to convert to O_n^*) will be assumed to be independent of C_I. These assumptions are justified by the good agreement of the calculated rate curves with the experiment.

2. 5. Analytical and Numerical Solutions of the Agglomeration/Emission Equations

In a general case, the evolution of a system of oxygen clusters and interstitials is described by the two rate equations (8) and (4) for two interrelated dynamic variables, N (the concentration of TDs, the emitters) and N_V (the concentration of vacancy clusters, the absorbers). The Si_I concentration is expressed through these variables by using the balance equation (6).

In an earlier stage, when vacancy clusters still play an insignificant role, the rate curve is determined by one simple equation following from Eqs. (7) and (8):

$$dN/dt = G_0 - N/\tau_a, \quad (9)$$

where τ_a is the effective (sink-dependent) TD lifetime

$$1/\tau_a = 1/\tau - \mu\alpha/\beta D_i. \quad (10)$$

The solution of Eq. (9) is a simple exponential growth of $N(t)$ with saturation. On the plateau, the value of N is $G_0\tau_a$; it increases with decreasing sink power, and the first half of the rate curves in Fig. 2 is qualitatively accounted for by this simplified theory.

To describe the net rate curves, one has to integrate Eqs. (8) and (4) numerically, for which purpose one can conveniently introduce scaling factors, namely, $S = G_0\tau$ for the thermal-donor concentration, $S_V = \alpha\chi\tau$ for the vacancy cluster concentration, and $S_I = G_0/\alpha$ for the concentration of the self-interstitial clusters.

After the transition to normalized (divided by the above factors) variables and a dimensionless time $x = t/\tau$, the system of equations will include two dimensionless parameters, namely, the reduced catalytic coefficient A,

$$A = \alpha\chi/G_0\mu\tau, \quad (11)$$

and the reduced sink power B,

$$B = \beta D_I/\alpha\mu\tau. \quad (12)$$

The equations for the normalized variables, labeled by the old symbols N, N_V, and C_I, assume the simple form

$$dN/dx = 1 + C_I - N, \quad (13)$$

$$dN_V/dx = (N - C_I N_V)/A, \quad (14)$$

$$C_I = N/(N_V + B). \quad (15)$$

The lifetime τ and the intrinsic generation rate G_0 were found from a rate curve, obtained under vacuum annealing (where the effect of interstitials is insignificant), and were determined to be $\tau = 5$ h and $G_0 = 8.6 \times 10^{10}$ cm^{-3} s^{-1}. The parameters A and B were chosen as best fits for curves *1* and *2* in Fig. 2 (recall that the value of B for vacuum annealing is not an independent parameter; it is 14 times the value of B for annealing in air followed by slow cooling). The final results are as follows: $A = 20$, $B = 1.1$ for annealing in air with

quenching, $B = 1.6$ for annealing in air with subsequent slow cooling, and $B = 23$ for vacuum annealing.

The corresponding calculated curves for all three (dimensionless) variables are presented in Fig. 5; curves *1*, *2*, and *3* refer to three anneal regimes with different sink powers *B*. The curves of Fig. 5a, recalculated for the dimensional variable, are also shown in Fig. 2.

The curves with anneal regime switching (Fig. 3) were calculated for a stepwise change of sink power *B* made at the corresponding instants of time (from 1.1 to 23 in Fig. 3a and from 23 to 1.1 in Fig. 3b). This procedure does not involve any new fitting parameters; while the calculated curves do not precisely coincide with the experimental transition portions, they are close to them. The fast falloff of the *A*/*V* transient curve in Fig. 3a is due to the fact that the Si_I concentration decreased in a jump [expression (6) or (15)] and the TD generation rate dropped accordingly to become lower than the loss rate (N/τ in the dimensional form).

Similarly, the fast rise of the transient curve *V*/*A* in Fig. 3b is caused by the stepwise increase in C_I and the corresponding strong increase in the generation rate.

2. 6. Estimation of the Model Parameters

Based on the emission-induced generation rate of the vacancy clusters O_nV specified above (their concentration is three orders of magnitude lower than *N* at anneal times of approximately a few hours; that is, $\mu t/2$ is in the order of 10^{-3}), the emission frequency μ can be estimated as 10^{-7} s^{-1} at 500°C. After this, we find $\alpha\chi = 4 \times 10^9$ cm^{-3} s^{-1} from Eq. (11). For a given void sink power ($\beta = 150$ cm^{-2}, $B = 1.6$) for annealing in air followed by slow cooling, expression (12) yields $\alpha/D_I = 4 \times 10^4$ cm^{-2}. The two products estimated above allow one to determine $D_I\chi = 10^5$ cm^{-1} s^{-1}. Using the interstitial diffusion coefficient specified earlier ($D_I = 4 \times 10^{-5}$ cm^2/s), we obtain $\alpha = 1.5$ s^{-1} and $\chi = 3 \times 10^9$ cm^{-3}. One can now estimate the scaling factors S_I and S_V needed to reduce the dimensionless concentrations in Figs. 5b and 5c to their absolute values, $S_I = G_0/\alpha = 7 \times 10^{10}$ and $S_V = \alpha\chi\tau = 8 \times 10^{13}$ cm^{-3}.

One of the most important consequences that can be drawn from these estimates is the conclusion that the O_nV vacancy clusters are poor absorbers of interstitials. Indeed, the absorption rate (which can also be called the rate of recombination of the two defects O_nV and Si_I) is RC_IN_V, where *R* is the recombination coefficient, which, according to Eq. (4), is equal to μ/χ. On the other hand, if the recombination were diffusion limited, *R* would be equal to $4\pi rD_I$, where *r* is the capture radius (of the order of the interatomic distance 3×10^{-8} cm). The ratio of the actual to diffusion-limited values of *R* is $\mu/(4\pi rD_i\chi) = 2 \times 10^{-6}$. In other words, there exists an appreciable barrier E_r to recombination; it reduces the rate of the reaction by a factor $\exp(-E_r/kT)$, from which one obtains $E_r = 0.87$ eV.

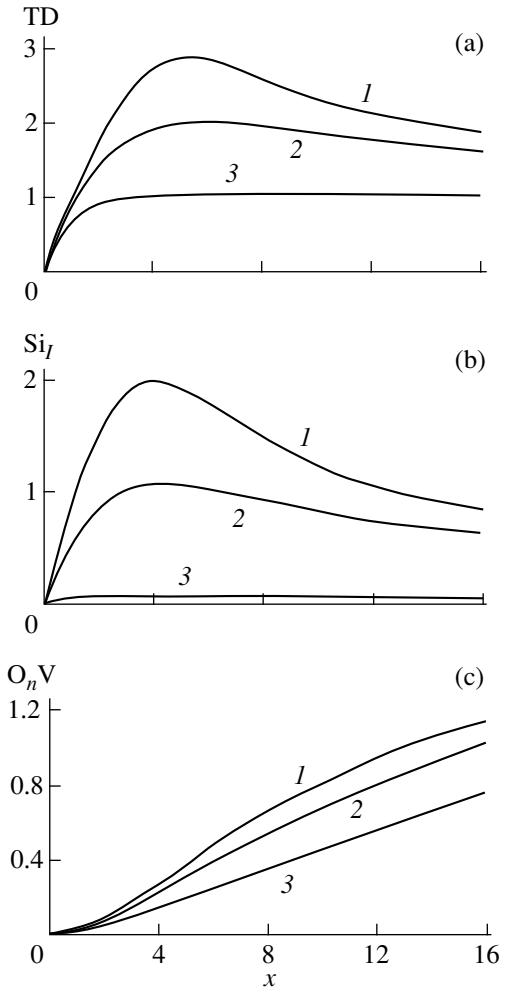

Fig. 5. Normalized concentrations of various defects calculated as functions of dimensionless time *x*: (a) thermal donors, (b) self-interstitials (Si_I), and (c) O_nV vacancy clusters for different sink parameters (curves *1–3* correspond to $B = 1.1$, 1.6, and 23, respectively, for the three different anneal regimes).

For some quantities, one can also estimate the activation energies (which characterize temperature dependence). For the TD loss frequency $1/\tau$ and the emission frequency μ, this can be done by using the simple expression $\nu\exp(-E/kT)$, with the prefactor $\nu = 10^{13}$ s^{-1}. Such an estimate of the emission constant χ is based on the above-mentioned barrier factor to recombination. Thus, the following activation energies were obtained: 2.65 eV for $1/\tau$, 3.1 eV for the emission frequency μ, and 2 eV for the emission constant χ.

The dimensionless time $x = t/\tau$ varies within a broad range at 500°C, where τ is relatively short. As *T* decreases, the lifetime grows rapidly, up to 15 h at 480°C and up to 80 h at 450°C, and the accessible dimensionless-time interval contracts. According to

Fig. 5a, at small t/τ, the difference between the three anneal regimes is small; this is what accounts for the convergence of the rate curves as T is reduced (Fig. 4).

2.7. Oxygen Loss Effect

The formation of oxygen clusters brings about a gradual decrease in the concentration C of the oxygen monomer. Accordingly, the generation rate parameters G_0 and α, which are power-law functions of C, decrease with time. This effect has been ignored up to now in order to focus the main attention on the key phenomenon, namely, the participation of silicon self-interstitials in the TD formation. In actual fact, the monomer loss $C(t)$ can considerably affect the shape of a rate curve (so that the drop in the generation rate during long time intervals is caused not only by the decrease in the C_I but also by the decrease in C). Taking into account the decrease in C would in no way be difficult (one may assume the loss of ten monomer atoms per cluster [22]). However, because of the formidable mathematical complication of the model involved, this will be analyzed in a separate publication.

3. CONCLUSIONS

Thus, a systematic dependence of TD concentration on the anneal conditions was found by annealing identical silicon samples in three different regimes (in air at two different cooling rates and in vacuum). These results are considered as arguments for silicon self-interstitials (Si_I) playing an important part in the low-temperature anneal process. The TD generation rate becomes greatly enhanced if the concentration C_I of these atoms is high enough (above 10^{10} cm^{-3}). The magnitude of C_I is controlled, in its turn, by the thermal donor clusters O_n (the main Si_I emitters), by the power of the Si_I sinks, and also, under prolonged annealing, by the vacancy clusters O_nV (which are products of the emission and, at the same time, act as absorbers of Si_I atoms).

The dependence of the rate curves on the anneal conditions originates from the fact that the latter strongly affect the Si_I sink power. Under relatively clean conditions, i.e., under annealing in vacuum, the sample surface is the major sink. In this case, the C_I concentration is low and TD generation remains practically unenhanced. When annealing in air, the surface as a sink becomes passivated, and the volume sinks (voids in the vacancy-type silicon) become dominant. In this case, C_I increases with time to such a level that TD generation is substantially enhanced. If annealing in air is followed by quenching, part of the voids become passivated (decorated) and C_I increases still more, which entails a corresponding increase in the generation rate.

The qualitative theory, built in terms of the simplest model (with thermal donors of various sizes described as identical defects with averaged properties), reduces to two rate equations in two dynamic variables, one of them being the TD concentration; the other, the vacancy cluster concentration.

An interesting consequence of this model is that under vacuum annealing the TD generation should become greatly enhanced with increasing sample thickness, i.e., with decreasing power of the main (surface) sink. This effect saturates at thicknesses of approximately a few millimeters, where the surface sink compares in power with the bulk sink. In samples of such thickness, there should form a strongly pronounced depth profile for the thermal donor concentration N, copying the Si_I distribution. The enhancement of TD generation with increasing sample thickness and the depth profile of N were actually observed [25], but in this particular case hydrogen rather than Si_I could act as the catalyst. A comprehensive study of the N depth profile in thick samples could yield direct evidence of the catalytic effect of self-interstitial atoms.

REFERENCES

1. G. D. Watkins, in *Proceedings of the 14 International Conference on Defects in Semiconductors* (1986), p. 953.
2. P. Wagner and J. Hage, Appl. Phys. A **A49** (2), 123 (1989).
3. V. V. Voronkov, Semicond. Sci. Technol. **8**, 2037 (1993).
4. V. M. Babich, N. I. Bletskan, and E. F. Venger, *Oxygen in Single Crystals of Silicon* (Interpres, Kiev, 1977).
5. A. R. Bean and R. C. Newman, J. Phys. Chem. Solids **33** (2), 255 (1972).
6. J. Leroueille, Phys. Status Solidi A **67** (1), 177 (1981).
7. R. C. Newman, A. R. Brown, R. Murray, *et al.*, in *The Electrochemical Society Proceedings Series*, Vol. 90-7: *Semiconductor Silicon*, Ed. by H. R. Huff, K.G. Barraclough, and J. Chikawa (Electrochemical Society, Pennington, 1990); Proc.–Electrochem. Soc. **90-7**, 734 (1990).
8. H. J. Stein and S. Hahn, in *Defect Control in Semiconductors*, Ed. by K. Sumino (Elsevier, Amsterdam, 1990), Part 1, p. 241.
9. C. S. Chen, C. F. Li, H. J. Ye, *et al.*, J. Appl. Phys. **76**, 3347 (1994).
10. D. Yang, R. Fan, L. Li, *et al.*, J. Appl. Phys. **80**, 1493 (1996).
11. V. V. Voronkov, Kristallografiya **38** (1), 150 (1993) [Crystallogr. Rep. **38**, 79 (1993)].
12. V. V. Voronkov and R. Falster, J. Cryst. Growth **194**, 76 (1998).
13. R. Falster, M. Pagani, D. Gambaro, *et al.*, Solid State Phenom. **57–58**, 129 (1997).
14. J. A. Griffin, J. Hartung, J. Weber, *et al.*, Appl. Phys. A **A48**, 47 (1989).
15. A. Hara, M. Aoki, M. Koizuka, and T. Fukuda, J. Appl. Phys. **75**, 2929 (1994).
16. R. Falster, Z. Laczik, G. R. Booker, *et al.*, in *Defect Engineering in Semiconductor Growth. Processing and*

Device Technology, Ed. by S. Ashok, J. Chevallier, K. Sumino, and E. Weber (Materials Research Society, Pittsburgh, 1992); Mater. Res. Soc. Symp. Proc. **262**, 945 (1992).

17. J. Frenkel, *Kinetic Theory of Liquids* (Nauka, Leningrad, 1975; Clarendon Press, Oxford, 1946).
18. M. Jacob, P. Pichler, H. Ryssel, and R. Falster, J. Appl. Phys. **82**, 182 (1997).
19. M. Jacob, P. Pichler, H. Ryssel, *et al.*, Solid State Phenom. **57–58**, 349 (1997).
20. V. V. Voronkov and R. Falster, J. Cryst. Growth **204**, 462 (1999).
21. M. Jacob, P. Pichler, and R. Falster, private communication (1997).
22. S. A. McQuaid, M. J. Binns, C. A. Londos, *et al.*, J. Appl. Phys. **77**, 1427 (1995).
23. G. D. Watkins, in *The Electrochemical Society Proceedings Series*, Vol. 99-1: *Defects in Silicon III*, Ed. by T. Abe, W. M. Bullis, S. Kobayashi, *et al.* (Pennington, 1999), p. 38.
24. V. V. Voronkov and R. Falster, J. Appl. Phys. **86** (11), 5975 (1999).
25. A. Hara, M. Koizuka, M. Aoki, *et al.*, Jpn. J. Appl. Phys. **33**, 5577 (1994).

Translated by G. Skrebtsov

Physics of the Solid State, Vol. 42, No. 11, 2000, pp. 2030–2038. Translated from Fizika Tverdogo Tela, Vol. 42, No. 11, 2000, pp. 1976–1984.

SEMICONDUCTORS AND DIELECTRICS

The Fine Structure of Excitonic Levels in CdSe Nanocrystals

S. V. Gupalov and E. L. Ivchenko

Ioffe Physicotechnical Institute, Russian Academy of Sciences, ul. Politekhnicheskaya, 26, St. Petersburg, 194021 Russia
e-mail: goupalov@coherent.ioffe.rssi.ru

Received April 13, 2000

Abstract—The fine structure of the exciton ground level in a spherical nanocrystal of a zincblende or a wurtzite structure semiconductor was calculated with the inclusion of short- and long-range (nonanalytical), exchange-interaction components. The band-parameter dependence of the long-range exchange-interaction contribution to the spin Hamiltonian describing the exciton ground-level splitting was found. A study was made of the effect exerted on the exciton-level fine structure by the difference between the background dielectric permittivities of the nanocrystal and of the dielectric host in which it was grown. © *2000 MAIK "Nauka/Interperiodica".*

Glasses activated by nanocrystals became popular model objects for use in investigating quantum size effects in semiconducting, quasi-zero-dimensional systems starting from the early 1980s, when it was shown that carriers present in semiconductor nanocrystals embedded in a wide-bandgap glass host are subject to three-dimensional quantum confinement [1–3].

A large number of publications have recently appeared which deal with the exchange interaction between the electron and the hole in nanocrystals, which are small in comparison to the exciton Bohr radius a_B in a bulk semiconductor [4–11]. This interest stems from the fact that, because of the strong, three-dimensional, spatial compression of the electron and hole wave functions, the exchange-induced, exciton level splittings become very large compared with those in bulk semiconductors (while remaining, at the same time, small in comparison with the characteristic size-quantization energies) and increase as R^{-3}, with decreasing nanocrystal radius R, whereas the size-quantized energy scales increase as R^{-2}. This dependence of the exchange splitting of the exciton ground level was observed experimentally in CdSe nanocrystals [5–10] and was determined to pertain to the effect of the analytical (short-range) part of the exchange interaction only. As shown in our related briefs [12, 13], the long-range or, as it is called sometimes, nonanalytical part of exchange interaction results in the same dependence of the exchange splitting on the radius, and its contribution to this splitting is of the same order of magnitude as that due to the analytical part. The purpose of the present work is to present a self-consistent theory of exchange interaction between the electron and the hole in a spherical quantum dot of a semiconductor with a zincblende or wurtzite structure and its generalization, taking into account the difference between the dielectric permittivities of the nanocrystal and the host.

1. ELECTRON–HOLE EXCHANGE INTERACTION IN THE EXCITON

A self-consistent theory of electron–hole exchange interaction in semiconductors was developed by Pikus and Bir [14–16] and Denisov and Makarov [17]. Considered in the effective-mass approximation, the Coulomb interaction operator between the electron and the hole in a semiconductor crystal includes three contributions, corresponding to the direct Coulomb interaction ($\mathcal{H}^C$) and the long-range ($\mathcal{H}^{\text{long}}$) and short-range ($\mathcal{H}^{\text{short}}$) exchange interactions, respectively. We introduced two-particle excited states of the crystal $|m, \mathbf{k}_e; n, \mathbf{k}_h\rangle$, where $\mathbf{k}_{e,h}$ is the electron or hole wave vector and the indices m and n label degenerate states of the electron in the conduction band (representation Γ_c) and of the hole in the valence band (representation Γ_v), respectively, at the point of the extremum $k_{e,h} = 0$ (the Γ point). We shall first consider a semiconductor of cubic symmetry exhibiting a zincblende structure; the case of a wurtzite structure crystal is discussed in Section 6. The matrix elements of the $\mathcal{H}^C$ and $\mathcal{H}^{\text{long}}$ operators between the above two-particle states can be written in the form [14–16, 18]

$$\mathcal{H}^C_{m'n',\,mn}(\mathbf{k}'_e, \mathbf{k}'_h, \mathbf{k}_e, \mathbf{k}_h) = -\frac{1}{V}\frac{4\pi e^2}{\kappa_0|\mathbf{k}_e - \mathbf{k}'_e|^2}\delta_{m'm}\delta_{n'n}\delta_{\mathbf{k}_e+\mathbf{k}_h,\,\mathbf{k}'_e+\mathbf{k}'_h}, \quad (1)$$

$$\mathcal{H}^{\text{long}}_{m'n',\,mn}(\mathbf{k}'_e, \mathbf{k}'_h, \mathbf{k}_e, \mathbf{k}_h) = \frac{1}{V}\frac{4\pi e^2\hbar^2}{\kappa_b m_0^2 E_g^2}\frac{(\mathbf{K}\mathbf{p}_{m'n'})(\mathbf{K}\mathbf{p}_{mn})^*}{K^2}\delta_{\mathbf{k}_e+\mathbf{k}_h,\,\mathbf{k}'_e+\mathbf{k}'_h}. \quad (2)$$

Here, $\mathbf{K}$ is the total wave vector $\mathbf{k}_e + \mathbf{k}_h = \mathbf{k}'_e + \mathbf{k}'_h$; m_0 is the free-electron mass; E_g is the gap width; $\mathbf{p}_{m\bar{n}} = \langle m|\mathbf{p}|\bar{n}$ is the matrix element of the momentum opera-

tor calculated between the electron Bloch functions $|m, \mathbf{k} = 0\rangle$ and $|\bar{n}, \mathbf{k} = 0\rangle$ (the hole state $n, \mathbf{k}$ and the electron state $\bar{n}, -\mathbf{k}$ are related through time-reversal operation); κ_0 and κ_b are the low-frequency and high-frequency (at the electron–hole excitation frequency) dielectric permittivities, respectively; e is the electronic charge; and V is the crystal volume. Note that the long-range exchange interaction is sometimes called nonanalytical, because the limit of the matrix element in Eq.(2) for $\mathbf{K} \longrightarrow 0$ depends on the way in which $\mathbf{K}$ tends to zero.

The exchange interaction in Eq.(2) involves only electron–hole pair states that are optically active in the dipole approximation. Such states may be specified by the total angular momentum of the pair $I = 1$, and the long-range exchange interaction operator in Eq.(2) can be cast in an invariant form [13]:

$$\mathcal{H}^{\text{long}}(\mathbf{k}'_e, \mathbf{k}'_h, \mathbf{k}_e, \mathbf{k}_h) = \frac{4\pi\hbar^2 e^2 P_0^2}{\kappa_b m_0^2 E_g^2}\left[1 - \frac{(\mathbf{K}\hat{\mathbf{I}})^2}{K^2}\right]\delta_{\mathbf{K},\mathbf{K}'}, \tag{3}$$

where

$$P_0^2 = \sum_{m,n}\left|p^{\alpha}_{m\bar{n}}\right|^2 \tag{4}$$

and the 3×3 matrices $\hat{I}_\alpha$ ($\alpha = x, y, z$) are the matrices of the $I = 1$ angular momentum projections.

The matrix element of the long-range, exchange, interaction operator written in the coordinate representation has the form [14–16]

$$\mathcal{H}^{\text{long}}_{m'n',mn}(\mathbf{r}'_e, \mathbf{r}'_h, \mathbf{r}_e, \mathbf{r}_h) = -\delta(\mathbf{r}_e - \mathbf{r}_h)\delta(\mathbf{r}'_e - \mathbf{r}'_h) \times \frac{\hbar^2 e^2}{\kappa_b m_0^2 E_g^2}\sum_{\alpha\beta} p^{\alpha}_{m',\bar{n}'} p^{\beta *}_{m\bar{n}} \frac{\partial^2}{\partial r_{e\alpha}\partial r_{e\beta}}\frac{1}{|\mathbf{r}_e - \mathbf{r}'_e|}, \tag{5}$$

where the α and β indices run through the values x, y, and z. Note that because

$$(\mathbf{a}\nabla)(\mathbf{b}\nabla)\frac{1}{r} = \frac{1}{r^3}\left[3\frac{(\mathbf{ar})(\mathbf{br})}{r^2} - \mathbf{ab}\right] - \frac{4\pi}{3}\mathbf{ab}\delta(\mathbf{r}), \tag{6}$$

where $\mathbf{a}$ and $\mathbf{b}$ are arbitrary vectors, the matrix element of the long-range exchange interaction operator in Eq.(5) contains the contact term

$$\Delta\mathcal{H}^{\text{long}}_{m'n',mn}(\mathbf{r}'_e, \mathbf{r}'_h, \mathbf{r}_e, \mathbf{r}_h) = \delta(\mathbf{r}_e - \mathbf{r}_h)\delta(\mathbf{r}'_e - \mathbf{r}'_h)\delta(\mathbf{r}_e - \mathbf{r}'_e) \times \frac{4\pi}{3}\frac{\hbar^2 e^2}{\kappa_b m_0^2 E_g^2}\sum_{\alpha} p^{\alpha}_{m',\bar{n}'} p^{\alpha *}_{m\bar{n}}. \tag{7}$$

A contribution to the short-range (analytic) interaction is provided by Fourier components of the Coulomb potential with wave vectors $\mathbf{b} + \mathbf{k}'_e - \mathbf{k}_e$, where $\mathbf{b}$ are nonzero reciprocal-lattice vectors. For small enough values of k_e and k_h, satisfying the criterion of applicability of the effective-mass approximation, the operator $\mathcal{H}^{\text{short}}$ takes the form of contact interaction and can be presented as

$$\mathcal{H}^{\text{short}}_{m'n',mn}(\mathbf{r}'_e, \mathbf{r}'_h, \mathbf{r}_e, \mathbf{r}_h) = \Delta^{\text{short}}_{m'n',mn} a_0^3 \delta(\mathbf{r}_e - \mathbf{r}_h)\delta(\mathbf{r}_e - \mathbf{r}'_e)\delta(\mathbf{r}_h - \mathbf{r}'_h), \tag{8}$$

where a_0 is the lattice constant and a_0^3 is factored out so that the coefficients $\Delta^{\text{short}}_{m'n',mn}$ have the dimensions of energy. The dependence of these coefficients on band indices is determined using symmetry considerations, while their absolute values are determined from a comparison of the theory with the results of an experimental study of the exciton-level fine structure (see, e.g., [19]). The number of linearly independent coefficients coincides with that of the irreducible representations contained in the direct product $\Gamma_c \times \Gamma_v$.

Note that the short-range part of exchange interaction is sometimes defined [4, 20] as the sum of the analytic exchange interaction in Eq.(8) and the contact part of the nonanalytic exchange interaction in Eq.(7). The short-range exchange interaction defined in this way is written in the form of Eq.(8), but with a renormalized constant

$$\Delta^{\text{short}}_{m'n',mn} a_0^3 = \Delta^{\text{short}}_{m'n',mn} a_0^3 + \frac{4\pi}{3}\frac{\hbar^2 e^2}{\kappa_b m_0^2 E_g^2}\sum_{\alpha} p^{\alpha}_{m',\bar{n}'} p^{\alpha *}_{m\bar{n}}. \tag{9}$$

2. EXCITON QUANTIZATION IN SPHERICAL NANOCRYSTALS

In the case of strong quantization ($R \ll a_B$), the wave function of an electron–hole pair is determined primarily by the reflections of the electron and the hole from the quantum-dot walls, whereas the Coulomb interaction between them is merely a weak perturbation. Then, in zero approximation, the envelope of the exciton, two-particle, wave function can be written as the product

$$\Psi^{\text{exc}}(\mathbf{r}_e, \mathbf{r}_h) = \psi^{(e)}(\mathbf{r}_e)\psi^{(h)}(\mathbf{r}_h), \tag{10}$$

where $\psi^{(e)}(\mathbf{r}_e)$ and $\psi^{(h)}(\mathbf{r}_h)$ are the one-particle wave functions of the electron and the hole, respectively, and are localized in the quantum dot.

The electronic states in a spherical quantum dot are characterized by electron, orbital, angular momentum l_e. The lowest energy corresponds to the electron state described by a spherical wave with an orbital angular momentum $l_e = 0$. For an infinitely high barrier, the electron wave function can be written as

$$\psi^{(e)}_m(\mathbf{r}_e) = \frac{1}{\sqrt{2\pi R}}\frac{\sin(\pi r_e/R)}{r_e}|m\rangle, \tag{11}$$

where the spin index m assumes the values $\pm 1/2$.

The envelope of the ground-state wave function of a size-quantized hole in the spin–orbit split-off band Γ_7 in cubic semiconductors of the crystalline class T_d coincides with that in Eq. (11).

The state of a quantum-confined hole in a fourfold spin-degenerate band Γ_8 (the hole spin $J_h = 3/2$, its projection $n = \pm 3/2, \pm 1/2$) is not characterized by any definite value of the orbital angular momentum l_h. Neglecting the warping of constant-energy surfaces (spherical approximation), the total hole momentum $\mathbf{F}_h = \mathbf{J}_h + \mathbf{l}_h$ may be considered a good quantum number [21]. Such a state is $(2F_h + 1)$-fold degenerate due to the projection F_z of the angular momentum $\mathbf{F}_h$ on the z axis. For the ground state, we have $F_h = 3/2$ and $F_z = \pm 3/2, \pm 1/2$. The wave function of the hole in this state can be written [22]

$$\psi_{F_z}^{(h)}(\mathbf{r}_h) = \sum_n \mathcal{R}_{n, F_z}(\mathbf{r}_h)|n\rangle, \tag{12}$$

where the components of matrix $\hat{\mathcal{R}}(\mathbf{r})$ can be expressed through Wigner's 3jm symbols:

$$\mathcal{R}_{n, F_z}(\mathbf{r}) = R^{-3/2} \sum_{l_h = 0.2} f_{l_h}\left(\frac{r}{R}\right)(-1)^{3/2 - l_h + F_z} \times 2\sum_\mu \begin{pmatrix} 3/2 & l_h & 3/2 \\ n & \mu & -F_z \end{pmatrix} Y_{l_h\mu}\left(\frac{\mathbf{r}}{r}\right), \tag{13}$$

where $Y_{l_h\mu}$ are the normalized spherical functions,

$$f_{l_h}(x) = \mathcal{C}\left[j_{l_h}(\varphi^{(h)}x) + (-1)^{l_h/2}\frac{j_2(\varphi^{(h)})}{j_2(\sqrt{\beta}\varphi^{(h)})} j_{l_h}(\sqrt{\beta}\varphi^{(h)}x)\right], \tag{14}$$

j_{l_h} are spherical Bessel functions, $\beta = (\gamma_1 - 2\gamma)/(\gamma_1 + 2\gamma)$ is the light-to-heavy hole mass ratio, γ_1, γ are the Luttinger parameters in the spherical approximation, $\varphi^{(h)}$ is the first root of the equation

$$j_0(x)j_2(\sqrt{\beta}x) + j_2(x)j_0(\sqrt{\beta}x) = 0, \tag{15}$$

and $\mathcal{C}$ is found from the normalization condition

$$\int_0^1 [f_0^2(x) + f_2^2(x)]x^2 dx = 1.$$

Because in the ground state $F_h = J_h$, the $\psi_{F_z}^{(h)}(\mathbf{r}_h)$ and $|n\rangle$ functions transform in accordance with the same representation of the rotation group. Therefore, the matrix $\hat{\mathcal{R}}(\mathbf{r})$ must be a spherical invariant. It can be written in invariant form as [12, 13]

$$\hat{\mathcal{R}}(\mathbf{r}) = \frac{1}{\sqrt{4\pi}R^{3/2}}\left\{ f_0\left(\frac{r}{R}\right) - f_2\left(\frac{r}{R}\right)\left[\left(\hat{\mathbf{J}}\frac{\mathbf{r}}{r}\right)^2 - \frac{5}{4}\right]\right\}, \tag{16}$$

where $\hat{J}_\alpha$ are the 4×4 matrices of the $J_h = 3/2$ angular momentum projections ($\alpha = x, y, z$).

For $\beta \longrightarrow 1$, the light- and heavy-hole subbands in a bulk semiconductor merge to form one degenerate band. As follows from Eqs. (14) and (16) in this limit, the wave-function envelope of a size-quantized hole in the ground state does not depend on spin indices and coincides with the envelope of the function in Eq.(11).

3. ELECTRON–HOLE EXCHANGE INTERACTION IN A NANOCRYSTAL OF A SEMICONDUCTOR WITH A SIMPLE BAND STRUCTURE

To make a comparative estimation of the short- and long-range exchange-interaction contributions to the exciton-level splitting, let us first consider the optical transitions between a simple conduction band Γ_6 and a simple valence band Γ_7 in zincblende structure semiconductors (crystal class T_d). In this case, taking into account the spin degeneracy of the electron and the hole state, the 1s exciton energy level is fourfold degenerate. Because the direct product $\Gamma_6 \times \Gamma_7$ reduces to irreducible representations Γ_5 and Γ_2 [23], one may conveniently replace the $|m, n\rangle$ basis ($m, n = \pm 1/2$), in which the matrix elements in Eqs. (2), (5), and (8) are written, with the basis of the states $|\Gamma_5, \nu\rangle$ ($\nu = x, y, z$) and $|\Gamma_2\rangle$. The $|\Gamma_5, \nu\rangle$ state is optically active for light linearly polarized in the ν direction, while the $|\Gamma_2\rangle$ state is inactive. If the energy is reckoned from the Γ_2 level, then in the new basis, the nonzero components of the short- and long-range exchange terms will have the form

$$\mathcal{H}_{\nu'\nu}^{\text{short}}(\mathbf{k}_e', \mathbf{k}_h', \mathbf{k}_e, \mathbf{k}_h) = \Delta_{ST}^{\text{bulk}}\pi a_B^3 \delta_{\nu\nu'}\delta_{\mathbf{KK}'},$$
$$\mathcal{H}_{\nu'\nu}^{\text{long}}(\mathbf{k}_e', \mathbf{k}_h', \mathbf{k}_e, \mathbf{k}_h) = \hbar\omega_{LT}\pi a_B^3 \frac{K_\nu K_{\nu'}}{K^2}\delta_{\mathbf{KK}'}, \tag{17}$$

where a_B is the Bohr radius of excitons in a bulk semiconductor, $\Delta_{ST}^{\text{bulk}}$ is the magnitude of the exciton level splitting into a singlet and a triplet, and $\hbar\omega_{LT}$ is the longitudinal–transverse exciton splitting. Because the exchange splitting of exciton levels is small compared to the size-quantization level separations, the electron–hole exchange interaction in a nanocrystal can be taken into account using perturbation theory. As follows from Eq.(17), the exciton splitting in a spherical nanocrystal

of radius $R \ll a_B$ into a singlet and a triplet is [12]

$$\Delta_{ST}^{QD}(R) = \pi C\left(\Delta_{ST}^{\text{bulk}} + \frac{1}{3}\hbar\omega_{LT}\right)\left(\frac{a_B}{R}\right)^3, \quad (18)$$

where

$$C = \int_0^\pi \frac{\sin^4 x}{x^2}dx \approx 0.672. \quad (19)$$

In the derivation of Eq.(18), the potential barrier at the nanocrystal boundary was assumed to be infinitely high. In this case, the wave-function envelopes of both the electron and the hole coincide with the envelope of the function in Eq.(11) and vanish at the nanocrystal boundary. Assuming, for the purpose of estimation, that $\Delta_{ST}^{\text{bulk}} \sim 0.1$ meV and $\hbar\omega_{LT} \sim 1$ meV, we come to the conclusion that, of the two terms in Eq.(18), the long-range contribution to the splitting Δ_{ST}^{QD} is dominant.

Note that, in the case of the $\Gamma_6 \times \Gamma_7$ exciton, only the contact part (7) of the long-range exchange interaction contributes to the exchange splitting in Eq.(18). This follows from the fact that the noncontact part of the long-range exchange interaction, having the character of a dipole–dipole interaction, transforms according to a T_d-group representation that does not contain the identity representation.

4. EXCHANGE INTERACTION OF THE ELECTRON AND THE HOLE IN A SEMICONDUCTOR NANOCRYSTAL WITH A COMPLEX-STRUCTURE VALENCE BAND

Now, let us consider a $\Gamma_6 \times \Gamma_8$ exciton in a nanocrystal of radius $R \ll a_B$. The electron and hole wave functions are presented in this case by expressions (11) and (12), respectively. The short-range exchange interaction is [7]

$$\hat{\mathcal{H}}^{\text{short}}(\mathbf{k}_e', \mathbf{k}_h', \mathbf{k}_e, \mathbf{k}_h) = -\frac{2}{3}\varepsilon_{\text{exch}}a_0^3(\boldsymbol{\sigma}\mathbf{J})\delta_{\mathbf{K}\mathbf{K}'}, \quad (20)$$

where $\varepsilon_{\text{exch}}$ is the exchange-interaction constant and σ_α are the Pauli matrices acting on the electronic spin. For the long-range part in Eq.(2), we obtain

$$\hat{\mathcal{H}}^{\text{long}}(\mathbf{k}_e', \mathbf{k}_h', \mathbf{k}_e, \mathbf{k}_h) = \frac{4\pi}{\kappa_b}\left(\frac{\hbar e p_{cv}}{m_0 E_g}\right)^2 \delta_{\mathbf{K}\mathbf{K}'}\frac{1}{K^2}$$
$$\times\left\{\frac{3}{8}K^2 - \frac{1}{6}(\mathbf{J}\mathbf{K})^2 - \frac{1}{9}K^2(\boldsymbol{\sigma}\mathbf{J})\right.$$
$$+\frac{1}{6}\left[(\boldsymbol{\sigma}\mathbf{J})\left((\mathbf{J}\mathbf{K})^2 - \frac{5}{4}K^2\right) + \left((\mathbf{J}\mathbf{K})^2 - \frac{5}{4}K^2\right)(\boldsymbol{\sigma}\mathbf{J})\right] \quad (21)$$
$$\left.-\frac{1}{3}\left[(\boldsymbol{\sigma}\mathbf{K})(\mathbf{J}\mathbf{K}) - \frac{1}{3}K^2(\boldsymbol{\sigma}\mathbf{J})\right]\right\},$$

where $p_{cv} = i\langle S|\hat{p}_x|X\rangle$ is the interband matrix element of the momentum operator.

The Hamiltonian of the electron–hole exchange interaction in a quantum dot of radius $R \ll a_B$ can be written as

$$\hat{H}_{\text{exch}} = -\bar{\eta}(\boldsymbol{\sigma}\mathbf{J}). \quad (22)$$

Here,

$$\bar{\eta} = \left(\frac{a_B}{R}\right)^3\left(\chi(\beta)\hbar\omega_{TF} + \frac{\pi}{9}\zeta(\beta)\hbar\omega_{LT}\right),$$

$$\hbar\omega_{TF} = \frac{2}{\pi}\left(\frac{a_0}{a_B}\right)^3\varepsilon_{\text{exch}}, \quad (23)$$

$$\hbar\omega_{LT} = \frac{4}{\kappa_b a_B^3}\left(\frac{e\hbar p_{cv}}{m_0 E_g}\right)^2;$$

$$\chi(\beta) = \frac{1}{6}\int_0^1 dx \sin^2(\pi x)\left(f_0^2(x) + \frac{1}{5}f_2^2(x)\right); \quad (24)$$

$$\zeta(\beta) = \frac{1}{(2\pi)^3}\int_0^\infty dy y^2[I_0(y) + I_2(y)]^2, \quad (25)$$

$$I_l(y) = 2\sqrt{2\pi}(-1)^{l/2}\int_0^1 dx x f_l(x)\sin(\pi x) j_l(xy).$$

Expression (24) for the short-range contribution to the parameter $\bar{\eta}$ was derived in [7]. Expression (25) for the parameter $\zeta(\beta)$, determining the long-range contribution, can be recast in the form

$$\zeta(\beta) = \frac{1}{2\pi}\int_0^1 dx \sin^2(\pi x)[f_0^2(x) + f_2^2(x)]$$
$$+\frac{1}{(2\pi)^3}\int_0^\infty dy y^2 2I_0(y)I_2(y). \quad (26)$$

The $\chi(\beta)$ and $\zeta(\beta)$ functions are plotted in Fig. 1.

Note that, in contrast to the $\Gamma_6 \times \Gamma_7$ exciton, here not only the contact but also the noncontact part of the nonanalytic exchange interaction contributes to the long-range term. The contribution to the splitting from the contact part is

$$-\frac{\hbar\omega_{LT}}{3}\left(\frac{a_B}{R}\right)^3\chi(\beta)(\boldsymbol{\sigma}\mathbf{J}).$$

In the limit as $\beta \longrightarrow 1$, the noncontact part vanishes, leaving us with

$$\zeta(\beta \longrightarrow 1) = \chi(\beta \longrightarrow 1)3/\pi = C,$$

where C is determined by expression (19). A comparison of the $\chi(\beta)$ and $\zeta(\beta)$ functions shows that for $\beta < 1$

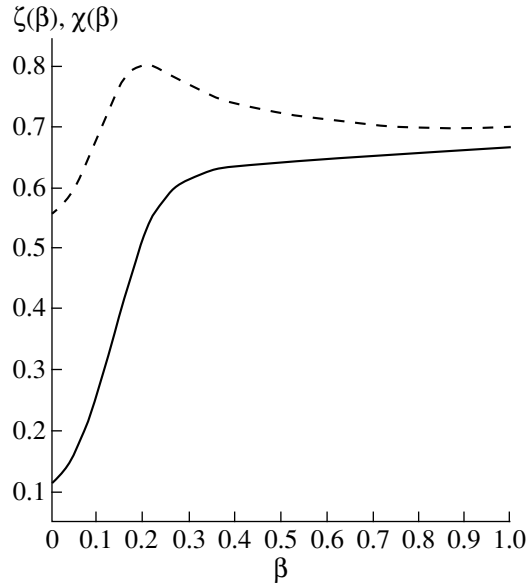

Fig. 1. Functions ζ(β) (solid line) and χ(β) (dashed line).

the contribution of the noncontact part to the exchange splitting is opposite in sign to that of the contact part, so that the noncontact part reduces the total contribution of the long-range exchange interaction to the exciton level splitting.

5. INCLUSION OF THE BACKGROUND PERMITTIVITIES OF THE NANOCRYSTAL AND THE HOST

We shall use the approach developed in [14–16] to calculate the contribution of long-range exchange interaction to the exciton ground-level splitting in a nanocrystal, taking into account the difference between the background permittivities of the nanocrystal and the host. This approach is based on a solution of the problem of interaction between two electrons occupying states near the Γ point in the valence band and in the conduction band, respectively. The Coulomb interaction potential of these electrons has the form

$$V_{\text{bulk}}(\mathbf{r}, \mathbf{r}') = \frac{e^2}{\kappa_1|\mathbf{r}-\mathbf{r}'|},$$

where κ_1 is the permittivity at the exciton resonance frequency.

The Coulomb interaction potential between two point charges in a spherical semiconductor nanocrystal synthesized in a host with a background permittivity κ_2 contains an additional term due to the surface charge induced on the sphere [24, 25]:

$$V_{QD}(\mathbf{r}, \mathbf{r}') = \frac{e^2}{\kappa_1|\mathbf{r}-\mathbf{r}'|} + \delta V_{QD}(\mathbf{r}, \mathbf{r}'), \tag{27}$$

where

$$\delta V_{QD}(\mathbf{r}, \mathbf{r}') = e^2\frac{\kappa_1-\kappa_2}{\kappa_1}\sum_{l=0}^{\infty}\frac{4\pi}{2l+1}\frac{l+1}{\kappa_1 l+\kappa_2(l+1)}\frac{r^l r'^l}{R^{2l+1}} \times \sum_{l_z=-l}^{l} Y^*_{ll_z}\left(\frac{\mathbf{r}}{r}\right)Y_{ll_z}\left(\frac{\mathbf{r}'}{r'}\right). \tag{28}$$

According to Eq.(5), this term produces an additional term in the electron–hole long-range exchange-interaction operator

$$\delta\mathscr{H}^{\text{long}}_{m'n', mn}(\mathbf{r}'_e, \mathbf{r}'_h, \mathbf{r}_e, \mathbf{r}_h) = -\delta(\mathbf{r}_e-\mathbf{r}_h)\delta(\mathbf{r}'_e-\mathbf{r}'_h) \times \frac{\hbar^2}{m_0^2E_g^2}\sum_{\alpha\beta}p^{\alpha}_{m'\bar{n}'}p^{\beta *}_{m\bar{n}}\frac{\partial^2}{\partial r_{e\alpha}\partial r_{e\beta}}\delta V_{QD}(\mathbf{r}_e, \mathbf{r}'_e), \tag{29}$$

which yields a corresponding contribution to the exchange splitting of the exciton level:

$$\Delta H_{m'F'_z, mF_z}(\kappa_1, \kappa_2) = \sum_{n', n}\int d\mathbf{r}_1\int d\mathbf{r}_2\int d\mathbf{r}'_1\int d\mathbf{r}'_2 C_{F'_z, n'}(\mathbf{r}'_1) \times \delta\mathscr{H}^{\text{long}}_{m'n', mn}(\mathbf{r}'_1, \mathbf{r}'_2, \mathbf{r}_1, \mathbf{r}_2)C_{n, F_z}(\mathbf{r}_1). \tag{30}$$

The matrix $\hat{C}(\mathbf{r})$ for the $\Gamma_6\times\Gamma_7$ exciton in the ground state is proportional to the identity matrix and has the form

$$\hat{C}(\mathbf{r}) = \frac{1}{2\pi R}\frac{\sin^2(\pi r/R)}{r^2}, \tag{31}$$

while for the ground state of the $\Gamma_6\times\Gamma_8$ exciton, this matrix is proportional to the product of the scalar envelope from Eq.(11) by matrix (16):

$$C_{n, F_z}(\mathbf{r}) = \frac{1}{\sqrt{2\pi R}}\frac{\sin(\pi r/R)}{r}\mathscr{R}_{n, F_z}(\mathbf{r}). \tag{32}$$

Expression (30) can be recast to

$$\Delta H_{m'F'_z, mF_z}(\kappa_1, \kappa_2) = \frac{\hbar^2e^2(\kappa_1-\kappa_2)}{m_0^2E_g^2\kappa_1} \times \sum_{l=0}^{\infty}\frac{4\pi}{2l+1}\frac{l+1}{\kappa_1 l+\kappa_2(l+1)}\frac{1}{R^{2l+1}}\sum_{l_z=-l}^{l} I^{(l, l_z)}_{m'F'_z}I^{(l, l_z)*}_{mF_z}, \tag{33}$$

where

$$I^{(l, l_z)}_{mF_z} = \sum_n\int d\mathbf{r}C_{F_z, n}(\mathbf{r})(\mathbf{p}_{m\bar{n}}\nabla)\left[r^lY_{ll_z}\left(\frac{\mathbf{r}}{r}\right)\right]. \tag{34}$$

The quantities $I^{(l, l_z)}_{mF_z}$ can be simplified if one takes into account that the matrix element of the covariant cyclic component p_σ ($\sigma = \pm1, 0$) of the momentum operator, which is calculated using conduction- and valence-

band Bloch functions, is expressed through Wigner's 3*jm* symbol

$$\langle m|p_\sigma|\bar{n}\rangle = \sqrt{3}P_0(-1)^{3/2+J_h-\sigma}\begin{pmatrix} \frac{1}{2} & J_h & 1 \\ m & n & -\sigma \end{pmatrix}, \quad (35)$$

where $J_h = 1/2$ for the $\Gamma_6 \times \Gamma_7$ exciton, $J_h = 3/2$ for the $\Gamma_6 \times \Gamma_8$ exciton, the constant P_0 is defined in Eq.(4), and the canonical basis of the Bloch functions $|m\rangle$, $|n\rangle$ are used [23]. Then, after some manipulations, one obtains for the $\Gamma_6 \times \Gamma_7$ exciton

$$I_{mF_z}^{(l,l_z)} = \frac{(-1)^{l_z+1}\sqrt{3}p_{cv}\delta_{l1}}{\sqrt{2\pi}}\begin{pmatrix} \frac{1}{2} & \frac{1}{2} & 1 \\ F_z & m & -l_z \end{pmatrix}, \quad (36)$$

and expression (18) for the triplet–singlet ground-state splitting of the $\Gamma_6 \times \Gamma_7$ exciton can be recast to [12]

$$\Delta_{ST}^{QD}(R) = \left(\pi C\Delta_{ST}^{\text{bulk}} + \frac{1}{3}\pi C\hbar\omega_{LT} + \frac{1}{2}\hbar\omega_{LT}\frac{\kappa_1-\kappa_2}{\kappa_1+2\kappa_2}\right)\left(\frac{a_B}{R}\right)^2. \quad (37)$$

Taking into account Eqs.(13) and (32), we obtain for the $\Gamma_6 \times \Gamma_8$ exciton

$$I_{mF_z}^{(l,l_z)} = \frac{(-1)^{l_z+1}\sqrt{6}p_{cv}\delta_{l1}}{\sqrt{\pi}} \times \begin{pmatrix} \frac{3}{2} & \frac{1}{2} & 1 \\ F_z & m & -l_z \end{pmatrix}\int_0^1 f_0(x)\sin(\pi x)x\,dx. \quad (38)$$

Note that

$$I_{mF_z}^{(3,l_z)} \propto \begin{pmatrix} \frac{3}{2} & \frac{1}{2} & 3 \\ F_z & m & -l_z \end{pmatrix} = 0,$$

because the three numbers (3/2, 1/2, 3) do not satisfy the rule of the triangle. Taking into account the difference between the background permittivities of the nanocrystal and the host, expression (23) can be rewritten as

$$\bar{\eta} = \left(\frac{a_B}{R}\right)^3\left(\hbar\omega_{TF}\chi(\beta) + \frac{\pi\hbar\omega_{LT}\zeta(\beta)}{9} + \frac{1}{3}\hbar\omega_{LT}\frac{\kappa_1-\kappa_2}{\kappa_1+2\kappa_2}\left[\int_0^1 f_0(x)\sin(\pi x)x\,dx\right]^2\right). \quad (39)$$

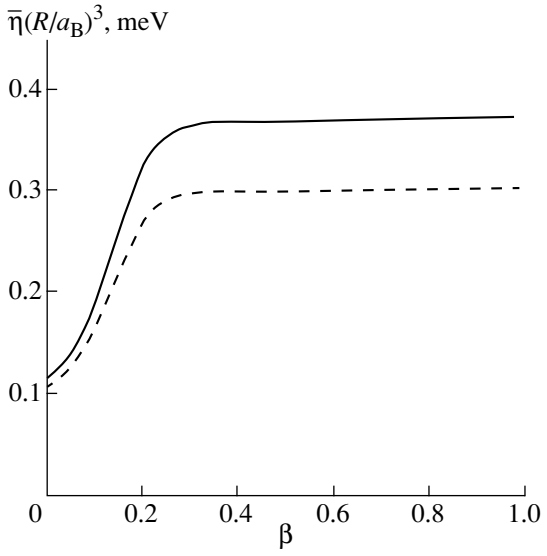

Fig. 2. Dependence of the quantity $\bar{\eta}(R/a_B)^3$ on the parameter β calculated with (solid line) and without (dashed line) inclusion of the difference in the background permittivity between the nanocrystals and the host.

For $\beta \longrightarrow 1$, the square of the integral in the brackets tends to 1/2 and the envelopes of the electron and hole wave functions coincide; for $\beta < 1$, the overlap between them decreases and the integral in the brackets in Eq.(39) decreases.

Figure 2 shows the dependence of the quantity $\bar{\eta}(R/a_B)^3$ on the parameter β with the difference between the background permittivities of the nanocrystal and the host included (solid line) and disregarded (dashed line). For κ_2, the typical value of the squared refractive index of glass, $\kappa_2 = 2.25$, was taken, while the other parameters were taken equal to those of CdSe ($\kappa_1 = 8.4$). One readily sees that taking into account the difference in the background permittivities between the nanocrystal and the host results in an increase in $\bar{\eta}$.

6. THE FINE STRUCTURE OF THE EXCITON GROUND LEVEL IN WURTZITE NANOCRYSTALS

In the case of hexagonal crystals with wurtzite structure, one has to add a term responsible for the crystal-field splitting [22] to the Luttinger Hamiltonian, describing states near the top of the valence band of a bulk cubic semiconductor:

$$\hat{\mathcal{H}}_{cr} = -\frac{\Delta_{cr}}{2}\left(J_z^2 - \frac{5}{4}\right).$$

Therefore, the fine structure of the exciton ground state in a wurtzite-lattice nanocrystal, taking into account the

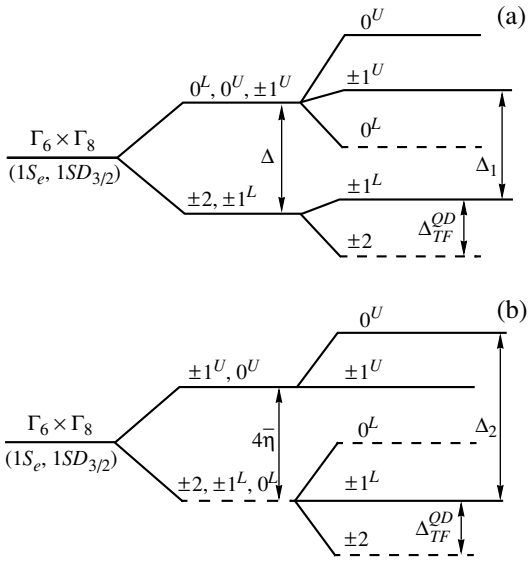

Fig. 3. Diagram of exciton level splitting into five sublevels for a hexagonal nanocrystal. For conveniency, the fine structure obtained neglecting (a) exchange interaction or (b) crystal-field splitting is also shown.

crystal-field and exchange splittings, is described by a spin Hamiltonian:

$$\Delta H = -\frac{\Delta}{2}\left(J_z^2 - \frac{5}{4}\right) - \bar{\eta}(\boldsymbol{\sigma}\mathbf{J}), \tag{40}$$

where $\Delta = \Delta_{cr}\nu(\beta)$,

$$\nu(\beta) = \int_0^1 dx x^2 \left(f_0^2(x) - \frac{3}{5}f_2^2(x)\right). \tag{41}$$

Expression (41) was derived in [22]. Note that the parameters $\hbar\omega_{TF}$ and $\hbar\omega_{LT}$, which were introduced in Eq.(23), have a simple physical meaning for a bulk hexagonal crystal; namely, $\hbar\omega_{TF}$ is the splitting of the 1*s* exciton level *A* ($\Gamma_7 \times \Gamma_9$ representation of group C_{6v}) induced by the short-range exchange interaction, with the split-off states having angular-momentum projections ±2 and ±1 on the C_6 axis, respectively, and $\hbar\omega_{LT}$ is the longitudinal–transverse splitting for the exciton propagating in the plane perpendicular to the C_6 axis. The fine structure of exciton levels in CdSe nanocrystals was studied in [5–10]. The description of the exchange splitting presented in [5–10] took into account only the first term in expression (23). According to [19], $\hbar\omega_{TF} \approx 0.12$ meV and $\hbar\omega_{LT} \approx 0.95$ meV; one can extrapolate that for $\beta = 0.3$ the ratio of the second (long-range) term to the first (short-range) term is approximately 3.

Figure 3 presents exciton level diagrams described by Hamiltonian (40) and by each of its terms separately. The excitonic sublevels are labeled in accordance with the magnitude of the projection of the total electron–hole pair, angular momentum $F_z + m$ on the C_6 axis. If one takes into account only the crystal-field splitting and neglects the exchange contribution, the exciton ground level splits into two states differing in the modulus of the projection of the total hole angular momentum (Fig. 3a). The projection of the total hole angular momentum $F_z = \pm1/2$ corresponds to the upper state, while the lower state has the projection $F_z = \pm3/2$. Conversely, if one neglects the crystal-field splitting and includes only the exchange contribution, the exciton ground level will split into two sublevels corresponding to different values for the total angular momentum F_{ex} of the electron–hole pair (Fig. 3b). $F_{ex} = 1$ corresponds to the upper (optically active) sublevel, while the lower sublevel (inactive) has $F_{ex} = 2$. Taking both terms in Hamiltonian (40) into account results in a splitting of the exciton ground level into five sublevels (Figs. 3a, 3b). The relative oscillator strengths of the corresponding transitions were calculated in [7]. The states $\pm1^U$, $\pm1^L$, and 0^U are optically active in the dipole approximation, while the transitions to the ±2 and 0^L states are forbidden in the same approximation. At the same time, the "dark" state ±2 turns out to be the lowest in energy, so that the low-temperature photoluminescence is due to the radiative recombination from this state. Therefore, one can determine the splitting between the $\pm1^L$ and ±2 levels experimentally from the Stokes shift of the luminescence [5–10]. The splittings between the $\pm1^U$ and ±2 levels and between 0^U and ±2 can be derived from luminescence excitation spectra, but the $\pm1^U$ and 0^U states cannot be resolved in such a manner [6, 9].

The splitting $\Delta_{TF}^{QD}(\bar{\eta})$ between the ±2 and $\pm1^L$ states is given by the expression

$$\Delta_{TF}^{QD}(\bar{\eta}) = 2\bar{\eta} + \frac{\Delta}{2} - \sqrt{4\bar{\eta}^2 + \frac{\Delta^2}{4} - \bar{\eta}\Delta}. \tag{42}$$

For large radii, where $\bar{\eta} \ll \Delta$, Δ_{TF}^{QD} is approximately equal to $3\bar{\eta}$. For $\Delta \longrightarrow \infty$, $\beta \longrightarrow 1$, and $\hbar\omega_{TF} = \Delta_{ST}^{bulk}$ in particular, expression (42) transforms into Eq.(18). For small radii, where $\bar{\eta} \gg \Delta$, we have $\Delta_{TF}^{QD} \approx 3\Delta/4$. If one neglects the long-range exchange contribution, the parameter $\bar{\eta}$ in Eq.(42) is replaced by the parameter

$$\eta = \left(\frac{a_B}{R}\right)^3 \chi(\beta)\hbar\omega_{TF},$$

which is approximately one fourth of $\bar{\eta}$ for $\beta = 0.3$. Figure 4 presents the calculated dependence of the splitting Δ_{TF}^{QD} on the nanocrystal radius. The solid and dashed lines were calculated including and neglecting the difference between the background permittivities of the nanocrystal and the host, respectively. The dotted

line plots expression (42) with the parameter $\bar{\eta}$ replaced by η. The filled [8] and open [6] circles refer to experimental points. The values of the Luttinger parameters used in the calculation are [26] ($\gamma_1 = 2.04$ and $\gamma = 0.58$, for which $\beta = 0.275$). The triangles identify the values of the splitting Δ_{TF}^{QD} calculated using the pseudopotential method [11].

The splittings Δ_1 and Δ_2, between the $\pm 1^U$ and $\pm 1^L$, and between the $\pm 0^U$ and $\pm 1^L$ sublevels, are given by the expressions

$$\Delta_1(\bar{\eta}) = 2\sqrt{4\bar{\eta}^2 + \frac{\Delta^2}{4} - \bar{\eta}\Delta}, \quad (43)$$

$$\Delta_2(\bar{\eta}) = 2\bar{\eta} + \frac{\Delta}{2} + \sqrt{4\bar{\eta}^2 + \frac{\Delta^2}{4} - \bar{\eta}\Delta}, \quad (44)$$

respectively.

For large radii ($\bar{\eta} \ll \Delta$) we have $\Delta_1 \approx \Delta - 2\bar{\eta}$ and $\Delta_2 \approx \Delta + \bar{\eta}$. For small radii ($\bar{\eta} \gg \Delta$), $\Delta_1 \approx 4\bar{\eta} - \Delta/2$ and $\Delta_2 \approx 4\bar{\eta} + \Delta/4$. Figure 5 presents the splittings Δ_1 and Δ_2 calculated as functions of the nanocrystal radius. The pair of solid (dashed) curves corresponds to the calculation with inclusion (without inclusion) of the difference between the background permittivities of the nanocrystal and the host. The upper curve in each pair describes the $\Delta_2(R)$ relation, while the lower curve is $\Delta_1(R)$. The dotted curves were calculated from expressions (43) and (44), in which the parameter $\bar{\eta}$ was replaced by η. The open [6] and filled [9] circles are experimental data.

7. DISCUSSION OF RESULTS

As seen from Figs. 4 and 5, the curves calculated with inclusion of long-range exchange interaction agree with the experimental data obtained for the splittings Δ_1 and Δ_2, whereas in the case of the Δ_{TF}^{QD} splitting, the calculation made for nanocrystals of small radius disagrees substantially with the experimental data. It is, however, this splitting that is particularly sensitive to the nanocrystal shape. Indeed, as pointed out above, we have $\Delta_{TF}^{QD} \approx 3\Delta/4$ for small radii. On the other hand, a weak deviation of the nanocrystal shape from the spherical is usually delineated by the introduction of a volume-conserving, homogeneous, uniaxial strain along the hexagonal crystallographic axis C_6, as a result of which the nanocrystal assumes the shape of an oblong or an oblate ellipsoid of rotation [5–7]. Taking this strain into account results in a renormalization of the quantity Δ, which becomes larger by an amount proportional to R^{-2} [27]. Because it is for small-radius nanocrystals that a deviation from the spherical shape is most probable, it is no wonder that our theory is at odds with the experiment in this case. At the same time,

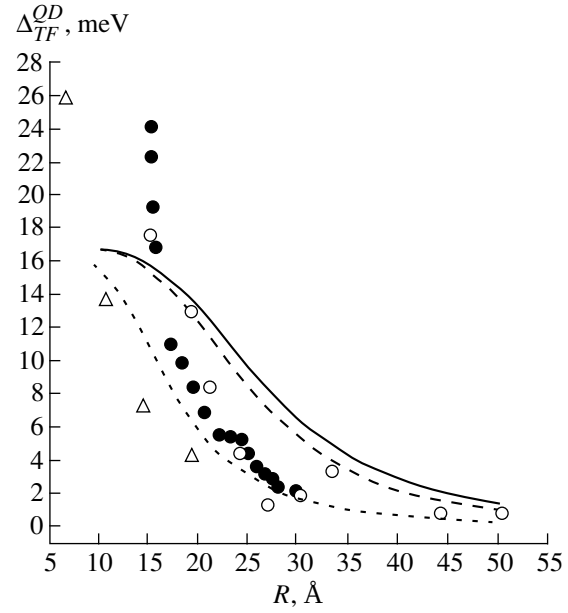

Fig. 4. Dependence of the splitting Δ_{TF}^{QD} on nanocrystal radius calculated for $\kappa_1 = 8.4$ and $\kappa_2 = 2.25$ (solid line) and $\kappa_1 = \kappa_2 = 8.4$ (dashed line), taking into account both the short-range and long-range exchange contributions. The dotted line presents the calculation made neglecting long-range exchange interaction. The filled [8] and open [6] circles refer to the experimental values of the splitting, and the triangles are the splitting Δ_{TF}^{QD} calculated using the pseudopotential method [11].

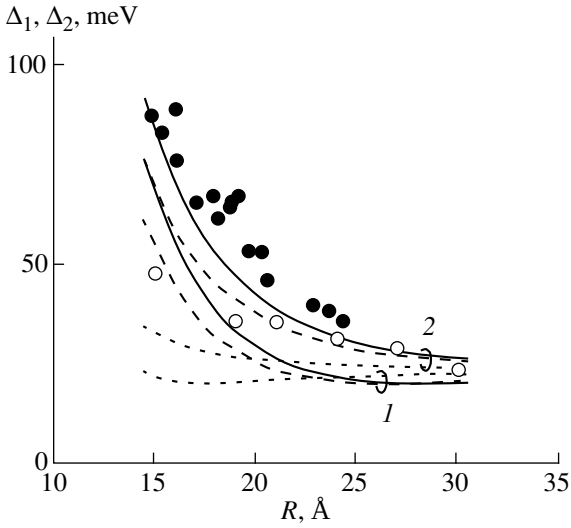

Fig. 5. Dependences of the splittings Δ_1 (*1*) and Δ_2 (*2*) on nanocrystal radius calculated for $\kappa_1 = 8.4$ and $\kappa_2 = 2.25$ (solid lines) and $\kappa_1 = \kappa_2 = 8.4$ (dashed lines), taking into account both the short-range and long-range exchange contributions. The dotted lines represent the calculation made neglecting the long-range exchange interaction. The experimental values of the splitting are shown by the filled [9] and open [6] circles.

the splittings Δ_1 and Δ_2 are less sensitive to a nonsphericity of quantum dots. As seen from Fig. 5, the experimental points from [9] are better suited to the solid line ($\kappa_1 \neq \kappa_2$), while those from [6] are better suited to the dashed line ($\kappa_1 = \kappa_2$). This may be explained by the fact that the measurements of [9] were made on nanocrystals prepared by the thermally activated phase decomposition of a supersaturated solid solution of a semiconductor in a glass host [28]. In this case, the background permittivity of the host in which the nanocrystals are embedded should be set equal to the square of the refractive index of the glass. The study [6] was done on chemically synthesized nanocrystals with a different dielectric environment.

ACKNOWLEDGMENTS

The support of the Russian Foundation for Basic Research (grant no. 98-02-18267) is gratefully acknowledged.

REFERENCES

1. A. I. Ekimov and A. A. Onushchenko, Pis'ma Zh. Éksp. Teor. Fiz. **34** (6), 363 (1981) [JETP Lett. **34**, 345 (1981)].
2. A. I. Ekimov and A. A. Onushchenko, Fiz. Tekh. Poluprovodn. (Leningrad) **16** (7), 1215 (1982) [Sov. Phys. Semicond. **16**, 775 (1982)].
3. Al. L. Éfros and A. L. Éfros, Fiz. Tekh. Poluprovodn. (Leningrad) **16** (7), 1209 (1982) [Sov. Phys. Semicond. **16**, 772 (1982)].
4. T. Takagahara, Phys. Rev. B **47** (15), 4569 (1993).
5. M. Nirmal, D. J. Norris, M. Kuno, *et al.*, Phys. Rev. Lett. **75** (20), 3728 (1995).
6. D. J. Norris, Al. L. Éfros, M. Rosen, and M. G. Bawendi, Phys. Rev. B **53** (24), 16347 (1996).
7. Al. L. Éfros, M. Rosen, M. Kuno, *et al.*, Phys. Rev. B **54** (7), 4843 (1996).
8. M. Chamarro, C. Gourdon, P. Lavallard, *et al.*, Phys. Rev. B **53** (3), 1336 (1996).
9. M. Chamarro, M. Dib, C. Gourdon, *et al.*, Mater. Res. Soc. Symp. Proc. **454**, 396 (1997).
10. U. Woggon, F. Gindele, O. Wind, and C. Klingshirn, Phys. Rev. B **54** (3), 1506 (1996).
11. A. Franceschetti, L. W. Wang, H. Fu, and A. Zunger, Phys. Rev. B **58** (20), 13367 (1998).
12. S. V. Goupalov and E. L. Ivchenko, J. Cryst. Growth **184/185**, 393 (1998).
13. S. V. Goupalov and E. L. Ivchenko, Acta Phys. Pol. A **94** (2), 341 (1998).
14. G. E. Pikus and G. L. Bir, Zh. Éksp. Teor. Fiz. **60** (1), 195 (1971) [Sov. Phys. JETP **33**, 108 (1971)].
15. G. E. Pikus and G. L. Bir, Zh. Éksp. Teor. Fiz. **62** (1), 324 (1972) [Sov. Phys. JETP **35**, 174 (1972)].
16. G. L. Bir and G. E. Pikus, *Symmetry and Strain-Induced Effects in Semiconductors* (Nauka, Moscow, 1972; Wiley, New York, 1975).
17. M. M. Denisov and V. P. Makarov, Phys. Status Solidi B **56** (1), 9 (1973).
18. S.V. Gupalov, E. L. Ivchenko, and A. V. Kavokin, Zh. Éksp. Teor. Fiz. **113** (2), 703 (1998) [JETP **86**, 388 (1998)].
19. V. A. Kiselev, B. S. Razbirin, and I. N. Uraltsev, Phys. Status Solidi B **72** (1), 161 (1975).
20. K. Cho, Phys. Rev. B **14** (10), 4463 (1976).
21. D. Schechter, J. Phys. Chem. Solids **23**, 237 (1962).
22. Al. L. Éfros, Phys. Rev. B **46** (15), 7448 (1992).
23. E. L. Ivchenko and G. E. Pikus, *Superlattices and Other Heterostructures. Symmetry and Optical Phenomena* (Springer-Verlag, Berlin, 1997).
24. V. V. Batygin and I. N. Toptygin, *Problems in Electrodynamics* (Nauka, Moscow, 1970; Academic, London, 1964), Problem 158.
25. H. Haug and S.W. Koch, *Quantum Theory of the Optical and Electronic Properties of Semiconductors* (World Scientific, Singapore, 1993).
26. D. J. Norris and M. G. Bawendi, Phys. Rev. B **53** (24), 16338 (1996).
27. Al. L. Éfros and A. V. Rodina, Phys. Rev. B **47** (15), 10005 (1993).
28. A. I. Ekimov, J. Lumin. **70**, 1 (1996).

Translated by G. Skrebtsov

Physics of the Solid State, Vol. 42, No. 11, 2000, pp. 2039–2046. Translated from Fizika Tverdogo Tela, Vol. 42, No. 11, 2000, pp. 1985–1991.

SEMICONDUCTORS AND DIELECTRICS

An Analysis of the Thermoelectric Efficiency of *n*-$(Bi,Sb)_2(Te,Se,S)_3$ Solid Solutions within an Isotropic Scattering Model

V. A. Kutasov, L. N. Luk'yanova, and P. P. Konstantinov

Ioffe Physicotechnical Institute, Russian Academy of Sciences, ul. Politekhnicheskaya 26, St. Petersburg, 194021 Russia
e-mail: v.kutasov@shuvpop.ioffe.rssi.ru

Received April 13, 2000

Abstract—A study is reported on the thermoelectric properties of *n*-type solid solutions $Bi_2Te_{3-y}Se_y$ (y = 0.12, 0.3, 0.36), $Bi_{2-x}Sb_xTe_{3-y}Se_y$ (x = 0.08, 0.12; y = 0.24, 0.36), and $Bi_2Te_{3-z}S_z$ (z = 0.12, 0.21) as functions of carrier concentration within the 80- to 300-K range. It has been established that the highest thermoelectric efficiency Z is observed in the $Bi_2Te_{3-y}Se_y$ (y = 0.3) solid solution containing excess Te at optimum carrier concentrations (0.35×10^{19} cm^{-3}) and at temperatures from 80 to 250 K. The increase in Z in the $Bi_2Te_{3-y}Se_y$ solid solution compared with $Bi_{2-x}Sb_xTe_{3-y}Se_y$ and $Bi_2Te_{3-z}S_z$ is accounted for by the high mobility μ_0, an increase in the effective mass m/m_0 with decreasing temperature, the low lattice heat conductivity κ_L, and the weak anisotropy of the constant-energy surface in a model assuming isotropic carrier scattering. © *2000 MAIK "Nauka/Interperiodica".*

n-Bi_2Te_3-based solid solutions enjoy wide use as *n*-legs in multistage modules providing cooling below 150 K; this requires the development of thermoelectric materials with low carrier concentrations [$n = (3–4) \times 10^{18}$ cm^{-3}], which are optimal for the low-temperature domain [1, 2]. For this reason, analysis of the β parameter determining the ZT product, the key factor in the thermogenerator efficiency or the performance coefficient of a thermoelectric refrigerator, is of utmost importance. The corresponding expression is

$$ZT \sim \beta = \frac{2(2\pi)^{3/2}}{h^3 e} k_0^{7/2} \left(\frac{m}{m_0}\right)^{3/2} \mu_0 T^{5/2} \kappa_L^{-1}, \qquad (1)$$

where Z is the thermoelectric efficiency and m, μ_0, and κ_L are the effective density-of-states mass, the mobility taking the degeneracy and lattice heat conductivity into account. The quantities entering expression (1) are connected with the parameters of the constant-energy surface and the carrier scattering mechanisms, thus offering the possibility of relating the thermoelectric efficiency with these parameters for various temperatures, carrier concentrations, and solid-solution compositions.

1. MULTIVALLEY MODEL

The $(Bi,Sb)_2(Te,Se,S)_3$ solid solutions (space group $R\bar{3}m$) exhibit strongly anisotropic kinetic effects (except the thermopower), which is related to specific features of crystal structure and chemical bonding. The constant-energy surfaces of these materials are described in terms of a multivalley energy-spectrum model [3, 4], which relates the components of the tensors of electrical resistivity ρ_{ii}, Hall effect ρ_{ijk}, and magnetoresistance ρ_{ijk1} to the parameters determining the constant-energy ellipsoids u, v, and w. The parameters u, v, and w are connected with the components of the inverse effective-mass tensor $\overleftrightarrow{\alpha}$

$$u = \alpha_{11}/\alpha_{22}, \quad v = \alpha_{33}/\alpha_{22}, \quad v - w = \alpha_{23}^2/\alpha_{22}^2. \qquad (2)$$

The tilt angle (θ) of the principal axes of constant-energy ellipsoids with respect to the crystallographic axes is given by the expression

$$\tan 2\theta = 2\alpha_{23}/(\alpha_{22} - \alpha_{33}). \qquad (3)$$

The inverse effective-mass tensor $\overleftrightarrow{\alpha}$ is defined in the following way with respect to the crystallographic axes:

$$\overleftrightarrow{\alpha} = m_0 \overleftrightarrow{T}(\theta) \overleftrightarrow{m}^{-1} \overleftrightarrow{T}^{-1}(\theta). \qquad (4)$$

The density-of-states effective mass is related to the effective-mass tensor components in the multivalley model through

$$m = N^{2/3}(m_1 m_2 m_3)^{1/3}, \qquad (5)$$

where N is the number of valleys and m_1, m_2, and m_3 are the principal components of the effective mass tensor.

Studies of the effect of constant-energy surface anisotropy on thermoelectric efficiency, made in terms

of the model with anisotropic carrier scattering [1, 2], showed that carrier scattering in $Bi_2Te_{3-y}Se_y$ solid solutions ($0.12 \le y \le 0.36$), with optimum carrier concentrations close to the filling of the second subband in the conduction band, is close to isotropic in the temperature interval $80 < T < 150$ K. Therefore, at optimal concentrations for the above temperature region, carrier scattering may be considered isotropic. In this case, the relaxation time depends only on energy using the power-law relation

$$\tau = \tau_0 E^{r_{\text{eff}}}, \qquad (6)$$

where τ_0 is an energy-independent factor and r_{eff} is an effective scattering parameter [5], which takes into account, besides the main mechanism of scattering from the lattice acoustic vibrations, the other possible (impurity and interband) scattering mechanisms.

2. THERMOPOWER AND ELECTRICAL CONDUCTIVITY

The study of the thermoelectric properties of $(Bi,Sb)_2(Te,Se,S)_3$ solid solutions was made on samples prepared through directed crystallization (vertical zone leveling). The required carrier concentrations in the $Bi_2Te_{3-y}Se_y$ solid solutions (y = 0.12–0.36) were obtained by adding excess Te. In the $Bi_{2-x}Sb_xTe_{3-y}Se_y$ solid solutions (x = 0.08 and 0.12, y = 0.24 and 0.36), one used $CdCl_2$ in addition to excess Te. $Bi_2Te_{3-z}S_z$ (z = 0.12 and 0.21) was doped by introducing $CdCl_2$ into the solid solution.

Figures 1 and 2 present the experimental temperature dependences for the thermopower coefficient α and for the electrical conductivity σ, which were used to determine the product $(m/m_0)^{3/2}\mu_0$ entering expression (1), with due account of r_{eff}:

$$\mu_0\left(\frac{m}{m_0}\right)^{3/2} = \frac{\sigma\Gamma(r+3/2)}{2e(2\pi m_0 k_0 T/h^2)^{3/2} F_{r+1/2}(\eta)}, \qquad (7)$$

where $F(r, \eta)$ and $\Gamma(r + 3/2)$ are the Fermi integral and the gamma function, respectively, and η is the reduced Fermi energy.

As follows from Figs. 1 and 2, the temperature dependence of the thermopower coefficient α becomes weaker in the low-temperature domain ($80 < T < 150$ K), and with an increasing number of substituted atoms and with a carrier concentration increasing from 0.25 to 0.9×10^{19} cm^{-3} in the solid solutions studied. The weakening of the $\alpha = f(T)$ relation is indicated by

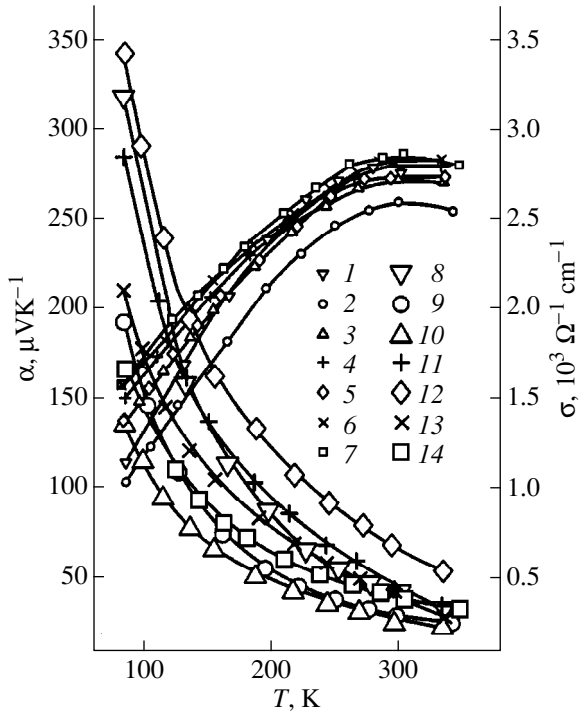

Fig. 1. Temperature dependences of the thermopower coefficient α (*1–7*) and of the electrical conductivity σ (*8–14*) in $Bi_2Te_{3-y}Se_y$ solid solutions with different values of n (10^{19} cm^{-3}): (y = 0.12) (*1, 8*) 0.35, (*2, 9*) 0.8; (y = 0.21) (*3, 10*) 0.65; (y = 0.3) (*4, 11*) 0.35, (*5, 12*), 0.8; (y = 0.36) (*6, 13*) 0.35, (*7, 14*) 0.9.

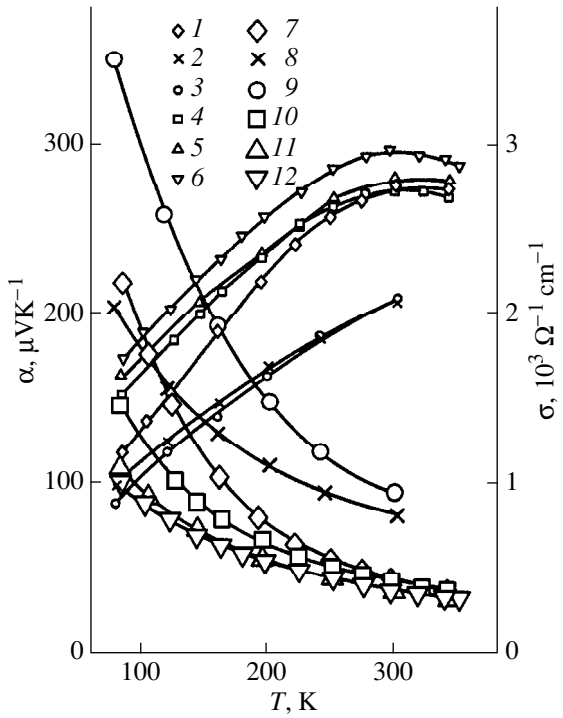

Fig. 2. Temperature dependences of the thermopower coefficient α (*1–6*) and of the electrical conductivity σ (*7–12*) in $(Bi,Sb)_2(Te,Se,S)_3$ solid solutions. $Bi_{2-x}Sb_xTe_{3-y}Se_y$, n (10^{19} cm^{-3}): (x = 0.08, y = 0.24) (*1, 7*) 0.7; (x = 0.12, y = 0.36) (*2, 8*) 0.4, (*3, 9*) 0.7. $Bi_2Te_{3-z}S_z$, n (10^{19} cm^{-3}): (z = 0.12) (*4, 10*) 0.4, (*5, 11*) 0.7; (z = 0.21) (*6, 12*) 0.9.

Table 1. The slopes of the temperature dependences $s_1 = d\ln\alpha/d\ln T$, $|s_2| = d\ln\sigma_0/d\ln T$, $|s_3| = d\ln((m/m_0)^{3/2}\mu_0)/d\ln T$, $|s_4| = d\ln\kappa_L/d\ln T$, and $s_5 = d\ln\beta/d\ln T$ in $Bi_{2-x}Sb_xTe_{3-y-z}Se_yS_z$ solid solutions obtained for $T < 150$ K

$Bi_2Te_{3-y}Se_y$							
y		$n \times 10^{19}$, cm^{-3}	s_1	$\|s_2\|$	$\|s_3\|$	$\|s_4\|$	s_5
0.12		0.35	0.86	1.65	1.7	0.75	1.61
		0.8	0.83	1.55	1.66	0.75	1.36
0.21		0.65	0.69	1.51	1.61	0.75	1.56
0.3		0.35	0.55	1.61	1.75	0.73	1.56
		0.65	0.53	1.51	1.57	0.7	1.5
0.36		0.35	0.5	1.42	1.63	0.72	1.52
		0.9	0.48	1.34	1.55	0.71	1.45
z		$Bi_2Te_{3-z}S_z$					
0.12		0.3	0.76	1.38	1.49	0.55	1.5
		0.7	0.58	1.08	1.35	0.49	1.47
0.21		0.9	0.67	0.93	1.26	0.46	1.35
x	y	$Bi_{2-x}Sb_xTe_{3-y}Se_y$					
0.08	0.24	0.7	0.51	1.19	1.4	0.67	1.66
0.12	0.36	0.4	0.46	0.99	1.22	0.71	1.68
		0.7	0.43	0.87	1.03	0.69	1.61

the decrease of the slopes $s_1 = d\ln\alpha/d\ln T$ (Table 1; Figs. 1, 2).

The temperature dependences of the electrical conductivity σ measured at low temperatures also become weaker (the slopes $|s_2| = d\ln\sigma_0/d\ln T$ decrease, where σ_0 is the electrical conductivity calculated for r_{eff} with inclusion of degeneracy, Table 1) with an increasing concentration n and an increasing number of substituted atoms in the solid solution (Figs. 1, 2); this is a result of the increasing number of scattering centers.

Figure 3 plots temperature dependences of the parameter $(m/m_0)^{3/2}\mu_0$. At low temperatures, the $Bi_2Te_{3-y}Se_y$ solid solution ($y = 0.12$–0.36) exhibited a decrease in $(m/m_0)^{3/2}\mu_0$ with an increasing carrier concentration n, which is associated with the decreasing mobility μ_0 (curves *1*, *4*, *6* and *2*, *5*, *7* in Fig. 3). As the concentration n in the solid solutions increases from 0.25 to 0.9×10^{19} cm^{-3}, the mobility μ_0, in agreement with our earlier data [2], decreases considerably faster than $(m/m_0)^{3/2}\mu_0$. This pattern of variation of the $(m/m_0)^{3/2}\mu_0$ quantity with n is governed by the concentration dependence of the average effective mass m/m_0, by which m/m_0 increases not only with an increasing carrier concentration [6] but also with a temperature decrease from 120 to 80 K [2].

In the low-temperature region, the parameter $(m/m_0)^{3/2}\mu_0$ was found to be the largest in the $Bi_2Te_{3-y}Se_y$ solid solution ($y = 0.3$) (curve *4* in Fig. 3). The sample with concentration $n \approx 0.35 \times 10^{19}$ cm^{-3} is also characterized by a large slope $|s_3| = d\ln(m/m_0)^{3/2}\mu_0/d\ln T$ (Table 1).

Compared with $Bi_2Te_{3-y}Se_y$, $Bi_2Te_{3-z}S_z$ samples exhibited a large decrease in the $(m/m_0)^{3/2}\mu_0$ parameter with an increasing concentration n (curves *8*, *9* in Fig. 3). As the temperature is reduced from 200 to 80 K, the parameter $(m/m_0)^{3/2}\mu_0$ decreases as a result of a considerable decrease in mobility with an increasing n and decreasing m/m_0. The weak, contrasted with $Bi_2Te_{3-z}S_z$, decrease in $(m/m_0)^{3/2}\mu_0$ in $Bi_{2-x}Sb_xTe_{3-y}Se_y$ solid solutions observed to occur at low temperatures, with the concentration n increasing from 0.4 to 0.7×10^{19} cm^{-3}, is determined by the temperature dependence of the effective mass m/m_0, which grows with decreasing temperature [6–8].

3. LATTICE HEAT CONDUCTIVITY

The experimental values of the heat conductivity κ were used to calculate the lattice heat conductivity κ_L (Fig. 4). The electronic heat conductivity κ_e needed to calculate the Lorenz number $L(r_{\text{eff}}, \eta)$ was found taking the effective scattering parameter into account. The result is

$$L = \left(\frac{k}{e}\right)^2 \times \left[\frac{(r+7/2)F_{r+5/2}(\eta)}{(r+3/2)F_{r+1/2}(\eta)} - \frac{(r+5/2)^2F^2_{r+3/2}(\eta)}{(r+3/2)^2F^2_{r+1/2}(\eta)}\right]. \quad (8)$$

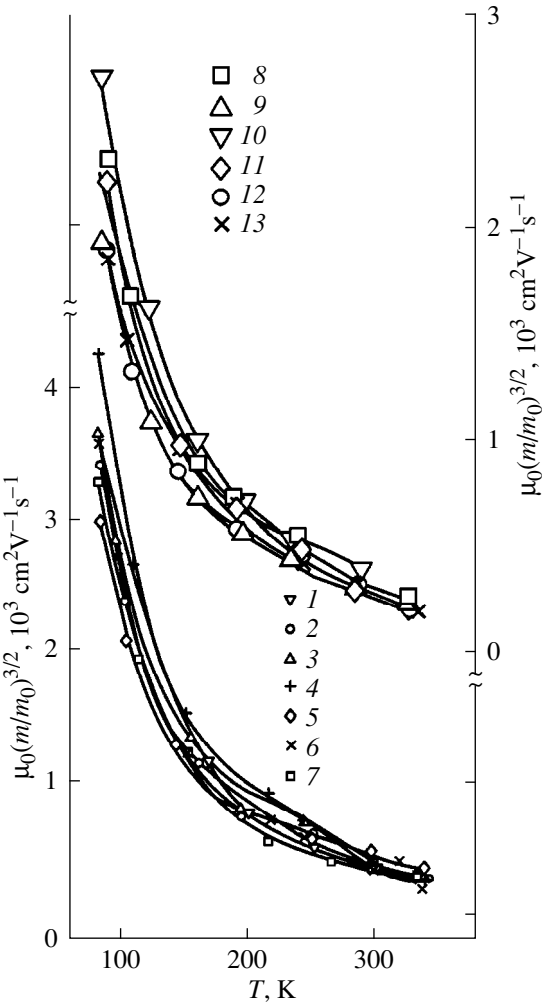

Fig. 3. Temperature dependences of the parameter $(m/m_0)^{3/2}\mu_0$ in $(Bi,Sb)_2(Te,Se,S)_3$ solid solutions. $Bi_2Te_{3-y}Se_y$, n (10^{19}cm^{-3}): (y = 0.12) (*1*) 0.35; (*2*) 0.8; (y = 0.21) (*3*) 0.65; (y = 0.3) (*4*) 0.35; (*5*) 0.8; (y = 0.36) (*6*) 0.35; (*7*) 0.9. $Bi_{2-x}Sb_xTe_{3-y}Se_y$, n (10^{19} cm^{-3}): (x = 0.08, y = 0.24) (*8*) 0.7; (x = 0.12, y = 0.36) (*9*) 0.4; (*10*) 0.7. $Bi_2Te_{3-z}S_z$, n (10^{19} cm^{-3}): (z = 0.12) (*11*) 0.4; (*12*) 0.7; (z = 0.21) (*13*) 0.9.

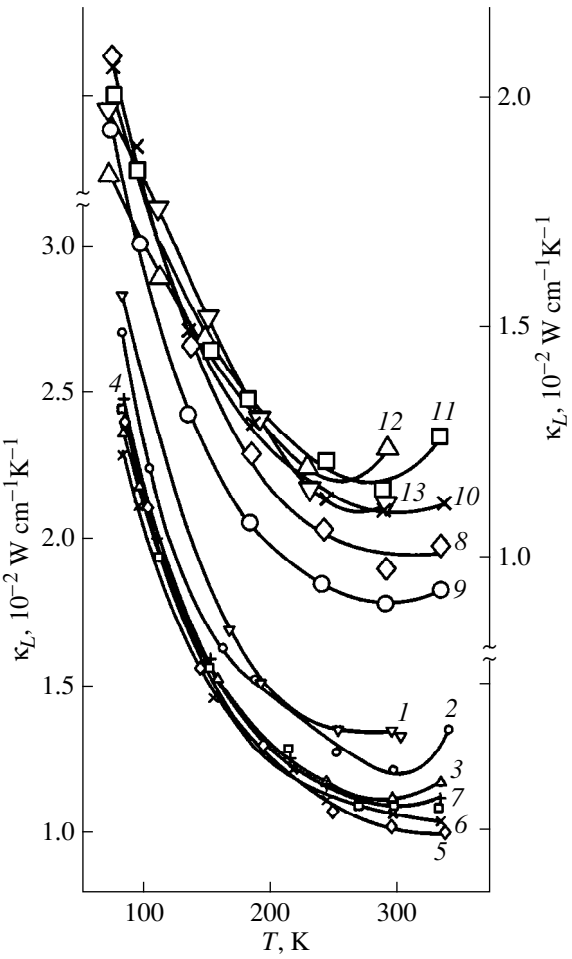

Fig. 4. Temperature dependences of the lattice heat conductivity κ_L in $(Bi,Sb)_2(Te,Se,S)_3$ solid solutions. Sample notation is the same as in Fig. 3.

By using r_{eff}, one can take into account not only a change of the scattering mechanisms in solid solutions but, albeit indirectly, the effect of a complex band structure on the lattice heat conductivity (through the concentration and temperature dependences of r_{eff} [5]).

The lattice heat conductivity κ_L decreases weakly in $Bi_2Te_{3-y}Se_y$ solid-solution samples with low carrier concentrations as y increases from 0.12 to 0.36 (curves *1*, *4*, *6* in Fig. 4). The weak variation of κ_L from the number of substituted Te atoms is due to the fact that a small number of Se atoms are sufficient for the absorption of practically all short-wavelength phonons, as a result of which an increase in the number of Se atoms cannot bring about a noticeable decrease in κ_L [9]. At higher carrier concentrations, the decrease in κ_L with increasing y in the $Bi_2Te_{3-y}Se_y$ solid solution becomes even more negligible (curves *1*, *2*, *4*, *5*, *6*, *7* in Fig. 4), because the distorted lattice regions may overlap at high impurity-atom concentrations. The slopes $|s_4| = d\ln\kappa_L/d\ln T$ (Table 1) also fall off slowly with increasing y in the $Bi_2Te_{3-y}Se_y$ solid solution.

The values of κ_L and of the $|s_4|$ slope for the $Bi_2Te_{3-z}S_z$ solid solution (curves *8–13* in Fig. 4) are smaller than those for $Bi_2Te_{3-y}Se_y$ (curves *1–7*). The κ_L decreases because S atoms scatter phonons more strongly than Se does and because the distortions of the Bi_2Te_3 lattice induced by the S $\longrightarrow$ Te substitution are larger than in the Se $\longrightarrow$ Te replacement due to the difference between the covalent radii of the S and Se atoms [9].

In $Bi_{2-x}Sb_xTe_{3-y}Se_y$ solid solutions (curves *8–10* in Fig. 4) where substitution (Sb $\longrightarrow$ Bi, Se $\longrightarrow$ Te) takes place on both Bi_2Te_3 sublattices, one observes a further decrease in κ_L compared with that in the $Bi_2Te_{3-y}Se_y$

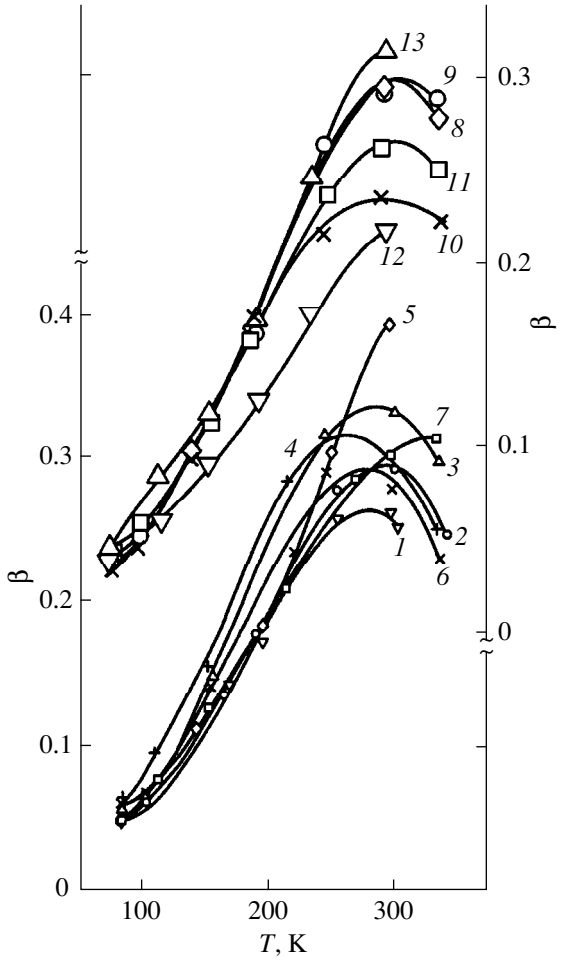

Fig. 5. Temperature dependences of the parameter β in $(Bi,Sb)_2(Te,Se,S)_3$ solid solutions. Sample notation is the same as in Fig. 3.

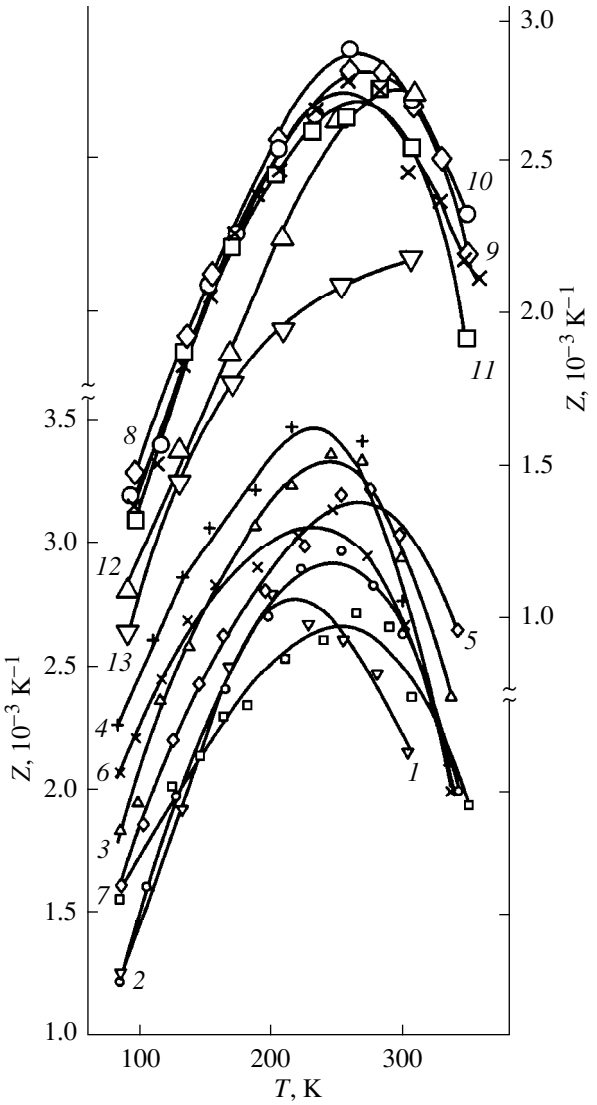

Fig. 6. Temperature dependences of the thermoelectric efficiency Z in $(Bi,Sb)_2(Te,Se,S)_3$ solid solutions. Sample notation is the same as in Fig. 3.

and $Bi_2Te_{3-z}S_z$ solid solutions, where atoms are substituted on one sublattice only (curves *8–10* in Fig. 4). This decrease in κ_L may be due to a change in the concentration of antisite Bi, brought about by the formation of the $Bi_{2-x}Sb_xTe_{3-y}Se_y$ solid solution [9].

The decrease in κ_L with increasing carrier concentration in the $Bi_2Te_{3-y}Se_y$ solid solution containing excess Te is due to the increase in phonon scattering from charged impurities as the number of scattering centers increases. The decrease of κ_L in the $Bi_{2-x}Sb_xTe_{3-y}Se_y$ and $Bi_2Te_{3-z}Se_z$ solid solutions containing $CdCl_2$ as a dopant, as well as excess Te, may be attributed to stronger scattering from charged impurities. The decrease in κ_L with increasing carrier concentration may also originate from the effect of the second subband in the solid-solution conduction band [10], resulting from additional heat transport by carriers, which, while being of two types, have the same sign.

4. THERMOELECTRIC EFFICIENCY

Data on the temperature dependences of $(m/m_0)^{3/2}\mu_0$ and κ_L permit one to calculate the parameter β (Fig. 5), which was observed to be the largest in the $Bi_2Te_{3-y}Se_y$ solid solution ($y = 0.3$) at low temperatures at the concentration $n = 0.35 \times 10^{19}$ cm^{-3}, which was found to be optimal for these low temperatures (curve *4* in Fig. 5). The increase in β and, hence, in the thermoelectric efficiency Z (curve *4* in Fig. 6) for $x = 0.3$ can be assigned to high mobility, to an increase in the density-of-states effective mass with decreasing temperature for $T <$ 150 K, and to the low lattice heat conductivity κ_L (curve *4* in Fig. 4). The weak decrease in κ_L at $y = 0.36$ does not compensate the decrease in the parameter

$(m/m_0)^{3/2}\mu_0$, which reduces the magnitude of β and, hence, the thermoelectric efficiency *Z* (curve *6* in Figs. 5, 6).

It should be noted that in $(Bi,Sb)_2(Te,Se,S)_3$ solid solutions, the slopes of the temperature dependences of all the quantities studied (Table 1) are different for the low- ($T < 150$ K) and high-temperature ($150 < T < 250$ K) regions, which may originate from the electron–phonon coupling being different in different temperature intervals [11]. The decrease of the slope $s_5 = d\ln\beta/d\ln T$ at low temperatures, compared with that at high temperatures, brings about an increase in thermoelectric efficiency.

Despite the decrease in κ_L (curves *8–13* in Fig. 4) in $Bi_2Te_{3-z}S_z$ ($z = 0.12$, 0.21) and $Bi_{2-x}Sb_xTe_{3-y}Se_y$ ($x = 0.08$, $y = 0.24$) solid solutions, the parameter β and the thermoelectric efficiency *Z* (curves *8–13*, Figs. 5, 6) are substantially lower than those in $Bi_2Te_{3-y}Se_y$ because of the considerable decrease in mobility.

5. PARAMETERS OF THE CONSTANT-ENERGY ELLIPSOIDS

Expression (5), taken together with the effective mass ratios m_i/m_j [4], offers a possible method of determining the orientation of the principal axes of the constant-energy ellipsoids (m_1, m_2, m_3) with respect to the crystallographic axes. This was done using the data on temperature dependences of effective-mass tensor-component ratios m_i/m_j in $(Bi,Sb)_2(Te,Se,S)_3$ solid solutions, which were obtained by us earlier [7, 8]. In the calculations of m_i, the *Z* (or *3*th) axis was directed along the threefold axis, the *X* (*1*th) axes were directed along the twofold axes (binary directions), and the *Y* (*2*th) axes were in the mirror planes (bisector directions).

Table 2 presents the ratios of components of the effective-mass tensors m_1, m_2, m_3 for the $(Bi,Sb)_2(Te,Se,S)_3$ solid solutions calculated from Eq. (5) for $T = 77$ and 150 K. The tilt angles θ of the principal ellipsoid axes (not listed in Table 2), with respect to the crystallographic axes, are 40°–44° for all

Table 2. Parameters of the constant-energy ellipsoids in *n*-$(Bi,Sb)_2(Te,Se,S)_3$ solid solutions

$Bi_2Te_{3-y}Se_y$						
no.	*y*		$n \times 10^{19}$, cm^{-3}	*T* = 77, 150 K		
				m_1	m_2	m_3
1	0.12		0.25	0.041	0.22	0.23
				0.043	0.23	0.2
2			0.7	0.027	0.94	0.17
				0.03	1.14	0.16
3	0.3		0.4	0.119	0.49	0.4
				0.067	0.85	0.3
4			1.1	0.055	1.26	0.25
				0.056	2.15	0.11
	x	*y*	$Bi_{2-x}Sb_xTe_{3-y}Se_y$			
5	0.2	0.3	1.1	0.05	0.34	0.2
				0.051	0.46	0.24
6	0.4	0.6	0.8	0.017	0.17	0.07
				0.015	0.15	0.05
	z		$Bi_2Te_{3-z}S_z$			
7	0.12		0.4	0.049	0.48	0.41
				0.615	0.52	0.23
8			1.3	0.068	0.83	0.17
				0.04	1.2	0.08
9	0.21		0.4	0.06	0.48	0.51
				0.04	1	0.21

Note: For each carrier concentration, the upper row gives the values of m_1, m_2, and m_3 for 77 K, while the lower one gives those for 150 K.

the solid solutions, with the exception of $Bi_2Te_{3-y}Se_y$ ($y = 0.12$), which exhibits a low concentration $n = 0.25 \times 10^{19}$ cm^{-3}, where $\theta \approx 22°$; thus, no effect of the second subband in the conduction band of the solid solution [10] is indicated. The values of m_2 and m_3 from Table 2 were used to construct projections on the *ZY* plane of one of the six equivalent constant-energy ellipsoids for the conduction band of the $(Bi,Sb)_2(Te,Se,S)_3$ solid solutions (Fig. 7).

The compression of the ellipsoids in the materials under study was found to be the largest in the binary direction (*X*). In the $Bi_2Te_{3-y}Se_y$ solid solution, the ellipsoids constructed for $T = 77$ K and low carrier concentrations are weakly extended along the *Y*' axis and tilted at an angle θ to the bisector crystallographic axis *Y* (solid lines in Fig. 7, ellipsoids *1*, *3*). As the temperature decreases, the ellipsoids become more and more extended along the *Y*' axis (along the bisector axis *Y* and with a tilt through an angle θ) while remaining compressed along the binary axis *X*' (dashed lines in Fig. 7, ellipsoids *1*, *3*). According to [1, 2], for the carrier concentrations specified, the scattering is only weakly anisotropic in the $Bi_2Te_{3-y}Se_y$ solid solution. The same orientation of the ellipsoids and a weak extension along the *Y*' axis are also characteristic of the $Bi_2Te_{3-z}S_z$ solid solution at low carrier concentrations (0.4×10^{19} cm^{-3}) (ellipsoids *7*, *8* in Fig. 7). However, the scattering anisotropy in $Bi_2Te_{3-z}S_z$ is larger than it is in $Bi_2Te_{3-y}Se_y$ at similar carrier concentrations.

As the concentration increases ($n \geq 0.7 \times 10^{19}$ cm^{-3}), the ellipsoids become progressively more extended along the *Y*' axis while remaining compressed along the binary axis *X*' (ellipsoids *2*, *4*, *8*, *9* in Fig. 7). This change in the ellipsoid parameters obtained in the model assuming isotropic carrier scattering indicates an increasing anisotropy in the constant-energy surface.

It should be noted that at high concentrations *n* in the $Bi_{2-x}Sb_xTe_{3-y}Se_y$ solid solution, a smaller ellipsoid elongation along *Y*' (ellipsoids *5*, *6* in Fig. 7) was observed compared with that observed for $Bi_2Te_{3-y}Se_y$ and $Bi_2Te_{3-z}S_z$. Thus, the extension of the ellipsoids in the $Bi_{2-x}Sb_xTe_{3-y}Se_y$ conduction band occurs at higher carrier concentrations than is the case with $Bi_2Te_{3-y}Se_y$ and $Bi_2Te_{3-z}S_z$, which is due to the variation of the mass parameters m_1, m_2, m_3 (Table 2) with concentration and solid-solution composition, as well as to the effect of carrier scattering anisotropy.

6. ANISOTROPY OF THE CONSTANT-ENERGY ELLIPSOID PARAMETERS AND THE THERMOELECTRIC EFFICIENCY

The results of the study on thermoelectric efficiency *Z* and the available data on the variation of the parameters of constant-energy ellipsoids for the $(Bi,Sb)_2(Te,Se,S)_3$ solid solutions permit a coordinated analysis of these quantities. The largest values of *Z* were observed in the $Bi_2Te_{3-y}Se_y$ ($y = 0.3$) solid solution with excess Te (curve *4* in Fig. 6) at optimum carrier concentrations (0.35×10^{19} cm^{-3}) not only in the low-temperature region but also at higher temperatures, up to 250 K. At such concentrations *n*, the single-conduction-band model is valid for the $Bi_2Te_{3-y}Se_y$ solid solution [10], the constant-energy ellipsoids are slightly extended along the *Y* axis with a tilt angle θ, and the carrier scattering anisotropy is the weakest in comparison with the solid solutions, with $y = 0.12$ and 0.36. At higher carrier concentrations, where *Z* decreases (curve *5* in Fig. 6), the ellipsoid parameters change (the ellipsoids extend) and the anisotropy of the constant-energy surface increases, as does that of the carrier scattering.

At low enough carrier concentrations ($n = 0.4 \times 10^{19}$ cm^{-3}), the thermoelectric efficiency *Z* of the $Bi_2Te_{3-z}S_z$ solid solution (curve *11* in Fig. 6) is lower than that of $Bi_2Te_{3-y}Se_y$, with no appreciable changes in the ellipsoid shape parameters being observed in

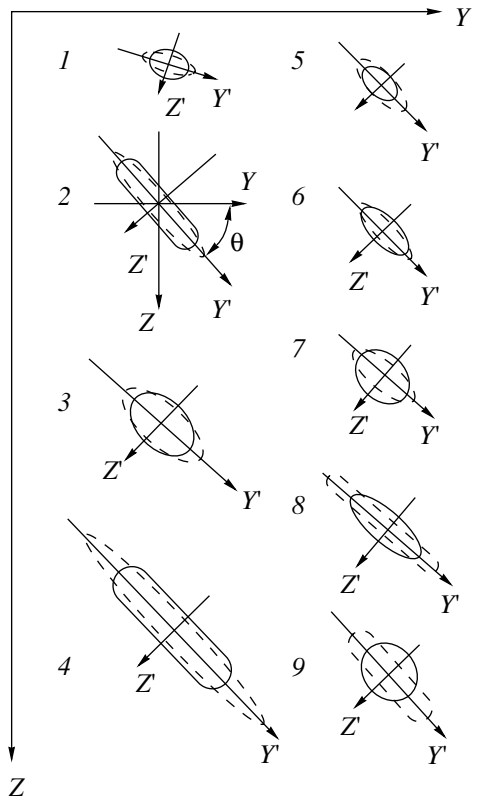

Fig. 7. Projections of one of the six equivalent constant-energy ellipsoids on the mirror plane *YZ* constructed for the conduction band of the $(Bi,Sb)_2(Te,Se,S)_3$ solid solutions at $T = 77$ (solid lines) and $T = 150$ K (dashed lines). $Bi_2Te_{3-y}Se_y$, n (10^{19} cm^{-3}): ($y = 0.12$) (*1*) 0.25, (*2*) 0.7; ($y = 0.3$) (*3*) 0.4, (*4*) 1.1. $Bi_{2-x}Sb_xTe_{3-y}Se_y$, n (10^{19} cm^{-3}): ($x = 0.2$, $y = 0.3$) (*5*) 1.1; ($x = 0.4$, $y = 0.6$) (*6*) 0.8. $Bi_2Te_{3-z}S_z$, n (10^{19} cm^{-3}): ($z = 0.12$) (*7*) 0.4, (*8*) 1.3; ($z = 0.21$) (*9*) 0.4.

these solid solutions (ellipsoids *3*, *7* in Fig. 7; Table 2). This decrease in Z can be explained as being due to a difference in carrier scattering anisotropy between $Bi_2Te_{3-y}Se_y$ and $Bi_2Te_{3-z}S_z$. A study of the galvanomagnetic properties of the $Bi_2(Te,Se,S)_3$ solid solutions made within the anisotropic scattering model [1, 2] showed that in $Bi_2Te_{3-y}Se_y$ ($y = 0.3$) the ratios of the relaxation time tensor components obtained within the temperature interval $80 \le T \le 150$ K for a concentration $n = 0.35 \times 10^{19}$ cm^{-3} are $\tau_{22}/\tau_{11} \approx (0.95–1.2)$ and $\tau_{33}/\tau_{11} \approx (0.65–0.9)$ as T is varied from 80 to 150 K. The close-to-unity ratio τ_{22}/τ_{11} implies a weak scattering anisotropy in the $Bi_2Te_{3-y}Se_y$ ($y = 0.3$) solid solution in both the bisector and binary directions. The small difference (of no more than 30%) between the τ_{22}/τ_{11} and τ_{33}/τ_{11} ratios is associated with the weak anisotropy in the mirror plane (YZ). In the $Bi_2Te_{3-z}S_z$ solid solution ($z = 0.21$, $n = 0.4 \times 10^{19}$ cm^{-3}, $80 \le T \le 150$ K), the ratio $\tau_{22}/\tau_{11} \approx (0.2–0.5)$, which gives evidence for a higher scattering anisotropy compared with that in the binary direction in $Bi_2Te_{3-y}Se_y$. Thus, the thermoelectric efficiency in the solid solutions studied is effected by an increase in carrier scattering anisotropy to a larger extent than by a change in the parameters of the constant-energy ellipsoids.

REFERENCES

1. M. V. Vedernikov, V. A. Kutasov, L. N. Luk'yanova, and P. P. Konstantinov, in *Proceedings of the XVII International Conference on Thermoelectrics, Nagoya, 1998*, p. 121.
2. V. A. Kutasov, L. N. Luk'yanova, and P. P. Konstantinov, Fiz. Tverd. Tela (St. Petersburg) **41** (2), 187 (1999) [Phys. Solid State **41**, 164 (1999)].
3. J. R. Drabble, R. D. Groves, and R. Wolfe, Proc. Phys. Soc. London **71** (3), 430 (1958).
4. L. P. Caywood and G. R. Miller, Phys. Rev. **2** (8), 3210 (1970).
5. V. A. Kutasov and L. N. Luk'yanova, Fiz. Tverd. Tela (Leningrad) **26** (8), 2501 (1984) [Sov. Phys. Solid State **26**, 1515 (1984)].
6. V. A. Kutasov and L. N. Luk'yanova, Fiz. Tekh. Poluprovodn. (Leningrad) **23** (4), 652 (1989) [Sov. Phys. Semicond. **23**, 408 (1989)].
7. V. A. Kutasov and L. N. Luk'yanova, Phys. Status Solidi B **154**, 669 (1989).
8. V. A. Kutasov and L. N. Luk'yanova, Fiz. Tverd. Tela (Leningrad) **29** (10), 2966 (1987) [Sov. Phys. Solid State **29**, 1705 (1987)].
9. B. M. Gol'tsman, V. A. Kudinov, and I. A. Smirnov, *Semiconducting Thermoelectric Materials Based on Bi_2Te_3* (Nauka, Moscow, 1972).
10. H. Kohler, W. Haigis, and A. von Middendorff, Phys. Status Solidi B **78** (2), 637 (1976).
11. G. N. Ikonnikova, V. A. Kutasov, and L. N. Luk'yanova, Fiz. Tverd. Tela (Leningrad) **32** (11), 3350 (1990) [Sov. Phys. Solid State **32**, 1937 (1990)].

Translated by G. Skrebtsov

Physics of the Solid State, Vol. 42, No. 11, 2000, pp. 2047–2053. Translated from Fizika Tverdogo Tela, Vol. 42, No. 11, 2000, pp. 1992–1997.

SEMICONDUCTORS AND DIELECTRICS

Electronic Band Structure of In_2S_3 and $CdIn_2S_4$ Semiconductor Spinels from the Data of X-ray Spectroscopy and Theoretical Calculations

A. A. Lavrent'ev, N. Yu. Safontseva, V. A. Dubeĭko, B. V. Gabrel'yan, and I. Ya. Nikiforov

Don State Technical University, Rostov-on-Don, 344010 Russia

e-mail: root@sintez.rnd.su

Received March 16, 2000; in final form, April 28, 2000

Abstract—The electronic band structure of the chalcogenide spinels In_2S_3 and $CdIn_2S_4$ has been studied using the FEFF8 program. It is shown that the valence band top is formed by the S *p* states mixed with the In *s* and In *p* states for In_2S_3 or with the Cd *s*, Cd *p*, In *s*, and In *p* states for $CdIn_2S_4$. Compared to In_2S_3, the presence of Cd atoms in the nearest environment of S atoms in $CdIn_2S_4$ does not considerably affect the electronic band structure. In $CdIn_2S_4$ the Cd 4*d* states, as well as the In 4*d* states, form a narrow localized band shifted deep into the valence band. The theoretical results are in good agreement with the experimental x-ray photoelectron and x-ray spectra. © *2000 MAIK "Nauka/Interperiodica".*

1. INTRODUCTION

Nonmagnetic compounds of the $A^{II}B_2^{III}C_4^{VI}$ type, in which the cations have filled *d* shells, are characterized by a broad transparency region, high nonlinear susceptibility and natural birefringence, optical activity, high photosensitivity, and intense luminescence [1]. These merits, in a combination with the large optical band gap E_g (according to different authors, E_g for $CdIn_2S_4$ lies in the range 2.0–2.3 eV [2]), render the $A^{II}B_2^{III}C_4^{VI}$ compounds promising for use in optoelectronics.

The $CdIn_2S_4$ compound crystallizes in the normal spinel structure, which belongs to the space group O_h^7 ($Fd3m$). The cubic unit cell of the spinel contains eight $CdIn_2S_4$ formula units with the lattice parameter a = 10.797 Å [2] and the anionic parameter u = 0.386 [3]. The sulfur atoms in $CdIn_2S_4$ form a face-centered cubic sublattice with the closest packing. As in all normal spinels, the high-valence indium atoms occupy sixteen octahedral holes and the cadmium atoms with a lower valence fill eight tetrahedral holes in the unit cell. Each sulfur atom has three octahedrally coordinated indium atoms and one tetrahedrally coordinated cadmium atom as the nearest neighbors. The shortest interatomic distances in $CdIn_2S_4$ are as follows: $R_{Cd–S}$ = 2.543 Å, $R_{In–S}$ = 2.586 Å, and $R_{S–S}$ = 3.481 Å.

The indium sulfide In_2S_3 studied in this work also has a spinel structure with a tetragonal superstructure due to a vacancy disordering. The sulfur atoms form the closest cubic packing. One unit cell contains 32 sulfur atoms. The indium atoms are distributed over two regular systems with multiplicities of 8 (tetrahedral holes) and 16 (octahedral holes). However, compared to $CdIn_2S_4$, among all the above 24 holes in the unit cell of In_2S_3, only 21 holes are occupied, and three holes (1/3, 2, and 2/3) remain unoccupied [4]. The crystal lattice parameter a = 10.74 Å and the parameter u = –0.136 [4] were used in further calculations for In_2S_3. The shortest interatomic distances in In_2S_3 are as follows: $R_{In^1–S}$ = 2.53, $R_{In^2–S}$ = 2.572, and $R_{S–S}$ = 3.463 Å.

The electronic band structure of $CdIn_2S_4$ and In_2S_3 was studied both theoretically by using band-structure calculations [3, 5–11] and experimentally with x-ray photoelectron (XPS) [12], ultraviolet photoelectron (UPS) [13], and x-ray [14, 15] spectroscopy. Goodenough [5] noted that knowledge of the electronic band structure of the In_2S_3 nonmagnetic spinel can be very useful in investigating the structure of more complex spinels with transition *d* metals (for example, $CdIn_2S_4$). However, in all the cited works, the densities of states were not determined in the band calculations of In_2S_3 and $CdIn_2S_4$, which made their comparison with experimental results more difficult. In this respect, the experimental and theoretical data on local partial densities of states in In_2S_3 and $CdIn_2S_4$ are of fundamental importance, because this information, first, allows one to determine with confidence the energy distribution of electronic states with a specific symmetry and their contributions to the electronic subbands and, second, provides the basis for the conclusion about the hybridization of electronic states in these compounds.

2. EXPERIMENTAL TECHNIQUE

Sulfides are very convenient objects because the experimental sulfur *K* x-ray spectra are rather informa-

1063-7834/00/4211-2047$20.00 © 2000 MAIK "Nauka/Interperiodica"

tive by virtue of their fine resolved structure. This is explained by the fact that the width of the sulfur *K*-edge core level is small (0.57 eV [16]), and this broadening does not lead to a considerable "smearing" of the fine structure in the experimental sulfur *K* x-ray spectra. The sulfur *K*-edge x-ray fluorescence spectra and sulfur *K* x-ray absorption spectra of the In_2S_3 and $CdIn_2S_4$ compounds were measured on a DRS-2 spectrograph with photographic recording. The Johann focusing was used in the DRS-2 spectrograph, and the energy resolution was equal to approximately 0.2 eV. The $(10\bar{1}1)$ quartz crystal with a bending radius of 50 cm served as a dispersive element. For the sulfur *K* spectra, the reference lines were the Bi $M\alpha_1$ and Bi $M\beta$ lines in the first-order reflection with energies of 2422.5 and 2525.6 eV, respectively [16]. Each spectrum was obtained by averaging the data for three films after the photometric measurements at 250 equidistant points.

The sulfur primary $L_{2,3}$ spectra of In_2S_3 and $CdIn_2S_4$ were taken on an RSM-500 spectrometer. A concave spherical grating of radius $R = 2$ m with 600 rulings per millimeter (the wavelengths fall in the range from ~20 Å to 550 Å) was used as a dispersive element in the spectrometer. The grating was coated with a thin layer of gold in order to increase the intensity and to enhance the contrast of the spectra. The spectra were recorded with a secondary emission electron multiplier of an open type, which could operate in spectrometers under a high vacuum, but, unlike counters, had no windows. In measurements of the sulfur $L_{2,3}$ spectra, the Zr $M\zeta$ line ($\lambda = 81.75$ Å; $E = 151.65$ eV [17]) was used as the reference line. The spectra of the *K* and *L* series were matched on the same energy scale against the energy of the sulfur $K\alpha_1$ line.

As a whole, the S *K* x-ray spectrum reflects the energy distribution of the S *p* partial states [18]; hence, its main maximum *A* (Figs. 1, 2) for all the studied compounds determines the energy location of the greater part of these states in the valence band. The other features in the structure of the S *K* spectrum can be attributed to the S *p* states mixed with the partial states of the other atoms bonded to the sulfur atoms in the compound. This can be treated as a manifestation of the hybridization of electronic states due to the interatomic interaction in the chemical compound (this interpretation was successfully applied, for example, to sulfides, in our earlier works [14, 19, 20]). In turn, the S $L_{2,3}$ spectrum reflects the energy distribution of the S *s* partial states [18].

The In L_1 x-ray emission spectra of the In_2S_3 and $CdIn_2S_4$ semiconductor compounds were also recorded on a DRS-2 spectrograph (for greater detail, see [21]). Figures 1 and 2 demonstrate the In L_1 x-ray emission spectra together with the adjacent long-wavelength spectral range approximately 25 eV in length. The In L_1 emission band represents the L_{γ_4} line, which corresponds to the L_1–εp transitions from the L_1 level to the levels of the valence band. The shape of this line reflects the energy distribution of the density of states in the valence band, which have the *p* symmetry and are localized in a polyhedron of the indium atoms. A small structural feature, which was referred to as $L_{\beta_2^1}$ [21], is observed in the long-wavelength range of the L_1 spectrum. This feature was assigned to the L_1–$N_{4,5}$ transition. Despite the fact that the center of gravity of the $L_{\beta_2^1}$ feature on the energy scale is located approximately 10 eV below the valence band bottom, this feature can be interpreted in terms of the possible hybridization of states in solids, which gives rise to an admixture of the In *p* states with the In $N_{4,5}(4d)$ states. Therefore, the $N_{2,3}$ and $N_{4,5}$ states manifest themselves in the In L_1 emission spectrum. The energy locations of the latter states in Figs. 1 and 2 are shown by the In 4*d* lines, which were brought into coincidence with the corresponding peaks in the x-ray photoelectron spectra.

3. CALCULATION TECHNIQUE

Over twenty years, many researchers have run into serious problems when interpreting the results of calculations of the x-ray absorption near-edge structure (XANES) spectra in the range approximately 40 eV above the absorption edge, which is characterized by a strong photoelectron scattering (see, for example, [22, 23]). The available XANES codes, which deal with the full multiple scattering calculations [22, 23], are limited in accuracy for the necessity of using large basis sets and the absence of self-consistent potentials. At the same time, the results of calculations of the electronic structure with ground state potentials by conventional methods [24, 25], as a rule, depend on the lattice periodicity or disregard the core hole and the intrinsic energy effects (when the exchange–correlation potential is taken to be independent of the energy of an outcoming photoelectron).

In this work, the sulfur *K* x-ray absorption spectra and the partial density of states for the In_2S_3 and $CdIn_2S_4$ semiconductor compounds were calculated using the new FEFF8 code [26, 27]. This program makes it possible to perform *ab initio* calculations of the self-consistent crystal muffin-tin potentials with a sufficient number of loops (up to 30) and also to calculate the XANES spectra for arbitrary systems without any constraints on symmetry and periodicity within the real-space full multiple scattering (RSMS) approximation taking into account a fully relaxed hole at the core level. In addition to the x-ray absorption spectra, the FEFF8 program permits calculations of the electronic structure: the local partial densities of states (LDOS), the charge electron densities $\rho(r)$, and the charge transfer between atoms of the studied compounds. Compared to other techniques for calculating the electronic structure, the real-space multiple-scattering approach

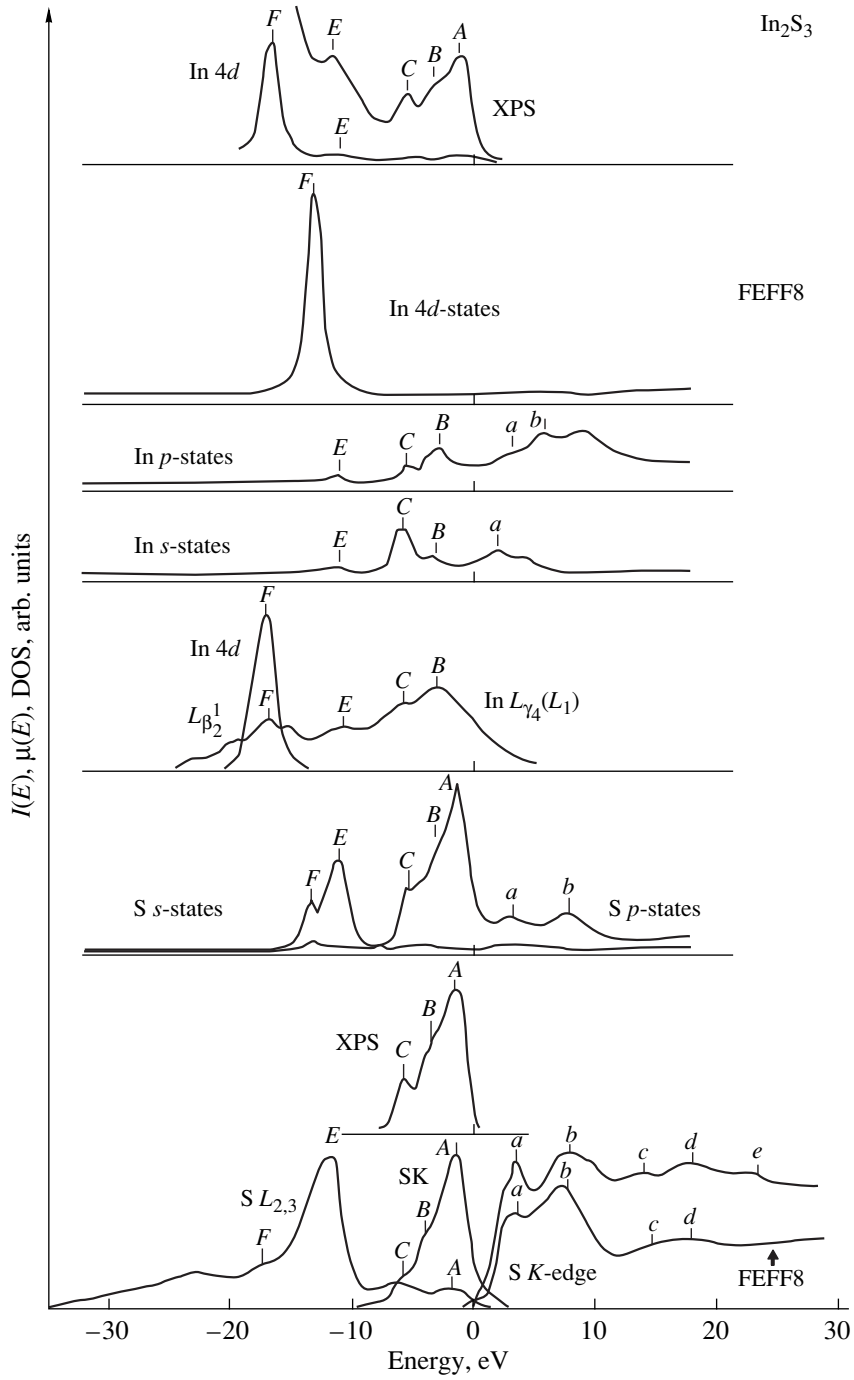

Fig. 1. Experimental and theoretical data on the electronic band structure of the In_2S_3 semiconductor compound. The XPS spectrum is taken from [12]. The energy is reckoned from the valence band top E_V.

has the advantage that the integration is carried out over the complex energy region without determination of the energy eigenvalues.

All the theoretical x-ray spectra and the local partial densities of states were *ab initio* calculated within the dipole approximation without fitting parameters according to the scheme recommended by the authors of the FEFF8 code [26, 27]. The self-consistent muffin-tin potentials were determined for clusters composed of 35 atoms (the SCF subprogram). These potentials were used to calculate the absorption spectra and the local partial densities of states within the full multiple scattering approximation for clusters consisting of 87 atoms (the FMS subprogram). Then, in addition to these clusters, the paths of single scattering in the largest cluster (permissible in the FEFF8 code) containing

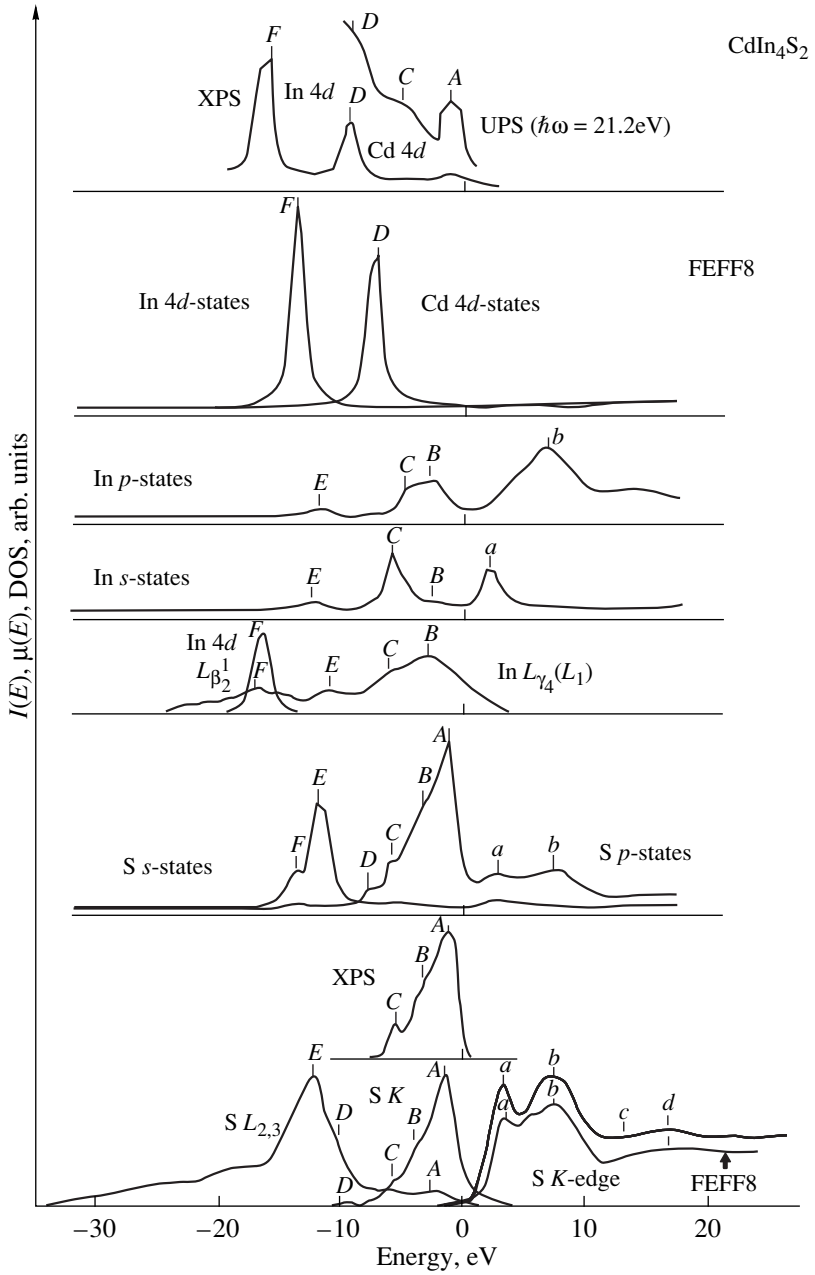

Fig. 2. Experimental and theoretical data on the electronic band structure of the $CdIn_2S_4$ semiconductor compound. The XPS and UPS spectra are taken from [12] and [13], respectively. The energy is reckoned from the valence band top E_V.

up to 1000 atoms were included in the calculations (the NLEG2 subprogram). The maximum path length (RPATH) was equal to ~16 Å for each studied compound. It should be noted that, among all the possible two-way scattering paths, only significant paths whose amplitude was no less than 4% of the maximum scattering path were taken into consideration (the CRITERIA subprogram). The crystal potentials were constructed with due regard for the exchange interaction in the Hedin–Lundqvist approximation (the EXCHANGE 0 subprogram). Because the Debye temperature for many compounds is an uncertain quantity, the DEBYE subprogram (as for the other specific parameters taken into account by different subprograms of the FEFF8 program) was commented out in the XANES calculations of In_2S_3 and $CdIn_2S_4$. The location of the Fermi level E_0 was automatically determined with an accuracy of 1 eV in the self-consistent crystal potential calculations provided by the FEFF8 code. No shift in the real value of the energy that changes the E_0 location in the final data files of the XANES calculations was made, and the

Energy location of the characteristic peaks (eV) attributed to the valence bands of In_2S_3 and $CdIn_2S_4$

Compound		Peak					
		A	*B*	*C*	*D*	*E*	*F*
In_2S_3	x-ray spectrum (S)	1.5	3.8	5.8	–	11.9	17.3
	XPS [12]	1.5	3.9	5.9	–	11.8	17.0
	S *p*	1.5	3.4	5.5	–	–	–
	S *s*	–	–	–	–	11.2	13.5
	In *s*	–	3.2	5.9	–	11.8	–
	In *p*	–	3.1	5.7	–	11.2	–
	In 4*d*	–	–	–	–	–	13.5
$CdIn_2S_4$	x-ray spectrum (S)	1.5	3.7	5.7	9.6	11.3	17.0
	x-ray spectrum (In)	–	3.3	5.8	–	–	17.0
	XPS [12]	1.6	3.9	5.9	9.7	–	16.8
	UPS [13]	1.5	–	6.0	9.9	–	–
	S *p*	1.5	3.9	6.1	8.0	–	–
	S *s*	–	–	–	–	12.1	14.1
	In *s*	–	3.0	6.1	–	12.8	–
	In *p*	–	3.0	5.0	–	12.1	–
	Cd 4*d*	–	–	–	7.4	–	–
	In 4*d*	–	–	–	–	–	14.0

Note: The energy is reckoned from the valence band top E_V.

CORRECTION subprogram providing this possibility was commented out.

4. RESULTS AND DISCUSSION

Figure 1 displays the S *K* and S $L_{2,3}$ x-ray emission spectra and the S *K* absorption edge, which were obtained by A. A. Lavrent'ev (one of the authors of this work), and also the x-ray photoelectron spectrum (XPS) taken from [12]. As can be seen, these spectra are compared with the local partial densities of states, which were calculated for indium and sulfur atoms in the In_2S_3 compound with the use of the FEFF8 program. The theoretical and experimental data in Figs. 1 and 2 were brought into coincidence on the same energy scale with respect to the main maximum *A* in the S *K* spectrum, which reflects the energy distribution of the S *p* partial states and determines the energy location of the greater part of these states in the valence band. The other features in the structure of the S *K* spectrum (*B* and *C*) can be assigned to the S *p* states mixed with the partial states of the indium atom involved in this compound. Similarly, the S $L_{2,3}$ spectrum is interpreted as the energy distribution of the S *s* occupied states, and its main maximum *E* corresponds to the energy location of their greater part.

It can be seen from Fig. 1 that the upper part of the valence band in In_2S_3 is formed by the S *p* states (the *A* maximum). The *B* shoulder in the S *K* spectrum can be attributed to the S *p* states mixed with the In *s* and In *p* states. This is confirmed by the curve of the In *p* states, whose main maximum coincides in energy location with the *B* shoulder, and also by the curve of the In *s* states, which shows a certain feature in this energy range (see table). This inference is corroborated by the experimental In L_{γ_4} spectrum [21], which reflects the energy distribution of the In *p* and In *s* states. The main maximum of this spectrum is located near the *B* peak in the curve of the In *p* states, and the *C* shoulder coincides in energy location with the main maximum in the curve of the In *s* states. In this range of energies, the S *K* spectrum also contains the *C* shoulder. This indicates that the S *p* states are mixed with both In *p* and In *s* states and that the In–S chemical bond in the In_2S_3 compound has a covalent component. The *E* shoulders in the curves of the In *s* and In *p* states are caused by the mixing of the S *s* states with the indium states of the relevant symmetry. The In *d* states form a narrow localized band, which is shifted deep into the valence band (the *F* maximum). The shift found from the maxima in the x-ray photoelectron spectrum [12] and from the In $L_{\beta_2^1}$ line [21] is equal to ~12 eV. However, the energy locations of the main maximum *F* in the curves of the

In *d* partial densities of states, which were calculated with the FEFF8 code, considerably differ from the experimental data (see table). Note that the performed calculations revealed a general tendency in the above shift. The In *d* states virtually do not contribute to the chemical bonding in the In_2S_3 compound. At the same time, the low-energy shoulders *F* in the S $L_{2,3}$ spectrum and the theoretical curve of the S *s* states suggest only an insignificant mixing of these states with the In *d* states.

The sulfur x-ray absorption spectrum near the main edge (*a*) reflects the energy distribution of the S *p* free states. Analysis of the theoretical and experimental S *K* edges and the calculated partial densities of free states (Fig. 1) shows that the conduction band bottom is formed by the strongly mixed S *p* free states and the In *p* and In *s* unoccupied states (the maxima *a* and *b* in the corresponding curves). The features *c* and *d* in the experimental S *K* edge, which are located at ~13 and ~18 eV above the valence band top E_v, are also revealed in our calculation and reside in the theoretical S *K* edge.

A comparison of the experimental and theoretical results shows that the performed calculations are in good agreement with the experimental data and reflect the energy distribution of the partial densities of states in the valence band within 20 eV from its top and in the conduction band within 17 eV with respect to E_v.

Analysis of the electronic band structure of the $CdIn_2S_4$ compound (Fig. 2) revealed that the valence band top is also formed by the S *p* states. This is confirmed by the energy location of the *A* maximum in the S *K* spectrum, x-ray photoelectron spectrum (XPS) [12], ultraviolet photoelectron spectrum (UPS) [13], and theoretical curve of the S *p* states. The shoulders *B* and *C* in the curves displayed in Fig. 2 result from the mixing of the S *p* states with the strongly mixed In *s* and In *p* states. The low-energy maximum *E* in the curves of the In *s* and In *p* states is associated with an admixture of the S *s* states shifted deep into the valence band by ~11 eV, which is supported by the experimental S $L_{2,3}$ x-ray emission spectrum.

As follows from the comparison of the electronic structures for $CdIn_2S_4$ and In_2S_3, the presence of the cadmium atoms as the nearest neighbors of the sulfur atoms does not considerably affect the chemical bounding. This is explained by the fact that the Cd *d* states, as well as the In *d* states, form a narrow localized band shifted deep into the valence band by ~10 eV. The energy location of the main maximum *D* in the curve of the Cd 4*d* states, as for the In 4*d* states, disagrees with the data of the ultraviolet photoelectron [13] and x-ray photoelectron [12] spectroscopy. However, the distance between the *F* and *D* peaks in the above curves corresponds to the experimental value (see table). The shoulders *D* in the S *K* spectrum and in the curve of the S *p* states are due to an insignificant mixing of S *p* states with Cd *d* states.

According to the XANES calculations of the S *K* absorption edge (Fig. 2), the conduction band bottom in the $CdIn_2S_4$ compound, as in In_2S_3, is formed by the mixed S *p* free states and the In *p* and In *s* states. However, the *A* maximum in the S *K* edge for the $CdIn_2S_4$ compound is associated with the hybridization of the S *p* and In *s* states, unlike the In_2S_3 compound, for which the In *p* states are also observed near the main absorption edge. The *c* feature in the experimental S *K* edge was not revealed in our calculations, unlike the *D* maximum observed in the theoretical curve (Fig. 2).

5. CONCLUSION

The above analysis demonstrated that the FEFF8 program allows one to reveal the principal features near the main absorption edge and also to trace the formation of the valence band top and the conduction band bottom by the partial states of all the atoms involved in the compound composition. This makes it possible to compare the theoretical results with both absorption spectra and the energy locations of the main maxima in the emission spectra.

REFERENCES

1. A. N. Georgobiani, S. I. Radautsan, and I. M. Tiginyanu, Fiz. Tekh. Poluprovodn. (Leningrad) **19** (2), 193 (1985) [Sov. Phys. Semicond. **19**, 121 (1985)].
2. *Physicochemical Properties of Semiconducting Materials: A Handbook*, Ed. by A. V. Novoselova and V. B. Lazarev (Nauka, Moscow, 1979).
3. W. Rehwald, Phys. Rev. **155** (3), 861 (1967).
4. G. V. Bokiĭ, *Introduction to Crystal Chemistry* (Mosk. Gos. Univ., Moscow, 1954).
5. J. B. Goodenough, J. Phys. Chem. Solids **30** (2), 261 (1969).
6. F. Meloni and G. Mula, Phys. Rev. B **2** (2), 392 (1970).
7. S. Katsuki, J. Phys. Soc. Jpn. **33** (6), 1561 (1972).
8. M. Inoue and M. Okazaki, J. Phys. Soc. Jpn. **36** (3), 780 (1974).
9. A. Baldereschi, F. Meloni, F. Aymerichi, and G. Mula, in *Proceedings of the Third International Conference on Ternary Compounds* (Edinburgh, England, 1977); Inst. Phys. Conf. Ser. **35**, 193 (1977).
10. G. Guizzetti and F. Meloni, Nuovo Cimento D **1** (4), 503 (1982).
11. N. Serra, F. Meloni, and A. Baldereschi, Nuovo Cimento D **2** (6), 1754 (1983).
12. H. Ihara, H. Abe, S. Endo, and T. Irie, Solid State Commun. **28** (7), 563 (1978).
13. F. Cerrina, C. Quaresima, I. Abbati, *et al.*, Solid State Commun. **33** (4), 429 (1980).
14. A. N. Gusatinskii, A. A. Lavrentyev, M. A. Blokhin, and V. Yu. Slivka, Solid State Commun. **57** (6), 389 (1986).
15. C. Sugiura, H. Yorikawa, and S. Muramatsu, J. Phys. Soc. Jpn. **66** (2), 503 (1997).
16. M. A. Blokhin and I. G. Shveĭtser, *A Handbook on X-ray Spectroscopic Analysis* (Nauka, Moscow, 1982).

17. M. O. Krause, Phys. Lett. A **A74** (5), 303 (1979).

18. A. Meisel, G. Leonhardt, and R. Szargan, *Röntgenspektren und chemische Bindung* (Akademische Verlagsgesellschaft Geest U. Portig, Leipzig, 1977; Naukova Dumka, Kiev, 1981); *X-ray Spectra and Chemical Binding* (Springer-Verlag, New York, 1989).

19. A. A. Lavrentyev, A. N. Gusatinskii, M. A. Blokhin, *et al.*, J. Phys. C: Solid State Phys. **20**, 3445 (1987).

20. A. A. Lavrentyev, A. N. Gusatinskii, I. Ya. Nikiforov, *et al.*, J. Phys.: Condens. Matter **5**, 1446 (1993).

21. A. N. Gusatinskiĭ, M. A. Blokhin, P. Shumikhen, A. A. Lavrent'ev, and S. S. Mikhaĭlova, Available from VINITI, No. 569-81 (Rostov-on-Don, 1981).

22. P. J. Durham, J. B. Pendry, and C. H. Hodges, Comput. Phys. Commun. **25**, 193 (1982).

23. Z. Y. Wu, G. Ouvrard, P. Gressier, and C. R. Natoli, Phys. Rev. B **55** (16), 10382 (1997).

24. J. E. Muller, O. Jepsen, and J. W. Wilkins, Solid State Commun. **42** (5), 365 (1982).

25. R. C. Albers, A. K. McMahan, and J. E. Muller, Phys. Rev. B **31** (6), 3435 (1985).

26. A. L. Ankudinov, B. Ravel, J. J. Rehr, and S. D. Conradson, Phys. Rev. B **58** (12), 7565 (1998).

27. A. L. Ankudinov, J. Synchrotron Radiat. **6** (3), 236 (1999).

Translated by O. Borovik-Romanova

Physics of the Solid State, Vol. 42, No. 11, 2000, pp. 2054–2060. Translated from Fizika Tverdogo Tela, Vol. 42, No. 11, 2000, pp. 1998–2003.

SEMICONDUCTORS AND DIELECTRICS

Electrically Stimulated Movement of Edge Dislocations in Silicon in the Temperature Range 300–450 K

A. A. Skvortsov, A. M. Orlov, V. A. Frolov, and A. A. Solov'ev

Ul'yanovsk State University, ul. L'va Tolstogo 42, Ul'yanovsk, 432700 Russia

e-mail: scvor@sv.uven.ru

Received March 3, 2000; in final form, May 10, 2000

Abstract—The movement of edge dislocations and the related acoustic emission of Si (111) carrying a direct current of density $0.5–5 \times 10^5$ A/m^2 in the [110] direction are studied in the temperature range T = 300–450 K. It is shown that the basic mechanism of dislocation movement is the electric wind determining the magnitude of the effective charge (per atom of the dislocation line) Z_{eff} = 0.06 (*n*-Si) and –0.01 (*p*-Si). Matching theory with experimental data has made it possible to determine the main contribution of edge dislocations to the acoustic-emission response of the silicon samples under investigation. The characteristic transition frequencies of dislocations in *n*- and *p*-Si from one metastable state into another are found to be $f_{\max}$ = 0.1–0.5 Hz. The numerical values of the diffusion coefficient for atoms in the dislocation impurity atmosphere are estimated as 3.2×10^{-18} m^2/s (*n*-Si) and 1.5×10^{-18} m^2/s (*p*-Si). © *2000 MAIK "Nauka/Interperiodica".*

It is well known that dislocations considerably affect the electrophysical properties of semiconductors [1]. Like doping impurities, dislocations in semiconductors play the role of electrically active centers [2] whose motion modifies the electrical properties of crystals. Moreover, they actively interact with dopant atoms, leading to the formation of impurity atmospheres [3, 4]. Such a rearrangement determines the behavior of linear defects in external perturbing electric fields. The experiments with elemental semiconductors at high [1] or room (T_R) temperatures under an additional mechanical loading [1, 5] provide an apt illustration of such an effect. However, the information obtained in this case was obviously insufficient in describing the mechanism of the electroplastic effect in the studied elemental semiconductors. Moreover, there is practically no information on the transport processes occurring at the dislocation core during its electrically stimulated motion at room temperature. For this reason, this work aims at analyzing the electrically stimulated transport of edge dislocations in silicon loaded with an impurity cloud near room temperature.

The experiments were made on dislocation-free *n*- and *p*-type silicon plates of the (111) orientation having a size of $60 \times 12 \times 0.4$ mm with a fixed value of resistivity ρ ranging from 0.05 to 0.005 Ω cm. Edge dislocations were introduced by a three-support bending of the plates in the [111] direction at 1000°C for 30 min [6]. As the sag changed to 800 μm, the dislocation density attained 10^6 cm^{-2} and was fixed for each object.

In our experiments, we first analyzed the dislocation structure of the sample to establish the dominance of the edge component, after which room-temperature electrical annealing of dislocation-containing and dislocation-free samples was carried out, followed by an analysis of the migration of the linear defects.

The effect of dislocation anharmonism on the change in Young's modulus E was detected during the bending of silicon single crystals. Since the anisotropy factor for silicon is ~1.5 [7] and the velocities of propagation of sound in different directions differ insignificantly (by ~2% [8]), we can base our analysis on the nonlinear Hooke law for isotropic bodies:

$$\sigma = E\varepsilon = E_0\varepsilon + \alpha\varepsilon^2 + \beta\varepsilon^3; \quad (1)$$

this law leads to the following expression for the elastic energy per unit volume of the crystal:

$$W = \frac{1}{2}E_0\varepsilon^2 + \frac{1}{3}\alpha\varepsilon^3 + \frac{1}{4}\beta\varepsilon^4. \quad (2)$$

Here and below, α and β are linear combinations of the third- and fourth-order elastic moduli (Pa), respectively; ε is the elastic strain; and E_0 is Young's modulus for the linear Hooke law.

The modulus α in Eq. (2) is the coefficient of an odd power of elastic strain; consequently, the alternating contribution of this term to the elastic energy depends on the sign of ε. For example, in the case of a sag, the "upper" half of the plate experiences compression relative to the neutral layer ($\alpha\varepsilon^3 < 0$), while the "lower" half is subjected to extension ($\alpha\varepsilon^3 > 0$), so that averaging over the cross section gives zero [9]. On the other hand, in a composition with β, any alternating deformation leads to the same variation of W. While calculating the contribution of dislocations to nonlinear moduli, we

must take into account the lattice β_l, dislocation β_d, and the concentration β_c anharmonism:[1]

$$\beta = \beta_l + \beta_d + \beta_c. \quad (3)$$

According to Nikitin [10], in the presence of a dislocation structure, we have

$$\beta_d = \frac{(1 + 3\nu - 7\nu\sin^2\theta)N_d L^4 \Omega^4 E_0^4}{160(1 + \nu - 3\nu\sin^2\theta)^4 b^2 g^3 \mu^3} \quad (4)$$

and $\beta_l \ll \beta_d$. Here, Ω is the orientation factor; N_d and L are the dislocation density and length, respectively; $\nu = 0.27$ is the Poisson ratio for silicon; and θ is the angle between the Burgers vector **b** and the dislocation axis [10]. For an edge dislocation in silicon, the sign of the modulus $\beta \approx \beta_d$ is positive, while for a dominating screw component it is negative. Consequently, by measuring the value of β for a dislocation-containing sample with a low concentration of charge carriers, we are able to further understand the nature of linear defects in semiconductors.

The sign of β was verified experimentally using a compound vibrator technique. Piezoceramic pickups with two metallized faces were glued to the end faces of the plates. The pickup width was made as close to the plate width as possible, while the length of the pickups was 6–8 mm.

Bending of plates along the [111] direction was carried out on a specially designed device with spherical supports of diameter 0.5 mm, which reduced the effect exhibited by the support–crystal contacts on the elastic energy transport. The sag of the plates was measured by a micrometer to within ±2.5 μm. The maximum sag of the crystal at the center of the plate was 800 μm for a span of 55 mm between the supports. The complete destruction of the sample took place for larger strains.

The plate under investigation was connected to the feedback circuit of an rf resonant amplifier. The resonance frequency amplitude was monitored with the help of an S1-83 oscilloscope and an RChZ-07-0002 frequency meter. The strain dependence of the elastic wave velocity in the semiconductor was measured in the frequency range 3–7 MHz. First, the oscillatory circuit was tuned to a resonance frequency, followed by a subsequent 3-min holding of this frequency in the on state. This allowed us to attain thermal equilibrium and to reduce the resonance frequency drift. Then, a frequency meter recording was taken upon the loading and unloading of the crystals. The relative change in frequency associated with a drift in the parameters of the outer medium did not exceed 10^{-5}.

If longitudinal vibrations are excited in a semiconducting silicon plate of length L_{PL} and thickness h_{PL} subjected to three-support bending, the total strain will be the sum of the vibrational ε_k and static ε_0 strains. The parameters of the vibrations will be characterized in this case by Young's modulus [10]:

$$E = E_0\left(1 + \left(\frac{3\beta}{2E_0} - \frac{\alpha^2}{E_0^2}\right)\frac{h_{PL}^2}{6r_{PL}^2}\right). \quad (5)$$

Here, the radius of curvature r_{PL}^2 for a small sag is determined by the second derivative of the plate profile $y(x)$. For the loading procedure with a fixed distance ρ between the supports used, the plate profile can be described by the well-known function [10]

$$y(x) = d\left(-\frac{4x^3}{p^3} + \frac{6x^2}{p^2} - 1\right), \quad (6)$$

where d is the sag.

In order to determine the elastic moduli, we used a measuring circuit, including a feedback oscillator with the resonance condition determined by the resultant phase

$$\varphi = 2\pi f \int_{-0.5L_{PL}}^{0.5L_{PL}} \frac{dx}{v(x)}$$

$$= \frac{2\pi f}{v_0} \int_{-0.5L_{PL}}^{0.5L_{PL}} \frac{dx}{\sqrt{\left(1 + \left(\frac{3\beta}{2E_0} - \frac{\alpha^2}{E_0^2}\right)\frac{h_{PL}^2}{6r_{PL}^2}\right)}} = 2\pi N, \quad (7)$$

$$N = 1, 2, 3\ldots$$

Here, $v = \sqrt{\frac{E}{d_{\mathrm{Si}}}}$ is the velocity of sound in the crystal and d_{Si} is the density of silicon.

The integration of this equation, while taking Eqs. (5) and (6) into account, makes it possible to derive an expression for the relative change in the frequency $\Delta f = f - f_0$ of generation of ultrasonic signals in an oscillatory system with a deformed plate:

$$\frac{\Delta f}{f} \approx \frac{df}{f} = \frac{4h_{PL}^2}{p^3 L_{PL}}(\Delta d)^2\left(\frac{3\beta}{2E_0} - \frac{\alpha^2}{E_0^2}\right). \quad (8)$$

Here, f_0 and d_0 denote the self-oscillation frequency and the sag in the absence of deformation; f and d are the frequency and sag under bending, respectively; and $\Delta d = d - d_0$.

For the sake of simplifying the subsequent analysis, we write expression (8), taking into account Eq. (3), in the form of the corresponding equations

$$\left\{\frac{\Delta f}{(\Delta d)^2}\right\}_s = 4\left(\frac{(h_{PL})^2}{p^3 L_{PL}}\right)_s f_s\left[\frac{3(\beta_p + \beta_c)}{2E_0}\right], \quad (9)$$

[1] The concentration anharmonism is identified with the contribution of the free charge carriers to the nonlinear elastic modulus β.

$$\left\{\frac{\Delta f}{(\Delta d)^2}\right\}_d = 4\left(\frac{(h_{PL})^2}{p^3 L_{PL}}\right)_d f_d\left[\frac{3\beta}{2E_0}\right] \quad (10)$$

for dislocation-free (subscript "*s*") and dislocation-containing ("*d*") silicon which take into account the absence of the term α in the case of sample bending.

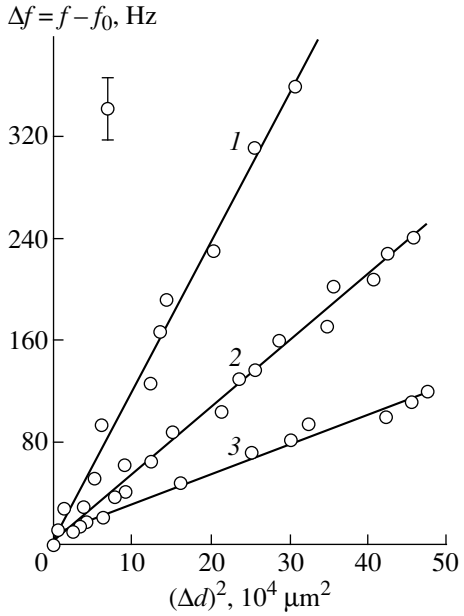

Fig. 1. Effect of the sag *d* on the variation of vibrational frequency of samples with different density of dislocations: (*1*) 8×10^4, (*2*) 7×10^5, and (*3*) 2×10^6 cm^{-2}.

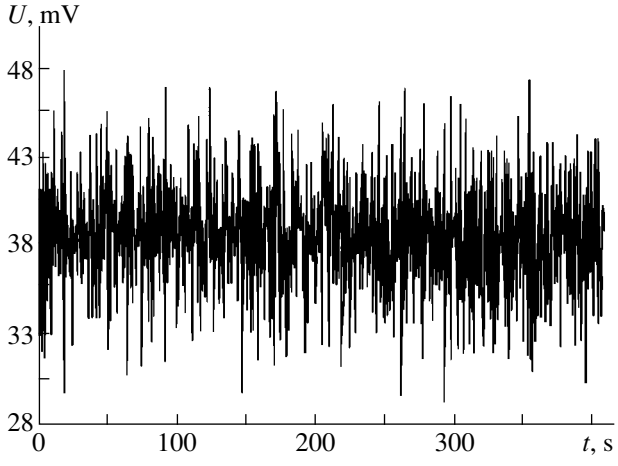

Fig. 2. Oscillogram of the acoustic emission signal $U(t)$ emerging in the course of electrical annealing of silicon (0.005 Ω cm) dislocation-containing plates (4×10^5 cm^{-2} of the *n* type for a current density $j = 2.7 \times 10^5$ A/m^2 and T = 410 K).

It can be easily seen that the right-hand sides of Eqs. (9) and (10) determine the slope of the experimental curves plotted in the Δf vs. $(\Delta d)^2$ coordinates and that their difference gives the value of the dislocation contribution to the modulus being measured:

$$\Delta\beta = \beta - \beta_p - \beta_c = \frac{E_0}{6 f_d}\left(\frac{p^3 L_{PL}}{h_{PL}^2}\right)_d \left(\frac{\Delta f}{\Delta d^2}\right)_d - \frac{E_0}{6 f_s}\left(\frac{p^3 L_{PL}}{h_{PL}^2}\right)_s \left(\frac{\Delta f}{\Delta d^2}\right)_s. \quad (11)$$

It can be seen that the dislocation contribution to the corresponding modulus can be obtained by comparing $\Delta\beta$ for samples with different values of dislocation density N_d. The effects associated with the contribution of free charge carriers to the nonlinear modulus β are excluded in this case.

The results of these investigations are presented in Fig. 1. It can easily be seen that $\beta_d > 0$ for the dislocation structure of *n* silicon, which indicates the edge nature of the dislocations under investigation. A similar situation is also observed for *p* silicon.

Thus, the deformation conditions used for both the donor and acceptor silicon facilitate the emergence of predominantly edge dislocations with an angle $\theta \approx 90°$ between the Burgers vector and the dislocation axis, which follows directly from Eq. (4). Analysis of the mobility of edge defects in an electric field was carried out by acoustic-emission methods [11] and by the selective etching of the semiconductor surface [12]. For this purpose, silicon plates were chemically polished and etching was started, after the annealing process under a load was completed, in order to determine the initial positions of the dislocations.

Exposure to a current without additional mechanical loading ($j = 1–7 \times 10^{-5}$ A/m^2) was carried out for a span of 20–40 h in a thermostat in a special fastening unit. The current contacts were formed by using In–Ga eutectic.

After electrothermal annealing in the temperature range 300–450 K, repeated etching and an analysis of the dislocation pattern were carried out. The separation between dislocation etch pits was measured with the help of an MII-4 microscope under ×450 magnification. In some experiments, the dislocation structure of the sample before and after electrical exposure was photographed and the paths were analyzed by measuring the photographic negatives. The results obtained by using both methods were found to be in good agreement.

Along with controllable etching, the acoustic emission (AE) method was actively used. The AE signals were detected by a piezoelectric transducer mounted on the surface of the plate under investigation [11]. The electric response $U(t)$ from the transducer (Fig. 2) was

fed to a storage oscilloscope S9-8. The information was then fed to a computer in order for the spectral composition of the AE signal $U(\omega)$ to be calculated using the algorithm of fast Fourier transformation based on the Welch periodogram analysis [13]. A typical spectrum of an acoustic-emission response in the course of electrothermal annealing of dislocation-containing silicon is shown in Fig. 3.

The results of analysis proved that the presence of a stable AE response from dislocation-containing samples during electric annealing is associated with the motion of dislocations. This is confirmed by the radical difference in the acoustic emissions of dislocation-free and dislocation-containing silicon plates, as well as by the increase in the AE signal amplitude resulting from an increase in the dislocation density in samples under invariable parameters of electrical exposure [11].

It is well known that the effect of an electric field on dislocations is the result of the combined action [12, 14–16] of forces of ion drag and electron (hole) wind:

$$\begin{aligned}\mathbf{F}_{\text{eff}} &= (eZ_iN_{at} + ep\sigma_{ip}l_pN_{at} - en\sigma_{in}l_nN_{at})\mathbf{E} \\ &= eZ_{\text{eff}}N_{at}\mathbf{E},\end{aligned} \tag{12}$$

where σ_{in} and σ_{ip} are the average electron and hole scattering cross sections per atom on a dislocation line, respectively; N_{at} is the number of atoms on a dislocation line; n, p, l_n, and l_p are the equilibrium concentrations and mean free paths of electrons and holes; e is the elementary charge; and Z_i and Z_{eff} are the Coulomb and effective charges per atom on a dislocation line, respectively. The sign of the effective charge of a dislocation determines the direction of the electron transport forces. The total force determining the motion of a linear defect with a velocity V can be written in the form

$$\begin{aligned}\mathbf{F} &= eZ_{\text{eff}}N_{at}\mathbf{E} - \mathbf{F}_t(V) \\ &= Z_{\text{eff}}N_{at}\mathbf{E} - \frac{\pi c_0\gamma L}{2D_dkT}V\ln\frac{Vr_0}{D_d},\end{aligned} \tag{13}$$

where $\mathbf{F}_t$ is the dislocation drag force depending on the dislocation length L, on the diffusion coefficient D_d of atoms in the dislocation impurity atmosphere, on the equilibrium concentration c_0 of an impurity in a defect-free region of the crystal, and on the dimensional constant γ.

Drag processes are manifested especially clearly in doped semiconductors due to the impurity segregation near the dislocation core and the formation of impurity atmospheres whose characteristic size can be estimated as [5]

$$r_0^{n+2} = n(n+2)\frac{DWb^nt}{kT}, \tag{14}$$

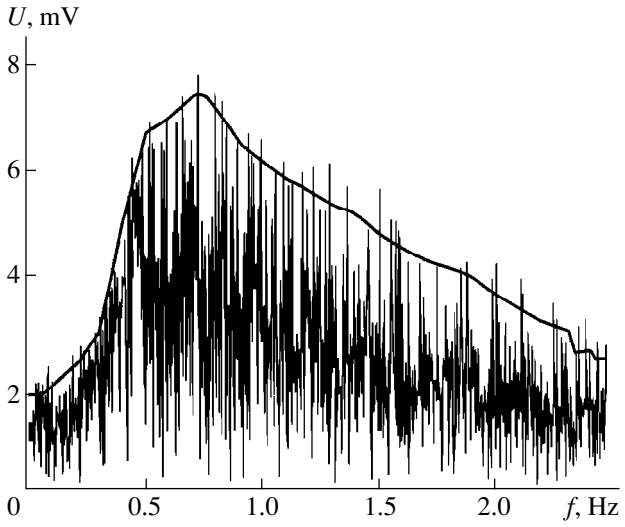

Fig. 3. Spectral density of the acoustic-emission signal after Fourier's transformation of the signal $U(t)$. The principal curve corresponds to the smoothing of the $U(\omega)$ signal.

where D is the bulk diffusion coefficient for impurity atoms, W is the binding energy, kT is the thermal energy, and t is the duration of thermal treatment.

Near room temperature and at low current densities, the probability of detachment of a dislocation from the Cottrell atmosphere can be neglected even when taking thermal activations into consideration. The presumed mechanism of dislocation motion is associated with the transition of a dislocation (or its fragment) to a neighboring metastable state with a diffusion drag of impurity atoms corresponding to its new position. In this case, the dislocation can move only in the form of the "dislocation–impurity cloud" object [17]. The motion of this system is controlled by the diffusion of atoms dissolved in the dislocation core [14, 17].

Thus, in the presence of a constant force $\mathbf{F}$, the thermally activated motion of a "loaded" dislocation can be described by the equation [3, 14]

$$V = V_0\exp\left(-\frac{E_{p2} - Fb}{kT}\right), \tag{15}$$

assuming the form

$$V = V_0\exp\left(-\frac{E_{p2} - eZ_{\text{eff}}N_{at}Eb + F_tb}{kT}\right), \tag{16}$$

where E_{p2} is the Peierls barrier of the second kind.

In analyzing the effects of an electric field on the mobility of linear defects in silicon, it is necessary to take into account the acceptor properties of linear defects in n-Si and the donor–acceptor properties in p-Si [2]. The distance over which the field of a charged dislocation is compensated by the field of ionized

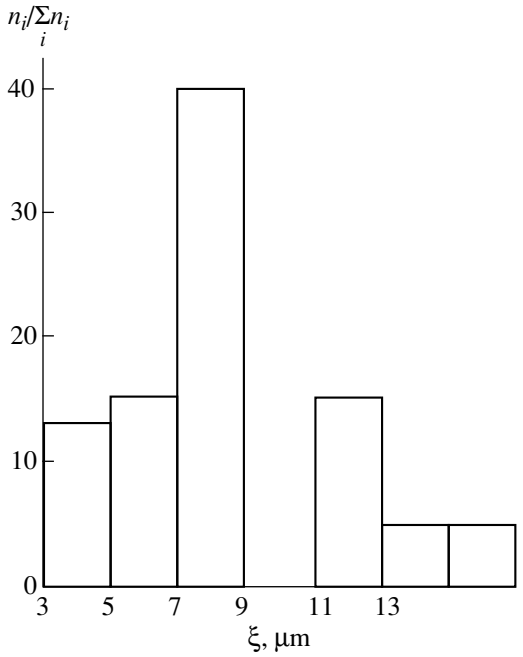

Fig. 4. Distribution of dislocation paths (ξ) in *n* silicon ($N_d = 5 \times 10^{24}$ m^{-3}) during electrical annealing with $j = 0.5 \times 10^5$ A/m^2.

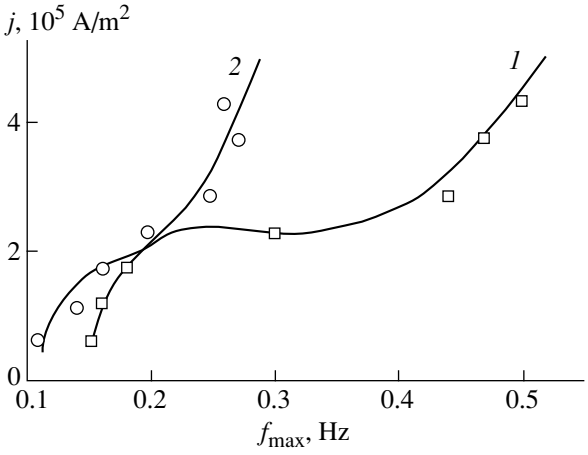

Fig. 5. Current dependence of the maximum of acoustic emission spectrum for silicon. Symbols correspond to experimental results and continuous curves are the results of calculations: (*1*) *n* type ($N_d = 5 \times 10^{24}$ m^{-3}) and (*2*) *p* type ($N_d = 2 \times 10^{24}$ m^{-3}).

donors for silicon is estimated as $R \approx 2$ nm [2]. Consequently, in view of complete screening, the main contribution to the force action on dislocations under current loading comes from the electron or hole wind, which, hence, determines the displacement of the "dislocation–impurity cloud" object in the direction of motion of the majority charge carriers.

Analysis of the paths of linear defects, which was carried out for 80 individual dislocations, indicates that the preferred motion of edge dislocations in *n*-Si is towards the positive electrode. Analysis of dislocation-containing *p*-Si reveals that the velocity of linear defects has the opposite direction; that is, they move towards the negative electrode. The results of these investigations are presented in Fig. 4. An increase in the "current load" accelerates the motion of edge dislocations in Si, which invariably affects the acoustic emission of the samples [11].

Our acoustoemission experiments on the samples under investigation demonstrated a regular displacement of the acoustoemission spectrum towards higher frequencies and an increase in the emission response amplitude (Fig. 5) upon a perturbation of the system by an electric current. The electrically stimulated changes in the average velocity of the directional motion of dislocations and the characteristic frequency of the AE spectrum are well correlated. For example, an increase in j in n silicon (0.05 Ω cm) from 4×10^5 to 6×10^5 A/m^2 leads to an increase in V, as well as in the f_{max}, by a factor of 1.5. Such a correlation makes it possible to connect the peak of the AE signal spectrum with the characteristic frequency of transition of dislocations from one metastable state to another:

$$V = af_{max}, \tag{17}$$

where a is the magnitude of a jump. It can be said, moreover, that the very existence of the acoustoemission response points towards the hopping nature of the dislocation movement [18]. Indeed, using the experimental values of the dislocation velocity $V = 0.5 \times 10^{-10}$ m/s and the characteristic values of $f_{max} = 0.15$ Hz for $j = 0.5 \times 10^5$ A/m^2, we can easily calculate the Peierls period $a \sim 0.3$ nm (which is in accordance with the values for covalent crystals), as well as the dislocation mobility $\mu_d = 1.4 \times 10^{-12}$ m^2/(V s).

Thus, the electric current passing through the samples expels dislocations even at room temperature. In this case, the increase in the current load increases the rate of dislocation-induced transitions and, hence, the drift velocity of dislocations, which is directly reflected in the spectra of acoustic-emission responses. Thus, the recording of emission processes makes it possible to trace *in situ* the dynamics of dislocations in a semiconductor.

Let us analyze the relation between f_{max} and the current density through the sample. For this purpose, we rewrite Eq. (17) by taking into account Eqs. (13) and

Basic electrical transport parameters

Sample	ρ, Ω m	c_0, m^3	Φ_1, m^2/A	Φ_2, s	Φ_3, s	Φ_4, 1/s	Z_{eff}, 1/atom	V_0, m/s	D_d, m^2/s
n-Si	10^{-4}	5×10^{24} phosphorus	3×10^{-7}	7.27×10^{-6}	4.23	1.77	0.06	4.1×10^{-5}	3.2×10^{-18}
p-Si	5×10^{-4}	2×10^{24} boron	3.5×10^{-7}	1.36×10^{-5}	8.34	0.86	−0.01	2.2×10^{-5}	1.5×10^{-18}

(16) and present it first as the relation

$$f_{\max}a = V_0\exp\left(-\frac{E_{p2}}{kT}\right)$$

$$\times\exp\left(\frac{\left(eZ_{\text{eff}}N_{at}\rho j - \frac{\pi c_0\gamma L}{2D_d kT}f_{\max}a\ln\left(\frac{f_{\max}ar_0}{D_d}\right)\right)b}{kT}\right), \quad (18)$$

and, for the convenience of subsequent graphic analysis, we then rewrite it in the form

$$j = \frac{1}{\Phi_1}\left(\frac{E_{p2}}{kT} + \ln(\Phi_2 f_{\max}) + \Phi_3 f_{\max}\left(\ln\frac{f_{\max}}{\Phi_4}\right)\right), \quad (19)$$

where the constants are given by

$$\Phi_1 = \frac{eZ_{\text{eff}}N_{at}b\rho}{kT}; \quad \Phi_2 = \frac{a}{V_0};$$

$$\Phi_3 = \frac{\pi c_0\gamma Lba}{2D_d(kT)^2}; \quad \Phi_4 = \frac{D_d}{ar_0}.$$

It can be seen that an increase in the current load must be accompanied by a displacement of the maximum of the AE spectrum along the frequency axis. Figure 5 illustrates this graphically for donor and acceptor silicon, demonstrating good agreement between the experimental results and Eq. (19) for the obtained values of Φ_i (see table), r_0 = 6 nm, and the Peierls barrier of the second type ($E_{p2} \approx 0.5$ eV) [11]. This makes it possible to determine the effective charge Z_{eff}, the diffusion coefficient D_d, and the preexponential factor V_0 in Eq. (15). The obtained values of the main parameters of electrical transport are presented in the table.

It can be seen that the numerical values of V_0, D_d, and Z_{eff} determined from the acoustic-emission response and from the displacement of dislocation etching pits in perturbing electric fields are reasonable. Exaggerated values of D_d as compared to bulk diffusion [19] may indicate that diffusion is facilitated in the dislocation core region in the presence of an electric field and in the presence of a field of long-range internal stresses in a deformed crystal, but they also indicate a same order of magnitude as that of grain-boundary diffusion for T_R [20]. Unfortunately, we are not aware of any data on the electrically stimulated drift of dislocation–impurity structures that would aid in formulating a comparative analysis.

Thus, we have analyzed the motion of edge dislocations in silicon in the 300- to 450-K temperature range. It has been proven that the dominating mechanism of transport under electrical action is the force of the electron (for *n*-Si) or hole (for *p*-Si) wind determining the sign of the effective charge of an edge dislocation surrounded by an impurity cloud. The obtained results indicate the impossibility of the detachment of a dislocation from an impurity cloud under the current and thermal loads used in our studies, though their motion is limited by the diffusion of atoms to the core in an electric field and in the field of internal stresses of a dislocation. The proposed mechanism of displacement is associated with a transition of a dislocation (or its fragment) to an adjacent metastable state with a diffusion drag of impurity atoms corresponding to its new position.

ACKNOWLEDGMENTS

This research was supported financially by the Ministry of Higher Education under the program "Degradation Processes in Multilayered Thin-Film Structures" and by the Russian Foundation for Basic Research, grant no. 98-02-0335.

REFERENCES

1. T. Suzuki, H. Yosinaga, and S. Takeucti, *Dislocation Dynamics and Plasticity* (Syokabo, Tokyo, 1986; Mir, Moscow, 1989).
2. V. B. Shikin and Yu. V. Shikina, Usp. Fiz. Nauk **165** (8), 887 (1995).
3. J. P. Hirth and J. Lothe, *Theory of Dislocations* (McGraw-Hill, New York, 1967; Atomizdat, Moscow, 1972).
4. N. K. Nechvolod, *Creep of Crystalline Solids under Low Temperatures* (Vishcha Shkola, Kiev, 1980).
5. J. Friedel, *Dislocations* (Pergamon, Oxford, 1964; Mir, Moscow, 1967).
6. V. L. Bonch-Bruevich and S. G. Kalashnikov, *Physics of Semiconductors* (Nauka, Moscow, 1990).
7. C. Kittel, *Introduction to Solid State Physics* (Wiley, New York, 1976; Nauka, Moscow, 1978).
8. *Physical Quantities. Handbook*, Ed. by I. S. Grigor'ev and E. Z. Meĭlikhov (Énergoizdat, Moscow, 1991).
9. L. D. Landau and E. M. Lifshitz, *Course of Theoretical Physics*, Vol. 7: *Theory of Elasticity* (Nauka, Moscow, 1982; Pergamon, New York, 1986).

10. K. E. Nikitin, Fiz. Tverd. Tela (St. Petersburg) **36** (12), 3587 (1994) [Phys. Solid State **36**, 1909 (1994)].
11. A. M. Orlov, A. A. Skvortsov, and V. A. Frolov, Pis'ma Zh. Tekh. Fiz. **25** (3), 28 (1999) [Tech. Phys. Lett. **25**, 95 (1999)].
12. L. B. Zuev, *Physics of Electric Plasticity of Alkali Halide Crystals* (Nauka, Novosibirsk, 1990).
13. S. L. Marple, Jr., *Digital Spectral Analysis with Application* (Prentice-Hall, Englewood Cliffs, 1987; Nauka, Moscow, 1990).
14. V. I. Spitsin and O. A. Troitskiĭ, *Electric Plastic Deformation of Metals* (Nauka, Moscow, 1985).
15. V. B. Fiks, *Ionic Conduction in Metals and Semiconductors (Electron Transfer)* (Nauka, Moscow, 1969).
16. V. Ya. Kravchenko, Zh. Éksp. Teor. Fiz. **51**, 1676 (1966) [Sov. Phys. JETP **24**, 1135 (1966)].
17. M. A. Aliev, Kh. O. Alieva, and V. V. Seleznev, Fiz. Tverd. Tela (Leningrad) **41** (6), 1028 (1999) [Phys. Solid State **41**, 936 (1999)].
18. V. D. Natsik and K. A. Chishko, Fiz. Tverd. Tela (Leningrad) **14** (11), 3126 (1972) [Sov. Phys. Solid State **14**, 2678 (1972)].
19. B. I. Boltaks, *Diffusion in Semiconductors* (Fizmatgiz, Moscow, 1961; Academic, New York, 1963).
20. L. N. Larikov and V. I. Isaĭchev, *Diffusion in Metals and Alloys: A Reference Book* (Naukova Dumka, Kiev, 1987).

Translated by N. Wadhwa

Physics of the Solid State, Vol. 42, No. 11, 2000, pp. 2061–2069. Translated from Fizika Tverdogo Tela, Vol. 42, No. 11, 2000, pp. 2004–2011.

SEMICONDUCTORS AND DIELECTRICS

Spin Echo Generated by Resonance Transitions between Laboratory Coordinate Frame Levels and Quasi-Energy Levels

A. R. Kessel', R. É. Zinatullin, and I. S. Donskaya

Kazan Institute of Engineering Physics, Russian Academy of Sciences, Sibirskiĭ trakt 10, Kazan, 420029 Tatarstan, Russia
e-mail: kessel@dionis.kfti.kcn.ru

Received February 15, 2000; in final form, April 25, 2000

Abstract—The general rules governing the transition to a new representation in which the Hamiltonian of interaction with an alternating field contains constant terms are formulated. Diagonalization of this Hamiltonian leads to the formation of quasi-stationary energy levels. The possibility of the existence of a temperature at the quasi-energy levels is considered separately. A three-level spin system is used as an example to show that another specially selected alternating magnetic field can excite resonance transitions between the energy levels in the laboratory coordinate frame and the energy levels in the new representation. Expressions for free-precession and spin echo signals, which carry information concerning quasi-stationary energy levels, are derived.

INTRODUCTION

An interesting fact was observed by Redfield [1]: if the alternating field is so strong that interaction with it considerably exceeds the interaction with the sources of energy level broadening, a new effect called spin quantization is observed in the alternating field. This quantization is responsible for the emergence of spin quasi-stationary energy levels.

Formally, a static field $H_{\text{eff}} = \sqrt{H_1^2 + (H_0 - \omega/\gamma)^2}$ (H_0 is a constant magnetic field and H_1 is the amplitude of an alternating magnetic field perpendicular to H_0 and rotating with a frequency ω in the direction of precession) in a rotating coordinate frame (RCF) can be put in correspondence with Zeeman's quasi-stationary energy levels separated by an interval $\hbar\omega_{\text{eff}} = \hbar\gamma H_{\text{eff}}$ [1, 2].

It was shown experimentally [1] that quasi-energy levels indeed exist in the sense that magnetic resonance can be observed on them with the help of an appropriately chosen second alternating current. Spin levels in the RCF were also recognized thermodynamically; spin temperature and canonical distribution were introduced for them [1]. Adiabatic demagnetization [3, 4] and spin–spin and spin–lattice relaxation [5] were studied both theoretically and experimentally in the RCF. The existence of spin quantization in the field of a high-intensity acoustic wave and the trapping of nondiagonal components of the nuclear quadrupole electrical moment associated with it were studied in [6]. It is interesting to note that the quasi-energy spectrum of the nuclei in the case of quantization in an acoustic field is identical to the nuclear quadrupole resonance (NQR) spectrum, whereas in the laboratory coordinate frame (LCF), the nuclei possess a Zeeman spectrum. Spin quantization in a strong alternating magnetic field was also studied in detail for the case when the spin system in the LCF possesses the NQR spectrum [7–11].

In the case of a nonequidistant spectrum, the transition to the RCF is replaced by a transition to a new representation in which the Hamiltonian of interaction with the alternating field contains terms that do not depend explicitly on time. Transition to the new representation is expedient only over a certain part of the LCF Hamiltonian, after which the possibility of exciting spin transitions between quasi-energy levels, as well as between the LCF and quasi-energy levels, becomes quite obvious.

In this work, we study the transient processes in a nonequidistant three-level twofold degenerate spin system (the spins $I = 5/2$ are placed in an electric field of axial symmetry) in which two energy levels are transferred to the quasi-stationary state by exciting an individual resonance transition and the third level pertains to the LCF. The investigated transient processes emerge as a result of pulsed excitation of resonance transitions between quasi-stationary and LCF levels.

1. SPECTRUM OF A SPIN SYSTEM IN THE ALTERNATING-FIELD REPRESENTATION

In order to study the effect of resonance transitions between LCF and quasi-energy levels on the spin system, one should consider a spin system with three or more nonequidistant energy levels. An alternating stationary resonance field is used to create quasi-energy levels on two of these levels, while the remaining levels

1063-7834/00/4211-2061$20.00

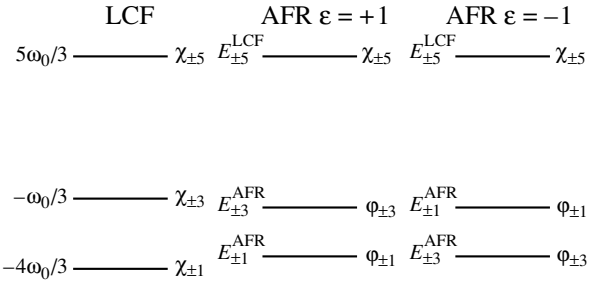

Fig. 1. Energy spectrum and wave functions in the LCF and AFR.

are barely perturbed by this field. The transient processes are triggered by radiofrequency (rf) pulses which serve as resonance pulses for an LCF level and a quasi-energy level.

Let us consider the NQR spectrum of nuclei with spin $I \geq 5/2$. Three twofold degenerate NQR energy levels with spin I = 5/2 possess the required nonequidistant spectrum (the complications caused by twofold degeneracy are not manifested in the dynamics).

In the case of a nonequidistant spectrum, it is convenient to use the projection operators $\hat{P}_{mn}$ that have matrix elements $\langle \chi_{m'}|\hat{P}_{mn}|\chi_{n'}\rangle = \delta_{mm'}\delta_{nn'}$ in the $\hat{I}_z$ representation, thus having the multiplication rule $\hat{P}_{mn}\hat{P}_{kl} = \delta_{nk}\hat{P}_{ml}$ take place for them. In terms of these projection operators, the NQR Hamiltonian for spin $I = 5/2$ has the following form in an axially symmetric electric crystal field:

$$\hat{H}_0 = \frac{\hbar\omega_0}{3}[5(\hat{P}_{5,5} + \hat{P}_{-5,-5}) - (\hat{P}_{3,3} - \hat{P}_{-3,-3}) - 4(\hat{P}_{1,1} + \hat{P}_{-1,-1})], \quad (1)$$

$$\omega_0 = \frac{6e^2Qq}{4I(2I-1)},$$

where eq is the electric field gradient at the nucleus, ω_0 is the resonance frequency of the lower transition, and eQ is the nuclear quadrupole electrical moment. The NQR energy levels and the corresponding wave functions χ_m are shown in Fig. 1.

Interaction with the alternating fields has the form

$$\hat{H}_a^t = -\gamma\mathbf{H}_a(t)\hat{\mathbf{I}} = \hbar\sum_m f_m(\hat{P}_{m+1,m} + \hat{P}_{m,m+1})\cos(\omega_a t + \theta_a), \quad (2)$$

$$\hat{H}_b^t = -\gamma\mathbf{H}_b(t)\hat{\mathbf{I}} = i\hbar\sum_m g_m(\hat{P}_{m+1,m} + \hat{P}_{m,m+1})\cos(\omega_b t + \theta_b), \quad (3)$$

$$\theta_a = \varphi_a - \omega_a t_{0a}, \quad \theta_b = \varphi_b - \omega_b t_{0b},$$

where $f_m = \gamma H_a\langle \chi_m|\hat{I}_x|\chi_{m+1}\rangle$; $g_m = \gamma H_b\langle \chi_m|\hat{I}_x|\chi_{m+1}\rangle$; t_{0a} and t_{0b} are the instants of time corresponding to the application of alternating fields $\mathbf{H}_a(t)$ and $\mathbf{H}_b(t)$, respectively; and H_a, H_b and φ_a, φ_b are their amplitudes and initial phases, respectively. The magnetic fields $\mathbf{H}_a(t)$ and $\mathbf{H}_b(t)$ are directed along x and y axes in the LCF. Their frequencies are close to the resonance frequencies $\omega_a \approx \omega_0$ and $\omega_b \approx 2\omega_0$ of the Hamiltonian (1).

The alternating magnetic field $\mathbf{H}_a(t)$ is used in the formation of quasi-stationary energy levels, and the field $\mathbf{H}_b(t)$ is applied for studying these levels by exciting resonance transitions between them.

In order to find the quasi-energy levels associated with the amplitude of the alternating field $\mathbf{H}_a(t)$, we must go over to the new representation in such a way that (I) the unitary operator $\exp\left(\frac{i\hat{H}_1 t}{\hbar}\right)$ of transformation to the new representation commutes with the Hamiltonian $\hat{H}_0$, (II) the Hamiltonian $\hat{H}_a^t(t)$ contains terms that do not depend explicitly on time, and (III) the "center of gravity" of the operator is preserved; i.e., the condition $\mathrm{Tr}(\hat{H}_1) = 0$ is satisfied.

In the general case, condition (I) is satisfied by the operator $\hat{H}_1 = \sum_m a_m\hat{P}_{mm}$, whose coefficients are subjected to the constraint $a_{\pm3} - a_{\pm1} = \hbar\omega_a$ owing to condition (II), while condition (III) leads to the relation $\sum_m a_m = 0$. These equalities do not completely define the coefficients a_m.

The following requirements can be additionally introduced from the physical considerations: (IV) The energy levels of Hamiltonian (1) are twofold degenerate and the alternating field excites transitions of identical intensities between the states $\chi_m \leftrightarrow \chi_{m+1}$ and $\chi_{-m} \leftrightarrow \chi_{-(m+1)}$; hence the twofold degeneracy of spin levels can be naturally preserved in the new representation by putting $a_m = a_{-m}$. (V) The alternating field $\mathbf{H}_a(t)$ induces resonance transitions between the states $\chi_{\pm1} \leftrightarrow \chi_{\pm3}$ at the resonance frequency $\omega_a \approx \omega_0$ and leaves the states $\chi_{\pm5}$ unperturbed; hence, it is natural to impose the requirement that a transition to the new representation associated with $\mathbf{H}_a(t)$ must not affect $\chi_{\pm5}$, i.e., that the equalities $a_{\pm5} = 0$ must be satisfied.

Taking into account requirements (IV) and (V), the operator $\hat{H}_1$ can be defined accurately, except for the sign. From the physical considerations we choose the positive sign

$$\hat{H}_1 = \frac{\hbar\omega_a}{2}(\hat{P}_{3,3} + \hat{P}_{-3,-3} - \hat{P}_{1,1} - \hat{P}_{-1,-1}). \quad (4)$$

For any operator $\hat{A}$, the transition to the generalized interaction representation (GIR) is accomplished with the help of the relation

$$\hat{A}(t) = \exp\left(i\frac{\hat{H}_1}{\hbar}t\right)\hat{a}\exp\left(-i\frac{\hat{H}_1}{\hbar}t\right). \quad (5)$$

Let us pass to the operator $\hat{H}_1$ in the GIR, in which the spin Hamiltonian is defined as

$$\hat{H} = \hat{H}_2 + \hat{H}_a^t(t) + \hat{H}_b^t(T), \quad (6)$$

where

$$\hat{H}_2 = \hat{H}_0 - \hat{H}_1 = \frac{5\hbar\omega_0}{3}\hat{P}_{\pm5,\pm5} - \left(\frac{\hbar\omega_0}{3} + \frac{\hbar\omega_a}{2}\right)\hat{P}_{\pm3,\pm3} - \left(\frac{4\hbar\omega_0}{3} - \frac{\hbar\omega_a}{2}\right)\hat{P}_{\pm1,\pm1}. \quad (7)$$

The interaction Hamiltonian of spin with an alternating magnetic field $H_a(t)$ can be written in the GIR in the form

$$\hat{H}_a^t(t) = \hat{H}_a^{\text{const}}(t) + \hat{H}_a^{2t}(t), \quad (8)$$

where

$$\hat{H}_a^{\text{const}}(t) = \frac{\hbar f_1}{2}[\hat{P}_{3,1}\exp(-i\theta_a) + \hat{P}_{1,3}\exp(i\theta_a)], \quad (9)$$

$$\hat{H}_a^{2t}(t) = \frac{\hbar f_1}{2} \times (\hat{P}_{3,1}\exp[i(2\omega_a t + \theta_a)] + \hat{P}_{1,3}\exp[-i(2\omega_a t + \theta_a)]) + \hbar f_3\left[\hat{P}_{5,3}\exp\left(-i\frac{\omega_a}{2}t\right) + \hat{P}_{3,5}\exp\left(i\frac{\omega_a}{2}t\right)\right]\cos(\omega_a t + \theta_a). \quad (10)$$

It seems natural that the spin spectrum in the GIR should be determined by the Hamiltonian $\hat{H}_2$, i.e., the part left after the transition to the GIR of the Hamiltonian $\hat{H}_0$ which defines the energy spectrum in the LCF (Fig. 1). However, we assume that the spin spectrum in the GIR is determined by all time-independent terms in Hamiltonian (6):

$$\hat{H}_3 = \hat{H}_0 - \hat{H}_1 + \hat{H}_a^{\text{const}}(t) \equiv \hat{H}_2 + \hat{H}_a^{\text{const}}(t). \quad (11)$$

This assumption is a continuation of Redfield's ideas on quantization in the RCF along an alternating field amplitude. As a result, the Hamiltonian $\hat{H}_3$ in the GIR assumes the form

$$\hat{H}_3 = \frac{5\hbar\omega_0}{3}\hat{P}_{5,5} - \left(\frac{\hbar\omega_0}{3} + \frac{\hbar\omega_a}{2}\right)\hat{P}_{3,3} - \left(\frac{4\hbar\omega_0}{3} - \frac{\hbar\omega_a}{2}\right)\hat{P}_{1,1} + \frac{\hbar f_1}{2}[\hat{P}_{3,1}\exp(-i\theta_a) + \hat{P}_{1,3}\exp(i\theta_a)]. \quad (12)$$

The representation in which the Hamiltonian $\hat{H}_3$ containing effective interaction with the alternating field $\mathbf{H}_a(t)$ is diagonal will be called the alternating-field representation (AFR).

The generalized quasi-stationary levels, or the energy levels in the AFR, are defined as follows:

$$E_5^{\text{AFR}} = \frac{5\hbar\omega_0}{3}, \quad E_3^{\text{AFR}} = -\frac{5\hbar\omega_0 - 3\varepsilon\hbar\kappa}{6}, \quad E_1^{\text{AFR}} = -\frac{5\hbar\omega_0 + 3\varepsilon\hbar\kappa}{6}, \quad (13)$$

where we have used the notation

$$\Delta = |\omega_a - \omega_0|, \quad \varepsilon = \text{sgn}(\omega_a - \omega_0),$$
$$\kappa = \sqrt{\Delta^2 + f_1^2}, \quad \omega_a = \omega_0 - \varepsilon\Delta.$$

The eigenfunctions corresponding to these levels are

$$\varphi_5 = \chi_5, \quad \varphi_3 = \chi_3\cos\lambda + \varepsilon\chi_1\exp(i\theta_a)\sin\lambda, \quad \varphi_1 = \chi_1\cos\lambda - \varepsilon\chi_3\exp(-i\theta_a)\sin\lambda, \quad (14)$$

in which the parameter λ is defined by the condition $\tan 2\lambda = \frac{f_1}{\Delta}$.

Let us now introduce, for the sake of convenience, the projection operators $\hat{R}_{mn}$ in the basis of the wave functions φ_m:

$$\langle\varphi_{m'}|\hat{R}_{mn}|\varphi_{n'}\rangle = \delta_{mm'}\delta_{nn'}.$$

The operators $\hat{R}_{mn}$ and $\hat{P}_{mn}$ are connected through simple linear relations which can be used to obtain the following expression for the operator $\hat{H}_3$ in the AFR wherein it is diagonal:

$$\hat{H}_3 = \sum_m E_m^{\text{AFR}}\hat{R}_{mm}. \quad (15)$$

The resonance frequencies in the AFR are defined as (see Fig. 1)

$$\Omega_{5,3} = \frac{5\omega_0 - \varepsilon\kappa}{2}, \quad \Omega_{5,1} = \frac{5\omega_0 + \varepsilon\kappa}{2}, \quad \Omega_{3,1} = \varepsilon\kappa. \quad (16)$$

The operator $\hat{H}_3$ in the AFR plays the role of the Hamiltonian $\hat{H}_0$ in the LCF.

In conformity with constraint (V) imposed on the operator $\hat{H}_1$, we obtain

$$E_5^{\mathrm{AFR}} = E_5^{\mathrm{LCF}} \equiv \frac{5\hbar\omega_0}{3}, \quad \varphi_5 = \chi_5. \tag{17}$$

This fact leads to the assumption that, upon the transition to the AFR, this energy level remains an energy level in the LCF, while the energy levels E_3^{AFR} and E_1^{AFR} are the AFR energy levels.

Let us write down the resonance terms of the Hamiltonian $\hat{H}_b^t(t)$ corresponding to transitions between the LCF levels and the quasi-energy levels at frequencies $\Omega_{5,3}$ and $\Omega_{5,1}$:

$$\begin{aligned}\hat{H}_b^{res}(t) = \frac{i\hbar g_3}{2}\Big[&\exp\Big(-i\Big[\Big(\omega_b + \frac{\omega_a}{2}\Big)t + \theta_b\Big]\Big)\\ &\times(\hat{R}_{5,3}\cos\lambda - \varepsilon\hat{R}_{5,1}\exp(-i\theta_a)\sin\lambda)\\ &-\exp\Big(i\Big[\Big(\omega_b + \frac{\omega_a}{2}\Big)t + \theta_b\Big]\Big)\\ &\times(\hat{R}_{3,5}\cos\lambda - \varepsilon\hat{R}_{1,5}\exp(i\theta_a)\sin\lambda)\Big].\end{aligned} \tag{18}$$

Interaction with any other field whose amplitude is smaller than the energy E_m^{AFR} can also be presented in terms of the projection operators $\hat{R}_{mn}$ in the resonance approximation.

2. DESCRIPTION OF TRANSIENT PROCESSES IN THE AFR

The results of the action of an electromagnetic pulse at the frequency ω_b depend to a considerable extent on the occupancy N_m^{AFR} of the quasi-energy levels in the AFR. If we measure time from the instant of application of the rf field $\mathbf{H}_a(t)$, the electromagnetic field $\mathbf{H}_b(t)$ starts acting from the instant of time $\tau_1 \geq 0$. Figure 2 shows the general diagram for the application of the rf field $\mathbf{H}_a(t)$ and the field pulses $\mathbf{H}_b(t)$. There, τ_2 is the time interval between the instants of application of the first and second pulses of the field $\mathbf{H}_b(t)$, and t_1 and t_2 are their respective durations. Depending on the initial form of the density matrix, two interesting limiting cases are observed:

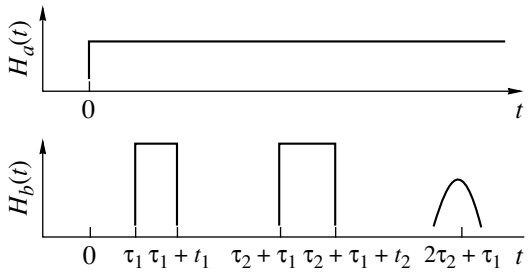

Fig. 2. Schematic diagram showing the application of an rf field $H_a(t)$ and field pulse $H_b(t)$ (the expected instant of emergence of the spin-echo signal is also indicated).

(1) The interval after which the transient processes start is much shorter than the spin–lattice relaxation time $\tau_1 \ll T_2$. In this case, the initial value of the density matrix corresponds to the thermodynamic equilibrium at the LCF levels:

$$\hat{\rho}^{(0)} = \hat{\rho}(t=0) = \sum_m \frac{1}{6}\Big(1 - \frac{E_m}{kT}\Big)\hat{P}_{mm}. \tag{19}$$

In contrast, in the AFR, the density matrix in Eq. (19) has the form

$$\begin{aligned}\hat{\rho}^0 = &\frac{1}{6}\Big(1 - \frac{E_5}{kT}\Big)\hat{R}_{5,5}\\ &+\frac{1}{6}\Big[\Big(1 - \frac{E_3}{kT}\Big)\cos^2\lambda + \Big(1 - \frac{E_1}{kT}\Big)\sin^2\lambda\Big]\hat{R}_{3,3}\\ &+\frac{1}{6}\Big[\Big(1 - \frac{E_3}{kT}\Big)\sin^2\lambda + \Big(1 - \frac{E_1}{kT}\Big)\cos^2\lambda\Big]\hat{R}_{1,1}\\ &+\frac{E_3 - E_1}{6kT}\varepsilon\frac{\sin 2\lambda}{2}[\exp(-i\varphi_a)\hat{R}_{3,1} + \exp(i\varphi_a)\hat{R}_{1,3}].\end{aligned} \tag{20}$$

(2) By the beginning of the transient processes in the spin system, thermodynamic equilibrium is already established on the quasi-energy levels in the AFR ($\tau_1 \gg T_2$). In this case, the initial density matrix for transient processes is defined by the relation

$$\hat{\rho}^0 = \frac{1}{6}\sum_m\Big(1 - \frac{E_m^{\mathrm{AFR}}}{kT_{\mathrm{AFR}}}\Big)\hat{R}_{mm} \tag{21}$$

with a certain temperature T_{AFR}, which is generally different from the lattice temperature.

In this section, main attention will be paid to the first case. We shall solve the problem of spin dynamics in the AFR, which coincides in general with the problem of computing the spin echo in the LCF, but this shall be done using Hamiltonian (15), the initial density matrix in Eq. (20), and the interaction with the "external" alternating resonance field in the form of Eq. (18).

Passing again to the interaction representation with respect to the Hamiltonian $\hat{H}_3$, we can write

$$\hat{\rho}' = \exp\Big(i\frac{\hat{H}_3}{\hbar}t\Big)\hat{\rho}\exp\Big(-i\frac{\hat{H}_3}{\hbar}t\Big),$$

$$\hat{H}_b^{res'}(t) = \exp\left(i\frac{\hat{H}_3}{\hbar}t\right)\hat{H}_b^{res}(t)\exp\left(-i\frac{\hat{H}_3}{\hbar}t\right).$$

The change in the density matrix induced by Hamiltonian (18) is defined by von Neumann's equation

$$i\hbar\frac{\partial}{\partial t}\langle m|\hat{\rho}'|n\rangle$$

$$= \sum_r [\langle r|\hat{\rho}'|n\rangle\langle m|\hat{H}_b^{res}(t)|r\rangle\exp(i\Omega_{mr}t)$$

$$-\langle m|\hat{\rho}'|r\rangle\langle r|\hat{H}_b^{res}(t)|n\rangle\exp(i\Omega_{rn}t)\,].$$

Here and below, the matrix elements involve the wave functions φ_m. This leads to a complete system of equations of motion for the density matrix elements.

This system of equations has a general solution in the resonance approximation ($g_3 \ll \kappa, 2\omega_0$) for the cases when the exciting pulses cover both transitions $E_5^{AFR} \longleftrightarrow E_3^{AFR}$ and $E_5^{AFR} \longleftrightarrow E_1^{AFR}$ (which is true for $\kappa t_i \ll 1$, where t_i is the duration of the ith pulse) or when only one transition is covered ($\kappa t_i \gg 1$). For example, if only one level E_3^{AFR} is covered under resonance conditions at the frequency

$$\omega_b = \omega_b^+ \equiv 2\omega_0 + \frac{\varepsilon}{2}(\Delta + \kappa), \qquad (22)$$

the solutions for the matrix elements at the end of the first pulse for $t = \tau_1 + t_1$ and up to the onset of the second excitation pulse at $t = \tau_2 + \tau_1$ are given by

$$\rho'_{5,5}(t) = -\frac{\hbar\omega_0}{6kT}\frac{1}{2}(2+\cos^2\lambda)\cos 2\alpha_1 + \frac{1}{2}(\rho^0_{5,5}+\rho^0_{3,3}),$$

$$\rho'_{3,3}(t) = \rho^0_{3,3},$$

$$\rho'_{1,1}(t) = \frac{\hbar\omega_0}{6kT}\frac{1}{2}(2+\cos^2\lambda)\cos 2\alpha_1 + \frac{1}{2}(\rho^0_{5,5}+\rho^0_{3,3}),$$

$$\rho'_{5,3}(t) = \rho'^*_{3,5}(t)$$

$$= -\frac{\hbar\omega_0}{6kT}\frac{\sin 2\lambda}{2}\sin 2\alpha_1\exp[i(\omega_b^+\tau_1-\varphi_b)],$$

$$\rho'_{5,1}(t) = \rho'^*_{1,5}(t) = -\frac{\hbar\omega_0}{6kT}\frac{\varepsilon}{2}(2+\cos^2\lambda)\sin 2\alpha_1 \qquad (23)$$

$$\times\exp[i(\omega_b^+\tau_1-\varphi_b-\varphi_a)],$$

$$\rho'_{3,1}(t) = \rho'^*_{1,3}(t)$$

$$= \frac{\hbar\omega_0}{6kT}\varepsilon\frac{\sin 2\lambda}{2}\cos\alpha_1\exp[-i\varphi_a],$$

$$\alpha_1 = \frac{\sin\lambda}{2}g_3t_1.$$

Following the action of the second pulse ($t \geq \tau_2 + \tau_1 + t_2$), the density matrix elements are defined as

$$\rho'_{5,3}(t) = \rho'^*_{3,5}(t) = -\frac{\hbar\omega_0}{6kT}\frac{\sin 2\lambda}{2}\exp[-i\varphi_b]$$

$$\times(\sin\alpha_1\cos\alpha_2\exp[i\omega_b^+\tau_1]$$

$$+\cos\alpha_1\sin\alpha_2\exp[i(\omega_b^+[\tau_2+\tau_1]-\varphi_b)]),$$

$$\rho'_{5,1}(t) = \rho'^*_{1,5}(t) = -\frac{\hbar\omega_0}{6kT}\frac{\varepsilon}{2}(2+\cos^2\lambda)$$

$$\times\exp[-i(\varphi_b+\varphi_a)](\sin 2\alpha_1\cos^2\alpha_2\exp[i\omega_b^+\tau_1]$$

$$+\cos 2\alpha_1\sin 2\alpha_2\exp[i\omega_b^+(\tau_2+\tau_1)]$$

$$-\sin 2\alpha_1\sin^2\alpha_2\exp[i\omega_b^+(2\tau_2+\tau_1)]),$$

$$\rho'_{3,1}(t) = \rho'^*_{1,3}(t) = \frac{\hbar\omega_0}{6kT}\varepsilon\frac{\sin 2\lambda}{2}\exp(-i\varphi_a) \qquad (24)$$

$$\times(\cos\alpha_1\cos\alpha_2-\sin\alpha_1\sin\alpha_2\exp[i\omega_b^+\tau_2]),$$

$$\rho'_{5,5}(t) = \frac{\hbar\omega_0}{6kT}\frac{1}{2}(2\cos^2\lambda)[\sin 2\alpha_1\sin 2\alpha_2\cos(\omega_b^+\tau_2)$$

$$-\cos 2\alpha_1\cos 2\alpha_2] + \frac{1}{2}(\rho^0_{5,5}+\rho^0_{1,1}),$$

$$\rho'_{1,1}(t) = -\rho'_{5,5}(t) + \rho^0_{5,5} + \rho^0_{1,1},$$

$$\rho'_{3,3}(t) = \rho^0_{3,3}, \quad \alpha_2 = \frac{\sin\lambda}{2}g_3t_2.$$

Similar results are obtained in the case of excitation at the other frequency investigated,

$$\omega_b = \omega_b^- \equiv 2\omega_0 + \frac{\varepsilon}{2}(\Delta - \kappa), \qquad (25)$$

as well as in the case when transitions at both resonance frequencies ω_b^+ and ω_b^- are excited to the same extent.

3. RESPONSE OF THE SPIN SYSTEM TO A SINGLE PULSE AND TO TWO PULSES

In order to cover all spins contributing to the nonuniform broadening of a resonance line, the alternating field pulses used for exciting the transition should be so short that the condition $t_i\sigma < 1$ is satisfied, where σ is the width of the inhomogeneously broadened steady-state resonance line. Hence, the wavepacket of the pulse covers nearly all nuclear spins (in the case of its tuning at the center of the resonance line). In this case, each spin is under the exact conditions for resonance at the natural frequency

$$\omega_0 = \omega_Q + \delta, \qquad (26)$$

where ω_Q is the mean resonance frequency and δ is a random deviation from ω_Q caused by the imperfection of the crystal field in the vicinity of the given spin.

The frequency of the alternating field $\mathbf{H}_a(t)$ has not been specified thus far. We shall now consider the case when the broadening field is tuned at the center of the resonance line:

$$\omega_a = \omega_Q. \tag{27}$$

In this case, $\Delta = |\delta|$ and $\varepsilon = \mathrm{sgn}(\delta)$.

Let us calculate the y component of magnetization of the sample, which defines the signals of free precession and spin echo:

$$\begin{aligned} M_y(t) &= \sum_k M_k^y(t) \\ &= \gamma\hbar\sum_k \langle \hat{I}_k^y(t)\rangle = \gamma\hbar\sum_k \mathrm{Tr}(\hat{\rho}_k(t)\hat{I}_k^y), \end{aligned} \tag{28}$$

where the operators $\hat{\rho}_k(t)$ and $\hat{I}_k^y$ must be taken in the same representation, the simplest one being the interaction representation with respect to $\hat{H}_3$.

We introduce the notation $M_\omega^y(\omega_1, \omega_2, \ldots)$ for the part of $M_y(t)$ oscillating at the frequency ω after the exposure of the spin system to pulses of the alternating field containing the frequencies $\omega_1, \omega_2, \ldots$ It follows from formulas (23) and (24) (as well as from the analogous relations for the case when we have $\omega_b = \omega_b^-$ and the ω_b pulse covers both frequencies $\omega_b^\pm$) that the quantity $M_y(t)$ can be presented as the sum of two terms:

$$M_y(t) = M_{2\omega_Q}^y(\omega_1, \omega_2, \ldots) + M_{\omega_Q}^y(\omega_1, \omega_2, \ldots), \tag{29}$$

oscillating at the natural NQR frequencies $2\omega_Q$ and ω_Q.

One part of the y component, $M_{\omega_Q}^y(\omega_1, \omega_2, \ldots)$, oscillates at the frequency ω_Q at which the strong alternating field $\mathbf{H}_a(t)$ acts. Hence, it is quite difficult to register transient processes at this frequency of NQR. On account of the nonlinear effects in the apparatus, the broadening field overlaps the signal and distorts it. Hence, we confine the calculations to the part $M_{2\omega_Q}^y(\omega_1, \omega_2, \ldots)$.

Substituting expressions (23) for the density matrix after the action of one exciting pulse in formula (28), we arrive at the following values for the y component of the magnetization in the LCF:

$$\begin{aligned} M_{2\omega_Q}^y(\omega) &= \frac{\sqrt{5}N\gamma\hbar^2\omega_Q}{6kT} \\ &\times \sin[2\omega_Q(t-\tau_1) + \varphi_b]\overline{W(\omega)}. \end{aligned} \tag{30}$$

The bar over the envelope $W(\omega)$ of the free precession signal indicates its averaging over the difference δ between resonance frequencies. We shall assume that the distribution of the difference δ is described by the normal distribution law

$$\begin{aligned} \overline{W(\omega)} &= \frac{1}{N}\sum_{k=1}^{n} W(\omega_k) \\ &= \frac{1}{\sqrt{2\pi}\sigma}\int_{-\infty}^{+\infty} \exp\left(-\frac{\delta^2}{2\delta^2}\right) W(\omega, \delta)\,d\delta. \end{aligned} \tag{31}$$

The general expressions for $W(\omega, \delta)$ are cumbersome and will not be presented here.

In the absence of the broadening field ($f_1 = 0$), signals at the frequency ω_Q vanish since, in this case, $\rho_{3,1}(t) = \rho_{1,3}(t) = 0$ in the LCF and expression (30), for which

$$W(\omega_b^+) = 0,$$

$$W(\omega_b^-) = W(\omega_b^+, \omega_b^-) = \sin(2\xi_1)\cos[2\delta(t-\tau_1)],$$

$$(\xi_1 = g_3 t_1/2),$$

is transformed into an expression for a conventional signal describing free precession at the frequency $2\omega_Q$, which emerges after the passage of one pulse.

In the opposite limiting case of large f_1 $\left(\lambda = \frac{\pi}{4}, \kappa = f_1\right)$, we can write

$$\begin{aligned} \overline{W(\omega_b^\pm)} &= \frac{5\sqrt{2}}{8}\sin(\sqrt{2}\xi_1)K^\pm\left(x - x_1, b, \frac{x-x_1}{5}\right) \\ &- \frac{\sqrt{2}}{4}\sin\left(\frac{\xi_1}{\sqrt{2}}\right)K^\mp\left(x - x_1, b, \frac{x+x_1}{5}\right), \\ \overline{W(\omega_b^+, \omega_b^-)} &= \frac{5}{8}\sin 2\xi_1 K\left(x - x_1, b, \frac{x-x_1}{5}\right) \\ &+ \frac{1}{4}\sin^2\left(\frac{\xi_1}{2}\right)\sin\xi_1 K\left(x - x_1, b, \frac{x-3x_1}{5}\right) \\ &- \frac{1}{4}\cos^2\left(\frac{\xi_1}{2}\right)\sin\xi_1 K\left(x - x_1, b, \frac{x+x_1}{5}\right), \\ K &= K^+ + K^-, \end{aligned} \tag{32}$$

where

$$K^\pm(x, b, z) = \frac{1}{\sqrt{2\pi}}\int_0^{+\infty} \exp\left(-\frac{y^2}{2}\right)\cos(xy \pm zb)\,dy$$

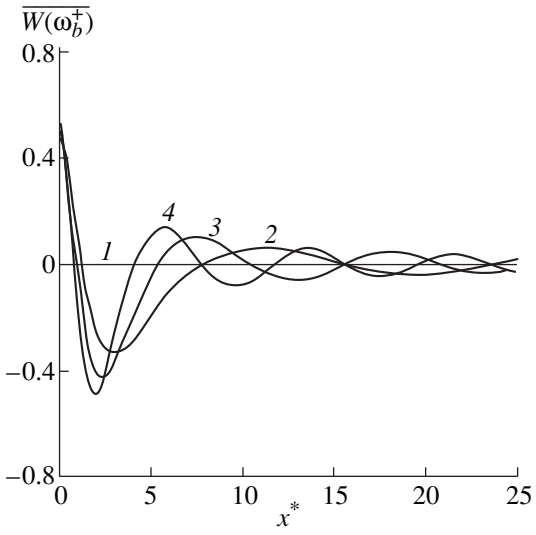

Fig. 3. Envelope of the free precession signal for the exciting frequency ω_b^+ for b = (*1*) 0, (*2*) 2, (*3*) 3, and (*4*) 4; $X^* = X - X_1$, $X_1 = 5\pi$.

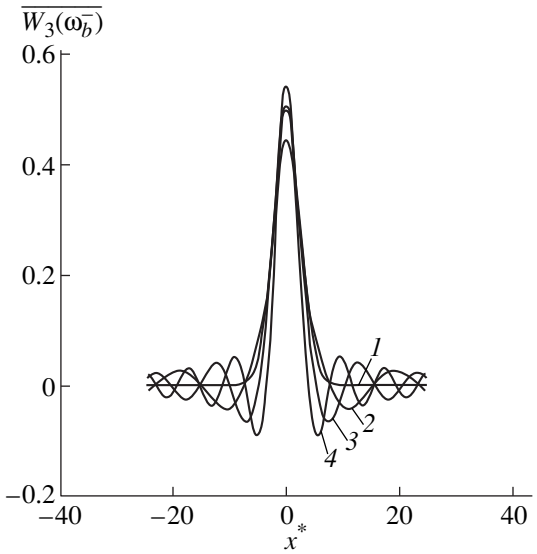

Fig. 4. Envelope of the free-precession signal for the exciting frequency ω_b^- for b = (*1*) 0, (*2*) 2, (*3*) 3, and (*4*) 4; $X^* = X - 2X_2 - X_1$.

$$= \exp\left(-\frac{x^2}{2}\right)A(x)\sin[zb + \Phi(x)],$$

$$A(x) = \sqrt{\frac{1}{4} + \frac{x^2}{2\pi}\left\{{}_1F_1\left(\frac{1}{2}; \frac{3}{2}; \frac{x^2}{2}\right)\right\}^2}, \tag{33}$$

$$\Phi(x) = \arctan\left[\pm\sqrt{\frac{2}{\pi}}x_1F_1\left(\frac{1}{2}; \frac{3}{2}; \frac{x^2}{2}\right)\right],$$

and ${}_1F_1(\alpha; \gamma; z)$ is the confluent hypergeometric function [12].

Here, we have passed to the dimensionless quantities

$$y = \frac{\delta}{\sigma}, \quad x = \frac{5\sigma t}{2}, \quad x_1 = \frac{5\sigma\tau_1}{2}, \quad b = \frac{f_1}{\sigma}. \tag{34}$$

Figure 3 shows the envelopes of the decay of free precession as a function of the amplitude b of the pumping field. It can be seen that, for $b = 0$ and excitation at frequency ω_b^+, the response of the spin system vanishes. As seen from the results obtained by Low and Norberg [13], the response associated with the excitation at frequency ω_b^- coincides with the Fourier transform of the steady-state resonance line shape used by us. With increasing b, the free precession signal experiences beats at frequencies that vary gradually with increasing b.

Analogous computations were made for the magnetization of the spin system after two pulses. The echo response is described by the expression

$$M^y_{2\omega_Q}(\omega) = -\frac{\sqrt{5}N\gamma\hbar^2\omega_Q}{6kT} \times \sin[2\omega_Q(t - 2\tau_2 - \tau_1) + \varphi_b]\overline{W_3(\omega)}. \tag{35}$$

In the limit of strong fields, we can write

$$\overline{W_3(\omega_b^\pm)} = \frac{5\sqrt{2}}{8}\sin(\sqrt{2}\xi_1)\sin^2\left(\frac{\xi_2}{\sqrt{2}}\right) \times K^\pm\left(x - 2x_2 - x_1, b, \frac{x - 2x_2 - x_1}{5}\right), \tag{36}$$

where

$$\xi_2 = \frac{g_3t_2}{2}, \quad x_2 = \frac{2\sigma\tau_2}{5}.$$

The envelope of the echo signal experiences beats just like the free precession signal (Fig. 4). It can be seen from Figs. 3 and 4 that there exists a certain point x^{**} at which the plots of several transient signals intersect the abscissa (time) axis. It would be interesting to understand the meaning of these points. For this purpose, we use the analytic expressions (32) and (36) in the strong-field approximation. In this case, the free induction and spin echo signals can be schematically presented in the form

$$\overline{W_n(\omega)} = \sum_{i=0} B_iK(x, b, z_i), \quad z_i = \frac{x}{5} + C_i, \tag{37}$$

where B_i are certain constants which do not depend on the parameter b in Eq. (34), C_i is a linear combination

of the intervals between the onset of the first and second pulses, and x is measured from the center of the echo signal.

Note that $|x^{**}| \geq 15$ in Figs. 3 and 4; these results are in good agreement with the approximation for large x. For $x \longrightarrow \infty$, we can use relations (33) in their limiting form

$$\Phi^{\pm}(x) \longrightarrow \frac{\pi}{2}(1 \mp \operatorname{sgn} x),$$

$$K^{\pm}(x, b, z) \longrightarrow \operatorname{sgn} x \exp\left(-\frac{x^2}{2}\right) A(x) \sin(zb).$$

In this case, formula (37) is a superposition of sinusoids. It is well known that a superposition of several sinusoids with different phases and amplitudes, but with the same frequency, leads to the formation of a single sinusoid with the same frequency and with modified values of the amplitude and phase:

$$\overline{W_n(\omega)} \longrightarrow \exp\left(-\frac{x^2}{2}\right) A(x) B(b) \sin\left[\frac{bx}{2} + \varphi(b)\right], \quad (38)$$

where $B(b)$ and $\phi(b)$ are certain functions of B_i and bC_i.

It can be seen from formula (38) that different $\overline{W_n(\omega)}\big|_{b = b_k}$ curves for signals $\overline{W_n(\omega)}$ corresponding to various values b_k of the parameter b must intersect the abscissa axis at the points x_n^{**}, if the conditions

$$x_n^{**} = \frac{5}{b_k}[\pi n - \varphi(b_k)] \quad (n \text{ is an integer})$$

are satisfied. We can determine the amplitude b of the pumping field by measuring the separation between the nearest points of intersection of the abscissa axis with the curves of the transient signals (Figs. 3 and 4): $b_k = 5\pi(x_{n+1}^{**} - x_n^{**})^{-1}$.

4. TRANSIENT PROCESSES UNDER CONDITIONS OF EXISTENCE OF SPIN TEMPERATURE FOR QUASI-ENERGY LEVELS

If the interval of time τ_1 between the application of the pumping field $\mathbf{H}_a(t)$ and the onset of the first pulse $\mathbf{H}_b(t)$ is quite large ($\tau_1 > T_1, T_2$), spin temperature can be introduced for quasi-energy levels [5].

The initial density matrix is defined in this case by formula (21), which can be used to carry out all operations described in the previous section. This gives

$$M^y_{2\omega_Q}(\omega) = \frac{5\sqrt{5} N\gamma\hbar^2\omega_Q}{24kT_{\mathrm{AFR}}} \sin(2\omega_Q t + \varphi_b)\overline{W(\omega)}. \quad (39)$$

In a strong alternating field ($f_1 \gg \sigma$), the expressions for $\overline{W(\omega)}$ assume a compact form:

$$\overline{W(\omega_b^{\pm})} = \frac{\sqrt{2}}{2}\sin(\sqrt{2}\xi_1) K^{\pm}\left(x, b, \frac{x}{5}\right),$$
$$\overline{W(\omega_b^{+}, \omega_b^{-})} = \frac{1}{2}\sin 2\xi_1 K\left(x, b, \frac{x}{5}\right). \quad (40)$$

After the action of a double pulse, the signals of transient processes at the frequency $2\omega_Q$ are defined as

$$M^y_{2\omega_Q}(\omega) = \frac{5\sqrt{5} N\gamma\hbar^2\omega_Q}{24kT_{\mathrm{AFR}}}(\sin[2\omega_Q t + \varphi_b]\overline{W_1(\omega)}$$
$$+ \sin[2\omega_Q(t - \tau_2) + \varphi_b]\overline{W_2(\omega)}$$
$$- \sin[2\omega_Q(t - 2\tau_2 - \tau_1) + \varphi_b]\overline{W_3(\omega)}), \quad (41)$$

where

$$\overline{W_1(\omega_b^{\pm})} = \frac{\sqrt{2}}{2}\sin(\sqrt{2}\xi_1)\cos^2\left(\frac{\xi_2}{\sqrt{2}}\right) K^{\pm}\left(x, b, \frac{x}{5}\right),$$
$$\overline{W_2(\omega_b^{\pm})} = \frac{\sqrt{2}}{2}\cos(\sqrt{2}\xi_1)$$
$$\times \sin(\sqrt{2}\xi_2) K^{\pm}\left(x - x_1, b, \frac{x - x_2}{5}\right), \quad (42)$$
$$\overline{W_3(\omega_b^{\pm})} = \frac{\sqrt{2}}{2}\sin(\sqrt{2}\xi_1)$$
$$\times \sin^2\left(\frac{\xi_1}{\sqrt{2}}\right) K^{\pm}\left(x - 2x_2, b, \frac{x - 2x_2}{5}\right).$$

It should be observed that $M^y_{\omega_Q}(\omega_1, \omega_2, \ldots)$ differs from zero only when the ω_b pulses simultaneously cover both resonance frequencies $\omega_b^{\pm}$.

A comparison of the results presented here and in the previous section shows that the nature of enveloping signals of transient processes does not change due to the existence of the spin temperature characterizing the occupancies of the quasi-energy levels. Calculations reveal only a difference in amplitude:

$$\frac{M^y_{2\omega_Q}(\omega)\big|_{T = T_{\mathrm{LCF}}}}{M^y_{2\omega_Q}(\omega)\big|_{T \to T_{\mathrm{AFR}}}} = \frac{2T_{\mathrm{AFR}}}{T_{\mathrm{LCF}}}.$$

Thus, one can expect a difference in the amplitudes, which is determined by the ratio of temperatures. This makes it possible to study the kinetics of the attainment of equilibrium and the stabilization of the spin temperature of the quasi-energy levels in the above experiments upon variation of the interval between the onset of pumping and exciting pulses.

The publications [1–11] cited in the Introduction contain details of execution and theoretical interpretation of various experiments involving quasi-energy levels. Since the energy levels in any representation can be considered only indirectly through their influence on the observable quantities, it can be concluded that quasi-energy levels are as real as the energy levels in the LCF.

However, the problem of excitation of resonance transitions between the LCF and AFR levels remains unsolved. The results of this work demonstrate the possibility and the formulation of the conditions for the existence of these processes, as a well as a computation of certain effects associated with quantization in a strong alternating field, which induces such transitions. In the procedure considered here, a strong resonance field creates energy levels associated with one transition in the nonequidistant nuclear spin spectrum, while the other rf field excites transitions between these levels and the level that does not participate in the creation of the quasi-energy spectrum, i.e., the LCF energy level. The manifestation of quantization due to a strong rf field in signals of transient processes induced by the second rf field is demonstrated. It is found that the envelopes of these signals are subjected to beats with a frequency determined by the spacing between quasi-energy levels. Among other things, the measurement of the period of beats makes it possible to determine the amplitude of the alternating field in the sample. It would be interesting to study the kinetics of equilibrium stabilization and the spin temperature of the quasi-energy levels in the framework of the approach presented in this paper.

REFERENCES

1. A. Redfield, Phys. Rev. **98** (6), 1787 (1955).
2. I. I. Rabi, N. F. Ramsay, and J. Schwinger, Rev. Mod. Phys. **26** (1), 167 (1954).
3. C. P. Slichter and W. C. Holton, Phys. Rev. **122** (6), 1701 (1961).
4. A. G. Anderson and S. R. Hartman, Phys. Rev. **128** (5), 2023 (1966).
5. M. Goldman, *Spin Temperature and Nuclear Magnetic Resonance in Solids* (Clarendon Press, Oxford, 1970; Mir, Moscow, 1972).
6. A. R. Kessel' and M. M. Shakirzyanov, Akust. Zh. **23** (3), 469 (1977) [Sov. Phys. Acoust. **23**, 263 (1977)].
7. A. R. Kessel' and M. M. Shakirzyanov, Zh. Éksp. Teor. Fiz. **83** (3), 1100 (1982) [Sov. Phys. JETP **56**, 624 (1982)].
8. V. A. Golenishchev-Kutuzov, V. A. Kirsanov, and V. F. Tarasov, Pis'ma Zh. Éksp. Teor. Fiz. **39** (9), 407 (1984) [JETP Lett. **39**, 491 (1984)].
9. V. A. Kirsanov, V. F. Tarasov, and M. M. Shakirzyanov, Fiz. Tverd. Tela (Leningrad) **27** (5), 1554 (1985) [Sov. Phys. Solid State **27**, 938 (1985)].
10. A. R. Kessel and O. S. Zueva, Physica (Amsterdam) **19** (1), 205 (1977); Phys. Lett. A **68A** (4), 347 (1978); Zh. Éksp. Teor. Fiz. **73** (6), 2169 (1977) [Sov. Phys. JETP **46**, 1136 (1977)].
11. N. E. Aĭnbinder and G. B. Furman, Zh. Éksp. Teor. Fiz. **85** (3), 988 (1983) [Sov. Phys. JETP **58**, 575 (1983)]; N. E. Ainbinder, G. A. Volgina, A. N. Osipenko, and G. B. Furman, J. Mol. Struct. **64**, 214 (1983).
12. I. S. Gradshteĭn and I. M. Ryzhik, *Table of Integrals, Series, and Products* (Nauka, Moscow, 1971; Academic, New York, 1980).
13. I. J. Low and R. E. Norberg, Phys. Rev. **107** (1), 46 (1957).

Translated by N. Wadhwa

Physics of the Solid State, Vol. 42, No. 11, 2000, pp. 2070–2075. Translated from Fizika Tverdogo Tela, Vol. 42, No. 11, 2000, pp. 2012–2016.

SEMICONDUCTORS AND DIELECTRICS

Effect of an Electric Field on Brucite Dehydroxylation

E. A. Kalinichenko and A. S. Litovchenko

Institute of Geochemistry, Mineralogy, and Ore Formation, National Academy of Sciences of Ukraine, Kiev, 252680 Ukraine

Received February 11, 2000; in final form, April 20, 2000

Abstract—The dehydroxylation of brucite has been investigated in electric fields up to 400 kV/m at $T = 623$ K. It is revealed that this reaction in the presence and absence of the field is a diffusion-controlled process, and its rate is governed by the diffusion rate of "slow" protons (the O^{2-} states) in the $Mg(OH)_2$ crystal structure. A decrease in the activation energy for diffusion of these protons in an electric field can be explained by both the additional energy acquired by the proton upon its migration through a distance of about 10^3 A and a certain decrease in the potential barrier. It is shown that the found decrease in height of this barrier can be caused by the ionic polarization of the brucite lattice in an electric field whose effect on the barrier depends on the net dipole moment responsible for the generation of dipoles in the structural region of radius ~200 Å. © *2000 MAIK "Nauka/Interperiodica".*

1. INTRODUCTION

Although a large number of works have been dedicated to the study of the dehydroxylation effect, the physical mechanism of this phenomenon is not completely understood and its elucidation calls for further investigation. Explorations into the influence of different external factors on the process under consideration provide a means of solving many important problems concerning, in particular, possible paths of traveling protons, height and shape of structural potential barriers, etc.

Investigations into the effect of an external electric field on the dehydroxylation of layered structures have received little attention. It was found that this process is usually accompanied by an increase in the electrical conductivity owing to the contribution of protons [1] and by a deterioration of the dielectric and strength properties of the materials involved [2]. From the data on the dehydroxylation of brucite and gibbsite in an electric field [3], it was assumed that protons can tunnel during reaction over considerable distances in the crystal lattice and, most likely, can also be transferred by a specific charged complex. The authors of [4, 5] studied the proton conductivity in kaolinite, brucite, and gibbsite and made the conclusion that two mechanisms of proton transfer can be realized in similar structures: the migration of excess mobile protons in the protonic conduction band lying above the potential barriers ($E_{act} \sim$ 2.1 eV for the $Mg(OH)_2$ lattice) and the migration of the O^{2-} states over the crystal (the O^{2-} ion located in the lattice at the hydroxyl site takes up a proton from the nearest OH group; $E_{act} \sim 0.87$ eV for $Mg(OH)_2$]). It should be noted that the authors of the aforementioned works, for the most part, qualitatively described the experimental results within the appropriate models and approximately estimated the heights of the energy barriers.

At present, many researchers believe that the dehydroxylation reaction at a local level is attended by the transfer of a proton from a particular OH group to the nearest neighboring OH group [6, 7]. However, the migration of protons over large distances in the crystal is often treated as a probable mechanism of the reaction at high temperatures occurring when a considerable number of OH groups have already dissociated [7].

In this respect, it was of interest to investigate the effect of an electric field on the dehydroxylation reaction with the use of a technique providing the direct determination of the degree of conversion from the change in the number of hydroxyl groups in a sample. The data obtained by this method directly reflect the kinetics of the dehydroxylation reaction (the decomposition of the structural OH groups), which can provide useful information on the mechanism of this process.

In this work, we elucidated how the external direct electric field ($E = 0$–400 kV/m) affects the dehydroxylation kinetics of the $Mg(OH)_2$ brucite at $T = 623$ K by using the Mn^{2+} ESR technique. The degree of conversion α (the relative decrease in the number of OH groups in a sample) was determined from the decrease in the peak intensity of the Mn^{2+} line in the ESR spectrum of the brucite sample ($g_{eff} = 2.1478 \pm 0.0005$). Although the spectra were recorded at room temperature, the kinetic data thus obtained seem to be reliable.

It should be noted that brucite was chosen for the investigation of the dehydroxylation reaction in an electric field, because the kinetics and mechanism of dehydroxylation of this mineral in the absence of an electric field were studied in sufficient detail by other methods [5, 8, 9].

1063-7834/00/4211-2070$20.00

2. EXPERIMENTAL TECHNIQUE

2.1. Sample Preparation

A natural x-ray pure brucite sample was used in our experiments. The brucite structure is built up of the $Mg(OH)_2$ octahedra, which form the layers. The unit cell is trigonal ($a = b = 3.12$ and $c = 4.73$ Å): the Mg^{2+} ion lies in the (001) plane and the O^{2-} ions are located above and below the (001) plane at a distance of $0.22c$. The protons are situated at a distance of 0.98 Å from each oxygen ion along the c axis [10].

For our experiments, we chose the sample in which a part of the Mg^{2+} ions (0.06%) was replaced by Mn^{2+} ions. The Mn^{2+} ESR spectrum of the initial polycrystalline sample contains six hyperfine structure lines ($S_N = 5/2$ and $I_N = 5/2$ for Mn^{2+}) with constant $A = (-85.0 \pm 0.4) \times 10^{-4}$ T, which agrees with the data reported in [10, 11]. The heat treatment of the sample at $T = 850$ K leads to the disappearance of the above ESR lines and the appearance of a sextet with $g_0 = 2.0015 \pm 0.0001$ and $A = (82.2 \pm 0.5) \times 10^{-4}$ T, which corresponds to the Mn^{2+} ions located in the MgO structure [11].

Two cubic $Mg(OH)_2$ samples (with the edge $l = 5$ mm) were simultaneously heat-treated for a given time (5–500 min) in air at temperature $T = 623$ K [at this temperature, the dehydroxylation rate is maximum (Fig. 1)]: the check sample was measured at $E = 0$ ($E \equiv |\mathbf{E}|$) and the other sample was in the electric field ($\mathbf{E} \parallel$ (001) plane). The electric current passing through the crystal was monitored in order to avoid the possible influence of breakdown and electrolysis on the experimental data.

After heat treatment at the given temperature, the samples were cooled down to room temperature and were then investigated by the ESR technique.

2.2. Measurements

In this work, the degree of conversion α was determined from the Mn^{2+} ESR spectra according to the procedure described in [12]: the weights of several samples were measured and their ^1H NMR and Mn^{2+} ESR spectra were recorded prior to and after heat treatment in the temperature range $400 < T < 800$ K for 60 min. All the spectra were measured at room temperature.

The ESR spectra of these samples were used to determine the quantity

$$\nu(T) = I/I_0,$$

where I_0 and I are the peak intensities (peak heights) of the first Mn^{2+} hyperfine line ($g_{\text{eff}} = 2.1478$) in the ESR spectra recorded for the same sample prior to and after the heat treatment at temperature T for 60 min, respectively. The data obtained by the gravimetric method and ^1H NMR spectroscopy were processed according to the procedure described in [12].

The results obtained are displayed in Fig. 1. The degree of conversion α can be calculated from the ν values, which were determined from the ESR spectra of the studied samples. For example, at $\nu = 0.5$ (Fig. 1), $\alpha_1 = w_G$ and $\alpha_2 = 1 - w$; therefore, $\alpha = (\alpha_1 + \alpha_2)/2 = 0.4$.

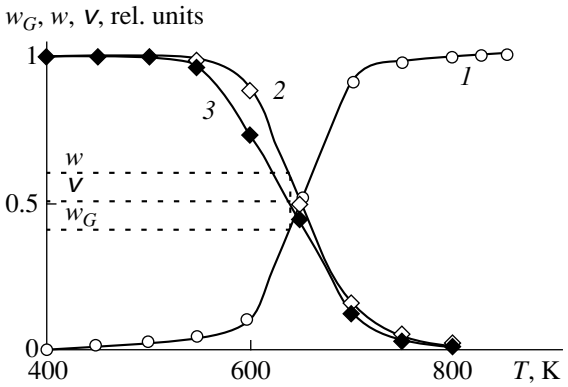

Fig. 1. Temperature dependences of (*1*) the relative weight loss $w_G(T) = 1 - G/G_0$, (*2*) relative decrease in the integrated intensity of the NMR line for hydroxyl groups $w(T) = H/H_0$, and (*3*) relative change in the peak intensity of the first hyperfine structure line $\nu(T)$ in the Mn^{2+} ESR spectrum for a brucite sample ($g_{\text{eff}} = 2.1478$). Heat treatment time is 60 min.

As in [12], it can easily be shown that, under experimental conditions, the time required for heating the sample to the furnace temperature T is $t_1 \cong 30$ s and the time of its subsequent cooling is $t_2 \cong 40$ s. Therefore, the shortest time of heat treatment of the sample in a furnace (300 s) is sufficient for heating the sample to the temperature T. It should also be mentioned that, upon heating of the crystal, the reaction rate increases to a maximum value (attainable at T) for time t_1. However, upon cooling in air, the reaction proceeds with a decreasing rate for time t_2. These effects, to some extent, compensate for each other.

Consequently, there are strong grounds to believe that the kinetic curves obtained in the present work adequately describe the dehydroxylation reaction at a specified temperature (the direct determination of α for the sufficiently precisely measured time t at the known temperature).

3. RESULTS AND DISCUSSION

3.1. Kinetics and Mechanism of Dehydroxylation

The kinetic curves for dehydroxylation of a brucite crystal at $T = 623$ K in air at different strengths of the applied electric field are depicted in Fig. 2.

Note that an increase in the electric field strength from 200 to 300 kV/m leads to a substantial increase in the reaction rate. At $E \leq 200$ kV/m, the dehydroxylation reaction proceeds rather slowly (at $E = 200$ kV/m, the value of $\alpha \approx 0.9$ can be reached only for $t \sim 500$ min), whereas at $E \geq 300$ kV/m, the reaction is virtually completed after a time $t \cong 50$ min.

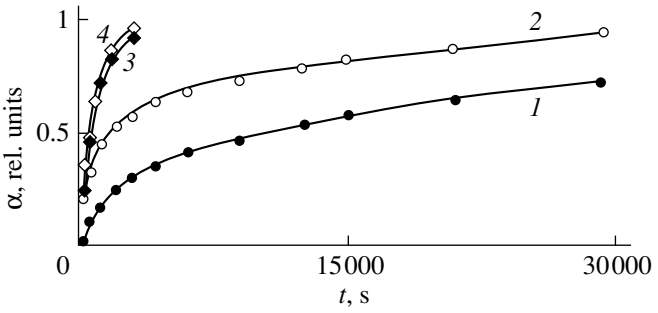

Fig. 2. Dehydroxylation kinetics of the brucite crystal at T = 623 K in an electric field at different strengths (kV/m): (*1*) 0, (*2*) 200, (*3*) 300, and (*4*) 400. Points are the experimental data.

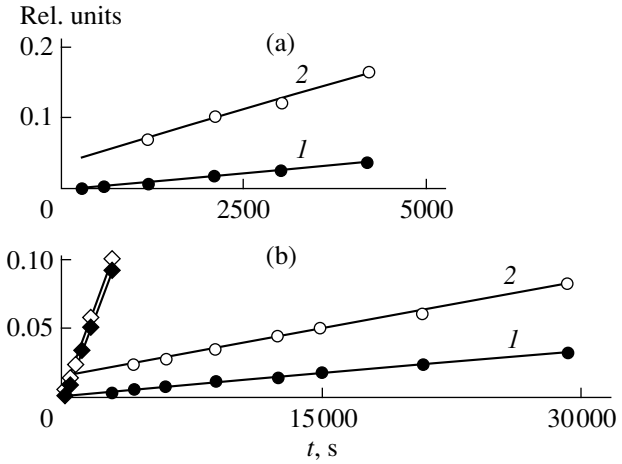

Fig. 3. Kinetic curves for the functionals in the left-hand sides of (a) Eq. (1) and (b) Eq. (2). Designations of the curves are the same as in Fig. 2.

In order to elucidate the possible mechanism of the reaction, the experimental data obtained were processed on several coordinate systems.

It was found that the dehydroxylation of a brucite crystal at the initial stage ($\alpha \le 0.34$) at E = 0 and 200 kV/m is adequately described by the following equation (the functional in the left-hand side of this equation is represented in Fig. 3a):

$$(1-(1-\alpha)^{1/2})^2 = \frac{k_s(t-t_s)}{r^2}, \quad (1)$$

where k_s is the diffusion coefficient of particles migrating at the initial stage of the dehydroxylation, t_s is the induction period, and r is the characteristic size of the crystal.

Equation (1) was obtained from the "contracting-circle" equation, which is often used for describing the dehydroxylation of laminated minerals with due regard for the fact that a decrease in the reaction rate with time is caused by diffusion processes due to an increase in the thickness of a product layer or its cracking (this implies that the movement of the interface is determined by the parabolic law $\delta = \sqrt{k_{dif}t}$ (where k_{dif} is the diffusion coefficient of migrating particles) for this diffusion-controlled growth of nuclei) [9].

At E = 300 and 400 kV/m and at the later stages of the reaction ($\alpha \ge 0.34$) when E = 0 and 200 kV/m, the kinetic curve is well represented by the following equation (the functional in the left-hand side of this equation is shown in Fig. 3b):

$$(1+(z-1)\alpha)^{2/3} + (z-1)(1-\alpha)^{2/3} - z = \frac{2(1-z)k_v(t-t_v)}{r^2}, \quad (2)$$

where k_v is the diffusion coefficient of particles migrating at the later stage of the reaction, t_v is the induction period (at $E \ge 300$ kV/m), and z is the ratio between the molar volumes of the product and the reagent (z = 0.65 for $Mg(OH)_2$).

Equation (2) was derived from the "contracting-sphere" equation for reactions proceeding in the bulk of spherical particles of radius r with due regard for the fact that the reaction rate is limited by the diffusion processes mentioned above [9].

The table lists the parameters k_s, t_s, k_v, and t_v, which were calculated by the least-squares method from the experimental data (r = 2.5 mm).

Thus, the results obtained in this work are in agreement with the existing concepts [3, 5] on the mechanism of brucite dehydroxylation. The stage of nucleation—the decomposition of OH groups in the $Mg(OH)_2$ lattice and the formation of structural water molecules—is not limited. The dehydroxylation of the studied brucite crystal is the diffusion-controlled process at both E = 0 and $E \ne 0$. The elimination of the resulting H_2O molecules from the lattice occurs when the product–reactant reaction interface is approached.

It should be noted that, according to [6, 7, 13], the structural water molecule is formed upon the transition of the proton from the hydroxyl group to a vacant site in the nearest unit cell of brucite over the barrier with a height of about 2.8 eV. This brings about the formation

Parameters obtained for the contracting-circle and contracting-sphere equations

E, kV/m	k_s, 10^{-10} m^2/s	t_s, s	k_v, 10^{-10} m^2/s	t_v, s
0	0.593	275	0.071	–
200	3.680	70	0.147	–
300	–	–	2.140	245
400	–	–	2.240	190

of a nucleation center—the H_2O molecule and the OH group are located in the same unit cell. Most likely, the product (one O^{2-} ion) can be formed in this unit cell when the water molecule leaves the lattice and the proton of the remaining hydroxyl group escapes from the crystal structure [5]. Therefore, it is quite probable that in the case when the protons occur at the product–reactant interface and then migrate into the lattice, they can activate the remaining nucleation centers, i.e., contribute to the development of an active zone in front of the interface [9].

Since the relative change in the number of hydroxyl groups in the sample was determined in the experiment, the above conclusions regarding the diffusion-controlled mechanism enabled us to argue that further formation of structural water molecules (i.e., a decrease in the number of OH groups) is determined by the rate of escape of the H_2O molecules from the crystal and, hence, quite possibly, by the number of protons at the interface and their migration.

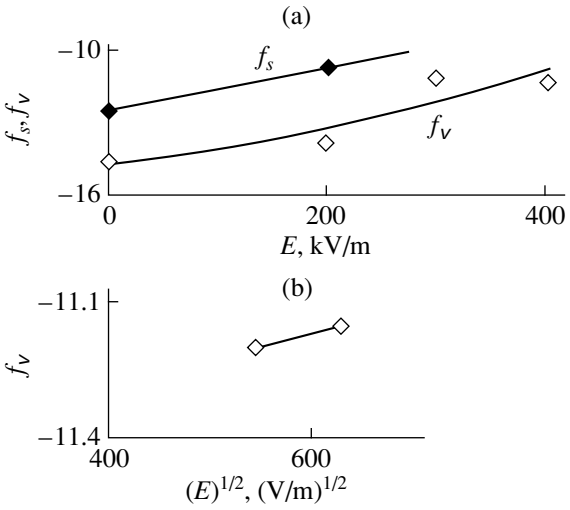

Fig. 4. Effect of the external electric field on (a) f_s and f_v and (b) f_v at the field strength $E \geq 300$ kV/m.

3.2. Effect of an Electric Field on the Diffusion Coefficient of Migrating Particles

As follows from the foregoing, it is this migration of protons (which occur at the product–reactant interface) in the crystal structure that, most likely, limits the interface movement, i.e., the reaction rate. Then, k_s and k_v are the diffusion coefficients of these protons in the sample lattice at the early and later stages of dehydroxylation, which can be evaluated from the relationship

$$k_s = \nu_0 d_s^2 e^{-U^s/k_B T}, \quad (3)$$

where $\nu_0 = 1.07 \times 10^{14}$ s^{-1} [13], k_B is the Boltzmann constant, $d_s = 3.12$ Å is the distance to the nearest lattice sites, and U^s is the activation energy of diffusion (for k_v, the relationship is similar to Eq. (3) and contains $d_v^2 \cong 3.12 \times 4.73$ Å^2).

It turned out that, in this case, the activation energies of diffusion are equal to 0.62 and 0.71 eV (at $E = 0$) and somewhat decrease to 0.53 eV (at $E = 400$ kV/m) with an increase in the strength of the applied electric field. These activation energies at $E = 0$ are very close to the activation energy (~0.87 eV) obtained by Wengeller *et al.* [5] for the diffusion of the so-called slow protons. The latter process can be represented as the migration of the O^{2-} state over the crystal: the hydroxyl proton transfers to the oxygen ion and the O^{2-} ion formed in the adjacent lattice site takes up a proton from another OH group. It should be mentioned that a small number of such protons occurs in the initial structure under normal conditions, but their concentration substantially increases in the course of dehydroxylation [5].

Therefore, the movement of the reaction interface upon dehydroxylation of the brucite crystal is most likely governed by the diffusion rate of slow protons (the O^{2-} states).

The dependences of the quantities $f_s = \ln(k_s/\nu_0 d_s^2)$ and $f_v = \ln(k_v/\nu_0 d_v^2)$ on the external electric field strength are shown in Fig. 4. It was found that these dependences can be represented as

$$f_s = a_s + b_s E, \quad E < 300 \text{ kV/m}, \quad (4)$$

where $a_s = -12.49$ and $b_s = 9.133 \times 10^{-6}$ m/V (from the data obtained at $E = 0$ and 200 kV/m), and

$$f_v = a_v + b_v E + c_v E^2, \quad E \leq 400 \text{ kV/m}, \quad (5)$$

where $a_v = -14.73$, $b_v = 5.347 \times 10^{-6}$ m/V, and $c_v = 1.116 \times 10^{-11}$ (m/V)^2 (Fig. 4a).

The character of the dependences $f_s(E)$ and $f_v(E)$ suggests that an increase in the rate of brucite dehydroxylation (according to the available data) can be caused by the following factors: at the initial stage of the reaction, it is the additional energy acquired by the proton upon its migration in the electric field, and, at the later stage, it is also a certain decrease in the activation energy for diffusion of slow protons due to the polarization of the brucite crystal upon application of the electric field. Apparently, a change in the brucite structure at $E \neq 0$ is accompanied by the generation of electric dipoles in the mineral lattice, and the potential barrier somewhat decreases in the field of these dipoles.

Let us now consider in greater detail the exponent in formula (3). This expression can be written as

$$-\frac{U}{k_B T} \cong -\frac{U_0 - eSE_v - \varepsilon_0 \beta E_v^2}{k_B T}, \quad (6)$$

where U_0 is the activation energy at $E = 0$, S is the distance at which the proton migrates, e is its charge, ε_0 is

the dielectric constant, β is the polarizability, and $E_v = (\varepsilon_0 + 2)E/3 \cong 3E$ is the local electric field strength in the bulk (the dielectric constant of brucite $\varepsilon \cong 7.0$) [14].

From the data obtained for the early stage of the reaction (at $E < 300$ kV/m) and relationships (4) and (6), it is possible to evaluate only the quantities $U_0^s = 0.67$ eV and $S \approx 1500$ Å.

For the later stage of the brucite dehydroxylation, according to formulas (5) and (6), we have $U_0^v = 0.79$ eV, $S \approx 950$ Å, and $\beta = 1.2 \times 10^{-21}$ m^3.

As follows from the results obtained, the slow proton can migrate over large distances in the bulk of the sample, which agrees with the data available in the literature [7].

In order to determine the type of particular polarization that makes the largest contribution to β, it is necessary to estimate the magnitude of the dipoles $p_i = \varepsilon_0 \beta_i E_v$ ($p_i \equiv |\mathbf{p}_i|$), which appear in the unit cell of brucite upon application of the electric field due to a certain displacement of ions in the lattice; that is,

$$p_i = 2R2e \cong 2.87 \times 10^{-38} E,$$

where $R = 2eE_v/k$ is the change in the distance between the positions of Mg^{2+} ions in the lattice in the presence and absence of an electric field, $2e$ is the charge of the Mg^{2+} ion, and k is the stiffness coefficient ($k \cong 10$ N/m).

As a result, we obtain $\beta_i \cong 1.08 \times 10^{-27}$ m^3 for the unit cell of brucite. A comparison of the ionic polarization with $\beta_d \cong 1.78 \times 10^{-36}$ m^3 (the maximum dipole polarization)[1] and $\beta_e \cong 9.86 \times 10^{-29}$ m^3 (the electron polarization) demonstrates that the ionic polarization of the lattice of this mineral in the electric fields is predominant: $\beta_0 = \beta_i + \beta_d + \beta_e \cong \beta_i$.

The high value of β can be explained by the fact that the net dipole moment (whose magnitude determines the effect of the electric field on the barrier) is formed by dipoles in a large structural region:

$$\beta \cong n\beta_i.$$

Consequently, this region in the crystal should involve $n \sim 10^6$ unit cells (the radius of the region is ~200 Å). It is worth noting that the obtained radius is of the same order of magnitude as the estimated sizes of the structural cluster whose ions form the potential barrier for the proton in muscovite and whose thermal vibrations are responsible for variations in parameters of this barrier [12].

A further increase in the electric field strength up to 400 kV/m leads to an insignificant increase in the dehydroxylation rate. This indicates that the prebreakdown voltages are achieved (in the experiment, the electric current increases and the breakdown is sometimes observed at $E > 400$ kV/m)[2] when the electrical conductivity σ obeys the Frenkel law [15]

$$\ln(\sigma/\sigma_0) = c_0\sqrt{E},$$

where σ_0 is the electrical conductivity in weak fields and c_0 is the constant.

Note that, at $E = 300$ and 400 kV/m (Fig. 4b), we have

$$f_v = h\sqrt{E} + g,$$

where $h = 5.43 \times 10^{-4}$ (m/V)$^{1/2}$ and $g = -11.5$. As can be seen, $h \cong c_0$ [15]; hence, it is quite probable that the electrical conductivity of brucite upon its dehydroxylation is primarily determined by the diffusion of slow protons.

4. CONCLUSION

It was demonstrated that the dehydroxylation of the brucite crystal in the presence and absence of an electric field is a diffusion-controlled process.

The kinetics of the process under consideration is adequately described by the contracting-circle and contracting-sphere equations with due regard for the decrease in crystal volume in the course of the reaction.

An increase in the dehydroxylation rate in the electric field is primarily caused by an increase in the diffusion coefficient of slow protons (the O^{2-} states). This can be explained by a decrease in the activation energy of diffusion from 0.79 to 0.53 eV owing to the additional energy acquired by the proton upon its migration in the electric field over a distance of ~10^3 Å and also a certain decrease in the potential barrier height due to the polarization of the brucite crystal upon application of the electric field. In this case, the electric dipole moments can likely arise in the lattice, and their field induces a certain distortion and a decrease in the potential barrier. The radius of the structural region whose net dipole moment determines the effect of the electric field on the barrier is equal to ~200 Å.

REFERENCES

1. A. S. Litovchenko and V. V. Mazykin, Phys. Status Solidi A **81**, K47 (1984).
2. A. S. Litovchenko, V. A. Chernenko, I. V. Matyash, and O. D. Ishutina, Phys. Status Solidi A **93**, K9 (1986).
3. K. J. D. McKenzie, J. Therm. Anal. **5**, 19 (1973).
4. G. C. Maiti and F. Freund, Clays Clay Miner. **16**, 395 (1981).
5. H. Wengeller, R. Martens, and F. Freund, Ber. Bunsenges. Phys. Chem. **84**, 874 (1980).

[1] This value was obtained with due regard for the fact that the OH dipole is located perpendicularly to the (001) plane and its maximum deviation from the normal does not exceed 1×10^{-4} at the applied fields E.

[2] The data obtained at $E > 400$ kV/m are not discussed in the present work.

6. G. W. Brindley and J. Lemaitre, in *Chemistry of Clays and Clay Minerals*, Ed. by A. C. D. Newman (London Scientific Technical, Essex, 1987), p. 319.
7. A. A. Ogloza and V. M. Malhotra, Phys. Chem. Miner. **16**, 378 (1989).
8. M. C. Ball and N. F. W. Taylor, Mineral. Mag. **32** (6), 754 (1961).
9. M. Brown, D. Dollimore, and A. Galway, in *Reactions in the Solid State*, Ed. by C. Tipper and C. Bamford (Elsevier, Amsterdam, 1980; Mir, Moscow, 1983).
10. W. A. Pieczonka, H. E. Petch, and A. B. Mclay, Can. J. Phys. **39**, 145 (1961).
11. S. A. Altshuler and B. M. Kozyrev, *Electron Paramagnetic Resonance in Compounds of Transition Elements* (Nauka, Moscow, 1972; Halsted, New York, 1975).
12. E. A. Kalinichenko, A. S. Litovchenko, A. M. Kalinichenko, *et al.*, Phys. Chem. Miner. **24** (7), 520 (1997).
13. R. Martens and F. Freund, Phys. Status Solidi A **37** (1), 97 (1976).
14. W. B. Mils, *The Linear Electric Field Effect in Paramagnetic Resonance* (Clarendon, Oxford, 1976; Naukova Dumka, Kiev, 1982).
15. A. S. Zingerman, Usp. Fiz. Nauk **46** (4), 450 (1952).

Translated by O. Borovik-Romanova

Physics of the Solid State, Vol. 42, No. 11, 2000, pp. 2076–2082. Translated from Fizika Tverdogo Tela, Vol. 42, No. 11, 2000, pp. 2017–2023.

DEFECTS, DISLOCATIONS, AND PHYSICS OF STRENGTH

Thermal Hardening of Ni_3Ge Alloy Single Crystals with an $L1_2$ Superstructure at Low Temperatures

V. A. Starenchenko*, Yu. V. Solov'eva*, V. I. Nikolaev, V. V. Shpeĭzman**, and B. I. Smirnov****

** Tomsk State Architectural and Construction University, Tomsk, 634003 Russia*

*** Ioffe Physicotechnical Institute, Russian Academy of Sciences, Politekhnicheskaya ul. 26, St. Petersburg, 194021 Russia*

e-mail: dekan@oof.tisi.tomsk.su

Received March 20, 2000; in final form, April 5, 2000

Abstract—The mechanical properties and the dislocation structure of Ni_3Ge alloy single crystals have been experimentally studied at low temperatures. It is found that the flow stresses increase beginning with 4.2 K, and the observed rise in the stresses depends on the orientation of the strain axes of the crystals. The dislocation structure is investigated thoroughly. It is revealed that the mean density of dislocations and the interdislocation interaction parameter α anomalously increase as the temperature increases in the range 4.2–293 K. The mechanisms providing an explanation for the temperature anomaly of flow stresses and the α parameter are considered. The activation energy of thermal hardening is evaluated. It is assumed that the low activation energies of thermal hardening are due to the motion of dislocations at velocities close to the velocity of sound at these temperatures. *© 2000 MAIK "Nauka/Interperiodica".*

1. INTRODUCTION

Single-phase ordered alloys exhibit a wide variety of mechanical properties. The property of thermal hardening, which, at the early stages of investigations, was assumed to be unique and characteristic only of specific alloys, appeared to be inherent in almost every simple ordered superstructure ($L1_2$, B_2, $L1_0$, and $D0_{19}$). However, the mechanisms responsible for the increase in the flow stresses and the yield point with an increase in the temperature can differ considerably for each group of alloys. In this work, we considered the features in the mechanical behavior of Ni_3Ge alloy single crystals, which belong to a large group of intermetallic alloys with an $L1_2$ superstructure. Of particular interest is the investigation into the temperature anomaly of the mechanical properties of these alloys in the low-temperature range near the liquid-helium temperature. For the most part, the investigations have been limited by the boiling temperature of liquid nitrogen (77 K). The temperature range from 4.2 to 77 K remains poorly investigated for a number of reasons. First and foremost, this is caused by methodological problems, which stem from the necessity of using special equipment for the performance of mechanical testing at low temperatures. On the other hand, many researchers *a priori* believed that the flow stresses should substantially increase beginning with higher temperatures. However, Takasugi and Yoshida [1] studied the $Ni_3(Si,Ti)$ alloys and showed that an anomaly in the mechanical characteristics is already observable upon heating in the temperature range from 4.2 to 77 K. In this respect, it was of interest to examine the low-temperature anomaly for other alloys with a similar superstructure.

2. SAMPLES AND EXPERIMENTAL TECHNIQUE

The experiments were performed with Ni_3Ge alloy single crystals grown by the Czochralski technique from nickel (N-1 grade) and high-purity germanium (99.999%). Samples $3 \times 3 \times 6$ mm in size were cut from a single-crystal ingot by the electric-spark method. The face orientation was determined with the use of the Laue method.

The single crystals were tested on an Instron 1342 universal testing machine with an Oxford helium cryostat at the Ioffe Physicotechnical Institute, Russian Academy of Sciences. The samples were cooled down to 77 K with liquid nitrogen. Liquid helium was supplied to the cryostat with two pumps in order to ensure a weak evacuation in the cryostat. In addition to the standard isothermal testing at 4.2 and 77 K upon uniaxial compression at a rate of 4×10^{-4} s^{-1}, the samples were compressed upon a stepwise change in the temperature. After the deformation (by ~0.1 mm, $\Delta\varepsilon \approx 1.5\%$) and recording of a portion of the deformation curve at a specified temperature of testing (beginning with 4.2 K), the sample was heated by ΔT = 10–20 K (in the range 4.2–77 K) or ΔT = 90 K (at higher temperatures) at ε = const and, again, was subjected to the

deformation, etc. As a result, we constructed the compression diagram consisting of portions of the deformation curves (load P versus change of sample length) obtained at different temperatures (Fig. 1). Then, this diagram was used for determining the flow stresses at different temperatures and the sign and magnitude of the stress jump with a change in the temperature. From the obtained diagrams, we determined the temperature dependences of the shear flow stresses, which were taken equal to the flow stresses at 4.2 K plus the stress jumps caused by the changes in the temperature, that is,

$$\tau = \tau_{4.2} + \sum_i \Delta\tau_{\Delta T_i}.$$

The dislocation structure was studied with a UÉMV-100K electron microscope. In order to obtain the image of the dislocation structure, the studied sample was cut by the electric-spark method into thin plates parallel to the glide planes. These plates were mechanically or electrolytically thinned to a foil. The dislocation structure in the foil was examined under the electron microscope operating in the transmission mode. The observations were performed at magnifications $M = (20–36) \times 10^3$. The mean dislocation density was measured with the use of the linear-intercept method. A rectangular mesh was superposed on a micrograph. The mean dislocation density was calculated from the formula

$$\rho = M/t(n_1/1_1 + n_2/1_2),$$

where M is the micrograph magnification; t is the foil thickness; n_1 and n_2 are the numbers of intersections with horizontal and vertical lines, respectively; and 1_1 and 1_2 are the total lengths of the horizontal and vertical lines, respectively. The foil thickness was determined from the thickness extinction contours at the foil edge. As a rule, the foil thickness was equal to $(1.2–1.7) \times 10^3$ Å.

3. MECHANICAL PROPERTIES

The mechanical testing of the Ni_3Ge alloy single crystals revealed that the temperature anomaly of the flow stresses is observed beginning with the liquid-helium temperature (4.2 K). As is seen from Fig. 1, out of 23 temperature steps $\Delta T > 0$ (for all the orientations), only three steps correspond to $\Delta\tau \le 0$, and all the other stress jumps are positive; i.e., the flow stresses τ increase with an increase in the temperature (see insets in Fig. 2). However, it can be seen that the lower the temperature, the smaller the change in $\tau(T)$, and the τ stresses at the [111] and [234] orientations remain unchanged in the range 4.2–20 K. Figure 2 displays the temperature dependences of the yield point for the Ni_3Ge single crystals at three orientations of the compression axis. The anomalous shape of the dependence $\tau(T)$ is observed even beginning with a temperature of 4.2 K. As follows from the figure in which the low-temperature portions of the thermal hardening curves are

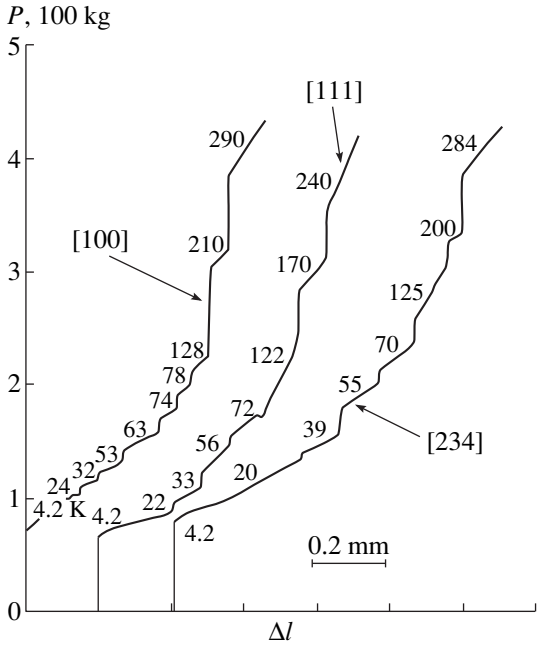

Fig. 1. Compression diagrams of Ni_3Ge single crystals for different orientations upon a stepwise change in temperature.

matched to their high-temperature portions [2] for the three orientations under consideration, the thermal hardening effect depends on the orientation of the compression axis. This indicates that the Schmid–Boas law is violated and agrees with the results obtained for thermal hardening in the temperature range above 77 K [2, 3]. The behavior of the dependence $\tau(T)$ in the range from 4.2 to 77 K virtually corresponds to its variation in the range above 77 K, and the flow curves $\tau(\varepsilon)$ (Fig. 3) have the shape of smooth convex downward curves. An increase in the temperature from 4.2 to 77 K weakly affects the flow curves: their shape only slightly changes in this temperature range. In our earlier work [2], we proposed the method for determining the activation energy of thermal hardening from the temperature dependences of the flow stresses. With this method, we obtained the activation energies of the low-temperature thermal hardening from the temperature dependences of the yield point for the Ni_3Ge single crystals of different orientations. It was found that the activation energies U_d in the low-temperature range upon compression along the [001], [234], and [111] axes are equal to $(0.84 \pm 0.16) \times 10^{-2}$, $(1.3 \pm 0.1) \times 10^{-2}$, and $(1.7 \pm 0.3) \times 10^{-2}$ eV, respectively. These energies are close to the corresponding activation energies in the temperature range 77–293 K [2], which suggests that there is one mechanism of thermal hardening in the temperature range 4.2–293 K.

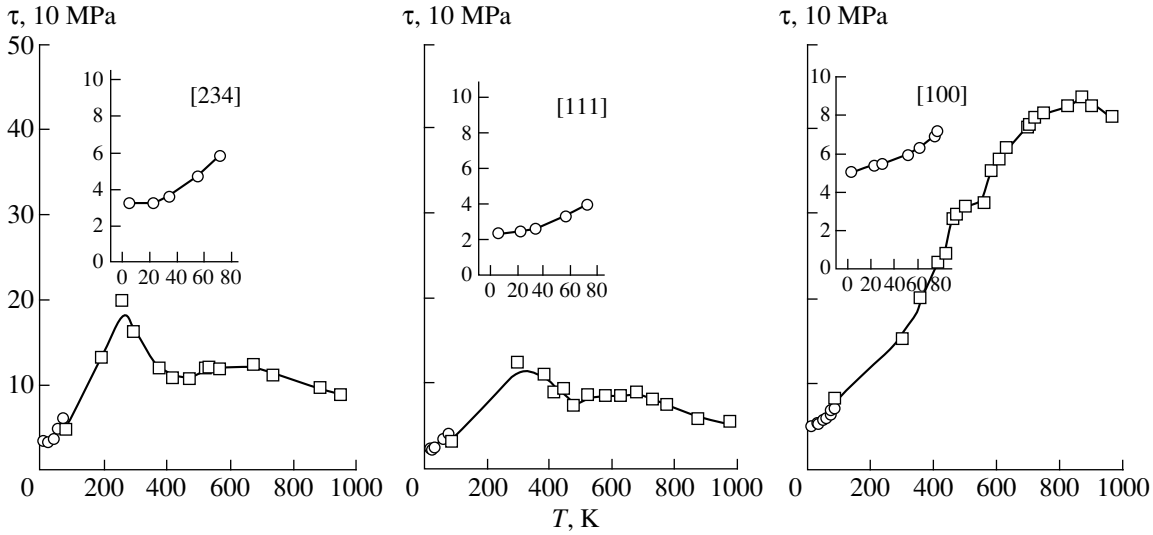

Fig. 2. Temperature dependences of the yield point (flow stresses) for Ni_3Ge single crystals at three orientations of the compression axis.

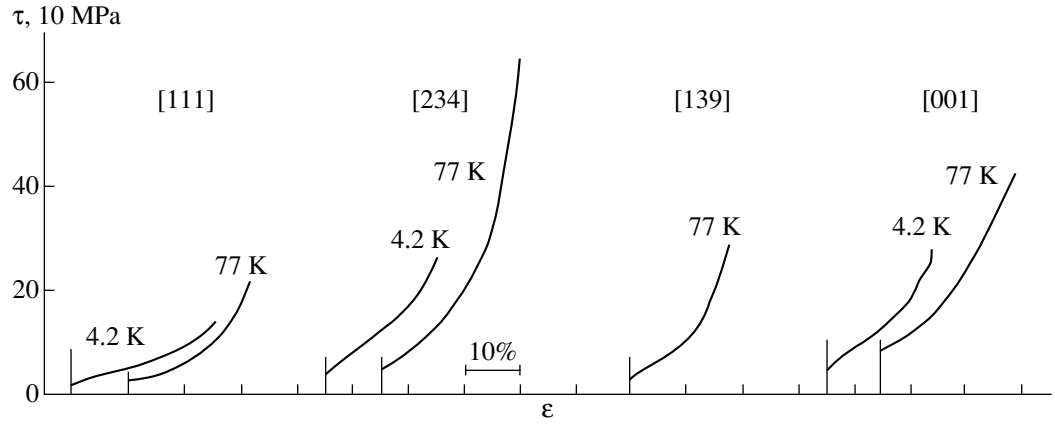

Fig. 3. Flow curves τ(ε) under low-temperature strain.

4. DISLOCATION STRUCTURE

Numerous electron microscopic investigations into the dislocation structure of the $L1_2$ alloys showed that the main structural elements of dislocations at temperatures in the range of the anomalous temperature dependence of the yield point are long rectilinear anchored screw segments [4]. However, at temperatures below 100 K, or in the case of small strains (below the macroscopic yield point), the dislocation structure does not exhibit these features and is formed by curvilinear dislocations [5]. Unlike the data obtained in [5], our observations revealed that the long rectilinear dislocation segments lying along close-packed directions of the ⟨110⟩ type are observed in the Ni_3Ge alloy even at $T = 4.2$ K (Fig. 4). The examination of the fine structure of these barriers allows us to assume that the rectilinear dislocations observed can be the Kear–Wilsdorf barriers or barriers similar to them [4, 6, 7]. Dipoles of different configurations are also revealed. Superdislocations are not split, which indicates a high energy of antiphase boundaries in the octahedron plane. An increase in the strain leads to a decrease in the number and length of rectilinear dislocations. The curvilinear dislocations with numerous kinks and reacted portions appear in the structure. An increase in the temperature up to 77 K does not result in considerable qualitative changes in the dislocation structure (Figs. 5a, 5b). A change in the orientation of the strain axis of the single crystal (for the studied [234], [139], and [100] orientations) virtually does not affect the qualitative features of the dislocation structure at these temperatures. The structure remains highly homogeneous and predominantly consists of long rectilinear dislocations.

The direct observations of the dislocation structure enabled us to evaluate its quantitative parameters. The

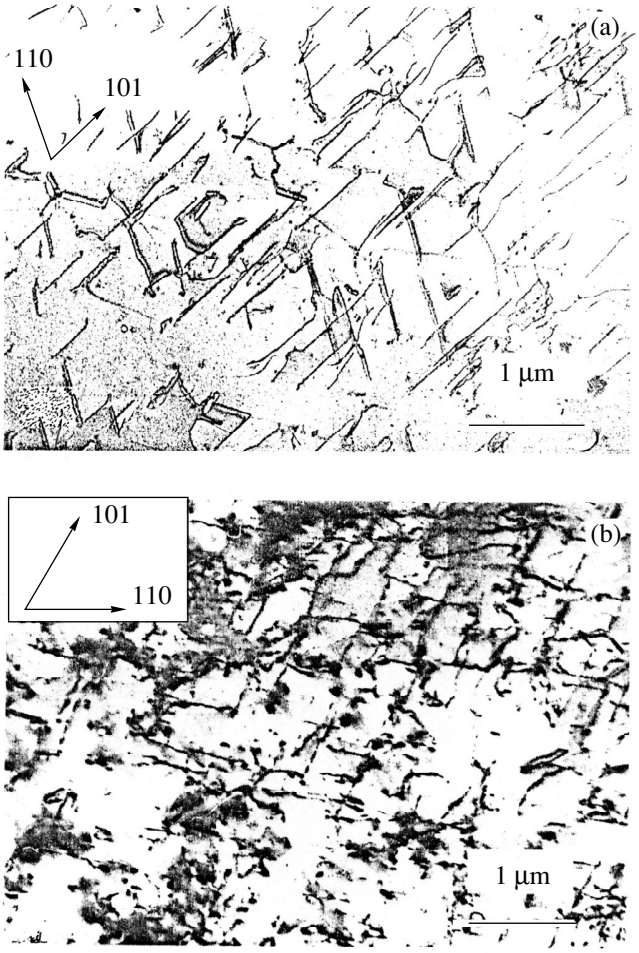

Fig. 4. Dislocation structures of the Ni_3Ge single crystals strained along the [234] axis at a temperature of 4.2 K. Strain ε (%): (a) 5 and (b) 15.

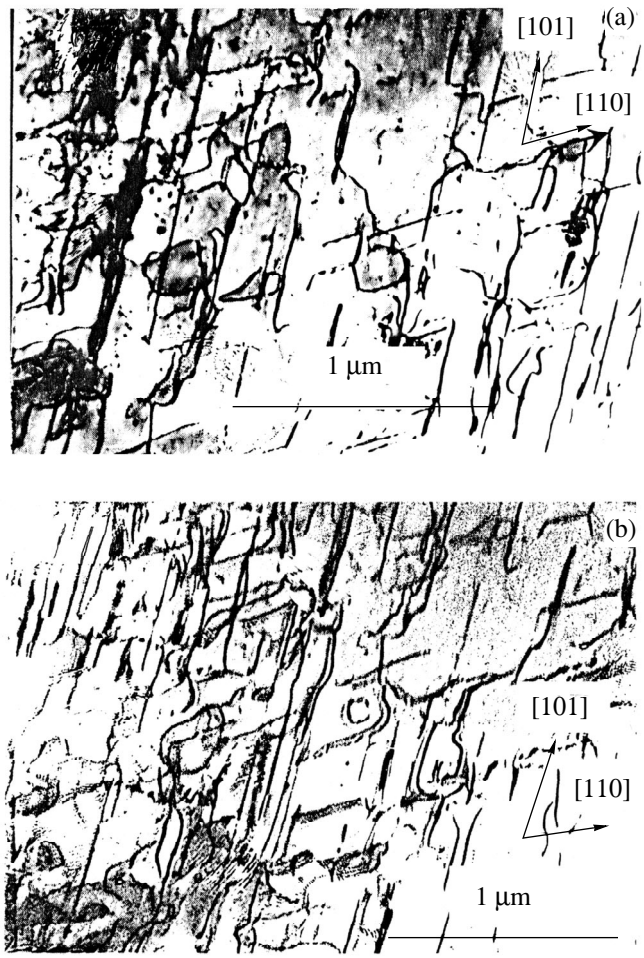

Fig. 5. Dislocation structures of the Ni_3Ge single crystals strained along the [234] axis at a temperature of 77 K. Strain ε (%): (a) 20 and (b) 23.

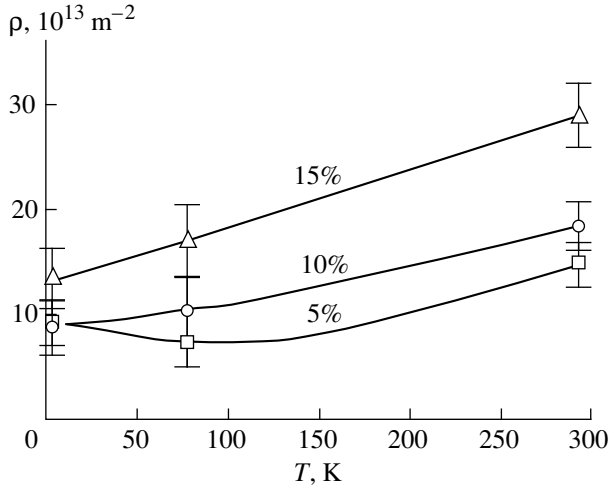

Fig. 6. Temperature dependences of the mean dislocation density for different strains of the Ni_3Ge single crystals at the [234] orientation.

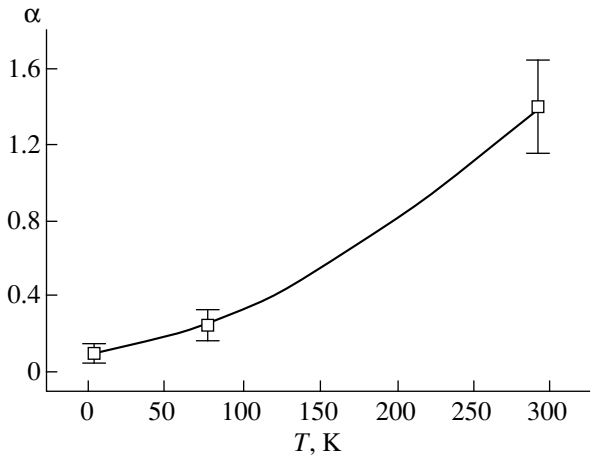

Fig. 7. Temperature dependence of the interdislocation interaction parameter α.

mean scalar dislocation density was measured as a function of the temperature and the strain. Figure 6 demonstrates the low-temperature portion of the temperature dependence of the mean dislocation density for the [234] orientation, which was studied in greater detail. The interdislocation interaction parameters α were determined from the relationship $\tau = \tau_F + \alpha Gb\rho^{1/2}$ (where G is the shear modulus and b is the Burgers vector) and the experimental data on the dislocation density ρ and the shear stresses τ. The temperature dependence of the α parameter is depicted in Fig. 7. It is worth noting that the interdislocation interaction parameter in this temperature range increases with a rise in the temperature, which indicates an anomalous change in the character of the interdislocation interaction.

5. DISCUSSION

A number of mechanisms based on the concept of the self-anchoring of superdislocations were proposed to explain the thermal hardening in alloys with the $L1_2$ superstructure [4, 8]. A change in the resistance to the dislocation motion is explained by the fact that driven and driving superpartial dislocations lose the common glide plane. Apparently, this can be caused by the cross sliding of screw dislocations (the Kear–Wilsdorf mechanism [4]) and the trapping of point defects by edge superdislocations, which are partly pinned as a result of thermal fluctuations of the superpartial dislocation portions [8]. The splitting of a superpartial dislocation can essentially depend on the velocity of the dislocation motion, and, hence, a change in the velocity can lead to a change in the activation energy for the self-anchoring of superdislocations. This is associated with the fact that the stress fields of dislocations depend on the velocity of their motion. At high velocities V of the dislocation motion, when $V \longrightarrow c_s$ (where c_s is the velocity of sound), the interaction forces between the parallel dislocations sliding in the same plane become less than those between the immobile dislocations by a factor of approximately $\gamma = 1 - V^2/c_s^2$ [9].

The activation energy for the formation of a superpartial dislocation junction can be approximately evaluated as the energy required for the displacement of a driving partial dislocation from the equilibrium distance r_1 (determined by the equilibrium between the elastic and the surface tension forces) toward a driven dislocation at distances of the order of the Burgers vector

$$\Delta U' = \int_{r_1}^{b} \tau b l_{cs} dr - \zeta^* l_{cs}(r_1 - b) \approx \frac{\gamma G b^2 l_{cs}}{2\pi}\left(\ln\frac{\gamma G b}{2\pi\zeta^*} - 1\right), \quad (1)$$

where τb is the interaction force between partial dislocations per unit length (without regard for the fine structure of superpartial dislocations, the interaction force between them can be approximately taken equal to the interaction force between screw dislocations: $\tau b \approx \gamma G b^2/2\pi r_1$); l_{cs} is the length of the superdislocation segment, which experiences the junction formation; $r_1 = \gamma G b^2/2\pi\zeta^*$; and ζ^* is the effective surface energy of a planar defect linking partial dislocations. In order to estimate the value of γ, let us consider the motion of a superdislocation loop. We assume that the superdislocation is a linear defect with the effective mass m^*. Then, the motion of the dislocation with a unit length can be described by the equation

$$\frac{m^*}{\sqrt{\left[1 - \left(\frac{1}{c_s}\frac{dx}{dt}\right)^2\right]}}\frac{d^2x}{dt^2} = \tau_{\text{dyn}} b - \tau_j b - B\frac{dx}{dt}, \quad (2)$$

where τ_{dyn} is the stress causing the dislocation motion in the shear region ($\tau_{\text{dyn}} = \alpha_{\text{dyn}} Gb\rho^{1/2}$) [9, 10], τ_j is the stress due to the motion of superdislocation jogs, and $B\frac{dx}{dt}$ is the viscous drag force. For the screw dislocation, τ_j can be represented as $\tau_j = p_j \xi \rho \langle \Delta E_k \rangle x/b$, where p_j is the fraction of jog-forming dislocations, ξ is the fraction of the dislocation forest, ρ is the dislocation density, $\langle \Delta E_k \rangle$ is the mean energy of the formation of a point defect arising upon the motion of a jog, and x is the dislocation path. In this case, relationship (2) takes the form

$$\frac{d^2x}{dt^2} = \left(\frac{\tau_{\text{dyn}} b}{m^*} - \frac{B}{m^*}\frac{dx}{dt} - \frac{p_j \xi \rho_0 \langle \Delta E_k \rangle}{m^* b} x\right) \times \sqrt{1 - \left(\frac{1}{c_s}\frac{dx}{dt}\right)^2}. \quad (3)$$

Let the initial conditions be $x = 0$, $t = 0$, and $dx/dt = 0$. The coefficients in the equation will be calculated with the following parameters: $\rho_0 = 10^8$ cm^{-2}, $G = 7 \times 10^{11}$ dyn/cm^2, $b = 5 \times 10^{-8}$ cm, $(\Delta E_k) = 1$ eV, $p_j = 0.5$, $\xi = 0.5$, and $B = 10^{-5}$ Pa [11].

According to [12], $m^* = db^2/4\pi\ln(R/r)$. Setting the density $d = 8$ g/cm^3 and $R/r_0 = 10$, we obtain $m^* \approx 8.6 \times 10^{-16}$ g/cm.

Assume that τ_{dyn} is equal to $\alpha_{\text{dyn}} Gb\rho_0^{1/2}$, where $\alpha = 0.3$ [9, 10]. The numerical solution of Eq. (3) for different parameters α_{dyn} is shown in Fig. 8.

The maximum velocity of the dislocation is achieved at a distance of 1.5 μm, which is considerably less than the shear region sizes (no less than 10 μm) observed in alloys with the $L1_2$ superstructure [11]. This implies that the dislocation acquires the maximum velocity of motion prior to reaching the boundary of the

shear region. The highest velocities for different dynamic stresses lie in the range 1450–2600 m/s (the experimentally obtained velocities of dislocations near the yield point are close in the order of magnitude to the velocities obtained in [13]), and, hence, the values of γ can fall in the range 0.8–0.2. In this case, the activation energy of junction formation can decrease by a factor of 1.3–5. For comparison, we note that the energies of the antiphase boundary in alloys with a low ordering energy (for example, Ni_3Fe, in which the anomalous effect is small) and a high ordering energy (for example, Ni_3Ge, in which the anomalous effect is pronounced) differ approximately four or five times.

Therefore, it can be supposed that the moving superdislocations, to a large extent, are susceptible to thermoactivated junction formation and the development of jogs, which result in the self-braking of dislocations. This can account for the low activation energies of self-braking superdislocations in the low-temperature range, because the motion of dislocations at low temperatures due to a decrease in the dynamic drag coefficient can occur at higher velocities compared to that at high temperatures.

The formation of the Kear–Wilsdorf barrier on a free dislocation segment changes the contact interdislocation interaction and can bring about a change in the strength of interdislocation interactions, which, in turn, can lead to a change in the interdislocation interaction parameter.

Let us now evaluate the change in the interdislocation interaction parameter due to the formation of the Kear–Wilsdorf barrier on a free segment of the shear-forming dislocation.

It was assumed that thermal fluctuations gave rise to N barriers per unit area in the shear region, which were subsequently suppressed in a further motion of the dislocation loop. As was shown earlier [14], the mean length of these barriers can be taken equal to approximately $\rho^{-1/2}$, i.e., equal to the length of the free dislocation segment.

The deformation work done by the external stress τ is equal to the work expended on extending the dislocation loops. Then,

$$\tau = \frac{\delta A}{bS}, \tag{4}$$

where S is the mean area occupied by the dislocation loop upon the formation of the shear region. The quantity δA can be represented as the sum

$$\delta A = \delta A_s + \delta A_\rho + \delta A_f, \tag{5}$$

where A_s is the work on the suppression of the Kear–Wilsdorf barriers, A_ρ is the work to overcome dislocation forest, and A_f is the friction work. The work on the suppression of the Kear–Wilsdorf barriers is given by

$$\delta A_s = NS\rho^{-1/2}\Delta U, \tag{6}$$

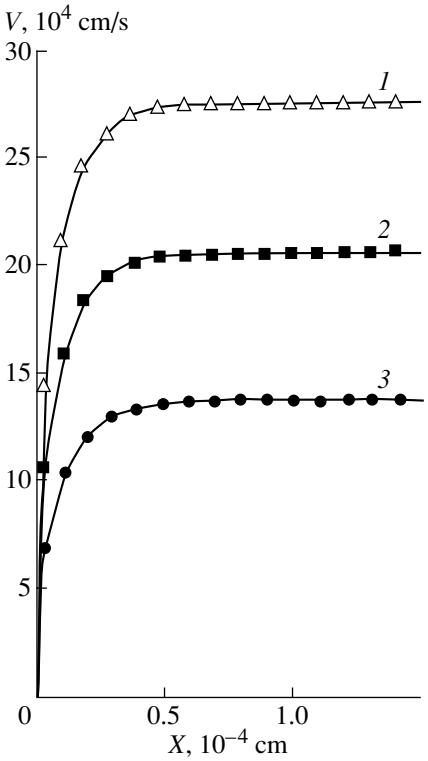

Fig. 8. Dependences of the dislocation velocity V on the distance X from the source at different α_{dyn}: (*1*) 0.4, (*2*) 0.3, and (*3*) 0.2.

where ΔU is the energy of the Kear–Wilsdorf barrier per unit length.

In [15], it was shown that

$$N = \frac{\nu b}{V}\frac{w_s}{l_{cs}^2}\exp\left(-\frac{U}{kT}\right), \tag{7}$$

where ν is the Debye frequency; w_s is the fraction of screw dislocations; l_{cs} is the length of the dislocation portion which experiences the thermoactivated junction formation; U is the activation energy for formation of the Kear–Wilsdorf barrier; and V is the mean velocity of dislocation motion. Then,

$$\frac{dA_s}{dS} = \Delta\tau_s \cong \frac{\nu b}{V}\frac{w_s}{l_{cs}^2}\Delta U\exp\left(-\frac{U}{kT}\right)\rho^{1/2}. \tag{8}$$

Thus, the contribution to the resistance to the motion of shear-forming dislocations turns out to be proportional to the square of the dislocation density. This leads to a strong increase in the interdislocation interaction parameter, which, according to formula (8), is described by the relationship

$$\alpha = \alpha_0\exp\left(-\frac{U}{kT}\right). \tag{9}$$

This expression makes it possible to determine the activation energy U from the experimental dependence

$\alpha(T)$. By using the data on the dependence $\alpha(T)$ displayed in Fig. 7, we obtain the activation energy $U = (2.0 \pm 0.8) \times 10^{-2}$ eV, which is close to the activation energy U_d obtained in the present work for this temperature range. This gives grounds to believe that the proposed mechanism of the influence of the Kear–Wilsdorf barriers on the α parameter is true.

6. CONCLUSION

The following features of the Ni_3Ge alloy single crystals were experimentally established: (1) the flow stresses anomalously increase beginning with a temperature of 4.2 K, and the activation energy of thermal hardening in this case is equal to a few hundredths of an electron-volt, (2) the observed increase in the yield point in the temperature range 4.2–77 K depends on the orientation of the strain axis of the crystal, (3) the variation in the temperature from 4.2 to 77 K does not lead to considerable qualitative changes in the dislocation structure, and (4) the interdislocation interaction parameter exhibits an anomalous temperature dependence in the low-temperature range. The mechanisms providing an explanation for the temperature anomalies in the flow stresses and the α parameter were considered, and our conclusion supports the Kear–Wilsdorf mechanism. It was assumed that the low activation energies of thermal hardening are due to the motion of dislocations at velocities close to the velocity of sound at these temperatures.

ACKNOWLEDGMENTS

This work was supported by the International Association of Assistance for the promotion of co-operation with scientists from the New Independent States of the former Soviet Union (project INTAS no. 97-31994) and the Russian Foundation for Basic Research (project no. 00-01-00482).

REFERENCES

1. T. Takasugi and M. Yoshida, Philos. Mag. A **67**, 447 (1993).
2. V. A. Starenchenko, Yu. V. Solov'eva, Yu. A. Abzaev, *et al.*, Fiz. Tverd. Tela (S.-Peterburg) **38**, 3050 (1996) [Phys. Solid State **38**, 1668 (1996)].
3. H.-R. Pak, T. Saburi, and S. J. Nenno, J. Jpn. Inst. Met. **39**, 1215 (1975).
4. B. H. Kear and H. G. B. Wilsdorf, Trans. Metall. Soc. AIME **224**, 382 (1962).
5. R. A. Mulford and D. P. Pope, Acta Metall. **21**, 1375 (1973).
6. D. Caillard, N. Clement, and A. Couret, Philos. Mag. Lett. **58**, 263 (1988).
7. A. Korner, H. P. Karntaler, and C. Hitzenberger, Philos. Mag. **56**, 73 (1987).
8. P. A. Flinn, Trans. Metall. Soc. AIME **218**, 145 (1960).
9. J. P. Hirth and J. Lothe, *Theory of Dislocations* (McGraw-Hill, New York, 1967; Atomizdat, Moscow, 1972).
10. L. E. Popov, V. A. Starenchenko, and S. V. Kolupaeva, Model. Mekh. **3**, 123 (1989).
11. L. E. Popov, V. S. Kobytev, and T. A. Kovalevskaya, *Plastic Deformation in Alloys* (Metallurgiya, Moscow, 1984).
12. V. S. Kobytev, V. A. Starenchenko, S. P. Zhukovskiĭ, and V. P. Chubis, *Atomic Ordering and Its Influence on the Properties of Alloys* (Tomsk, 1978).
13. V. A. Starenchenko, V. S. Kobytev, and L. E. Popov, Available from VINITI No. 299-78 (TISI, Tomsk, 1978).
14. V. A. Starenchenko, Yu. A. Abzaev, and L. G. Chernykh, Metallofizika (Kiev) **8**, 22 (1987).
15. V. I. Al'shits and V. G. Indenbom, *Dynamics of Dislocations* (Naukova Dumka, Kiev, 1978).

Translated by O. Borovik-Romanova

Physics of the Solid State, Vol. 42, No. 11, 2000, pp. 2083–2088. Translated from Fizika Tverdogo Tela, Vol. 42, No. 11, 2000, pp. 2024–2028.

DEFECTS, DISLOCATIONS, AND PHYSICS OF STRENGTH

Defect Ensembles on the Surface of Loaded Metals as a Result of Their Reversible Aggregation

H. G. Kilian*, V. I. Vettegren, and V. N. Svetlov****

** Abteilung of Experimentelle Physik, Universität Uhm, D-89069 Ulm, Germany*

*** Ioffe Physicotechnical Institute, Russian Academy of Sciences, Politekhnicheskaya ul. 26, St. Petersburg, 194021 Russia*

e-mail: Victor.Vettegren@pop.ioffe.rssi.ru

Received March 24, 2000; in final form, April 17, 2000

Abstract—The structures of nanodefect ensembles formed on the surfaces of copper, gold, and molybdenum under a load have been investigated. The properties of the defect ensembles are described in the framework of the reversible aggregation model. The size distribution of nanodefects is thermodynamically determined by the maximum "entropy of their mixing" with atoms of the crystal lattice. The entropy of mixing reaches a maximum value at a small concentration of defects due to a considerable difference in the sizes of defects and atoms. This concentration agrees closely with the experimental data. The reduced size distribution of defects is universal. © *2000 MAIK "Nauka/Interperiodica".*

1. INTRODUCTION

Recent investigations [1–4] of the surfaces of metals (Cu, Au, Mo, and Pd) under tensile stresses by scanning tunneling microscopy (STM) demonstrated that defects of a nanometric size are formed on the metal surface (Fig. 1). The nanodefects have the shape of a prism (Fig. 2) whose walls are parallel to the glide planes [2]. All the defects can be divided into two groups. The "smallest-sized," rapidly fluctuating defects belong to the first group, and the second group involves "large-sized" quasi-stationary defects whose mean lifetime is three or four orders of magnitude longer than that of the former defects. The mean sizes of the defects increase with time, and the time dependence of the defect concentration exhibits a quasi-periodic behavior (Fig. 3).

In this paper, the size distribution of defects on the surfaces of copper, gold, and molybdenum at different times after the loading is described within the model of their reversible aggregation [5]. The main inference drawn is that the distribution has a universal form which accounts for the optimum properties of the defect ensembles (the principle of the maximum entropy [6, 7]).

As can be seen from Fig. 4, the defects are formed and annihilate through the motion of material strips whose width varies from 5 to 50 nm [2–4]. We believe that this example is a sufficient demonstration of the occurrence of dynamic processes on the surface; therefore, we can consider the formation and annihilation of defect ensembles as a result of their reversible aggregation.

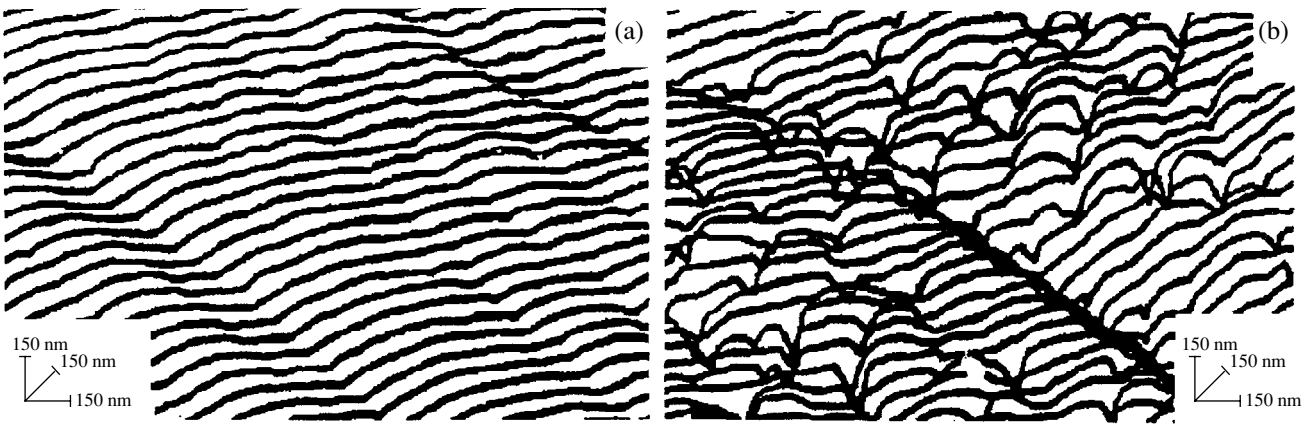

Fig. 1. Fragments of the topograms of the copper surface (a) prior to loading and (b) within 21 h after applying a load of 420 MPa.

1063-7834/00/4211-2083$20.00 © 2000 MAIK "Nauka/Interperiodica"

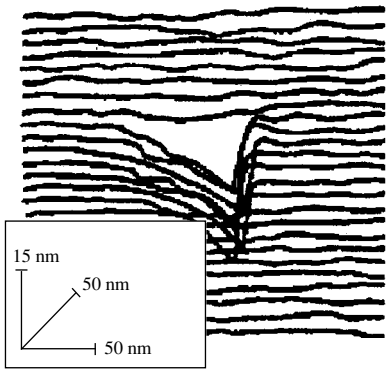

Fig. 2. A quasi-stationary defect formed on the gold surface under a load.

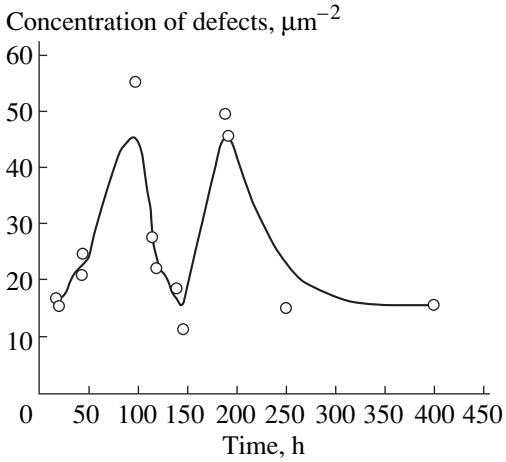

Fig. 3. Time dependence of the defect concentration on the copper surface under a load of 380 MPa.

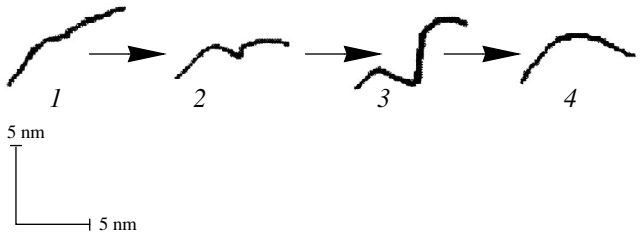

Fig. 4. Cross-sections of a smallest-sized defect on the gold surface under a load of 220 MPa at different instants of time *t* (s): (*1*) 0, (*2*) 38, (*3*) 76, and (*4*) 114.

It seems likely that the stationary size distribution in systems with fluctuation superstructures can be rapidly attained even in a nonequilibrium state. For example, it was found that the size distribution of carbon black aggregates formed under nonequilibrium conditions in filled rubbers is identical in shape to the stationary distribution obtained by a numerical solution of the fundamental Smoluchowski equation [8]. It is worth noting that the hysteresis of the stress–strain curves under cyclic loading of a rubber can also be described using the invariant relaxation distribution mode, which follows from the same stationary size distribution of molecular aggregates [9, 10].

In the case when the aggregation occurs through the coalescence of ensembles, the size distribution in each of them should be "optimized," even though each ensemble contains a nonequilibrium number of components. It is evident that the equilibrium is established upon relaxation when the system passes through a sequence of quasi-stationary states, and the entropy production in the relaxation processes is minimized [11, 12]. Such a behavior should be typical of the systems with a large number of equivalent subunits in which identical processes proceed independently of one another.

2. MODEL

In the model, the defect size is expressed by the number y of atoms involved in the defect, and the defect energy is measured in terms of $y\Delta U_0$, where ΔU_0 is the energy required to change the length of the defect wall by one interatomic distance. Under the reversibility conditions, the size distribution of defects is represented by the following relationship [5]:

$$n(y) = n_0 y^2 \exp(-\beta y \Delta U_0), \qquad (1)$$

where $\beta \equiv \frac{1}{k_B T}$, k_B is the Boltzmann constant, T is the temperature, and n_0 is the normalization constant. The entropy of the defect ensemble is maximum.

The lifetime of different atomic configurations on the walls of quasi-stationary defects is three or four orders of magnitude shorter than the mean time of defect relaxation [2–4]. Consequently, throughout the lifetime of a quasi-stationary defect, a large number of different atomic configurations are generated on its walls, and the atomic structure of the walls changes independently. According to thermodynamics, the defects with identical sizes, but with different internal structures, should be treated as different entities [6, 7]. The continuously varying configurations of a defect ensemble can be described as fluctuations of a multicomponent liquid in a loaded crystal lattice, which are stabilized by the "entropy of mixing." At equilibrium, the entropy of mixing should be maximum. For this reason, the preexponential factor in relationship (1) for the size distribution of defects includes y^2 [5].

The mean size $\langle y \rangle$ of a defect is given by [5]

$$\langle y \rangle = \frac{\int y^3 \exp(-\beta y \Delta U_0) dy}{\int y^2 \exp(-\beta y \Delta U_0) dy} = \frac{3 k_B T}{\Delta U_0}. \qquad (2)$$

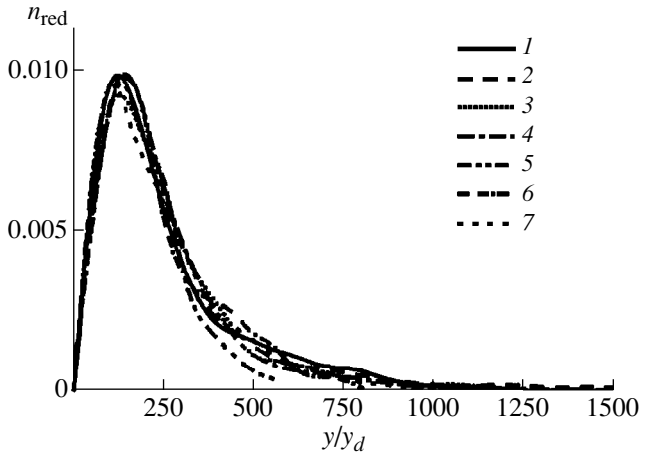

Fig. 5. Reduced distributions of the defects formed on the surfaces of (*1*–*5*) copper, (*6*) gold, and (*7*) molybdenum at different loads σ and loading times *t*. Load σ (MPa), time *t* (s): (*1*) 380, 16; (*2*) 380, 45; (*3*) 400, 117; (*4*) 380, 403; (*5*) 400, 21; (*6*) 320, 60; and (*7*) 800, 60.

3. COMPARISON WITH THE EXPERIMENT

According to the model of reversible aggregation, the reduced distribution $n_{red}(\eta)$ [see formula (1)] can be written as

$$n_{red}(\eta) = \frac{n(\eta)}{n_0(\beta\Delta U_0)^2} = \eta^2\exp(-\eta), \qquad (3)$$

where $\eta \equiv \dfrac{3y}{\langle y\rangle}$ is a universal function [5].

The reduced size distributions of defects on the surface were calculated for one, two, and ten samples of molybdenum, gold, and copper at room temperature, respectively. The load applied to the copper samples ranged from 350 to 420 MPa, and the loading time varied from 16 to 403 h. For the gold samples, the applied load was equal to 320 MPa, and the loading durations were 60 and 125 h. In the case of molybdenum samples, the load was 800 MPa, and the loading time was 60 h.

It was found that the reduced size distributions for all the studied samples have an identical shape within the limits of experimental error. This is illustrated in Fig. 5, in which the experimental distributions are plotted as a function of $\eta = 3y/\langle y\rangle = y/\langle y_d\rangle$. In this figure, the maximum of each distribution is shifted to the same position ($\langle y_d\rangle = 25$), and its magnitude n_{res} is fitted to a value of ≈0.09 by the corresponding variation in the parameter n_0.

As can be seen from Fig. 5, the symmetry predicted by the reversible aggregation model can be observed in real situations. Therefore, even under nonequilibrium conditions, the structure of defect ensembles formed on the surface of loaded metals corresponds to the maximum entropy.

At the same time, for an adequate description of the distribution, it is often necessary to use two (rather than one) distributions defined by formula (1), that is,

$$n(y) = n_{01}y^2\exp(-\beta y\Delta U_{01}) + n_{02}y^2\exp(-\beta y\Delta U_{02}). \quad (4)$$

As an example, Fig. 6 shows the depth distributions of defects formed on the surfaces of loaded samples of copper and gold, which were calculated from relationship (4). It can be seen that this expression adequately describes the experimental data. Moreover, this expression adequately represents the size distribution of the defects on the surfaces of all the studied samples of copper, gold, and molybdenum.

This result indicates that the topologically identical defect structure is realized on the surfaces of all the studied metals.

The main fitting parameters $\beta\Delta U_{01}$ and $\beta\Delta U_{02}$ are listed in the table. As is seen from the table, the ΔU_{01} values for the studied metals fall in the range (0.045–0.088)k_BT. (It is of interest that the standard energy of aggregate formation on the surface of the poly(methyl methacrylate) vitreous polymer at the glass transition temperature T_g = 384 K is of the same order of magnitude: $\Delta U_0 = 0.012k_BT$ [5].)

The energies ΔU_{02} and the mean defect sizes $\langle y_1\rangle$ and $\langle y_2\rangle$ are also presented in the table. It is seen that the ratio between the mean sizes of defects and the ratio

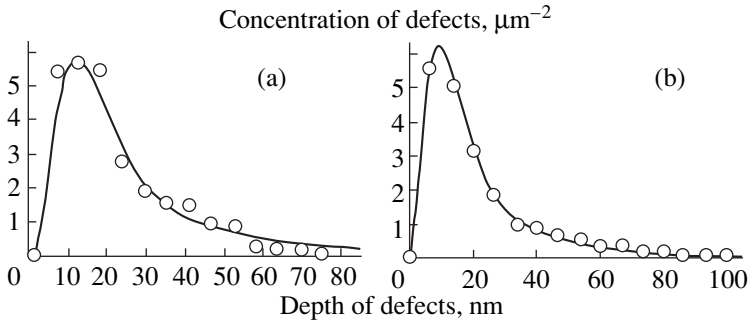

Fig. 6. Depth distributions of the defects formed on the surface of (a) gold within 60 h after applying a load of 350 MPa and (b) copper within 16 h after applying a load of 380 MPa. Solid lines correspond to the calculations according to Eq. (4).

Standard aggregation energies (calculated per interatomic distance) and mean sizes of defects formed on the metal surfaces under a load

σ, MPa	*t*, h	$\beta\Delta U_{01}$	$\beta\Delta U_{02}$	$\frac{\langle y_1\rangle}{\langle y_a\rangle}$	$\frac{\langle y_2\rangle}{\langle y_a\rangle}$	$\frac{\langle y_2\rangle}{\langle y_1\rangle}$	$\frac{\gamma}{\gamma_0}$
			Cu				
380	16	0.045	0.015	67	200	3.0	1.85
	45	0.047	0.015	64	200	3.1	1.85
	117	0.047	0.015	64	200	3.1	3.7
	187	0.047	0.015	64	190	3.0	3.7
	403	0.047	0.016	64	190	3.0	1
420	21	0.05	0.015	67	215	3.2	3.7
	43	0.045	0.013	67	213	3.0	4.5
400	144	0.05	0.017	60	215	3.2	1.1
	192	0.045	0.015	67	200	3.0	3.3
			Au				
350	60	0.06	0.016	50	130	2.7	1.85
	125	0.06	0.02	50	210	4.2	1.1
			Mo				
800	60	0.088	0.025	34	110	3.2	1

between the standard energies of their formation $\frac{\langle y_2\rangle}{\langle y_1\rangle} = \frac{\Delta U_{01}}{\Delta U_{02}}$ are approximately equal to 3. This result is difficult to interpret in the framework of classical kinetics. The model that provides an explanation for the "magic" number 3 will be described in a separate work.

The smallness of the ΔU_{01} and ΔU_{02} energies (compared to $k_B T$) allows the possibility of forming and rearranging the defect ensembles on the surfaces of loaded metals due to thermal fluctuations.

If two consecutive ensembles of defects are independently formed, the relationship for the preexponential factor in Eq. (1) under equilibrium conditions takes the form

$$n_{0k} = \frac{(1-p_k)^3}{2}, \quad (5)$$

where $p_k \equiv \exp(-\beta\Delta U_k)$ and $k = 1, 2$.

Since $\frac{\Delta U_{01}}{\Delta U_{02}} \approx 3$, at the equilibrium state, the ratio between the preexponential factors $\gamma \equiv \frac{n_{02}}{n_{01}}$ in expression (1) for two ensembles following each other should be $\gamma_0 = 1/27$. The parameter $\frac{\gamma}{\gamma_0} = \frac{27 n_{01}}{n_{02}}$ can be used to estimate the "distance" from the equilibrium. The $\frac{\gamma}{\gamma_0}$ values presented in the table indicate that the equilibrium is not universally attained, and the "distance from the equilibrium" essentially depends on the experimental conditions (the applied load and loading time).

Thus, the hierarchical equilibrium in the optimized defect structure on the surface of loaded metals, as a rule, is not established. This is also evidenced by the oscillations of the defect concentration (Fig. 3). However, the size distributions of defects are always identical in shape. Most likely, the time required for attaining this form of the size distribution is considerably shorter than the time taken to record the topogram (in our case, this time is equal to approximately 40 min [1]).

4. EQUILIBRIUM CONCENTRATION OF DEFECTS

The question now arises as to whether the defect concentration on the surface of loaded metals can be calculated in our case.

Let us consider the equivalent subsystems of defects, which are substantially larger than the STM scanned area. If these subsystems are optimized, the following relationship (saturation condition) should be met [5]:

$$\langle y_c\rangle \beta\Delta U_{ca} = 3 = \beta T \langle \Delta S_{ca}\rangle = \beta T k_B \langle \ln\Omega_{ca}\rangle, \quad (6)$$

where ΔU_{ca} is the standard energy of formation of a superaggregate from defects, and the product $k_B \ln(\Omega_{ca})$ characterizes the standard entropy of aggregation ΔS_{ca}.

Our experimental data allow us to interpret the entropy term in Eq. (6). We assume that defects with the mean volume $\langle y_c\rangle$ are randomly distributed over the lat-

tice consisting of atoms whose volume is y_a. Then, the fluctuations of the structural ensemble can be represented as a mixing of large-sized defects and small-sized atoms. The partial entropy s_c is determined by the following relationship [8, 13, 14]:

$$s_c = \frac{\partial \Delta S_{\text{mix},d}}{\partial n_c} = k_B\left(\ln(\varphi_c) + 1 - \frac{y_c}{\langle y_c\rangle}\right), \quad (7)$$

where $\varphi_c = \dfrac{y_c x_c}{y_c x_c + y_c(1-x_c)}$ is the volume concentration of defects.

Equation (6) can be rewritten as

$$s_c = \left(\ln\varphi_c + 1 - \frac{y_c}{\langle y_c\rangle}\right) = \langle \ln\Omega_{ca}\rangle = 3. \quad (8)$$

At $y_c \gg y_a$, $\dfrac{y_c}{\langle y_c\rangle} \approx 1$, and from relationship (8), it follows that $\varphi_c \approx x_c$.

The partial molar entropy of the mixture under consideration is approximately equal to the entropy of the ideal mixture [5, 13, 14]

$$k_B\langle \ln\Omega_{ca}\rangle \approx -k_B \ln x_c. \quad (9)$$

Substitution of this relationship into expression (8) gives the molar concentration of defects

$$x_c \approx e^{-3} = 0.05. \quad (10)$$

This value is in excellent agreement with the concentration ($x_{\text{exp}} = 0.050 \pm 0.003$), which was obtained from the topograms at the instants of time when the concentration reached its maximum values (Fig. 3). Since the mean sizes of quasi-stationary defects $\langle y_c\rangle$ are considerably larger than the atomic sizes (see table), our approximation is completely justified.

5. COROLLARY OF THE MODEL

It is expedient to calculate the ratio L/d_c, where L is the mean distance between two neighboring defects with the mean size $d_c = \varepsilon y_c$ (the parameter ε is determined by the geometric shape of the defect). Since $d_c/L \approx x_c$, it follows from relationship (8) that

$$\frac{L}{d_c} = \frac{1}{\sqrt[3]{x_c}} \approx e. \quad (11)$$

Therefore, the ratio $\dfrac{L}{d_c}$ for the optimized aggregate of defects is equal to $e \approx 2.7$. As follows from the calculations, $\dfrac{L}{d_c} = 2.6$–2.8 at the instants of time when the defect concentration is close to maximum. This result agrees well with the statement that the structure of the defect ensembles is thermodynamically optimized.

It is worth noting that the same ratio $L/d_c \approx e$ was obtained for cracks in different solids prior to their fracture [15, 16]. Apparently, the structure of crack ensembles under these conditions is also close to the thermodynamically optimized structure.

According to our concept based on the experimental data, the hierarchically organized ensembles (such as the defect ensembles on the surface of loaded metals) rapidly attain the quasi-stationary state even under nonequilibrium conditions. This evolution of ensembles becomes possible when they consist of large-sized equivalent subsystems in which the processes occur on different time scales. For example, in our experiments, the smallest-sized defects are formed and relax rather rapidly, whereas the large-sized quasi-stationary defects undergo a slower evolution.

Most likely, the structure of the ensembles of the defects formed on the surface of loaded metals is thermodynamically optimized. This assumption is corroborated by their successful description in terms of the reversible aggregation of atoms and defects. In particular, it was proven that, according to the thermodynamic principle of symmetry [5, 8, 14], the reduced size distribution of defects [relationship (3)] has a universal form. At the same time, the experimental concentration of defects ($x_c \approx 0.05$) is correctly reproduced provided that the entropy of mixing of the ensemble of defects and atoms is maximum.

ACKNOWLEDGMENTS

This work was supported by the Volkswagen-Stiftung, grant no. 1/72 638.

REFERENCES

1. V. I. Vettegren, S. Sh. Rakhimov, and V. N. Svetlov, Fiz. Tverd. Tela (S.-Peterburg) **37** (4), 913 (1995) [Phys. Solid State **37**, 495 (1995)]; Fiz. Tverd. Tela (S.-Peterburg) **37** (12), 3635 (1995) [Phys. Solid State **37**, 2001 (1995)]; Fiz. Tverd. Tela (S.-Peterburg) **38** (2), 590 (1996) [Phys. Solid State **38**, 323 (1996)]; Fiz. Tverd. Tela (S.-Peterburg) **38** (4), 1142 (1996) [Phys. Solid State **38**, 632 (1996)]; Fiz. Tverd. Tela (S.-Peterburg) **39** (9), 1560 (1997) [Phys. Solid State **39**, 1389 (1997)]; Fiz. Tverd. Tela (S.-Peterburg) **40** (12), 2180 (1998) [Phys. Solid State **40**, 1977 (1998)].
2. V. I. Vettegren, V. L. Gilyarov, S. Sh. Rakhimov, and V. N. Svetlov, Fiz. Tverd. Tela (S.-Petersburg) **40** (4), 668 (1998) [Phys. Solid State **40**, 614 (1998)].
3. V. I. Vettegren, S. Sh. Rakhimov, and V. N. Svetlov, Proc. SPIE—Int. Soc. Opt. Eng. **3345**, 226 (1998).
4. V. I. Vettegren, S. Sh. Rakhimov, and V. N. Svetlov, Neorg. Mater. **35** (6), 756 (1999).
5. H. G. Kilian, R. Metzler, and B. Zink, J. Chem. Phys. **107** (20), 8697 (1997).
6. E. W. Montroll and M. F. Shlesinger, J. Stat. Phys. **32** (2), 209 (1983).
7. F. Reif, *Statistical and Thermal Physics* (McGraw-Hill, 1998).

8. H. G. Kilian, A. Rosa, H. Hild, and O. Marti, Rubber Chem. Technol. (in press).
9. V. Kraus, H. G. Kilian, and W. V. Soden, Prog. Colloid Polym. Sci. **90** (1), 27 (1992).
10. V. Kraus and H. G. Kilian, Makromol. Chem., Macromol. Symp. **76** (1), 113 (1993).
11. R. Haase, *Thermodynamik der Irreversiblen Prozesse* (Steinkopff, Darmstadt, 1963).
12. J. Meixner and H. G. Reik, in *Handbuch der Physik* (Springer-Verlag, Berlin, 1959), Vol. III/2.
13. R. Haase, *Thermodynamik der Mischphasen* (Springer-Verlag, Berlin, 1956).
14. P. J. Flory, *Principles of Polymer Chemistry* (Cornell Univ. Press, New York, 1953).
15. V. S. Kuksenko, V. S. Ryskin, V. I. Betechtin, and A. I. Slutsker, Int. J. Fract. Mech. **11** (4), 829 (1975).
16. V. A. Petrov, A. Ya. Bashkarev, and V. I. Vettegren, *Physical Principles for the Prediction of Fracture in Structural Materials* (Politekhnika, St. Petersburg, 1993).

Translated by O. Borovik-Romanova

Physics of the Solid State, Vol. 42, No. 11, 2000, pp. 2089–2092. Translated from Fizika Tverdogo Tela, Vol. 42, No. 11, 2000, pp. 2029–2032.

MAGNETISM AND FERROELECTRICITY

The Effect of Intercalation by 3*d* Elements on the Structure and Physical Properties of Titanium Diselenide M_xTiSe_2 (M = Cr, Fe, Co)

A. V. Kuranov, V. G. Pleshchev, A. N. Titov, N. V. Baranov, and L. S. Krasavin

Ural State University, pr. Lenina 51, Yekaterinburg, 620083 Russia
e-mail: Valery.Pleschov@usu.ru

Received January 13, 2000

Abstract—The dependences of the structural parameters and the electrical and magnetic properties of titanium diselenide, intercalated by chromium, iron, and cobalt on the intercalant concentration and temperature were studied experimentally. The possibility of the involvement of *d* electrons in the formation of interlayer covalent bonds in relation to the 3*d*-shell filling of intercalated ion is discussed. © *2000 MAIK "Nauka/Interperiodica".*

Titanium dichalcogenides have a hexagonal layered structure of the CdI_2 type, with the [X–Ti–X] blocks separated by appreciable spacings which far exceed the interatomic spacings within the blocks. This feature of the crystal structure allows for the introduction of a considerable amount of other atoms which are in the octahedral positions [1], between the blocks of the host lattice. Many articles are concerned with the study of these compounds, which are intercalated by alkaline metals and silver (see, for example, [2]). Investigations into the intercalation of titanium dichalcogenides by 3*d*-transition elements have recently been developed. This allows for the extra possibility of wide-ranging modification of their magnetic properties and the development of quasi-two-dimensional magnetic materials. The possibility of realizing a wide spectrum of magnetic states, from spin glass to magnetic ordering, has been shown for these materials, in particular, for titanium disulfide [3]. The M_xTiSe_2 compounds (M = V, Cr, Mn, Fe, Co, Ni, Cu) with a small intercalant content (x = 0.10, 0.20) are paramagnets, with the temperature dependence of the magnetic susceptibility obeying the Curie–Weiss law [4]. However, the most interesting magnetic properties are revealed at large intercalant concentrations. There is evidence that antiferromagnetic ordering is observed in Fe_xTiSe_2 [5] and that the temperature dependence of magnetic susceptibility passes through a maximum in $Co_{0.05}TiSe_2$ [6] with an increasing 3*d*-element concentration. Various observed properties could be associated with the electronic structure of the intercalant atoms (with a number of *d* electrons, the character of their distribution over *d* orbitals, etc.). In addition, the intercalation of *d* transition element atoms having directed orbitals can considerably affect the conduction electron state.

In this work, the behavior of the structural parameters, the electrical conductivity, the thermoelectric coefficient, and the magnetic susceptibility of titanium diselenides intercalated by chromium, iron, and cobalt has been investigated for a wide range of concentrations.

1. EXPERIMENTAL METHOD

Samples of the composition of Fe_xTiSe_2, Co_xTiSe_2, and Cr_xTiSe_2 ($0 < x \le 0.5$) were made by sintering preliminary prepared titanium diselenide and a consistent quantity of 3*d* metal (the purity of the components was 99.9%) by means of solid-phase reactions in evacuated quartz ampoules at a temperature of 900°C. Then, the samples were pressed into pellets and homogenized at the same temperature. At the last stage of preparation, the samples were quenched in water so that the same initial state of the samples would be provided. X-ray analysis (made using a DRON-3M diffractometer with CuK_α irradiation) did not reveal any inclusions of other phases in the samples prepared.

The investigation into the kinetic characteristics (conductivity and thermopower) was carried out on rectangular cold-pressed samples using the standard four-probe technique in the temperature range 80–400 K.

The magnetic susceptibility (χ) was measured by the Faraday method in the temperature range 80–400 K.

2. EXPERIMENTAL RESULTS AND DISCUSSION

The dependences of the unit-cell parameters on the concentration of intercalated atoms are presented in Fig. 1. The data from [4, 7] are also presented in this figure. These data, as can be seen, agree with ours. It is notable that the unit-cell parameters of all the systems investigated show a similar behavior; in the concentration range $0 < x < 0.25$, an increase in the intercalant

1063-7834/00/4211-2089$20.00

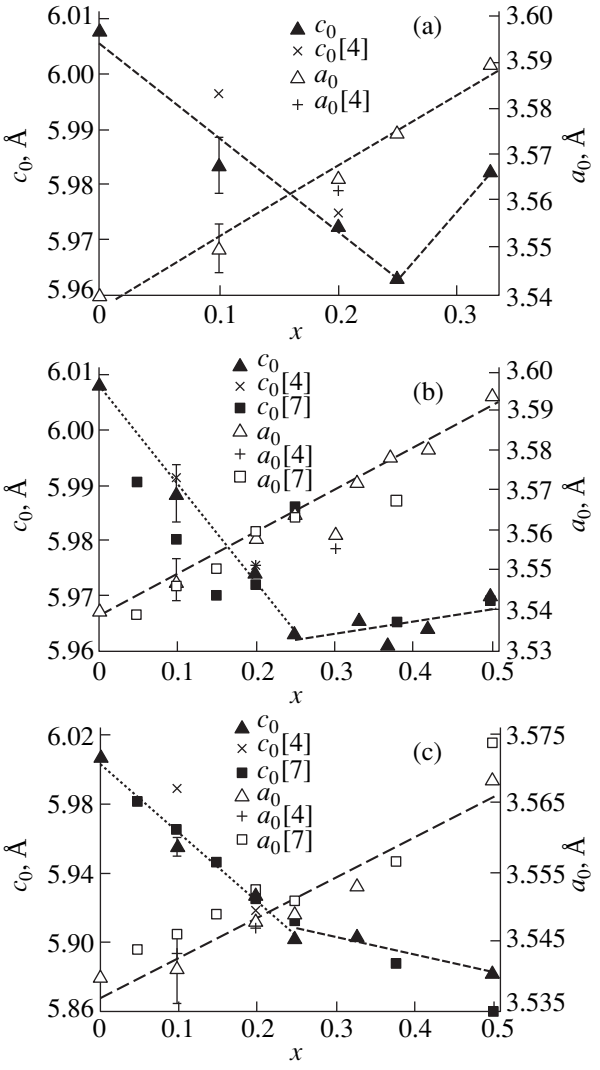

Fig. 1. Dependences of the crystal lattice parameters a_0 and c_0 on the intercalant content x for (a) Cr_xTiSe_2, (b) Fe_xTiSe_2, and (c) Co_xTiSe_2.

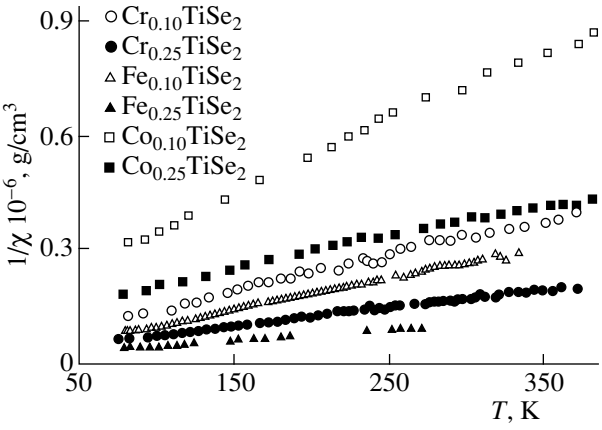

Fig. 2. Temperature dependences of the inverse magnetic susceptibility $1/\chi$ for M_xTiSe_2 (x = 0.10, 0.25).

concentration results in a monotonic increase in the a_0 parameters and a decrease in the c_0 parameters. Such behavior in the structural parameters radically differs from that observed in titanium diselenide intercalated by alkaline metals. As was shown in [2], the introduction of alkaline metals is accompanied by a simultaneous increase in both parameters. A decrease in the c_0 parameter in the systems intercalated by 3*d* metals was interpreted earlier as evidence of hybridization of the 3*d* states of intercalant atoms with the *p*–*d* states of the atoms in a $TiSe_2$ layer [4, 8]. Such bonding, as was shown for Ti_xTiTe_2 [9] and Fe_xTiTe_2 [10], results in the creation of localized electron states. It follows from Fig. 1 that, after the $M_{0.25}TiSe_2$ composition is reached, the parameter c_0 ceases to decrease (in Fe_xTiSe_2), decreases more slowly (in Co_xTiSe_2), or begins to increase (in Cr_xTiSe_2). As the intercalant atoms reside on sites separated by some interatomic spacings at $x < 0.25$, they can be considered as isolated from each other. On further intercalation, intercalant atoms find themselves in the neighboring sites and form clusters. Therefore, this turnover in the c_0 parameter dependence could be associated with a crossover from a dilute to a concentrated solid solution.

The "parent" $TiSe_2$ compound is a Pauli paramagnet [11] with a magnetic susceptibility magnitude of 5.2×10^{-7} cm^3/g at room temperature. The intercalation of 3*d* elements results in an increase in the magnetic susceptibility magnitude (Fig. 2). All the samples investigated in the temperature range studied (except for $Fe_{0.5}TiSe_2$ and $Co_{0.5}TiSe_2$) revealed a paramagnetic behavior with the magnetic-susceptibility temperature dependence close to the Curie law. The experimental dependences of $\chi(T)$ can be represented in the form

$$\chi(T) = C/(T - \Theta) + \chi_d + \chi_p, \qquad (1)$$

where C is the Curie constant; Θ is the paramagnetic Curie temperature; and χ_d and χ_p are the temperature-independent terms due to the diamagnetism of the filled electron shells and the paramagnetism of the free charge carriers, respectively. The preliminary estimate of the χ_d value was done in accordance with expression [12]

$$\chi = -Z_i(e^2/\hbar c)^2 N_A a_0^3/6\langle(r/a_0)\rangle^2, \qquad (2)$$

where Z_i is the atomic number of the element, a_0 is the Bohr radius, and r is the electron orbit radius.

From the subsequent approximation of the magnetic susceptibility temperature dependences, the values of the parameters entering Eq. (1) were determined and the effective magnetic moments of the intercalant atoms were calculated. The results of the calculations are presented in the table.

The values of the effective magnetic moments for Cr, Fe, and Co, calculated with regard to their different valence and spin states, are shown in Fig. 3 (curves); the dots are the experimentally determined values for

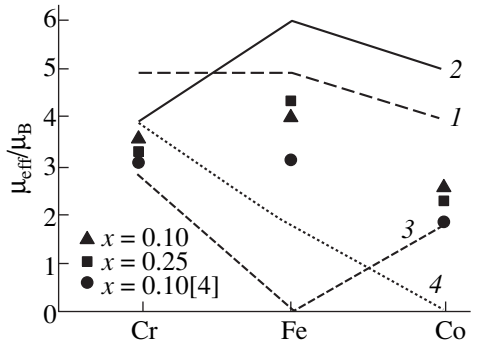

Fig. 3. Effective magnetic moments calculated for the free ions (lines), and the experimentally determined values (dots) for the three elements intercalated in the M_xTiSe_2 compounds. The keys (*1*, *2*) and (*3*, *4*) denote the high- and low-spin states, respectively, of the ions M^{2+} (*1*, *3*) and M^{3+} (*2*, *4*).

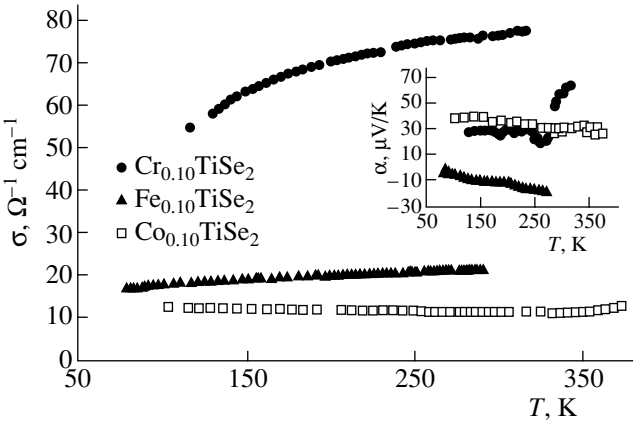

Fig. 4. Temperature dependence of the conductivity σ and thermoelectric coefficient α (inset) for $M_{0.10}TiSe_2$.

the intercalant ions in the Cr_xTiSe_2, Fe_xTiSe_2, and Co_xTiSe_2 systems for $x = 0.10$ and 0.25. A comparison of the data presented shows that the experimental data for iron and cobalt are the closest to the values for Fe^{2+} and Co^{2+}, while the trivalent state is more probable for chromium. This conclusion is also supported by the fact that the octahedral coordination is the most favorable to the Cr^{3+} ion, which is argued by the estimates of the stabilization energy for the differently coordinated chromium ions [13]. It can be seen that the experimentally determined effective magnetic moments of the chromium, iron, and cobalt atoms turned out to be less than the corresponding values of the spin moments of the Cr^{3+}, Fe^{2+}, and Co^{2+} ions.

The reason for this could be the possible hybridization considered above of the 3*d* states of intercalated atoms with states in the $TiSe_2$ layers. The data obtained show that the concentration dependences of the magnetic moments correlate with the c_0 parameter behavior for the systems studied; the values of μ_{eff} decrease with a contraction of the crystal lattice. The paramagnetic Curie temperatures for most of the samples investigated have a negative sign and are not large in magnitude. This is indicative of the presence of antiferromagnetic interactions, and therefore, antiferromagnetic ordering upon temperature lowering might be expected in these materials. Such ordering was observed in the Fe_xTiSe_2 system at $x \geq 0.25$ [5] and observed by us for $Fe_{0.5}TiSe_2$.

The as-grown titanium diselenide is a semimetal with respect to the electrical properties, with its conductivity being 900 Ω^{-1} cm^{-1} at room temperature [11]. The investigations of the electrical properties have shown that, for all the systems studied, a strong decrease in the electrical conductivity of the samples intercalated is observed in comparison to the electrical conductivity of $TiSe_2$. This takes place in spite of an increase in the concentration of the electrons added to the crystal lattice with the intercalant atoms (Fig. 4). The sign of the thermoelectric coefficient of most samples indicates a *p*-type conductivity, typical of the as-grown titanium diselenide. Such kinetic properties let us suggest that the electrons are bound in a potential well created by the intercalant atoms. The band structure of the compounds intercalated by the transition elements seems to undergo qualitative changes, and a band of localized states is formed. This results in an increase in the density of states at the Fermi level, which is indicated by an increase in the Pauli magnetic susceptibility with an increasing intercalant concentration (see table).

Effective magnetic moments (μ_{eff}), the paramagnetic Curie temperatures (Θ), and the Pauli magnetic susceptibility (χ_p) for the M_xTiSe_2 systems

x	μ_{eff}/μ_B	Θ, K	$\chi_p \times 10^6$, cm^3/g
	Cr_xTiSe_2		
0.10	3.6	–6.6	0.99
0.20	3.1	–7.4	1.15
0.25	3.2	–17.7	1.43
0.33	2.6	12.5	3.05
	Fe_xTiSe_2		
0.05	4.9	–5.6	0.71
0.10	4.0	3.1	0.95
0.25	4.2	–19.9	1.49
0.37	3.3	6.5	2.58
0.42	3.3	–5.1	1.29
	Co_xTiSe_2		
0.10	2.5	–34.6	0.75
0.20	2.4	–85.5	1.15
0.25	2.3	–66.1	1.09
0.33	1.6	–65.1	1.88

The results presented on the concentration dependence of the structural parameters and electrical and magnetic characteristics of the titanium diselenides intercalated by different transition metals show general tendencies for all the intercalant atoms investigated. These tendencies independently argue for the creation of the localized electronic states due to the intercalation.

The dissimilarities observed in the concentration dependences of the physical properties resulting from the intercalation by the different elements (the concentration dependence of the c_0 parameter at $x > 0.25$, the different relative change in the lattice parameters and in the effective magnetic moment) can be associated with the peculiarities in the structure of the 3*d* shells of the atoms intercalated. The most essential difference between them is that the Cr^{3+} ion has partially filled only three out of five *d* orbitals, whereas Fe^{2+} and Co^{2+} ions have electrons in a high-spin state in all *d* orbitals. The orbitals with a *z* component of the electron density are directed towards the ligands. Therefore, they are favorably disposed towards the formation of the molecular orbitals with the atoms in the environment. It might be expected that these electrons in particular are the most strongly hybridized and delocalized at the formation of the covalent bonds. In actual fact, at the intercalation by cobalt and iron, a decrease in the c_0 parameter continues up to significantly higher intercalant concentrations than in the samples intercalated by chromium. The relative decrease in the c_0 parameter is a maximum for the Co_xTiSe_2 system. It should be noted that, in contrast to Fe^{2+} and Co^{2+}, the Cr^{3+} ions are typically in a singlet ground state. Therefore, the chromium atoms are less favorably disposed towards hybridization, resulting in the energy lowering (due to the degeneracy lifting) and the distortion of the crystal lattice.

An increase in the *d* electron delocalization extent leads to a monotonic decrease in μ_{eff}. A value of 1.6 μ_B for $Co_{0.33}TiSe_2$ is consistent formally with one unpaired electron in one of the cobalt *d* orbitals. With the introduction of iron, the effective magnetic moment is equal to 4.9 μ_B for the composition with $x = 0.05$ and decreases to 3.3 μ_B at $x = 0.42$. In the intercalation by chromium, the involvement of *d* electrons in the orbital hybridization is to the smallest extent; this is in accordance with the smallest relative change in μ_{eff}.

Thus, as a result of this study, it has been shown that the intercalation of titanium dichalcogenides by 3*d* transition metals generally results in the localization of the conduction electrons. However, the extent of the localization and the material properties associated with it depend heavily on the filling of the impurity 3*d* shell and on the involvement of the *d* electrons in the covalent bonding.

ACKNOWLEDGMENTS

This work was supported by the Russian Foundation for Basic Research, project no. 98-03-32656, and the Ministry of Education of the Russian Federation, project no. 97-0-7.1-169.

REFERENCES

1. F. Raaum, F. Gronvold, A. Kjekshus, and H. Haraldsen, Z. Anorg. Chem. **317**, 91 (1962).
2. R. H. Friend, Rev. Chim. Miner. **19**, 467 (1982).
3. M. Inoue, M. Koyano, H. Negichi, *et al.*, Phys. Status Solidi B **132**, 295 (1985).
4. Y. Tazuke and T. Takeyama, J. Phys. Soc. Jpn. **66**, 827 (1997).
5. M. Buhannic, P. Colombet, M. Danot, and G. Calvarin, J. Solid State Chem. **69**, 280 (1987).
6. V. G. Pleshchev, A. N. Titov, and A. V. Kuranov, Fiz. Tverd. Tela (S.-Peterburg) **39**, 1618 (1997) [Phys. Solid State **39**, 1442 (1997)].
7. Y. Arnaod, M. Chevreton, A. Aheuanjinou, *et al.*, J. Solid State Chem. **17**, 9 (1976).
8. R. H. Friend and A. D. Yoffe, Adv. Phys. **36** (1), 1 (1987).
9. O. Yu. Pankratova, L. I. Grigor'eva, R. A. Zvinchuk, and A. V. Suvorov, Zh. Neorg. Khim. **38**, 410 (1993).
10. V. G. Pleshchev, A. N. Titov, S. G. Titova, and A. V. Kuranov, Neorg. Mater. **33**, 1333 (1997).
11. L. S. Krasavin, A. N. Titov, and V. M. Antropov, Fiz. Tverd. Tela (S.-Peterburg) **40**, 2165 (1998) [Phys. Solid State **40**, 1962 (1998)].
12. N. W. Ashcroft and N. D. Mermin, *Solid State Physics* (Holt, Rinehart and Winston, New York, 1976; Mir, Moscow, 1979), Vol. 2.
13. S. Krupička, *Physik der Ferrite und der verwandten magnetischen Oxide* (Academia, Prague, 1973; Mir, Moscow, 1976), Vol. 1.

Translated by N. Kovaleva

Physics of the Solid State, Vol. 42, No. 11, 2000, pp. 2093–2096. Translated from Fizika Tverdogo Tela, Vol. 42, No. 11, 2000, pp. 2033–2035.

MAGNETISM AND FERROELECTRICITY

Identity Period and Thermal Expansion Coefficient for Rare-Earth Hexaborides at Temperatures of 5–320 K

N. N. Sirota*, V. V. Novikov, and A. V. Novikov*****

**Moscow State University of Environmental Engineering, ul. Pryanishnikova 19, Moscow, 127550 Russia*

***Bryansk State Pedagogical University, Bezhitskaya ul. 14, Bryansk, 241036 Russia*

****Podol'e Technological University, Khmel'nitskiĭ, Ukraine*

Received January 24, 2000

Abstract—The temperature dependences of the lattice spacing and thermal expansion coefficient for five hexaborides MB_6 (M = Ce, Pr, Nd, Gd, and Tb) are experimentally investigated. © *2000 MAIK "Nauka/Interperiodica".*

In recent years, great interest has been expressed by researchers in the properties of lanthanide hexaborides at low temperatures. This is explained by a unique combination of the physical and physicochemical properties inherent in compounds of this series. Considerable attention has been given to the study of magnetic transformations in the majority of rare-earth hexaborides at liquid-helium temperatures [1–6]. However, the properties of their crystal lattices over a wide range of low temperatures have been not adequately investigated [7–13].

Lattice spacing a for rare-earth hexaborides

T, K	a, Å						
	CeB_6	PrB_6	NdB_6	EuB_6	GdB_6	TbB_6	DyB_6
4.2	4.13482	4.12727	4.12232	4.18061	4.00163	4.09646	4.09513
6	4.13491	4.12730	4.12240	4.18068	4.10162	4.09645	4.09505
8	4.13492	4.12735	4.12245	4.18075	4.10161	4.09644	4.09501
10	4.13493	4.12739	4.12249	4.18091	4.10160	4.09643	4.09499
12	4.13493	4.12741	4.12253	4.18105	4.10155	4.09641	4.09494
14	4.13493	4.12743	4.12253	4.18109	4.10148	4.09639	4.09491
16	4.13493	4.12744	4.12253	4.18113	4.10151	4.09641	4.09489
18	4.13493	4.12745	4.12255	4.1814	4.10156	4.09643	4.09489
20	4.13493	4.12746	4.12257	4.18116	4.10162	4.0946	4.09477
22						4.09644	4.09429
24						4.09642	4.09411
26						4.09640	4.09372
28						4.09640	4.09296
30	4.13499	4.12750	4.12260	4.181119	4.10171	4.09643	4.09290
32						4.09648	4.09290
34						4.09655	4.09320
40	4.13505	4.12756	4.12262	4.18125	4.10181	4.09676	4.09332
60	4.13522	4.12771	4.12283	4.18139	4.10210	4.09707	4.09374
80	4.13542	4.12786	4.12308	4.18148	4.10240	4.09756	4.09423
100	4.13562	4.12809	4.12334	4.18167	4.10276	4.09798	4.09453
140	4.13608	4.12875	4.12397	4.18212	4.10352	4.09882	4.09561
180	4.13671	4.12955	4.12465	4.18266	4.10430	4.09993	4.09646
220	4.13740	4.13039	4.12537	4.18325	4.10524	4.10060	4.09743
260	4.13817	4.13127	4.12610	4.18389	4.10625	4.10170	4.09840
300	4.13899	4.13220	4.13299	4.18456	4.10724	4.10274	4.09938
320	4.13943	4.13267	4.12754	4.18490	4.10789	4.10323	4.09992

1063-7834/00/4211-2093$20.00 © 2000 MAIK "Nauka/Interperiodica"

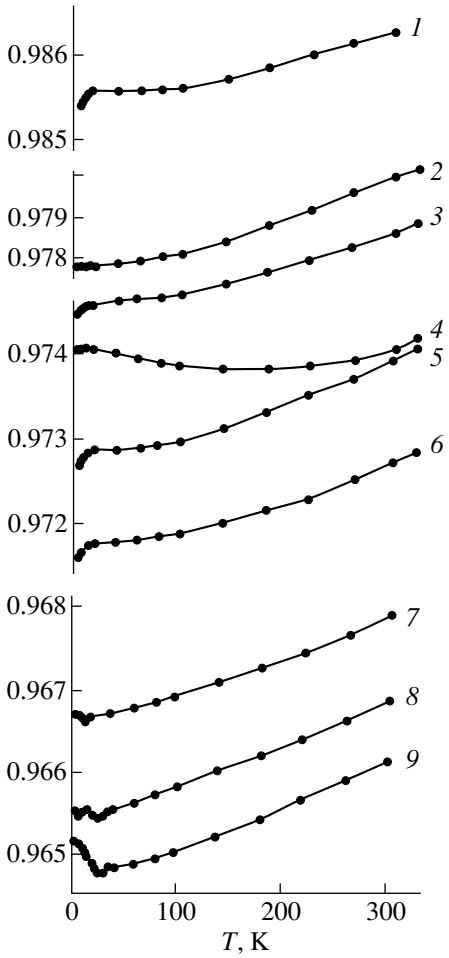

Fig. 1. Temperature dependences of the interplanar distance $d_{411}(T)$ for (*1*) europium, (*2*) lanthanum, (*3*) cerium, (*4*) samarium, (*5*) praseodymium, (*6*) neodymium, (*7*) gadolinium, (*8*) terbium, and (*9*) dysprosium.

This paper reports the results of the experimental investigation into the lattice spacing of five hexaborides MB_6 (M = Ce, Pr, Nd, Gd, and Tb) and the data on the LaB_6, SmB_6, EuB_6, and DyB_6 hexaborides studied in our earlier works [14–16].

The sample preparation procedure and the x-ray diffraction experiment were similar to those described earlier in [14]. The temperature dependences of the interplanar distance $d_{411}(T)$ for the studied hexaborides are displayed in Fig. 1. The lattice spacings are given in the table and in [14].

The temperature dependences of the linear thermal expansion coefficients α for hexaborides were determined by differentiation of the graphically smoothed curves $d_{411}(T)$ (Fig. 2).

As was noted earlier in [14–16], the dependences $\alpha(T)$ for rare-earth hexaborides exhibit a number of characteristic features. The magnetic ordering observed in the majority of the studied hexaborides leads to the appearance of pronounced anomalies in the $\alpha(T)$ curves.

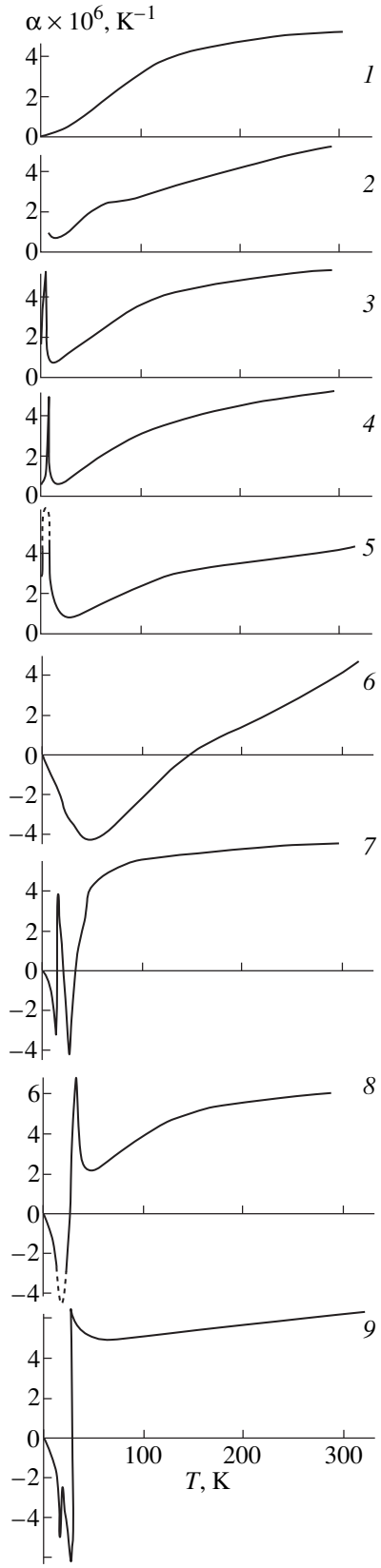

Fig. 2. Temperature dependences of the linear thermal expansion coefficient $\alpha(T)$ for (*1*) LaB_6, (*2*) CeB_6, (*3*) PrB_6, (*4*) NbB_6, (*5*) SmB_6, (*6*) EuB_6, (*7*) GdB_6, (*8*) TbB_6, and (*9*) DyB_6.

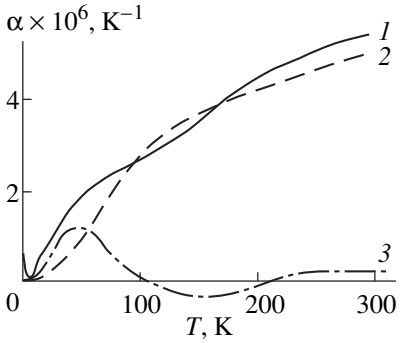

Fig. 3. Temperature dependences of (*1*) the thermal expansion coefficient $\alpha(T)$ for cerium hexaboride, (*2*) its regular (lattice) component $\alpha_L(T)$, and (*3*) the excess thermal expansion coefficient $\Delta\alpha(T) = \alpha(T) - \alpha_L(T)$.

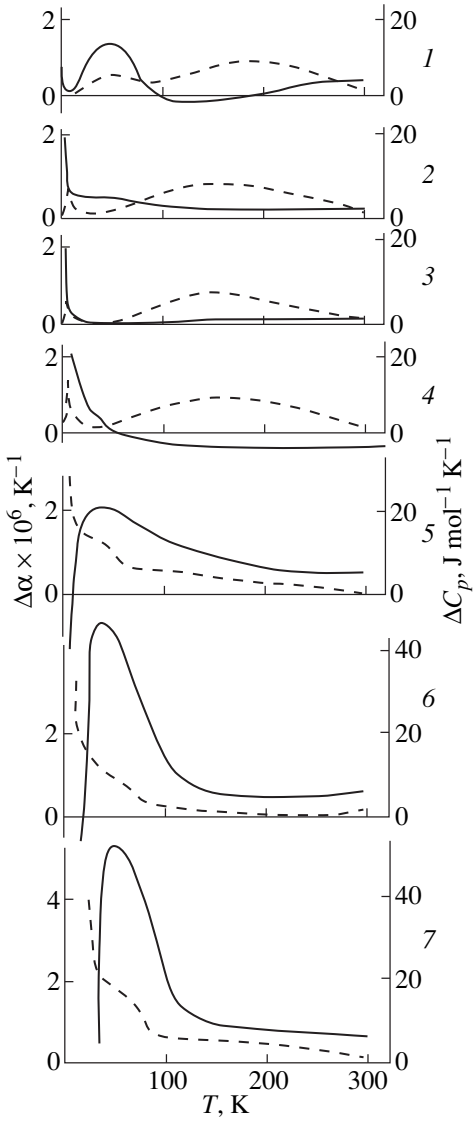

Fig. 4. Temperature dependences of the excess thermal expansion coefficient $\Delta\alpha(T)$ (solid lines) and excess heat capacity $\Delta C_p(T)$ (dashed lines) for hexaborides of (*1*) cerium, (*2*) praseodymium, (*3*) neodymium, (*4*) europium, (*5*) gadolinium, (*6*) terbium, and (*7*) dysprosium.

At high temperatures, the $\alpha(T)$ dependences virtually flatten out. The thermal expansion coefficient of hexaborides at $T = 300$ K increases only slightly with an increase in the atomic number of the metal. The origin of the negative thermal expansion coefficient for SmB_6, which was discussed in [10], calls for further analysis.

After separating out the lattice contribution to the thermal expansion coefficient, the deviations of the components from the thermal expansion coefficient manifest themselves more clearly. Since the crystal structures of lanthanum and rare-earth hexaborides are identical, the ratio between their lattice contributions to the $\alpha(T)$ quantities is equal to that of the corresponding lattice components of the heat capacity: $\alpha_L(LaB_6)/\alpha_L(MB_6) = C_L(LaB_6)/C_L(MB_6)$ [17]. By assuming that the thermal expansion coefficient of LaB_6 contains only the lattice component, i.e., $\alpha_L(LaB_6) = \alpha(LaB_6)$, and using the temperature dependences of the lattice components of the heat capacity [18], we determined the lattice components of the thermal expansion coefficient $\alpha_L(MB_6)$ for rare-earth hexaborides and its excess component relative to the lattice component: $\Delta\alpha(T) = \alpha(T) - \alpha_L(T)$. As an example, Fig. 3 depicts the dependences $\alpha(T)$, $\alpha_L(T)$, and $\Delta\alpha(T)$ for cerium hexaborides. The $\Delta\alpha(T)$ curves for all the studied hexaborides are displayed in Fig. 4. For comparison, this figure demonstrates the temperature dependences of the excess heat capacity for the studied hexaborides: $\Delta C(T) = C(T) - C_L(T)$ [18]. Judging from the curves $\Delta\alpha(T)$ and $\Delta C(T)$, the processes of splitting the energy levels responsible for the Schottky contribution to the heat capacity virtually do not affect the thermal expansion of rare-earth hexaborides. An appreciable value of $\Delta\alpha(T)$ near $T = 40$ K for CeB_6, a weak maximum of $\Delta\alpha(T)$ for PrB_6, and clear maxima for GdB_6, TbB_6, and DyB_6 correlate with the anomalies in the heat capacity and, most likely, result from the Jahn–Teller effect [11].

REFERENCES

1. Y. Peysson, C. Ayache, J. Rossat-Mignod, *et al.*, J. Phys. (Paris) **47** (1), 113 (1986).
2. K. Segawa, A. Tomita, K. Iwashita, *et al.*, J. Magn. Magn. Mater. **104–107**, 1233 (1992).
3. K. Iwashita, T. Matsumura, K. Segawa, and S. Kunii, Physica B (Amsterdam) **186–188**, 636 (1993).
4. M. Sera, S. Kobayashi, M. Hiroi, *et al.*, Phys. Rev. B **54** (8), 5207 (1996).
5. Degiorgi, E. Felder, H. R. Ott, *et al.*, Phys. Rev. Lett. **79** (25), 5134 (1997).
6. M. Sera, M. Hiroi, N. Kobayashi, and S. Kunii, J. Phys. Soc. Jpn. **67** (2), 629 (1998).
7. N. N. Zhuravlev, A. A. Stepanov, Yu. B. Paderno, and G. V. Samsonov, Kristallografiya **7** (4), 791 (1962) [Sov. Phys. Crystallogr. **7**, 639 (1962)].
8. H. G. Smith, G. Dolling, and T. Goto, Solid State Commun. **53** (1), 15 (1985).

9. S. Kunii, J. Phys. Soc. Jpn. **57** (1), 361 (1988).
10. P. A. Alekseev, E. S. Konovalova, V. N. Lazukov, *et al.*, Fiz. Tverd. Tela (Leningrad) **30** (7), 2024 (1988) [Sov. Phys. Solid State **30**, 1167 (1988)].
11. S. Nakamura, T. Goto, S. Kunii, *et al.*, J. Phys. Soc. Jpn. **63** (2), 623 (1994).
12. V. A. Trunov, A. L. Malyshev, D. Yu. Chernyshov, *et al.*, Fiz. Tverd. Tela (S.-Peterburg) **36** (9), 2687 (1994) [Phys. Solid State **36**, 1465 (1994)].
13. M. K. Blomberg, M. J. Merisalo, M. M. Korsukova, and V. N. Gurin, J. Alloys Compd. **217**, 123 (1995).
14. N. N. Sirota, V. V. Novikov, V. A. Vinokurov, and Yu. B. Paderno, Fiz. Tverd. Tela (S.-Peterburg) **40** (11), 2051 (1998) [Phys. Solid State **40**, 1856 (1998)].
15. N. N. Sirota, V. V. Novikov, and A. A. Sidorov, Fiz. Tverd. Tela (S.-Peterburg) **42** (2), 193 (2000) [Phys. Solid State **42**, 199 (2000)].
16. N. N. Sirota and V. V. Novikov, J. Mater. Process. Manuf. Sci. **7** (1), 111 (1998).
17. S. I. Novikov, *Thermal Expansion of Solids* (Nauka, Moscow, 1974).
18. V. V. Novikov, Fiz. Tverd. Tela (S.-Peterburg) **42**, 12 (2000) [Phys. Solid State **42** (2000) (in press)].

Translated by O. Borovik-Romanova

Physics of the Solid State, Vol. 42, No. 11, 2000, pp. 2097–2102. Translated from Fizika Tverdogo Tela, Vol. 42, No. 11, 2000, pp. 2036–2041.

MAGNETISM AND FERROELECTRICITY

Induced Magnetic Superstructure in the $FeBO_3$: Mg Weak Ferromagnet

A. A. Karaev*, B. Yu. Sokolov*, and Yu. M. Fedorov†**

**Tashkent State University, Universitetskaya ul. 95, Vuzgorodok, Tashkent, 700095 Uzbekistan*

***Kirenskiĭ Institute of Physics, Siberian Division, Russian Academy of Sciences, Akademgorodok, Krasnoyarsk, 660036 Russia*

Received February 18, 2000

Abstract—The domain structure of a $FeBO_3$: Mg single crystal was studied with a polarizing microscope. It was found that application of a magnetic field along the hard axis in the basal plane of this weak ferromagnet gives rise, within a certain field-strength interval, to a magnetic superstructure observed against the background of the macrodomain structure of the sample. The magnetic superstructure is visually represented as a quasi-periodic system of bands oriented perpendicular to the applied field, with an alternating magneto-optic image contrast along an axis coinciding with the magnetic-field direction. The absence of sharp changes in the contrast of the magnetic superstructure image along this axis is explained as being due to the smooth variation of the sublattice magnetic-moment azimuth with spatial coordinates. The results obtained are discussed within the parameters of the instability of a uniform magnetic state of a system in the random field induced by a magnetic field. © *2000 MAIK "Nauka/Interperiodica".*

The instability of a uniform magnetic state of a ferromagnet, caused by a weak random field which makes the state with nonuniform magnetization energetically favorable, was first discussed in [1]. That publication stimulated numerous experimental and theoretical investigations aimed at studying the effect of a random field on the magnetic state of a magnet. Those studies stimulated, in particular, the discovery of the existence of a microdomain structure in dilute uniaxial antiferromagnets through the use of neutron-diffraction and magnetic measurements [2, 3]. The ambiguous behavior of such a structure in a magnetic field with respect to the instant of its application (before cooling below the magnetic-transition temperature or after it) indicated that the forming magnetic states are metastable. A microdomain structure was also observed, in addition to the uniaxial, in easy-plane antiferromagnets containing extended or point defects [4]. It was shown that, depending on the correlation length of the random anisotropic fields, there may form both a structure with domains having a uniform antiferromagnetism vector and an amorphous magnetic structure with the antiferromagnetism vector varying continually in direction in the basal plane [4].

A particular place among easy-plane antiferromagnets is occupied by weak ferromagnets; their ferromagnetic moment permits one to control their magnetic structure through the application of a weak magnetic field, which makes it possible, in principle, to follow the effects associated with the presence of a random field (induced, for instance, by the randomness of the exchange or by local variations of the competing anisotropic interactions) fairly easily. To study random-field effects, we have carried out an experimental investigation of the influence of diamagnetic impurity ions on the stability of a uniform magnetic state of a weak ferromagnet in an external magnetic field.

1. SAMPLES AND EXPERIMENTAL TECHNIQUE

The study was performed on an $FeBO_3$ single crystal (space group D_{3d}^6), in which part of the Fe^{3+} ions was replaced by Mg diamagnetic ions. Magnetic inhomogeneities were revealed by magneto-optic visualization of the domain structure of the sample. The choice of the subject for the study and of the experimental technique used therein was motivated primarily by the fact that the behavior of the $FeBO_3$ domain structure had been thoroughly investigated and, therefore, one could carefully analyze the differences in the magnetic response between nominally pure (impurity-free) crystals and crystals diluted by a diamagnetic impurity. In addition to this, the magnetic, optical, and magneto-optic properties of iron borate are well known (see, e.g., [5]). $FeBO_3$ is a two-sublattice weak ferromagnet with a Néel temperature T_N = 348 K, below which a stable domain structure is observed to exist. $FeBO_3$ is practically transparent to visible light for wavelengths $\lambda <$ 500 nm, and its magneto-optic properties are governed primarily by the Faraday effect and magnetic linear dichroism [6].

† Deceased.

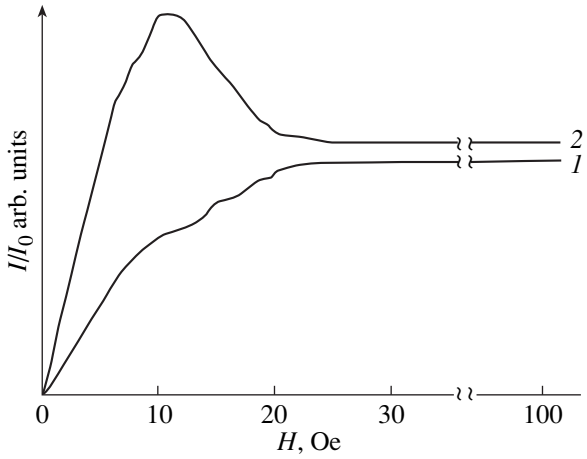

Fig. 1. Field dependences of a magneto-optic signal obtained at $T = 80$ K for different orientations of magnetization. (*1, 2*) Vector **H** is parallel and perpendicular to the domain wall direction.

The charge used to prepare the samples contained magnesium oxide and iron oxide in a weight ratio of ~0.1%. After synthesis, plates ~100 μm thick and ~3 mm wide were cut from the $FeBO_3$: Mg single crystals, such that the principal symmetry axis of the crystal, C_3, coincided with the normal to the sample plane. To relieve the mechanical stress and to make the impurity distribution over the volume more uniform, the samples thus prepared were annealed in air for 10 h at $T = 500$°C. Magnetic measurements showed that the magnesium impurity, compared with pure $FeBO_3$, did not noticeably affect the T_N of the samples.

The domain structure was studied using a polarizing microscope with a camera attachment. The measurements were carried out in transmission at the edge of the transparency window ($\lambda \approx 500$ nm), under normal light incidence, and in the geometry of nearly crossed axes of the polarizer–sample–analyzer system at 80 K (see below). In addition, the magnetic-field and orientation dependences of the intensity variation of light passed through the polarizer–sample–analyzer system, I/I_0 (where I_0 is the light intensity in zero magnetic field H and I is that at $H \neq 0$), were measured. The magnetic field was produced by two pairs of Helmholtz coils. The magnetization system permitted the orientation of the **H** vector along any direction in the basal plane of the sample at $|\mathbf{H}| = \text{const}$. The orientation of the sample, as well as the measurement of the I/I_0 ratio, was executed using the technique described in detail in [6].

2. EXPERIMENTAL RESULTS

An analysis of the field dependence of the magneto-optic signal $I(H)/I_0$, obtained at $T = 80$ K from regions of the sample comparable in size with its transverse dimensions, revealed magnetization curves of two types. The $I(H)/I_0$ dependences of the first kind (curve *1* in Fig. 1) reflect the well-known behavior of magnetic moments under increasing H, namely, an increase in the integrated ferromagnetic, **m**, and antiferromagnetic, **l**, moments through a decrease in their disorder. Curves of this kind were observed under a field application along the boundaries of the domain structure observed in the demagnetized state in the sample (Fig. 2a).

$I(H)/I_0$ dependences of the second type (curve *2* in Fig. 1) were observed under the application of a field perpendicular to the domain boundaries of the demagnetized sample. The pattern of the magneto-optic signal disagreed with the behavior of the moments **m** and **l** in a magnetic field; indeed, as H increases from zero, the I/I_0 ratio grows to a value in excess of its saturated level, to finally reach saturation at $H > 20$ Oe. As proceeds from our results, this type of $I(H)/I_0$ dependence is not observed for $T > 120$ K.

The observed anomalous pattern of the field dependence of the magneto-optic signal can be assigned to the formation, in the course of magnetization, of wedge-shaped magnetic domains, in which the rotation of the plane of polarization increases through the interference of birefringence and the Faraday effect [7]. However, this phenomenon takes place only when the direction of light propagation deviates considerably from the crystal optical axis, which was not the case in our experiment. Furthermore, it was earlier established that the $I(H)/I_0$ dependences of the second type were not observed in an identical geometry on nominally pure $FeBO_3$ crystals.

In order to study the behavior of the magnetic state of a $FeBO_3$: Mg crystal in the course of magnetization, visual representations of the evolution of the domain structure of the sample under study were analyzed. Figure 2a displays a fragment of the surface of a sample maintained at $T = 80$ K in zero magnetic field. The sample is seen to be broken down into domains with distinct boundaries. As field H was applied in the sample plane in the direction perpendicular to the domain walls, the crystal first crossed over to the single-domain structure, after which a quasi-periodic system of alternating bands with fuzzy boundaries and different contrast (Fig. 2b) was observed in fields corresponding to the anomaly in the $I(H)/I_0$ dependence. As the field was increased even more, the modulation of the magneto-optic image contrast on the sample surface disappeared. It was found that the observed band structure formed under a field applied close to the three directions in the crystal basal plane, which, judging from the domain wall orientation in the demagnetized state, are hard-magnetization axes of in-plane crystallographic anisotropy. Figure 3 illustrates the angular pattern of the above structure, relating the applied field strength to the **H** vector azimuth.

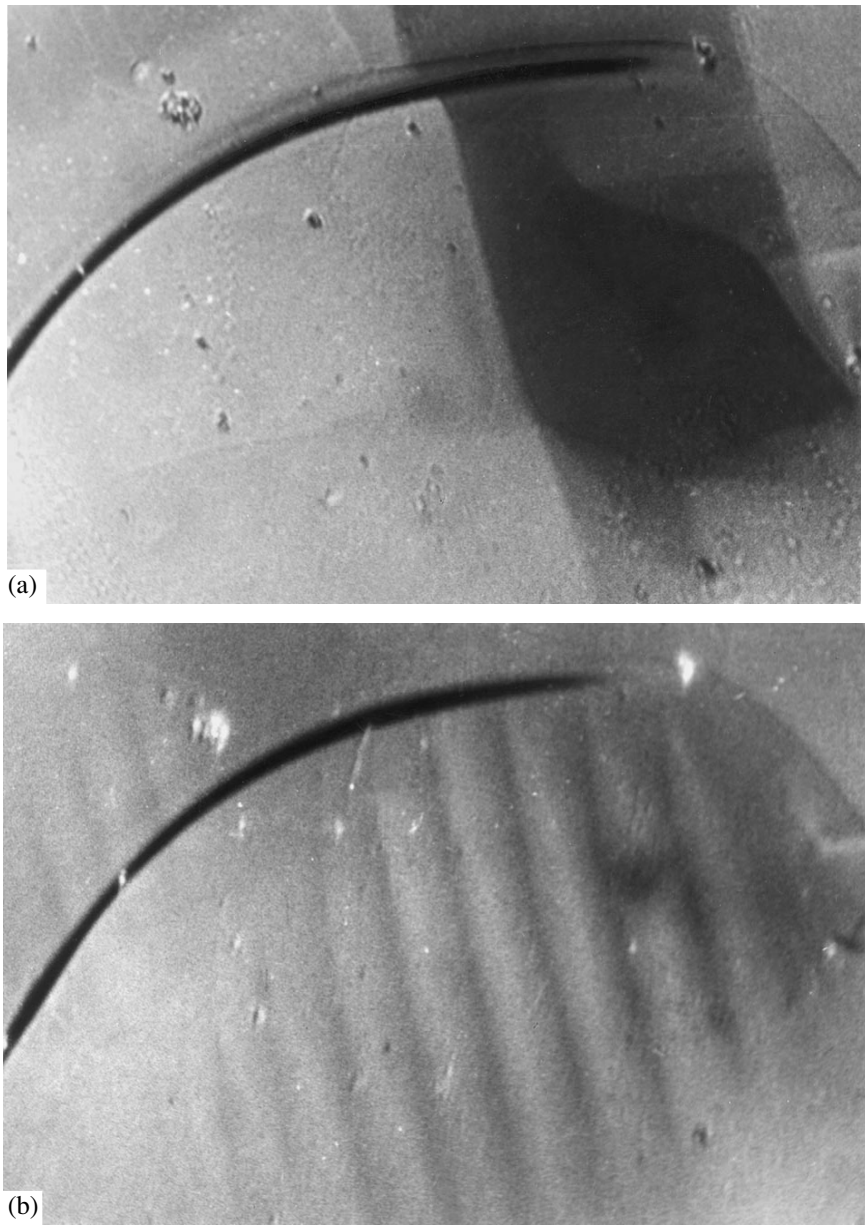

Fig. 2. Sample surface image obtained in polarized light at $T = 80$ K. H (Oe): (a) 0, (b) 12.

Studies showed that the average period of the quasi-periodic band structure with a varying magneto-optic contrast depends on H. Figure 4 presents a typical dependence of the spatial period d of the observed structure on the magnetic field applied along the normal to its wavefront. Of importance is the discontinuous change in period d in a field through a change in the number of bands fitting within the measured length, which is shown in Fig. 4 in the form of steps. In addition to this pinning effect, one observed a hysteresis in the values of d as the field H decreased (i.e., under reverse magnetization); in other words, the average period of the structure is smaller under a decreasing field than under an increasing field.

3. DISCUSSION OF THE RESULTS

One could conceive of three reasons for the formation of the observed system of bands with different magneto-optic contrasts. This structure may actually represent interference bands produced by a system of domain walls inclined to the crystal basal plane, a stripe-domain structure, or again an image of a spatially modulated (incommensurate) structure in the spin system of the crystal.

The first phenomenon is observed at large angles of light incidence on the sample surface [7], a geometry which, as already mentioned, was not used in our experiment. As for the possibility of the existence of a

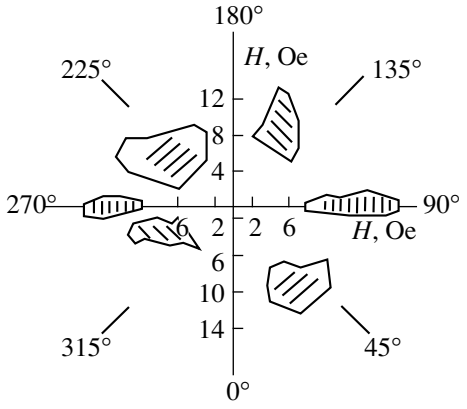

Fig. 3. Diagram illustrating the existence of contrast modulation in the sample surface image in the azimuth–applied-field plane. The hatched areas identify the regions where band structures with different magneto-optic contrast set in, and the orientation of the hatching corresponds to that of the wavefronts of the observed structure.

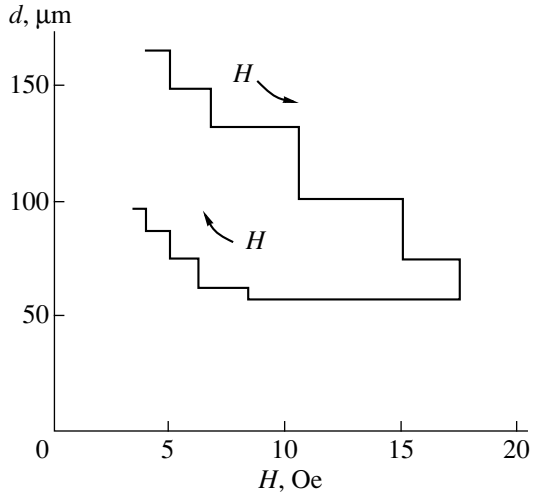

Fig. 4. Field dependence of the spatial period of the quasi-periodic structure of bands with different magneto-optic contrast.

stripe-domain structure, it can hold only if one assumes that impurity states in $FeBO_3$: Mg affect the hexagonal anisotropy constant to the extent that the ferromagnetism vector leaves the basal plane (in these conditions, in order to reduce the magnetostatic energy, the sample must break up into stripe domains). Furthermore, in a doped crystal, the sixth-order anisotropy constant must become noticeable in comparison with the second-order constant, which is unlikely, because the ions introduced into the crystal are diamagnetic. It is, in addition, known [8] that an increase of field H applied in the basal plane of such systems results in an increase in the period of the stripe structure; our experiment, however, revealed the reverse relationship (Fig. 4).

The absence of sharp boundaries in the image of the forming structure suggests that **m**, rather than being an alternating quantity, as is the case with a conventional domain structure, varies only in magnitude. This means that a spatially modulated magnetic state is induced in the $FeBO_3$: Mg, dilute, weak ferromagnet within a certain magnetic-field interval. Therefore, in order to analyze the results obtained, we employ the theory of the transition of a system from a uniform magnetic state to an incommensurate structure (see, e.g., [9, 10]).

It is well known [10, 11] that magnetic anisotropy in the easy plane in rhombohedral antiferromagnets gives rise to the formation of six directions in this plane, along which the uniform sublattice moments are in a stable state. These directions are turned through the angles $\pm\pi/3$ with respect to one another and are crystallographically equivalent. Thus, without any loss of generality, one can assume that the antiferromagnetism vector in an external field H is aligned with an axis close to one of these six directions. Assuming now that the angle β by which vector **l** is canted from the given axis, chosen here as the x axis, is small, the thermodynamic potential of the crystal can be written in a form similar to that obtained in [10]

$$F(\beta) = \int [1/2A\beta^2 + 1/4B\beta^4 + 1/2\alpha(\beta')^2 + 1/4\gamma(\beta'')^2 + mh\beta + 1/2\eta lh(\beta')^2 + \dots]dx, \quad (1)$$

where the single and double primes on β denote the corresponding derivative, and the external magnetic field **H** ∥ **x** is taken into account by adding two symmetry-allowed terms: the first of them, $mh\beta$ ($h = HM$, where M is the sublattice moment), is the Zeeman contribution to the crystal energy, while the second, $1/2\eta lh(\beta')^2$, is invariant under space and time inversion. Inclusion of this term into expansion in Eq. (1) merely renormalizes the coefficient of the first derivative and makes it dependent on the external field H.

Within this model, the transition to a nonuniform magnetic state takes place when the coefficient of the first derivative, $1/2(\alpha + \eta lh)$, is less than zero. In other words, for $\eta < 0$, a modulated state will be induced in the medium under an external field $h > \alpha/\eta l$. In an analysis of the effect of a field H on such a transition, the Zeeman contribution to the thermodynamic potential of the system was first taken into account in [12], where it was shown that a functional similar to Eq. (1) can be minimized using a function of the type

$$\beta(x) = \beta_0 + \xi \exp(ikx) + \text{c.c.},$$

where β_0 and $\xi$are parameters depending, in a complex way, on h and the coefficients A, B, α, γ, and η of the potential in Eq. (1), and the wave vector is defined as [10]

$$k = [|\alpha + \eta lh|/2\gamma]^{1/2}. \quad (2)$$

Expression (2) is a good description, at least qualitatively, of the experimental H dependence of the period of the structure. Indeed, as follows from Eq. (2), the period of the structure $d = 2\pi/k = 2\pi[2\gamma/|\alpha + \eta lh|]^{1/2}$ should decrease with an increasing magnetic field, exactly as was observed in the experiment (see Fig. 4).

Thus, in accordance with the above model, when a magnetic field, applied along the anisotropy axis in the basal plane of a $FeBO_3$: Mg crystal, reaches the critical level $h = \alpha/\eta l$, it induces a phase transition from a uniform to a modulated magnetic state. The axis along which the state is modulated is oriented along the **H** vector, and the magnetic superstructure can be conceived of as a ripple-on phase, where the azimuth of the local antiferromagnetism vector undergoes oscillations relative to a constant deviation angle from the anisotropy axis. The above assumptions suggest that there should be three directions along which the magnetic state of a crystal can be modulated, which is in accordance with the diagram in Fig. 3.

Note that the one-dimensional spatial orientation of vector **l** is an oversimplified case, and that, in actual fact, there is probably also modulation along the axis perpendicular to the basal plane of the crystal. However, because of the small thickness of the sample studied and the small amplitude of the oscillations, this relation will manifest itself in the form of an effective decrease in the antiferromagnetism vector compared with its magnitude in the uniform state.

Now consider the physical meaning of the gradient terms in potential Eq. (1). The introduction of Mg ions into the iron borate lattice gives rise to distortions associated with the difference between the ionic radii of Fe and Mg (and, possibly, with the difference between their charge states). This may produce a random anisotropy, which will induce local canting of vector **l**(**m**) from the directions determined by the crystallographic anisotropy. On the whole, the equilibrium magnetic structure of the crystal will be determined by the competition between the random anisotropy, on the one hand, and the crystallographic anisotropy and the dc magnetic field, on the other. A similar situation was considered for thin polycrystalline magnetic films [13], where the role of the random anisotropy was played by the crystallographic anisotropy in crystallites whose axes were randomly oriented with respect to one another. The factors governing the orientation were the induced anisotropy and the external field H. Assuming these interactions to be also essential for $FeBO_3$: Mg and using the results obtained in [13], one can recast the expression for the modulation period in the form

$$d = 2\pi[2J/(h - K)]^{1/2},$$

where J is the exchange constant and K is the crystallographic-anisotropy energy density. A similar relation can be obtained from Eq. (2) by setting $J = \gamma/\eta l$ and $K = \alpha/\eta l$. We readily see that the coefficients of expansion in Eq. (1) do not have a simple physical meaning and that they represent, rather, some combinations of the exchange and anisotropy constants.

In conclusion, we turn back to the question of the reason for the anomalous field dependence of the I/I_0 ratio (Fig. 1). Using Jones' matrix obtained for rhombohedral weak ferromagnets in [6], one can write a column matrix describing the polarization state of the light at the exit from the crystal. On multiplying it by a conjugate row matrix and making fairly cumbersome manipulations, we obtain the following relation (to within terms linear in magneto-optic coefficients) for the relative intensity of the light passing through a polarizer–sample–analyzer system:

$$I/I_0 = 1 + Q(\delta)\sin\varphi + R\cos 3(\varphi + \varphi_1) + S(\vartheta, \Psi)\sin 2(\varphi + \varphi_2), \quad (3)$$

where ϑ and Ψ are the azimuths of the polarizer and analyzer, respectively, reckoned from the direction of the C_2 axis in the basal plane of the crystal; φ is the azimuth of the ferromagnetism vector relative to the same axis; δ is the angle by which the direction of light propagation deviates from the optical axis; φ_1 and φ_2 are constants; $Q(\delta)$ and R are magneto-optic coefficients, which determine the Faraday rotation of the plane of light polarization induced by the components of vector **m**, transverse and longitudinal with respect to the light propagation direction; and $S(\vartheta, \Psi)$ is the magneto-optic coefficient accounting for the contribution of the magnetic linear dichroism to the magneto-optic rotation. When the direction of light propagation exactly coincides with the optical axis of the crystal ($Q = 0$ for $\delta = 0$), the magnitude of the magneto-optic signal is determined only by the last two terms in Eq. (3).

As is evident from the structure of the above relation, in the case of the field oriented along the hard-magnetization axis, the anomaly in the $I(H)/I_0$ dependence may be due to the fact that the vector **m** in the modulated state cants away from the direction of the applied field, which should increase the contribution of the magnetic linear dichroism to the magneto-optic signal. In saturating fields, vector **m** aligns with the field ($\varphi = \pi/2$), and the contribution due to the dichroism term in Eq. (3) decreases.

ACKNOWLEDGMENTS

This study was supported in part by INTAS, grant no. 97-0366.

REFERENCES

1. Y. Imry and S. Ma, Phys. Rev. Lett. **35** (7), 1399 (1975).
2. R. J. Birgeneau, H. Yoshizawa, R. A. Cowley, *et al.*, Phys. Rev. B: Condens. Matter **28** (3), 1438 (1983).
3. H. Ikeda, J. Phys. C: Solid State Phys. **16** (11), L1033 (1983).

4. E. B. Sonin, J. Phys. C: Solid State Phys. **13** (17), 3293 (1980).
5. G. A. Smolenskiĭ, V. V. Lemanov, G. M. Nedlin, M. P. Petrov, and R. V. Pisarev, *Physics of Magnetic Dielectrics* (Nauka, Leningrad, 1974).
6. Yu. M. Fedorov, A. A. Leksikov, and A. E. Aksenov, Fiz. Tverd. Tela (Leningrad) **26** (1), 220 (1984) [Sov. Phys. Solid State **26**, 128 (1984)].
7. J. Haisma and W. T. Stacy, J. Appl. Phys. **44** (7), 3367 (1973).
8. M. Yang and M. W. Muller, J. Appl. Phys. **45** (9), 4130 (1974).
9. A. Michelson, Phys. Rev. B: Solid State **16** (1), 577 (1977).
10. A. Michelson, Phys. Rev. B: Solid State **16** (1), 585 (1977).
11. E. A. Turov, *Physical Properties of Magnetically Ordered Crystals* (Akad. Nauk SSSR, Moscow, 1963; Academic, New York, 1965).
12. I. E. Dikshteĭn, F. V. Lisovskiĭ, E. G. Maksvetova, and V. V. Tarasenko, Fiz. Tverd. Tela (Leningrad) **25** (9), 2545 (1983) [Sov. Phys. Solid State **25**, 1465 (1983)].
13. H. Hoffman, Phys. Status Solidi B **6** (3), 733 (1964).

Translated by G. Skrebtsov

Physics of the Solid State, Vol. 42, No. 11, 2000, pp. 2103–2108. Translated from Fizika Tverdogo Tela, Vol. 42, No. 11, 2000, pp. 2042–2047.

MAGNETISM AND FERROELECTRICITY

Transport Parameters of Granular $La_{0.67}Ca_{0.33}MnO_3$ Films Grown on an *R*-Plane Sapphire

Yu. A. Boĭkov*, D. Erts, and T. Claeson*****

**Ioffe Physicotechnical Institute, Russian Academy of Sciences, Politekhnicheskaya ul. 26, St. Petersburg, 194021 Russia*

***Latvian University, Riga, LV 1586 Latvia*

****Physics Department, Chalmers Institute of Technology, Göteborg, S-41296 Sweden*

Received March 2, 2000

Abstract—Precisely (100)-oriented, 200-nm thick $La_{0.67}Ca_{0.33}MnO_3$ films have been grown by laser ablation on a sapphire (*R*-plane) substrate covered by a (100)$SrTiO_3$/(001)$Bi_2SrNb_2O_9$/(001)CeO_2 trilayer buffer. The azimuthal misorientation of crystal grains (50–300 nm) in the $La_{0.67}Ca_{0.33}MnO_3$ films decreased by about 40% as the condensation temperature was increased ered from 760 to 810°C. The lattice parameter of the grown manganate films was reduced to 3.81–3.82 Å by enriching them with oxygen. The maximum in the temperature dependence of the electrical resistivity of the $La_{0.67}Ca_{0.33}MnO_3$ films grown was shifted toward lower temperatures by 20–50 K relative to its position for bulk ceramic samples of a stoichiometric composition. The largest magnetoresistance (MR = 42% at H = 0.4 T) was found in $La_{0.67}Ca_{0.33}MnO_3$ films with a Mn^{4+} concentration on the order of 50% (T = 166 K). © *2000 MAIK "Nauka/Interperiodica".*

The process of ferromagnetic spin ordering in $La_{1-x}Ca_xMnO_3$ perovskite-like manganates is accompanied by an increase in the effective carrier mobility [1] and, as a consequence, by a drop in the electrical resistivity ρ [2–4]. The temperature of the ferromagnetic phase transition T_C depends on x involved in the chemical formula [5], the oxygen concentration [6], and the magnetic field [4, 6] and can be substantially increased under hydrostatic pressure [7]. The increase in T_C in a magnetic field accounts for the anomalously high magnetoresistance (MR) of epitaxial films and bulk ceramic samples of $La_{1-x}Ca_xMnO_3$ ($T < T_C$). The high values of the MR and of the temperature coefficient of resistivity β make $La_{1-x}Ca_xMnO_3$ thin films promising for use in magnetic-field detectors and sensors of IR detectors ($T < T_C$) [3].

The maximum temperature of the ferromagnetic phase transition in $La_{1-x}Ca_xMnO_3$ stoichiometric bulk ceramic samples and epitaxial films is reached at $x \approx 0.33$ (T_C = 250–270 K [4, 5]). The T_C can be increased up to 300 K by properly breaking the stoichiometry on the cation sublattice of $La_{1-x}Ca_xMnO_3$, for instance, by inducing a lanthanum deficiency [8] or by doping the solid solution with silver [9].

The magnetoresistance of $La_{1-x}Ca_xMnO_3$ films depends strongly on their microstructure which, in its turn, is governed to a considerable extent by the material used as the substrate [10].

To make perovskite-like manganate films attractive for practical use, they should be grown on substrates of the materials employed in microelectronics. In this work, we have studied the structure and electrophysical parameters of thin $La_{0.67}Ca_{0.33}MnO_3$ (LCMO) films grown by laser ablation on a sapphire substrate coated by a trilayer buffer heterostructure.

1. EXPERIMENT

An excimer laser (KrF, λ = 248 nm, τ = 30 ns) was used to ablate a stoichiometric LCMO target prepared by standard ceramic technology. The laser radiation density on the target surface was 1.5 J/cm^2. The oxygen pressure during LCMO film growth was maintained within the 0.48–0.50-mbar interval. The substrates chosen for the growth of LCMO films were polished $(1\underline{1}02)Al_2O_3$ plates (*R*-plane, 5 × 5 × 0.5 mm). To achieve the growth of a precisely oriented (both azimuthally and with respect to the normal to the substrate plane) LCMO film, a trilayer buffer (80 nm)$SrTiO_3$/(15 nm)$Bi_2SrNb_2O_9$/(80 nm)CeO_2 (STO/BSNO/CO) was grown on the sapphire surface by laser ablation. The LCMO films were grown at three different substrate temperatures (T_s), namely, 760, 780, and 810°C.

The structure and the phase composition of the films making up the LCMO/STO/BSNO/CO/Al_2O_3 multilayer heterostructure were studied with a Philips X'pert MRD x-ray diffractometer (ω/2θ and φ scans and rocking curves). The cell parameters of the grown manganate films were calculated from the x-ray data obtained. The lattice parameter along the normal to the substrate plane, c, was determined from an ω/2θ scan obtained in

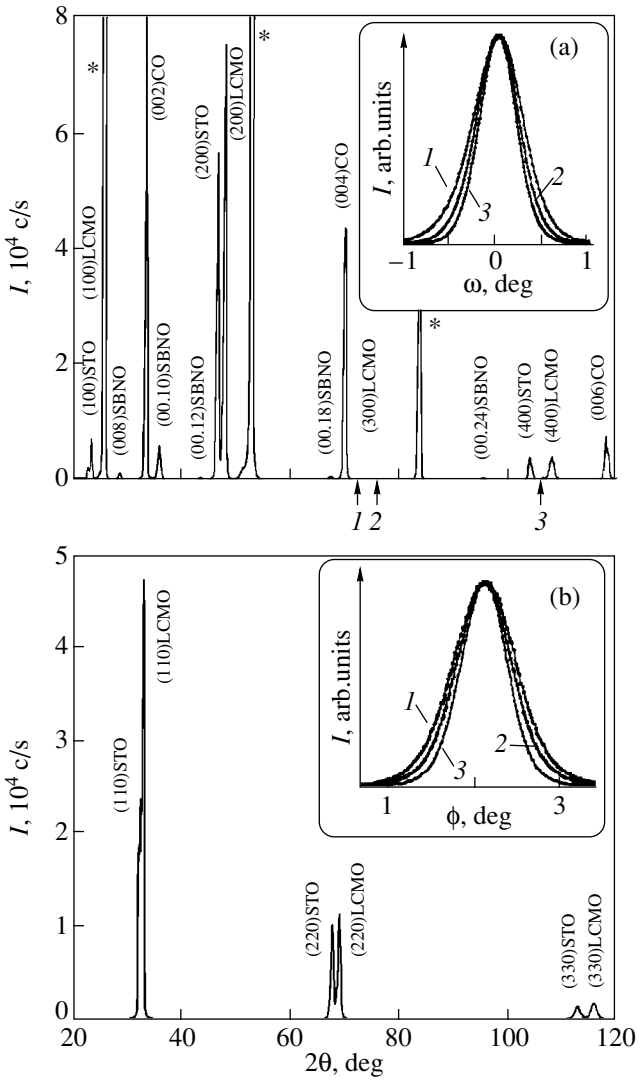

Fig. 1. (a) X-ray diffractogram (ω/2θ, CuK_α) for an LCMO/STO/BSNO/CO heterostructure grown on the $(1\underline{1}02)Al_2O_3$ surface. The diffractogram was obtained with the incident and reflected x-ray beams being in the plane normal to the substrate plane: (*) x-ray peaks from the substrate, (*1*) (300)STO peak, (*2*) (00.20)BSNO peak, and (*3*) (00.26)BSNO peak. The inset shows rocking curves obtained for the (200)LCMO x-ray reflection from manganate films grown at T_s = (°C): (*1*) 760, (*2*) 780, and (3) 810. (b) X-ray diffractogram (ω/2θ, CuK_α) for the same heterostructure obtained with the incident and reflected x-ray beams contained in a plane normal to (110)LCMO. The inset shows peaks in the x-ray ϕ scans obtained for the (110)LCMO reflection for manganate films grown at T_s = (°C): (*1*) 760, (*2*) 780, and (*3*) 810.

the conditions where the (100) plane in the LCMO film was perpendicular to the plane containing both the incident and reflected x-ray beams. To determine the lattice parameter *a* in the substrate plane, the ω/2θ x-ray scan was recorded in the conditions where the (110) plane in the grown LCMO film was normal to both the incident and reflected x-ray beams. The morphology of the grown manganate films was studied with a CamScan-IIIa atomic-force microscope.

The resistance *R* of the LCMO films was measured in the van der Pau geometry with a Hewlett-Packard 4263A LCR meter at a frequency of 100 Hz, both with and without the application of a 0.4-T magnetic field. The magnetic field was oriented perpendicular to the LCMO film plane. The electrical resistivity of the manganate films was calculated from the relation $\rho = (\pi d/\ln 2)R$ [11], where d = 200 nm is the LCMO film thickness. The four silver contacts (d_1 = 100 nm) at the corners of the square were thermally deposited from a tungsten boat.

2. EXPERIMENTAL RESULTS AND DISCUSSION

The fairly large difference between the lattice parameters of LCMO and Al_2O_3 complicates the growth of precisely oriented films of a perovskite-like manganate directly on the sapphire surface, thus making necessary the introduction of a thin buffer layer. The buffer permits one not only to reduce the elastic strain energy in the nucleus/substrate system, but also to suppress the chemical interaction between the aluminum in the sapphire and the calcium in the LCMO phase adsorbed on its surface. A thin (001)CO buffer layer was successfully used [12] to grow $YBa_2Cu_3O_{7-\delta}$ epitaxial films on the *R*-plane of the sapphire. Unfortunately, diffusive exchange of the components results in a drastic degradation of the microstructure and the parameters of an LCMO film grown directly on $(001)CO \parallel (1\bar{1}02)Al_2O_3$. Strontium titanate is more stable chemically with respect to LCMO than cerium dioxide, and (100)STO matches well in the lattice parameters to (100)LCMO. To preclude the formation of (110)STO || (001)CO-oriented grains in the bulk of the STO layer [13], a thin film of the BSNO layered ferroelectric was sandwiched between the strontium titanate and the cerium dioxide. The specific features of the growth of a thin (001)CO layer on $(1\underline{1}02)Al_2O_3$, of a (001)BSNO layer on (001)CO, and of a (100)STO layer on (001)BSNO were considered in [12, 13]. The inset to Fig. 4a schematically shows the four-layer heterostructure LCMO/STO/BSNO/CO grown on the sapphire *R*-plane.

2.1. The Structure of a Trilayer Buffer

As follows from x-ray diffraction data, the layers making up the STO/BSNO/CO trilayer buffer had a preferred orientation to the substrate surface, both in the azimuthal direction and relative to the substrate normal (see Figs. 1a, 1b and the inset to Fig. 2). We used the x-ray scans of Figs. 1 and 2 to obtain the following orientation relationships for the layers making up the trilayer buffer heterostructure STO/BSNO/CO grown

on $(1\bar{1}02)Al_2O_3$: (100)[010]STO ‖ (001)[110]BSNO ‖ (001)[110]CO.

The FWHM of the rocking curves for the (200)STO and (002)CO x-ray reflections from the STO/BSNO/CO buffer heterostructure was practically the same, 0.5°–0.6° (Fig. 2), and approximately twice that measured for the (024) reflection from the substrate. The rocking curve FWHM for the (00.10) x-ray reflection from the BSNO layer was approximately 1.0° (Fig. 2). The broadening of the rocking curve peak for the x-ray reflection from the layered ferroelectric compared to the corresponding figures for the STO and CO indicates degradation of the BSNO microstructure because of its small thickness and interaction with the cerium dioxide.

As follows from the x-ray data shown in the inset in Fig. 2, the BSNO layer was grown on the CO surface without any misorientation in the substrate plane, which indicates a good lattice match between (001)BSNO and (001)CO. The parameter of the CO cubic unit cell is 5.41 Å [13–15], and the constants *a* and *b* of the orthorhombic unit cell of BSNO are approximately equal to 5.51 Å. The STO layer grown was turned azimuthally through 45° relative to the BSNO (inset in Fig. 2).

Because of a considerable mismatch between the lattice parameters, the cerium dioxide layer grown on $(1\bar{1}02)Al_2O_3$ had a granular structure. As follows from the peak widths in the ϕ scans for the (111)CO x-ray reflection, the azimuthal misorientation of crystal grains in the CO layer is about 1.3°. It is the azimuthal grain misorientation in the CO layer that also accounts for the noticeable grain misorientation in the LCMO films grown on the STO/BSNO/CO trilayer buffer (see table).

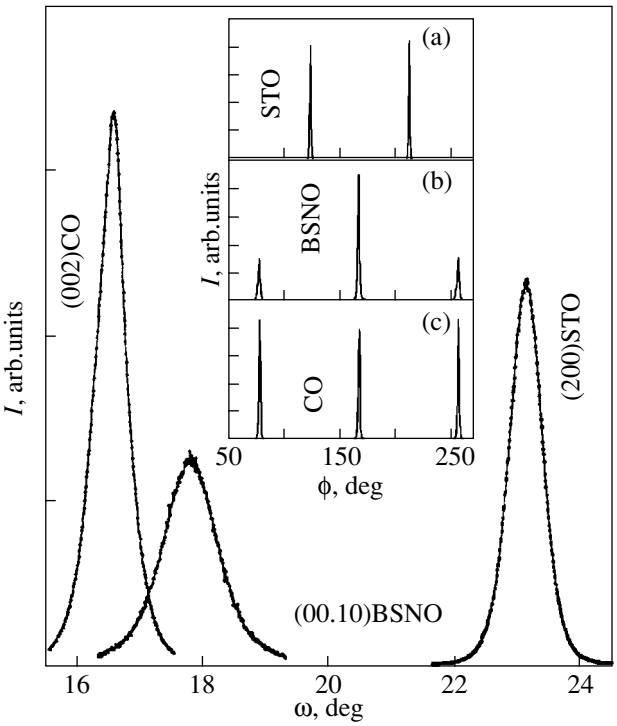

Fig. 2. Rocking curves (CuK_α) obtained for the (002)CO, (00.10)BSNO, and (200)STO x-ray reflections from an LCMO/STO/BSNO/CO heterostructure grown on $(1\bar{1}02)Al_2O_3$ at T_s = 780°C. The inset shows ϕ scans for (a) (111)STO, (b) (115)BSNO, and (c) (117)CO for the same heterostructure.

2.2. The Structure and Parameters of LCMO Films

The surface of the LCMO films grown on (100)STO ‖ (001)BSNO ‖ (001)CO ‖ $(1\underline{1}02)Al_2O_3$ was uneven because of grains 50–300 nm in size (Figs. 3a, 3b). The crystal grains in the LCMO film had a preferred orientation relative to the substrate surface, both azimuthally and with respect to the substrate normal, and (100)[010]LCMO ‖ (100)[010]STO (Figs. 1a, 1b). The preferred orientation of grains in the LCMO films did not change under variation of the substrate temperature T_s within the 760–810°C interval. As follows from the surface images of the LCMO films grown at the substrate temperatures of 760 and 810°C (Fig. 3), the density of grains rising above the surface of the manganate films by 20–30 nm decreased with increasing T_s. The atomic-force micrographs of the surface of the LCMO films grown at T_s = 810°C clearly exhibit growth steps (Fig. 3b).

The microstructure in the bulk of grains in LCMO films became more ordered with an increasing condensation temperature, which is evidenced by the decreasing width of the rocking curves measured for the (200)LCMO reflection (see table and the inset in Fig. 1a). The increase in T_s was also accompanied by a decrease in the azimuthal rotation angle of the crystal grains in the manganate film (see the inset of Fig. 1b and table).

Condensation temperatures and structural and electrophysical parameters of LCMO films

N	T_s, °C	*a*, Å	*c*, Å	Rocking curve FWHM, deg	ϕ-Scan peak FWHM, deg	a_{eff}, Å	T_ρ, K	T_{MR}, K	–*MR*, %
1	760	3.813	3.815	0.61	1.3	3.814	205	166	42
2	780	3.815	3.815	0.54	1.1	3.815	223	190	39
3	810	3.823	3.819	0.46	0.9	3.819	238	215	33

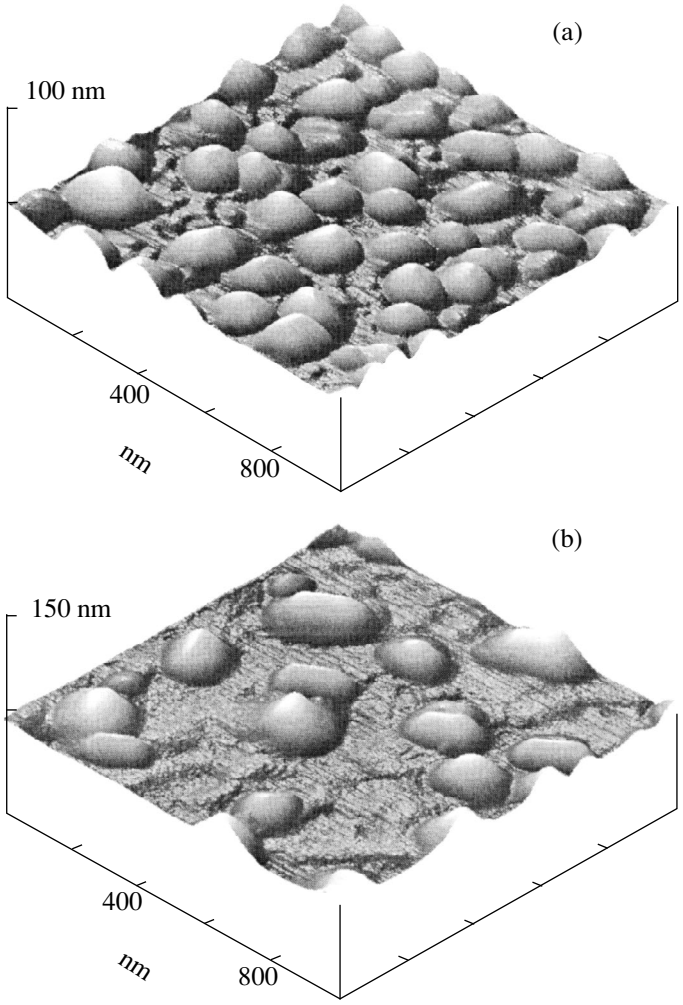

Fig. 3. Surface morphology of 200-nm thick LCMO films grown on STO/BSNO/CO/Al_2O_3 at T_s (°C): (a) 760 and (b) 810. The images were obtained with an atomic-force microscope. The surface of the film grown at T_s = 810°C exhibits characteristic growth steps with a height multiple of the unit cell parameter.

The lattice parameter of the $La_{1-x}Ca_xMnO_3$ solid solutions decreases approximately linearly with increasing the relative concentration of Mn^{4+} ions from zero (x = 0) to 100% (x = 1) [16]. This reflects the difference in the ionic radii between Mn^{4+} (r = 0.60 Å) and Mn^{3+} (r = 0.66 Å [17]). According to [6], the parameter of the pseudocubic unit cell of bulk ceramic LCMO samples of stoichiometric composition, in which approximately 33% of manganese ions are in the 4+ state, is 3.87 Å.

The parameters a and c for the LCMO films grown at the substrate temperatures of 760 and 780°C practically coincided (see table). The increase in the parameter a of the manganate film grown at 810°C compared with the parameter c is due to tensile stresses in the substrate plane. The mechanical stresses were generated in the LCMO films because of the difference in the temperature coefficients of expansion between the manganate film and the sapphire substrate and, partially, as a result of the positive lattice mismatch between STO and LCMO (the lattice parameter of strontium titanate is larger than that of LCMO).

The specific feature of LCMO films grown on the STO/BSNO/CO trilayer buffer is the substantially smaller effective unit cell parameter ($a_{eff} = V_c^{1/3}$, where $V_c = cxa^2$, see table) compared with the corresponding figures obtained on bulk ceramic samples. The low values of a_{eff} measured on the grown LCMO films argue for a high Mn^{4+} concentration.

A decrease in the lattice parameter compared with that of ceramic samples of a stoichiometric composition was also found to occur in LCMO films grown on single-crystal strontium-titanate plates [10]. The decrease in a_{eff} observed for the manganate films formed on single-crystal (100)STO substrates is, how-

ever, not as large as that in the LCMO films prepared in this work on STO/BSNO/CO/Al_2O_3.

The concentration of Mn^{4+} ions in perovskite-like manganates can be increased substantially (up to 35% [16]) by enriching the LCMO with oxygen above the stoichiometric level. The enrichment of $La_{1-x}Ca_xMnO_3$ solid solutions by oxygen is favored by the introduction of defects into the cation sublattice. The lattice parameter of La_xMnO_{3-y} films was found [8] to decrease systematically with an increasing lanthanum deficiency, which is assigned [8] to the growth of the relative oxygen concentration.

One of the most probable reasons for the oxygen enrichment of LCMO films grown on STO/BSNO/CO is the diffusion of lanthanum ions from the LCMO film into the strontium titanate layer on whose surface this film forms. The possibility of using Group-III elements to dope the (Ba,Sr)TiO_3 ceramic was pointed out in [18]. The diffusive exchange of the components between the manganate film and the trilayer buffer STO/BSNO/CO is favored by the high grain-boundary density in the layers making up the LCMO/STO/BSNO/CO/Al_2O_3 heterostructure. Doping strontium titanate with lanthanum should result in an increase in the oxygen vacancy concentration [18]. Oxygen-deficient STO films are characterized by large lattice-parameter values compared with those for stoichiometric STO single crystals (a = 3.905 Å [15]). The unit-cell parameters of the STO layer in the buffer heterostructure measured in the substrate plane and along its normal practically coincided and varied from 3.911 to 3.914 Å.

The temperature dependences of the electrical resistivity ρ of the LCMO films studied exhibit a clearly pronounced maximum (Fig. 4a). The temperature of the maximum in ρ, T_ρ, increased with increasing T_s (see table). The maximum in the ρ(T) curve shifted by 3–5 K toward higher temperatures when the resistance of the LCMO film was measured in a magnetic field of 0.4 T (Fig. 4a). The maximum in the temperature dependence of ρ for LCMO films grown on STO/BSNO/CO/Al_2O_3 was shifted considerably (by 20–50 K) to lower temperatures compared to its position on the corresponding curves for bulk ceramic LCMO samples of a stoichiometric composition and for annealed films grown on (100)$LaAlO_3$ single-crystal substrates [4]. In bulk ceramic LCMO films with a close-to-stoichiometric composition, about one-third of the manganese ions reside in the Mn^{4+} charge state, and the films have the lowest values of ρ [16, 19]. The values of a_{eff} derived from the x-ray studies, combined with the available data [5, 16] on the dependence of the lattice parameter of the corresponding bulk ceramic samples on the Mn^{4+} concentration, lead to the conclusion that about 50% of the manganese ions in the LCMO films grown on STO/BSTO/CO/Al_2O_3 are in the 4+ charge state. The phase-transition temperature T_C of ceramic LCMO

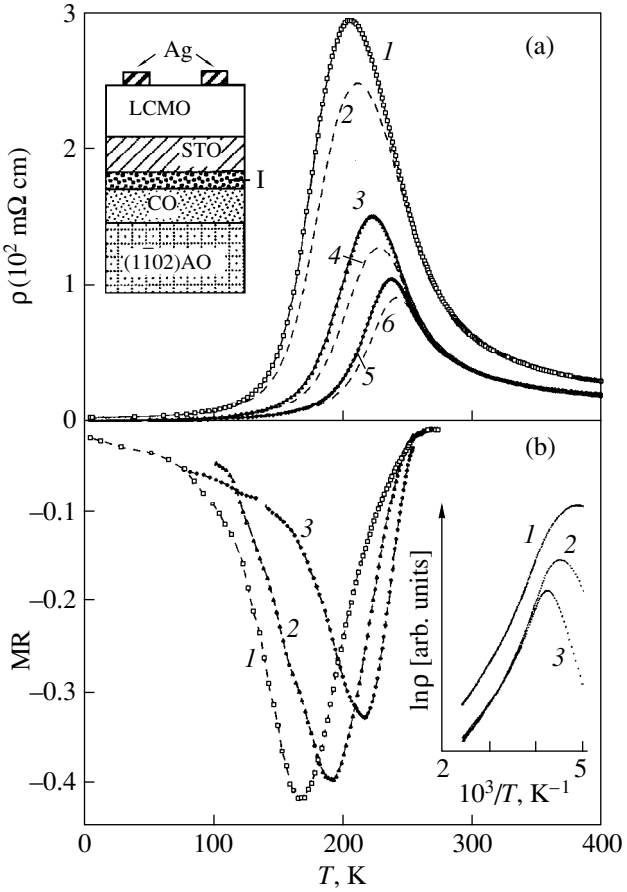

Fig. 4. (a) Temperature dependences of the electrical resistivity ρ of LCMO films grown on STO/BSNO/CO/Al_2O_3 at T_s (°C): (*1*, *2*) 760, (*3*, *4*) 780, and (*5*, *6*) 810. Curves *2*, *4*, and *6* were measured in a 0.4-T magnetic field. The inset shows a schematic of the four-layer heterostructure grown on the *R*-plane of a sapphire: (I) BSNO layer and (1$\bar{1}$02)AO refers to the sapphire substrate. (b) Temperature dependences of the magnetoresistance (MR) of LCMO films grown on STO/BSNO/CO/Al_2O_3 at T_s (°C): (*1*) 760, (*2*) 780, and (*3*) 810. The inset shows ln ρ(1/T) relations measured at temperatures close to T_ρ for the LCMO films grown on STO/BSNO/CO/Al_2O_3 at T_s (°C): (*1*) 760, (*2*) 780, and (*3*) 810.

samples decreased substantially (by ~40 K) as the Mn^{4+} concentration increased within the 30–50% interval [16]. The increase in the conductivity of LCMO films with increasing T_s is due to both an increase in the effective carrier concentration and the increase in the carrier mobility as a result of improving the film structure, in particular, of the decrease in the grain boundary density.

The exponential decrease of the electrical resistivity of LCMO films with increasing temperature for $T > T_\rho$ [20] was attributed to a manifestation of the polaron mechanism of conduction. The depletion of the regions adjoining the grain boundaries in a majority of the carriers because of a deviation from stoichiometry can also lead to an exponential growth of the film resistivity

with decreasing temperature [10]. The temperature dependences of the grown LCMO films measured at temperatures from T_ρ to 300 K could be well matched by the relation $\ln\rho \sim E_A/kT$, where k is the Boltzmann constant. The values of the activation energy E_A derived for LCMO films from the slope of the $\ln\rho(1/T)$ plot (see inset in Fig. 4b) were only weakly dependent on T_s and varied from 120 to 130 meV.

For the LCMO films, the maximum magnetoresistance (in absolute magnitude) $MR = [\rho(H = 0.4\ \text{T}) - \rho(H = 0\ \text{T})]/\rho(H = 0.4\ \text{T})$ was observed at a temperature T_{MR} lower than T_ρ by 20–40 K (see table). The difference $T_\rho - T_{MR}$ increased with decreasing T_s. The peak in the $MR(T)$ dependence for the LCMO films grown on STO/BSNO/CO was considerably broader than that typically observed on stoichiometric LCMO films grown on a (100)$LaAlO_3$ substrate and annealed in oxygen [4]. The shift of the magnetoresistance peak toward lower temperatures and its fairly large width are accounted for by the coexistence in LCMO films of regions with ferromagnetic and antiferromagnetic spin ordering. The existence of phases with ferromagnetic and antiferromagnetic ordering in the bulk of $La_{1-x}Ca_xMnO_3$ ceramic samples with Mn^{4+} concentrations close to 50% was established in experiments with neutron diffraction [16].

Thus, LCMO films grown on the sapphire *R*-plane with an intermediate STO/BSNO/CO trilayer buffer had a polycrystalline structure. The crystal grains in the manganate films (50–300 nm) had a preferred orientation both azimuthally and relative to the normal to the substrate plane. Increasing the growth temperature of LCMO films favored improvement of the microstructure in the grain bulk and reduced the azimuthal grain misorientation. As T_s was lowered, an increase in the Mn^{4+} concentration brought about an increase in the electrical resistivity of the manganate films and the maximum in the $\rho(T)$ dependence shifted toward lower temperatures. The magnetoresistance peak for the LCMO films was observed at temperatures lower by 20–40 K than the maximum in the corresponding temperature dependences of the electrical resistivity. The fairly large MR measured in LCMO films at low temperatures is accounted for by the substantial misorientation of the spins on manganese ions in different regions of a film.

ACKNOWLEDGMENTS

This research was done within the framework of scientific cooperation between the Russian Academy of Sciences and the Royal Swedish Academy. This study was supported in part by the Russian Foundation for Basic Research, grant no. 98-02-18222, and the TFR 240-97-382 project.

REFERENCES

1. C. Zener, Phys. Rev. **82**, 403 (1951).
2. S. Jin, T. H. Tiefel, M. McCormack, *et al.*, Science **264**, 413 (1994).
3. A. Goyal, M. Rajeswari, R. Shreekala, *et al.*, Appl. Phys. Lett. **71**, 2535 (1997).
4. M. F. Hundley, M. Hawley, R. H. Heffner, *et al.*, Appl. Phys. Lett. **67**, 860 (1995).
5. G.-Q. Gong, C. Canedy, G. Xiao, *et al.*, Appl. Phys. Lett. **67**, 1783 (1995).
6. H. L. Ju, J. Gopalakrishnan, J. L. Peng, *et al.*, Phys. Rev. B: Condens. Matter **51**, 6143 (1995).
7. Y. Moritomo, A. Asamitsu, and Y. Tokura, Phys. Rev. B: Condens. Matter **51**, 16491 (1995).
8. A. Gupta, T. R. McGuire, P. R. Dancombe, *et al.*, Appl. Phys. Lett. **67**, 3494 (1995).
9. R. Shreekala, M. Rajeswari, S. P. Pai, *et al.*, Appl. Phys. Lett. **74**, 2857 (1999).
10. Yu. A. Boikov, D. Erts, and T. Claeson, submitted to Mater. Sci. Eng. B.
11. T. I. Kamins, J. Appl. Phys. **42** (11), 4357 (1971).
12. Yu. A. Boikov, T. Claeson, D. Erts, *et al.*, Phys. Rev. B: Condens. Matter **56**, 11312 (1997).
13. Yu. A. Boikov and Z. Ivanov, J. Alloys Compd. **251**, 193 (1997).
14. G. A. Smolenskiĭ, V. A. Bokov, V. A. Isupov, N. N. Kraĭnik, and R. E. Shur, *Ferroelectrics and Antiferroelectrics* (Nauka, Leningrad, 1971).
15. R. W. G. Wyckoff, *Crystal Structures* (Interscience, New York, 1964), Vol. 2, p. 394.
16. E. O. Wollan and W. C. Koehler, Phys. Rev. **100**, 545 (1955).
17. R. C. Weast, *Handbook of Chemistry and Physics* (CRC Press, Cleveland, 1974), p. F-198.
18. B. Huybrechts, K. Ishizaki, and M. Takata, J. Mater. Sci. **30**, 2463 (1995).
19. J. H. van Santen and G. H. Jonker, Physica (Amsterdam) **16**, 599 (1950).
20. M. Jaime, M. B. Salamon, K. Pettit, *et al.*, Appl. Phys. Lett. **68**, 1576 (1996).

Translated by G. Skrebtsov

Physics of the Solid State, Vol. 42, No. 11, 2000, pp. 2109–2112. Translated from Fizika Tverdogo Tela, Vol. 42, No. 11, 2000, pp. 2048–2051.

MAGNETISM AND FERROELECTRICITY

Effect of the Spin–Orbit Interaction of Ni^{2+} Ions with a Triplet Orbital Ground State on the Magnetostriction of $NiFe_{0.5}Cr_{1.5}O_4$ Ferrite

L. G. Antoshina, A. N. Goryaga, and R. R. Annaev

Moscow State University, Vorob'evy gory, Moscow, 119899 Russia

Received March 10, 2000

Abstract—The magnetization σ and the longitudinal ($\lambda_{\parallel}$) and transverse ($\lambda_{\perp}$) magnetostrictions of the $NiFe_{0.5}Cr_{1.5}O_4$ ferrite containing the tetrahedral ions Ni^{2+} with the triplet orbital ground state have been investigated for the first time at a temperature of 4.2 K in fields up to 55 kOe. It is revealed that the $NiFe_{0.5}Cr_{1.5}O_4$ ferrite exhibits an anomalously large magnetic anisotropy (H_c = 12.5 kOe) and magnetostrictions ($\lambda_{\parallel} \approx -870 \times 10^{-6}$ and $\lambda_{\perp} \approx 800 \times 10^{-6}$). In strong fields, the magnetostrictions $\lambda_{\parallel}$ and $\lambda_{\perp}$ are found to be anisotropic in character; i.e., the susceptibility $\Delta\lambda_{\parallel p} < 0$ and $\Delta\lambda_{\perp p} > 0$. The conclusion is drawn that the studied compound is characterized by two paraprocesses: one paraprocess in the *B* sublattice has an exchange nature, and the second process in the *A* sublattice is due to the spin–orbit interaction of Ni_A^{2+} ions. © *2000 MAIK "Nauka/Interperiodica".*

It is known that, among 3*d* ions, only ions whose ground state in the crystal field of cubic symmetry is the triplet orbital state (the effective orbital angular momentum **I** = 1) exhibit a strong spin–orbit interaction. In this case, the orbital angular momentum of the 3*d* ions is incompletely "frozen" by the crystal field, and the magnetic properties of these ions are determined by the total angular momentum **J**. Therefore, in magnetic compounds containing these 3*d* ions, the spin–orbit interaction at $T < T_C$ (where T_C is the Curie temperature) results in the ordering of the orbital angular momenta with respect to the ordered spin momenta. For spinel ferrites, this leads to a noncollinear magnetic ordering in the magnetic sublattice containing these 3*d* ions.

Consequently, in spinel ferrites, the application of a magnetic field should induce a strong paraprocess (true magnetization) without regard to the particular sublattice which is occupied by the 3*d* ions with the triplet orbital ground state. If the 3*d* ions in spinel ferrites occur in the sublattice responsible for the magnetic moment of the ferrite, the application of the magnetic field **H** should lead to an increase in the total magnetic moment $\mathbf{M}_\Sigma$ of the ferrite due to an increase in the projection $\mathbf{M}_\mathbf{J}$ onto the field direction. In the case when the 3*d* ions occupy the sublattice that is not responsible for the magnetic moment of the ferrite, the total magnetic moment $\mathbf{M}_\Sigma$ of the ferrite increases at the expense of a decrease in the projection $\mathbf{M}_\mathbf{J}$ onto the direction of the **H** field. We assume that this paraprocess should also be accompanied by a change in the dimensions of the spinel crystal lattice, i.e., by a substantial magnetostriction of the paraprocess λ_p. The data on the behavior of magnetostrictions of this paraprocess in spinel ferrites containing the above 3*d* ions are unavailable. In this respect, it was of interest to perform an experimental study which could corroborate this assumption. At the same time, only a complex investigation into the behavior of the longitudinal and transverse magnetostrictions and magnetization can solve the problem under consideration.

In this work, we investigated the magnetization and magnetostriction of the $NiFe_{0.5}Cr_{1.5}O_4$ ferrite. In this compound, the 3*d* ions (Ni_A^{2+}) with the triplet orbital ground state occupy the tetrahedral sublattice that is not responsible for the magnetic moment of the ferrite. With allowance made for the energy of the preferred occupation of particular crystallographic sites by ions, the cation distribution in the ferrite has the following form: $Ni_{0.5}^{2+}Fe_{0.5}^{3+}[Ni_{0.5}^{2+}Cr_{1.5}^{3+}]O_4$. We assume that the magnetic structure of this ferrite should be noncollinear in both the *B* sublattice (due to the Cr_B^{3+}–Cr_B^{3+} direct negative interionic exchange) and the *A* sublattice owing to the spin–orbit interaction between the Ni_A^{2+} ions.

The $NiFe_{0.5}Cr_{1.5}O_4$ ferrite sample was prepared by the ceramic technique. The first annealing was carried out at a temperature of 1000°C for 5 h, and the second annealing was performed at 1350°C for 6 h with a subsequent slow cooling. Both annealings were carried out in air. The x-ray diffraction analysis performed at room temperature revealed that the synthesized sample was a

1063-7834/00/4211-2109$20.00 © 2000 MAIK "Nauka/Interperiodica"

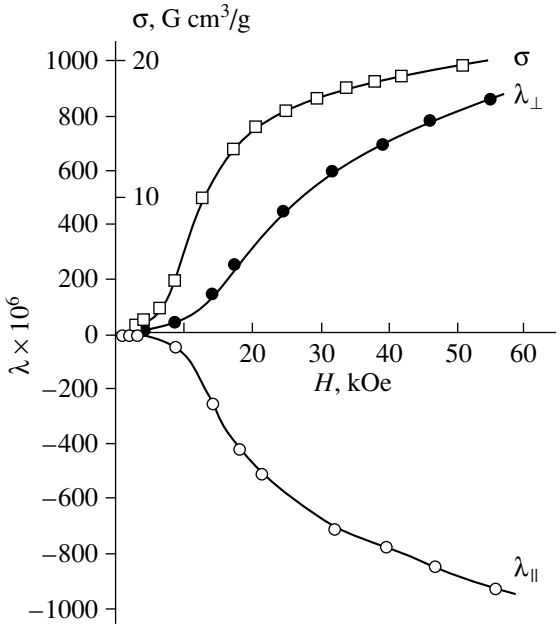

Fig. 1. Isotherms of the magnetization $\sigma(H)$ and the longitudinal $\lambda_{\parallel}(H)$ and transverse $\lambda_{\perp}(H)$ magnetostrictions for the $NiFe_{0.5}Cr_{1.5}O_4$ ferrite at $T = 4.2$ K.

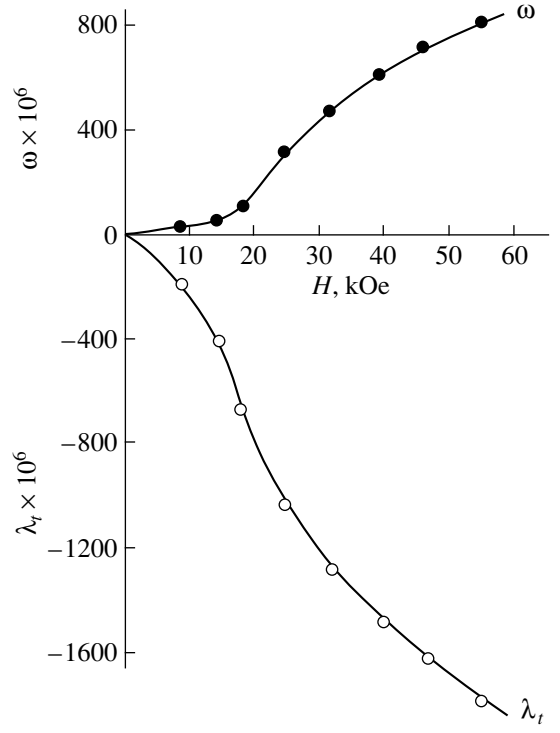

Fig. 2. Isotherms of the volume $\omega(H)$ and anisotropic $\lambda_t(H)$ magnetostrictions for the $NiFe_{0.5}Cr_{1.5}O_4$ ferrite at $T = 4.2$ K.

single-phase compound with the lattice parameter a = 8.32 Å. The magnetization was measured by the ballistic technique, and the magnetostriction was determined by the tensometric method. The measurements were carried out in a superconducting solenoid in magnetic fields up to 55 kOe at a temperature of 4.2 K.

It was found that the $NiFe_{0.5}Cr_{1.5}O_4$ ferrite at 4.2 K has a large coercive force (H_c = 12.5 kOe). This suggests that the ferrite containing the 3*d* ions with the triplet orbital ground state possesses a large magnetic anisotropy.

Figure 1 displays the isotherms $\sigma(H)$, $\lambda_{\parallel}(H)$, and $\lambda_{\perp}(H)$. It can be seen that no saturation is observed in all the isotherms. Furthermore, the magnetostriction of this ferrite is anomalously large. For example, in the magnetic field H = 50 kOe at 4.2 K, the longitudinal magnetostriction $\lambda_{\parallel} \approx -870 \times 10^{-6}$ and the transverse magnetostriction $\lambda_{\perp} \approx 800 \times 10^{-6}$. In strong fields, the $\lambda_{\parallel}$ and $\lambda_{\perp}$ magnetostrictions have an anisotropic character; i.e., the magnetostriction susceptibility $\Delta\lambda_{\parallel p} < 0$ and $\Delta\lambda_{\perp p} > 0$. It should be noted that, in the ferrite–chromite materials with a spinel structure free from 3*d* ions with the triplet orbital ground state, the magnetostriction, as a rule, is substantially less, and the magnetostriction susceptibilities $\Delta\lambda_{\parallel}$ and $\Delta\lambda_{\perp}$ in strong fields have an isotropic character.

Reasoning from our assumption that the magnetic structure in the *A* sublattice is noncollinear owing to the spin–orbit interaction between the Ni_A^{2+} ions, the ferrite under consideration should be characterized by two paraprocesses. The first paraprocess is associated with an increase in the projection of the magnetic moment $\mathbf{M_B}$ of the *B* sublattice at the expense of a decrease in the angle between the magnetic moments of the Cr_B^{3+} ions, and the other paraprocess is due to a decrease in the projection of the magnetic moment $\mathbf{M_A}$ of the *A* sublattice of the Ni_A^{2+} ions onto the direction of the field **H**. The first paraprocess has an exchange nature, and the second paraprocess shows a spin–orbit nature.

By using the formulas for the volume magnetostriction $\omega = \lambda_{\parallel + 2\lambda_{\perp}}$ and the anisotropic magnetostriction $\lambda_t = \lambda_{\parallel - \lambda_{\perp}}$, we constructed the isotherms $\omega(H)$ and $\lambda_t(H)$ at T = 4.2 K (Fig. 2). It turned out that the anisotropic magnetostriction λ_t drastically increases beginning with weak magnetic fields, whereas the volume magnetostriction ω remains virtually zero in fields less than 20 kOe and increases beginning only with the field H = 20 kOe ($\omega \approx 820 \times 10^{-6}$ at H = 55 kOe). It was found that the large magnetic anisotropy of the spinel ferrites containing the 3*d* ions with the triplet orbital ground state is accompanied by an anomalously large anisotropic magnetostriction λ_t (for example, $\lambda_t = -1800 \times 10^{-6}$ at H = 50 kOe).

For comparison, Fig. 3 shows the isotherms of the σ magnetization, the longitudinal $\lambda_{\parallel}$ and transverse $\lambda_{\perp}$ magnetostrictions at 80 K for the nickel ferrite–chromite $Fe^{3+}[Ni^{2+}Fe_{0.1}^{3+}Cr_{0.9}^{3+}]O_4$ (x = 0.9), in which

the Ni^{2+} ions are absent in the *A* sites. Since the coercive force H_c for this sample is equal to ≈0.2 kOe at 80 K, the magnetic fields up to 12 kOe are large enough for the study of the longitudinal $\lambda_{\parallel}$ and transverse $\lambda_{\perp}$ magnetostrictions. It can be seen that, for this sample, the $\lambda_{\parallel}$ magnetostriction is one order of magnitude less than that for the $NiFe_{0.5}Cr_{1.5}O_4$ sample and the paraprocess is attended by the negative isotropic magnetostriction; i.e., $\Delta\lambda_{\parallel p} < 0$ and $\Delta\lambda_{\perp p} < 0$. This paraprocess has an exchange nature and is brought about by the noncollinear magnetic structure in the *B* sublattice due to the strong negative direct exchange $Cr_B^{3+} - Cr_B^{3+}$. The calculated isotherms of the volume magnetostriction $\omega(H)$ and the anisotropic magnetostriction $\lambda_t(H)$ are also displayed in Fig. 3. At H = 12 kOe, $\omega \approx -52 \times 10^{-6}$ and $\lambda_t = -73 \times 10^{-6}$.

Hoppe and Hirst [1] theoretically proved that the ordering of both the spin momenta **S** and the orbital momenta **L** should be observed in the case when the ionic magnetic compounds contain the 3*d* ions which are involved in the superexchange interaction and whose ground state is the triplet orbital state. In turn, this leads to the formation of new ordered magnetic phases. These authors also demonstrated that the phase transitions associated with the ordering of the orbital momenta **L** should occur at temperatures below the temperature of the spin ordering. The conclusions made in [1] can be successfully applied to explain the anomalous behavior of the magnetic and magnetostriction properties of the $NiFe_{0.5}Cr_{1.5}O_4$ ferrite, because it contains the Ni_A^{2+} magnetic ions, which participate in the superexchange interaction and whose ground state in the crystal field of cubic symmetry is the triplet orbital state.

In the ferrite–chromite materials with a spinel structure, the paraprocess induced by a change in the degree of noncollinearity in the ferrite sublattices in strong fields should be accompanied by the isotropic susceptibilities $\Delta\lambda_{\parallel}$ and $\Delta\lambda_{\perp}$. Hence, it was of interest to elucidate why the anisotropic magnetostriction susceptibilities $\Delta\lambda_{\parallel p} < 0$ and $\Delta\lambda_{\perp p} > 0$ are observed in the strong fields for the $NiFe_{0.5}Cr_{1.5}O_4$ sample in which 3*d* ions with the triplet orbital ground state occupy the *A* sublattice that is not responsible for the total magnetic moment of this ferrite.

However, it should be taken into account that the degree of noncollinearity in the *B* sublattice can decrease in weak fields, because the negative interaction between the *A* and *B* sublattices favors this process. At the same time, the negative interaction between the *A* and *B* sublattices hinders an increase in the degree of noncollinearity in the *A* sublattice. Consequently, it can be inferred that, in the $NiFe_{0.5}Cr_{1.5}O_4$ ferrite, the paraprocess proceeds in the *B* sublattice in weak fields and in the *A* sublattice in stronger fields. Moreover, it should be remembered that, in the case when the 3*d* ion has the orbital angular momentum *l*, its displacement in response to the magnetic field should affect the arrangement of the O^{2-} anions in the crystal lattice due to the Stark effect (**E** × **l**). This gives grounds to assume

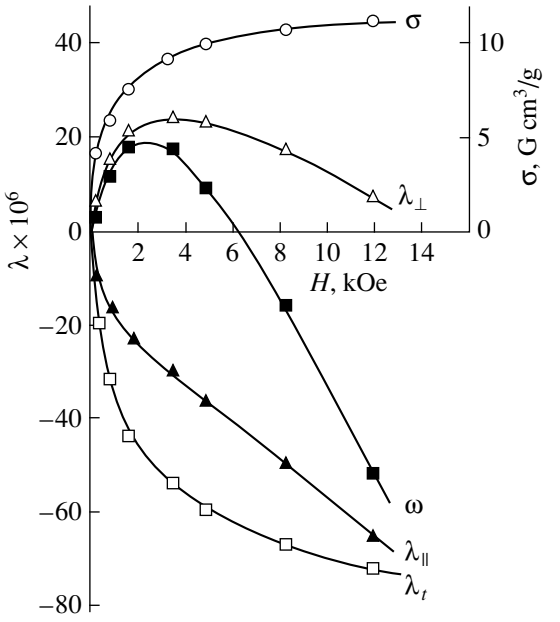

Fig. 3. Isotherms of the magnetization $\sigma(H)$ and the longitudinal $\lambda_{\parallel}(H)$, transverse $\lambda_{\perp}(H)$, volume $\omega(H)$, and anisotropic $\lambda_t(H)$ magnetostrictions for the $NiFe_{1.1}Cr_{0.9}O_4$ ferrite at T = 80 K.

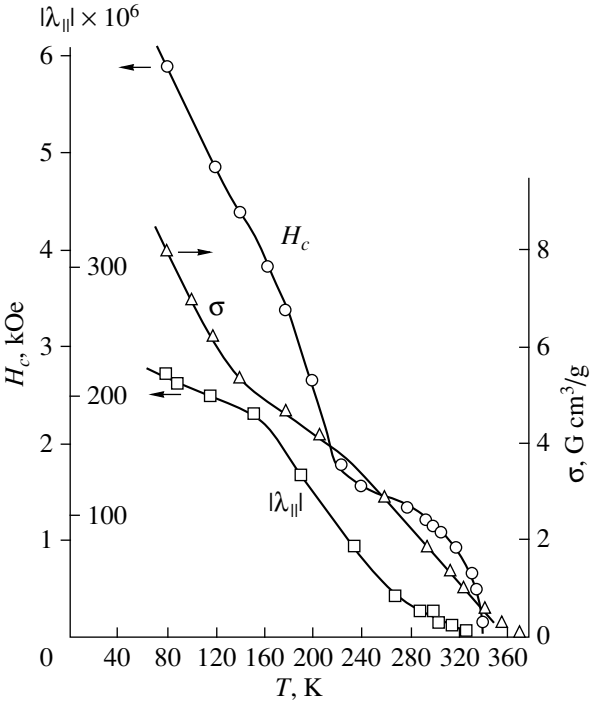

Fig. 4. Temperature dependences of the magnetization $\sigma(T)$ and the longitudinal magnetostriction $\lambda_{\parallel}(T)$ (in magnitude) at H = 12.7 kOe and the coercive force $H_c(T)$ for the $NiFe_{0.5}Cr_{1.5}O_4$ ferrite.

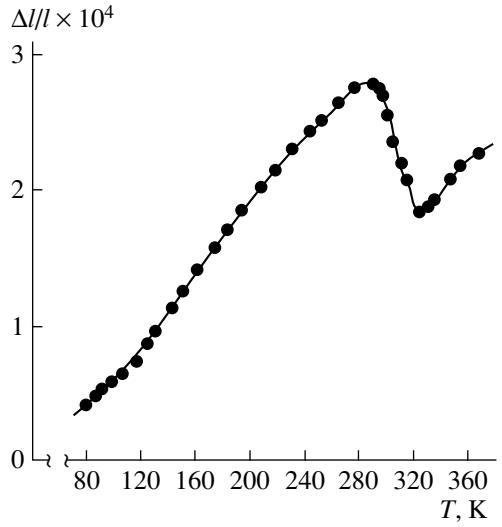

Fig. 5. Temperature dependence of the thermal linear expansion $\Delta l/l(T)$ for the $NiFe_{0.5}Cr_{1.5}O_4$ ferrite.

that the considerable magnetostriction and the anisotropic character of its susceptibilities $\Delta\lambda_{\parallel p} < 0$ and $\Delta\lambda_{\perp p} > 0$ in strong fields are governed by the displacement of the O^{2-} anions.

Our calculations of the energy of the effective spin–orbit interaction λ/S for the Ni^{2+} ion in the field of cubic symmetry led to $\lambda/S = (230 \pm 15)$ cm^{-1}, because $\lambda = -(230 \pm 15)$ cm^{-1}, $S = 1$, and $l = 1$ [2]. Therefore, this ferrite should undergo a crystallographic transition at temperatures below 300 K due to the spin–orbit interaction between the Ni^{2+} tetrahedral ions. It is known that the spin–orbit interaction between the Ni_A^{2+} ions in the $NiFe_{0.5}Cr_{1.5}O_4$ ferrite brings about a distortion of the crystal lattice with $c/a < 1$ at $T \approx 200$ K [3].

The temperature dependences $\sigma(T)$ and $\lambda_{\parallel}(T)$ (in magnitude) in the magnetic field $H = 12.7$ kOe and the dependence $H_c(T)$ for the $NiFe_{0.5}Cr_{1.5}O_4$ ferrite are displayed in Fig. 4. It can be seen that the magnetostriction $\lambda_{\parallel}$ and the coercive force H_c increase beginning with the temperature $T \leq 280$ K. This suggests that the crystal lattice distortions due to the spin–orbit interaction between the Ni^{2+} tetrahedral ions also should be observed at $T \leq 280$ K. Our investigation into the temperature dependence of the linear thermal expansion conclusively confirmed this fact (Fig. 5). As follows from the experimental data, the linear thermal expansion coefficient α changes its sign from positive to negative at $T \leq 320$ K and becomes positive again at $T \leq 280$ K. It is not improbable that the temperature range 280–320 K is the transition region. Thus, the experimental data obtained made it possible to assume that the transition temperature for the ferrite under consideration is equal to 300 ± 20 K. This result is in good agreement with the calculation of the effective spin–orbit interaction energy $\lambda 1S = (320 \pm 20)$ K for the Ni_A^{2+} ions.

REFERENCES

1. B. Hoppe and L. L. Hirst, J. Phys. C: Solid State Phys. **16**, 1919 (1983).
2. A. Abragam and B. Bleaney, *Electron Paramagnetic Resonance of Transition Ions* (Clarendon Press, Oxford, 1970; Mir, Moscow, 1972), Vol. 2.
3. T. R. McGuire and S. W. Greenwald, in *Solid State Physics in Electronics and Telecommunications*, Vol. 3: *Magnetic and Optical Properties* (Academic, New York, 1960), Part 1, p. 50.

Translated by O. Borovik-Romanova

Physics of the Solid State, Vol. 42, No. 11, 2000, pp. 2113–2115. Translated from Fizika Tverdogo Tela, Vol. 42, No. 11, 2000, pp. 2052–2053.

MAGNETISM AND FERROELECTRICITY

Colossal Room-Temperature Magnetoresistance of $La_{1/3}Nd_{1/3}Sr_{1/3}MnO_3$ Single Crystals

A. I. Abramovich and A. V. Michurin

Moscow State University, Vorob'evy gory, Moscow, 119899 Russia
e-mail: abram@ofef343.phys.msu.su

Received April 17, 2000

Abstract—Replacement of one half of the neodymium ions by lanthanum in $Nd_{2/3}Sr_{1/3}MnO_3$ is shown to result in a considerable increase in the Curie temperature. The single-crystal $La_{1/3}Nd_{1/3}Sr_{1/3}MnO_3$, whose Curie point lies at 315 K, has been found to exhibit a record-high magnetoresistance of 27% in a weak magnetic field of 8.4 kOe in the temperature range above room temperature. *© 2000 MAIK "Nauka/Interperiodica".*

Rare-earth manganites with a perovskite structure are presently a subject of intense investigation. These materials are characterized by a strong coupling of the electronic and spin subsystems with the crystal lattice, which gives rise to anomalies in the magnetic, electrical, optical, and elastic properties. The most unusual effect is certainly the colossal magnetoresistance (CMR) observed in manganites near the phase transition from the paramagnetic state to the ferromagnetic state. This phenomenon is of interest from a theoretical standpoint (the nature of the CMR still remains largely unclear) and for the potential of its practical application. The materials exhibiting CMR can be employed as highly sensitive transducers for magnetic-storage read heads. To become attractive for applications, the CMR in these materials should be observable (i) within a broad temperature range close to room temperature and (ii) in weak magnetic fields. However, the CMR in manganites is usually seen in strong magnetic fields of 6–13 T. The record-high CMR of 96% in a weak magnetic field of 0.67 T was observed in the $La_{1/3}Nd_{1/3}Ca_{1/3}MnO_3$ ceramic, but it was at 90 K [1]. $La_{0.7}Sr_{0.3}MnO_3$ is known to have the highest Curie temperature T_C = 370 K, but this compound has metallic conduction, and its magnetoresistance is considerably smaller than that of semiconductor manganites [2]. The materials exhibiting room-temperature CMR are few. These are, for instance, thin films of $La_{0.77}Sr_{0.23}MnO_3$ [3] and $La_{0.67}Sr_{0.33}MnO_3$ [4], whose magnetoresistance (MR) is 13% in a magnetic field of 11 kOe and 22% at 6 T, respectively. This justifies the search for materials exhibiting CMR near room temperature.

We studied earlier the $Nd_{2/3}Sr_{1/3}MnO_3$ ceramic [5] with the CMR observed within a broad temperature range from 80 to 280 K in weak magnetic fields (the T_C of this compound is 243 K). $Nd_{2/3}Sr_{1/3}MnO_3$ has a high conductivity; hence, exchange interaction through carriers is dominant in this compound. In this case, the Curie temperature is given by the expression

$$T_C \sim zt\nu, \tag{1}$$

where t is the transfer integral (the conduction-band width W is proportional to t), z is the coordination number of the magnetic ion (Mn in our case), and ν is the number of carriers per magnetic ion [6]. By substituting La for Nd in $Nd_{2/3}Sr_{1/3}MnO_3$, we intended to increase the Curie temperature using the following line of reasoning. In an undistorted perovskite structure, the Mn–O–Mn bond angle is known to be 180°. Replacement of the Nd ions by the smaller Sr ions results in a lattice distortion. One could thus anticipate that partial replacement of the Nd ions by the larger La ions would bring the bond angle closer to 180°, with a corresponding increase in the conduction-band width. Indeed, in the one-electron approximation, the width of the conduction band in manganites is proportional to $\cos^2\theta$ [7], and, hence, the transfer integral t increases, thus entailing an enhancement of the exchange through the current carriers. In accordance with expression (1), the Curie temperature also increases.

The $La_{1/3}Nd_{1/3}Sr_{1/3}MnO_3$ single crystal was grown by a crucibleless zone-melting technique and has an orthorhombic structure (space group *Pnma*). The initial ac magnetic susceptibility was measured with an F5063 ferrometer, and the resistance and magnetoresistance, by the conventional four-probe method.

Figure 1 presents the temperature dependence of the initial magnetic susceptibility $\chi(T)$ measured in an ac magnetic field (f = 8 kHz, $H_\sim$ = 1 Oe). The pattern of the $\chi(T)$ curve is seen to be typical of ferromagnets. The value of T_C, found as the temperature of the minimum in the $\partial\chi/\partial T(T)$ curve, turned out to be 315 K. The electrical resistivity ρ is observed to increase rapidly near

1063-7834/00/4211-2113$20.00

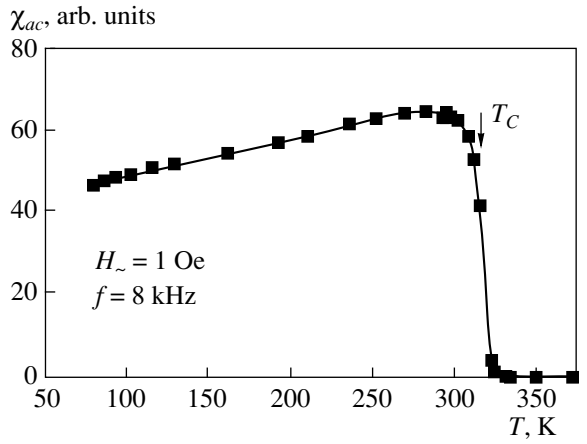

Fig. 1. Temperature dependence of the initial magnetic susceptibility.

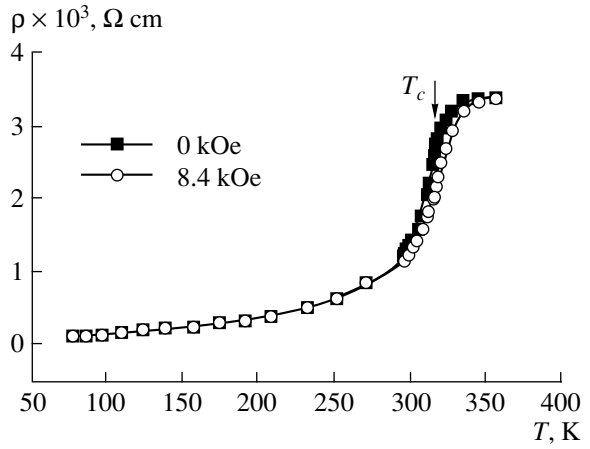

Fig. 2. Temperature dependence of the electrical resistivity.

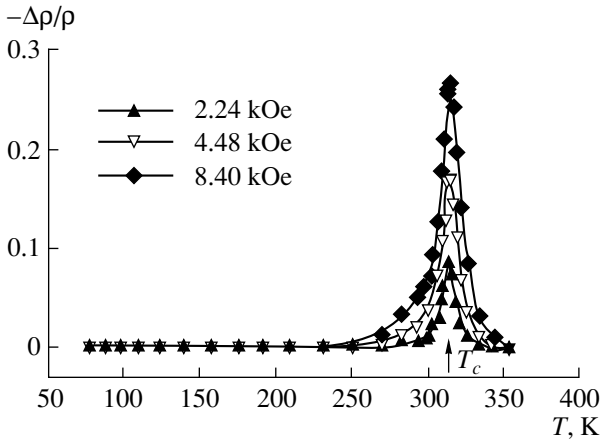

Fig. 3. Temperature dependence of the magnetoresistance in various magnetic fields.

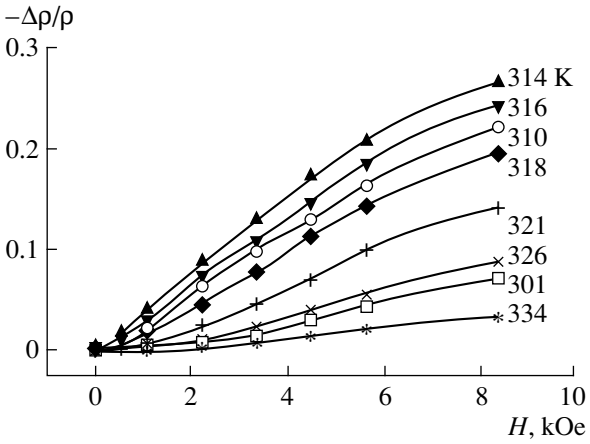

Fig. 4. Magnetoresistance isotherms in the region of the Curie point.

T_C, while application of a magnetic field brings about a decrease in ρ (Fig. 2). Figure 3 displays the temperature dependences of the MR in various magnetic fields. One readily sees a sharp maximum in the absolute value of the MR at T_C, which is characteristic of single crystals and epitaxial films. The negative MR [the MR was determined as $(\rho_H - \rho_0)/\rho_0$] reaches 27, 18, and 9% in magnetic fields of 8.4, 4.5, and 2.2 kOe, respectively. The MR isotherms remain far from saturation up to the maximum measurement field of 8.4 kOe (Fig. 4). The behavior of the electrical resistivity and magnetoresistance displayed in Figs. 2 and 3 is characteristic of a conducting magnetic two-phase state [8]. The $La_{1/3}Nd_{1/3}Sr_{1/3}MnO_3$ compound is a heavily Sr-doped antiferromagnetic semiconductor $La_{1/3}Nd_{2/3}MnO_3$, which exhibits metallic conduction below T_C (Fig. 2). It was shown [9] that there are two mechanisms by which magnetic impurities in manganites of this type with strong *p–d* exchange can affect the resistivity, namely, (i) scattering of carriers reducing their mobility and (ii) the formation of their band tail consisting of localized states. In the vicinity of T_C, the mobility of the carriers decreases strongly, and they undergo partial localization in the band tail. A magnetic field inhibits the magnetic-impurity scattering of the carriers, and they delocalize from the band tail, a process giving rise to the CMR.

ACKNOWLEDGMENTS

The authors are indebted to Yu.M. Balbashov for the preparation of the single crystal and for its characterization.

This study was supported by the Russian Foundation for Basic Research, grant no. 96-15-96429, NATO-HTECH LG 972942, and INTAS-97-open-30253.

REFERENCES

1. G. H. Rao, L. R. Sun, J. K. Liang, *et al.*, Appl. Phys. Lett. **69** (3), 424 (1996).
2. A. Urushibara, Y. Moritomo, T. Arima, *et al.*, Phys. Rev. B: Condens Matter **51**, 14103 (1995).
3. O. Yu. Gorbenko, R. V. Demin, A. R. Kaul', *et al.*, Fiz. Tverd. Tela (S-Peterburg) **40** (2), 290 (1998) [Phys. Solid State **40**, 263 (1998)].
4. J. C. Chen, S. C. Law, L. C. Tung, *et al.*, Phys. Rev. B: Condens Matter **60** (17), 12143 (1999).
5. A. I. Abramovich, L. I. Koroleva, A. V. Michurin, *et al.*, in *Proceedings of the II International Conference on Magnetoelectronics, Yekaterinburg, 2000*, p. 131.
6. É. L. Nagaev, *Physics of Magnetic Semiconductors* (Nauka, Moscow, 1979).
7. Y. Tokura and Y. Tomioka, J. Magn. Magn. Mater. **200** (1), 1 (1999).
8. É. L. Nagaev, Usp. Fiz. Nauk **166** (8), 833 (1996).
9. E. L. Nagaev, Phys. Lett. A **211** (5), 313 (1996).

Translated by G. Skrebtsov

Physics of the Solid State, Vol. 42, No. 11, 2000, pp. 2116–2122. Translated from Fizika Tverdogo Tela, Vol. 42, No. 11, 2000, pp. 2054–2059.

MAGNETISM AND FERROELECTRICITY

The Generalized Domain Structure Parameter for Magnetically Soft Materials and Its Application for Quantitative Description of a Family of Dynamic Hysteresis Loops

A. I. Kadochnikov and G. S. Korzunin

Institute of Metal Physics, Ural Division, Russian Academy of Sciences, ul. S. Kovalevskoĭ 18, Yekaterinburg, 620219 Russia
e-mail: korzunin@imp.uran.ru

Received January 12, 2000; in final form, April 21, 2000

Abstract—A generalized interpretation of the processes of dynamic magnetization reversal in magnetically soft electrically conducting materials is proposed. It can be used for obtaining a simple and quite accurate mathematical description for a family of dynamic hysteresis loops. *© 2000 MAIK "Nauka/Interperiodica".*

The dynamic hysteresis loop of a magnetically soft material can be treated as its main characteristic. It is better to speak of a family of such loops since they depend on the frequency and amplitude of the remagnetizing field (or magnetic induction), as well as on the magnetization reversal conditions, i.e., on the form of the time dependence of the external field or the magnetic induction flux. The reasons behind the difference between the dynamic and static hysteresis loops cannot be treated as definitely established, since certain facts cannot be explained within the framework of the traditional concepts [1]. In practice, one could disregard this circumstance if a satisfactory quantitative description of the loops and their dependence on the conditions under which the magnetization reversal is performed could be obtained at least by phenomenological methods. Such a description is extremely important for applied electrical engineering.

But is it possible in principle to find such a description? An affirmative answer to this question is unlikely, since it is well known that the process of magnetic reversal in ferromagnetic materials is quite complicated and a large number of reasonable assumptions have been put forth about the diverse possible mechanisms of retardation (relaxation) of this process. However, it will be shown below that a quite rational quantitative description for a family of hysteresis loops can nevertheless be obtained by adopting certain generalized assumptions concerning the magnetization reversal processes. One such assumption concerns eddy currents, while another pertains to a different type of phenomena that retard the magnetic reversal and were called the magnetic viscosity because of V.K. Arkad'ev [2]. As regards eddy currents, the basic reason behind the difficulties is quite obvious; it should be borne in mind that, in thin materials with a coarse domain structure, eddy currents are induced as a result of the motion of each individual domain wall, and the eddy current lines obtained as a result of their summation most likely have a configuration other than the simple one assumed in the classical theory of eddy currents. They may have a quite "intricate" form, which means that classical formulas for calculating eddy currents and their effect on the dynamic hysteresis loop do not always reflect the actual effects.

Let us examine how this circumstance can be taken into consideration. In real materials, the configuration of domain walls is by no means a regular pattern. Moreover, the motion of domain walls itself does not obey simple laws and may be quite diverse. For example, the mobility of walls may differ in value even for walls of the same type. However, statistical laws may come into play in a situation like this. For example, if a magnet is quite bulky and the domain walls are small in comparison, the configurations of eddy current lines will differ only insignificantly from those used in the classical computations of the eddy-current effect. In other words, the effect of the domain structure on eddy currents will be statistically insignificant. It can be asked whether some simple statistical law is also followed, at least approximately, in the case when the domain size is comparable with the thickness of the magnetic tape or strips used for constructing the magnetic cores of electrical devices.

An endeavor to establish such a regularity was made in [3]. This endeavor can be briefly described as follows. We proceed from the Pry–Bean model [4], which is a simple model, but the most characteristic, describing the domain structure and the movement of domain walls. On the one hand, this model corresponds to the

1063-7834/00/4211-2116$20.00

strongest manifestation of the "bendings" of the classical eddy current lines that are associated with the domain structure and "enhance" the integrated eddy-current effects. On the other hand, this model requires comparatively simple computations. It was shown in [5] that it can be used for calculating not only the energy losses due to the excitation of eddy currents, but also the dynamic component of the hysteresis loop associated with them. An analysis of this computation and its comparison with the classical approach suggests [3] that they lead approximately to the same result if the actual electrical conductivity γ in the classical formulas is replaced by an "equivalent" quantity γ_{eq}, which is larger than γ and depends on the size (width) of the domains. The ratio $\lambda = \gamma_{eq}/\gamma$ is a measure of the effect of the domain structure on eddy currents. The fact that the theoretical and actual eddy current losses become equal as a result of such a substitution is trivial. The main point is that the shape of the dynamic hysteresis loops corresponding to the given magnetization reversal is preserved.

The next step involves the extension of this result to more complicated domain structures. In other words, we treat this result as a statistical precept and seek its verification from a comparison of the theoretical and experimental hysteresis loops. We will dwell on this aspect later and at this stage formulate only the main aim of this research. As a matter of fact, a significant drawback of our previous publication [3] is that, although the replacement of γ by γ_{eq} in classical computations was substantiated approximately by tangible theoretical results, no direct comparison was made between the dynamic hysteresis loops calculated from the Pry–Bean model and those obtained from the formulas of the classical model of uniform magnetization in which γ is replaced by γ_{eq}. The main purpose of this research is to make such a comparison to show that, under standard conditions of magnetization reversal in the tapes made of magnetically soft electrically conducting materials, this simplifying procedure leads to results that do not differ significantly from the ideal results. This opens up the possibility of a remarkably simple quantitative description of the dynamic magnetization reversal cycles.

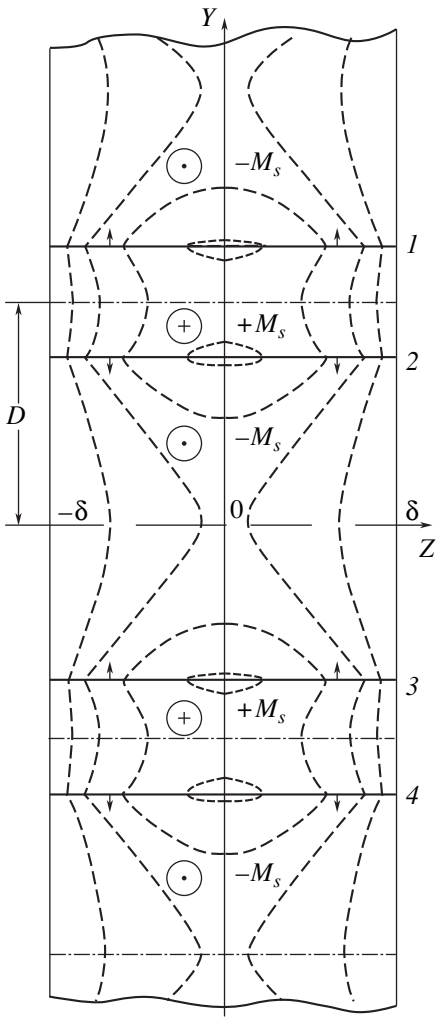

Fig. 1. The Pry–Bean domain structure model in the cross section of a ferromagnetic tape. The dashed curves are some of the eddy current lines; the domain walls are marked by *1–4*.

1. FORMULATION OF THE PROBLEM

Let us now formulate this problem in the specific language of computational procedures. In order to demonstrate in principle the variations introduced by the domain structure to the classical computation of eddy currents, Pry and Bean chose a simple model for thin materials (e.g., for strip-wound cores), which consists of domains separated by plane domain walls parallel to one another and perpendicular to the lateral faces of the strip. A stripe domain structure is formed on these surfaces, while the cross section displays the pattern shown in Fig. 1. In the demagnetized state, all domains are equal. When a magnetic field is applied perpendicular to the plane of Fig. 1, adjacent domain walls are displaced identically in opposite directions. In such a model, the description of the time variation of the average magnetization is equivalent to specifying the velocity of each domain wall as a function of time, which makes it possible to use the Maxwell equations for calculating the components of the induced eddy current density at each point of the strip. By way of an example, the dashed curves in Fig. 1 show some of the eddy current lines corresponding to this model under certain conditions of magnetization reversal [5]. This pattern of lines differs significantly from the classical pattern in the model of uniform magnetization.

The formulas for the components of the eddy current density can be used to obtain an expression for calculating the eddy current losses (which was done by Pry and Bean), as well as a formula for calculating the corresponding dynamic hysteresis loops [5] without

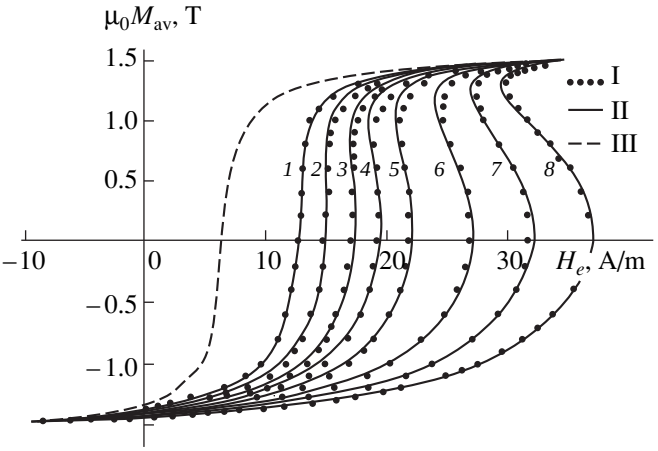

Fig. 2. Ascending branches of the dynamic hysteresis loops for the Fe 3% Si alloy of thickness 0.28 mm with a Goss texture, calculated without taking into account the magnetic viscosity for the case of magnetization reversal at a frequency of 50 Hz in the regime of sinusoidal induction with an amplitude of 1.5 T: I—according to the Pry–Bean model; II—by the model of uniform magnetization with a replacement of γ by γ_{eq}: d = 0.4 (curve *1*), 1.3 (*2*), 1.9 (*3*), 2.4 (*4*), 3 (*5*), 4 (*6*), 5 (*7*), and 6 (*8*); III—static magnetization reversal curve.

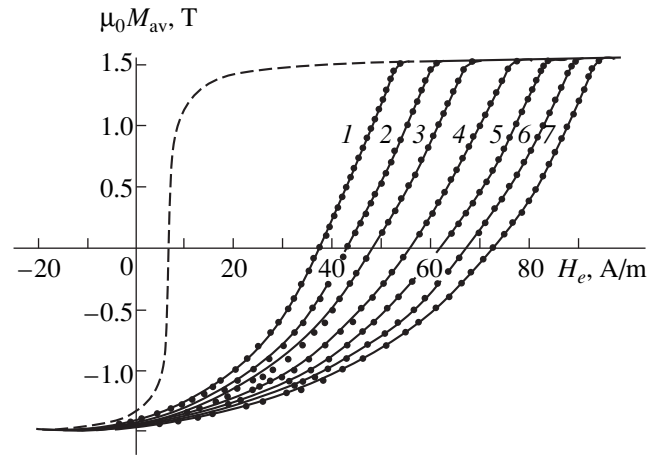

Fig. 3. The same as in Fig. 2 for the sinusoidal field regime with an amplitude 100 A/m; d = 0.4 (curve *1*), 1.3 (*2*), 2 (*3*), 3 (*4*), 4 (*5*), 5 (*6*), and 6 (*7*).

taking the magnetic viscosity into account. The latter formula can be presented in the form

$$H_e(t) = H_{st}(B_{av}) + \frac{8}{\pi^3}\gamma\delta D\frac{dB_{av}}{dt} \times \sum_{n=1}^{\infty}\frac{\cosh\alpha_n + \cosh\left(\alpha_n\frac{B_{av}}{\mu_0 M_s}\right)}{(2n+1)^3\sinh\alpha_n}. \quad (1)$$

Here, B_{av} is the magnetic induction averaged over the strip cross section, which varies periodically with time t; $H_e(t)$ is the value of the external magnetic field strength at the same instants of time t; $H_{st}(B_{av})$ is the quasi-static component of this field; δ and γ are the half-thickness and electrical conductivity of the magnetic tape, respectively; D is the average domain width (the separation between the centers of adjacent domains in Fig. 1); M_s is the saturation magnetization; μ_0 is the magnetic constant; and $\alpha_n = 0.5\pi(2n+1)(D/\delta)$. If the magnetic reversal conditions are specified, i.e., the periodic time dependence $B_{av}(t)$ or $H_e(t)$ is known, the dependence of B_{av} on H_e, i.e., the dynamic hysteresis loop, can be calculated from formula (1).

On the other hand, the classical theory, which presumes the absence of a domain structure, i.e., a constant value of the permeability, leads to the following relation for the dynamic hysteresis loop in the simplest case of a weak surface effect:

$$H_e(t) = H_{st}(B_{av}) + \frac{1}{3}\gamma\delta^2\frac{dB_{av}}{dt}. \quad (2)$$

The main aim of this research is to demonstrate graphically that in some specific situations the dynamic loops calculated from formula (1) are very close to the loops calculated by using the simple formula (2), in which the actual electrical conductivity γ is replaced by the "equivalent" ("effective") electrical conductivity γ_{eq}, which depends on the domain structure parameter $d = D/\delta$. This would confirm the results obtained by us earlier [3] by making some simplifying assumptions following only approximately from the theoretical curves presented in that work. On the other hand, these results form the basis for a satisfactory description of the family of dynamic hysteresis loops [6].

2. RESULTS OF CALCULATIONS

The dashed curves in Figs. 2 and 3 show the ascending branch of an experimental static hysteresis loop for an iron–silicon (Fe 3 wt % Si) alloy of 0.28 mm thickness with a Goss texture obtained as a result of magnetization reversal from the induction $-B_m$ = –1.5 T to $+B_m$ = +1.5 T. The remaining curves in Figs. 2 and 3, depicted by solid lines and dots, are the ascending branches of the theoretical dynamic hysteresis loops at a frequency of 50 Hz. Figure 2 corresponds to a preset sinusoidal induction flux for a magnetization amplitude $\mu_0 M_m$ = 1.5 T, while Fig. 3 corresponds to a preset sinusoidal external field with an amplitude H_m = 100 A/m. The dotted curves were obtained as a result of calculations using formula (1), i.e., from the Pry–Bean model with different values of the domain structure parameter d in the range 0.4–6.0. The solid curves were obtained by using formula (2), in which γ is replaced by γ_{eq}; the values of the latter are selected in such a way as to attain the maximum agreement with the curves obtained from

formula (1). It can be seen that this agreement is quite good, especially in the case of a sinusoidal external field. The dependence of the ratio $\lambda = \gamma_{eq}/\gamma$ on the domain structure parameter can be defined as [5]

$$\lambda = 0.81d + \exp[-0.81d(1 + 0.1d)]. \quad (3)$$

For small values of this parameter ($d \le 0.4$), the eddy currents induced in the cross section of the tape differ insignificantly from the classical results ($1 \le \gamma_{eq}/\gamma \le 1.05$). The larger the value of d, the higher the equivalent electrical conductivity γ_{eq} for neutralizing the effect of the domain structure on the eddy currents and hence on the dynamic hysteresis loop.

Thus, a clearly evident confirmation is obtained for the principle that the eddy currents in a tape with a domain structure can be calculated using the classical formulas for the case of uniform magnetization with the only difference being that the actual electrical conductivity γ should be replaced by the equivalent conductivity γ_{eq}, which depends on the relative size of the domains.

3. GENERALIZATION OF THE RESULTS OBTAINED

The curves shown in Figs. 2 and 3 confirm this principle only for the Pry–Bean model. One can naturally ask whether this simple result can be generalized to other domain structures prevailing in real ferromagnetic materials used in electrical engineering. We believe that this assumption can be made a working hypothesis if the real dynamic hysteresis loops are consistent with it. It is presumed that the Pry–Bean model is indeed the fundamental model, i.e., the most suitable one for rigorously demonstrating the effect of the domain structure on eddy currents, and that a stripe domain structure is indeed observed as a local effect in various crystallites of polycrystalline materials, although with different separations between the domain walls. Hence, it is expedient to introduce the concept of a certain generalized (effective) domain structure parameter d_{eff}, whose value is determined by the spread of the real values of d and, in addition, which statistically takes into account various departures from the Pry–Bean model, including the bending of walls, the presence of 90° walls, different wall mobilities, etc. Naturally, a direct evaluation of the quantity d_{eff} as a result of observations of the domain structures can lead only to an estimate of its value. On the other hand, indirect evaluations in terms of the quantity $\lambda = \gamma_{eq}/\gamma$ using formula (3) can be carried out only if the theoretical and experimental hysteresis loops do not differ significantly.

However, a considerable difficulty encountered in this direction is that real materials are subjected not only to eddy currents, but also to other relaxation mechanisms hindering the process of dynamic magnetization reversal (magnetic viscosity with a small relaxation time). Thus, it was shown earlier [1] that there are cases in which the observed discrepancy between the theoretical and experimental dynamic hysteresis loops cannot be attributed in any way to eddy currents only, irrespective of the level of their "intricacy." Among the known (though not necessarily investigated thoroughly) mechanisms of magnetic viscosity with a small relaxation time, we can single out, above all, the mechanisms of "friction" experienced by a domain wall during its movement, which leads to the emergence of the "friction force," proportional to the velocity of the domain wall, in the equation of motion of the domain wall. Such a friction may be due to the interaction with pinning centers [7–9] and with dislocations [10, 11], to magnetostriction [12], or to spin–spin and spin–lattice processes of magnetization relaxation [13]. In addition, the magnetic viscosity may be due to the pinning of domain walls at voids and inclusions [7, 14, 15], retarding Barkhausen pulses [16, 17], thermal activation of the motion of domain walls from metastable states, i.e., the effect of thermal fluctuations [18], and other processes [19, 20]. It was mentioned in a recent publication [21] that even spin relaxation (damping of the free precession of spins), characterized by a time constant of the order of 10^{-7} s, may affect the hysteretic magnetization reversal in modern magnetic materials. This relaxation may occur even at the acoustic frequencies of the external field, since the time in which a domain wall can pass through a given point (corresponding to the magnetic moment reversal at this point) in materials with a coarse domain structure may be small and comparable with 10^{-7} s.

It can be asked whether these mechanisms of magnetic viscosity with a small relaxation time can be described quantitatively by a statistical law. An analysis of the data obtained in numerous experiments leads to the conclusion [6] that such a statistical law can be written in the form of a modified magnetic viscosity equation

$$\mu_0 \frac{\partial M}{\partial t} = r \exp\left(-3.5\frac{M^2}{M_s^2}\right)[H - H_{st}(M)]. \quad (4)$$

Here, r is the magnetic viscosity characterizing the relaxation properties of the material under the given conditions of magnetization reversal.

It was also shown in [1] that for moderate magnetization reversal rates, when the surface effect is weak, it is possible to derive an equation of dynamic magnetization reversal, which can be used to calculate the

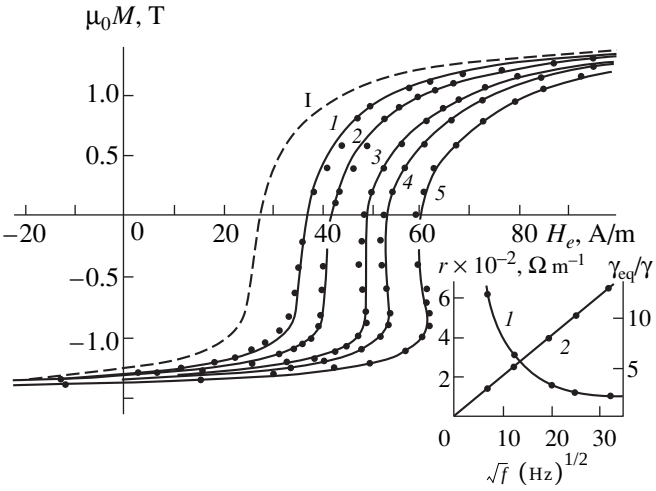

Fig. 4. Ascending branches of the hysteresis loops for electrical-sheet steel of 0.08 mm thickness under sinusoidal magnetic induction: I—static loop; curves *1*–*5* are the experimental points of dynamic loops for various frequencies of magnetization reversal f (Hz): 60 (curve *1*), 150 (*2*), 400 (*3*), 600 (*4*), and 1000 (*5*). The solid curves correspond to the theoretical dynamic loops. The inset shows the dependences of r (curve *1*) and γ_{eq}/γ (curve *2*) on $\sqrt{f}$.

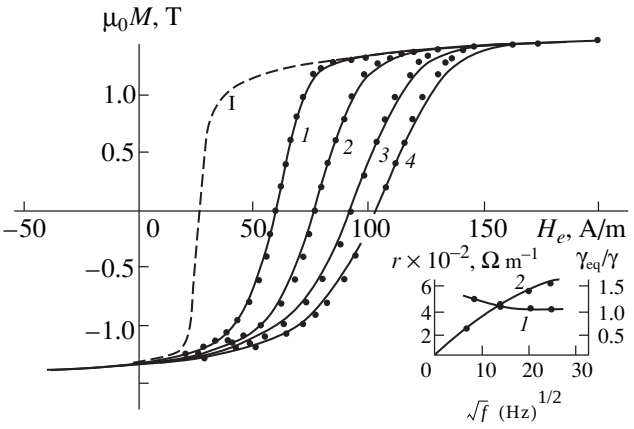

Fig. 5. The same as in Fig. 4 for a sinusoidal external field and various magnetization reversal frequencies f (Hz): 50 (curve *1*), 200 (*2*), 400 (*3*), and 600 (*4*).

dynamic hysteresis loop for given remagnetization conditions. This equation has the form

$$H_e(t) = H_{st}(M_{av}) + \frac{\mu_0}{r}\exp\left[3.5\left(\frac{M_{av}}{M_s}\right)^2\right]\frac{dM_{av}}{dt} + \frac{1}{3}\gamma_{eq}\delta^2\mu_0\frac{dM_{av}}{dt} \quad (5)$$

and differs from Eq. (2) only in that it contains an additional "viscosity" term and that γ in the "eddy-current" term is replaced by γ_{eq}. In order to calculate the hysteresis loop with the help of this equation, we must specify the time dependence of the magnetization averaged over the tape cross section, $M_{av}(t)$, or of the external magnetic field $H_e(t)$. In addition, Eq. (5) contains two unknown constants, viz., the quantity γ_{eq} (or $\lambda = \gamma_{eq}/\gamma$), characterizing the effect of the domain structure on eddy currents, and the viscosity r characterizing the relaxation properties of the magnetic material. The problem can now be formulated as follows: can we select these two fitting parameters λ and r for each specific dynamic hysteresis loop in such a way that the experimental and theoretical hysteresis loops are close to each other? Some examples of an affirmative answer to this question are given in [6]. We will present here one more example that extends the list of materials for which the effectiveness of the approach developed here for describing the dynamic properties of magnetic materials has been proved.

4. EXPERIMENTAL DATA

Two wound toroidal samples made of electrical-sheet steel 3424 of 0.08 mm thickness with nearly identical static hysteresis loops were chosen for specific measurements. One of them was tested in a sinusoidal magnetic induction flux (the results are presented in Fig. 4), and the other was tested in a sinusoidal external field (Fig. 5). Static magnetization reversal curves were measured on a ballistic setup and are shown by dashed lines in Figs. 4 and 5. The points on the dynamic hysteresis loops were determined by measurements on a ferrograph with a half-period cutoff, specially designed and fabricated at the Metrological Institute, Yekaterinburg. In the sinusoidal induction regime with an amplitude $B_m = 1.48$ T, measurements were made at frequencies of 50, 150, 400, 600, and 1000 Hz. In the sinusoidal field regime with an amplitude $H_m = 200$ A/m, dynamic hysteresis loops were measured at frequencies of 60, 200, 400, and 600 Hz. Measurements at higher frequencies in both cases led to a departure from the "weak surface effect" conditions.

5. RESULTS FOR SINUSOIDAL MAGNETIC INDUCTION

Calculations of the dynamic hysteresis loop with the help of formula (5) are especially simplified if the induction B_{av} averaged over the tape cross section depends on time t according to a sinusoidal law $B_{av} = B_m \sin\omega t$ and if the small difference between the induction B and the magnetization M multiplied by the magnetic constant μ_0 is disregarded, i.e., if we assume that $B \cong \mu_0 M$. By specifying the numerical values of the parameters

$$\Omega = \omega/r, \quad \Theta = (1/3)\gamma_{eq}\delta^2\omega, \quad (6)$$

we can calculate the value of $H_e(t)$ corresponding to each instantaneous value of $\mu_0 M_{av}(t)$, i.e., determine the

coordinates of the point on the dynamic magnetization reversal curve (the ascending branch of the dynamic hysteresis loop).

By requiring that this curve pass through the dynamic coercive field point H_{cd} at which $M_{av} = 0$ and $\mu_0(dM_{av}/dt) = \omega\mu_0 M_m$, we obtain from Eqs. (4) and (5)

$$\Omega + \Theta = (H_{cd} - H_c)/\mu_0 M_m,$$

where H_c is the static coercive field. Thus, it remains for us to determine in fact only one of the parameters in Eq. (6) corresponding to the best agreement between the theoretical and the experimental magnetization reversal curves.

Figure 4 shows the experimental points on the ascending branches of the dynamic hysteresis loops, while the solid lines are the corresponding theoretical magnetization reversal curves. The values of the parameters $\lambda = \gamma_{eq}/\gamma$ and r, calculated from Eq. (6) by using the obtained values of Ω and Θ, are presented in the same figure as the functions of the square root of the magnetization reversal frequency f. As in [6], the viscosity r was found to be directly proportional to $\sqrt{f}$. The parameter $\lambda = \gamma_{eq}/\gamma$, characterizing the effect of the domain structure on eddy currents, decreases sharply with increasing frequency, which indicates the familiar intensive splitting of domains [13]. Since the quantity λ is related to the generalized parameter d of the domain structure through formula (3), the results obtained can be used to estimate the average (effective) domain width. It is found that $D = 1.3$ mm at a frequency $f = 50$ Hz, $D = 0.34$ mm at $f = 400$ Hz, and $D = 0.18$ mm at $f = 1000$ Hz. The reasonably good matching of the theoretical and the experimental magnetization reversal curves shown in Fig. 4 leads to the conclusion that Eq. (5) can be used for describing the dynamics of magnetization reversal of the thinnest electrical-sheet steel.

6. RESULTS FOR A SINUSOIDAL EXTERNAL FIELD

If the magnetization reversal occurs under the action of a sinusoidal external field $H_e(t) = H_m \sin\omega t$, the calculations of the dynamic loop are a bit more complicated than in the case of a given sinusoidal magnetic induction, since they require a numerical solution of the differential equation (5). The static magnetization reversal curve can be defined in the form of an approximating function. For this purpose, it is best to use a spline [22] whose coefficients have been determined beforehand. The difficulty lies in finding a steady-state periodic solution. For this purpose, the initial value of M_{av} corresponding to the steady-state process of periodic variation of magnetization must be determined meticulously at some "initial" instant of time. For the type of magnetization reversal curves shown in Fig. 5 (having a gently sloping initial segment), it is best to use the fact that if the starting point is chosen to the left of the ordinate axis, the results of computations do not depend significantly on the initial value of M_{av} if it lies within the interval in which the numerical computational procedure is stable. Subsequent computations can be made without any difficulty by using the standard techniques.

The results of these calculations, which are presented in Fig. 5, are in accord with the experimental points. In this case, the parameter λ slowly approaches unity, varying from 1.2 at a frequency 60 Hz to 1.0 at a frequency 600 Hz, i.e., the splitting of domains in this case is insignificant in the given frequency range. As regards the viscosity r, its dependence on $\sqrt{f}$ is nonlinear in this case in contrast to all previously investigated materials [6].

7. CONCLUSION

Thus, it has been shown graphically in the present work that the theoretical dynamic hysteresis loops remain practically unchanged if the complex calculations of eddy currents in materials where magnetization reversal occurs as a result of displacement of domain walls are reduced to simple classical calculations based on the model of uniform magnetization in which the actual electrical conductivity γ is replaced by the equivalent conductivity γ_{eq}, the ratio γ_{eq}/γ serving as a measure of the effect of the domain structure on the eddy currents. This serves as the basis for the derivation of the simple dynamic magnetic reversal equation (5) which can be used to calculate the dynamic hysteresis loops for different frequencies and amplitudes of the applied action. The effectiveness of this equation is confirmed, among other things, by the example of the low-frequency magnetization reversal of the thinnest electrical-sheet steel of 0.08 mm thickness both in a sinusoidal induction flux and in a sinusoidal external magnetic field. This material obeys the dynamic magnetic reversal equation as do most of the materials investigated earlier [6].

REFERENCES

1. A. I. Kadochnikov, Fiz. Met. Metalloved. **83** (1), 37 (1997).
2. B. Wwedensky, Ann. Phys. **66**, 110 (1921).
3. A. I. Kadochnikov, Élektrichestvo **2**, 39 (1994).
4. R. H. Pry and C. P. Bean, J. Appl. Phys. **29** (3), 532 (1958).
5. A. A. Siventsev, A. I. Kadochnikov, and V. V. Leonov, Fiz. Met. Metalloved. **38** (3), 529 (1974).
6. A. I. Kadochnikov, Fiz. Met. Metalloved. **83** (2), 89 (1997).
7. G. L. Houze, J. Appl. Phys. **38** (3), 1089 (1967).
8. Z. J. Chen and D. C. Jiles, IEEE Trans. Magn. **29** (6), 2554 (1993).

9. G. H. Wantenaar, G. V. Wilson, D. H. Chaplin, and S. J. Cambell, J. Magn. Magn. Mater. **89** (1–2), 13 (1990).
10. D. D. Mishin, Izv. Akad. Nauk SSSR, Ser. Fiz. **34** (2), 233 (1970).
11. P. Gaunt, Philos. Mag. B **48** (3), 261 (1983).
12. F. N. Dunaev, Fiz. Met. Metalloved. **29** (5), 937 (1970).
13. V. A. Zaĭkova, I. E. Startseva, and B. F. Filippov, *Domain Structure and Magnetic Properties of Electrical Steels* (Nauka, Moscow, 1992).
14. D. J. Seagle and S. H. Charap, J. Appl. Phys. **53** (11), 8299 (1982).
15. K. J. Overshott and S. Hill, in *Proceedings of 2nd Conference on Advances in Magnetic Material Applications, London, 1976*, p. 29.
16. R. V. Telesnin, Dokl. Akad. Nauk SSSR **59** (5), 887 (1948).
17. E. P. Dzaganiya, Fiz. Met. Metalloved. **20** (2), 204 (1965).
18. E. Kneller, *Ferromagnetismus* (Springer, Berlin, 1962).
19. P. Mazzetti, IEEE Trans. Magn. **14** (5), 758 (1978).
20. J. V. Morgen and K. J. Overshott, J. Appl. Phys. **53** (11), 8293 (1982).
21. A. I. Kadochnikov, Fiz. Met. Metalloved. **76** (3), 108 (1993).
22. A. I. Kadochnikov, E. B. Khan, and N. B. Lobanova, Defektoskopiya, No. 11, 75 (1992).

Translated by N. Wadhwa

Physics of the Solid State, Vol. 42, No. 11, 2000, pp. 2116–2122. Translated from Fizika Tverdogo Tela, Vol. 42, No. 11, 2000, pp. 2054–2059.

MAGNETISM AND FERROELECTRICITY

The Generalized Domain Structure Parameter for Magnetically Soft Materials and Its Application for Quantitative Description of a Family of Dynamic Hysteresis Loops

A. I. Kadochnikov and G. S. Korzunin

Institute of Metal Physics, Ural Division, Russian Academy of Sciences, ul. S. Kovalevskoĭ 18, Yekaterinburg, 620219 Russia
e-mail: korzunin@imp.uran.ru

Received January 12, 2000; in final form, April 21, 2000

Abstract—A generalized interpretation of the processes of dynamic magnetization reversal in magnetically soft electrically conducting materials is proposed. It can be used for obtaining a simple and quite accurate mathematical description for a family of dynamic hysteresis loops. *© 2000 MAIK "Nauka/Interperiodica".*

The dynamic hysteresis loop of a magnetically soft material can be treated as its main characteristic. It is better to speak of a family of such loops since they depend on the frequency and amplitude of the remagnetizing field (or magnetic induction), as well as on the magnetization reversal conditions, i.e., on the form of the time dependence of the external field or the magnetic induction flux. The reasons behind the difference between the dynamic and static hysteresis loops cannot be treated as definitely established, since certain facts cannot be explained within the framework of the traditional concepts [1]. In practice, one could disregard this circumstance if a satisfactory quantitative description of the loops and their dependence on the conditions under which the magnetization reversal is performed could be obtained at least by phenomenological methods. Such a description is extremely important for applied electrical engineering.

But is it possible in principle to find such a description? An affirmative answer to this question is unlikely, since it is well known that the process of magnetic reversal in ferromagnetic materials is quite complicated and a large number of reasonable assumptions have been put forth about the diverse possible mechanisms of retardation (relaxation) of this process. However, it will be shown below that a quite rational quantitative description for a family of hysteresis loops can nevertheless be obtained by adopting certain generalized assumptions concerning the magnetization reversal processes. One such assumption concerns eddy currents, while another pertains to a different type of phenomena that retard the magnetic reversal and were called the magnetic viscosity because of V.K. Arkad'ev [2]. As regards eddy currents, the basic reason behind the difficulties is quite obvious; it should be borne in mind that, in thin materials with a coarse domain structure, eddy currents are induced as a result of the motion of each individual domain wall, and the eddy current lines obtained as a result of their summation most likely have a configuration other than the simple one assumed in the classical theory of eddy currents. They may have a quite "intricate" form, which means that classical formulas for calculating eddy currents and their effect on the dynamic hysteresis loop do not always reflect the actual effects.

Let us examine how this circumstance can be taken into consideration. In real materials, the configuration of domain walls is by no means a regular pattern. Moreover, the motion of domain walls itself does not obey simple laws and may be quite diverse. For example, the mobility of walls may differ in value even for walls of the same type. However, statistical laws may come into play in a situation like this. For example, if a magnet is quite bulky and the domain walls are small in comparison, the configurations of eddy current lines will differ only insignificantly from those used in the classical computations of the eddy-current effect. In other words, the effect of the domain structure on eddy currents will be statistically insignificant. It can be asked whether some simple statistical law is also followed, at least approximately, in the case when the domain size is comparable with the thickness of the magnetic tape or strips used for constructing the magnetic cores of electrical devices.

An endeavor to establish such a regularity was made in [3]. This endeavor can be briefly described as follows. We proceed from the Pry–Bean model [4], which is a simple model, but the most characteristic, describing the domain structure and the movement of domain walls. On the one hand, this model corresponds to the

1063-7834/00/4211-2116$20.00

strongest manifestation of the "bendings" of the classical eddy current lines that are associated with the domain structure and "enhance" the integrated eddy-current effects. On the other hand, this model requires comparatively simple computations. It was shown in [5] that it can be used for calculating not only the energy losses due to the excitation of eddy currents, but also the dynamic component of the hysteresis loop associated with them. An analysis of this computation and its comparison with the classical approach suggests [3] that they lead approximately to the same result if the actual electrical conductivity γ in the classical formulas is replaced by an "equivalent" quantity γ_{eq}, which is larger than γ and depends on the size (width) of the domains. The ratio $\lambda = \gamma_{eq}/\gamma$ is a measure of the effect of the domain structure on eddy currents. The fact that the theoretical and actual eddy current losses become equal as a result of such a substitution is trivial. The main point is that the shape of the dynamic hysteresis loops corresponding to the given magnetization reversal is preserved.

The next step involves the extension of this result to more complicated domain structures. In other words, we treat this result as a statistical precept and seek its verification from a comparison of the theoretical and experimental hysteresis loops. We will dwell on this aspect later and at this stage formulate only the main aim of this research. As a matter of fact, a significant drawback of our previous publication [3] is that, although the replacement of γ by γ_{eq} in classical computations was substantiated approximately by tangible theoretical results, no direct comparison was made between the dynamic hysteresis loops calculated from the Pry–Bean model and those obtained from the formulas of the classical model of uniform magnetization in which γ is replaced by γ_{eq}. The main purpose of this research is to make such a comparison to show that, under standard conditions of magnetization reversal in the tapes made of magnetically soft electrically conducting materials, this simplifying procedure leads to results that do not differ significantly from the ideal results. This opens up the possibility of a remarkably simple quantitative description of the dynamic magnetization reversal cycles.

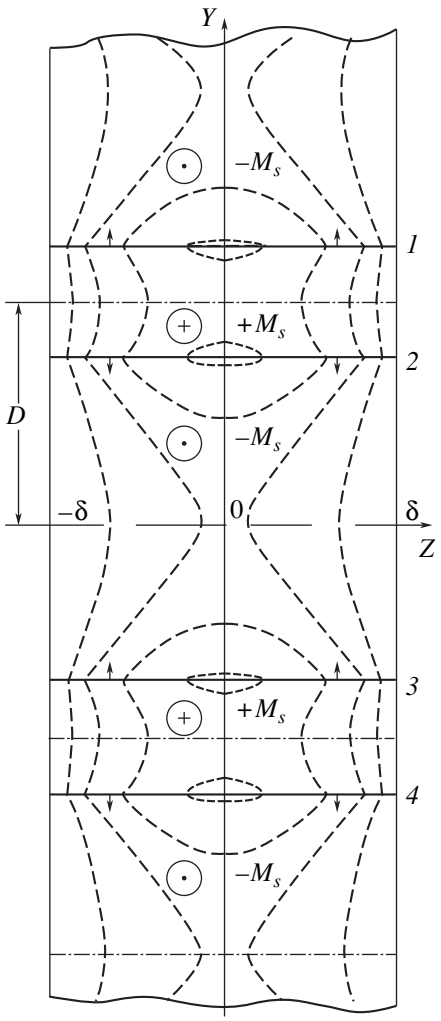

Fig. 1. The Pry–Bean domain structure model in the cross section of a ferromagnetic tape. The dashed curves are some of the eddy current lines; the domain walls are marked by *1–4*.

1. FORMULATION OF THE PROBLEM

Let us now formulate this problem in the specific language of computational procedures. In order to demonstrate in principle the variations introduced by the domain structure to the classical computation of eddy currents, Pry and Bean chose a simple model for thin materials (e.g., for strip-wound cores), which consists of domains separated by plane domain walls parallel to one another and perpendicular to the lateral faces of the strip. A stripe domain structure is formed on these surfaces, while the cross section displays the pattern shown in Fig. 1. In the demagnetized state, all domains are equal. When a magnetic field is applied perpendicular to the plane of Fig. 1, adjacent domain walls are displaced identically in opposite directions. In such a model, the description of the time variation of the average magnetization is equivalent to specifying the velocity of each domain wall as a function of time, which makes it possible to use the Maxwell equations for calculating the components of the induced eddy current density at each point of the strip. By way of an example, the dashed curves in Fig. 1 show some of the eddy current lines corresponding to this model under certain conditions of magnetization reversal [5]. This pattern of lines differs significantly from the classical pattern in the model of uniform magnetization.

The formulas for the components of the eddy current density can be used to obtain an expression for calculating the eddy current losses (which was done by Pry and Bean), as well as a formula for calculating the corresponding dynamic hysteresis loops [5] without

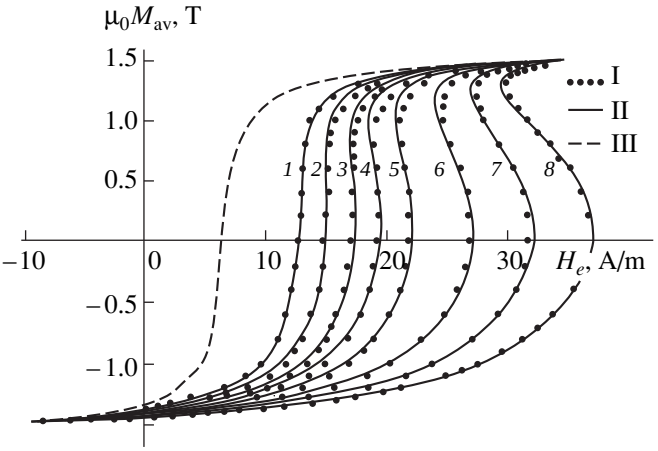

Fig. 2. Ascending branches of the dynamic hysteresis loops for the Fe 3% Si alloy of thickness 0.28 mm with a Goss texture, calculated without taking into account the magnetic viscosity for the case of magnetization reversal at a frequency of 50 Hz in the regime of sinusoidal induction with an amplitude of 1.5 T: I—according to the Pry–Bean model; II—by the model of uniform magnetization with a replacement of γ by γ_{eq}: d = 0.4 (curve *1*), 1.3 (*2*), 1.9 (*3*), 2.4 (*4*), 3 (*5*), 4 (*6*), 5 (*7*), and 6 (*8*); III—static magnetization reversal curve.

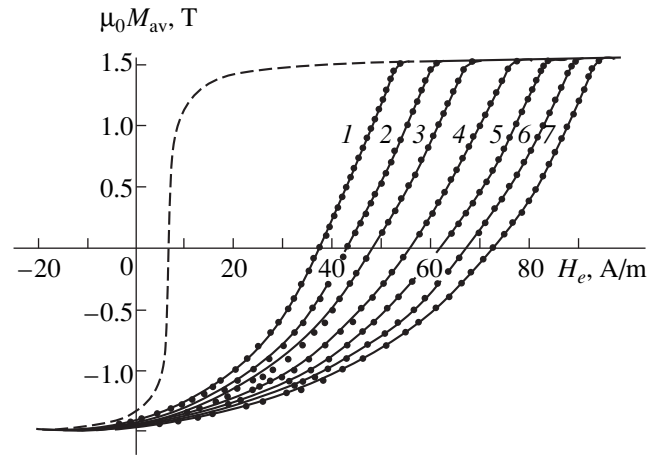

Fig. 3. The same as in Fig. 2 for the sinusoidal field regime with an amplitude 100 A/m; d = 0.4 (curve *1*), 1.3 (*2*), 2 (*3*), 3 (*4*), 4 (*5*), 5 (*6*), and 6 (*7*).

taking the magnetic viscosity into account. The latter formula can be presented in the form

$$H_e(t) = H_{st}(B_{av}) + \frac{8}{\pi^3}\gamma\delta D\frac{dB_{av}}{dt} \times \sum_{n=1}^{\infty}\frac{\cosh\alpha_n + \cosh\left(\alpha_n\frac{B_{av}}{\mu_0 M_s}\right)}{(2n+1)^3\sinh\alpha_n}. \quad (1)$$

Here, B_{av} is the magnetic induction averaged over the strip cross section, which varies periodically with time t; $H_e(t)$ is the value of the external magnetic field strength at the same instants of time t; $H_{st}(B_{av})$ is the quasi-static component of this field; δ and γ are the half-thickness and electrical conductivity of the magnetic tape, respectively; D is the average domain width (the separation between the centers of adjacent domains in Fig. 1); M_s is the saturation magnetization; μ_0 is the magnetic constant; and $\alpha_n = 0.5\pi(2n+1)(D/\delta)$. If the magnetic reversal conditions are specified, i.e., the periodic time dependence $B_{av}(t)$ or $H_e(t)$ is known, the dependence of B_{av} on H_e, i.e., the dynamic hysteresis loop, can be calculated from formula (1).

On the other hand, the classical theory, which presumes the absence of a domain structure, i.e., a constant value of the permeability, leads to the following relation for the dynamic hysteresis loop in the simplest case of a weak surface effect:

$$H_e(t) = H_{st}(B_{av}) + \frac{1}{3}\gamma\delta^2\frac{dB_{av}}{dt}. \quad (2)$$

The main aim of this research is to demonstrate graphically that in some specific situations the dynamic loops calculated from formula (1) are very close to the loops calculated by using the simple formula (2), in which the actual electrical conductivity γ is replaced by the "equivalent" ("effective") electrical conductivity γ_{eq}, which depends on the domain structure parameter $d = D/\delta$. This would confirm the results obtained by us earlier [3] by making some simplifying assumptions following only approximately from the theoretical curves presented in that work. On the other hand, these results form the basis for a satisfactory description of the family of dynamic hysteresis loops [6].

2. RESULTS OF CALCULATIONS

The dashed curves in Figs. 2 and 3 show the ascending branch of an experimental static hysteresis loop for an iron–silicon (Fe 3 wt % Si) alloy of 0.28 mm thickness with a Goss texture obtained as a result of magnetization reversal from the induction $-B_m$ = –1.5 T to $+B_m$ = +1.5 T. The remaining curves in Figs. 2 and 3, depicted by solid lines and dots, are the ascending branches of the theoretical dynamic hysteresis loops at a frequency of 50 Hz. Figure 2 corresponds to a preset sinusoidal induction flux for a magnetization amplitude $\mu_0 M_m$ = 1.5 T, while Fig. 3 corresponds to a preset sinusoidal external field with an amplitude H_m = 100 A/m. The dotted curves were obtained as a result of calculations using formula (1), i.e., from the Pry–Bean model with different values of the domain structure parameter d in the range 0.4–6.0. The solid curves were obtained by using formula (2), in which γ is replaced by γ_{eq}; the values of the latter are selected in such a way as to attain the maximum agreement with the curves obtained from

formula (1). It can be seen that this agreement is quite good, especially in the case of a sinusoidal external field. The dependence of the ratio $\lambda = \gamma_{eq}/\gamma$ on the domain structure parameter can be defined as [5]

$$\lambda = 0.81d + \exp[-0.81d(1 + 0.1d)]. \quad (3)$$

For small values of this parameter ($d \le 0.4$), the eddy currents induced in the cross section of the tape differ insignificantly from the classical results ($1 \le \gamma_{eq}/\gamma \le 1.05$). The larger the value of d, the higher the equivalent electrical conductivity γ_{eq} for neutralizing the effect of the domain structure on the eddy currents and hence on the dynamic hysteresis loop.

Thus, a clearly evident confirmation is obtained for the principle that the eddy currents in a tape with a domain structure can be calculated using the classical formulas for the case of uniform magnetization with the only difference being that the actual electrical conductivity γ should be replaced by the equivalent conductivity γ_{eq}, which depends on the relative size of the domains.

3. GENERALIZATION OF THE RESULTS OBTAINED

The curves shown in Figs. 2 and 3 confirm this principle only for the Pry–Bean model. One can naturally ask whether this simple result can be generalized to other domain structures prevailing in real ferromagnetic materials used in electrical engineering. We believe that this assumption can be made a working hypothesis if the real dynamic hysteresis loops are consistent with it. It is presumed that the Pry–Bean model is indeed the fundamental model, i.e., the most suitable one for rigorously demonstrating the effect of the domain structure on eddy currents, and that a stripe domain structure is indeed observed as a local effect in various crystallites of polycrystalline materials, although with different separations between the domain walls. Hence, it is expedient to introduce the concept of a certain generalized (effective) domain structure parameter d_{eff}, whose value is determined by the spread of the real values of d and, in addition, which statistically takes into account various departures from the Pry–Bean model, including the bending of walls, the presence of 90° walls, different wall mobilities, etc. Naturally, a direct evaluation of the quantity d_{eff} as a result of observations of the domain structures can lead only to an estimate of its value. On the other hand, indirect evaluations in terms of the quantity $\lambda = \gamma_{eq}/\gamma$ using formula (3) can be carried out only if the theoretical and experimental hysteresis loops do not differ significantly.

However, a considerable difficulty encountered in this direction is that real materials are subjected not only to eddy currents, but also to other relaxation mechanisms hindering the process of dynamic magnetization reversal (magnetic viscosity with a small relaxation time). Thus, it was shown earlier [1] that there are cases in which the observed discrepancy between the theoretical and experimental dynamic hysteresis loops cannot be attributed in any way to eddy currents only, irrespective of the level of their "intricacy." Among the known (though not necessarily investigated thoroughly) mechanisms of magnetic viscosity with a small relaxation time, we can single out, above all, the mechanisms of "friction" experienced by a domain wall during its movement, which leads to the emergence of the "friction force," proportional to the velocity of the domain wall, in the equation of motion of the domain wall. Such a friction may be due to the interaction with pinning centers [7–9] and with dislocations [10, 11], to magnetostriction [12], or to spin–spin and spin–lattice processes of magnetization relaxation [13]. In addition, the magnetic viscosity may be due to the pinning of domain walls at voids and inclusions [7, 14, 15], retarding Barkhausen pulses [16, 17], thermal activation of the motion of domain walls from metastable states, i.e., the effect of thermal fluctuations [18], and other processes [19, 20]. It was mentioned in a recent publication [21] that even spin relaxation (damping of the free precession of spins), characterized by a time constant of the order of 10^{-7} s, may affect the hysteretic magnetization reversal in modern magnetic materials. This relaxation may occur even at the acoustic frequencies of the external field, since the time in which a domain wall can pass through a given point (corresponding to the magnetic moment reversal at this point) in materials with a coarse domain structure may be small and comparable with 10^{-7} s.

It can be asked whether these mechanisms of magnetic viscosity with a small relaxation time can be described quantitatively by a statistical law. An analysis of the data obtained in numerous experiments leads to the conclusion [6] that such a statistical law can be written in the form of a modified magnetic viscosity equation

$$\mu_0 \frac{\partial M}{\partial t} = r \exp\left(-3.5\frac{M^2}{M_s^2}\right)[H - H_{st}(M)]. \quad (4)$$

Here, r is the magnetic viscosity characterizing the relaxation properties of the material under the given conditions of magnetization reversal.

It was also shown in [1] that for moderate magnetization reversal rates, when the surface effect is weak, it is possible to derive an equation of dynamic magnetization reversal, which can be used to calculate the

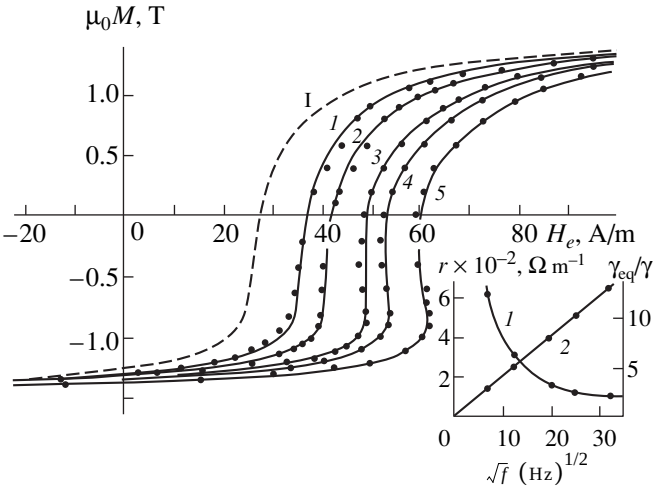

Fig. 4. Ascending branches of the hysteresis loops for electrical-sheet steel of 0.08 mm thickness under sinusoidal magnetic induction: I—static loop; curves *1*–*5* are the experimental points of dynamic loops for various frequencies of magnetization reversal f (Hz): 60 (curve *1*), 150 (*2*), 400 (*3*), 600 (*4*), and 1000 (*5*). The solid curves correspond to the theoretical dynamic loops. The inset shows the dependences of r (curve *1*) and γ_{eq}/γ (curve *2*) on $\sqrt{f}$.

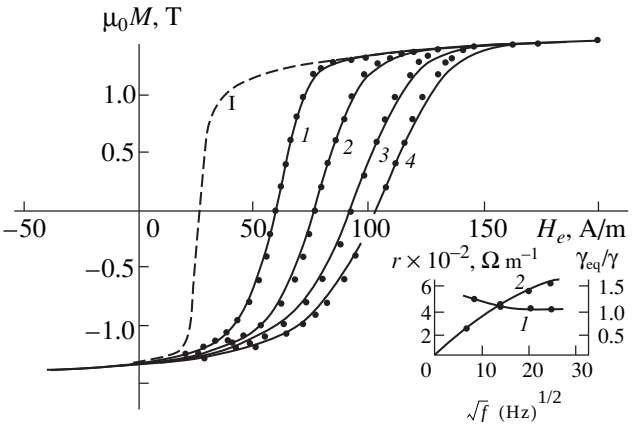

Fig. 5. The same as in Fig. 4 for a sinusoidal external field and various magnetization reversal frequencies f (Hz): 50 (curve *1*), 200 (*2*), 400 (*3*), and 600 (*4*).

dynamic hysteresis loop for given remagnetization conditions. This equation has the form

$$H_e(t) = H_{st}(M_{av}) + \frac{\mu_0}{r}\exp\left[3.5\left(\frac{M_{av}}{M_s}\right)^2\right]\frac{dM_{av}}{dt} + \frac{1}{3}\gamma_{eq}\delta^2\mu_0\frac{dM_{av}}{dt} \quad (5)$$

and differs from Eq. (2) only in that it contains an additional "viscosity" term and that γ in the "eddy-current" term is replaced by γ_{eq}. In order to calculate the hysteresis loop with the help of this equation, we must specify the time dependence of the magnetization averaged over the tape cross section, $M_{av}(t)$, or of the external magnetic field $H_e(t)$. In addition, Eq. (5) contains two unknown constants, viz., the quantity γ_{eq} (or $\lambda = \gamma_{eq}/\gamma$), characterizing the effect of the domain structure on eddy currents, and the viscosity r characterizing the relaxation properties of the magnetic material. The problem can now be formulated as follows: can we select these two fitting parameters λ and r for each specific dynamic hysteresis loop in such a way that the experimental and theoretical hysteresis loops are close to each other? Some examples of an affirmative answer to this question are given in [6]. We will present here one more example that extends the list of materials for which the effectiveness of the approach developed here for describing the dynamic properties of magnetic materials has been proved.

4. EXPERIMENTAL DATA

Two wound toroidal samples made of electrical-sheet steel 3424 of 0.08 mm thickness with nearly identical static hysteresis loops were chosen for specific measurements. One of them was tested in a sinusoidal magnetic induction flux (the results are presented in Fig. 4), and the other was tested in a sinusoidal external field (Fig. 5). Static magnetization reversal curves were measured on a ballistic setup and are shown by dashed lines in Figs. 4 and 5. The points on the dynamic hysteresis loops were determined by measurements on a ferrograph with a half-period cutoff, specially designed and fabricated at the Metrological Institute, Yekaterinburg. In the sinusoidal induction regime with an amplitude $B_m = 1.48$ T, measurements were made at frequencies of 50, 150, 400, 600, and 1000 Hz. In the sinusoidal field regime with an amplitude $H_m = 200$ A/m, dynamic hysteresis loops were measured at frequencies of 60, 200, 400, and 600 Hz. Measurements at higher frequencies in both cases led to a departure from the "weak surface effect" conditions.

5. RESULTS FOR SINUSOIDAL MAGNETIC INDUCTION

Calculations of the dynamic hysteresis loop with the help of formula (5) are especially simplified if the induction B_{av} averaged over the tape cross section depends on time t according to a sinusoidal law $B_{av} = B_m \sin\omega t$ and if the small difference between the induction B and the magnetization M multiplied by the magnetic constant μ_0 is disregarded, i.e., if we assume that $B \cong \mu_0 M$. By specifying the numerical values of the parameters

$$\Omega = \omega/r, \quad \Theta = (1/3)\gamma_{eq}\delta^2\omega, \quad (6)$$

we can calculate the value of $H_e(t)$ corresponding to each instantaneous value of $\mu_0 M_{av}(t)$, i.e., determine the

coordinates of the point on the dynamic magnetization reversal curve (the ascending branch of the dynamic hysteresis loop).

By requiring that this curve pass through the dynamic coercive field point H_{cd} at which $M_{av} = 0$ and $\mu_0(dM_{av}/dt) = \omega\mu_0 M_m$, we obtain from Eqs. (4) and (5)

$$\Omega + \Theta = (H_{cd} - H_c)/\mu_0 M_m,$$

where H_c is the static coercive field. Thus, it remains for us to determine in fact only one of the parameters in Eq. (6) corresponding to the best agreement between the theoretical and the experimental magnetization reversal curves.

Figure 4 shows the experimental points on the ascending branches of the dynamic hysteresis loops, while the solid lines are the corresponding theoretical magnetization reversal curves. The values of the parameters $\lambda = \gamma_{eq}/\gamma$ and r, calculated from Eq. (6) by using the obtained values of Ω and Θ, are presented in the same figure as the functions of the square root of the magnetization reversal frequency f. As in [6], the viscosity r was found to be directly proportional to $\sqrt{f}$. The parameter $\lambda = \gamma_{eq}/\gamma$, characterizing the effect of the domain structure on eddy currents, decreases sharply with increasing frequency, which indicates the familiar intensive splitting of domains [13]. Since the quantity λ is related to the generalized parameter d of the domain structure through formula (3), the results obtained can be used to estimate the average (effective) domain width. It is found that $D = 1.3$ mm at a frequency $f = 50$ Hz, $D = 0.34$ mm at $f = 400$ Hz, and $D = 0.18$ mm at $f = 1000$ Hz. The reasonably good matching of the theoretical and the experimental magnetization reversal curves shown in Fig. 4 leads to the conclusion that Eq. (5) can be used for describing the dynamics of magnetization reversal of the thinnest electrical-sheet steel.

6. RESULTS FOR A SINUSOIDAL EXTERNAL FIELD

If the magnetization reversal occurs under the action of a sinusoidal external field $H_e(t) = H_m \sin\omega t$, the calculations of the dynamic loop are a bit more complicated than in the case of a given sinusoidal magnetic induction, since they require a numerical solution of the differential equation (5). The static magnetization reversal curve can be defined in the form of an approximating function. For this purpose, it is best to use a spline [22] whose coefficients have been determined beforehand. The difficulty lies in finding a steady-state periodic solution. For this purpose, the initial value of M_{av} corresponding to the steady-state process of periodic variation of magnetization must be determined meticulously at some "initial" instant of time. For the type of magnetization reversal curves shown in Fig. 5 (having a gently sloping initial segment), it is best to use the fact that if the starting point is chosen to the left of the ordinate axis, the results of computations do not depend significantly on the initial value of M_{av} if it lies within the interval in which the numerical computational procedure is stable. Subsequent computations can be made without any difficulty by using the standard techniques.

The results of these calculations, which are presented in Fig. 5, are in accord with the experimental points. In this case, the parameter λ slowly approaches unity, varying from 1.2 at a frequency 60 Hz to 1.0 at a frequency 600 Hz, i.e., the splitting of domains in this case is insignificant in the given frequency range. As regards the viscosity r, its dependence on $\sqrt{f}$ is nonlinear in this case in contrast to all previously investigated materials [6].

7. CONCLUSION

Thus, it has been shown graphically in the present work that the theoretical dynamic hysteresis loops remain practically unchanged if the complex calculations of eddy currents in materials where magnetization reversal occurs as a result of displacement of domain walls are reduced to simple classical calculations based on the model of uniform magnetization in which the actual electrical conductivity γ is replaced by the equivalent conductivity γ_{eq}, the ratio γ_{eq}/γ serving as a measure of the effect of the domain structure on the eddy currents. This serves as the basis for the derivation of the simple dynamic magnetic reversal equation (5) which can be used to calculate the dynamic hysteresis loops for different frequencies and amplitudes of the applied action. The effectiveness of this equation is confirmed, among other things, by the example of the low-frequency magnetization reversal of the thinnest electrical-sheet steel of 0.08 mm thickness both in a sinusoidal induction flux and in a sinusoidal external magnetic field. This material obeys the dynamic magnetic reversal equation as do most of the materials investigated earlier [6].

REFERENCES

1. A. I. Kadochnikov, Fiz. Met. Metalloved. **83** (1), 37 (1997).
2. B. Wwedensky, Ann. Phys. **66**, 110 (1921).
3. A. I. Kadochnikov, Élektrichestvo **2**, 39 (1994).
4. R. H. Pry and C. P. Bean, J. Appl. Phys. **29** (3), 532 (1958).
5. A. A. Siventsev, A. I. Kadochnikov, and V. V. Leonov, Fiz. Met. Metalloved. **38** (3), 529 (1974).
6. A. I. Kadochnikov, Fiz. Met. Metalloved. **83** (2), 89 (1997).
7. G. L. Houze, J. Appl. Phys. **38** (3), 1089 (1967).
8. Z. J. Chen and D. C. Jiles, IEEE Trans. Magn. **29** (6), 2554 (1993).

9. G. H. Wantenaar, G. V. Wilson, D. H. Chaplin, and S. J. Cambell, J. Magn. Magn. Mater. **89** (1–2), 13 (1990).
10. D. D. Mishin, Izv. Akad. Nauk SSSR, Ser. Fiz. **34** (2), 233 (1970).
11. P. Gaunt, Philos. Mag. B **48** (3), 261 (1983).
12. F. N. Dunaev, Fiz. Met. Metalloved. **29** (5), 937 (1970).
13. V. A. Zaĭkova, I. E. Startseva, and B. F. Filippov, *Domain Structure and Magnetic Properties of Electrical Steels* (Nauka, Moscow, 1992).
14. D. J. Seagle and S. H. Charap, J. Appl. Phys. **53** (11), 8299 (1982).
15. K. J. Overshott and S. Hill, in *Proceedings of 2nd Conference on Advances in Magnetic Material Applications, London, 1976*, p. 29.
16. R. V. Telesnin, Dokl. Akad. Nauk SSSR **59** (5), 887 (1948).
17. E. P. Dzaganiya, Fiz. Met. Metalloved. **20** (2), 204 (1965).
18. E. Kneller, *Ferromagnetismus* (Springer, Berlin, 1962).
19. P. Mazzetti, IEEE Trans. Magn. **14** (5), 758 (1978).
20. J. V. Morgen and K. J. Overshott, J. Appl. Phys. **53** (11), 8293 (1982).
21. A. I. Kadochnikov, Fiz. Met. Metalloved. **76** (3), 108 (1993).
22. A. I. Kadochnikov, E. B. Khan, and N. B. Lobanova, Defektoskopiya, No. 11, 75 (1992).

Translated by N. Wadhwa

Physics of the Solid State, Vol. 42, No. 11, 2000, pp. 2123–2128. Translated from Fizika Tverdogo Tela, Vol. 42, No. 11, 2000, pp. 2060–2065.

MAGNETISM AND FERROELECTRICITY

The Role of the Spatial Distribution of Local Polarization Perturbations in the Posistor Effect Onset

A. N. Pavlov, I. P. Raevskiĭ, and V. P. Sakhnenko

Research Institute of Physics, Rostov State University, Rostov-on-Don, 344104 Russia

Received March 3, 2000

Abstract—The electrical resistance of polycrystalline ferroelectric semiconductors is defined by the potential barriers due to the existence of local charged surface states at crystallite boundaries. The barrier screening depends on the state of the ferroelectric system and is maximal during spontaneous-polarization switching. It is shown in this paper that the local perturbation of the ferroelectric system, resulting from the repolarization and appearing as a domain wall between the regions with different polarization directions, has a zigzag configuration. The electric field in the vicinity of the zigzag domain wall is stabilized and coincides with the coercive field, which provides low potential barriers in the ferroelectric phase compared with the paraelectric phase. The repolarization processes become inefficient in the potential barrier screening at the transition from the ferroelectric to the paraelectric phase. As a result, a sharp increase in the electrical resistance is observed at the ferroelectric–paraelectric phase transition, called the posistor effect. © *2000 MAIK "Nauka/Interperiodica"*.

The resistance of polycrystalline ferroelectric semiconductors of the oxygen-octahedron type decreases by several orders of magnitude at the transition from the paraelectric to the ferroelectric phase [1]. This effect is known as the effect of the positive temperature coefficient of resistance, or the posistor effect. This phenomenon could be related to the crystallite boundary potential barriers drastically changing in magnitude at the ferroelectric phase transition. The potential barriers mentioned are due to the presence of local charged surface states of the acceptor-type at the crystallite boundaries with the activation energy of $E_s \sim 1$ eV and the density of $N_s \sim 10^{14}$ cm^{-2} [1]. The resistance of polycrystalline ferroelectric semiconductors is mainly determined by the charge screening of these surface states, which is due to the response of both the electronic and the ionic subsystems. The response of the electronic subsystem results in the creation of an electron-deficient Schottky region near the charged crystallite boundaries. The electric field associated with the surface states at the crystallite boundaries is concentrated in this region. The response of the ionic subsystem forced by this field can reveal both the polarization and the repolarization character. The polarization of the ionic subsystem occurs in the paraelectric phase. This can also occur in the ferroelectric phase when the direction of the spontaneous polarization P_s in the crystallite bulk (where all fields compensate each other) coincides with the direction of the electric field strength E in the Schottky region ($\mathbf{P}_s \uparrow\uparrow E$). The repolarization occurs in the ferroelectric phase when the direction of P_s in the crystallite bulk is opposite to the direction of the electric field in the Schottky region ($\mathbf{P}_s \uparrow\downarrow E$) and the field strength E is larger than the coercive field E_c. In accordance with [2], the polarization response in the ferroelectric phase does not provide efficient screening of the potential barriers, compared with the screening in the paraelectric phase, and, hence, it has not resulted in the posistor effect. The repolarization response was shown to play a crucial role in the screening of the potential barriers and the posistor effect onset [2]. However, an analysis of the repolarization was done in [2] in terms of the polarization metastable states, described via the theoretical hysteresis loop. These states are not stable, and the repolarization region appears instead like a domain wall between two head-to-head domains [3]. This region is a strong local perturbation of the ferroelectric system, because the thickness of the domain wall is $l_c \sim 10^{-6}$ cm [4]. The structure of this region and its role in the posistor effect onset are analyzed in this paper. The domain wall has a negative repolarization bound charge with a density of $\sigma_p = \mathrm{div}\mathbf{P}$. For the most efficient screening of the electric field, the wall should be oriented relative to the direction of P_s in the crystallite bulk so that the negative bound charge and the positive space charge in the Schottky region compensate each other. The space charge is defined by the ionized donor states with a density of $N_d \sim 10^{19}$ cm^{-3}, and the neutralization of the total repolarization charge $\Delta P = 2P_s \sim 10^{-5}$ C cm^{-2} occurs at a distance of $l_p = 2P_s/qN_d \sim 10^{-5}$ cm (here, q is the elementary electronic charge). As long as $l_c \ll l_p$, the domain wall will be oriented at an angle θ to the P_s direction. This angle is given by the expression

$$\sin\theta = \frac{l_c q N_d}{2P_s}. \quad (1)$$

1063-7834/00/4211-2123$20.00

Then, the boundary between the head-to-head domains will have a zigzag wedge shape, which was observed experimentally in [5, 6].

1. CALCULATION RESULTS

The zigzag structure of the domain wall can be found solving the equation of state for the ferroelectric system.

We assume that $\mathbf{P}_s$ is parallel to the [001] direction, taken as the Z axis. A normal vector to the domain wall is directed at the angle $\pi/2 - \theta$ to the Z axis and lies in the (011) plane, denoted as the YZ plane. Then, the thermodynamic potential for the tetragonal phase is given by the expression

$$\Phi = \frac{1}{2}\alpha P_z^2 + \frac{1}{4}\beta P_z^4 + \frac{1}{6}\gamma P_z^6 + \frac{1}{2}\chi\left[\frac{1}{A^2}\left(\frac{dP_z}{dz}\right)^2 + \frac{1}{B^2}\left(\frac{dP_z}{dy}\right)^2\right], \quad (2)$$

where

$$A = \sin\theta, \quad B = \cos\theta. \quad (3)$$

Minimizing expression (2), we arrive at the equation of state

$$\chi\left[\frac{1}{A^2}\left(\frac{d^2P_z}{dz^2}\right) + \frac{1}{B^2}\left(\frac{d^2P_z}{dy^2}\right)\right] = \alpha P_z + \beta P_z^3 + \gamma P_z^5. \quad (4)$$

At $\theta \longrightarrow \pi/2$, a solution to Eq. (4) is given by the expression

$$P_{z1} = P_0\frac{c_2^{0.5}\,\mathrm{sn}(\eta z A)}{(\mathrm{sn}^2(\eta z A) - 1 + c_2)^{0.5}}. \quad (5)$$

Here, sn is an elliptic function and P_0 is a variable parameter,

$$\eta = P_0^2\sqrt{\frac{\gamma}{6\chi}}\sqrt{c_1(1-c_2)}, \quad (6)$$

$$c_{1,2} = -\delta \pm \sqrt{\delta^2 - 2\delta - \tau}, \quad (7)$$

$$\delta = \frac{1}{2} + \frac{3\beta}{4\gamma P_0^2}, \quad (8)$$

$$\tau = \frac{3\alpha}{\gamma P_0^4}. \quad (9)$$

The structure reveals an energy minimum at $P_0 \longrightarrow P_s$. In this limit, Eq. (5) can be rewritten as

$$P_{z1} = P_s\frac{\sinh(\eta z A)}{\left(\cosh^2(\eta z A) + \dfrac{2\gamma P_s^2}{4\gamma P_s^2 + 3\beta}\right)^{0.5}}. \quad (10)$$

Here, sinh and cosh are the hyperbolic sine and cosine, respectively.

We represent P_z in the form

$$P_{z2} = P_{z1} + f(y). \quad (11)$$

At $f \longrightarrow 0$, we can find a particular solution for f from the equation of state, which has the form

$$f = P_0\sin(\eta y B). \quad (12)$$

We seek the general solution of the equation of state in the form of a linear combination of the particular solutions (10) and (12)

$$P_z = P_s \times\left\{\frac{\sinh(\eta z A)}{\left(\cosh^2(\eta z A) + \dfrac{2\gamma P_s^2}{4\gamma P_s^2 + 3\beta}\right)^{0.5}} + g(z)\sin(\eta y B)\right\}, \quad (13)$$

where $g(z)$ is a function of z to be determined.

According to the numerical calculations, $g(z)$ can be approximated by the relation

$$g = 1 - \mathrm{sgn}(z)\frac{\sinh(\eta z A)}{\left(\cosh^2(\eta z A) + \dfrac{2\gamma P_s^2}{4\gamma P_s^2 + 3\beta}\right)^{0.5}}. \quad (14)$$

Graphs of the dependencies described by Eqs. (13) and (14) are presented in Figs. 1 and 2 for $BaTiO_3$ at the temperature $T = 115$ K and $\theta = 3°$. The resulting wedge-shaped structure is the zigzag domain boundary. The periodicity of this structure is illustrated in Fig. 2 by the boundary line between regions with opposite polarization directions. The polarization distribution having a wedge-shaped structure is extended along the [001] direction, and its length is $\sim l_p$. The coercive electric field E_c, at which the polarization P switching begins, is stabilized within the structure described; the space charge in the Schottky region and the bound repolarization charge compensate each other, and the electric field strength E, directed toward the crystallite boundary, no longer increases. The value of E_c can be estimated accounting for the thermal activation processes of the polarization P_s switching in the regions whose size is of the order of the coherent length ξ [4]. Let the E_c value be equal to the electric field strength at which the region that was not repolarized is too small to be considered as continuous. Consequently, its relative content is less than 0.15 [7]. In this case, $W_I/W_{II} = 0.85/0.15$. Here, W_I is the probability for the ferroelectric system being in state I, corresponding to one of the thermodynamic potential minima, where $\Phi = \Phi_0 - E_cP_s$; W_{II} is the probability for the system being in

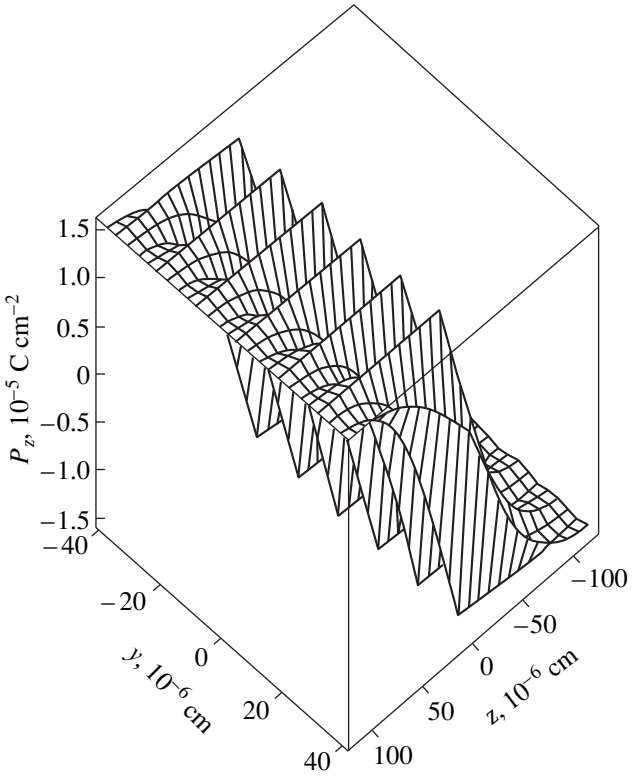

Fig. 1. Distribution of the polarization P resulting from the repolarization in the Schottky region.

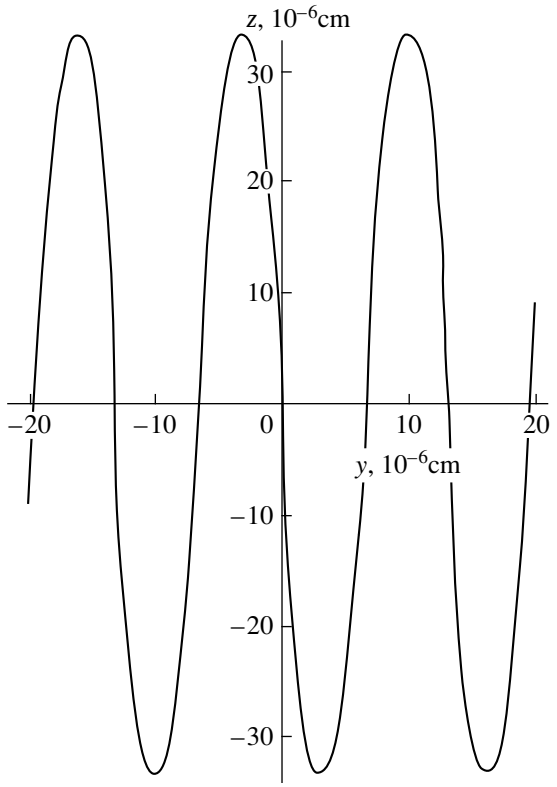

Fig. 2. The boundary line between the regions with the opposite polarization P directions resulting from the repolarization in the Schottky region.

state II, corresponding to the other thermodynamic potential minimum, where $\Phi = \Phi_0 + E_c P_s$.

$$W_{\mathrm{I}} \sim \exp(-(|\Phi_0| - E_c P_s)V_c/kT);$$
$$W_{\mathrm{II}} \sim \exp(-(|\Phi_0| + E_c P_s)V_c/kT). \quad (15)$$

Here, Φ_0 is the thermodynamic potential at $P = P_s$, k is the Boltzmann constant, and $V_c = \xi^3$. For E_c parallel to the pseudocubic [001] direction, we obtain the expression

$$E_c = \frac{kT}{2P_{sz}\xi^3 V_c}\ln\frac{W_1}{W_2}. \quad (16)$$

Here, $\xi \sim (\chi\varepsilon_{zz}\varepsilon_0)^{0.5}$ [4], ε_{zz} is the dielectric permittivity in the pseudocubic [001] direction, ε_0 is the electric constant, and P_{sz} is the spontaneous polarization in the pseudocubic [001] direction. The results of the E_c calculation for $BaTiO_3$ by using Eq. (16), presented in Fig. 3, are in qualitative and quantitative agreement with the experimental data, shown in the inset of Fig. 3. The calculations were performed for $\chi\varepsilon_0 \sim 6 \times 10^{-16}$ cm^2 [8], and the experimental values of P_{sz} and ε_{zz} taken from [9]. The value of E_c was obtained to be about 10^3 V/cm, which is of the same order of magnitude as the experimentally determined coercive fields [10]. This is of principal importance in the posistor effect theory and implies that the field screening is more efficient in the ferroelectric phase than in the paraelectric one. In the latter, the electric field strength reaches the value of $E_{pe} = l_p q N_d/\varepsilon\varepsilon_0 \sim 10^4$ V/cm at a distance of $\sim l_p$ from the Schottky region boundary [1]. Here, $\varepsilon \approx 10^4$ is the dielectric permittivity in the paraelectric phase near the

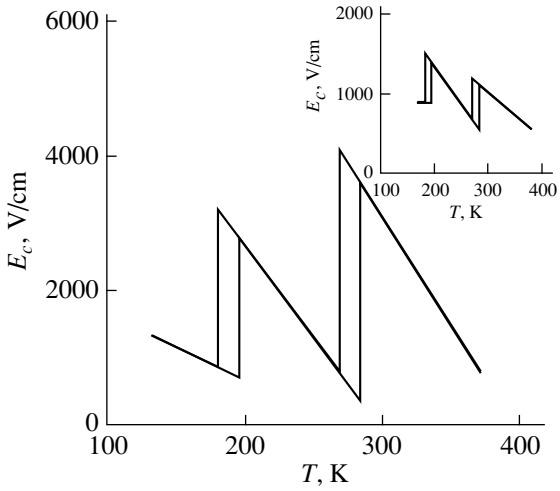

Fig. 3. The theoretical temperature dependence of the coercive field E_c for $BaTiO_3$ (the experimental one is in the inset).

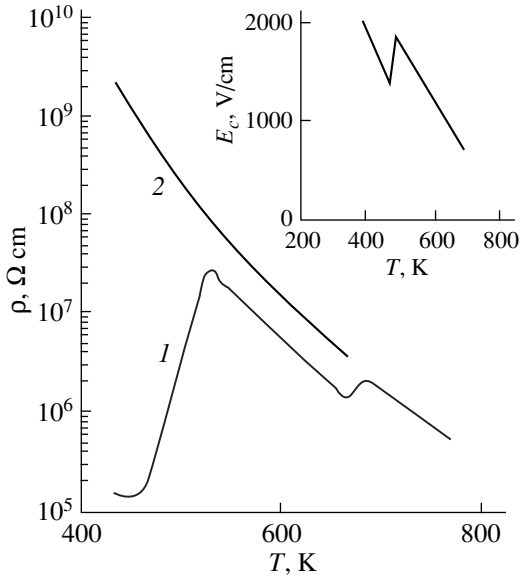

Fig. 4. The experimental temperature dependences of the resistivity ρ of the unpolarized (curve *1*) and the polarized (curve *2*) polycrystalline $KNbO_3$. The experimental temperature dependence of the coercive field E_c for the $KNbO_3$ crystal is shown in the inset.

phase transition point. If the length of the repolarization region l_p is comparable to the Schottky region length l_s defined by the electrical neutrality condition, the potential barrier in the ferroelectric phase $q\varphi_{0fe}$ is determined by the formula

$$\varphi_{0fe} \approx l_s E_c = \frac{N_s E_s}{N_d}. \quad (17)$$

This potential barrier is not high in comparison to the potential barrier in the paraelectric phase, $q\varphi_{0pe}$ [11]

$$\varphi_{0pe} = \frac{qN_s^2}{2\varepsilon\varepsilon_0 N_d}. \quad (18)$$

From Eqs. (17) and (18), we obtain the relation $\varphi_{0fe}/\varphi_{0pe} = E_c 2\varepsilon\varepsilon_0/(qN_s) \sim 0.1$.

The sharp changes in the electrical resistivity (curve *1* in Fig. 4) [12] and in the coercive field (the inset in Fig. 4) [13] were observed experimentally in polycrystalline $KNbO_3$ in the region where the transition occurs from one ferroelectric phase to the other. The correlation observed in the behavior of ρ and E_c can be explained by the following. The coercive field drastically changes in $KNbO_3$ during the transition from one ferroelectric phase to the other, and, therefore, the screening of the potential barriers related to the repolarization also changes drastically. This results in a sharp change in the electrical resistivity during the transition from one ferroelectric phase to the other.

The phenomenon described above should be particularly characteristic of an unpolarized polycrystalline ferroelectric, where the polarization P_s switching is possible on either side of the crystallite boundary. In a polarized polycrystalline ferroelectric, the polarization P_s switching can occur only on one side of the crystallite boundary. On the other side, we will have only the substance polarization, which is of far less importance in the screening than the repolarization is. Therefore, the barrier potential and, consequently, the electrical resistivity in the direction parallel to the polarization direction are larger in the polarized polycrystalline ferroelectric than in the unpolarized one. This is in accordance with the experimental data for $KNbO_3$ [13] (curve *2* in Fig. 4) and $BaTiO_3$ [14].

The qualitative considerations presented above were tested applying the theoretical calculations based on the model proposed. For this purpose, the negatively charged boundary between the crystallites arranged in the (110) plane has been considered. There is a mobile-charge-depleted Schottky region near the crystallite boundary, which causes the screening of the boundary surface charge. Therefore, no electric field is produced outside of the Schottky region by the surface charge owing to the screening effect. The linear size l_s of this region in the approximation of "complete depletion," meaning the total absence of the mobile charge carriers in it, is defined by the electrical neutrality condition

$$l_s\sigma = qn_s = \frac{qN_s}{1 + \exp(E_F - E_s - q\varphi_0/kT)}. \quad (19)$$

Here, σ is the space charge density in the Schottky region, n_s is the density of the filled localized states at the boundary between the crystallites, φ_0 is the value of the potential φ at the boundary, and E_F is the Fermi energy. For the donor states with a small activation energy, we have $\sigma = qN_d$. The value of the current density j (for the current along the [001] direction) was determined in the diffusion-drift approximation [15] by using the expression

$$j = \frac{kT\mu N_d}{\int_{-z_l}^{z_r} \exp[-q(\varphi + u)/kT]dz} \times \left[1 - \exp\left(\frac{-qu}{kT}\right)\right] = \frac{u}{\rho d}. \quad (20)$$

Here, μ is the mobility of free charge carriers, u is the external voltage value calculated per one crystallite, d is the crystallite thickness, and ρ is the resistivity.

The integration in Eq. (20) is executed over the space charge region near the charged boundary between the crystallites, z_r and $-z_l$ are the coordinates of the Schottky region boundary.

The calculation of the electrical characteristics (including ρ) by using formula (20) requires knowing

the distributions of P, φ, and E. These values are determined from the system of equations

$$\nabla\varphi = -E, \tag{21}$$

$$\varepsilon_0 \nabla E = \sigma - \nabla P, \tag{22}$$

as well as from the equation of state P resulting from the minimization of the thermodynamic potential and accounting for the influence of the electric field produced by the charged crystallite boundary on the polarization.

In this case, the possibility of the polarization P switching in the field E_c caused by the zigzag domain wall formation should be considered. The calculations of ρ by using relation (20) for $KNbO_3$ are presented in Fig. 5. The following values for the parameters are used in the calculations: $N_d = 10^{18}$ cm^{-3}, $N_s = 3 \times 10^{14}$ cm^{-2}, $E_s = 1.2$ eV, $\mu = 0.5$ cm^2 V^{-1} s^{-1}, and $d = 4 \times 10^{-3}$ cm. Sharp drops in ρ are observed at the phase transitions to the low-temperature phases (curve *1* in Fig. 5). The character of the change in ρ and the drop values in ρ agree quite well with the experimental data (Fig. 4). The calculation of ρ for the unpolarized state (curve *1* in Fig. 5) was done at the polarization configuration having $\mathbf{P}_s \uparrow\downarrow \mathbf{E}$ on both sides of the crystallite boundary, resulting in the smallest potential barrier value. In the Schottky region, where $\mathbf{P}_s$ and $\mathbf{E}$ have opposite directions, after reaching the value of E_c by the electric field, the repolarization begins. The proliferation of the wedges occurs with the polarization opposite to the $\mathbf{P}_s$ direction. As a result, the density of the repolarization charge is compensated completely by the density of the free charge ($\nabla P = \sigma = qN_d$), and the electric field has a fixed strength of E_c in the repolarization region. The calculation of ρ for the polarized state (curve *2* in Fig. 5) was done at the polarization configuration having $\mathbf{P}_s \uparrow\uparrow \mathbf{E}$ on one side of the crystallite boundary and $\mathbf{P}_s \uparrow\downarrow \mathbf{E}$ on the other. In the polarized state, the repolarization occurs only on one side of the crystallite boundary. On the other side, the polarization occurs, and the screening of the electric field is less efficient, resulting in a larger value of the potential barrier $q\varphi_{0p}$ compared with that of the unpolarized state, $q\varphi_{0up}$. The screening in the latter case can occur due to the repolarization on both sides of the crystallite boundary. The calculations for $KNbO_3$ at $T = 500$ K give the values $q\varphi_{0up} = 0.6$ and $q\varphi_{0p} = 0.9$ eV.

Thus, the character of the screening determines the values of the potential barriers in polycrystalline ferroelectric semiconductors. The screening is the most efficient when, on both sides of the crystallite boundary, the direction of the electric field in the Schottky region has the direction opposite to the spontaneous polarization in the crystallite bulk, resulting in the repolarization. In this case, the domain wall between the regions

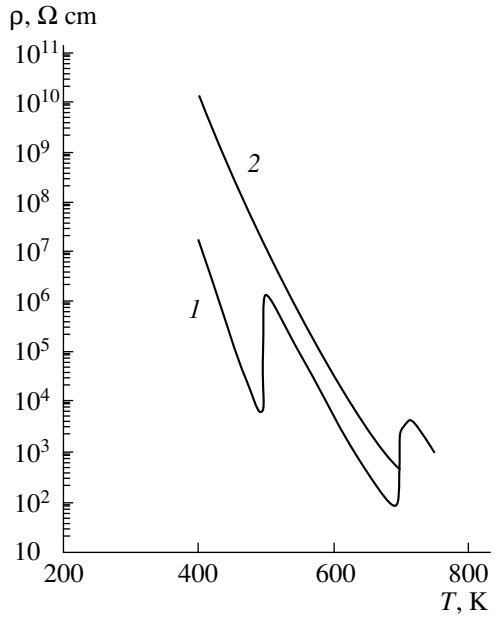

Fig. 5. The theoretical temperature dependences of the resistivity ρ of the unpolarized (curve *1*) and the polarized (curve *2*) polycrystalline $KNbO_3$.

with different polarization directions, being the local polarization perturbation, has a zigzag shape. The electric field in this zigzag repolarization region is stabilized at the coercive field value, resulting in the most efficient screening of the potential barriers in the ferroelectric phase, compared with the paraelectric one, and the posistor effect takes place. When the coercive field changes sharply during the transition from one ferroelectric phase to the other, the screening of the potential barriers and the resistivity change drastically. This is particularly relevant for the unpolarized polycrystalline ferroelectrics, where the repolarization P is possible on either side of the crystallite boundary. In the polarized polycrystalline ferroelectric, the repolarization P occurs only on one side of the crystallite boundary, whereas on the other side, only the substance polarization occurs, which is of far less importance in the screening of the potential barriers than the repolarization is. Therefore, the potential barriers and the resistivity for the polarized polycrystalline ferroelectrics turn out to be larger than for the unpolarized ones.

The analysis of the experimental and theoretical results presented above allows us to reach the following conclusion. Due to the action of the electric field of the charged surface states at the crystallite boundaries in polycrystalline ferroelectric semiconductors, the zigzag region of the local polarization perturbations appears. It provides for efficient screening of the boundary electric field and results in the anomalies in the resistivity as the ferroelectric system state is changed.

REFERENCES

1. W. Heywang, J. Am. Ceram. Soc. **47** (10), 484 (1964).
2. A. N. Pavlov, Fiz. Tverd. Tela (S.-Peterburg) **36** (3), 579 (1994) [Phys. Solid State **36**, 319 (1994)].
3. V. M. Fridkin, *Photoferroelectrics* (Nauka, Moscow, 1976; Springer, Berlin, 1979).
4. G. A. Smolenskiĭ, V. A. Bokov, V. A. Isupov, *et al*., *Ferroelectrics and Antiferroelectrics* (Nauka, Leningrad, 1971).
5. E. G. Fesenko, V. G. Gavrilyachenko, and A. F. Semenchev, *Domain Structure of Multiaxial Ferroelectric Crystals* (Rostov. Gos. Univ., Rostov-on-Don, 1990).
6. E. G. Fesenko, V. G. Gavrilyachenko, M. A. Martynenko, and A. F. Semenchev, Izv. Akad. Nauk SSSR, Ser. Fiz. **39** (4), 762 (1975).
7. G. N. Dul'nev and V. V. Novikov, *Transport Processes in Inhomogeneous Medium* (Énergoatomizdat, Leningrad, 1991).
8. L. P. Kholodenko, *Thermodynamical Theory of $BaTiO_3$ Type Ferroelectrics* (Znanie, Riga, 1971).
9. W. J. Merz, Phys. Rev. **76**, 1221 (1949).
10. H. H. Wieder, J. Appl. Phys. **26**, 1479 (1955).
11. *Semiconductors Based on Barium Titanate* (Énergoizdat, Moscow, 1982).
12. I. P. Raevskiĭ, E. I. Bondarenko, A. N. Pavlov, *et al.*, Fiz. Tverd. Tela (Leningrad) **26** (4), 1219 (1984) [Sov. Phys. Solid State **26**, 741 (1984)].
13. S. Triebwasser, Phys. Rev. **101** (3), 993 (1956).
14. I. P. Raevskiĭ, E. I. Bondarenko, A. N. Pavlov, *et al.*, Zh. Tekh. Fiz. **55** (3), 603 (1985) [Sov. Phys. Tech. Phys. **30**, 351 (1985)].
15. G. T. Mallik and P. R. Emtage, J. Appl. Phys. **39** (6), 3088 (1968).

Translated by N. Kovaleva

Physics of the Solid State, Vol. 42, No. 11, 2000, pp. 2129–2136. Translated from Fizika Tverdogo Tela, Vol. 42, No. 11, 2000, pp. 2066–2073.

MAGNETISM AND FERROELECTRICITY

Ferroelectric Properties of Strontium Barium Niobate Crystals Doped with Rare-Earth Metals

T. R. Volk*, V. Yu. Salobutin, L. I. Ivleva***, N. M. Polozkov***, R. Pankrath****, and M. Woehlecke******

** Shubnikov Institute of Crystallography, Russian Academy of Sciences, Leninskiĭ pr. 59, Moscow, 117333 Russia*

*** Tver State University, Sadovyĭ per. 35, Tver, 170002 Russia*

**** Research Center for Laser Materials and Technology, Institute of General Physics, Russian Academy of Sciences, ul. Vavilova 38, Moscow, 117942 Russia*

***** Fachbereich Physik, Universität Osnabrück, Barbarastrasse 7, D 49076 Osnabrück, Germany*

e-mail: volk@ns.crys.ras.ru

Received March 3, 2000; in final form, April 7, 2000

Abstract—The influence of doping of the $Sr_xBa_{1-x}Nb_2O_6$ ($x = 0.61$) crystals (SBN-0.61) by rare-earth element (RE) dopants has been investigated. Taking into account the data available in the literature, it is demonstrated that the introduction of all rare-earth metals is accompanied by a substantial decrease in the temperature of the phase transition T_p and an increase in its smearing. The shift in the T_p temperature for certain rare-earth metals ranges up to 20 K per atomic percent of dopant in the crystal. It is experimentally established that, in the SBN-0.61 : Yb, SBN-0.61 : Ce, SBN-0.61 : Tm, SBN-0.61 : La, and SBN-0.61 : (Ce + La) crystals, a decrease in T_p brings about a considerable increase in the permittivity and the piezoelectric and electrooptical coefficients. The conclusion is drawn that the doping by rare-earth metals provides a means of optimizing the properties of strontium barium niobates. The pulse switching of the SBN-0.61 and SBN-0.61 : RE crystals is studied for the first time. It is found that the switching is characterized by a number of features, the most important of which is a decrease in the switched charge after the application of external fields. This effect associated with the specific features of the switching in the relaxor ferroelectric is assumed to be responsible for the instability of the parameters for strontium barium niobate material. *© 2000 MAIK "Nauka/Interperiodica".*

1. INTRODUCTION

Ferroelectric crystals $Sr_xBa_{1-x}Nb_2O_6$ (SBN-x) possess unique properties from the viewpoint of basic research and different practical (optical, pyroelectric, and piezoelectric) applications [1, 2]. They show considerable promise owing to strong dependences of the phase transition temperature T_p and the relaxor characteristics on the composition (the [Sr]/[Ba] ratio), which make it possible to vary different parameters over a wide range. From the available data, it follows that the doping of SBN-0.61 by La [3], Tb [4], and Ce [5, 6], as well as an increase in the [Sr]/[Ba] ratio, leads to a substantial decrease in the T_p temperature. There is good indirect evidence that the doping by other rare-earth metals (RE) produces a similar effect [7]. The doping of SBN-0.61 by rare-earth metals and an increase in the [Sr]/[Ba] ratio result in an increase the piezoelectric (for SBN-0.61 : La [3] and SBN-0.61 : Ce [8]) and electrooptical (for SBN-0.61 : Ce [9]) coefficients.

Despite the fact that the strontium barium niobates doped with rare-earth metals are very promising materials, the works dealing with physical (in particular, ferroelectric) properties of these crystals are few in number; the exception is provided by the works concerned with holographic recording in SBN-0.61 : Ce (see, for example, [10]). For comparison, we note that, in undoped strontium barium niobates, the influence of the [Sr]/[Ba] ratio on the phase transition and the relaxor characteristics has been studied thoroughly [1, 11–13].

The pulse switching in strontium barium niobate (SBN) crystals merits detailed consideration. The exploration of this process is of special interest with respect to the problem of producing regular domain structures for the realization of quasi-phase matching conditions, which provide the conversion of optical frequencies (see, for example, review [14]). There are several publications on the second harmonic generation of IR radiation with the use of the domain structure in strontium barium niobates [15, 16] and the laser generation with self-frequency doubling by microdomains in SBN : Nd [17]. However, so far as we know, the studies on the pulse switching of strontium barium niobate crystals have never been published. Since the static hysteresis loops for strontium barium niobates have specific features due to the relaxor properties [18], it can be expected that the kinetics of pulse switching also exhibits characteristic features.

This paper reviews the investigation into the influence of selected rare-earth metals on the ferroelectric properties of the SBN-0.61 crystals. First and foremost, in order to reveal the general character of the RE effect

1063-7834/00/4211-2129$20.00 © 2000 MAIK "Nauka/Interperiodica"

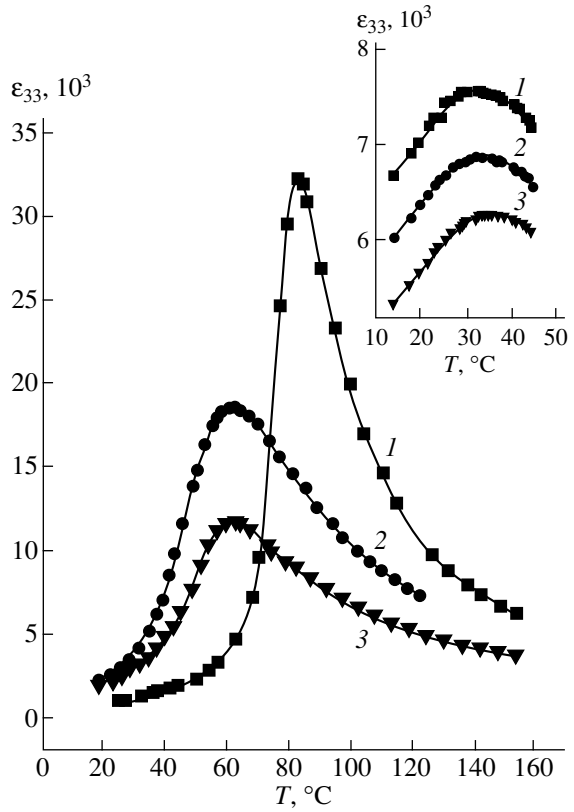

Fig. 1. Temperature dependences of the permittivity for (*1*) SBN-0.61, (*2*) SBN-0.61 : Yb, and (*3*) SBN-0.61 : Ce crystals at a frequency of 1 kHz. The inset shows the dependence $\varepsilon_{33}(T)$ for the crystal SBN-0.61 : (1 wt % La + 0.01 wt % Ce) at frequencies of (*1*) 0.1, (*2*) 1.0, and (*3*) 20.0 kHz.

on the phase transition, we increased the number of the studied SBN-0.61 : RE compositions. The influence of Nd, Yb, and Tm dopants and a combined doping were studied in this work for the first time. Then, we evaluated how the selected rare-earth metals affect the piezoelectric and electrooptical properties of strontium barium niobates. Moreover, we examined the pulse switching of undoped SBN-0.61 and doped SBN-0.61 : Ce crystals. The choice of the Ce dopant in this case was dictated by the fact that, as was shown in the recent work [6], the SBN : Ce crystal exhibits new optical effects, which are specific to photorefractive ferroelectrics and can be associated with the influence of switching on the holographic characteristics.

It should be emphasized that this paper presents the results of a preliminary study. In general, the search for techniques of optimizing the properties of strontium barium niobates for different applications is the main purpose of the investigation of strontium barium niobates doped with rare-earth metals.

2. STUDIED CRYSTALS

The SBN-0.61 and SBN-0.61 : RE (where RE = Ce, La, La + Ce, Nd, Tm, and Yb) crystals were studied in this work. The SBN-0.61 : Ce, SBN-0.61 : La, SBN-0.61 : Tm, and SBN-0.61 : Yb crystals were grown by the Czochralski method. The profiled SBN and SBN-0.61 : Nd crystals and the codoped SBN-0.61 : (La + Ce) crystals were grown by the Stepanov method [19]. For doping, the rare-earth metal oxides were introduced into the melt. All the crystals, except for SBN-0.61 : Ce, were grown at the Research Center for Laser Materials and Technology, Institute of General Physics, Russian Academy of Sciences. The SBN-0.61 : Ce crystals were grown at the Physical Faculty of the Osnabrück University (Germany). The weight concentrations given below refer to the oxide concentration in the melt, and the corresponding molar and atomic concentrations in crystals were determined with a Camebax microanalyzer. The distribution coefficients for different rare-earth metals in SBN-0.61 are given in [19].

3. EFFECT OF RARE-EARTH METAL DOPANTS ON THE PHASE TRANSITION TEMPERATURE IN SBN-0.61 CRYSTALS

The temperature dependences of the permittivity ε_{33} were studied using thin plates of the *z*-cuts with electrodes made of a silver paste or evaporated gold. The measurements were carried out in the frequency range from 100 Hz to 20 kHz with a measuring field amplitude of no higher than 0.5 V/cm. Figure 1 depicts the dependences $\varepsilon_{33}(T)$ for the undoped SBN-0.61 crystal and the SBN-0.61 crystals doped with Ce, Yb, and La + Ce (inset) at a frequency of 1 kHz. As is known, the undoped SBN crystals of different compositions exhibit a frequency dependence of the temperature T_{max} at a maximum of T_{max}, which is characteristic of relaxors, and the dependence becomes stronger with an increase in the [Sr]/[Ba] ratio [11–13]. A similar frequency dependence of T_{max} was also found for SBN : La [3] and SBN : Tb [4]. In the studied SBN : RE crystals, an increase in the field frequency also leads to a decrease in the ε_{33} maximum and a shift in T_{max} toward the high-temperature range (see the inset in Fig. 1). As a whole, the effect of rare-earth metals on the frequency dependences of ε_{33} is qualitatively similar to the effect of an increase in the [Sr]/[Ba] ratio.

Table 1 presents the temperatures T_{max} at a frequency of 1 kHz for the crystals studied in the present work, the data obtained in our previous work [6] for SBN-0.61 : Ce, and the results taken from [4] for SBN-0.61 : Tb. As is seen from Table 1 and Fig. 1, the introduction of rare-earth metals brings about a sharp decrease in T_{max} and an increase in the smearing of the phase transition.

In the SBN-0.61 : Ce crystals, the shift in T_{max} linearly depends on the atomic concentration of Ce in the crystal: $T_{max} = 80–25[Ce]$ [6]. We roughly evaluated the shift ΔT_{max} per atomic percent of dopant in the crystal for other rare-earth metals (Table 1) under the assumption that, by analogy with SBN-0.61 : Ce, ΔT_{max} in each

Table 1. Effect of rare-earth metal dopants on the phase transition temperature of the SBN-0.61 crystals

Crystal	Dopant concentration		T_{max}, °C (1 kHz)	ΔT_{max} per atomic percent of dopant, K
	in melt, wt %	in crystal, at. %		
SBN-0.75			48	
SBN-0.61			83	
SBN-0.61 : Tm_2O_3	2.0	1.4	54–56	18
SBN-0.61 : Nd_2O_3	1.0	1.4	58–60	17–18
SBN-0.61 : La_2O_3	1.0	0.9	61	22
SBN-0.61 : CeO_2	0.4	0.66	63	
SBN-0.61 : CeO_2 [6]	1.6	2.1	27–30	25
SBN-0.61 : La + Ce	1 + 0.01		35–37	
SBN-0.61 : Yb_2O_3	2.6	2.6	62	7
SBN-0.61 : Tb_2O_3 [4]	1.0		70	≤10

Table 2. Parameters of the SBN and SBN : RE crystals at room temperature

Crystal*	ε_{33} (1 kHz)	d_{33}, C/N, 10^{-12}	r_{33}, pm/V	$V_{\lambda/2}$, V
SBN-0.75	3500		770	80
SBN-0.61	800	140	250	250
SBN-0.61 : 0.4% CeO_2	1500	190	330 [9]	
SBN-0.61 : 0.5% Tm_2O_3	2000			180
SBN-0.61 : 2.6% Yb_2O_3	2500	210		130
SBN-0.61 : 1% La_2O_3	1800			160
SBN-0.61 : (1% La + 0.01% Ce)	6000			130
SBN-0.61 : (1% La + 0.1% Ce)	8000			≤100

* The dopant concentration in the melt is given in wt %.

case linearly depends on the dopant concentration. (The Tb_2O_3 concentration in the melt was given in [4]; therefore, for the upper estimate of ΔT_{max} in SBN-0.61 : Tb, we assumed that the distribution coefficient k_{eff} for Tb is approximately equal to 0.5–0.6, which, on the average, is typical of rare-earth metals in strontium barium niobates.) It is seen from Table 1 that the shift in the phase transition temperature is as much as 20 K per 1 at. % Ce, Tm, La, and Nd.

The most intriguing result was obtained for the codoped SBN : (La + Ce) crystals, which were grown with the aim of their usage in the holography. In these crystals, the La_2O_3 concentration (1 wt %) is considerably higher than the CeO_2 concentration (0.01 and 0.1 wt %). Therefore, it could be expected that the phase transition temperature in these crystals should be close to T_{max} for SBN-0.61 : 1 at. % La, because the doping with 0.1 wt % CeO_2 (0.2 at. % Ce) leads to a shift in T_{max} by no more than 5 K [6]. However, the effect of the codoping appears to be nonadditive and anomalously strong: $T_{max} \approx$ 37–40°C in the crystals SBN-0.61 : 1 at. % La : Ce (see the inset in Fig. 1). Moreover, according to the estimates based on the microanalysis, the La concentrations in the crystals SBN-0.61 : 1 at. % La and SBN-0.61 : 1 at. % La : Ce are virtually identical, which means that the large difference between T_{max} in these crystals cannot be explained by different concentrations of the La dopant. In the SBN-0.61 : (La + Ce) crystals, the phase transition is the most smeared, and the frequency dispersion of ε_{33} is the most pronounced (inset in Fig. 1).

Despite an increase in the smearing of the phase transition upon doping with rare-earth metals, the Curie–Weiss law is fulfilled in good approximation in the frequency range from 100 Hz to 20 kHz for all the studied SBN-0.61 : RE crystals with the exception of SBN-0.61 : (La + Ce).

4. EFFECT OF RARE-EARTH METAL DOPANTS ON SOME PARAMETERS OF SBN-0.61 CRYSTALS

The doping of the SBN-0.61 crystals by all the rare-earth metal dopants is accompanied by an increase in the permittivity ε_{33} under normal conditions (Table 2), which is caused by a decrease in the temperature T_p and

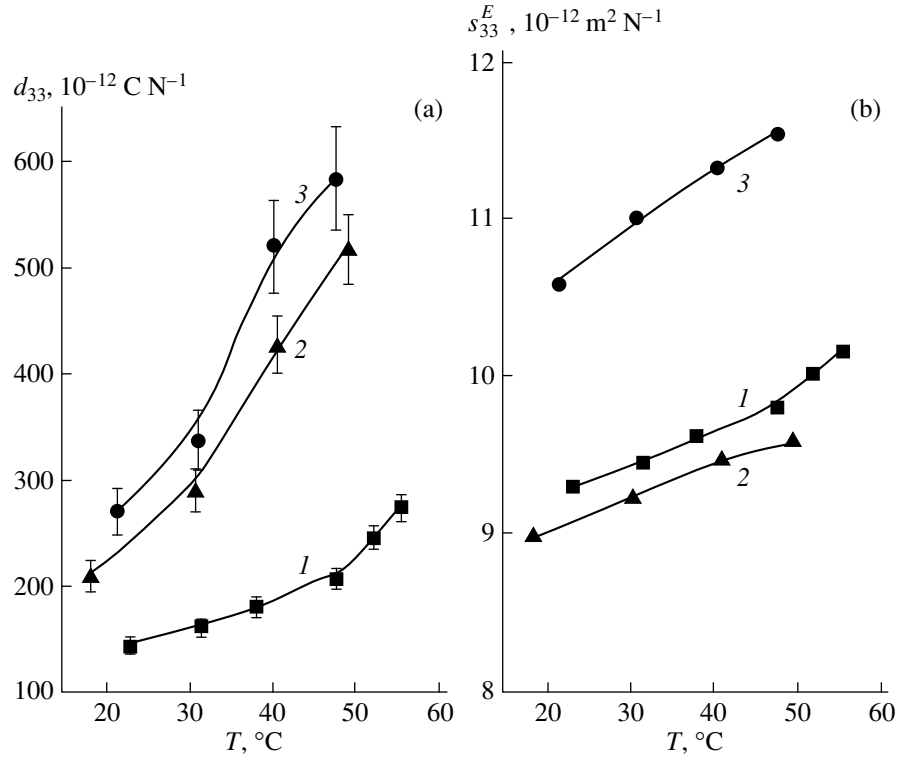

Fig. 2. Temperature dependences of (a) the piezoelectric coefficient and (b) the elastic compliance for (*1*) SBN-0.61, (*2*) SBN-0.61 : Yb, and (*3*) SBN-0.61 : Ce crystals.

the smearing of the phase transition. An increase in ε_{33} should result in an increase in a number of parameters. This can be demonstrated by the example of the piezoelectric and electrooptical properties of the SBN-0.61 : RE crystals. The piezoelectric coefficients d_{33} and half-wave voltages $V_{\lambda/2}$ were evaluated at room temperature (Table 2).

The piezoelectric coefficients d_{33} for the crystals preliminarily polarized by an external field were measured in the frequency range from 100 kHz to 5 MHz by using the resonance–antiresonance method [20]. The calculations were performed by the formula

$$d_{33} = \frac{\pi}{4}\sqrt{\frac{\varepsilon_{33}\varepsilon_0(f_r - f_a)}{\rho f_r^3 h^2}},$$

where f_r and f_a are the resonance and antiresonance frequencies, respectively; ρ is the crystal density taken equal to the density of the undoped SBN-0.61 crystal [7]; and h is the crystal thickness along the polar axis. The error of measurements was no more than 10%. The d_{33} coefficient obtained for the undoped SBN-0.61 crystal (Table 2) agrees well with the reference data [2, 7] (however, its value is less than $d_{33} = 190 \times 10^{-12}$ C/N determined in [3]).

Figure 2a displays the temperature dependences of d_{33} for the crystals SBN-0.61, SBN-0.61 : 0.66 at. % Ce, and SBN-0.61 : 2.6 at. % Yb. The doping with rare-earth metals brings about a substantial increase in the piezoelectric coefficients over the entire temperature range. The temperature dependences of the elastic compliance s_{33}^E calculated from the resonance frequencies are shown in Fig. 2b. These dependences are similar to the dependences $s_{33}^E(T)$ obtained for SBN : Ce in [8]. From Figs. 2a and 2b, it follows that an increase in d_{33} upon doping with rare-earth metals is predominantly determined by an increase in ε_{33}. At the same time, for each specific SBN : RE crystal, an increase in d_{33} with temperature is contributed by both $\varepsilon_{33}(T)$ and $s_{33}^E(T)$.

The half-wave voltages $V_{\lambda/2}$ were measured by the standard polarization-optical method with a He–Ne laser (λ = 0.63 μm) as a radiation source. The angle between the polarizations of radiation and crossed polarizers was 45°, the propagation vector of radiation was perpendicular to the polar axis z, and the field was applied along the z axis. The $V_{\lambda/2}$ voltages were determined by the dynamic technique in a 50-Hz sinusoidal field. The $V_{\lambda/2}$ voltages obtained for the undoped SBN-0.61 crystal (Table 2) are in good agreement with the reference data [2, 5]. An appreciable decrease in $V_{\lambda/2}$ for all the SBN-0.61 : RE crystals as compared to that for the undoped SBN-0.61 crystal indicates the corresponding increase in the linear electrooptical coefficient r_y. The $V_{\lambda/2}$ value ≤100 V for the codoped SBN-

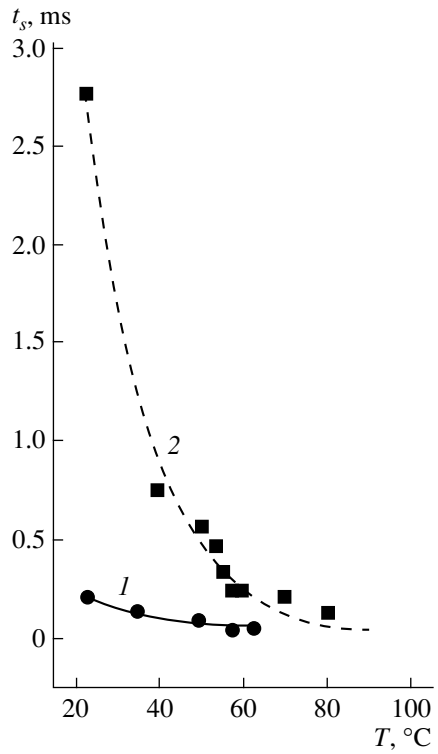

Fig. 3. Temperature dependences of the switching time for (*1*) SBN-0.61 and (*2*) SBN-0.61 : Ce crystals in a field of 5 kV/cm.

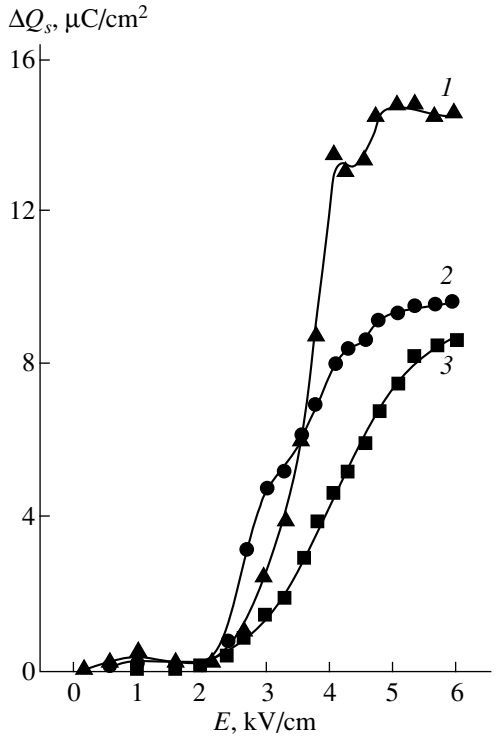

Fig. 4. Field dependences of the switched charge for (*1*) nonpolarized SBN-0.61 : Ce crystals, (*2*) after the polarization of crystals in an external field of 4 kV/cm at room temperature, and (*3*) after the polarization of crystals in an external field of 2 kV/cm upon slow cooling from 120 °C to room temperature.

0.61 : (La + Ce) crystals is close to the lowest known voltage (50–75 V) found for the SBN-0.75 crystals [2]. Note that $V_{\lambda/2}$ in our SBN-0.75 crystals is equal to 80 V (Table 2).

5. FEATURES OF FERROELECTRIC SWITCHING IN STRONTIUM BARIUM NIOBATE CRYSTALS

As far as we know, there are no works dealing with the pulse switching of strontium barium niobate crystals. In this respect, we studied first the undoped SBN-0.61 crystals. Then, for the most part, the SBN-0.61 : 0.66 at. % Ce crystals were investigated for comparison. For these crystals at room temperature, the spontaneous polarization P_s calculated from pyroelectric measurements is equal to 16–20 μC cm^{-2}.

The switching currents excited in the crystals by single-shot rectangular pulses with a width of 0.1 s and a short rise time ≤0.1 μs were measured by the Merz method (see, for example, [21]). The pulse amplitude was as large as 8 kV/cm, and the pulse separation was equal to several minutes. Plates 1–2 mm thick were used in the experiments. The shape of the switching current i_s observed in the studied crystals is identical to a characteristic pulse shape presented in monographs for model ferroelectrics [21]. The switching current i_s, the switched charge ΔQ_s (the integral of the switching current i_s over the time), and the switching time t_s were studied as a function of pulse amplitude and temperature. The time corresponding to 90% of the switched charge was taken as the switching time t_s [21].

The switching process in undoped and doped strontium barium niobates obeys general regularities characteristic of model ferroelectrics [21] and, at the same time, shows a number of specific features of fundamental importance. The switching kinetics in the fields corresponding to the "full" switching (for more detail, see below) over the entire temperature range is described by the activation dependence $t_s^{-1} = t_\infty^{-1}\exp(-\alpha/E)$, where α is the activation field. The time t_s decreases as the phase transition is approached (Fig. 3), which is typical of ferroelectrics. The value of α for the SBN-0.61 : RE crystals is lower than that for the SBN-0.61 crystals. For example, the α values for the SBN-0.61 and SBN-0.61 : Ce crystals at T = 30°C are equal to 17 and 11 kV/cm, respectively. An increase in the temperature leads to a decrease in α for both crystals.

The doping with rare-earth metals results in a "retardation" of the switching. As is seen from the dependences $t_s(T)$ (Fig. 3), the time t_s for the SBN-0.61 : Ce crystal over the entire temperature range is consider-

ably (almost by an order of magnitude) longer than that for the undoped SBN-0.61 crystal.

A substantial difference between the switching characteristics of the nonpolarized ("polydomain") crystals and the crystals polarized in the external field is a fundamental feature of the pulse switching in the SBN and SBN : RE crystals. The dependences of the charge ΔQ_s on the switching field for the SBN-0.61 : Ce crystal are demonstrated in Fig. 4. Curve *1* was obtained for the polydomain crystal. In this case, the $\Delta Q_s(E)$ dependences are virtually identical for the switching fields of both signs. Curves *2* and *3* were derived for the same crystal preliminarily polarized in the external field under different conditions (in these cases, the $\Delta Q_s(E)$ dependences for the fields of opposite signs differ sharply). Note that curves *2* and *3* correspond to the switching in the fields with directions opposite to the direction of the polarizing field. Curve *2* characterizes the switching of the crystal polarized in a field of 4 kV/cm for 1 h at room temperature. Curve *3* describes the switching of the crystal in which a single-domain state was produced upon prolonged cooling from the paraelectric phase down to room temperature in a field of 2 kV/cm. In all the cases, the $\Delta Q_s(E)$ dependences flatten out, but the limiting values of ΔQ_s are different. The limiting value is maximum ($\Delta Q_s \approx P_s$) for the nonpolarized crystals. For the polarized crystals, ΔQ_s is substantially lower and decreases with an increase in the duration or amplitude of the polarizing field. After the prolonged application of the fields with alternating polarity to the polarized crystal, the value of ΔQ_s increases owing to a partial depolarization.

As noted above, the kinetic characteristics of switching $t_s(E)$ were studied in the fields corresponding to the full switching. The term full switching was used according to the commonly accepted terminology and only implies that the $t_s(E)$ dependences were obtained in the fields at which $\Delta Q_s(E)$ flattens out. However, in the polarized crystals, ΔQ_s at the saturation is less than P_s (Fig. 4); i.e., the switched volume is considerably smaller than that in the polydomain crystal. Therefore, the values of t_s in the polydomain crystals are substantially larger than the times t_s observed in the same crystals after the preliminary polarization.

Another specific feature of the pulse switching in the SBN-0.61 and SBN-0.61 : RE crystals is the high values of the so-called fields of the onset of switching. For example, this threshold quantity under the field conditions used is equal to approximately 2 kV/cm (Fig. 4). At lower fields, the switching current is, at least, one order of magnitude less. The same features of the pulse switching (the high fields of the onset of switching and a decrease in the values of ΔQ_s and t_s due to the polarization in the external field) are observed in the SBN-0.75 crystals.

6. DISCUSSION

Let us discuss the experimental results in the order of their representation. Our experimental observations in agreement with the data available in the literature demonstrate that the doping of the strontium barium niobate crystals by all the studied rare-earth metal dopants leads to a considerable decrease in the phase transition temperature T_p. Most likely, this conclusion can be extended to all the rare-earth metal dopants. The influence of the rare-earth metals on the T_p temperature is much more efficient than the change in the [Sr]/[Ba] ratio. An increase in the Sr content from 61 to 75 at. % brings about a decrease in T_p from 80 to 40–50°C [1, 2] (Table 1), whereas the same result can be achieved by doping only with 1–2 at. % of the rare-earth metal. According to our results and the data available in the literature, it is possible to distinguish two groups of the rare-earth metal dopants which differ in the quantitative effect on the T_p temperature: RE1 = Ce, Tm, La, and Nd, for which $\Delta T_{max} \geq 20$ K, and RE2 = Tb and Yb, for which the effect is substantially less ($\Delta T_{max} \leq 10$ K).

The nature of a profound effect of the rare-earth metal dopants on the phase transition in strontium barium niobates and the difference in the influence of the two groups of dopants cannot be analyzed, because the location of rare-earth metal ions in the strontium barium niobate lattice is unknown. This problem was studied only for the Ce dopant. It was shown that Ce in the strontium barium niobate lattice predominantly occurs in the charge state 3+ [22, 23] and, most likely, replaces Sr [24]. The location of the Ce ions is uncertain, because the Sr ions are statistically distributed over two structural positions [1, 2]. It is obvious that the La [3], Tm [6], and Nd [17] dopants in the lattice also occur in the charge state 3+. In general, it is reasonable to assume that all the rare-earth metal ions, which have large ionic radii ($r_i \geq 0.85$ Å [25]), replace Sr^{2+} (r_i = 1.12 Å) or Ba^{2+} (r_i = 1.34 Å) rather than Nb^{5+} ($r_i \approx 0.7$ Å).

An increase in many parameters, specifically in the permittivity, over a wide range of temperatures is an important practical result of a decrease in the T_p temperature upon introduction of rare-earth metals. In this respect, of particular interest are the codoped SBN : (La + Ce) crystals, in which the permittivity ε_{33} is almost one order of magnitude larger than that in the undoped SBN-0.61 crystals, and a broad smearing of the phase transition (Fig. 1) ensures a rather weak temperature dependence of ε_{33}.

In oxygen octahedral ferroelectrics, the linear electrooptical coefficients and the permittivity ε_{33} are related by the known relationships [26]

$$r_{13} = 2g_{13}P_s\varepsilon_{33}\varepsilon_0,$$

$$r_{33} = 2g_{33}P_s\varepsilon_{33}\varepsilon_0,$$

where g_{ik} are the temperature-independent quadratic electrooptical coefficients in the corresponding cen-

trosymmetric phase. Consequently, an increase in ε_{33} upon doping with rare-earth metals should be attended by an increase in the r_{ij} coefficients. Our rather rough estimates of the $V_{\lambda/2}$ voltage (Table 2) indicate that the electrooptical coefficients r_{33} in all the studied crystals increase by a factor of approximately two. This is somewhat less than the magnitudes expected reasoning from an increase in the permittivity ε_{33} [in certain SBN : RE, ε_{33} is three or four times larger than that in SBN (Table 2)]. In part, this is explained by the fact that the spontaneous polarization in the SBN : RE crystals (P_s = 15–20 $\mu C/cm^2$) owing to the smearing of the phase transition is less than that in the SBN crystals ($P_s \geq 25$ $\mu C/cm^2$ [1, 2]). The doping with certain rare-earth metals (La and Yb) is not accompanied by the appearance of absorption bands in the visible spectral range. Therefore, these rare-earth metal dopants do not change the transmittance and can serve as efficient "controllers" of optical parameters such as the electrooptical coefficients, linear and nonlinear susceptibilities, etc. In order to increase the optical parameters of the strontium barium niobate crystals, the doping of the SBN-0.61 crystals by the rare-earth metals seems to be more efficient compared to an increase in the Sr content, because the SBN-0.61 crystals corresponding to the congruent melt [2] possess the best optical quality among all the SBN compositions. The doping of the SBN-0.61 crystals by the rare-earth metals with the use of appropriate technological procedures does not deteriorate the crystal homogeneity as particularly evidenced by a wide employment of the SBN-0.61 : Ce crystals in the holography [10].

Our inference regarding a substantial increase in the d_{33} coefficients in the SBN-0.61 : Ce and SBN-0.61 : Yb crystals (Table 2) suggests that these materials, similar to SBN : La [3], can find a wide use in piezoelectric engineering. Note that an increase in the piezoelectric coefficients is not an *a priori* obvious consequence of a decrease in the T_p temperature; for example, upon doping with Tb, the value of d_{33} remains virtually constant [4].

It is quite possible that the effect of rare-earth metal dopants on the T_p temperature in strontium barium niobates is not unique in character. For example, it was found that a heavy doping of SBN-0.61 by Cr leads to a substantial decrease in the T_p temperature [27]. However, unlike the doping with rare-earth metals, this interesting result is of no practical importance, because a strong optical absorption in the visible range, which appears in the highly doped SBN : Cr crystal, prevents the traditional use of this material in holography [10].

Now, we dwell on the results obtained for the pulse switching. A decrease in the switched charge upon application of fields is the most important finding. This is in agreement with the data obtained in [18, 28] on the irreproducibility of dielectric hysteresis loops in strontium barium niobates in static and quasi-static fields upon repeated cycling, which is attended by a change in the shape of loops and a decrease in their amplitudes. The results of optical experiments (the generation of the second harmonic of Nd–YAG laser radiation by the microdomain structure in SBN-0.6 upon switching) [15] also indirectly indicate a decrease in the switched charge after the repeated application of a pulsed field, as a result of which the intensity of the second-harmonic radiation turns out to be uncontrollable.

The regularities observed in the pulse switching can be interpreted in the framework of the model proposed in [18, 29] for explaining the "anomalous" field and the time dependences of the polarization P for the strontium barium niobate crystals. It can be assumed that the observed features are associated with the relaxor nature of the materials and stem from the occurrence of the strong randomly distributed internal field E_i in a polar crystal with an inhomogeneous distribution of its composition. The full repolarization of this crystal is achieved only in the case when the external field $|E| > |E_i|$ at each point in the bulk (i.e., in this case, the notion of the specific coercive field loses its meaning). Upon application of the field $|E| < |E_i|$, a part of the material transforms into a stable nonrepolarizable state. As a result, the switched charge in the field of the opposite sign becomes less than that in the nonpolarized crystal, which can be seen from Fig. 4. In our opinion, the model proposed in [18, 29] and the dependences $\Delta Q_s(E)$ obtained in this work (Fig. 4) partly explain the scatter in the P_s values available in the literature for strontium barium niobates (from 20 to 35 $\mu C/cm^2$ for SBN-0.61). It seems likely that only the limiting ("equilibrium" for a given polarizing field) value of $P_e < P_s$ was measured in a number of cases. As was shown in [29], the kinetics of polarization relaxation $P(t)$ in the given field E for strontium barium niobates is contributed to by fast and slow (of an order of 1 min) components. Thus, the full switching cannot be realized at all in the pulsed fields (in our case, with a pulse length of 0.1 s) up to very large amplitudes.

The results obtained in [18, 28] and this work demonstrate that the polarization in strontium barium niobates depends on the external fields, which, to a certain degree, explains the degradation or instability (noted in the literature) of different parameters (for example, the piezoelectric and electrooptical coefficients) during the practical use of strontium barium niobates. This degradation is one of the causes that restrict the application of strontium barium niobates. Therefore, from the practical standpoint, the problem of optimizing the properties of these materials for applications resides in a decrease in the energy of the potential barriers and the equalization of their distribution over the bulk (i.e., a decrease in the strength of the field E_i and an increase in the uniformity of its distribution). The observed decrease in the activation field of switching α upon doping with Ce, preliminary investigations, and the data obtained in [2, 4] suggest that this possibility, to

some extent, is provided by the doping with rare-earth metals.

7. CONCLUSION

The doping of strontium barium niobate crystals by the rare-earth metals leads to a sharp decrease in the phase transition temperature T_p. The shift in the T_p temperature per atomic percent of dopant in the crystal is equal to about 20 K for RE1 = Ce, Tm, La, and Nd and is less than 10 K for RE2 = Tb and Yb. Moreover, the smearing of the phase transition becomes more pronounced, which especially manifests itself in the codoped SBN : (La + Ce) crystals. This effect of the rare-earth metal dopants on the T_p temperature is accompanied by a considerable increase in the permittivity over a wide range of temperatures and, as a consequence, by a substantial rise in the piezoelectric and electrooptical coefficients. It is experimentally found that the piezoelectric coefficient d_{33} appreciably increases in the SBN-0.61 : Ce and SBN-0.61 : Yb crystals, and the half-wave voltage (for the 0.63-μm radiation) decreases in the SBN-0.61 : La, SBN-0.61 : Tm, SBN-0.61 : Yb, and SBN-0.61 : (Ce + La) crystals (in the last case, $V_{\lambda/2} \leq 100$ V). Consequently, the rare-earth metal dopants can be considered the efficient controllers of the practically important parameters for strontium barium niobate crystals.

The pulse switching of the undoped SBN-0.61 crystal and the SBN-0.61 : Ce crystal was investigated for the first time. It was found that, in addition to the common kinetic regularities characteristic of ferroelectrics, the switching in strontium barium niobate crystals of all the compositions exhibits a number of features, the most important of which is a decrease in the switched charge ΔQ_s upon the preliminary application of external fields. This effect that is evidently responsible for the instability of the parameters of strontium barium niobates (observed in practice) stems from the specific features of the polarization in the relaxor ferroelectric.

ACKNOWLEDGMENTS

We are grateful to V.V. Gladkiĭ for helpful remarks.

This work was supported by the Russian Foundation for Basic Research, project nos. 98-02-16384 and 00-02-16624.

REFERENCES

1. M. E. Lines and A. M. Glass, *Principles and Application of Ferroelectrics and Related Materials* (Clarendon, Oxford, 1977; Mir, Moscow, 1981).
2. Yu. S. Kuz'minov, *Ferroelectric Crystals for Control of Laser Radiation* (Nauka, Moscow, 1982).
3. R. R. Neurgaonkar, J. R. Oliver, W. K. Cory, *et al.*, Ferroelectrics **160**, 265 (1994).
4. P. L. Zhang, W. L. Zhong, Y. Y. Song, and H. C. Chen, Ferroelectrics **142**, 115 (1993).
5. N. Wittler, G. Greten, S. Kapphan, *et al.*, Phys. Status Solidi B **189**, K37 (1995).
6. T. Volk, Th. Woike, U. Doerfler, *et al.*, Ferroelectrics **203**, 457 (1997).
7. *Landolt–Börnstein physikalisch–chemische Tabellen* (Springer-Verlag, Berlin, 1990), New Series Vol. III/28a, p. 338.
8. B. M. Jin, Ruyan Guo, and A. S. Bhalla, Ferroelectrics **195**, 73 (1997).
9. U. Doerfler, R. Piechatzek, Th. Woike, *et al.*, Appl. Phys. B **B68** (5), 843 (1999).
10. R. R. Neurgaonkar, W. K. Cory, J. R. Oliver, and M. Khoshnevisan, Ferroelectrics **102**, 3 (1990).
11. J. Oliver, R. Neurgaonkar, and L. Corss, J. Appl. Phys. **64** (1), 37 (1988).
12. W. H. Huang, D. Viehland, and R. R. Neurgaonkar, J. Appl. Phys. **76** (1), 490 (1994).
13. D. Viehland, Z. Xu, and Weng-Hsing Huang, Philos. Mag. A **71** (2), 205 (1995).
14. M. Houe and P. D. Townsend, J. Phys. D: Appl. Phys. **28**, 1747 (1995).
15. Y. Y. Zhu, J. S. Fu, R. F. Xiao, and G. K. L. Wong, Appl. Phys. Lett. **70** (14), 1793 (1997).
16. S. Kawai, T. Ogawa, H. S. Lee, *et al.*, Appl. Phys. Lett. **73** (6), 768 (1998).
17. A. A. Kaminskiĭ, J. García-Sole, S. N. Bagaev, *et al.*, Kvantovaya Élektron. (Moscow) **25** (12), 1059 (1998).
18. V. V. Gladkiĭ, V. A. Kirikov, S. V. Nekhlyudov, *et al.*, Pis'ma Zh. Éksp. Teor. Fiz. **71** (1), 38 (2000) [JETP Lett. **71**, 24 (2000)].
19. L. I. Ivleva, N. V. Bogodaev, N. M. Polozkov, and V. V. Osiko, Opt. Mater. **4**, 168 (1995).
20. W. P. Mason, *Piezoelectric Crystals and Their Application to Ultrasonics* (Van Nostrand, New York, 1950; Inostrannaya Literatura, Moscow, 1952).
21. J. C. Burfoot, *Ferroelectrics: An Introduction to the Physical Principles* (Princeton, Toronto, 1967; Mir, Moscow, 1970).
22. N. C. Giles, J. L. Wolford, G. J. Edwards, and R. Uhrin, J. Appl. Phys. **77** (3), 976 (1995).
23. R. Niemann, K. Buse, R. Pankrath, and M. Neumann, Solid State Commun. **98**, 209 (1996).
24. Th. Woike, G. Weckwerth, H. Palme, and R. Pankrath, Solid State Commun. **102** (10), 743 (1997).
25. R. D. Shannon and C. T. Prewitt, Acta Crystallogr. B **25**, 925 (1969).
26. M. DiDommenico and S. H. Wemple, J. Appl. Phys. **40** (2), 720 (1969).
27. J. Seglins, S. Mendricks, R. Pankrath, *et al.*, Verh. DPG **1** (33), 601 (1998).
28. A. I. Burkhanov, A. V. Shil'nikov, and R. É. Uzakov, Kristallografiya **42** (6), 1069 (1997) [Crystallogr. Rep. **42**, 993 (1997)].
29. V. V. Gladkiĭ, V. A. Kirikov, S. V. Nekhlyudov, *et al.*, Fiz. Tverd. Tela (S.-Peterburg) **42** (7), 1296 (2000) [Phys. Solid State **42**, 1334 (2000)].

Translated by O. Borovik-Romanova

Physics of the Solid State, Vol. 42, No. 11, 2000, pp. 2137–2141. Translated from Fizika Tverdogo Tela, Vol. 42, No. 11, 2000, pp. 2074–2078.

MAGNETISM AND FERROELECTRICITY

On the Phase Transition in Foreign Phase Inclusions in CsH_2AsO_4, KD_2PO_4, and KH_2PO_4 Crystals

S. A. Gridnev and S. A. Kravchenko

Voronezh State Technical University, Moskovskiĭ pr. 14, Voronezh, 394026 Russia
e-mail: gridnev@nsl.vstu.ac.ru

Received April 18, 2000

Abstract—The low-frequency internal friction Q^{-1} and the shear modulus G in a paraelectric phase of CsH_2AsO_4, KD_2PO_4, and KH_2PO_4 ferroelectrics were studied using a reversed torsion pendulum method. Anomalies in the $Q^{-1}(T)$ and $G(T)$ dependences were observed above the Curie temperatures of these crystals, at temperatures 308, 253, and 293 K, respectively. The anomalies were associated with a first-order phase transition ($\bar{4}2m \longrightarrow mm2$) occurring in the foreign phase inclusions. © *2000 MAIK "Nauka/Interperiodica".*

Anomalies in various physical properties (electrical conductivity, dielectric, acoustic, thermal, optical, and other properties) have been discovered in KH_2PO_4-family crystals above the Curie temperature (T_C) by many researchers. As a rule, the anomalies were observed at temperatures near the thermal decomposition of the crystals [1–4]. The presence of the anomalies has been interpreted as a consequence of the high-temperature structural phase transitions in the solid phase [3, 5–7] or as the chemical decomposition of the crystals [4, 8]. High-temperature phase transitions are associated with H_2PO_4-group rotation around the crystallographic axes and with changes revealed in the hydrogen bonds and PO_4 groups [3, 5–7] involved. The results of investigations into the low-frequency elastic and inelastic properties of these crystals [9, 10] have shown that the temperature spectrum of internal friction Q^{-1} has a relatively complicated form. Along with the peaks in the temperature dependences of Q^{-1}, corresponding to the Curie temperatures and high-temperature phase transitions, there are peaks in Q^{-1} observed in the paraelectric phase slightly above T_C, but not identified in the origin.

Therefore, the aim of this work is to investigate the origin of anomalies of low-frequency internal friction and of the shear modulus in crystals of CsH_2AsO_4 (CDA), KD_2PO_4 (DKDP), and KH_2PO_4 (KDP) in the paraelectric phase under different external actions.

1. EXPERIMENTAL METHODS AND SAMPLES

The single crystals investigated were grown from supersaturated water solutions by the dynamic method, with adjustable temperature lowering. The specimens used for the measurements were in the form of $20 \times 2 \times 2$ mm rectangular bricks cut from homogeneous parts of crystal boules and polished with a wet fabric. The samples with *X* or *Z* orientation were oriented with their long side directed along the crystallographic *X* or *Z*, respectively.

The internal friction Q^{-1} and the shear modulus G were measured using an installation constructed on the basis of a reversed torsion pendulum [11] with a frequency of ~20 Hz and a deformation amplitude of $\sim 5 \times 10^{-5}$. The logarithmic decrement of the oscillations, divided by π, was chosen as the measure of internal friction. The systematic error was no more than 10% in Q^{-1} measurement and no more than 5% in the shear-modulus measurement. The installation also enabled us to take measurements of the sample torsion angle φ in the torsion pendulum as a function of temperature, and the automatic recording of $\varphi(T)$ curves was accomplished using an *XY* recorder. During measuring, the samples were placed in a thermostat, where a constant temperature was maintained and measured within an accuracy of 0.3 K in the temperature range from 90 to 370 K.

2. EXPERIMENTAL RESULTS AND DISCUSSION

The temperature dependences of internal friction Q^{-1} (curves *1*) and shear modulus G (curves *2*) for samples with an *X* orientation of the CDP, DKDP, and KDP crystals are presented in Figs. 1, 2, and 3, respectively. Two clear peaks are observed in the $Q^{-1}(T)$ dependences for all crystals in the temperature range investigated. These peaks are related to changes (softening) in the temperature behavior of the shear modulus G at temperatures T_C and T^*. As for the mechanical loss near T_C, the mechanism of the damping of low-frequency elastic oscillations at the first-order phase tran-

1063-7834/00/4211-2137$20.00

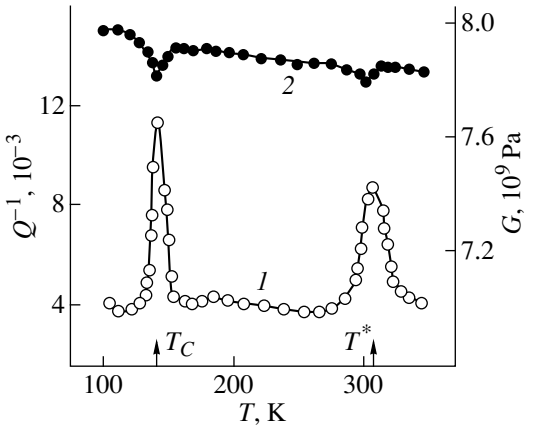

Fig. 1. Temperature dependences of (*1*) the internal friction Q^{-1} and (*2*) the shear modulus G of a CsH_2AsO_4 crystal at a heating rate of 0.5 K/min.

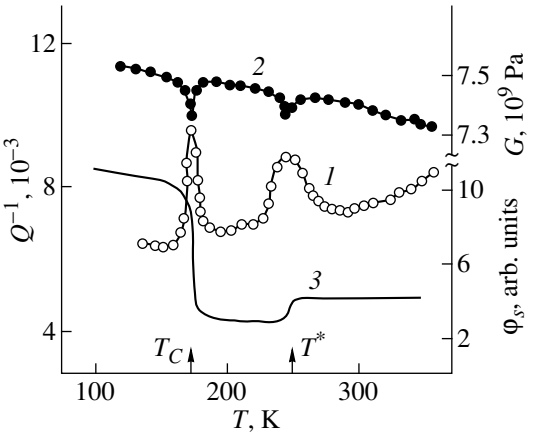

Fig. 2. Temperature dependences of (*1*) the internal friction Q^{-1}, (*2*) the shear modulus G, and (*3*) the spontaneous torsion angle φ_s of the KD_2PO_4 crystal.

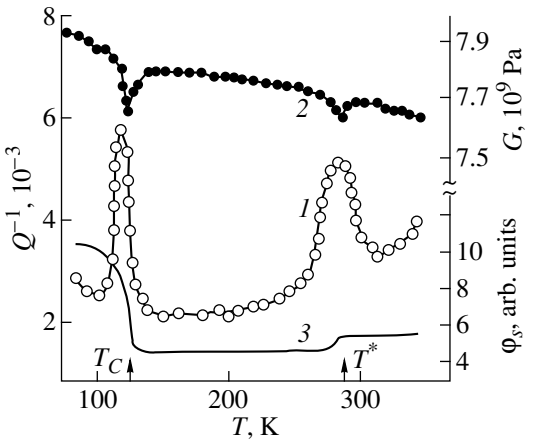

Fig. 3. Temperature dependences of (*1*) the internal friction Q^{-1}, (*2*) the shear modulus G, and (*3*) the spontaneous torsion angle φ_s of the KH_2PO_4 crystal.

sition responsible for the peak in Q^{-1} was considered, in detail, in [9, 12] and will not be discussed in this article.

To investigate the origin of the anomalies in Q^{-1} and G at the temperature T^*, measurements of $Q^{-1}(T)$, $G(T)$, and $\varphi(T)$ were taken at different rates of temperature change and different external mechanical strain amplitudes, etc. To get rid of the influence of the sample prehistory on the values measured, the samples were processed to achieve the same initial state. For this purpose, after each measurement, the samples were kept in a vacuum of about 10^{-2} torr in isothermal conditions at room temperature for twelve hours.

Analyzing the results presented in Figs. 1–3, it should be noted that the anomalies in Q^{-1} and G near T^* were observed in all the crystals studied. This fact suggests that the mechanism responsible for the observed anomalies is common for crystals of the KH_2PO_4 group. This mechanism is practically independent of deuteration and isomorphic ion substitution, which affect only the magnitude of the anomalies and the temperatures at which they are observed.

It is seen from the figures that the peaks in Q^{-1} at temperatures T^* for different crystals correlate with the softening of the shear modulus G. This softening has the same character here as at the phase transitions at T_C but is slightly smaller in magnitude. A temperature hysteresis of 5 K is observed in Q^{-1} and G measurements in a cycle of heating and subsequent cooling at a 1 K/min rate of temperature change. The temperature dependences of Q^{-1} were studied at different frequencies in the range from 6 Hz to 150 kHz. It was found that the height of the peak at T^* varies inversely with frequency, while there is no appreciable shift in the Q^{-1} peak position with temperature. Such behavior of the internal friction peak is characteristic of low-frequency relaxation processes associated with phase transition [12]. However, no peculiarities were observed, in the vicinity of this Q^{-1} peak, in the temperature behavior of the dielectric permittivity ε_{33} at a frequency of 1.5 kHz, nor were any observed in that of the electrical conductivity. This reasoning will be discussed later.

We suggest that the peak of the mechanical loss at T^* is due to the fluctuation mechanism associated with the nucleation of the new phase and the movement of the phase boundary throughout a system of stoppers [9, 12]. Hence, for the case of sufficiently low oscillation amplitudes of the sample, the height of the peak Q_m^{-1} is given by the equation:

$$Q_m^{-1} = \frac{G\beta x_s^2 m}{kT}\frac{}{\omega}, \qquad (1)$$

where m is the rate of the phase transformation (that is, the specific volume of the substance undergoing the phase transition per unit time), β is the effective volume of the critical nucleus, G is the shear modulus, x_s is the jump in the spontaneous deformation at the phase tran-

sition point, ω is the frequency, k is the Boltzmann constant, and T is the temperature.

As can be seen from formula (1), the fluctuation mechanism of Q^{-1} not only explains the peak height Q_m^{-1} varying as the reciprocal of the frequency, but also predicts the linear dependence of Q_m^{-1} on the rate of temperature change V (proportional to m). Indeed, such dependences of Q_m^{-1} on V were observed in the experiment for all crystals investigated (see, for example, Fig. 4 for a CDA crystal). The estimates show that the effects observed are not associated with the temperature flattening over the sample volume due to the finite value of thermal diffusivity nor with the influence of thermoelastic deformations on the experimentally measured values of Q^{-1} and G. In actual fact, the largest temperature difference ΔT along the sample radius r, caused by the thermal diffusivity χ of the material, can be estimated from the expression

$$\Delta T = \frac{Vr^2}{2\chi}. \qquad (2)$$

Substituting the values of $r = 1$ mm, $\chi = 10^{-3}$ cm^2/s [13], and the rate $V = 2.5$ K/min (the largest observed in the experimental conditions), we obtain $\Delta T = 0.1$ K, which is noticeably smaller than the Q^{-1} peak width which is equal to ≅30 K. This temperature difference along the sample thickness causes thermoelastic deformation

$$x_T = \alpha_T \Delta T/2, \qquad (3)$$

where α_T is the coefficient of linear expansion. Putting $\alpha_T = 4 \times 10^{-5}$ K^{-1} [13] at $T = 300$ K and $\Delta T = 0.1$ K, we obtain $x_T = 2 \times 10^{-6}$, which is an order of magnitude smaller than the deformation amplitudes used in the experiment.

Formula (1) allows one to estimate the jump in the spontaneous deformation x_s at the phase transition temperatures T_C and T^* by using the internal-friction experimental data. We assume that the critical nucleus volume is of the same order of magnitude as the size of Känzig's regions, $\beta \cong 10^{-19}$ cm^3 [14]. Substituting the available experimental data in Eq. (1), we determine for the CDA, DKDP, and KDP crystals the respective values of $x_s = 10 \times 10^{-3}$, 5×10^{-3}, and 1.5×10^{-3} at the T_C and $x_s = 3 \times 10^{-3}$, 9.8×10^{-4}, and 5×10^{-4} at the T^*.

In accordance with Eq. (1), the low-frequency internal friction at the first-order phase transition is dictated by phase transition kinetics and, in the case of isothermal measurements of Q^{-1}, with the temperature being fixed ($V \longrightarrow 0$), the time dependences for Q^{-1} should be observed. An example of these dependences for the CDA crystal is shown in Fig. 5. Similar dependences were obtained for the KDP and DKDP crystals. It has been recognized that $Q^{-1}(t)$ dependences are

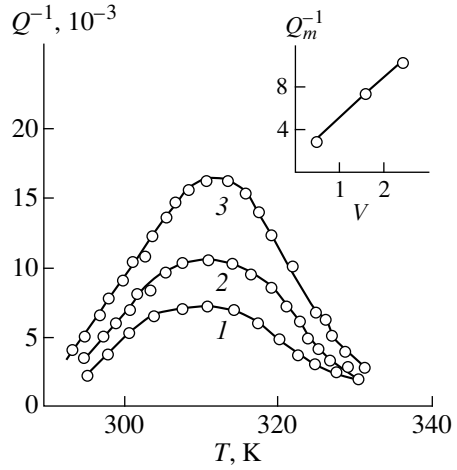

Fig. 4. Temperature dependences of Q^{-1} near T^* of a CsH_2AsO_4 crystal at different heating rates V: (*1*) 0.5, (*2*) 1, and (*3*) 2.5 K/min. The dependence of the Q_m^{-1} peak height on the heating rate V is shown in the inset.

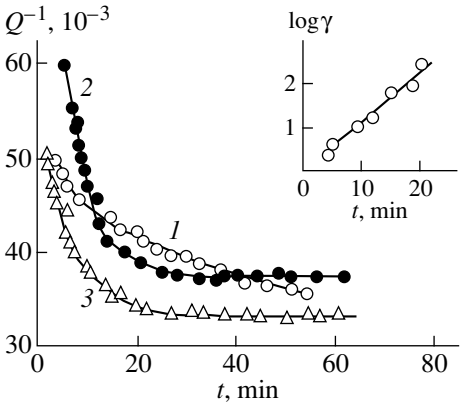

Fig. 5. Time dependences of Q^{-1} near T^* of a CsH_2AsO_4 crystal at different temperatures: (*1*) 298, (*2*) 308, and (*3*) 318 K. The dependence of log γ on time at $T = 318$ K is shown in the inset.

approximated sufficiently by exponential functions of the type

$$Q^{-1}(t) = Q_\infty^{-1} + (Q_0^{-1} - Q_\infty^{-1})\exp(-t/\tau), \qquad (4)$$

where Q_0^{-1} is the internal friction at the initial instant of time, Q_∞^{-1} is the internal friction at $t \longrightarrow \infty$, and τ is the relaxation time.

The possibility of this approximation is confirmed by the fact that the experimental points lie well enough on the straight lines (the inset in Fig. 5) in the coordinates $\log\gamma = \log(Q_0^{-1} - Q_\infty^{-1})/(Q^{-1} - Q_\infty^{-1})$ and time t. The relaxation time τ, estimated by Eq. (4), decreases

with a temperature rise, and the τ temperature dependence obeys the Arrhenius equation

$$\tau = \tau_0 \exp\left(\frac{U}{kT}\right), \quad (5)$$

where τ_0 is the preexponential factor depending only slightly on temperature, k is the Boltzmann constant, and U is the activation energy.

Calculating the experimental results using formula (5) gives the value of $\tau_0 = 1.6$ min and the barrier height $U = 0.1$ eV, which is close to the interaction energy of a phase boundary and a point defect [12]. Thus, the Q^{-1} time dependences can be explained by the kinetics of the interfacial boundaries driven by the diffusive redistribution of point defects in a process of isothermal annealing and by the movement of the interfacial boundaries to the new, energetically more favorable positions in the course of time.

The physical nature of the mechanical relaxation at the first order phase transition implies that the rate of the phase boundary displacement in the process of the phase transition is limited by the thermal fluctuational mechanism of overcoming the potential barriers created by stoppers (point defects). In this case, the role of overheating (or supercooling) in the occurrence of internal friction is reduced to decreasing the height of the potential barriers due to the pressure applied to the phase boundary by the thermodynamically unstable phase. Obviously, the potential barriers for the moving interfacial boundary are created by its interaction with point defects of the crystal lattice. Under the experimental conditions, the Q^{-1} peak width in the temperature dependence is determined by the duration of the phase transition, while the Q^{-1} peak shape reflects the change in the phase transition rate with temperature.

The experimental data obtained suggest that, in the crystals investigated, the peculiarities of the internal friction and the shear modulus near T^* are associated with a new structural phase transition of the first order above T_C. This conclusion is also supported by the investigations of the temperature dependences of the sample spontaneous torsion angle φ_s in the torsion pendulum (curves *3* in Figs. 2, 3). It is seen that a discontinuous change occurs in φ_s in the paraelectric phase at temperatures close to T^*, as well as at the ferroelectric phase transition point T_C, the magnitude of the jump at T^* being noticeably smaller than that near T_C.

As is known [15], in the ferroelectrics with a spontaneous shear strain x_s occurring at T_C, the occurrence of this deformation in the absence of an external mechanical stress results in spontaneous sample twisting in the torsion pendulum as the temperature is varied and passes through the phase transition point. In this case, the angle of twist φ_s is equal to

$$\varphi_s = \left(\frac{3l}{4a}\right)x_s. \quad (6)$$

Here, l is the sample length and a is the cross-section size of the sample.

The jump in the strain at the Curie point calculated for a KDP crystal by using Eq. (6) is $x_{6s} = 1.4 \times 10^{-3}$, which is close to the value of $x_{6s} = 1.5 \times 10^{-3}$ presented in [16]. The jump in strain at the temperature T^* as estimated from the experimental value of the angle of the twist has noticeably smaller values of $x_6 = 3 \times 10^{-3}$, 8.5×10^{-4}, and 2.5×10^{-4} for CDA, DKDP, and KDP crystals, respectively.

Despite the fact that crystals of the KH_2PO_4 family are well studied, there is no available data in publications supporting the existence of a phase transition at temperatures close to T^* and based on structural investigations. Therefore, it is unlikely that such a phase transition, if it exists, occurs everywhere in the crystal volume. Apparently, it occurs only in some local regions, i.e., the foreign phase inclusions. This suggestion is based on the results of KDP crystal investigations using a transition electron microscopy method [17, 18], revealing inclusions of the rhombohedral phase (the point symmetry group *mm*2) in the tetragonal matrix ($\bar{4}2m$) at room temperature, well above T_C. The average size of the inclusions is about 500–4500 Å, and the total volume of the inclusions is not large, amounting to 1.5–5% in different crystals. We consider that the anomalies of Q^{-1} and G discovered in this work are associated with the structural phase transition in the inclusions, while the macroscopic tetragonal matrix symmetry remains unchanged. Inasmuch as the specific volume of the inclusions is small, the dielectric permittivity of this microheterogeneous system is mainly determined by the dielectric properties of the matrix, rather than by those of the inclusions, thereby explaining the absence of these dielectric anomalies at the temperature T^*.

The existence of the phase transition at T^* in the inclusions of the phase with the orthorhombic symmetry *mm*2 is supported by the orientational dependence of Q^{-1} and G observed in the experiments. The peak of the internal friction Q_m^{-1} and the softening of the shear modulus G are not observed at an arbitrary sample orientation relative to the crystallographic axes. The anomalies of Q^{-1} and G are clearly pronounced near T^* only for the samples with the X orientation and are completely absent for the samples with the Z orientation. The anomalous behavior of the elastic and inelastic properties of X-oriented samples can be explained in the following way. The external torsion stress produces shear stress components σ_5 and σ_6 and, consequently, is related to the parameter x_6 of the transition. At the torsion of Z-oriented samples, the components σ_4 and σ_5 appear, which do not involve x_6; therefore, the anomalies in Q^{-1} and G are absent near T^*.

Thus, there is a set of experimental data obtained in this work: the existence of the peak of the internal friction Q^{-1} and the shear modulus G softening, which are characteristic of the phase transitions; the hysteresis of Q^{-1} and G during a cyclic temperature variation; the slight dependence of the Q^{-1} peak position on frequency; the orientational dependence of Q^{-1} and G; the long-term mechanical relaxation in the isothermal sample kept in the temperature region of the Q^{-1} peak; and the discontinuous change in the shear strain component x_6 estimated from the internal friction and the angle of the spontaneous sample twisting in the torsion pendulum. Altogether, these experimental data let us conclude that the phase transition occurs at the temperature T^* in the inclusions in the crystals studied with the symmetry change $\bar{4}2m \longrightarrow mm2$. The reason for the appearance of the orthorhombic phase inclusions in the tetragonal matrix has not yet been established. There are some suggestions [18] to the effect that small concentrations of uncontrolled impurities (Fe^{3+}, Cr^{3+}, Ca^{2+}, and Al^{3+}) could create local deformations, resulting in orthorhombic distortions of the crystal lattice. It is quite possible that the different phosphate complexes (HPO_4^{-2}, $H_5P_2O_8^-$, and H_3PO_4), which are always present, even in carefully purified saturated water solutions of KH_2PO_4 [19], could function like these impurities.

ACKNOWLEDGMENTS

This work was supported by the Russian Foundation for Basic Research, project no. 98-02-16055.

REFERENCES

1. A. I. Baranov, V. P. Khiznichenko, and L. A. Shuvalov, Ferroelectrics **100**, 135 (1989).
2. A. T. Amandosov, I. A. Velichko, and L. N. Rashkovich, Kristallografiya **26** (2), 406 (1981) [Sov. Phys. Crystallogr. **26**, 231 (1981)].
3. K. Itoh, T. Matsubayashi, E. Nakamura, and H. Motegi, J. Phys. Soc. Jpn. **39** (3), 843 (1975).
4. J.-H. Park, K.-S. Lee, and J.-N. Kim, J. Korean Phys. Soc. **32**, S1149 (1998).
5. R. Blinc, V. Dinic, D. Kolar, *et al.*, J. Chem. Phys. **49** (11), 4996 (1969).
6. V. G. Gofman, M. D. Ivchenkova, A. V. Mishchenko, and B. U. Shaĭmerdinov, Kristallografiya **22** (5), 1107 (1977) [Sov. Phys. Crystallogr. **22**, 631 (1977)].
7. J. I. Nicholson and J. Soest, J. Chem. Phys. **60** (2), 715 (1974).
8. B.-K. Choi and S.-C. Chung, Ferroelectrics **155**, 153 (1994).
9. S. A. Gridnev and B. M. Darinskii, Phys. Status Solidi A **47**, 379 (1978).
10. S. A. Gridnev and S. A. Kravchenko, Ferroelectrics **186**, 313 (1996).
11. S. A. Gridnev, V. I. Kudryash, and L. A. Shuvalov, Izv. Akad. Nauk SSSR, Ser. Fiz. **43** (8), 1718 (1979).
12. S. A. Gridnev, Ferroelectrics **112**, 107 (1990).
13. *Acoustical Crystals: A Handbook*, Ed. by M. P. Shaskol'skaya (Nauka, Moscow, 1973).
14. W. Känzig, Helv. Phys. Acta **24**, 175 (1951).
15. S. A. Gridnev, A. V. Biryukov, and O. N. Ivanov, Fiz. Tverd. Tela (St. Petersburg) **41** (10), 1848 (1999) [Phys. Solid State **41**, 1697 (1999)].
16. F. Jona and G. Shirane, *Ferroelectric Crystals* (Pergamon, Oxford, 1962; Mir, Moscow, 1965).
17. E. I. Suvorova and V. V. Klechkovskaya, Kristallografiya **36** (3), 729 (1991) [Sov. Phys. Crystallogr. **36**, 405 (1991)].
18. E. I. Suvorova and V. V. Klechkovskaya, Ferroelectrics **144**, 245 (1993).
19. M. R. Cerreta and K. A. Berglund, J. Cryst. Growth **84**, 577 (1987).

Translated by N. Kovaleva

Physics of the Solid State, Vol. 42, No. 11, 2000, pp. 2142–2147. Translated from Fizika Tverdogo Tela, Vol. 42, No. 11, 2000, pp. 2079–2084.

MAGNETISM AND FERROELECTRICITY

Narrow-Band Holographic Interference $LiNbO_3$-Based Filters

I. F. Kanaev, V. K. Malinovskiĭ, and N. V. Surovtsev

Institute of Automatics and Electrometry, Siberian Division, Russian Academy of Sciences, Universitetskiĭ pr. 1, Novosibirsk, 630090 Russia
e-mail: mvk@iae.nsk.su

Received March 16, 2000; in final form, April 20, 2000

Abstract—New experimental data on antiparallel-beam holograms recorded in $LiNbO_3$, temperature fixation of the recorded holographic gratings, and the spectral characteristic of a narrow-band (0.01 nm) interference filter are reported. The effects of asymmetry in the diffraction efficiency and the emergence of satellites in the transmission spectrum of the filter are observed. These effects are explained using the birefringence properties of the crystal and the ability of holograms to transfer power between the beams in the course of recording. *© 2000 MAIK "Nauka/Interperiodica".*

The exposure of ferroelectric crystals to light causes a change (Δn) in their refractive index [1]. Wide-range applications of these materials in optical holographic storage devices based on the above effect were predicted as early as at the beginning of the seventies. These predictions have not been implemented completely because of a number of problems that have defied solution, such as low sensitivity and photoinduced destruction of coherent light beams, which accompanies the variation in Δn. However, the recently discovered possibility of using such materials for developing ultra narrow-band interference filters can be regarded as an important advancement in science and technology. Specimens of such filters (with a transmission band of 0.01 nm) have already been constructed on $LiNbO_3$ crystals [2]. The conventional modern narrow-band filters ($\Delta\lambda \geq 0.05$ nm), which are used, for example, in solar astronomy, contain up to 50 optical units and weigh not less than ten kilograms. In contrast to the traditional approaches, the $LiNbO_3$-based narrow-band filter is a small-size unit including 3–5 optical elements and weighing less than one kilogram. The small size and mass of filters based on ferroelectric crystals make it possible to use them in space vehicles, in transmission lines operating on optical waveguide channels, and for other purposes.

In the modern technology of interference filter preparation, layers with different refractive indices are deposited by sputtering. As a rule, several dozens of such layers are used. The advantage of ferroelectric crystals lies in the possibility of creating a three-dimensional sinusoidal refractive index grating with practically any period (or spacing Λ) and any number of cycles (or layers). The spectral half-width ($\Delta\lambda$) of the filter is determined by the thickness (L) of the medium [3]:

$$\Delta\lambda = \lambda^2/2nL. \quad (1)$$

Here, n is the average refractive index of the layers, and λ is the wavelength of light corresponding to the reflection maximum of the filter. It follows from Eq. (1) that the spectral width of the filter depends on the crystal thickness as $1/L$; consequently, by varying L, we can create a filter with any transmission spectral width.

In a ferroelectric crystal exposed to light, an electric current

$$j = \chi\beta I + D\chi\nabla I + \sigma E \quad (2)$$

is generated [4]. This current is the sum of the photogalvanic ($\chi\beta I$), diffusion ($D\chi\nabla I$), and conduction (σE) currents. Here, χ, β, and D are the optical absorption, photogalvanic, and diffusion coefficients, respectively; σ is the conductivity; E is the electric field (photoinduced or applied to the crystal); and $I(r)$ is the optical intensity distribution. The current j leads to a spatial redistribution of charges matched with the $I(r)$ distribution, resulting in the emergence of an electric field $E(r) \propto I(r)$. The induced field $E(r)$ changes the refractive index due to the electrooptical effect: $\Delta n_{ij} = r_{ijk}E_k$. The recording of the gratings of the refractive index is carried out with the help of two coherent laser beams (with the wave vectors k_1 and k_2). In the region where the beams (which are characterized by the input intensities I_{01} and I_{02}) overlap, a periodic distribution of light intensity is formed due to interference [3]:

$$I = I_0(1 + m\cos(K_{12}r)), \quad (3)$$

where $I_0 = I_{01} + I_{02}$, $m = 2\sqrt{I_{01}, I_{02}/(I_{01} + I_{02})}$ is the modulation coefficient, and $K_{12} = k_1 - k_2$ is the wave vector of the grating (the optical grating and the holographic grating being recorded).

The recorded grating is erased during filter operation under subsequent exposure of the crystal due to photoconduction. However, it was proved long ago [5]

that the grating can be fixed; i.e., the erasure time can be increased significantly. The model of fixation, which remains popular even now, was proposed in [5] and supported later by other authors. The process of fixation is described in this model as follows. The current j emerging as a result of exposure to light (formula (2)) is due to photoexcited electrons. In their motion, photoelectrons are trapped at relatively deep energy levels. Illumination by light having the distribution of Eq. (3) forms a sinusoidal profile of the occupancy of traps (becoming donors)—an "electron matrix." Subsequent heating of the crystal (after recording) leads to domination of ionic conductivity. An optically induced "electron matrix" is screened by ions; i.e., an "ion matrix" is also formed. After the crystal is cooled to the initial temperature, exposure to light with a uniform intensity leads to equalization of the electron population due to nonuniform absorption of the "electron matrix" and diffusion processes. This gives rise to fields produced by the distribution of ions, i.e., by the "ion matrix," which remains unaltered upon exposure to light.

In this paper, we present the experimental data concerning the recording of holographic filters in $LiNbO_3$ crystals. The factors affecting the quality of the interference gratings being recorded, the thermal fixation, and the spectral parameters of the gratings, which have rarely been discussed in the literature, are considered.

1. SOME PARAMETERS OF HOLOGRAPHIC GRATING RECORDING IN ANTIPARALLEL BEAMS

We studied pure and Fe-doped monocrystalline samples of $LiNbO_3$ by recording reflection holograms in counter-propagating beams (the angle φ between the beams was equal or close to 180°). The wavelength of the recording beams was $\lambda = 514.5$ nm, and the beam intensities were close ($I_{01} \approx I_{02} \approx 0.5$ W/cm^2). The minimum spacing of the grating $\Lambda = \lambda/(2n\sin\varphi) = 112$ nm. The grating vector $\mathbf{K}_{12}$ was parallel to the Z axis ($\mathbf{K}_{12} \parallel Z$, where Z is a third-order axis parallel to the vector of the spontaneous polarization of the crystal).

The diffraction efficiency η of the gratings being recorded increased with the concentration of the Fe impurity. For example, for a crystal thickness L_z along the Z axis equal to 3 mm, the diffraction efficiency in crystals of the rated purity was $\eta \le 0.01$, while in Fe-doped crystals with 0.01 and 0.1 wt % impurity concentrations, the value of η attained 0.3 and 0.8, respectively. In these Fe-doped crystals, the diffraction efficiency η becomes the same (0.8–0.9) upon an increase in the sample thickness to 10 mm. In nominally pure crystals with $L_z = 10$ mm, the value of η does not exceed 0.01–0.05.

It is worth noting that the diffraction efficiency is strongly asymmetric: for reading beams with the wave vector k_- directed opposite to the Z axis (or having a negative projection on this axis), the value of η considerably exceeds (by a factor of 3) its value for a reading beam with the vector k_+.

For relatively long periods of exposure, the recording beam power is transferred to the beams reflected in the crystal from its back faces. The most significant transfer (up to 80%) is carried out from the beam with the wave vector k_+.

2. FIXED HOLOGRAPHIC GRATINGS

We investigated $LiNbO_3$ crystals doped with Fe (0.01–0.1 wt %). Fixation was carried out by the thermal method: after hologram recording, the crystal was heated until diffraction practically completely disappeared, after which the heater was disconnected, and the crystal temperature returned to the initial value as a result of natural heat exchange. The gratings were restored by exposing the crystal to white light from a quartz incandescent lamp or to a laser beam incident on the crystal at an angle other than Bragg's angle or having a wavelength differing from the recording wavelength. The experimental setup allowed control of the diffraction intensity during heating, cooling, and restoring irradiation.

It was found that fixation takes place at temperatures of heating from 90 to 180°C. For complete erasure of the hologram, the crystal must be held in the thermostat approximately for an hour at 90°C, or for several minutes at 180°C. The experiments were made on five groups of crystals with different concentrations of Fe (from 0.01 to 0.1 wt %).

The value of η of a fixed grating decreases as compared to its initial value by a factor 1.2–4 depending on the thermal regime and recovery conditions, as well as on the Fe concentration in the samples. Good recovery takes place in crystals with a high concentration of Fe. However, in heavily doped crystals (with 0.1 wt % Fe), the fixed grating relaxes rapidly due to dark conductivity (the characteristic time is of the order of several hours at room temperature). Repeated exposure of such a crystal to homogeneous light restores the hologram, and the process of relaxation and restoration can be repeated many times.

The spectral characteristics of diffraction at fixed gratings were investigated according to the following diagram (Fig. 1). A polychromatic light beam is collimated into a parallel beam (k_0) and is directed to a $LiNbO_3$ crystal with a recorded grating. Light satisfying the Bragg condition ($k_d(\lambda) = k_0(\lambda) + K_{12}$) is diffracted into a parallel beam with k_d. Light beams that do not satisfy Bragg's relation for the recorded grating are transmitted through the crystal. Light diffracted at the grating is passed through the spectrometer to a photodetector. The normal $\mathbf{n}_s$ to the crystal face forms an angle with the grating vector $\mathbf{K}_{12}$, which ensures complete spatial separation of the diffracted beam and the beam reflected from the surface.

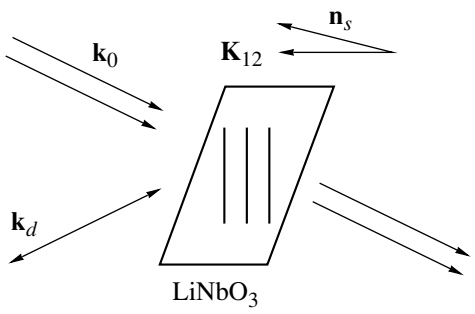

Fig. 1. Optical diagram of diffraction at a holographic filter.

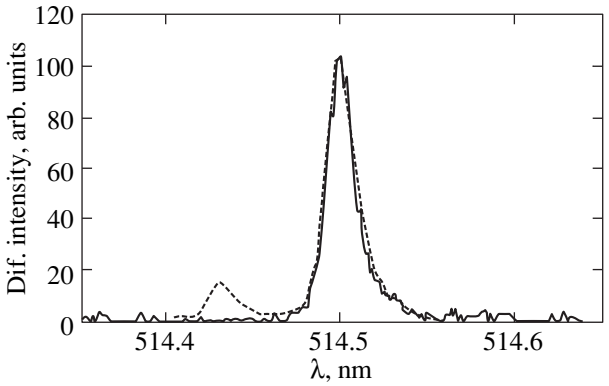

Fig. 2. Spectrum of the diffracted beam for an unpolarized (dashed curve) and a polarized (solid curve) light source.

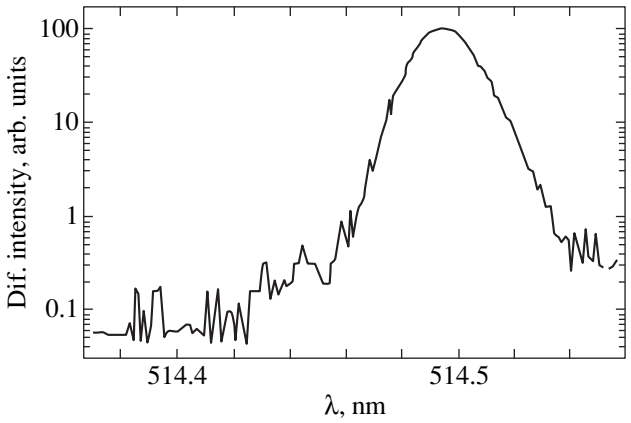

Fig. 3. Spectrum of the diffracted beam on the logarithmic scale for a polarized light source.

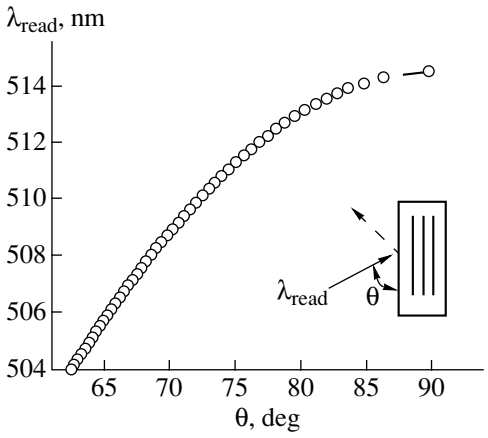

Fig. 4. Recording of the wavelength λ of the diffracted light as a function of the angle of incidence for a grating recorded in antiparallel beams with the wavelength 514.5 nm.

We will present below the spectral characteristics for a filter recorded in a sample of diameter 12 mm, L_z = 10 mm, and Fe concentration 0.01 wt %. The obtained diffraction efficiency of the fixed grating was ≥60%. On account of absorption in the crystal and reflection from the surfaces, the diffracted beam contains up to 15% of the light incident on the crystal and satisfying Bragg's condition. An incandescent lamp served as the source of the initial light. The spectra of light diffracted in the filter were measured on a two-grating spectrometer DFS-24.

When the crystal is illuminated by unpolarized white light, the spectrum of the diffracted beam displays two peaks (Fig. 2): the principal peak (λ = 514.5 nm) and an auxiliary peak displaced by 0.7 nm. Light polarizations in these beams are mutually perpendicular, and the intensities are approximately equal (the difference between the two peaks in Fig. 2 is due to the polarization selectivity of DFS-24). When the crystal is exposed to polarized light, only one peak is observed (see Fig. 2). The widths of the peaks shown in Fig. 2 were of the order of the instrumental resolution of the DFS-24 device, which was determined independently from the spectral response of the instrument to a laser line of 514.5 nm. According to estimates, the spectral width of the reflection line of the filter, taking into account the instrumental broadening, does not exceed 0.01 nm. In Fig. 3, the spectrum of diffracted light is shown on a logarithmic scale to characterize the efficiency of the suppression of the light that does not satisfy Bragg's condition near the diffraction maximum. It can be seen that the suppression of the intensity of the light detuned from the diffraction maximum by 0.1 nm is not worse than three orders of magnitude.

By varying the angle of incidence (Q) of the light beam on a crystal with a recorded holographic filter, we can displace the diffraction maximum of the filter in accordance with Bragg's condition for reflection holograms [3]

$$\Lambda^2 = \lambda^2/(n^2 - \cos^2 Q). \quad (4)$$

The theoretical curve presented in Fig. 4 shows that the spectral shift of the diffraction maximum (λ_{read}) can be as large as 10 nm or even larger. This possibility was

verified experimentally by analyzing the diffraction spectrum of the filter for different angles of incidence of the initial polychromatic light on the crystal. Figure 5 contains experimental data on the spectral characteristics of filters for three different angles Q.

We also studied the displacement of the spectral line of the filter under the action of an external field. It was found to be ±0.07 nm in a field of ±10 kV/cm applied along a direction perpendicular to the Z axis, and it is equal to zero if the field is applied along the Z axis. The result matches with the calculations based on the known electrooptical coefficients (this is clear from the analysis carried out in [6]). The choice of the recording geometry (i.e., $\mathbf{K}_{12} \parallel Z$) is optimal for obtaining a large η and for a considerable detuning from the effects of photoinduced scattering of light. However, the effect of the electric field on the position of the diffraction peak of the filter in this geometry is minimum as compared to some other orientations of $\mathbf{K}_{12}$ relative to the crystallographic axes of the crystal.

The results presented in Figs. 2, 3, and 5 were obtained on the grating which was recorded under the condition $\mathbf{K}_{12} \parallel Z$, and the polarizations of the recording beams were perpendicular to the plane of incidence ($\varphi \neq 180°$). If one of these conditions is violated, a second additional peak appears in the long-wave spectral range. Light polarizations of the right and left satellites are mutually perpendicular. The half-width of the spectral reflection line of the filter can increase considerably if the exposure time increases to the region of a slow increase in $\eta(t)$. Figure 6 illustrates the effect of these deteriorating factors on the spectral properties of the filter. In the course of the recording of this filter, the difference $\mathbf{K}_{12}$ was not parallel to Z, and they did not lie in the same plane, additionally the exposure time was tripled as compared to its optimal value.

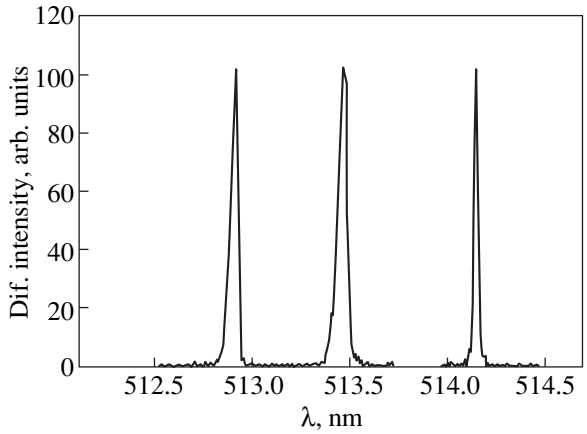

Fig. 5. Optical diffraction spectra for three different angles of incidence of a polychromatic beam.

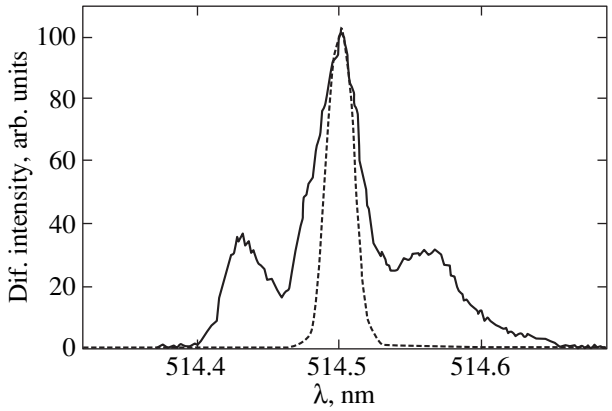

Fig. 6. Spectrum of the beam diffracted at a grating recorded under the following conditions: the difference $\mathbf{K}_{12}$ is not parallel to Z and does not lie in the same plane with Z (solid curve). The dashed curve corresponds to the resolution of the spectrometer.

3. DISCUSSION OF RESULTS

Here, we will explain the experimental results which do not require a detailed discussion of the mechanisms of recording and fixation on a microscopic level.

It follows from the results of experiments that the recording in principal beams can be worse (have a smaller value of η) than in the principal beam and the beam reflected from the back face. This is due to several factors. One of them is associated with the instability of the light wave phases in the bulk of the crystal. The phases of the principal beams vary stochastically on account of the relative mechanical vibrations of the elements of the optical system and the convective air flows, which are different in the regions where these beams propagate. This leads to spatial shifts of the interference peaks and, accordingly, to a decreased interference contrast and a decreased amplitude of the grating being recorded.

The interference pattern of the principal beam and the beam reflected from the back face does not experience any spatial displacement in the crystal. It is well known that antinodes (or interference maxima) are at a fixed distance from the reflecting face irrespective of the displacement of the crystal in any plane (except for rotational vibrations). Such a standing optical grating can easily be recorded without taking special measures for protection from the mechanical vibrations of the elements of the optical system and the convective flows of air.

There exists one more factor that affects simultaneously the value of η, its asymmetry, and the spectral resolution of the grating being recorded. It is associated with the transfer of power between the beams participating in the recording of the gratings. It is well known that the grating $\Delta n_h \cos(K_{12}x - \psi)$ is recorded in $LiNbO_3$ under the action of light with the distribution $I_0 \cos K_{12}x$. It is the sum of two gratings: $\Delta n_h \cos(K_{12}x - \psi) = \Delta n_n \cos K_{12}x + \Delta n_s \sin K_{12}x$, with $\Delta n_h = \sqrt{\Delta n_n^2 + \Delta n_s^2}$. One of them, viz., the undisplaced grating ($\Delta n_n \cos K_{12}x$),

coincides in phase with the optical interference grating, while the other grating ($\Delta n_s \sin K_{12}x$) is displaced by a quarter of the period ($\Lambda/4$). On the first grating, a time-dependent transfer of power is possible, but only if $I_{01} \neq I_{02}$ at the input surface of the crystal. The beam intensities I_1 and I_2 at the output surface can be written in the form (η_n is the diffraction efficiency of the undisplaced grating)

$$I_1 = I_{01}(1-\eta_n) + I_{02}\eta_n; \quad I_2 = I_{02}(1-\eta_n) + I_{01}\eta_n.$$

In the case of a displaced grating, an additional term $\pm 2\sqrt{I_{01}I_{02}(1-\eta_s)\eta_s}$ appears [7], which describes the interference energy transfer emerging as a result of the overlapping of two beams propagating in space with a phase shift equal to 0 or π. In the case of an undisplaced grating, the principal beams with intensities $I_{01}(1-\eta)$ and $I_{02}(1-\eta)$ and the diffracted beams ($I_{02}\eta$, $I_{01}\eta$) coinciding with them differ in phase by $\pm\pi/2$.

The interference transfer of power is asymmetric relative to the Z axis: it is positive for k_- beams and negative for k_+ beams. This asymmetry considerably affects the characteristics of recording in antiparallel beams. It was noted long ago [8] that, when a crystal is exposed to a single beam along the Z axis, the k_+beam can be completely transformed into the reflected k'_- beam, and vice versa, the reflected k'_+ beam can be transformed into the principal k_- beam. These are the effects of induced reflection and antireflection. In the former case, a low-intensity (reflected) beam is amplified, leading to the formation of an optical grating with improved contrast, and the grating being recorded is characterized by a large value of η. In the steady state, instead of passing through the crystal, the main beam k_+ can penetrate the crystal to a depth L_z at which the condition ($\eta_s \approx 0.5$) of a complete transfer of power is satisfied. The beam k_- is transmitted through the crystal and even is slightly intensified due to the transfer of the power of the reflected beam k'_+ to it. The asymmetry in the intensity variation of the k_+ and k_- beams on the $k_+ - k'_-$ and $k_- - k'_+$ gratings leads to the read-out asymmetry in η. It should be borne in mind that a reflected beam is also present in the readout. This means that the interference transfer of power between the k_+ and k_- beams persists during the readout. During the recording, the transfer of power between the principal beams also takes place. It can be noted that, for equal beam intensities at the entrance to the crystal, the transfer of power leads to an intensity disbalance and, accordingly, to a decrease in the interference contrast and in the amplitude of the grating being recorded. The recording on the principal grating $k_+ - k_- = K_{12}$ competes with the recording on the auxiliary grating $k_+ - k'_-$. When more exact conditions (the absence of a stochastic phase variation and an increase in the interference pattern contrast in the course of the transfer of power) are satisfied, the grating $k_+ - k'_-$ dominates in the recording, starting from a certain instant. The suppression of the k_+ beam caused by three factors (absorption and the transfer of power due to the two gratings $k_+ - k'_-$ and $k_+ - k_-$) leads to a decrease in its intensity with the increasing penetration depth. As a result, the effective thickness of the recorded lattice ($k_+ - k_- = K_{12}$) decreases, and the spectral resolution width increases in accordance with Eq. (1) (see Fig. 6).

It can be seen that the displaced grating leads to undesirable effects in the development of holographic interference filters. Its contribution can be minimized by using the optimal exposure time for the crystal during the recording of the holographic grating (at the initial instants of exposure, the recording of the principal grating $k_+ - k_- = K_{12}$ prevails in view of the larger magnitude of the interference maxima), by creating an antireflection coating (which reduces the intensity of the reflected beams), and by hermetically sealing or evacuating the optical system and eliminating its mechanical vibrations (which suppress the stochastic oscillations of the phases of the principal beams).

The reasons behind the emergence of satellites in the spectrum of diffracted light are associated with the anisotropic properties of the crystal, viz., electrooptics and birefringence. Let us consider the case when the vector K_{12} of the grating being recorded is parallel to the axis Z and $\varphi \neq 180°$. Depending on the direction of the polarization of the light beams, the following three cases are possible.

(1) Polarization is perpendicular to the plane of incidence of the beams relative to the Z axis. By definition, these are beams with ordinary polarization (e_o). They are used to record the grating with the vector $K_{12}^o = k_1^o - k_2^o$.

(2) When the polarization vector lies in the plane of incidence, the beam polarization is extraordinary (e_e). The grating being recorded is $K_{12}^e = k_1^e - k_2^e$.

(3) In the intermediate case, when the conditions of the first or second case are not satisfied for the polarization vector, the recording beams contain waves with the e_o and e_e polarizations. The gratings being recorded are K_{12}^o and K_{12}^e. The same situation is realized when the vector K_{12} is not parallel to Z.

When Bragg's conditions are satisfied, light beams with e_o, as well as e_e, polarization can experience diffraction on the same grating. If Bragg's condition (4) for the angle is satisfied for the e_o component of a beam of unpolarized white light, Bragg's condition for the e_e component of the beam is satisfied at another wavelength in accordance with (4). As a result, the readout in white light results in two diffraction peaks with

mutually perpendicular polarizations (λ_o and λ_e). A beam with the polarization e_e or e_o will undergo diffraction with the same, e_e or e_o, polarization.

The direction of the displacement of the second peak from the principal peak at λ_o (at which recording was carried out) can be determined from the equality $\Lambda_o = \Lambda_e$, since diffraction occurs on the same grating. This equality and Eq. (4) (where we put $Q \approx \pi/2$) lead to $\lambda_e n_e/n_o = \lambda_o$. Lithium niobate is a negative crystal, i.e., $n_o > n_e$. It can be seen that the λ_e is shifted relative to λ_o towards the short-wave region. If, however, λ_e is taken as the wavelength corresponding to the principal peak, the displacement takes place in the opposite direction. When the grating is recorded in beams with an intermediate polarization (between e_e and e_o), two gratings are recorded: K_{12}^e and K_{12}^o. In accordance with the above conclusion, the diffraction on these gratings results in the principal line (λ_o and λ_e) and in two satellites: the short-wave line with the polarization e_e and the long-wave line with the polarization e_o. In the principal line, light must be depolarized (in view of the presence of light with e_e and e_o polarizations).

Thus, we have analyzed experimentally the spectral characteristics of holographic filters based on $LiNbO_3$. It was proved that the characteristics of the filter can change depending on the recording and reading conditions.

The narrow-band ($\Delta\lambda \leq 0.01$ nm) interference filter created on the $LiNbO_3$ crystal as a result of our investigations is being tested at the Institute of Solar and Terrestrial Physics, Siberian Division, Russian Academy of Sciences. It is used for studying the intensity distribution of some spectral lines emitted from the Sun's surface.

ACKNOWLEDGMENTS

The authors are grateful to their colleagues V.M. Grigor'ev and P.G. Papushev from the Institute of Solar and Terrestrial Physics, Siberian Division, Russian Academy of Sciences, for their interest in this research and for organizing partial financial support for creating the filter. Thanks are also due to A.M. Pugachev for his active participation in the research at the initial stage.

This work was supported by the Russian Foundation for Basic Research, project no. 99-02-16697.

REFERENCES

1. A. Askin, C. D. Boyd, T. M. Dziedzic, *et al.*, Appl. Phys. Lett. **9**, 72 (1966).
2. G. A. Rakuljic and V. Leyva, Opt. Lett. **18** (6), 459 (1993).
3. R. J. Collier, C. B. Burckhardt, and L. H. Lin, *Optical Holography* (Academic, New York, 1971; Mir, Moscow, 1973).
4. M. E. Lines and A. M. Glass, *Principles and Applications of Ferroelectrics and Related Materials* (Oxford Univ. Press, Oxford, 1977; Mir, Moscow, 1981).
5. J. J. Amodei and D. L. Staebler, Appl. Phys. Lett. **18** (12), 540 (1971).
6. M. P. Petrov, S. I. Stepanov, and A. V. Khomenko, *Photosensitive Holographic Medium in Holography and Information Processing* (Nauka, Leningrad, 1983).
7. J. J. Amodei. Appl. Phys. Lett. **18** (1), 22 (1971).
8. I. F. Kanaev, V. K. Malinovskiĭ, and B. I. Sturman, Zh. Éksp. Teor. Fiz. **74** (5), 1599 (1978) [Sov. Phys. JETP **47**, 834 (1978)].

Translated by N. Wadhwa

Physics of the Solid State, Vol. 42, No. 11, 2000, pp. 2148–2150. Translated from Fizika Tverdogo Tela, Vol. 42, No. 11, 2000, pp. 2085–2086.

MAGNETISM AND FERROELECTRICITY

The Effect of Injected-Charge Spatial Distribution on the X-ray Induced Electron Emission Intensity in Ferroelectric Electrets

V. V. Kolesnikov and A. T. Kozakov

Research Institute of Physics, Rostov State University, pr. Stachki 194, Rostov-on-Don, 344104 Russia
e-mail: kozakov@iphys.rnd.runnet.ru

Received February 4, 2000; in final form, May 10, 2000

Abstract—The nonmonotonic behavior of electron emission intensity induced in a surface layer of a ferroelectric electret by soft x-ray irradiation with an injected charge depth is predicted using a model of an accelerating electric field. The predicted behavior is in agreement with the results of the model experiments. © *2000 MAIK "Nauka/Interperiodica".*

The electron emission induced from the surface of ferroelectric electrets by soft x-ray radiation has been called anomalous electron emission (AEE) due to some qualitative specifics in the physical behavior observed therein [1–3]. In accordance with the theoretical model proposed in [1], AEE is governed by the potential difference accelerating electrons in a crystal surface layer and favors their emission into a vacuum. The corresponding behavior of the electron potential energy $\varphi(z)$ near the surface is shown in the inset of Fig. 1 [1]. The effect is related to the nonlinearity of the equation of state of a ferroelectric, $E(P)$, which here indicates the dependence of an electric field E on polarization P. The effect is observed only if the total injected charge meets the condition $\sigma > P$. In accordance with the experimental evidence [1–3], this effect can result in an increase in the emission current by more than two orders of magnitude from its value for a neutral surface [4, 5]. It follows from the accelerating-field model [1] that the emission intensity depends on the spatial distribution $n(z)$ of the injected electron charge, particularly, on the depth of its occurrence in the surface layer, because this depth determines the width z_0 of the region of the anomalous behavior of the potential $\varphi(z)$ (Fig. 1) and the proximity of the strong electrical field region to the surface. As is shown below, this could be used for the direct experimental verification of the theoretical predictions in the proposed model.

We assume that the model dependence of $n(z)$ has the form

$$n(z) = \frac{\sigma_\infty}{\pi}\frac{\gamma}{(z-a)^2+\gamma^2}; \qquad (1)$$

therefore, there is a charge maximum at a distance a from the crystal surface. At $a < 0$, the charge density decreases monotonically with an increasing distance from the surface to the crystal bulk. The values of σ_∞ and γ are the model parameters.

The polarization distribution $P(z)$ in a ferroelectric is determined approximately by the expression [6]

$$P(z) \approx \int_0^z dz n(z) \qquad (2)$$

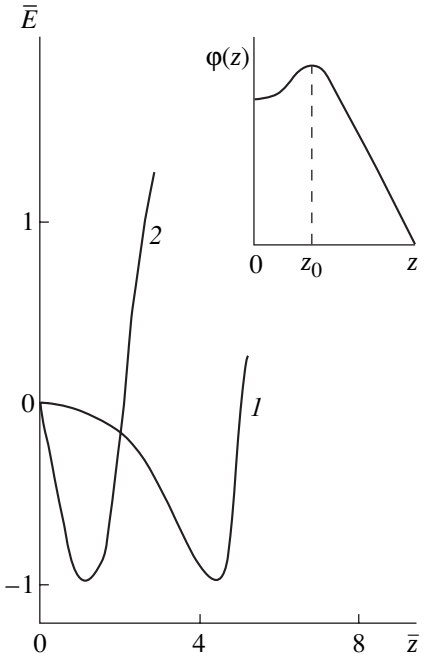

Fig. 1. Behavior of the normalized electrical field $\bar{E} = E/E_c$ in a surface layer of an electret for $\sigma_\infty/P_s = 2$ and $\bar{a} \equiv a/\gamma =$ (*1*) 5.0 and (*2*) 1.0 ($\bar{z} = z/\gamma$). The schematic behavior of the potential $\varphi(z)$ in accordance with [1] is shown in the inset.

1063-7834/00/4211-2148$20.00

or, allowing for (1),

$$\bar{P} \approx \frac{\sigma_\infty}{\pi P_s}\{\arctan(\bar{z}-\bar{a}) + \arctan\bar{a}\}, \qquad (2a)$$

where $\bar{z} = z/\gamma$, $\bar{a} = a/\gamma$, and $\bar{P} = P/P_s$.

For the equation of state $\bar{E} \equiv E/E_c = \frac{3\sqrt{3}}{2}\bar{P}(\bar{p}^2 - 1)$ (E_c is the coercive field) [6], the electrical field behavior in the surface layer is shown in Fig. 1 for two values of the parameter a (the field sign is consistent with the definition of the potential φ). As the parameter a decreases, the potential peak and the region of the strong electrical field approach the surface, which should lead to an increase in the emission intensity. However, a more detailed analysis shows that the dependence of these quantities on a is not monotonic. Specifically, from expression (2a), allowing for the condition $P(z_0) = P_s$ for $z_0(a)$, we find

$$\bar{z}_0 = \frac{1+\bar{a}^2}{\bar{a}-a_0}, \qquad (3)$$

where $a_0 = -\cot(\pi P_s/\sigma_\infty)$.

The dependence $z_0(a)$ (Fig. 2) has a minimum at $a = a_{\min} = \tan(\pi P_s/2\sigma_\infty)$, the minimum being equal to $z_0^{\min} = 2a_{\min}$. The value of z_0 decreases with increasing σ_∞, while at $a \longrightarrow a_0$, we have $z_0 \longrightarrow \infty$. For $\bar{a} < a_0$, the total injected charge in the crystal is $\sigma(a) < P_s$. Therefore, there is no region of the anomalous potential near the surface and, hence, the conditions for the anomalous electron emission are not met [1]. The position of the electric-field extremum is also determined by expression (3), in which the substitution $P_s \longrightarrow P_s/\sqrt{3}$ should be done in the a_0 definition. The peculiarities described in the behavior of the potential $\varphi(z)$ in the surface electret layer must result in the nonmonotonic dependence of the anomalous electron emission intensity on the position of the maximum a of the injected charge.

This effect is observed in the model experiments. The results of these experiments for $PbTiO_3$-based ceramic samples PKR-70, which are polarized using the method described in [7], are shown in the inset of Fig. 2: when the surface layer is mechanically removed, layer by layer the emission integral intensity I as a function of the thickness d of the layer removed has two maxima. The dependence $I(d)$ qualitatively agrees with the predictions made above using the model of the accelerating electric field. Moreover, this dependence suggests that there are two or more maxima in the distribution $n(z)$ of the injected charge in the surface layer of the ferroelectric electret. The influence of the ceramic microgranular structure on this effect is presently under investigation.

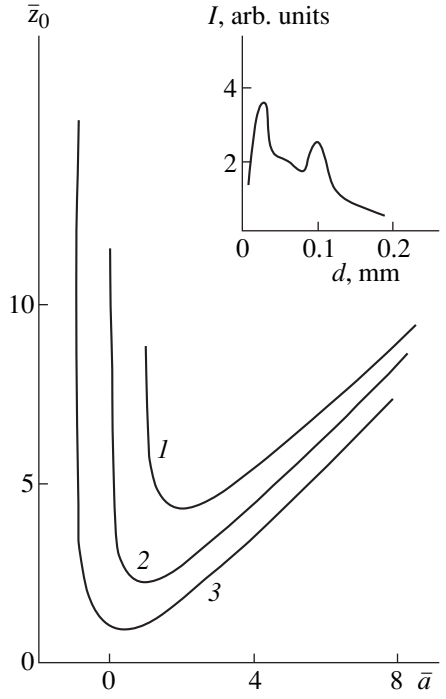

Fig. 2. Dependence of the dimensionless parameter $\bar{z}_0 = z_0/\gamma$ on the position $\bar{a} = a/\gamma$ of the injected-charge maximum for σ_∞/P_s = 1.4 (*1*), 2.0 (*2*), and 4.0 (*3*). The experimental $I(d)$ dependence for ferroelectric ceramic PKR-70 (see text) is shown in the inset.

In concluding, we note that the analysis presented above is valid for the case where the state of the sample is uniform over its plane. To investigate the problem of the stability of this state and the closely related problem of the description of the AEE spectrum shape [1–3], a more general theoretical approach is necessary, some aspects of which were considered in [3]. The important aspect of these investigations is, in particular, the description of the shape of the AEE spectrum, whose width may be as large as several hundred electronvolts [1–3]. The similarity in the spectrum shape of the electron emission measured from cold cathodes [8, 9] and of the AEE raises questions on the nature of the phenomena to be compared.

ACKNOWLEDGMENTS

The authors are grateful to I.V. Novikov for providing the experimental $I(d)$ dependence. This work was supported by the Government budget of the Research Institute of Physics, Rostov State University.

REFERENCES

1. A. T. Kozakov, V. V. Kolesnikov, V. P. Sakhnenko, *et al.*, Fiz. Tverd. Tela (St. Petersburg) **38** (8), 2524 (1996) [Phys. Solid State **38**, 1385 (1996)].

2. A. T. Kozakov, V. V. Kolesnikov, A. V. Nikol'skiĭ, and V. P. Sakhnenko, Fiz. Tverd. Tela (St. Petersburg) **39** (4), 679 (1997) [Phys. Solid State **39**, 594 (1997)].

3. V. V. Kolesnikov, A. T. Kozakov, and A. V. Nikol'skiĭ, Fiz. Tverd. Tela (St. Petersburg) **42** (1), 141 (2000) [Phys. Solid State **42**, 146 (2000)].

4. A. T. Kozakov, V. V. Kolesnikov, A. V. Nikol'skiĭ, and V. P. Sakhnenko, Fiz. Tverd. Tela (St. Petersburg) **36** (2), 317 (1994) [Phys. Solid State **36**, 173 (1994)].

5. V. V. Kolesnikov, A. T. Kozakov, A. V. Nikol'skiĭ, and V. P. Sakhnenko, Poverkhnost', No. 3, 915 (2000).

6. E. V. Chenskiĭ and V. V. Tarasenko, Zh. Éksp. Teor. Fiz. **88** (3), 1089 (1985) [Sov. Phys. JETP **61**, 639 (1985)].

7. A. T. Kozakov, I. V. Novikov, A. V. Nikol'skiĭ, and A. I. Klevtsov, Electronic Journal "*Issledovano v Rossii*," No. 58 (1999), http://zhurnal.mipt.rssi.ru/articles/1999/058.pdf.

8. A. Sh. Aĭrapetov, I. I. Ivanchik, A. N. Lebedev, *et al.*, Dokl. Akad. Nauk SSSR **311** (3), 594 (1990) [Sov. Phys. Dokl. **35**, 267 (1990)].

9. O. Auciello, M. A. Ray, D. Palmer, *et al.*, Appl. Phys. Lett. **66** (17), 2183 (1995).

Translated by N. Kovaleva

Physics of the Solid State, Vol. 42, No. 11, 2000, pp. 2151–2158. Translated from Fizika Tverdogo Tela, Vol. 42, No. 11, 2000, pp. 2087–2093.

LOW-DIMENSIONAL SYSTEMS AND SURFACE PHYSICS

Critical Thermodynamics of Two-Dimensional Systems in the Five-Loop Renormalization-Group Approximation

E. V. Orlov and A. I. Sokolov

St. Petersburg State University of Electrical Engineering, St. Petersburg, 197376 Russia
e-mail: ais@sokol.usr.etu.spb.ru

Received March 21, 2000

Abstract—The paper is devoted to the calculation of renormalization-group (RG) functions in the $O(n)$-symmetry two-dimensional model of the $\lambda\varphi^4$ type in the five-loop approximation and to an analysis of the critical behavior of systems described by this model. Five-loop expansions for the β function and the critical indices are determined in bulk theory. They are summed up using the Padé–Borel and Padé–Borel–Le Roy methods, making it possible to optimize the summation procedure and to estimate the accuracy of the obtained numerical values. It is shown that in the Ising ($n = 1$) case, as well as in other cases, the inclusion of the five-loop contribution to the β function displaces the coordinate of the Wilson fixed point only insignificantly, leaving it outside the interval formed by the results of computations on lattices; even "spreads" of the error in the renormalization group and lattice estimates do not overlap. This discrepancy is attributed to the effect of the nonanalytic component of the β function, which cannot be determined in perturbation theory. A computation of critical indices proves that, although the inclusion of the five-loop terms in the corresponding RG expansion slightly improves the concordance with the exact results, the nonanalytic contributions are apparently also significant in this case.

The renormalization group (RG) method is one of the most important analytical tools applied at present for a theoretical analysis of critical phenomena. It proved to be exceptionally efficient as applied to three-dimensional systems both for determining the quantitative characteristics of the critical behavior and for analyzing qualitative features of phase transitions. The calculation of multiloop RG expansions for an $O(n)$-symmetry model of the $\lambda\varphi^4$ type and their processing with the help of various methods of summation made it possible to obtain highly accurate values of critical indices, critical-amplitude ratios, and renormalized coupling constants [1–9] used as standards for comparing the predictions of the theory with the results of physical and computer experiments.

On the other hand, the advances of the RG method in the theory of phase transitions, which are quite obvious, lack sufficient theoretical substantiation. Indeed, all observables can be presented in this case in the form of a diverging power series in dimensionless renormalized coupling constants which are not small in the critical region. The construction of various iterative procedures on the basis of diverging RG expansions, the best of which exhibit rapid convergence and lead to matching numerical results, simplifies the problem, but naturally does not solve it. In this situation, alternative methods of verification of the reliability and efficiency of the RG method (primarily, its testing on certain exactly solvable models) become especially significant.

The two-dimensional Ising model, describing critical phenomena in a number of real physical objects, is a well-known example of an exactly solvable model of phase transitions. It is generally accepted that in the critical region this model is thermodynamically equivalent to the two-dimensional scalar theory of the $\lambda\varphi^4$ type, and hence its critical behavior can be analyzed using the RG method in analogy with three-dimensional systems. Quite recently, exact values of asymptotic critical indices were also determined for a family of two-dimensional models corresponding to conformal-invariant theories [10–12]. These models are characterized by n-component order parameters with nonintegral values of n, forming an infinite sequence converging to the point $n = 2$. They form a natural basis for further testing of the RG method in phase-transition theory.

Another circumstance stimulating the study of two-dimensional models by using the RG technique is that not all of the universal parameters characterizing their critical behavior are known or can be determined from the exact solutions obtained. As a matter of fact, these solutions are valid either in a zero field or only at the critical point, and hence they cannot be used, for example, to find the critical index of corrections to scaling ω or the renormalized dimensionless coupling constants g_{2n} appearing in the equation of state (a detailed analysis of questions associated with this problem can be found, for example, in [13, 14]). At the same time, the recent renormalization-group calculation of the universal value of the vertex g_6 for the two-dimensional Ising model [15] and a comparison of the result obtained with the lattice analogs [16, 17] proved that the RG method can be sufficiently efficient in such cases.

1063-7834/00/4211-2151$20.00

It should be noted that in the physical-dimensionality space the field-theoretical RG method was applied for the first time to the two-dimensional Ising model more than two decades ago. In the classical work [1], the RG functions of a two-dimensional model of the $\lambda\varphi^4$ type with $n = 1$ were calculated in the four-loop approximation. The summation of the obtained RG expansions by using the Padé–Borel–Le Roy method led to estimates of "large" critical indices γ and ν, which were found to be in accord with the Onsager values. However, the values 0.16, 0.08, and 0.06 obtained for "small" indices α, η, and β differ significantly from the exact values (0, 1/4, and 1/8). In addition, the comparatively small number of terms in the RG series and their stronger convergence than in the 3D case deteriorated the accuracy of the numerical results: the values of the corresponding "spreads" were found to be between ± 0.2 and ± 0.6 [1]. The application of more complicated summation methods [2] based on the Borel–Le Roy transformations and on the conformal mapping technique slightly improved the situation; the estimates $\alpha = 0.06 \pm 0.24$, $\eta = 0.13 \pm 0.07$, and $\beta = 0.08 \pm 0.26$ were obtained for small indices, but their difference from the exact values still remained too large, and the accuracy was quite low.

This work aims at the calculation of the RG functions in a two-dimensional $O(n)$-symmetry model of the $\lambda\varphi^4$ type in the five-loop approximation. These functions will be determined for an arbitrary n. Summation of the RG expansions will allow us to determine the coordinate of a nontrivial fixed point and the critical indices for the cases $n = 1$ and 0, which are interesting from the physical point of view and correspond to layered Ising ferromagnets and polymers, as well as for an exactly solvable model with $n = -1$. The article has the following structure. Section 1 is devoted to determining the RG expansions for the β function and critical indices. In Section 2, the Padé–Borel–Le Roy method of summation of the expansion of the β function is used to calculate the coordinate of a nontrivial (Wilson) fixed point g_4^* and the index ω of corrections to the scaling. Padé's approximants of several different types are used in this case, and the summation procedure is optimized. Section 3 contains an analysis of asymptotic critical indices for the above values of n, a comparison of the numerical results with the exact values and with the data of calculations on lattices, and a discussion of the efficiency of the field-theoretical RG method as applied to problems of the type under consideration.

1. FIVE-LOOP EXPANSIONS FOR THE β FUNCTION AND CRITICAL INDICES

Thus, the Hamiltonian of the model under consideration has the form

$$H = \int d^2x \left[\frac{1}{2}(m_0^2 \varphi_\alpha^2 + (\nabla \varphi_\alpha)^2) + \frac{\lambda}{24}(\varphi_\alpha^2)^2 \right], \qquad (1)$$

where φ_a is the real n-component vector field, the square of the "bare mass" m_0^2 is proportional to $T - T_c^{(0)}$, and $T_c^{(0)}$ is the phase transition temperature disregarding order parameter fluctuations.

We will calculate the β function and critical indices in the framework of bulk theory. In Green's function, the vertex part and the total three-leg vertex are assumed to be normalized for zero external momenta according to the conventional procedure

$$G_R^{-1}(0, m, g_4) = m^2, \quad \left. \frac{\partial G_R^{-1}(p, m, g_4)}{\partial p^2} \right|_{p^2 = 0} = 1, \qquad (2)$$

$$\Gamma_R(0, 0, 0, m, g) = m^2 g_4, \quad \Gamma_R^{(1,2)}(0, 0, m, g_4) = 1.$$

Since four-loop expansions for the β function and critical indices for $n = 1$ are known [1], we must obtain the corresponding series for arbitrary n and then calculate the five-loop contributions. The solution of the first problem is not complicated by any difficulties, since the combinatorial factors, tensor convolutions, and the numerical values of integrals of all one-, two-, three-, and four-loop Feynman diagrams were determined earlier [18]. Conversely, the integrals corresponding to five-loop vertex and mass diagrams have not been calculated for the 2D case and will be calculated here for the first time. Without going into the details of this computation, we consider the most significant aspects of the analysis.

The five-loop contribution to the total four-leg vertex is specified by the sum of 124 topologically different diagrams, which are compiled in [18]. Twenty-seven diagrams have a trivial structure in the sense that their integrals are the products of the integrals of lower-order diagrams. Several dozens of diagrams correspond to integrals which can easily be evaluated with the help of a computer, since they can be reduced to single or double integrals. However, the calculation of triple and more complex integrals cannot be carried out using standard packages and requires the application of appropriate programs, which were specially developed for this purpose. The calculation of 31 five-fold and three seven-fold integrals was the most time-consuming. The latter were evaluated to within four decimal places, but the relative total contribution of these three diagrams to the five-loop term was approximately equal to 2.5%. Because the remaining diagrams were calculated with errors that were several orders of magnitude lower, the accuracy of the final result was better than to five decimal places. As a matter of fact, the accuracy proved to be still higher, since the experience of performing operations with our programs shows that the error in such computations is actually an order of magnitude smaller than that declared by the corresponding option. For this reason, we will henceforth write the five-loop contribution to the β function to within six decimal places.

Thus, the expansion of the β function in the model with the Hamiltonian (1) has the form

$$\frac{\beta(g)}{2} = -g + g^2 - \frac{g^3}{(n+8)^2}(10.33501055n + 47.67505273) + \frac{g^4}{(n+8)^3}(5.0002759n^2 + 149.1518586n + 524.3766023) - \frac{g^5}{(n+8)^4}(0.08884291n^3 + 179.6975910n^2 + 2611.154798n + 7591.108694) + \frac{g^6}{(n+8)^5}(-0.00407946n^4 + 80.3096n^3 + 5253.56n^2 + 53218.6n + 133972). \quad (3)$$

The calculation of five-loop RG expansions for critical indices also required the computation of quite a family of multiple integrals, which turned out to be more complicated than in the case of the β function. Eventually, the following expressions were obtained for the indices γ and η:

$$\gamma^{-1} = 1 - \frac{n+2}{n+8}g + \frac{g^2}{(n+8)^2}(n+2)3.3756289 - \frac{g^3}{(n+8)^3}(4.6618848n^2 + 34.41848329n + 50.18942749) + \frac{g^4}{(n+8)^4}(0.31899304n^3 + 71.70330240n^2 + 429.4244948n + 574.5877236) - \frac{g^5}{(n+8)^5}(0.0938051n^4 + 85.4975n^3 + 1812.19n^2 + 8453.70n + 10341.1). \quad (4)$$

$$\eta = \frac{g^2}{(n+8)^2}(n+2)0.91708597 - \frac{g^3}{(n+8)^3}(n+2)0.05460898 + \frac{g^4}{(n+8)^4}(-0.09268446n^3 + 4.05641051n^2 + 29.2511668n + 41.5352155) - \frac{g^5}{(n+8)^5}(0.0709196n^4 + 1.05240n^3 + 57.7615n^2 + 325.329n + 426.896). \quad (5)$$

Here, as in the previous publications [1–3], instead of the renormalized coupling constant g_4, we used the dimensionless invariant charge proportional to it:

$$g = \frac{n+8}{24\pi}g_4, \quad (6)$$

which, in contrast to g_4, does not tend to zero as $n \longrightarrow \infty$, but attains a finite value equal to unity.

2. THE COORDINATE OF WILSON'S FIXED POINT IN THE FIVE-LOOP APPROXIMATION

The values of indices and other universal parameters characterizing a phase transition are determined by the coordinate of Wilson's fixed point g^*, which is a nontrivial solution to the equation $\beta(g) = 0$. Like other series of the renormalized perturbation theory, the expansion obtained by us for $\beta(g)$ is asymptotic; in order to find g^*, the series in Eq. (3) must be reduced to a convergent one, i.e., subjected to a rearrangement of its terms. This is usually done using the Borel–Le Roy transformation

$$f(x) = \sum_{i=0}^{\infty} c_i x^i = \int_0^{\infty} e^{-t} t^b F(xt)\,dt, \qquad F(y) = \sum_{i=0}^{\infty} \frac{c_i}{(i+b)!} y^i. \quad (7)$$

In order to evaluate the integral in Eq. (7), the Borel transform $F(y)$ of the required function must be continued analytically beyond the convergence range. To this end, we can use Padé's approximants $[L/M]$, which are the ratios of polynomials $P_L(y)$ and $Q_M(y)$ of the Lth and Mth degree, respectively, whose coefficients are defined unambiguously if the sum $L + M + 1$ coincides with the number of the known terms of the series, and $Q_M(0) = 1$. It was found that the best approximating properties are observed for the diagonal Padé approximants, for which $L = M$, or approximants close too them (see, for example, [19]). However, the number of roots, i.e., the number of approximant poles in the complex plane, increases with the degree of the denominator M. If at least some of these poles are close to the real semi axis $y > 0$, or, which is still worse, lie on this semi axis, the corresponding approximant becomes unsuitable for the summation of the series. In actual practice, this considerably limits the degree of the denominator from above and narrows the choice of admissible approximants. On the other hand, the presence of the adjustable parameter b in the Borel–Le Roy transfor-

Table 1. Coordinate of Wilson's fixed point for models with $n = 1, 0$, and -1 as calculated in four successive RG approximations and the resultant five-loop estimates of $g^*(n)$

n	[1/1]	[2/1]	[2/2]	[3/2]	g^*, 5-loop
1	2.4246	1.7508	1.8453	1.8286	1.837 ± 0.03
0	2.5431	1.7587	1.8743	1.8402	1.86 ± 0.04
–1	2.6178	1.7353	1.8758	1.8278	1.85 ± 0.05

mation makes it possible to optimize the summation procedure by attaining the most rapid convergence of the iterative process.

Taking into account what has been said above, we initially chose the following procedure for calculating the coordinate of the nontrivial fixed point g^* [6]. For each n, a nontrivial root of the equation $\beta(g) = 0$ was determined in four successive (two-, three-, four-, and five-loop) approximations, and the analytic continuation of the Borel transforms of the β function was carried out using symmetric or nearly symmetric Padé approximants: [1/1], [2/1], [2/2], and [3/2]. The parameter b was varied over wide limits and chosen such that the numerical results specified by higher (four- and five-loop) approximations coincided; i.e., the most rapid convergence of the iterative procedure was ensured. Unfortunately, the optimal values of b corresponding to the most rapid convergence proved to be quite close to the threshold values, i.e., the values beyond which working approximants acquire poles for positive values of y. In actual practice, this circumstance significantly affects the accuracy of the results obtained.

In order to avoid the problem of poles, we did not use the variation of b and confined the analysis (for small n) to a fixed value of this parameter (equal to zero), which corresponds to the Padé–Borel summation method. In this case, all the Padé approximants listed above are free from "hazardous" poles, and the iterative procedure converges quite rapidly. The results of computations for $n = 1, 0$, and -1 (exactly solvable models) given in Table 1 clearly illustrate the situation. It can be seen that the application of the approximants [1/1], [2/1], [2/2], and [3/2] for analytic continuation of the Borel transform gives estimates for g^* that rapidly approach asymptotic values; the process of attaining the asymptotic form has the form of damped oscillations. The presence of oscillations appears quite natural, since the series for the β function is alternating, and their damping reflects the Borel summability of the RG expansion. Consequently, it can be concluded that the asymptotic value of g^* must lie between the four- and five-loop estimates, and it is natural to take their half-sum as the final result. For example, having obtained $g^* = 1.8453$ and 1.8286 in the four- and five-loop approximations of the two-dimensional Ising model, respectively, we assume that $g^* = 1.837$ is the most probable coordinate of Wilson's fixed point. The estimates of g^* for other values of n are given in the last column of Table 1 and in the upper row of Table 2.

The accuracy of determining the coordinate of Wilson's fixed point was estimated as follows. We varied the parameter b from 0 to 10, i.e., over wide limits, and traced the ensuing variation of g^* obtained by averaging the four- and five-loop results. The range of variation of this average value was taken as the error in determining the numerical value of g^*. The estimate of error obtained in this way is quite conservative since it exceeds considerably (at least by a factor of two) the difference between the averaged and the five-loop val-

Table 2. Coordinate of Wilson's fixed point g^* and the critical index ω for $-1 \geq n \geq 32$ in the five-loop renormalization-group approximation

n	–1	0	1	2	3	4	8	16	32
					g^*				
RG, 5-loop	1.85(5)	1.86(4)	1.837(30)	1.80(3)	1.75(2)	1.70(2) ($b = 1$)	1.52(1) ($b = 1$)	1.313(3) ([4/1], [3/1])	1.170(2) ([4/1], [3/1])
HT exp [22, 23]		1.679(3)	1.754(1)	1.81(1)	1.724(9)	1.655(16)			
MC [25, 29]			1.71(12)	1.76(3)	1.73(3)				
SC [24]	1.473(8)	1.673(8)	1.746(8)	1.81(2)	1.73(4)				
ϵ-exp [23]		1.69(7)	1.75(5)	1.79(3)	1.72(2)	1.64(2)	1.45(2)	1.28(1)	1.16(1)
$1/n$-exp [23]					1.758	1.698	1.479	1.283	1.154
					ω				
RG, 5-loop	1.32(4)	1.31(3)	1.31(3)	1.32(3)	1.33(2)	1.37(3)	1.50(2)	1.70(1)	1.85(2)

Note: The values of g^* extracted from high-temperature (HT) expansions and strong-coupling (SC) expansions, as well as those calculated by the Monte Carlo (MC) method, obtained by the processing of ϵ expansion for g^* (ϵ-exp), and specified by the corresponding $1/n$ expansion ($1/n$-exp), are given for comparison.

ues of g^*. This allows us to treat this estimate as quite realistic.

Before using the values obtained for determining critical indices, it would be interesting to compare them with the values of g^* reported earlier in other publications. The coordinate of the fixed point for the two-dimensional Ising model was determined by the RG method in the physical-dimensionality space [1, 2, 20] from an analysis of high-temperature expansions [16, 21–23] with the help of the ϵ-expansion technique [23], the Monte Carlo method [25], and the strong-coupling method [24, 26]. The numerical value of g^* was obtained from the results of calculation on lattices with the help of the relation

$$\chi_4 = \left.\frac{\partial^3 M}{\partial H^3}\right|_{H=0} = -\chi^2 m^{-2} g_4, \qquad (8)$$

connecting the renormalized coupling constant $g_4 = (8\pi/3)g$ with the nonlinear χ_4 and conventional χ susceptibilities of the system in the critical region. The summation of four-loop RG expansions by the Padé–Borel ([3/1] approximant) and Padé–Borel–Le Roy methods, as well as by using the conformal mapping technique, led to the following estimates: $g^* = 1.88$ [20], 1.8 ± 0.3 [1], and 1.85 ± 0.1 [2], respectively. The processing of high-temperature expansions, as well as of strong-coupling expansions, made it possible to obtain close values characterized by a high expected accuracy: $g^* = 1.751$ [21], 1.7547 ± 0.002 [16], 1.7538 ± 0.0005 [22], and 1.746 ± 0.008 [24]. The summation of the ϵ-expansion for the renormalized coupling constant for $\epsilon = 2$ by using information on exact values of g^* for low-dimensional models ($D = 1$ and 0) led to the estimates of $g^* = 1.79 \pm 0.05$ and 1.75 ± 0.05 [23]. Finally, the Monte Carlo method and direct summation of the strong-coupling expansion for the β-function resulted in $g^* = 1.71 \pm 0.12$ [25] and 1.76 [26].

A comparison of these numbers with one another and with our result $g^* = 1.837 \pm 0.03$ leads to the following important conclusions. First, the lattice estimates of g^*, grouped around the value of $g^* = 1.75$, noticeably differ from their analogs obtained by the RG method in the four-loop approximation. Second, the inclusion of the five-loop contribution to the β-function, which improves considerably the expected accuracy in the determination of g^*, leads only to an insignificant displacement of the coordinate of the fixed point, leaving it outside the interval containing the results of the calculations on lattices. Moreover, even the spreads in the errors of the RG and lattice estimates do not overlap in the five-loop approximation. The reasons behind this discrepancy can be associated with the insufficient length of the available RG expansions and the slower convergence of iterations than in the $D = 3$ case on the one hand, and, on the other hand, with the presence of nonanalytic contributions to the RG functions, which cannot be determined from perturbation theory.

The first reason does not appear to be likely. Indeed, the series for the β function is alternating, and hence the dependence of g^* on the approximation order is oscillating by nature. This means that the inclusion of the six-loop term in the expansion of $\beta(g)$ leads to an increase in g^*, i.e., to a larger difference between the RG result and its lattice analogs. The perturbative contributions of higher orders might slightly reduce the six-loop estimate, but the value of g^* at any rate remains larger than that obtained in the five-loop approximation in view of the convergence of the iterative procedure. Consequently, the divergence under consideration cannot be eliminated in perturbation theory.

It is natural to attribute this divergence to the effect of the nonanalytic component of the β function. It is well known that field-theoretical functions must have singularities [27] (Dyson theorem) at the point $g = 0$, near which the weak-coupling expansions are constructed. In a theory of the $\lambda\varphi^4$ type, Wilson's fixed point itself can be singular for the β function [23, 28]. Numerous calculations made in recent decades show that the nonanalyticity of RG functions virtually does not affect the accuracy of determining the critical indices and other universal quantities characterizing the critical behavior of 3D systems. However, the role of singular terms must increase with decreasing dimensionality. The results obtained can be regarded as a convincing demonstration of the fact that the influence of nonanalytic terms for 2D objects is no longer negligibly small.

This conclusion is valid not only for the Ising model. For $n \neq 1$, the field-theoretical RG method also leads to estimates of g^*, which differ significantly from the numbers obtained by lattice calculations. For example, for $n = 0$, the method of high-temperature expansions and the RG analysis in the five-loop approximation give $g^* = 1.679 \pm 0.003$ [24] and 1.86 ± 0.04, respectively (see Table 1). With increasing n, the difference between the lattice and the RG estimates of the coupling constant decreases but remains comparable with the errors in determining g^* or exceeds them. This is clearly illustrated in Table 2, containing, in addition to five-loop RG estimates, the values of g^* for various values of n obtained from high-temperature expansions [22, 23] (row 2), strong-coupling expansions [24] (row 4), and the Monte Carlo method [25, 29] (row 3), as well as those leading to the ϵ expansion summed up taking into account the available exact values of g^* for $D = 1$ and 0 (row 5) and the $1/n$ expansion (row 6); the latter are borrowed from [23]. (In order to avoid a misunderstanding, we note that the models with $n > 1$ are considered here exclusively for testing the RG method rather than for describing the thermodynamics of real degenerate 2D systems, in which ferromagnetic transitions are known to be absent.) In order to determine g^* for $n = 16$ and 32, Padé approximants [4/1] and [3/1] were used, since the values of the coupling constant obtained on their basis depend on the parameter b only

Table 3. Critical indices for models with $n = 1$, 0, and –1 determined by the Padé–Borel summation of five-loop RG expansions

n	Method	g^*	γ	η	ν	α	β
1	RG	1.837	1.790	0.146	0.966	0.068	0.071
		1.754 (HT)	1.739	0.131	0.931	0.139	0.061
	Exact		7/4	1/4	1	0	1/8
			(1.75)	(0.25)			(0.125)
0	RG	1.86	1.449	0.128	0.774	0.452	0.049
		1.679 (HT)	1.402	0.101	0.738	0.524	0.037
	Exact		43/32	5/24	3/4	1/2	5/64
			(1.34375)	(0.20833)	(0.75)	(0.5)	(0.078125)
–1	RG	1.85	1.184	0.082	0.617	0.765	0.025
		1.473 (SC)	1.155	0.049	0.592	0.816	0.014
	Exact		37/32	3/20	5/8	3/4	3/64
			(1.15625)	(0.15)	(0.625)	(0.75)	(0.046875)

Note: The numerical values of these indices are also given for comparison.

slightly, and the approximants [3/2] and [2/2] become inapplicable for large values of n in view of the emergence of "hazardous" poles. It can be seen from Table 2 that the RG and lattice estimates of g^* are close to each other only for $n = 2$ and 3. This closeness, however, is accidental and does not change the conclusion concerning the systematic divergence of the field-theoretical and lattice estimates of the coordinate of the fixed point.

Apart from the numerical values of the coordinate of Wilson's fixed point, Table 2 also contains our estimates of the critical index $\omega = d\beta(g^*)/dg$ determining the temperature dependences of scaling corrections. The index ω was determined by numerical differentiation of the function $\beta(g)$ specified by the RG expansion summed up according to the Padé–Borel method (approximants [3/2] and [2/2]), and the error was taken as half the difference between the five- and four-loop estimates of this index. Since the diagonal and close-to-diagonal approximants acquire "hazardous" poles for $b = 0$ with increasing n (see above), the shift parameter for determining the index ω was taken as 1 for $n = 4$ and 8, while for $n = 16$ and 32, the approximants [4/1] and [3/1] were used (for $b = 0$).

3. CRITICAL INDICES: DISCUSSION OF RESULTS

Let us now determine the numerical values of the critical indices. It is well known that RG expansions for different indices differ considerably in their structure. For example, series (4) for γ^{-1} is alternating and is characterized by a regular behavior of the coefficients, which does not apply to the RG expansions of γ and ν. In order to ensure the highest rate of convergence of the iterative procedure, we carried out the Padé–Borel–Le Roy summation of the series for γ^{-1} and η, while the remaining critical indices were determined with the help of the well-known scaling relations. In order to verify the self-consistency of the obtained numerical results and to estimate their accuracy, we also calculated the indices

$$\eta^{(2)} = \frac{1}{\nu} + \eta - 2, \quad \eta^{(4)} = \frac{1}{\nu} - 2, \tag{9}$$

whose RG expansions have a regular structure. Since the RG method gives the coordinate of Wilson's fixed point which differs noticeably from the results of lattice calculations (see above), the critical indices were determined using both the renormalization-group and the lattice values of g^*. This enabled us to determine the values of g^* ensuring the closeness of RG estimates of critical indices to the exact values and to ascertain the extent of the sensitivity of these results to the value of g^*. While processing the RG expansion for γ^{-1}, we used the approximant [3/2], while the series for $\eta^{(i)}$ and η, which start from the first- and second-order terms in g, respectively, were summed up (after factoring out common multipliers) with the help of approximants [2/2] and [2/1]. The values of critical indices determined in this way were found to be weakly dependent on the parameter b, which can obviously be explained by the high symmetry of the approximants used.

The numerical results obtained for the models with $n = 1$, 0, and –1 for $b = 0$ are presented in Table 3. Although the values of critical indices are given in this table to the third decimal place, the actual accuracy of RG estimates is much lower. An estimate of its value can be obtained by calculating the index η in two different ways: summing up directly the series in Eq. (5) for this index or determining η as the difference of the series summed up for $\eta^{(2)}$ and $\eta^{(4)}$. In the Ising case, the value of η determined by the second method is equal to 0.093, i.e., differs from the direct estimate by 0.053; for

$n = 1$, this difference is 0.028. Although the attained accuracy is quite low, it nevertheless makes it possible to characterize the situation quite definitely. The inclusion of five-loop terms in RG expansions obviously leads to a certain decrease in the difference between the renormalization-group estimates and the exact values of critical indices. At the same time, this does not solve the problem of small indices, for which the discrepancy between the predictions of the RG method and the exact values remain on the order of the indices themselves. This conclusion does not depend on whether the values of g^* used for determining critical indices were obtained by the RG method or from the high-temperature expansions ($n = 1, 0$) and the strong-coupling expansion ($n = -1$).

Will the inclusion of the next terms in the RG expansion of critical indices change the situation? In all probability, it will not. Indeed, the series for γ^{-1} and η, as well as for the indices $\eta^{(2)}$ and $\eta^{(4)}$, are alternating, which leads to oscillating dependences of the numerical values of these indices on the approximation order. Since the five-loop estimates of critical indices are closer to the exact values than the four-loop estimates, the addition to the six-loop contributions must deteriorate (at least to a small degree) the quality of the RG estimates. This means that the discrepancy under consideration cannot be eliminated in perturbation theory. It can only be assumed that it originates from nonanalytic contributions to the indices. It was proved that these contributions for 2D models are significant.

In conclusion, let us consider the results of calculations of the critical index ω. It is well known that the true value of the index of scaling corrections in the two-dimensional Ising model remains disputable. The first RG computations in two dimensions (four-loop approximation) gave values of ω close to 1.3 [1, 2]. The summation of the ϵ expansion for $\epsilon = 2$ led to the estimate $\omega = 1.6 \pm 0.2$ [30]. This value is in good agreement with the predictions of the conformal-invariant theory, according to which $\omega = 4/3$ in the two-dimensional Ising model [31], and with the results of analysis of high-temperature expansions, according to which $\omega = 1.35 \pm 0.25$ [32]. On the other hand, all the above values contradict the results of exact calculations of the principal singular and correction terms for the susceptibility of the two-dimensional Ising model, which give $\omega = 1$ [33]. Moreover, it was found recently that the two-dimensional Ising model belonging to the family of conformal-invariant theories for which $\omega = 4/m$, with $m = 1, 2, 3, \ldots$, occupies a special place in this family: the index ω for this model must be equal to 2 [34] and not to 4/3 ($m = 3$ in the Ising model). The only perturbative estimate close to $\omega = 2$ was obtained from an analysis of the strong-coupling expansion for the β functions, according to which $\omega = 1.88$ [26]. On the contrary, it can be seen from Table 2 that the results of our calculations confirm the conclusion about the closeness of the index ω to 4/3 in the two-dimensional Ising model. The inclusion of the five-loop term in $\beta(g)$ made it possible to improve the accuracy of the estimates for ω as compared to the four-loop approximation and, accordingly, to make this conclusion more definite.

ACKNOWLEDGMENTS

We are grateful to B.N. Shalaev for numerous discussions of the critical thermodynamics of two-dimensional systems and for helpful suggestions.

This research was supported by the Ministry of Higher Education of the Russian Federation, grant no. 97-14.2-16, the International Science Foundation, A.I.S., grant no. p99-943, and the administration of St. Petersburg, E.V.O., grant no. 298496.

REFERENCES

1. G. A. Baker, B. G. Nickel, and D. I. Meiron, Phys. Rev. B **17** (3), 1365 (1978).
2. J. C. Le Guillou and J. Zinn-Justin, Phys. Rev. B **21** (9), 3976 (1980).
3. S. A. Antonenko and A. I. Sokolov, Phys. Rev. E **51** (3), 1894 (1995).
4. R. Guida and J. Zinn-Justin, Nucl. Phys. B **489** (3), 626 (1997).
5. H. Kleinert, Phys. Rev. D **57** (4), 2264 (1998).
6. A. I. Sokolov, Fiz. Tverd. Tela (S.-Peterburg) **40** (7), 1284 (1998) [Phys. Solid State **40**, 1169 (1998)].
7. R. Guida and J. Zinn-Justin, J. Phys. A **31** (40), 8103 (1998).
8. H. Kleinert, Phys. Rev. D **60**, 085001 (1999).
9. A. I. Sokolov, E. V. Orlov, V. A. Ul'kov, and S. S. Kashtanov, Phys. Rev. E **60** (2), 1344 (1999).
10. B. Nienhuis, Phys. Rev. Lett. **49** (15), 1062 (1982).
11. B. Nienhuis, J. Stat. Phys. **34**, 731 (1984).
12. D. Friedan, Z. Qiu, and S. Shenker, Phys. Rev. Lett. **52** (18), 1575 (1984).
13. J. Salas and A. Sokal, J. Stat. Phys. **98** (3/4) (2000) (in press); Preprint no. cond-mat/9904038 (1999).
14. M. Caselle, M. Hasenbusch, A. Pelissetto, and E. Vicari, Preprint no. hep-th/0003049 (2000).
15. A. I. Sokolov and E. V. Orlov, Phys. Rev. B **58** (5), 2395 (1998).
16. S. Y. Zinn, S. N. Lai, and M. E. Fisher, Phys. Rev. E **54** (2), 1176 (1996).
17. A. Pelissetto and E. Vicari, Nucl. Phys. B **522** (3), 605 (1998).
18. B. G. Nickel, D. I. Meiron, and G. A. Baker, Jr., *Compilation of 2-pt and 4-pt Graphs for Continuous Spin Model*, University of Guelph Report (1977).
19. G. A. Baker, Jr. and P. Graves-Morris, *Pade Approximants* (Addison-Wesley, Reading, 1981; Mir, Moscow, 1986).
20. I. O. Mayer, J. Phys. A **22** (14), 2815 (1989).
21. G. A. Baker, Jr., Phys. Rev. B **15**, 1552 (1977).
22. P. Butera and M. Comi, Phys. Rev. B **54** (22), 15828 (1996).

23. A. Pelissetto and E. Vicari, Nucl. Phys. B **519** (3), 626 (1998).
24. M. Campostrini, A. Pelissetto, P. Rossi, and E. Vicari, Nucl. Phys. B **459** (1), 207 (1996).
25. J. K. Kim and A. Patrascioiu, Phys. Rev. D **47**, 2588 (1993).
26. G. Jug and B. N. Shalaev, J. Phys. A **32** (42), 7249 (1999).
27. J. Zinn-Justin, *Quantum Field Theory and Critical Phenomena* (Clarendon, Oxford, 1996).
28. B. G. Nickel, Physica A (Amsterdam) **117**, 189 (1981).
29. J. Kim, Phys. Lett. B **345**, 469 (1995).
30. J. C. Le Guillou and J. Zinn-Justin, J. Phys. Lett. (Paris) **46**, L137 (1985); J. Phys. (Paris) **48**, 19 (1987); **50**, 1365 (1989).
31. B. Nienhus, J. Phys. A **15**, 199 (1982).
32. M. Barma and M. E. Fisher, Phys. Rev. Lett. **53** (20), 1935 (1984).
33. E. Barouch, B. M. McCoy, and T. T. Wu, Phys. Rev. Lett. **31** (23), 1409 (1973).
34. M. Henkel, *Conformal Invariance and Critical Phenomena* (Springer, New York, 1999).

Translated by N. Wadhwa

Physics of the Solid State, Vol. 42, No. 11, 2000, pp. 2159–2163. Translated from Fizika Tverdogo Tela, Vol. 42, No. 11, 2000, pp. 2094–2098.

LOW-DIMENSIONAL SYSTEMS AND SURFACE PHYSICS

Study of Lithium Adsorption on the TiO_2 Surface by Electron-Stimulated Desorption

V. N. Ageev and S. M. Solov'ev

Ioffe Physicotechnical Institute, Russian Academy of Sciences, Politekhnicheskaya ul. 26, St. Petersburg, 194021 Russia
e-mail: ageev@ms.ioffe.rssi.ru

Received March 16, 2000

Abstract—This paper reports on a study of electron-stimulated desorption (ESD) of O^+ and Li^+ ions from titanium dioxide as a function of the preheating temperature T and of the concentration of lithium adsorbed at 300 K, which was carried out with a static magnetic mass spectrometer combined with a retarding-field energy analyzer. For $T > 1500$ K, the TiO_2 surface undergoes irreversible rearrangement. At temperatures from 300 to 900 K and at lithium coverages $\Theta < 1$, the ESD cross sections of the O^+ and Li^+ ions vary in a reversible manner with temperature, while for lithium coverages $\Theta > 1$, the changes in the Li^+ and O^+ ESD cross sections become irreversible. For $\Theta < 1$, the appearance threshold of the Li^+ and O^+ ions is 25 eV, whereas for $\Theta > 1$, the ESD threshold of Li^+ ions shifts to 37 eV. © *2000 MAIK "Nauka/Interperiodica".*

Titanium dioxide is one of the most efficient catalysts for water photolysis [1] and for cleaning the polluted atmosphere and water basins of organic compounds [2]. It is also used to develop detectors of chemically aggressive gases [3] and in the preparation of barrier layers in field-effect transistors [4].

However, the atomic and electronic structure of TiO_2 is relatively unstable and changes already on heating to $T > 470$ K, the change depending on the pressure and composition of the gas in which the heating takes place [5, 6].

Alkali metals are employed as promoters in TiO_2-based catalysts, and they were established to modify the geometric and electronic surface structure of titanium dioxide [7–11].

There is a wealth of information on the adsorption of Na, K, and Cs on the (110) and (100) TiO_2 planes [12–17], which shows that, at low coverages, alkali metals are adsorbed in the ionic form, while at high coverages the adsorbed overlayer undergoes metallization. We are not aware, however, of any studies of lithium adsorption on the TiO_2 surface.

We studied electron-stimulated desorption (ESD) of alkali-metal ions and atoms from layers adsorbed on oxidized tungsten surfaces [18] and showed that adsorption of alkali metals attenuates the desorption of oxygen ions, the attenuation cross section decreasing as one crosses over from cesium to lithium [19].

This work investigates the ESD of lithium ions Li^+ from layers adsorbed on the surface of titanium dioxide and makes a comparison between the results obtained and similar relations measured for Li^+ ions escaping from the adlayers on oxidized tungsten.

1. EXPERIMENTAL TECHNIQUE

The experimental setup and the measurement technique employed have been described in considerable detail elsewhere [18]. Here, we briefly recall some specific features of the measurements and instrument design. The ESD ion currents were measured with a static magnetic mass spectrometer combined with a retarding-field energy analyzer.

The residual gas pressure in the instrument chamber did not exceed 10^{-9} Pa. The substrates were $20 \times 1 \times 0.01$-mm textured tungsten ribbons with a predominantly (100)-oriented surface, which was obtained by their ac heating at 2500 K for 10 h. To remove carbon, the ribbon was annealed at a temperature of about 1900 K and oxygen pressure of 10^{-4} Pa. The TiO_2 film was prepared by two techniques.

By the first technique, titanium was deposited on a tungsten substrate at room temperature to a thickness of 6–10 monolayers. The source of titanium was a titanium-iodide strip placed parallel to the ribbon and heated by passing an electric current through it. The titanium was oxidized at 1000 K in an oxygen atmosphere at a pressure of 10^{-5} Pa for 30 min. By the second technique, the titanium deposition was carried out directly onto a tungsten substrate heated to 1000 K at an oxygen pressure $\sim 10^{-5}$ Pa.

An analysis of the films prepared by both techniques, which was made by Auger electron and thermal desorption spectroscopy, revealed the presence of TiO_2 films.

Lithium was supplied by directly heated evaporators, in which a mixture of Li_2CO_3 with CaO was reduced by an aluminum powder. The concentration of

1063-7834/00/4211-2159$20.00

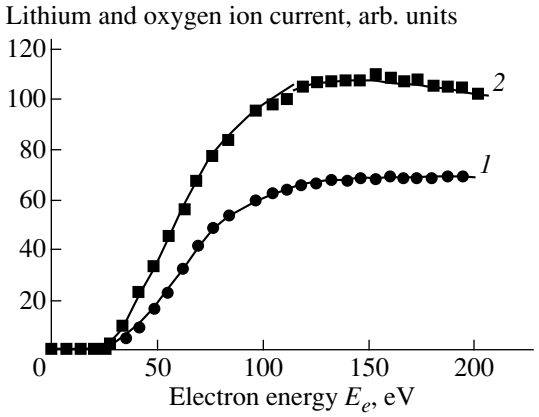

Fig. 1. Lithium (*1*) and oxygen (*2*) ion ESD yield q (arbitrary units) from a TiO_2 surface as a function of the primary-electron energy E_e. The surface was covered with lithium to a concentration of 2×10^{14} at./cm^2 at 300 K after a 10-s substrate heating at T = 1500 K. Electron current 10 μA.

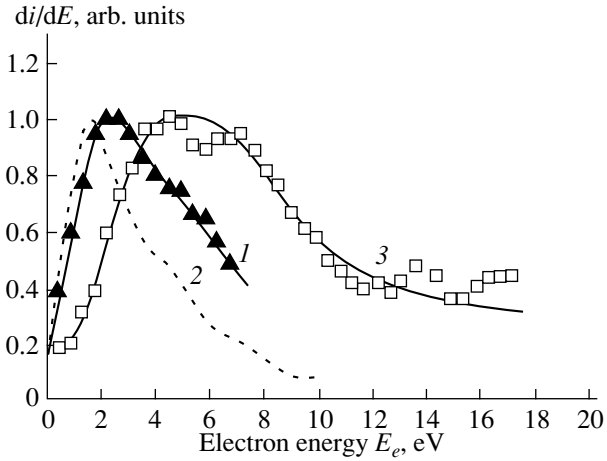

Fig. 2. Normalized energy distributions of Li^+ (curves *1*, *2*) and O^+ ions (curve *3*) obtained in ESD from TiO_2 (*1*, *3*) and WO_3 (*2*) surfaces covered with lithium to a concentration of 2×10^{14} at./cm^2 at 300 K after a 10-s substrate heating at T = 1500 K.

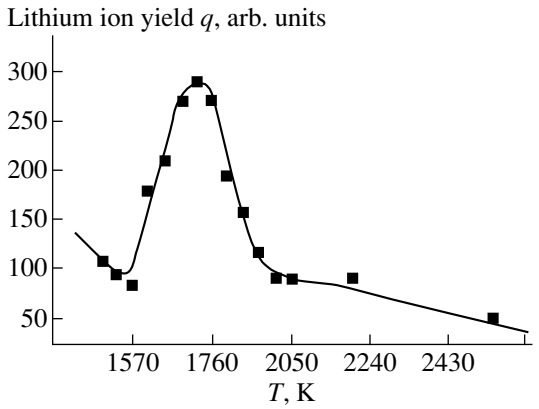

Fig. 3. Li^+ ion yield in ESD from a lithium adlayer of 2×10^{14} at./cm^2 deposited on TiO_2 at 300 K after a 5-s substrate heating at different temperatures T. Electron energy 190 eV.

the lithium deposited was determined from the deposition time under constant flux, whose magnitude was derived from measurements of the surface ionization current on a tungsten ribbon at saturation. The sticking coefficient was assumed to be equal to unity. The lithium concentration was monitored by observing the variation of the work function measured by the contact potential-difference method.

2. RESULTS OF THE MEASUREMENTS

Figure 1 presents the yield curves for Li^+ and O^+ ions obtained in ESD from a TiO_2 surface covered by a lithium adlayer with a lithium concentration of 2×10^{14} at./cm^2, which are plotted as a function of the primary electron energy. One observes the same appearance threshold near 25 eV for both ions, after which the ion yield tends gradually to saturation at electron energies above 150 eV. These plots are qualitatively similar to those obtained for the escape of Li^+ and O^+ ions from the surface of oxidized tungsten [18].

Figure 2 displays normalized Li^+ and O^+ energy distributions obtained in ESD from the TiO_2 surface at a concentration of adsorbed lithium of 2×10^{14} at./cm^2 and a primary-electron energy of 190 eV. The energy distribution for the O^+ ions is substantially broader than that for the Li^+ ions, and its maximum is shifted by 3 eV toward higher energies relative to that for the Li^+ ions. Note that the maximum of the distribution for the Li^+ ions escaping from TiO_2 lies about 1 eV higher than that for Li^+ ions desorbing from oxidized tungsten [18].

TiO_2 films grown at 1000 K undergo a noticeable rearrangement with increasing temperature, which becomes manifest in a change of the Li^+ ESD yield from the lithium overlayer deposited at room temperature. The results of these experiments are presented in Fig. 3. The substrate was heated for 5 s at the temperatures specified in the figure and then cooled down to room temperature, after which lithium was deposited on it to a concentration of 2×10^{14} at./cm^2. It is seen that, up to heating temperatures of about 1500 K, the Li^+ ion yield at a primary electron energy of $E_e \sim 190$ eV decreases slightly with increasing T, and for $T > 1570$ K, the yield grows rapidly to reach a maximum at $T \sim 1700$ K. For $T > 1760$ K, the Li^+ yield decreases and tends to zero for the anneal temperatures $T > 2300$ K. As follows from thermal desorption experiments, TiO_2 films start to disintegrate at $T > 1800$ K. The Li^+ ion yield depends not only on the temperature of the film preannealing but also on the duration of it. Figure 4 illustrates the dependence of the Li^+ yield for $E_e \sim 190$ eV on the TiO_2 film anneal time made at T = 1650 K following deposition of 2×10^{14} at./cm^2 of lithium at 300 K. The yield reaches a maximum at an anneal time of 5 min.

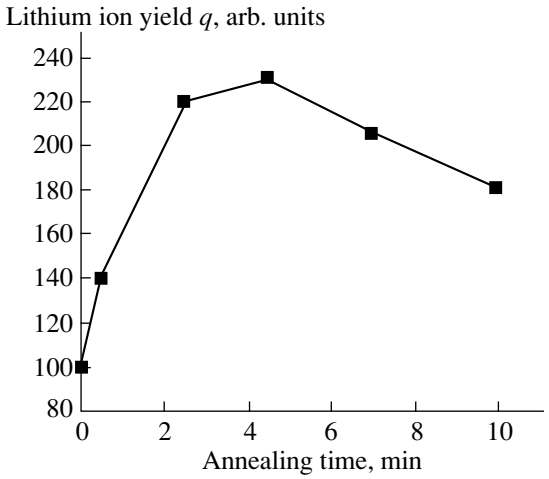

Fig. 4. Li^+ ion yield in ESD from a lithium adlayer of 2×10^{14} at./cm^2 deposited on TiO_2 at 300 K as a function of substrate heating time at T = 1650 K. Electron energy 190 eV, electron current 10 μA.

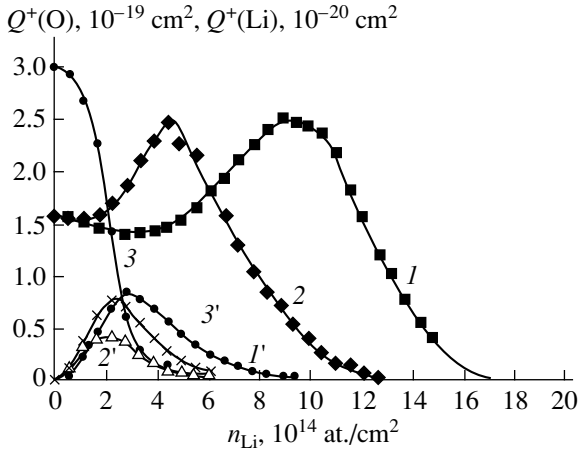

Fig. 5. ESD cross sections of O^+ (curves *1*–*3*) and Li^+ (curves *1*'–*3*') as functions of the concentration of lithium deposited at 300 K for various TiO_2 preanneal temperatures. T_{ann} (K): (*1*, *1*') 1200, (*2*, *2*') 1580, and (*3*, *3*') 1620. Electron energy 190 eV, electron current 10 μA.

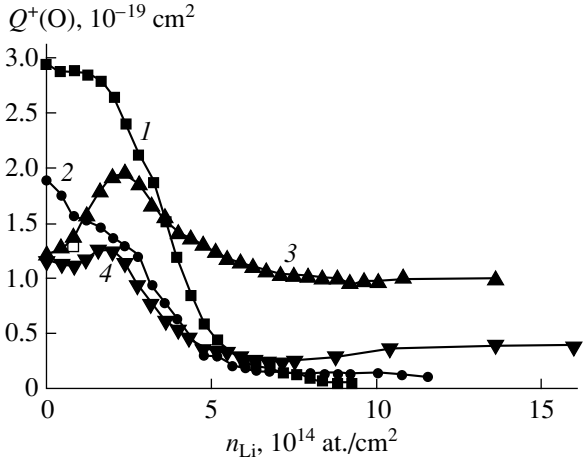

Fig. 6. O^+ ion ESD cross sections vs. lithium concentration on TiO_2 measured at different temperatures T (K): (*1*) 300, (*2*) 600, (*3*) 750, and (*4*) 900. Electron energy 190 eV, electron current 10 μA.

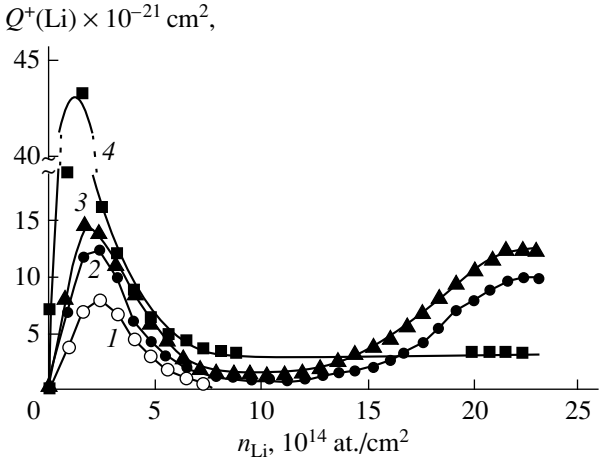

Fig. 7. Li^+ ion ESD cross sections vs. lithium concentration on TiO_2 measured at different temperatures T (K): (*1*) 300, (*2*) 600, (*3*) 750, and (*4*) 900. Electron energy 190 eV, electron current 10 μA.

Figure 5 shows the concentration dependences of the Li^+ and O^+ ESD cross sections obtained at a primary-electron energy of ~190 eV after TiO_2 film annealing at various temperatures for 10 s and lithium constant-flux deposition at room temperature. The ESD cross section of O^+ ions increases with an increasing lithium concentration for anneal temperatures below 1600 K and reaches a maximum at a lithium concentration whose value decreases with an increasing anneal temperature. For anneal temperatures above 1600 K, the ESD cross section of the O^+ ions decreases continuously with an increasing lithium concentration. As the deposited lithium concentration increases, the Li^+ ESD cross section passes through a maximum irrespective of the substrate anneal temperature. Note that, as the anneal temperature increases, the maximum ESD cross section is attained at progressively lower lithium concentrations and that the maximum lithium-ion ESD cross section varies nonmonotonically. It should be pointed out that the O^+ ESD cross section starts to increase simultaneously with a decrease in the Li^+ ESD cross section.

As the substrate anneal temperature is increased above 1700 K, the ESD cross sections of the O^+ and Li^+ ions decrease, thus implying disintegration of the TiO_2 film. Therefore, all subsequent experiments were performed at substrate temperatures below 1700 K, at which the TiO_2 film remained stable and lithium escaped from the surface without its disintegration. It was found that at substrate temperatures below 900 K

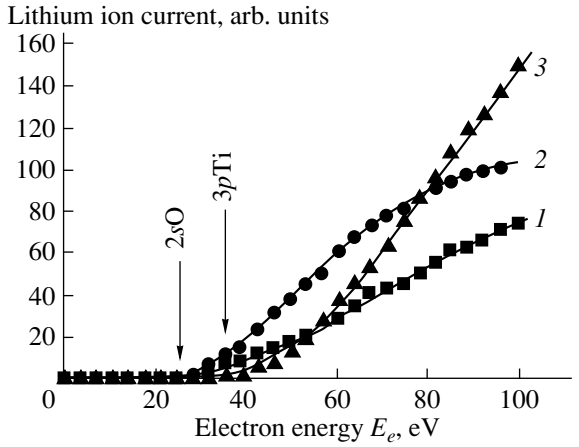

Fig. 8. Li^+ ion ESD current from a lithium adlayer deposited on TiO_2 at 300 K to a coverage (*1*) $\Theta < 1$ ML and (*3*) $\Theta > 1$ ML after substrate heating to $T = 1500$ K. Curve *2* was obtained after heating the substrate to $T > 1800$ K and lithium deposition at 300 K to $\Theta > 1$ML.

the ESD cross sections of Li^+ and O^+ ions vary with temperature in a reversible manner. Figures 6 and 7 plot ESD cross sections of the Li^+ and O^+ ions, obtained for various substrate temperatures at a primary electron energy of 190 eV, as functions of the deposited lithium concentration. Within the 300- to 500-K region, lithium attenuates the ESD cross section of O^+ ions, similar to the case of lithium adsorption on oxidized tungsten [19]. However, at temperatures of 600 to 900 K, the initial O^+ signal decreases substantially, which indicates either a decrease in the ESD cross section or a rearrangement of the TiO_2 surface. The latter appears more probable, because at $T = 750$ K and high lithium concentrations, the O^+ ESD cross section does not depend on the concentration of the deposited lithium (Fig. 6), which is similar to the ESD cross section of Li^+ ions (Fig. 7).

In Fig. 7, one can isolate two lithium concentration regions in which the Li^+ ESD cross section varies differently with increasing concentration. In the first region, where the lithium ion concentration is less than the monolayer coverage, the lithium cross section passes through a maximum whose height increases with increasing temperature. In the second region, for $\Theta > 1$ ML, the lithium-ion ESD cross section grows slowly to reach saturation at last. The cross section at saturation and the lithium concentration at which the saturation is reached are temperature dependent.

The Li^+ appearance threshold changes after the lithium concentration has increased above the monolayer coverage (Fig. 8). For lithium coverages $\Theta < 1$ ML, the Li^+ appearance threshold is close to 25 eV (curve *1*), while for $\Theta > 1$ ML, it shifts to 37 eV (curve *3*). Curve *2* obtained after the substrate was heated to $T > 1800$ K reveals two specific features, namely, the Li^+ appearance threshold at $E_e = 25$ eV and an additional threshold at $E_e = 37$ eV. This phenomenon apparently indicates that the substrate surface has become nonuniform as a result of this temperature treatment.

3. DISCUSSION OF RESULTS

The same appearance threshold for the Li^+ and O^+ ions at about 25 eV permits the suggestion that the ESD of both ions is initiated by ionization of the 2*s* energy level of oxygen [20]. Studies show that alkali metal atoms adsorb on the surface of oxide single crystals by the Stranski–Krastanow mechanism and, at least up to moderate coverages, occupy specific sites determined by the surface structure [21]. The decrease in the work function accompanying lithium adsorption on TiO_2 implies that lithium is adsorbed in the ionic form to comparatively high coverages. However, at coverages close to a monolayer, lithium adsorption becomes neutral because of the mutual depolarization of the adsorbed dipoles. Under these conditions, oxygen acquires a positive charge after the vacancy Auger decay at the oxygen 2*s* energy level and starts to repel the adjacent Li^+ positive ion. The O^+ ion, in its turn, can be repelled from a Ti^{4+} positive ion. The lower kinetic energy of the Li^+ and O^+ ions compared with that of these ions observed in ESD from tungsten oxide argues in favor of a lower binding energy of lithium and oxygen on titanium oxide compared with the tungsten oxide.

Ion ESD takes place usually from the uppermost layer of the substrate, and therefore the variation of the ion yield with temperature may be due to either a variation of the concentration of adsorbed particles or a change in the lifetime of the repulsive excited state. Heating the substrate to $T > 1500$ K (Fig. 3) results in a sharp increase in the Li^+ yield after lithium adsorption at 300 K and is accompanied by an increase in the O^+ yield. This effect is initiated apparently by reconstruction of the substrate surface under the ultrahigh-vacuum annealing conditions. Such a reconstruction was observed by means of a scanning tunneling microscope and by HEED [5]. The reconstruction gave rise to the formation of ridges propagating in the [110] and $[\bar{1}10]$ directions, which created a network with a cell size of about 4 nm. It is clear that the yield of Li^+ ions from lithium atoms adsorbed at the top of the ridges should be considerably higher than that from atoms adsorbed between the ridges, because the local surface potential at the ridge top should be lower.

At lithium coverages of less than one monolayer ($n < 10^{15}$ at./cm^2, Fig. 6), the ESD cross section of Li^+ ions increases reversibly with temperature up to $T \sim 900$ K. We relate this increase in the Li^+ ESD cross section to the increase in the average distance of lithium adatoms from the surface caused by transitions to higher vibrational levels and a change of the adatom

wave-function shape [18, 22]. The dependence of the O^+ ESD cross section on temperature is considerably more complex. Within the $T = 300–500$ K range, the O^+ ESD cross section decreases with an increasing surface coverage by lithium, and for coverages more than a monolayer it tends to zero. For $T > 600$ K, the O^+ ESD cross section passes through a maximum with an increasing lithium concentration and reaches saturation at coverages above one monolayer, as the Li^+ yield does. It may be conjectured that lithium forms some compounds with the oxygen of TiO_2 in these ranges of lithium concentrations and temperatures. It should be pointed out that the $TiO_2(110)$ surface undergoes rearrangement within the 770- to 830-K interval in the presence of oxygen with the formation of an irregular network of pseudohexagonal rosettes, and of small, (110)-oriented (1×1)-island bands in the 470- to 660-K region [6].

Rearrangement of the TiO_2 surface at lithium coverages above one monolayer is supported by the change in the Li^+ ESD appearance threshold from 25 to 37 eV. The 37-eV threshold can be associated with the ionization of the titanium core 3*p* level [20]; accordingly, the change in the Li^+ ESD threshold is apparently caused by a change in the Li position with respect to titanium and oxygen, and possibly, by a reaction of the substrate with the adsorbed lithium. The existence of two features in the Li^+ yield vs. electron energy curve (Fig. 8) implies the formation of two regions with different geometric structures on the surface, with a final surface rearrangement involving the formation of a new structure occurring at $T > 1800$ K.

ACKNOWLEDGMENTS

The authors are indebted to E.Yu. Afanas'eva for development of a method of preparing the TiO_2 oxide on a tungsten surface.

This study was supported by the Russian Foundation for Basic Research, grant no. 99-02-17972, the Russian State Program "Surface Atomic Structures," grant no. 4.5.99, and NATO, grant no. HTECH. LG. 97032.

REFERENCES

1. A. Fujishima and K. Honda, Nature **37**, 238 (1972).
2. A. L. Linsebigler, G. Lu, and J. T. Jates, Jr., Chem. Rev. **95**, 735 (1995).
3. K. D. Shierbaum, X. Wei-Xing, S. Ficher, and W. Gopel, in *Adsorption from Ordered Surfaces on Ionic Solids and Thin Films*, Ed. by E. Umbach and H. J. Freund (Springer, Berlin, 1993), p. 268.
4. E. Garfunkel, E. Gusev, and A. Vul', *Fundamental Aspects of Ultrathin Dielectrics on Si-based Devices* (Kluwer, Dordrecht, 1998).
5. H. Nörenberg, F. Dinelli, and G. A. D. Briggs, Surf. Sci. **436**, L635 (1999).
6. M. Li, W. Hebenstreit, L. Gross, *et al.*, Surf. Sci. **437**, 173 (1999).
7. H. Onishi, T. Aruga, Ch. Egawa, and Y. Iwasawa, Surf. Sci. **199**, 54 (1988).
8. H. Hird and R. A. Armstrong, Surf. Sci. **431**, L570 (1999).
9. M. A. San Miguel, C. J. Calzado, and J. F. Sanz, Surf. Sci. **409**, 92 (1998).
10. T. Bredow, E. Apra, M. Catti, and G. Pacchioni, Surf. Sci. **418**, 150 (1998).
11. J. Muscat, N. M. Harrison, and G. Thornton, Phys. Rev. B **59** (23), 15457 (1999).
12. R. Casanova, K. Probhakaran, and G. Thornton, J. Phys.: Condens. Matter **3**, S91 (1991).
13. B. E. Haydien and G. P. Nicholson, Surf. Sci. **274**, 277 (1992).
14. K. Prabhakaran, D. Puridie, R. Casanova, *et al.*, Phys. Rev. B **45**, 6969 (1992).
15. A. G. Thomas, P. J. Hardman, C. A. Muryn, *et al.*, J. Chem. Soc., Faraday Trans. **91**, 3569 (1995).
16. R. Heise and R. Courths, Surf. Sci. **331**, 1460 (1995).
17. J. Nerlov, S. V. Christensen, S. Wichel, *et al.*, Surf. Sci. **371**, 321 (1997).
18. V. N. Ageev, O. P. Burmistrova, and B. V. Yakshinskiĭ, Surf. Sci. **194**, 101 (1988).
19. V. N. Ageev, N. D. Potekhina, B. V. Yakshinskiĭ, *et al.*, Phys. Rev. B **54**, R5271 (1996).
20. *Practical Surface Analysis by Auger and X-ray Photoelectron Spectroscopy*, Ed. by D. Briggs and M. Seah (Wiley, New York, 1983; Mir, Moscow, 1987), p. 567.
21. Ch. T. Campbell, Surf. Sci. Rep. **27**, 1 (1997).
22. V. N. Ageev, S. T. Dzhalilov, N. I. Ionov, and N. D. Potekhina, Zh. Tekh. Fiz. **46** (5), 1019 (1976) [Sov. Phys. Tech. Phys. **21**, 596 (1976)].

Translated by G. Skrebtsov

Physics of the Solid State, Vol. 42, No. 11, 2000, pp. 2164–2167. Translated from Fizika Tverdogo Tela, Vol. 42, No. 11, 2000, pp. 2099–2102.

POLYMERS AND LIQUID CRYSTALS

Investigation of Third-Order Nonlinear Optical Susceptibility in Polymer Complexes of Diarylidenealkanones

A. V. Ten'kovtsev*, A. V. Yakimanskiĭ*, V. N. Lukoshkin, M. M. Dudkina*, and F. Boehme*****

**Institute of High-Molecular Compounds, Russian Academy of Sciences, St. Petersburg, 199004 Russia*

***Ioffe Physicotechnical Institute, Russian Academy of Sciences, Politekhnicheskaya ul. 26, St. Petersburg, 194021 Russia*

****Institut für Polumerforschung, Dresden, Germany*

Received March 2, 2000; in final form, May 10, 2000

Abstract—The third-order nonlinear optical susceptibility in polymer complexes of diarylidenealkanones has been investigated by the third harmonic generation technique at a wavelength of 1.06 μm. The macroscopic nonlinear susceptibility $\chi^{(3)}$ measured is compared with the calculated γ values of the second-rank molar hyperpolarizability tensor. It is demonstrated that low-molecular chromophores can be used in syntheses of the stable polymer composite systems with a high nonlinear optical susceptibility. A further improvement in the nonlinear optical properties of complexes between deprotonated chromophores and high-basicity polymers can be achieved using the proposed methods. © *2000 MAIK "Nauka/Interperiodica"*.

1. INTRODUCTION

In recent years, investigations into the nonlinear optical properties of different materials have attracted considerable attention, because they provide valuable information for structural analysis of these materials and their practical use in optoelectronic devices. Among a large number of materials with a pronounced nonlinear optical response, the compounds whose refractive indices can significantly change depending on the light intensity are of prime importance. This property provides a means of controlling the optical propagation in a medium with the use of light—purely optical gates, bistable devices, etc. It is known that, for the most part, organic compounds with a strongly delocalized conjugate π-electron system possess the required property [1].

In our earlier work [2], we reported that polyamidines with a high basicity can be used as H-bonding agents for nonlinear optical chromophores of the diarylidenealkanone series. Specifically, it was shown that 2,6-bis(4-hydroxybenzylidene)cyclohexanone forms strong complexes with aliphatic polyamidine, and one terminal OH group of the chromophore in these complexes is likely deprotonated by the polymer (Fig. 1).

This inference was confirmed by the change in color from light yellow to dark red upon mixing of the components, which was accompanied with a shift in the maximum of the absorption band of the chromophore by 130 nm [2]. The preliminary experiments demonstrated that films of this polymer complex exhibit a considerable efficiency of the third harmonic generation. In this respect, the purpose of this work was, first, to synthesize a large number of diarylidenealkanone chromophores with terminal OH groups and their complexes with high-basicity polyamidines and, second, to investigate the third harmonic generation properties of the films prepared from these complexes.

2. EXPERIMENTAL TECHNIQUE

Diarylidenealkanone complexes were synthesized according to the procedure described in [3] for preparing 2,6-bis(4-hydroxybenzylidene)cyclohexanone. The elemental composition determined by IR and NMR spectroscopy corresponded to the hypothetical structures of chromophores. The chemical structures of dibenzylidenealkanones synthesized in this work are depicted in Fig. 2.

The complexes of the studied chromophores with polyamidine (Fig. 3) were prepared by mixing the chro-

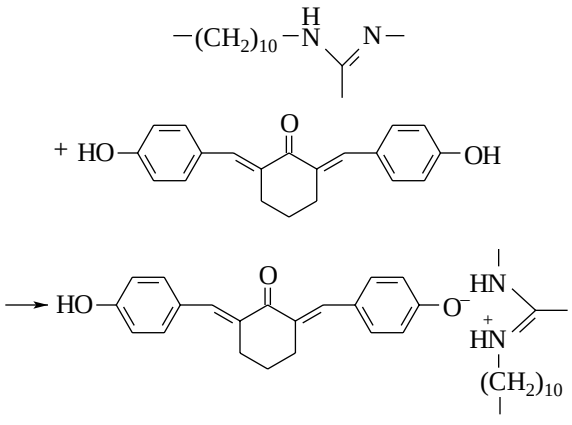

Fig. 1. Structure of the complexes studied.

1063-7834/00/4211-2164$20.00

mophore solutions in ethanol with an alcohol solution of polyamidine. The molar ratio between the chromophore and monomeric unit of the polymer was 0.5. Samples suitable for optical investigations were prepared by pouring the ethanol solutions of complexes onto a teflon substrate followed by evaporation of the solvent at room temperature and atmospheric pressure. Prior to the measurements, the films obtained were dried under vacuum (0.1 torr) to a constant weight.

3. DESCRIPTION OF THE PHYSICAL EXPERIMENT

The refractive index variation, which depends on the intensity of exciting radiation, is determined by the cubic term in the expansion of the macroscopic polarization of a dielectric in powers of the external electric field strength

$$P = \chi^{(1)}E + \chi^{(2)}EE + \chi^{(3)}EEE + \ldots,$$

where $\chi^{(n)}$ are the corresponding optical susceptibilities (nonlinear at $n > 1$).

At present, there are a number of widely accepted techniques for evaluating the third-order optical nonlinearities, for example, degenerate four-wave mixing [4], longitudinal scanning (Z-scan) method [5], the third harmonic generation technique, etc. Among these methods, the third harmonic generation is the simplest and most efficient (in technical realization) technique. Moreover, this method has the advantage that it furnishes a means for determining the electronic contribution to the third-order nonlinear optical susceptibility $\chi^{(3)}$.

In this work, the nonlinear optical properties of the synthesized materials were evaluated using the third harmonic generation technique. The excitation of samples was achieved with a pulsed neodymium-doped garnet laser (radiation wavelength, 1.06 μm; pulse length, 15 ns) operating in a Q-switching mode. The pulsed radiation power could be varied over a wide range (up to 30 mJ). A Gaussian spatial profile of the laser beam was specified by the higher-order transverse mode selection with the use of a mode control iris. The *p*-polarized radiation was focused onto the studied sample by using a convex spherical lens with F = 100 mm. A part of the radiation (4%) was separated with a beam splitter into a calibrated FD-24K photodiode. After focusing onto the sample, the third harmonic radiation was directed with the use of a lens system, first, at an entrance slit of an MDR-2 grating monochromator and, then, at a FEU-106 photomultiplier. Electric signals from both photodetectors were fed into integrating analog-to-digital converters and, through a KAMAK instrument interface, to a personal computer for further processing.

Since the determination of the absolute intensities of exciting radiation at the sample involved considerable difficulties, the nonlinear optical susceptibilities of the materials studied were estimated using the relative method based on comparison with a reference sample measured under identical conditions. The reference sample was a 0.5-mm-thick fused silica plate adjusted to the first maximum of the third harmonic intensity of the Maker fringes [6].

In this case, the susceptibility $\chi^{(3)}$ of the material can be determined from the simple relationship by comparing the intensities of the third harmonic signals from the studied and reference samples, that is,

$$\chi^{(3)} = \chi_s^{(3)}[I^{1/2}(3\omega)/l_c]/[I_s^{1/2}(3\omega)/l_{c,s}],$$

where $I(3\omega)$ and $I_s(3\omega)$ are the third harmonic intensities of the studied and reference samples, respectively; l_c and $l_{c,s}$ are the corresponding coherence lengths; and

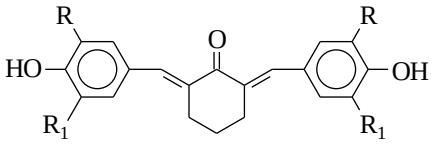

Ia, Ib

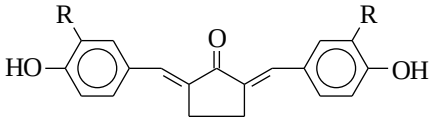

IIa, IIb

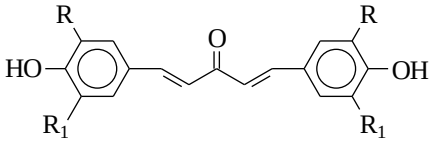

IIIa, IIIb

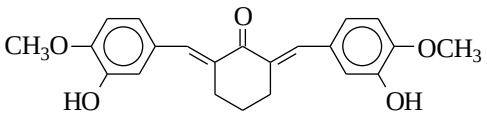

IV

Ia R = R_1 = H; Ib R = OCH_3, R_1 = H;
IIa R = R_1 = H; IIb R = OCH_3, R_1 = H;
IIIa R = R_1 = H; IIIb R = OCH_3; R_1 = H.

Fig. 2. Chemical structures of the chromophores used in syntheses of the complexes.

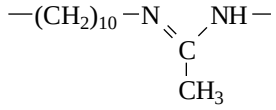

Fig. 3. Chemical structure of poly(1,10-decamethylene acetamidine).

Table 1. Cubic susceptibilities of the complexes

Chromophore	$\chi^{(3)} \times 10^{14}$ esu (experiment)	$\gamma \times 10^{36}$ esu (calculation)
Ia	10.7	53.8
Ib	33.7	59.6
IIa	10.0	
IIb	23.5	
IIIa	27.0	79.6
IIIb	38.2	89.9
IV	16.9	51.2

Table 2. Absorption band maxima for the chromophores and their complexes with polyamidine

Structure	λ_{max}, nm		
	chromophore	complex	
Ia	373	486	
Ib	386	494	
IIa	397	417	495
IIb	409	425	527
IIIa	380	478	
IIIb	394	512	
IV	380	378	

$\chi_s^{(3)} = 3.11 \times 10^{-14}$ esu for SiO_2 at $\lambda = 1.06$ μm. From this relationship, it follows that the susceptibility $\chi^{(3)}$ cannot be precisely determined when the coherence length of the studied material is unknown. However, the relative values of the cubic susceptibility can be qualitatively evaluated by ignoring the differences in coherence lengths for different compounds. The estimates obtained for the $\chi^{(3)}$ susceptibilities are listed in Table 1.

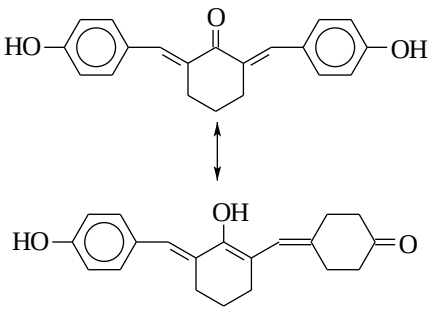

Fig. 4. Resonance forms of the 2,6-bis(4-hydroxybenzylidene)cyclohexanone monoanion.

4. DISCUSSION

The λ_{max} values characterizing the location of absorption band maxima for the chromophore complexes with polyamidine are given in Table 2. It can be seen from this table that, in all cases, except for the complex of chromophore IV, there are two absorption bands, of which the short-wavelength band corresponds to the nondeprotonated chromophore, and the long-wavelength band is attributed to the deprotonated chromophore. The bathochromic shift of the absorption band upon deprotonation of the chromophore is caused by the delocalization of the negative anionic charge as a result of the conjugation, which can be represented as a superposition of the benzenoid and quinoid resonance structures (Fig. 4).

Such a delocalization becomes impossible for the anion of chromophore IV, because the hydroxyl group in the phenyl ring occurs in the meta position with respect to the C=C double bond. Correspondingly, the interaction of chromophore IV with polyamidine does not lead to the bathochromic shift of the absorption band (Table 2). Furthermore, it can be seen from Table 2 that the introduction of electron-donating (auxochrome) groups into the benzylidene fragments brings about an increase in the bathochromic shift.

Table 1 presents the macroscopic susceptibilities $\chi^{(3)}$ measured for the chromophore complexes with polyamidine and the second-order molecular hyperpolarizabilities calculated by the PM3 method (intermediate neglect of differential overlap (INDO), version 3) [7]. It is evident that the introduction of auxochrome substituents into the benzylidene fragment also leads to an increase in $\chi^{(3)}$. Therefore, an increase in the electron density at the benzylidene fragment brings about an enhancement of the third harmonic signal of the chromophore complex with a high-basicity polyamidine. Moreover, it can be seen that the efficiency of the third harmonic generation for the polyamidine complexes of chromophores with the central cyclic fragment (based on cyclopentanone or cyclohexanone) is less than that for the complexes of acetone-based chromophores without central cyclic fragments. It is quite possible that a similar behavior is associated with a smaller π-conjugation in diarylidenecycloalkanones as compared to the acyclic analogues. This assumption is confirmed by the PM3 calculations, according to which diarylidenecycloalkanones adopt a nonplanar "banana-like" conformation (due to the repulsion between the ortho protons of the phenyl rings and the methylene protons of the central cyclic fragment), unlike a near-planar conformation of the acyclic chromophores (Fig. 5). It should be taken into account that the conformational rigidity of diarylidenecycloalkanones is considerably greater than that of their acyclic analogues. This is explained by the fact that the *s-cis-trans* isomerization becomes impossible because of the rotation of the O=C–C=C fragment about the single bond, which leads

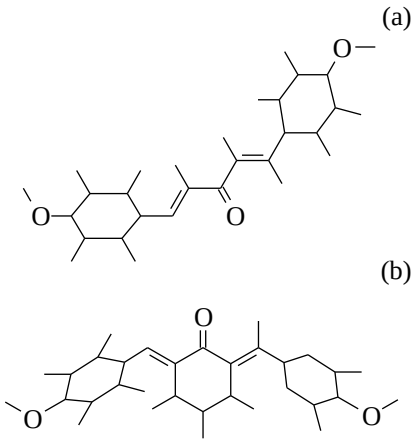

Fig. 5. Preferred conformations of compounds (a) IIIa and (b) Ia.

to the freezing of the nonplanar conformation of the chromophore.

It can be seen from Table 2 that, in the absorption spectra of the polyamidine complexes with chromophores, the short-wavelength bands that correspond to the molecular forms of these complexes (nondeprotonated chromophore) are very close in the location of their maxima (380–410 nm) to the wavelength of the third harmonic (355 nm). Consequently, the polyamidine complexes of chromophores in the molecular form can contribute to the total intensity of the third harmonic signal due to the resonant three-photon amplification. It seems likely that the three-photon resonance is responsible for the intensity of the third harmonic signal in the polyamidine complex of chromophore IV. At the same time, the polyamidine complexes of chromophores in the ionic form (for which the long-wavelength absorption bands have no tails in the vicinity of 355 nm) contribute to the third harmonic generation through a nonresonance mechanism. A comparison between the susceptibilities $\chi^{(3)}$ for the polyamidine complexes of chromophores Ib and IV allowed us to assume that the resonance and nonresonance contributions to the third harmonic generation are comparable in magnitude.

5. CONCLUSION

The results obtained in this work demonstrated that the low-molecular chromophores can be used in the preparation of the stable polymer composite systems with a high cubic nonlinear optical susceptibility. The use of simple chromophores (from the viewpoint of synthesis) makes it possible to obtain the $\chi^{(3)}$ values of the order of 10^{-12} esu. These values fall in the range of susceptibilities observed for a number of polymers whose synthesis is a very laborious procedure, for example, polythiophenes [8]. An insignificant modification of the chromophores studied in this work (the introduction of additional electron-donating substituents and an increase in the length of conjugation by introducing additional C=C bonds) can substantially increase the efficiency of the third harmonic generation in the complexes of the deprotonated chromophores with high-basicity polymers such as polyamidines. Similar investigations are being performed at the present time.

REFERENCES

1. *Nonlinear Properties of Organic Molecules and Crystals*, Ed. by D. S. Chemla and I. Zyss (Academic, Orlando, 1987; Mir, Moscow, 1989), Vol. 2.
2. F. Boehme, L. Haussler, and A. V. Yakimansky, Polym. Prepr. (Am. Chem. Soc. Div. Polym. Chem.) **40** (2), 1140 (1999).
3. B. Vorlander, Ber. Dtsch. Chem. Ges. **58**, 132 (1925).
4. T. Hattori and T. Kobayashi, Chem. Phys. Lett. **133** (2), 230 (1987).
5. M. Sheik-Bahae, A. A. Said, and E. W. van Stryland, Opt. Lett. **14** (4), 955 (1989).
6. K. Kubodera and H. Kobayashi, Mol. Cryst. Liq. Cryst., A **182**, 103 (1990).
7. J. J. P. Stewart, J. Comput. Chem. **24** (6), 791 (1989).
8. C. L. Callender, L. Robitaille, and M. Leclerc, Opt. Eng. **32** (9), 2246 (1993).

Translated by O. Borovik-Romanova

Physics of the Solid State, Vol. 42, No. 11, 2000, pp. 2168–2175. Translated from Fizika Tverdogo Tela, Vol. 42, No. 11, 2000, pp. 2103–2110.

FULLERENES AND ATOMIC CLUSTERS

Atomic-Core Dynamics and the Electronic Structure of Some Endo- and Exohedral Complexes of Fullerenes with Light Elements

P. V. Avramov[1, 3], S. A. Varganov[1], and S. G. Ovchinnikov[1, 2, 3]

[1]*Kirenskiĭ Institute of Physics, Siberian Division, Russian Academy of Sciences, Akademgorodok, Krasnoyarsk, 660036 Russia*

[2]*Krasnoyarsk State Technical University, Krasnoyarsk, Russia*

[3]*Krasnoyarsk State University, Krasnoyarsk, 660062 Russia*

e-mail: paul@post.krascience.rssi.ru

Received December 23, 1999; in final form, April 3, 2000

Abstract—The atomic and electronic structure of some endo-, exo-, and endo-exohedral complexes of the fullerene C_{60} with various guest atoms and molecules (He_n, H_2, and Li_2) are investigated using semiempirical and nonempirical quantum-chemical methods. The atomic core dynamics is studied by the method of molecular dynamics. It is shown that guest atoms and molecules in fullerene polyhedra acquire an orbital angular momentum due to the correlated motion of nuclei above the low-energy barriers of the potential surface within the carbon polyhedron even at low temperatures (from 4 to 78 K). The emergence of orbital angular momenta of nuclei of guest atoms and molecules is attributed to a change in the contribution of the orbital angular momentum of electrons to the potential surface of the complexes. The motion of Li ions in a polyhedron leads to blurring of the top of the valence band and to the emergence of a charge polarization wave in the carbon polyhedron. © *2000 MAIK "Nauka/Interperiodica".*

A large number of compounds of fullerenes with metals are known at present (see, for example, [1–3]). These materials can be divided into two large classes: endohedral complexes, in which metal atoms are inside the fullerene polyhedra, and exohedral complexes, in which metal atoms are located outside the polyhedra. Both classes have attracted considerable attention from researchers due to their unique chemical and physical properties, including their magnetic and superconducting characteristics. The most interesting metal–fullerene objects at present are probably exo- and endohedral fullerene complexes with alkali metals. This is primarily due to the fact that compounds of the K_3C_{60} and Rb_3C_{60} type [1, 4] are superconductors with rather high superconducting transition temperatures approaching 55 K. An elegant method of synthesis of the endohedrals $Li@C_{60}$, $Li_2@C_{60}$, and $Li_3@C_{60}$, in which fullerite C_{60} is bombarded by a beam of lithium ions with an energy up to 30 eV, was also developed recently [5].

Fullerene complexes with metals have been studied intensely for a long time by using both experimental (see, for example, [5–12]) and theoretical methods (see, for example, [1, 3, 13–27]). The electronic structure of metal complexes was studied by the method of electron spectroscopy. Weaver [9], for example, analyzed photoelectron spectra and inverse photoemission spectra of exohedral compounds of the K_xC_{60} type (Fig. 1).

It can be seen that the filling of the lower vacant orbital of C_{60} during doping by an alkali metal (potassium in our case) leads not only to a displacement of the occupied and vacant states, but also to a considerable change in the shape of the bands and a complex behavior of the Fermi level. A transition from pure C_{60} to KC_{60} leads to the disappearance of the band gap due to the formation of an impurity state on the one hand and a considerable (of the order of 1 eV) displacement of the first peak in the inverse emission spectrum on the other. A further increase in the extent of doping leads to a monotonic increase in the density of the impurity electron state, while the vacant state behaves in a more complex manner. For a doping degree of 2.5, it is displaced to the maximum extent on the energy scale (by 1.5 eV as compared to C_{60}), and then starts moving upwards along the energy scale again, and the band gap reappears for $x \approx 6$.

Another informative method of studying the electronic and atomic structures of both pure compounds and their complexes with metals is NMR and EPR spectroscopy. Almost immediately after the synthesis of the C_{60} molecule, it was established with the help of NMR spectroscopy that C_{60} molecules rotate in a solid at room temperature [28–30] at a frequency of the order of 10^{11} s^{-1} with randomly oriented rotational axes of the molecules. As the temperature is lowered to 250 K, the rotation becomes slower and ordered and the molecules now rotate only about a single axis [31, 32].

1063-7834/00/4211-2168$20.00

Similar results on the rotation of C_{60} molecules along a preferred axis of K_3C_{60} and Rb_3C_{60} crystals were obtained in [6] with the help of NMR spectroscopy. It was also pointed out that the freezing of rotation at a certain temperature plays an important role in the phase transitions in such materials.

Another important publication [11] in this field is also worth mentioning. Sato *et al.* [11] studied the molecular and intermolecular dynamics for solid $CeLa@C_{80}$. This compound was obtained in the course of beta decay of one of the ^{140}La atoms implanted in a carbon polyhedron. Sato *et al.* detected not only rotations of the molecules themselves, which were abruptly frozen at 160 K, but also rotations of Ce atoms, which persisted to temperatures of the order of 40 K.

The rapid migration of La ions in fullerene was also studied using the molecular dynamics method on the basis of the potential calculated in the LDA approach [33]. It was proved that La moves very rapidly along the tangent to a carbon polyhedron and performs one revolution in approximately one picosecond. Similar results were also obtained by Andreoni and Curioni [33, 34] for the endohedral $La@C_{82}$. These results led to the conclusion that the results of some experiments on the electronic and atomic structure should be interpreted taking the rotation into account. In particular, EPR spectroscopy cannot be used to extract the required information, since the characteristic time for EPR processes is an order of magnitude longer than the period of revolution of a La ion in the polyhedron.

A large number of endohedral fullerene complexes with individual atoms, as well as some molecules, have been obtained. It is obvious, however, that not all guest atoms and molecules can move in carbon polyhedra. In spite of the considerable interest of theoretical and experimental physicists in these exotic compounds, the coordination (location) of guest atoms and molecules that remain stationary in a polyhedron has not been determined in the general form. Indeed, only scant experimental information has been obtained on the structure of solids based on endohedra such as $Y@C_{82}$, for which it is known [10] that the yttrium atom is rigidly fixed to the carbon wall from inside, and endohedral molecules themselves in the molecular solid are arranged in a "head-to-tail" manner. These results were obtained, using a synchrotron source of radiation, by the methods of x-ray powder diffraction and maximum entropy. It was found that the yttrium atom is separated from the center of the C_{82} polyhedron by a distance of 3.14 Å. It was also shown that the rotation of the endohedral complex in the crystal lattice is suppressed, while C_{82} can rotate freely. The separation between the guest atom and the carbon wall in this case is approximately equal to 2.9 Å, which slightly exceeds the value predicted by quantum-chemistry methods.

For obvious reasons, the methods of coordination of guest atoms have been studied much better theoretically than experimentally. It was shown that some

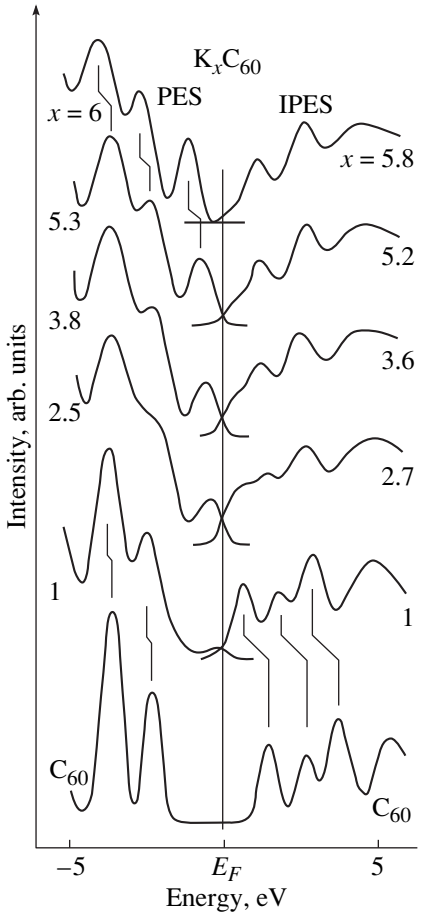

Fig. 1. Photoelectron spectra (PES) and inverse photoemission spectra (IPES) [9] of compounds of the K_xC_{60} type. For $x = 1$, the spectral intensity of the photoelectron spectrum at the Fermi level is low, while the first peak of the inverse photoemission spectrum is significant. However, the intensity of the photoelectron spectrum increases with doping, while the first peak of the inverse photoemission spectrum decreases.

atoms and ions like He and K^+ [16, 17, 25] must be coordinated at the center of a carbon polyhedron, while others, such as Li^+ and Na^+, must be coordinated at the carbon wall [13, 16, 35]. It is clear from the most general considerations that there exist five ways of coordinating a guest atom (at the center of a hexagon, at the center of a pentagon, at the edge between two hexagons, at the edge between a pentagon and a hexagon, and at the vertex of a truncated icosahedron). Obviously, in the presence of more than one guest atom, the number of possible arrangements of atoms within a carbon tetrahedron can be even greater.

An interesting theoretical publication [4] is also worth mentioning. Ramirez [4] proved that guest atoms can tunnel between the minima of a multivalley potential surface of an inner carbon wall. However, the problem was solved in the general form by using a model Hamiltonian under the assumption that the potential

surface over which the guest atom moves has twenty minima each of which lies above the center of a hexagon. The nature of the chemical interaction between the carbon wall and the guest atom was not considered.

This work is devoted to the study of the effects associated with the "flexibility" of the atomic core of endohedral complexes and the effect of the arrangement of guest atoms in a fullerene polyhedron on the electronic structure of these compounds.

1. METHODS AND OBJECTS OF INVESTIGATION

The electronic and atomic structures and the dynamic properties of a number of fullerene complexes with Li and He atoms, as well as with a hydrogen molecule, were investigated by the standard semiempirical quantum-chemistry PM3, MNDO, and INDO methods, the nonempirical Hartree–Fock method in the 3- to 21-G basis, and the molecular dynamics method, each method employing its own calculated potential. The GAMES program [36] (electronic structure and equilibrium atomic geometry) and the demonstration version of the "HyperChem-5.02" program (electronic structure, equilibrium atomic geometry, and molecular dynamics) were used for computer calculations. Such a variety of quantum-chemical methods is necessary for the following reasons.

(1) It is necessary to verify that the potentials obtained using different quantum-chemical methods (both nonempirical and semiempirical) lead to matching results in the molecular dynamics method.

(2) Unfortunately, none of the semiempirical methods possesses a parametrization for all the atoms constituting the chosen objects.

(3) It is impossible to make molecular-dynamic calculations in the quantum-chemical *ab initio* approach even on a small basis of the 3- to 21-G type for large systems (containing several dozens of carbon atoms like the C_{60} molecule) by using the existing computer facilities. (For example, a molecular-dynamic computation of the $Li_2@C_{60}$ system by the semiempirical MNDO method disregarding the symmetry of the duration of 1 ps and a step of 0.001 ps on a P-II 450 Dual 256 MB RAM computer requires more than a week of continuous operation.)

On the other hand, the semiempirical method can be successfully used to describe the electronic structure, as well as the equilibrium atomic geometry, of the C_{60} molecule itself and its derivatives doped with alkali metals in the case when the system has a closed electron shell (see, for example, [37] and some other publications). For example, the results obtained by the Hartree–Fock method in the 3- to 21-G basis were compared in [37] with the experimental photoelectron spectra and with the results of semiempirical computations by the PM3 and MNDO methods for endo- and exohedral complexes of C_{60} with the Li^+ ion and the Li_2 dimer. It was proved that semiempirical methods give results matching with the results of nonempirical calculations and correctly describe the experimental photoelectronic data taking into account systematic errors associated with the effects of strong electron correlations in these systems. By the way, such a result is not astonishing, especially in the case of endohedral complexes. As a matter of fact, all semiempirical methods correctly describe carbon-based systems with strong chemical bonds, such as fullerenes and their endoderivatives with alkali metals. In view of its unique electronic structure, the fullerene polyhedron is an oxidizer for alkali metals and attracts the *s* electrons of the metal. Thus, the bond in the molecule becomes mainly ionic (the charge of the alkali metal ion is of the order of +0.6). If, however, more than one guest atom (excluding the H_2 molecule) is implanted into the carbon polyhedron, the system, in addition, becomes stressed, since the internal volume is insufficient for their accommodation.

Thus, the choice of semiempirical quantum-chemical approaches for an extensive molecular-dynamic simulation of the behavior of such systems appears as justified and appropriate. In all cases, the calculated equilibrium geometry was used as the initial geometry in molecular-dynamic computations made under the assumption that the object under investigation is in a vacuum.

We analyzed the following objects.

(1) The C_{60} molecule with an icosahedral symmetry. The electronic structure and the equilibrium geometry were calculated in the restricted Hartree–Fock approximation by the nonempirical Hartree–Fock method in the 3- to 21-G basis and the semiempirical PM3 method. The length of the 6–6 bond in the *ab initio* approach and in the PM3 method amounted to 0.1367 and 0.1384 nm, respectively, while the length of the 6–5 bond was 0.1453 and 0.1457 nm, respectively. The molecular dynamics was calculated in the potential of the semiempirical PM3 method disregarding the symmetry.

(2) The C_{36} molecule with the D_{6h} symmetry. The electronic structure and the equilibrium geometry were calculated in the restricted Hartree–Fock approximation by the nonempirical Hartree–Fock method in the 3- to 21-G basis and the semiempirical PM3 method. The bond lengths in the *ab initio* approach and in the PM3 method were 0.1393 and 0.1411 nm, respectively, for the first type (6–6), 0.1438 and 0.1437 nm for the second type (6–5), 0.1415 and 0.1430 nm for the third type (6–5), and 0.1485 and 0.1499 nm for the fourth type (5–5). In order to verify these results, we made calculations in the 6- to 31-G basis and by the DFT B3LYP method. Both these calculations confirmed the correctness of computations in the 3- to 21-G basis and by the semiempirical PM3 method. The molecular dynamics was calculated using the potential

obtained by the semiempirical PM3 method and the nonempirical potential 3- to 21-G disregarding the symmetry.

(3) The endohedral complex $Li_2@C_{60}$, whose electronic structure and equilibrium geometry were calculated in the restricted Hartree–Fock approximation by the semiempirical MNDO method (a more detailed analysis of the electronic and atomic structures of this complex is given in [37]). The molecular dynamics was calculated in the potential of the semiempirical MNDO method disregarding the symmetry.

(4) The exohedral complex Li_2C_{60}, whose electronic structure and equilibrium geometry were calculated in the restricted Hartree–Fock approximation by the semiempirical MNDO method (see [37]). The molecular dynamics was calculated in the potential obtained by the semiempirical MNDO method.

(5) The endo-exohedral complex $Li[Li@C_{60}]$ (one of the ions is inside the polyhedron and the other is outside it), whose electronic structure and equilibrium geometry were calculated in the restricted Hartree–Fock approximation by the semiempirical MNDO method (see [37]). The molecular dynamics was calculated in the potential of the semiempirical MNDO method.

(6) The endohedral complex $Li@C_{60}^{+}$, whose electronic structure and equilibrium geometry were calculated in the restricted Hartree–Fock approximation by the semiempirical MNDO method (see [37]). The molecular dynamics was calculated in the potential of the semiempirical MNDO method.

(7) The endohedral complex $H_2@C_{36}$, whose electronic structure and equilibrium geometry were calculated in the restricted Hartree–Fock approximation by the nonsemiempirical Hartree–Fock method in the 3–21-G basis and by the semiempirical PM3 method. The structure of the polyhedron C_{36} in the complex was practically unchanged. The molecular dynamics was calculated in the potentials of the semiempirical PM3 method and in the nonempirical potential 3–21 G.

(8) The endohedral complex $H_2@C_{50}$, whose electronic structure and equilibrium geometry were calculated in the restricted Hartree–Fock approximation by the semiempirical PM3 method. The structure of the polyhedron C_{50} was chosen with the D_{5h} symmetry. The bond lengths were 0.1405 nm for the first type (6–6), 0.1378 nm for the second type (6–6), 0.1419 nm for the third type (6–5), 0.1474 nm for the fourth type (6–5), 0.1467 nm for the fifth type (6–5), and 0.1481 nm for the sixth type (5–5). The molecular dynamics was calculated in the potentials of the semiempirical PM3 method.

(9) The endohedral complex $H_2@C_{60}$, whose electronic structure and equilibrium geometry were calculated in the restricted Hartree–Fock approximation by the semiempirical PM3 method. The molecular dynamics was calculated in the potentials of the semiempirical PM3 method.

(10) A number of endohedral complexes $He_n@C_{60}$, $n = 2, 3, 4$, whose electronic structure and equilibrium geometry were calculated in the restricted Hartree–Fock approximation by the semiempirical INDO method. The length of the 6–6 bond was 0.1397 nm, while the length of the 6–5 bond was 0.1449 nm. The molecular dynamics was calculated in the potential of the semiempirical INDO method.

All calculations of the complexes with light elements were made without taking into account the symmetry of the system. The optimization of the geometry of these complexes in all the methods was carried out with a convergence parameter of 0.01 kcal/mol per atom of the complex.

At the present time, the method of molecular dynamics [38], which does not require the introduction of empirical intermolecular and interatomic potentials for computations, is widely used for studying the dynamic properties of molecular systems. Car and Parinello [38] specially introduced the term "nonempirical molecular dynamics" to emphasize that the potential of the system is not chosen parametrically, but calculated by quantum-chemical (including semiempirical) methods for any configuration in the course of computer simulation. They used the demonstration version of the Hyper-Chem-5.02 program for calculations using the nonempirical molecular dynamics method, which makes it possible to make calculations based on *ab initio*, as well as a number of semiempirical (INDO, MNDO, PM3, etc.), potentials. The elegance of some programs (including Hyper-Chem) for implementing the molecular dynamics method is also worth noting. The software was developed so that successive variation of atomic coordinates with time can be observed in the form of a dynamic picture, which provides a visual and convenient representation of the results of computations.

In the approach of molecular dynamics, the electron system is described by a set of wave functions $\{\psi_i(\mathbf{r})\}$ belonging to the ground state of the Born–Oppenheimer potential surface at any instant, which allows us to describe the collective motion of electrons and nuclei corresponding to a set of coordinates $\{\mathbf{R}_l\}$. In this case, the fixed kinetic energy of electrons remains small as compared to the kinetic energy of ions, which makes it possible to calculate the forces acting on the nuclei at any instant with the help of the Hellman–Feynman theorem for the electron systems corresponding to instantaneous nuclear configurations. The equations of motion of the complete dynamic system including the fictitious electron dynamics and real

ion dynamics are determined by the Lagrangian

$$L = \mu\sum_i\int dr|\dot{\psi}_i(r)|^2 + \frac{1}{2}\sum_l M_l\dot{R}_l^2 - E[\{\Psi_i\},\{R_l\},\{\alpha_\nu\}] + \sum_{i,j}\Lambda_{ij}\left(\int dr\psi_i^*(r)\psi_j(r) - \delta_{ij}\right) + \frac{1}{2}\sum_\nu \mu_\nu\dot{\alpha}_\nu^2,$$

where $E[\{\Psi_i\}, \{R_l\}, \{\alpha_\nu\}]$ is the total energy functional, which can be obtained using any quantum-chemical approach; the set $\{\alpha_\nu\}$ describes any possible external conditions, such as temperature, pressure, or volume; μ is the fictitious mass for the electron dynamics; and μ_ν is an arbitrary parameter of the appropriate dimensions. The matrix $\Lambda_{i,j}$ is a set of Lagrangian multipliers ensuring the orthonormality of $\{\Psi_i(\mathbf{r})\}$. From these equations, we can obtain the Euler–Lagrange equations of motion

$$\mu\ddot{\psi}_i(r,t) = -\frac{\delta E}{\delta\psi_i^*(r,t)} + \sum_k \Lambda_{ik}\psi_k(r,t),$$

$$M_l\ddot{R}_l = -\nabla_{R_l}E,$$

$$\mu_\nu\ddot{\alpha}_\nu = -(\delta E/\delta\alpha_\nu),$$

which describe the fictitious electron dynamics, ion dynamics, and the influence of external conditions (e.g., temperature), respectively.

The nonempirical molecular dynamics satisfies the Born–Oppenheimer approximation only under certain conditions. The situation with the choice of μ and other initial conditions for semiconductors and insulators is quite simple. However, a different situation prevails for systems in which the band gap is small and electrons interact strongly. This leads to thermal equilibrium between ions and electrons and violates the conditions of applicability of the Born–Oppenheimer approximation. In order to overcome these difficulties, the algorithm of thermostats [39] (one for ions and the other for electrons) is used in the nonempirical molecular dynamics. In this case, we have

$$\mu\ddot{\psi}_i(t) = -\hat{H}f_i|\psi_i(t)\rangle + \sum_k \Lambda_{ik}\psi_k(t) - \mu\dot{\eta}|\dot{\psi}_i(t)\rangle,$$

where f_i is the occupancy, and

$$M_l\ddot{R}_l = -\nabla_{R_l}E - M_l\dot{\xi}\dot{R}_l.$$

The thermostat variables η and ξ are determined by the equations

$$Q_e\ddot{\eta} = \left[\mu\sum_i\langle\dot{\psi}_i|\dot{\psi}_i\rangle - E_e\right],$$

$$Q_R\ddot{\xi} = \left[\mu\sum_l M_l\dot{R}_i^2 - gkT\right],$$

where Q_e and Q_R are the masses of the thermostats for the electron and ion components, respectively; E_e and T are the kinetic energy of electrons and the ionic temperature required by the conditions of the problem; and g is the number of degrees of freedom.

Time-dependent temperature fluctuations are included in the equations for the electron and ion thermostats, while the dynamics of the entire system obeys the principle of the thermodynamic-potential minimum. The simplest case of Newtonian dynamics describes the motion of the system in equilibrium, which allows us not only to study the dynamic properties of molecular and solid-state systems, but also to find effectively the equilibrium atomic structure.

It should be noted that, in the method of nonempirical molecular dynamics, the law of the conservation of energy (thermodynamic potential) is satisfied in the entire system, including in the electron and ion thermostats. This law can be written as

$$E = \mu\sum_i\langle\dot{\psi}_i|\dot{\psi}_i\rangle + \frac{1}{2}\sum_l M_l\dot{R}_l^2 + E[\{\psi_i\},\{R_l\}] + \frac{1}{2}Q_e\dot{\eta}^2 + \frac{1}{2}Q_R\dot{\xi}^2 + 2E_e\eta + gkT\xi,$$

while the energy of the electron–nucleus system without thermostats is not conserved because of thermal fluctuations. Consequently, for systems with nonrigid atomic cores, situations are possible when thermal conditions affect the electronic structure and the spectra of the systems under investigation as a result of the violation of the energy conservation law, since different atomic configurations must have different electronic spectra. In particular, rapid temperature rearrangements in the electronic spectra must lead to superpositions of the spectra corresponding to different configurations, which must be manifested in broadening and blurring of a number of spectral features.

2. RESULTS OF CALCULATIONS AND DISCUSSION

The electronic structure of the C_{60} molecule, as well as its dynamic properties in various conditions and states, has been studied comprehensively (see table). According to the results of our molecular-dynamic calculations, the C_{60} molecule rotates about its center of mass as a single entity. The period of rotation τ and the frequency $\nu = 1/\tau$ were determined from the time variation of the coordinates of the atoms forming the carbon polyhedron. An analysis of a free C_{60} molecule proved that the frequency of its rotation at 300 K amounts to 0.79×10^{10} s^{-1}. The experimental frequencies determined from the NMR spectra for the C_{60} molecule are 3.3×10^{11} s^{-1} in the gaseous phase at 300 K [28–30], 1.1×10^{11} s^{-1} in the solid phase at 300 K, and 5.0×10^8 s^{-1} below 260 K in the solid phase. It can be seen that our theoretical calculations based on the nonempir-

ical molecular dynamics method qualitatively describe the effect of the rotation of C_{60} molecules. The difference in the rotational frequencies is obviously due to the fact that semiempirical methods of calculations give, as a rule, exaggerated values of the energy and coupling constant and hence underestimate the change in the spacing between nuclei upon heating.

The rotation and the emergence of a nonzero orbital angular momentum of the entire molecule upon heating can be explained by the change in the total orbital angular momentum of the electron. Indeed, the total angular momentum of the system (the electron plus nuclear angular momenta) must be conserved, but an increase in temperature alters the effective nuclear spacing, and hence in the general form we can write

$$\langle \psi(r, R_0)|r\nabla|\psi(r, R_0)\rangle \neq \langle \psi(r, R_T)|r\nabla|\psi(r, R_T)\rangle.$$

This inequality holds since $\psi(r, R_0) \neq \psi(r, R_T)$, because the set of nuclear coordinates ($\{R_0\} \neq \{R_T\}$), which appear in the total electron wave function as parameters, changes with temperature. Consequently, the entire system must compensate for the change in the electron orbital angular momentum by the change in the ion orbital angular momentum, which is manifested in the rotation of molecules as a whole.

Nonempirical calculations of the lowest fullerene C_{36} in the 3- to 21-G basis at 300 K proved that this effect is also reproduced when the potential obtained by the *ab initio* method is used in the molecular dynamics. Since such computations require considerable time on computers, we could not estimate the rotational frequency of the molecule. As a matter of fact, the system is sort of "heated" in time due to the peculiarities of the algorithm in the molecular dynamics method using the system of thermostats. The typical time of heating is of the order of 0.2–0.3 ps, while a correct estimation of the rotational period can be made over time intervals equal to 0.5 ps. At the present time, the prevailing standard computer facilities do not allow us to carry out such a long simulation of the system behavior. The duration of intervals in our case was 0.1 ps, which required about two weeks of continuous operation of a P-II 450 Dual 256 MB RAM computer. The calculation of the rotational frequency of C_{36} using the semiempirical potential obtained using the PM3 method proved that the rotational frequency is slightly higher than for C_{60} and is equal to 3.2×10^{10} s^{-1}.

The *ab initio* calculations of the equilibrium atomic structure of the hypothetical endohedral complex $H_2@C_{36}$ in the 3- to 21-G basis revealed that the hydrogen molecule is located at the center of the carbon polyhedron. Calculations based on the molecular dynamics method at 300 K also demonstrated the flexibility of the coordination of the H_2 molecule in the polyhedron. The hydrogen molecule moves in a multivalley potential, hopping from one minimum to another. Effectively, such motion appears as the rotation of a molecule in the C_{36} polyhedron. However, the rotational frequency also could not be estimated in this case in view of limitations of the computer facilities. An analysis of molecular dynamics in the semiempirical PM3 potential revealed that the hydrogen molecule rotates in the polyhedron at a frequency of 4×10^{13} s^{-1}. It should be noted that the hydrogen molecule remains at the center of the carbon polyhedron.

Rotational frequencies of the Li_2 dimer and fullerene C_{60} in endohedral complexes $Li_2@C_{60}$ and $(Li_2@C_{60})_2$

Compound, temperature, K	Rotational frequency of Li_2 dimer, s^{-1}	Rotational frequency of fullerene C_{60}, s^{-1}
$Li_2@C_{60}$, 79	1×10^{12}	2.5×10^9
$Li_2@C_{60}$, 300	2.5×10^{12}	3.4×10^9
C_{60}, 300	–	7.9×10^9
Experimental frequency of rotation of the gas-phase C_{60} molecule at 300 K [28–30]	–	3.3×10^{11}
Experimental frequency of rotation of the C_{60} molecule in fullerite at 300 K [28–30]	–	1.1×10^{11}
Experimental frequency of rotation of the C_{60} molecule in fullerite below 260 K [28–30]	–	5.0×10^8

An analysis of the dynamics of the hypothetical $H_2@C_{50}$ system shows that the rotational frequency of the hydrogen molecule in this endohedral complex is slightly lowered (to 3×10^{13} s^{-1}) in view of the presence of a plateau on the potential surface within the carbon polyhedron. The hydrogen molecule is displaced by 0.09 nm from the center along the long axis of C_{50} in the course of its motion.

An analysis of the dynamics of the endohedral complex $H_2@C_{60}$ at 300 K proved that the hydrogen molecule in it does not rotate, but moves chaotically in the fullerene due to thermal fluctuations, which can be attributed to the presence of a large plateau (much larger than the hydrogen molecule) on the potential surface in the carbon polyhedron in all directions. For example, the displacement of the guest molecule from the center of C_{60} reaches 0.1 nm. An analysis of the system dynamics at 4 K revealed that the amplitude of motion of the hydrogen molecule decreases to 0.01 nm, but the system remains flexible all the same.

An analysis of the molecular dynamics for other interesting endohedral complexes of fullerene with helium atoms ($He_n@C_{60}$, $n = 2, 3, 4$) in the semiempirical INDO potential shows that such systems remain flexible at $T = 4$ K, the rotational frequencies of helium atoms for these objects being estimated as $(3–5) \times 10^{12}$ s^{-1}. An increase in temperature to 300 K leads to a noticeable increase (up to $(6–7) \times 10^{12}$ s^{-1}) in the rotational frequency of the helium atoms. It should be noted

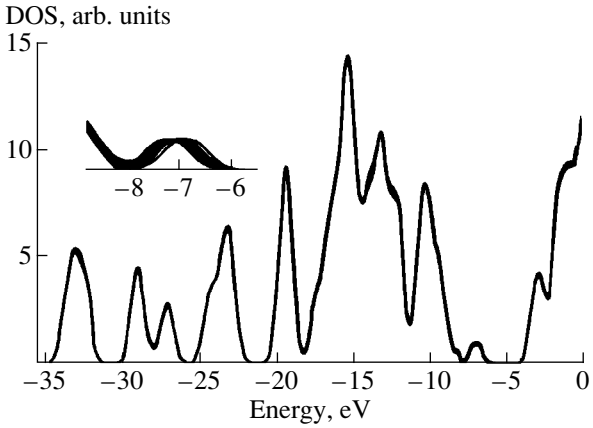

Fig. 2. Electronic structure observed in 16 stills of a dynamic picture superimposed and shot with a step of 0.01 ps calculated for the $Li_2@C_{60}$ complex at 300 K. It can be seen that the upper filled orbital (impurity electron state) changes its position with an amplitude of 1 eV. The inset shows the impurity state on a magnified scale.

that the carbon polyhedron in fact contains He_n molecules, the nuclear separation being 0.18 nm in all cases. (It should be noted that the calculation of the Van der Waals dimer He_2 by the INDO method gives 0.50 nm for the nuclear spacing, while in the *ab initio* approach (on the 6- to 31-G basis) this distance is 0.32 nm.)

Calculations of the electronic and atomic structures of Li-containing complexes show that lithium ions in the endohedral complex $Li_2@C_{60}$ are coordinated to the opposite vertices of the hexagons facing each other, so that the axis of the Li_2 fragment is just at the center of the polyhedron, the Li–Li separation being 0.299 nm, which is in accord with the C–C separation between the opposite carbon atoms from the base hexagons, while the Li–C distance (to carbon atoms belonging to hexagons) is 0.328 nm.

In the exohedral complex Li_2C_{60}, Li can be coordinated either to the center of a hexagon or to the center of a pentagon, the distance from the lithium ion being 0.232 nm to a carbon atom of the hexagon and 0.234 nm to a carbon atom of the pentagon.

In the endo-exohedral complex $Li[Li@C_{60}]$, the exohedral ion was coordinated to the center of a hexagon with the Li–C spacing equal to 0.231 nm, while the endohedral ion was coordinated to the center of a hexagon adjoining the hexagon to which the exohedral lithium is coordinated, the separation between the endohedral lithium ion and the carbon atom being 0.241 nm.

The coordination of lithium in the $Li@C_{60}^+$ complex takes place at the center of a hexagon, the Li–C distance being 0.2405 nm, while the separation between the lithium ion and the center of the hexagon is 0.1909 nm.

An analysis based on the molecular-dynamics method and the semiempirical potential demonstrates that endohedral Li ions in the $Li_2@C_{60}$ complex at 4 K are "frozen" to a carbon wall. At a temperature above 79 K, a dynamic transition takes place, in which the ions are dislodged from the equilibrium geometry and start rotating in the polyhedron at a frequency of 1.0×10^{12} s^{-1}, the carbon polyhedron itself also rotating at a frequency of 2.5×10^9 s^{-1}. (It should be emphasized that this dynamic transition temperature is just an estimate of the potential barrier height rather than a thermodynamic parameter. It was mentioned above that all calculations were made by the molecular-dynamics method, which does not comprehensively take into account thermal fluctuations and in fact simulates the thermodynamic equilibrium state.) At 300 K, the rotational frequency increases and attains 2.5×10^{12} s^{-1} for lithium ions and 3.4×10^9 s^{-1} for the carbon polyhedron (see table).

According to the results of similar molecular-dynamic calculations, the exohedral complex Li_2C_{60} is rigid up to 300 K. The outer Li ions just vibrate near their equilibrium positions above the centers of both the hexagons and the pentagons.

The behavior of the endohedral ion in the endo-exohedral complex $Li[Li@C_{60}]$ is much more complicated: at 77 K, it changes its coordination from the center of a hexagon to the edge between two adjacent hexagons to which the exo- and endohedral ions were coordinated at 4 K. At 300 K, the endohedral ion starts migrating in a solid angle of the order of 30° in the region of coordination of the exohedral lithium.

The calculations made by the molecular dynamics method in a semiempirical potential show that the endohedral Li ion in the $Li@C_{60}$ complex at 300 K moves at a frequency of the order of 5×10^{12} s^{-1}.

Let us now analyze the dependence of the electronic structure on the dynamic properties of the endohedral complex $Li_2@C_{60}$. Figure 2 presents the total densities of states plotted for 16 stills with an interval of 0.01 ps, obtained during dynamic filming of this complex. It can be seen that the impurity electronic state formed due to additional electrons supplied by Li atoms is "bloated." The change in the energies of the upper filled orbital due to the change in the coordination of Li ions under the action of thermal fluctuations is quite large (of the order of 1 eV). The motion of Li ions also gives rise to a polarization wave at the carbon polyhedron. The motion of lithium ions causes a change in the sign of the carbon atoms, whose effective charges can vary from a few hundredths of the electron charge to fifteen hundredths of the electron charge.

Thus, the calculations made by the method of nonempirical molecular dynamics lead to the following conclusions.

(1) Endohedral complexes of fullerenes with closed shells and light guest atoms and molecules that are not connected through covalent bonds with the carbon walls are flexible systems.

(2) This property can be explained by the low (of the order of tens of kelvins) potential barriers on the potential surface of atomic rearrangements in carbon polyhedra.

(3) The motion of ions within polyhedra under the action of thermal fluctuations blurs the top of the valence band consisting of an impurity electronic state and generates a polarization wave on the surface of a carbon polyhedron, which moves behind positively charged guest ions.

The files with dynamic pictures have been placed on the server of the Institute of Physics, Siberian Division, Russian Academy of Sciences (Kirensky.krascience.rssi.ru). The authors can also send them by e-mail: paul@post.krascience.rssi.ru.

ACKNOWLEDGMENTS

This work was carried out at the Collective Center Quantum-Chemical Calculations of Nanoclusters at the Krasnoyarsk Research and Education Center for High Technologies, financed by the Federal Program Supporting Integration of Higher Education and Fundamental Research, grant no. 69. This study was supported by the Russian Foundation for Basic Research for support, project no. 97-03-33684a, the State Program on HTSC, project no. 99019, and the State program "Fullerenes and Atomic Clusters," project no. 97018, and also the NATO Scientific Affairs Division, project PST.CLG 974818.

REFERENCES

1. A. V. Eletskiĭ and B. M. Smirnov, Usp. Fiz. Nauk **165** (9), 977 (1995).
2. C. T. White, J. W. Mintmire, R. C. Mowrwy, *et al.*, in *Buckminsterfullerenes*, Ed. by W. E. Billups and M. A. Ciufolini (VCH, New York, 1993).
3. W. Andreoni, Annu. Rev. Phys. Chem. **49**, 405 (1998).
4. A. R. Ramírez, Supercond. Rev. **1** (1–2), 1 (1994).
5. N. Krawez, A. Gromov, R. Tellgmann, and E. E. B. Campbell, in *Proceedings of XII International Winter School on Electronic Properties of Novel Materials—Progress in Molecular Nanostructures, Kirchberg, Tirol, 1998* (American Institute of Physics, Woodbury, 1998), p. 368.
6. Y. Yoshinari, H. Alloul, V. Brouet, *et al.*, Phys. Rev. B **54** (9), 6155 (1996).
7. T. Pichler, M. S. Golden, M. Knupfer, and J. Fink, in *Proceedings of the XII International Winterschool Electronic Properties of Novel Materials, 1998*, Ed. by H. Kuzmany, p. 271.
8. D. M. Poirier, M. Knupfer, J. H. Weaver, *et al.*, Phys. Rev. B **49** (24), 17403 (1994).
9. J. H. Weaver, Acc. Chem. Res. **25** (3), 143 (1992).
10. M. Takata, B. Umeda, E. Nishibori, *et al.*, Nature **377**, 46 (1995).
11. W. Sato, K. Sueki, K. Kikuchi, *et al.*, Phys. Rev. B **58** (16), 10850 (1998).
12. C. Gu, F. Stepniak, D. M. Poirier, *et al.*, Phys. Rev. B **53** (3), 1196 (1995).
13. J. Chioslovski and E. D. Fleischmann, J. Chem. Phys. **94** (5), 3730 (1991).
14. A. B. Roĭtsin, L. V. Artamonov, and A. A. Klimov, Fiz. Nizk. Temp. **23** (10), 1112 (1997) [Low Temp. Phys. **23**, 835 (1997)].
15. H. Mauser, T. Clark, and A. Hirsch, in *Proceedings of the XII International Winterschool on Electronic Properties of Novel Materials, 1998*, Ed. by H. Kuzmany, p. 202.
16. C. G. Joslin, J. Yang, C. G. Gray, and J. D. Poll, Chem. Phys. Lett. **211** (6), 587 (1993).
17. L. Pang and F. Brisse, J. Phys. Chem. **97** (33), 8562 (1993).
18. Y. S. Li and D. Tomanek, Chem. Phys. Lett. **221** (5), 453 (1994).
19. D. Tomanek and Y. S. Li, Chem. Phys. Lett. **243** (1), 42 (1995).
20. V. A. Levashov, A. A. Remova, and V. R. Belosludov, Pis'ma Zh. Éksp. Teor. Fiz. **65** (8), 647 (1997) [JETP Lett. **65**, 683 (1997)].
21. Y. Marryama, K. Ohno, K. Esfarjani, and Y. Kawazoe, Sci. Rep. Res. Inst. Tohoku Univ., Ser. A **41** (2), 183 (1996).
22. A. H. H. Chang, W. C. Ermler, and R. M. Pitzer, J. Chem. Phys. **94** (7), 5004 (1991).
23. J. Liu and S. Iwata, Phys. Rev. B **50** (8), 5552 (1994).
24. F. De Proft, C. van Alsenoy, and P. Geerlings, J. Phys. Chem. **100** (18), 7440 (1996).
25. S. Parchkovskii and W. Thiel, J. Chem. Phys. **106** (5), 1796 (1997).
26. Y. Wang and D. Tomanek, Chem. Phys. Lett. **208** (1–2), 79 (1993).
27. B. I. Dunlop, J. L. Ballester, and P. P. Schmidt, J. Phys. Chem. **96** (24), 9781 (1992).
28. Y. Maniwa, K. Mizoguchi, K. Kume, *et al.*, Solid State Commun. **80** (12), 609 (1991).
29. R. D. Johnson, C. S. Yannoni, H. C. Dorn, *et al.*, Science **225**, 1235 (1992).
30. R. Tycko, G. Dabbagh, R. M. Fleming, *et al.*, Phys. Rev. Lett. **67** (14), 1886 (1991).
31. P. A. Heiney, J. E. Fischer, A. R. McGhi, *et al.*, Phys. Rev. Lett. **66** (22), 2911 (1991).
32. R. Moret, P. A. Albouy, V. Agafonov, *et al.*, J. Phys. I **2** (5), 511 (1992).
33. W. Andreoni and A. Curioni, Phys. Rev. Lett. **77** (5), 834 (1996).
34. W. Andreoni and A. Curioni, Appl. Phys. A **A66**, 299 (1998).
35. J. L. Ballester and B. I. Dunlop, Phys. Rev. A **45** (10), 7985 (1992).
36. M. W. Schmidt, K. K. Baldridge, and J. A. Boatz, J. Comput. Chem. **14** (6), 1347 (1993).
37. S. A. Varganov, P. V. Avramov, and S. G. Ovchinnikov, Fiz. Tverd. Tela (St. Petersburg) **42** (2), 378 (2000) [Phys. Solid State **42**, 388 (2000)].
38. R. Car and M. Parinello, Phys. Rev. Lett. **55** (22), 2471 (1985).
39. P. E. Bloechl and M. Parinello, Phys. Rev. B **45** (11), 9413 (1992).

Translated by N. Wadhwa